Advances in Experimental Medicine and Biology 701

Joseph C. LaManna
Michelle A. Puchowicz
Kui Xu · David K. Harrison
Duane F. Bruley *Editors*

Oxygen Transport to Tissue XXXII

Springer

Advances in Experimental Medicine and Biology

Volume 701

For other titles published in this series, go to
www.springer.com/series/5584

Joseph C. LaManna • Michelle A. Puchowicz
Kui Xu • David K. Harrison • Duane F. Bruley
Editors

Oxygen Transport to Tissue XXXII

Springer

Editors
Joseph C. LaManna
Department of Physiology and Biophysics
Case Western Reserve University
School of Medicine
10900 Euclid Avenue
Cleveland Ohio 44106
USA
joseph.lamanna@case.edu

Michelle A. Puchowicz
Department of Nutrition
Case Western Reserve University
School of Medicine
Cleveland Ohio 44106
USA
michelle.puchowicz@case.edu

Kui Xu
Department of Neurology
Case Western Reserve University
School of Medicine
Cleveland Ohio 44106
USA
kui.xu@case.edu

David K. Harrison
Institute of Cellular Medicine
Newcastle University
Newcastle upon Tyne
United Kingdom
d.k.harrison@ncl.ac.uk

Duane F. Bruley
Synthesizer, Inc.
2773 Westminster Rd
Ellicott City Maryland 21043
USA
bruley@umbc.edu

ISSN 0065-2598
ISBN 978-1-4419-7755-7 e-ISBN 978-1-4419-7756-4
DOI 10.1007/978-1-4419-7756-4
Springer New York Dordrecht Heidelberg London

Library of Congress Control Number: 2011924351

Printed on acid-free paper

Springer is part of Springer Science+Business Media (www.springer.com)

Editors

Joseph C. LaManna
Department of Physiology and Biophysics
Case Western Reserve University School of Medicine
10900 Euclid Avenue
Cleveland Ohio 44106
USA
joseph.lamanna@case.edu

Michelle A. Puchowicz
Department of Nutrition
Case Western Reserve University School of Medicine
Cleveland Ohio 44106
USA
michelle.puchowicz@case.edu

Kui Xu
Department of Neurology
Case Western Reserve University School of Medicine
Cleveland Ohio 44106
USA
kui.xu@case.edu

David K. Harrison
Institute of Cellular Medicine
Newcastle University
Newcastle upon Tyne
United Kingdom
d.k.harrison@ncl.ac.uk

Duane F. Bruley
Synthesizer, Inc.
2773 Westminster Rd
Ellicott City Maryland 21043
USA
bruley@umbc.edu

Acknowledgments

Sponsors

As President of the 2009 Meeting of the International Society on Oxygen Transport to Tissue, held from July 5–9, 2009 in Cleveland, Ohio, USA, I would like to acknowledge the tremendous support of the following sponsors:

Rockland Technimed Ltd
PIONEERS IN MRI TISSUE VIABILITY IMAGING

Seahorse Bioscience

SHERWIN-WILLIAMS

ISCBFM
International Society for Cerebral Blood Flow & Metabolism

Case Western Reserve University EST. 1826

PERIMED

STARR Life Sciences Corp.

The University of Akron

HYPOXYGEN
Define your environment

Association Book Exhibit

Mr. and Mrs. Lawrence Boron

Special thanks also to Suzanne Foss, ISOTT Meeting Secretariat, and her volunteers: Girriso Benderro, D'Arbra Blankenship, Tim Darlington, Sylvia Hart, Eliza-

beth Hilow, Molly Karl, Elias Kikano, David Litvin, Obinna Ndubuizu, Jon Niemi, Ali Serhal, Xiaoyan Sun, Solomon Raju Bhupanapadu Sunkesula, Kevin Train, and Constantinos Tsipis.

Reviewers

The ISOTT 2009 editors would like to thank the following reviewers:

Scientific Review Panel

Donald G. Buerk (University of Pennsylvania, Philadelphia, USA)
Giuseppe Cicco (University of Bari, Italy)
Chris Cooper (University of Essex, Colchester, UK)
Paula Dore-Duffy (Wayne State University School of Medicine, Detroit, USA)
Andras Eke (Semmelweis University of Medicine, Budapest, Hungary)
Elaine Fisher (University of Akron, USA)
Albert Gjedde (University of Copenhagen, Denmark)
Jerry D. Glickson (University of Pennsylvania, Philadelphia, USA)
David K. Harrison (Newcastle University, Newcastle upon Tyne, UK)
Fahmeed Hyder (Yale University, New Haven, USA)
Kyung A. Kang (University of Louisville, USA)
Periannan Kuppusamy (Ohio State University, Columbus, USA)
Nicola Lai (Case Western Reserve University, Cleveland, USA)
Joseph C. LaManna (Case Western Reserve University, Cleveland, USA)
Arnulf G. Mayer (University of Mainz, Germany)
William Pearce (Loma Linda University School of Medicine, USA)
Michelle A. Puchowicz (Case Western Reserve University, Cleveland, USA)
Sophy Sundarajan (Case Western Reserve University, Cleveland, USA)
Ilias Tachtsidis (University College London, UK)
Eiji Takahashi (Saga University, Japan)
Oliver Thews (University of Mainz, Germany)
Sabine Van Huffel (Katholieke Universiteit Leuven, Belgium)
Peter W. Vaupel (University of Mainz, Germany)
William Welch (Georgetown University, Washington DC, USA)
David F. Wilson (University of Pennsylvania, Philadelphia, USA)
Martin Wolf (University of Zurich, Switzerland)
Christopher B. Wolff (St. Bartholomew's and the Royal London Hospital, London, UK)

Technical Reviewers

Laraine Visser-Isles (Rotterdam, The Netherlands)
Eileen Harrison (Durham, UK)

Organization of ISOTT 2009

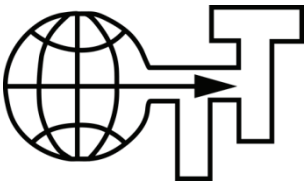

The 37th Annual Meeting of
the International Society on Oxygen Transport to Tissue
July 5–9, 2009, Cleveland, Ohio, USA

The International Society on Oxygen Transport to Tissue is an interdisciplinary society comprising about 250 members worldwide. Its purpose is to further the understanding of all aspects of the processes involved in the transport of oxygen from the air to its ultimate consumption in the cells of the various organs of the body.

The annual meeting brings together scientists, engineers, clinicians and mathematicians in a very unique international forum for the exchange of information and knowledge, the updating of participants on latest developments and techniques, and the discussion of controversial issues within the field of oxygen transport to tissue.

Founded in 1973, the society has been the leading platform for the presentation and discussion of many of the technological and conceptual developments within the field, both at the meetings themselves and in the proceedings of the society. These have been published in the "Advances in Experimental Medicine and Biology" series.

Examples of some of the areas in which members have made highly significant contributions to the field include spectrophotometric and magnetic resonance methods, electrode techniques, mathematical modeling of oxygen transport, and the understanding of local regulation of oxygen supply to tissue and fluorocarbons-blood substitutes.

Local Organizing Committee

Cynthia M. Beall (Cleveland, OH, USA)
Walter Boron (Cleveland, OH, USA)
Marco E. Cabrera[1] (Cleveland, OH, USA)
Jeffrey L. Duerk (Cleveland, OH, USA)
Serpil Erzurum (Cleveland, OH, USA
Elaine Fisher (Akron, OH, USA)
Charles L. Hoppel (Cleveland, OH, USA)
Periannan Kuppusamy (Columbus, OH, USA)
Richard Martin (Cleveland, OH, USA)
Gheorghe Mateescu (Cleveland, OH, USA)
Michelle A. Puchowicz (Cleveland, OH, USA)
Kingman P. Strohl (Cleveland, OH, USA)
Kui Xu (Cleveland, OH, USA)

[1] Deceased

Dedication

The 37th ISOTT Conference President, Joseph C. LaManna, would like to dedicate this volume in memory of **Marco E. Cabrera**, who had attended previous ISOTT meetings and was an integral part of the Local Organizing Committee for the Cleveland meeting before his sudden and untimely death in February, 2009.

Joseph C. LaManna and Marco E. Cabrera at ISOTT 2007, Uppsala, Sweden.

Marco E. Cabrera received his undergraduate degree in physics from the Universidad del Valle de Guatemala in 1978 and his Ph.D. degree in biomedical engineering from Case Western Reserve University in 1995. He achieved the rank of Associate Professor in the Departments of Pediatrics Biomedical Engineering, and Physiology and Biophysics. His research focused on regulation of energy metabolism in cardiac and skeletal muscles in response to exercise and adaptations to physical inactivity and training. It combined dynamic experimental measurements and computational models that encompassed mechanisms at the cellular, tissue, and whole body levels.

Marco believed passionately in a quantitative systems physiology approach for the in vivo study of organisms. His vision was endorsed by NIH funding of the Center for Modeling Integrated Metabolic Systems (MIMS). He was active professionally on the editorial board of the Journal of Biological Chemistry and assistant editor of Exercise and Sports Sciences Reviews as well as a Fellow of the American College of Sports Medicine and a member of the American Physiological Society, Biomedical Engineering Society, and American Society of Biochemistry and Molecular Biology.

Marco was a dear friend, valued research collaborator, and esteemed mentor. His ready smile, enthusiasm, and breadth of vision engaged many friends and collaborators. Marco's research scope encompassed a wide variety of fields including exercise physiology, human and animal performance evaluation, metabolic systems biology, mathematical modeling, and computer simulation. He had an exceptional ability to develop collaborations with theoretical and experimental researchers from different fields that could contribute to quantitative understanding of exercise and metabolism. Marco had a variety of wonderful collaborations locally at Case Western Reserve University, University Hospitals of Cleveland, and the Cleveland Clinic as well as nationally and internationally. To achieve the research goals that Marco set forth, his collaborators and students will continue along the path that he started.

Awards

The Melvin H. Knisely Award

The Melvin H. Knisely Award was established in 1983 to honor Dr. Knisely's accomplishments in the field of the transport of oxygen and other metabolites and anabolites in the human body. Over the years, he has inspired many young investigators and this award is to honor his enthusiasm in assisting and encouraging young scientists and engineers in various disciplines. The award acknowledges outstanding young investigators. This award was first presented during the banquet of the 1983 annual conference of ISOTT in Ruston, Louisiana. The award includes a Melvin H. Knisely plaque and a cash prize.

Melvin H. Knisely Award Recipients:

1983 Antal G. Hudetz, Hungary
1984 Andras Eke, Hungary
1985 Nathan A. Bush, USA
1986 Karlfried Groebe, Germany
1987 Isumi Shibuya, Japan
1988 Kyung A. Kang, Korea/USA
1989 Sanja Batra, Canada
1990 Stephen J. Cringle, Australia
1991 Paul Okunieff, USA
1992 Hans Degens, Netherlands
1993 David A. Benaron, USA
1994 Koen van Rossem, Belgium
1995 Clare E. Elwell, UK
1996 Sergei A. Vinogradov, USA
1997 Chris Cooper, UK
1998 Martin Wolf, Switzerland
1999 Huiping Wu, USA
2000 Valentina Quaresima, Italy
2001 Fahmeed Hyder, Bangladesh
2002 Geofrey De Visscher, Belgium
2003 Mohammad N. Khan, USA
2004 Fredrick Palm, Sweden
2005 Nicholas Lintell, Australia
2006 No award was made
2007 Ilias Tachtsidis UK
2008 Kazuto Masamoto, Japan
2009 Rossana Occhipinti, USA

The Dietrich W. Lübbers Award

The Dietrich W. Lübbers Award was established in honor of Professor Lübbers's long-standing commitment, interest, and contributions to the problems of oxygen transport to tissue and to the society. This award was first presented in 1994 during the annual conference of ISOTT in Istanbul, Turkey.

Dietrich W. Lübbers Award Recipients:

1983 Antal G. Hudetz, Hungary
1984 Andras Eke, Hungary
1985 Nathan A. Bush, USA
1986 Karlfried Groebe, Germany
1987 Isumi Shibuya, Japan
1988 Kyung A. Kang, Korea/USA
1989 Sanja Batra, Canada
1990 Stephen J. Cringle, Australia

1991 Paul Okunieff, USA
1992 Hans Degens, Netherlands
1993 David A. Benaron, USA
1994 Koen van Rossem, Belgium
1995 Clare E. Elwell, UK
1996 Sergei A. Vinogradov, USA
1997 Chris Cooper, UK
1998 Martin Wolf, Switzerland
1999 Huiping Wu, USA
2000 Valentina Quaresima, Italy
2001 Fahmeed Hyder, Bangladesh
2002 Geofrey De Visscher, Belgium
2003 Mohammad N. Khan, USA
2004 Fredrick Palm, Sweden
2005 Nicholas Lintell, Australia
2006 No award was made
2007 Ilias Tachtsidis UK
2008 Kazuto Masamoto, Japan
2009 Rossana Occhipinti, USA

The Britton Chance Award

The Britton Chance Award was established in honor of Professor Chance's long-standing commitment, interest, and contributions to the science and engineering aspects of oxygen transport to tissue and to the society. This award was first presented in 2004 during the annual conference of ISOTT in Bari, Italy.

Britton Chance Award Recipients:

2004 Derek Brown, Switzerland
2005 James Lee, USA
2006 Hanzhu Jin, China/USA
2007 Eric Mellon, USA
2008 Jianting Wang, USA
2009 Jessica Spires, USA

The Duane F. Bruley Award

The Duane F. Bruley Award was established in 2003 and first presented by ISOTT at the 2004 annual conference in Bari, Italy. This award was created to provide travel funds for student researchers in all aspects of areas of oxygen transport to tissue. The awards signify Dr. Bruley's interest in encouraging and supporting young researchers to maintain the image and quality of research associated with the society. As a co-founder of ISOTT in 1973, Dr. Bruley emphasizes cross-disciplinary research among basic scientists, engineers, medical scientists, and clinicians. His pioneering work constructing mathematical models for oxygen and other anabolite/metabolite transport in the microcirculation, employing computer solutions, were the first to consider system nonlinearities, time dependence, including multidimensional diffusion, convection, and reaction kinetics. It is hoped that receiving the Duane F. Bruley Award will inspire students to excel in their research and will assist in securing future leadership for ISOTT.

Duane F. Bruley Award Recipients:

2004 Helga Blocks (Belgium); Jennifer Caddick (UK); Charlotte Ives (UK); Nicholas Lintell (Australia); Leonardo Mottola (Italy); Samin Rezania

(Iran/USA); Ilias Tachtsidis (UK); Liang Tang (China/USA); Iyichi Sonoro (Japan); Antonio Franco (Italy)

2005 Robert Bradley (UK); Harald Oey (Australia); Kathy Hsieh (Australia); Jan Shah (Australia)

2006 Benn S. Gooch (UK); Ulf R. Jensen (Germany); Smruta S. Koppaka (USA); Daya Singh (UK); Martin Tisdall (UK); Bin Wong (China); Kui Xu (China/USA)

2007 Dominique De Smet (Belgium); Thomas Ingram (UK); Nicola Lai (USA); Andrew Pinder (UK); Joke Vanderhaegen (Belgium)

2008 Sebastiano Cicco (Italy)

2009 Lei Gao (UK); Obinna Ndubuizu (USA); Joke Vanderhaegen (Belgium); Jianting Wang (USA)

Preface

The International Society on Oxygen Transport to Tissue (ISOTT) is an interdisciplinary society comprising about 250 members worldwide. Its purpose is to further the understanding of all aspects of the processes involved in the transport of oxygen from the air to its ultimate consumption in the cells of the various organs of the body. Oxygen has played a substantial role in the evolution process of biological systems, including human, as the key molecule for energy production and genetic adaptation to the environment. Considering that the physiological function of oxygen is an extremely diverse and multidisciplinary research area, increased involvement of basic medical scientists, clinicians, and biomedical engineers in ISOTT was encouraged.

The annual meeting brings together scientists, engineers, clinicians and mathematicians in a unique international forum for the exchange of information and knowledge, the updating of participants on latest developments and techniques, and the discussion of controversial issues within the field of oxygen transport to tissue.

Founded in 1973, the society has been the leading platform for the presentation and discussion of many of the technological and conceptual developments within the field, both at the meetings themselves and in the proceedings of the society.

Examples of some of the areas in which members have made highly significant contributions to the field include Near Infrared Spectroscopy (NIRS) and other spectrophotometric and magnetic resonance methods, electrode techniques, mathematical modeling of oxygen transport, and the understanding of local regulation of oxygen supply to tissue and fluorocarbons-blood substitutes.

The 37th Annual ISOTT conference was held in Cleveland, Ohio, USA from July 5–9, 2009. The meeting consisted of one featured presentation by Jay Dean, Ph.D., from the Department of Molecular Pharmacology and Physiology, Hyperbaric Biomedical Research Laboratory at the University of South Florida. His topic was "Oxygen and the World War II Aviator." In addition, there were 21 featured lectures, 12 organized sessions, 56 general oral presentations, and 19 poster presentations. We welcomed 134 total participants comprised of 71 full, 13 social, 34 student, 10 daily, and 6 outside exhibitor registrations.

Our venue was the campus of Case Western Reserve University (CWRU), including the recently built Village at 115 dormitory-style housing facility where most

participants stayed. Participants were provided with many opportunities to interact, both scientifically and socially, during the conference and after hours in an informal atmosphere. Evening activities were structured to take advantage of Cleveland as well as CWRU's proximity to the University Circle cultural institutions. The highlight of the 2009 ISOTT meeting was the Closing Banquet held at the Rock and Roll Hall of Fame and Museum where several of our participants entertained us with their musical talents! Visit the website of http://www.case.edu/isott09/ to view information on the Annual Meeting in Cleveland, Ohio.

Joseph C. LaManna, Ph.D.
President, ISOTT 2009

Contents

Part IV Tumor Biology

Part I
Near Infrared Spectroscopy

Chapter 1

The Western Reserve, Edward Morley, and Oxygen

A Brief Historical Introduction

Joseph C. LaManna, Ph.D.

Abstract Edward Morley was an early member of the faculty of Western Reserve University in Cleveland. He was a very talented experimentalist who collaborated with Michelson of the Case School of Applied Science on the famous "Speed Of Light through the Ether" measurements in the 1880's. In the 1890's, Morley accomplished the difficult feat of providing the atomic weight of Oxygen, demonstrating by three separate quantitative methods and to the third decimal, that the atomic weight of oxygen was 15.879, significantly less than the 16 predicted by the then current "Prout Hypothesis.''

1.1 Introduction

The International Society for Oxygen Transport to Tissue held its annual meeting at Case Western Reserve University in Cleveland, Ohio in July of 2009. Although not chosen specifically for this reason, the site has significance for fields of study that involve Oxygen. This occasion allows us the opportunity to expound on the connection between oxygen and Case Western Reserve University. First, we will discuss the origin of the name of the university which is somewhat unusual. Then, we will summarize some of the contributions of Professor Edward Williams Morley to the science of Oxygen.

Department of Physiology and Biophysics, Case Western Reserve University, Cleveland, OH 44106, USA
e-mail: joseph.lamanna@case.edu

J.C. LaManna et al. (eds.), *Oxygen Transport to Tissue XXXII*, Advances in Experimental Medicine and Biology 701, DOI 10.1007/978-1-4419-7756-4_1,

1.2 The Western Reserve of Connecticut

At the time of the American Revolution there were a number of boundary disputes among the colonies. However, at the conclusion of the war, the new, pre-constitution government under the Articles of Confederation settled these disputes through the Northwest Ordinance of 1787. The original land grant for Connecticut had left the western border of the state undefined, and the state had laid claim to western lands extending into the northwest territory, the so-called "western reserve of Connecticut.'' Part of the 1787 resolution returned land to Pennsylvania that had been claimed by Connecticut and also took Erie from New York and gave it to Pennsylvania as a Great Lakes port for this state which became known as the Erie triangle. The western lands of Connecticut were incorporated into the "Northwest Territory,'' northwest of the Ohio river which was soon reorganized into 5 states including Ohio as the Northeast segment of the Northwest Territory. Moses Cleaveland was hired to survey the territory so that towns could be planned and land plots sold. The enlargement at left from the map of Figure 1 shows the location of the Western Reserve and indicates the location of the city of Cleveland, named for Moses. The first "a'' in "Cleveland'' was lost purportedly due to a misspelling on an early map. Ohio was admitted into the union as a state in 1803, and in 1826 Western Reserve College was established in the town of Hudson, 26 miles south of Cleveland.

1.3 Edward Williams Morley (1838–1923)

Edward Williams Morley was born in Newark, NJ in 1838. He graduated from Williams College in 1860 with an A.B. and completed a Master's there in 1863. His initial plan was to enter the ministry, receiving a divinity degree from Andover Theological Seminary 1864; however, he spent 1864–5 in the Sanitary Commission during the Civil War. After a few years he came to Ohio to serve as a minister in Twinsburg but was soon recruited to a teaching job at Western Reserve College in 1869. In 1882, he moved with the college to Cleveland, where he was also on the faculty of the School of Medicine as Professor of Chemistry and Toxicology [1]. He received an M.D. from Cleveland Medical College in 1877, and a Ph.D. from the University of Wooster in 1878. A number of short biographies are available [2, 3, 4, 5], and an excellent comprehensive monograph has recently appeared [1].

In Hudson, he supplemented his income by taking on the responsibility for maintaining the town clock and set up a telegraph line to Cleveland so he could access official railroad time. He also acted as a scientific consultant to industry and the civil courts. He introduced teaching laboratories for chemistry, and found time to establish a world class research facility, unusual in a small midwestern college setting. He put many custom features into his lab, including running gasoline lines for the lab burners, a system he built himself. He used gasoline because it was cheaper than natural gas. He was able to accomplish his studies despite having a full teaching load at Western Reserve and also commuting by train to the Cleveland Medical College,

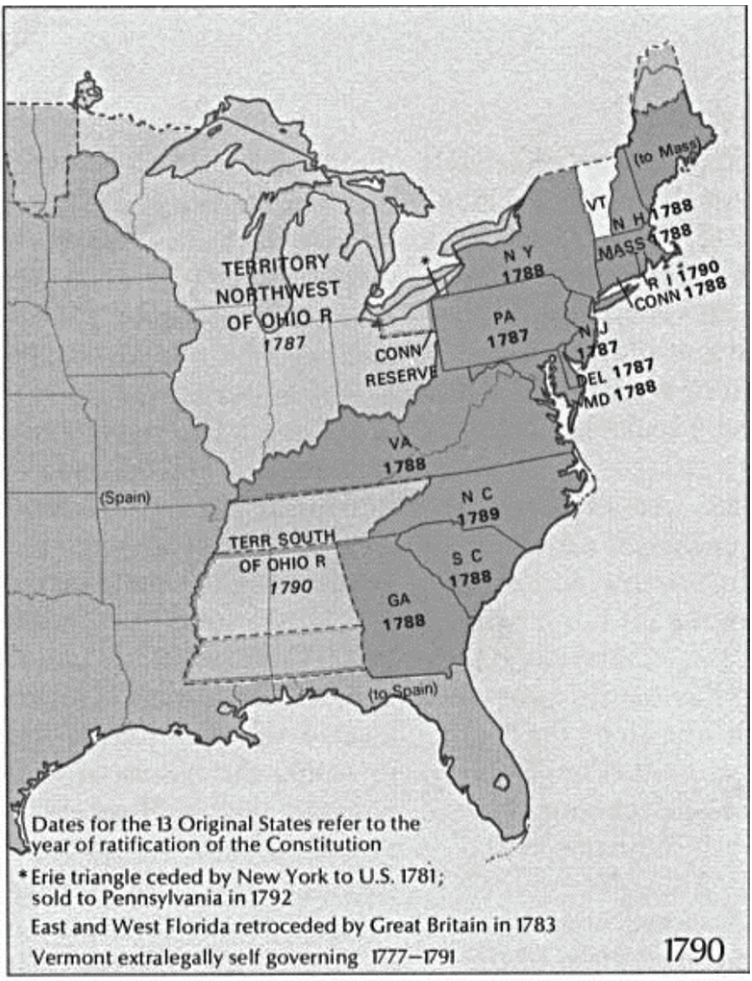

Fig. 1.1 Map of eastern USA showing states and territories as of 1790 (from the University of Texas maps).

Fig. 1.2 Map detail.

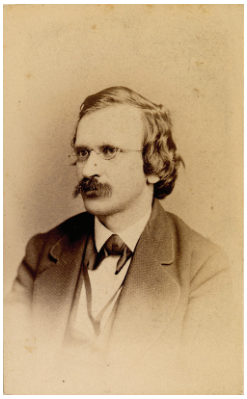

Fig. 1.3 Edward Morley ca. 1868. Property of CWRU Archives.

and his outside consultations. Edward Morley made three major contributions to science, two of them pertinent to Oxygen. His major contributions, in chronological order, were (1) determination of the constancy of the composition of the atmosphere, (2) the ether-drift experiment with Michelson, and (3) determination of the atomic weight of Oxygen.

1.4 The Composition of the Atmosphere (1879–1882)

In the 1800's, the relative contributions of Nitrogen and Oxygen in the air were determined. The composition of the atmosphere, 21% O_2 does not change appreciably with altitude or geography, i.e., there are no regional differences in the proportions of Oxygen and Nitrogen. Although Morley was not the only investigator to contribute to this conclusion, he was perhaps the most precise, designing an apparatus that was accurate to better than 1/400th of 1 percent accuracy (0.003%).

1.5 The Michelson–Morley Collaboration (1884–1887)

In 1882, Albert Michelson accepted the post as the first professor of physics at the Case School of Applied Science which had just been founded in Cleveland by Leonard Case adjacent to the location of Western Reserve College which was in the process of moving from Hudson. Michelson had designed an interferometer and Morley constructed it to exacting specifications, mounted it on a large marble slab, floated it on a pool of Mercury, and tried to detect changes in the interference pattern that would indicate a change in the speed of light if there were ether acting as a medium for light propagation. Finding no differences, they concluded that light

is propagated through a vacuum [6]. Their work became one of the most famous negative experiments in science history, made acceptable primarily because of Morley's reputation as an experimentalist. The level of precision necessary to make the measurement was unavailable without Morley's instrument.

1.6 The Atomic Weight of Oxygen (1884–1895)

Quantitative chemistry needed precise determination of atomic weights. At the time, the leading hypothesis was Prout's, which held that the elemental weights were integer multiples of that of Hydrogen. Morley demonstrated the weight of Oxygen to be 15.879, significantly less than the 16.0 demanded by Prout [7, 5]. The currently accepted weight of Oxygen is given as 15.874, a difference of only 0.005.

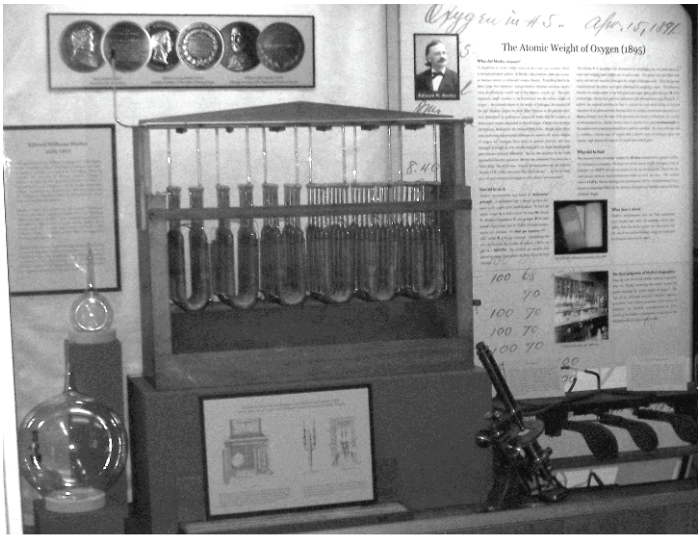

Fig. 1.4 Morley's apparatus for weighing Oxygen.

Morley's data were immediately accepted and praised by the international community for two main reasons: he was known to be an extremely precise and careful experimenter with great skills in building quantitative apparatus, and he used three different experimental methods to come up with the same estimate. In 1896 Morley took a leave of absence and toured Europe to the accolades of his peers.

1.7 The Rest of the Story

Case Institute of Technology (the former Case School of Applied Science) and Western Reserve University agreed to join together in 1965 during difficult financial times, to become the current Case Western Reserve University—CWRU. Morley returned from Europe to find his lab demolished. He never never again performed experimental science, but continued to teach until 1906 when he retired and moved east to West Hartford, Connecticut. He died in 1923, leaving all his scientific materials, notes, books, apparatus, medals, and a $100,000 grant to Williams College. He never received the Nobel Prize although he was in serious contention at least seven times. He received the Davy Medal of the Royal Society in 1907, The Elliot Cresson Medal of the Franklin Institute in 1912, and Willard Gibbs Medal from the American Chemical Society in 1917. He was President of the AAAS in 1895 and the American Chemical Society in 1899, and was elected to the National Academy of Science in 1897. He is one of the most illustrious members of the faculty of Case Western Reserve University. His enthusiasm for science, his hands-on experimental work, his attention to detail, his devotion to his students and his innovative approaches to the difficult questions of the day should still inspire us.

References

1. Hamerla RR (2006) An american scientist on the research frontier. Springer, Dordrecht.
2. Clarke FW (1927) Biographical Memoir Edward Williams Morley 1838–1923. Memoirs of the Narional Academy of Sciences 21:1–7.
3. Anon. (1917) Willard gibbs medal award. Journal of Industrial and Engineering Chemistry 9:615–616.
4. Booth HS (1923) American contemporaries: Edward Williams Morley. Journal of Industrial and Engineering Chemistry 15:194–195.
5. Fickinger W (2006) Physics at a research university: Case Western Reserve 1830-1890. Case Western University, Cleveland.
6. Michelson AA, Morley EW (1887) On the relative motion of the earth and the luminiferous ether. Am J Sci 34(series 3):333–345.
7. Hamerla RR (2003) Edward williams morley and the atomic weight of oxygen: the death of prout's hypothesis revisited. Ann Sci 60:351–372.

Chapter 2
Analysis of the Changes in the Oxidation of Brain Tissue Cytochrome-c-Oxidase in Traumatic Brain Injury Patients during Hypercapnoea
A Broadband NIRS Study

Ilias Tachtsidis, Martin M. Tisdall, Caroline Pritchard, Terence S. Leung, Arnab Ghosh, Clare E. Elwell, and Martin Smith

Abstract Using broadband near-infrared spectroscopy (NIRS) and cerebral microdialysis (MD), we investigated cerebral cellular metabolism and mitochondrial redox states, following hypercapnoea in 6 patients with traumatic brain injury (TBI). In all patients hypercapnoea increased intracranial pressure and cerebral blood flow velocity measured with transcranial Doppler. Despite the likely increase in cerebral oxygen delivery, we did not see an increase in the oxidation status of cytochrome-c-oxidase [oxCCO] in every patient. Analysis of the NIRS data demonstrated two patterns of the changes; Group A ($n = 4$) showed an increase in [oxCCO] of $0.34(\pm 0.34)\mu$M and Group B ($n = 2$) a decrease of $0.40(\pm 0.41)\mu$M. Although no obvious association was seen between the Δ[oxCCO] and the MD, measured changes in lactate and pyruvate concentrations. Further work using model informed data interpretation may be helpful in understanding the multimodal signals acquired in this heterogeneous patient group.

2.1 Introduction

Secondary cerebral damage after traumatic brain injury (TBI) is a multifactorial process with two components being of key importance—reduction in oxygen delivery below critical thresholds and failing cellular metabolism leading to an inability to utilise delivered oxygen and glucose. Global and regional derangements of cerebral oxygen delivery and utilisation often occur after TBI, rendering the brain susceptible

Ilias Tachtsidis, Terence S. Leung, Clare E. Elwell, and Martin Smith
Biomedical Optics Research Laboratory, Department of Medical Physics and Bioengineering, University College London, Gower Street, London WC1E 6BT, UK
e-mail: iliastac@medphys.ucl.ac.uk

Martin M. Tisdall, Caroline Pritchard, Arnab Ghosh, and Martin Smith
Neurocritical Care Unit, The National Hospital for Neurology and Neurosurgery, University College London Hospitals, Queen Square, London, UK

J.C. LaManna et al. (eds.), *Oxygen Transport to Tissue XXXII*, Advances in Experimental Medicine and Biology 701, DOI 10.1007/978-1-4419-7756-4_2,

to secondary injury processes. Modern protocolized TBI management strategies use a variety of modality techniques to monitor the injured brain and guide treatment. In addition within the context of attempting to minimise secondary injury after TBI, it appears vital to ensure adequate O_2 delivery to cerebral mitochondrial [1].

Hypercapnoea causes cerebral vasodilatation and would therefore be expected to increase cerebral oxygen delivery and, in turn, promote cerebral glucose utilization and oxidative metabolism to ensure maintenance of tissue high-energy phosphate reserves [2]. Using broadband near-infrared spectroscopy (BBS), we have recently demonstrated an increase in aerobic metabolism in the healthy human brain following hypercapnoea and hyperoxia [3] and during normobaric hyperoxia (NBH) after TBI [4]. The aim of this study was to investigate whether hypercapnoea also cause changes in cellular and mitochondrial redox state in TBI.

2.2 Methods

This study was approved by the Joint Research Ethics Committee of the National Hospital for Neurology and Neurosurgery and the Institute of Neurology. Since all of the patients were unconscious at the time of the study, written assent was obtained from their personal representatives. Six adult patients (5 male and 1 female) with a mean age of 40 years (range 22–51 years) were recruited into the study. The mean time between injury and study was 106 hours (range 38–298 hours).

Multimodality brain monitoring included intracranial pressure (ICP, Microsensor, Codman), brain tissue O_2 tension (Pbr_2, Licox PMO, Integra Neurosciences) and cerebral microdialysis. Microdialysate glucose, lactate and pyruvate concentrations were measured at the bedside using a CMA 600 analyser (CMA Microdialysis, Slona, Sweden). The mean blood flow velocity in the basal middle cerebral artery (Vmca) was measured using 2MHz transcranial Doppler ultrasonagraphy (Pioneer TC2020, Nicolet) as a surrogate of cerebral blood flow (CBF) [5]. For the purpose of this study the BBS optodes were placed 3.5cm apart in a black plastic holder and fixed to the upper forehead near to the invasive cerebral monitoring. The BBS system has been described elsewhere [6]; briefly, near-infrared spectra between 650 and 980nm were collected at 1Hz with a spectral resolution of 5nm. Absolute changes in concentrations of oxidised minus reduced cytochrome-c-oxidase ([oxCCO]), and oxygenated and deoxygenated haemoglobin concentrations ([HbO_2] and [HHb]) were calculated from changes in light attenuation. Correction factors for the wavelength dependence of the optical pathlength were applied to the chromophore absorption coefficients. The individual optical pathlength was calculated continuously using the second differential analysis of the 740nm water feature of the spectral data [7]. Change in total haemoglobin concentration ([HbT]) was derived from the sum of Δ[HbO_2] and Δ[HHb].

All patients received local protocolised intracranial pressure (ICP) and cerebral perfusion pressure (CPP) directed management based on international consensus guidance. During a period of cardiovascular stability, and whilst the patients were

being mechanically ventilated, the minute ventilation was reduced in a stepwise manner to produce an increase in $PaCO_2$ of approximately 1.5kPa. Cerebral microdialysate (MD) specimens were collected and analysed at intervals of 15–20min and arterial blood gases (ABG) for measurements of arterial carbon dioxide tension (PaCO2) and glucose concentrations were measured at intervals of 15–30min. All monitored variables were recorded on a personal computer and synchronised. Summary data were produced for the two phases of the study: baseline and hypercapnoea. For the continuously measured variables ([HbT], [oxCCO], ICP, and Vmca), a 10min mean and standard deviation for each phase were calculated, centred on the time of the ABG and MD sampling within that phase. Changes in the continuously measured variables between baseline and hypercapnoea were compared using a student's paired t-test (significance at $p < 0.05$). Results are presented as mean $\pm$ standard deviation.

2.3 Results

Group analysis demonstrated a significant mean increase in ICP (8.2 ± 4.2mmHg), Vmca ($25 \pm 18\%$), Δ[HbT] ($4.02 \pm 4.91\mu$M) and Δ[oxCCO] ($0.1 \pm 0.5\mu$M) during hypercapnoea. However, not all patients demonstrated an increase in Δ[oxCCO]; post-hoc analysis demonstrated two patterns of change in Δ[oxCCO] in response to hypercapnoea. Group A had an increase of $0.34 \pm 0.34\mu$M and Group B a decrease of $-0.40 \pm 0.41\mu$M (Figure 1 and Table 1). Figure 2 shows a typical example of the changes recorded from a patient from each group. In Group A $PaCO_2$ was significantly increased from baseline by 1.5 ± 0.8kPa, ICP by 8.9 ± 4.6mmHg, [HbT] by $3.27 \pm 5.73\mu$M, and Vmca by $22 \pm 11.3\%$. In Group B $PaCO_2$ was significantly increased from baseline by 2.1 ± 1.1kPa, ICP by 6.8 ± 4.5mmHg, [HbT] by $5.53 \pm 3.92\mu$M, and Vmca by $31 \pm 34.3\%$.

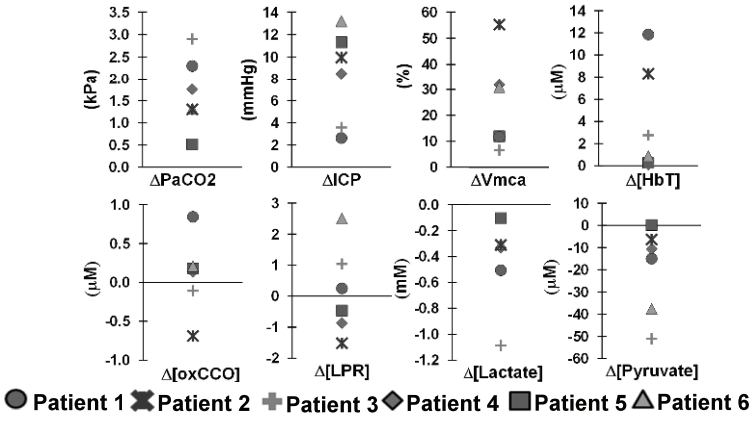

Fig. 2.1 Mean changes from baseline for each TBI patient.

Table 2.1 Summary values for measured variables in Group A (4 patients) and Group B (2 patients) during baseline and hypercapnoea. Data presented as mean ±standard deviation.

	Group A ($n = 4$)		Group B ($n = 2$)	
	Baseline	Hypercapnoea	Baseline	Hypercapnoea
$PaCO_2$ (kPa)	4.6(0.2)	6.1(0.7)	3.9(1.1)	6.0(0.0)
ΔVmca (%)	—	22(11.3)**	—	31(34.3)**
ICP (mmHg)	14.5(4.0)	23.4(7.9)**	7.5(5.5)	14.3(0.9)**
LPR*	23(10.1)	23(10.1)	20(5.5)	20(7.3)
Lactate (mM)	4.9(2.7)	4.6(2.6)	3.4(1.6)	2.7(1.0)
Pyruvate (μM)	209(27.3)	193(41.2)	166(32.5)	137(0.7)
Δ[oxCCO] (μM)	—	0.34(0.34)**	—	−0.40(0.41)**

*LPR is the lactate/pyruvate ratio.
**Student's paired t-test significance $p < 0.05$.

There was no association between the Δ[oxCCO] and the MD changes in lactate and pyruvate at any time. However, during hypercapnoea the mean MD lactate and pyruvate concentrations in Group A lay within reported normal levels and in Group B were at the low end and below reported normal levels, respectively [8].

2.4 Discussion

We have previously demonstrated that an increase in cerebral oxygen delivery secondary to hypercapnoea and hyperoxia results in an increase in aerobic metabolism in the healthy human brain [3]. We have also observed that NBH after TBI resulted in an increase in [oxCCO] consistent with an increase in aerobic metabolism secondary to the induced increase in cerebral oxygen delivery [4]. Hypercapnoea would be expected to increase cerebral oxygen delivery via an increase in CBF. However, despite the increase in Vmca and [HbT] in all patients in this study, only four of the six patients showed an increase in the oxidation status of [oxCCO]. Interestingly, and unlike the situation with NBH, changes in MD measured metabolic variables were not associated with the changes in the oxidation status of [oxCCO].

Unlike the effects of hyperoxia, hypercapnoea has multiple effects on cerebral physiology including CBF, pH, nitric oxide (NO) concentration, and cerebral oxygen consumption (CMRO2), and these might explain the variability of our results [9]. Also, there is wide heterogeneity of pathophysiological changes after TBI, both between and within patients. In the latter, it is also important to note that global and regional changes also evolve with time or in response to treatment [10]. In individual patients, metabolic supply and demand varies substantially; hypermetabolism, therapeutic sedation leading to reduced metabolic requirements or mitochondrial dysfunction may all be present. Due to the large variation between the injury and the time of the study in our patient group, the above variations could have affected our results. Further work is required to determine the relationship between changes in the continuously optically measured metabolic variable [oxCCO] (which demonstrated

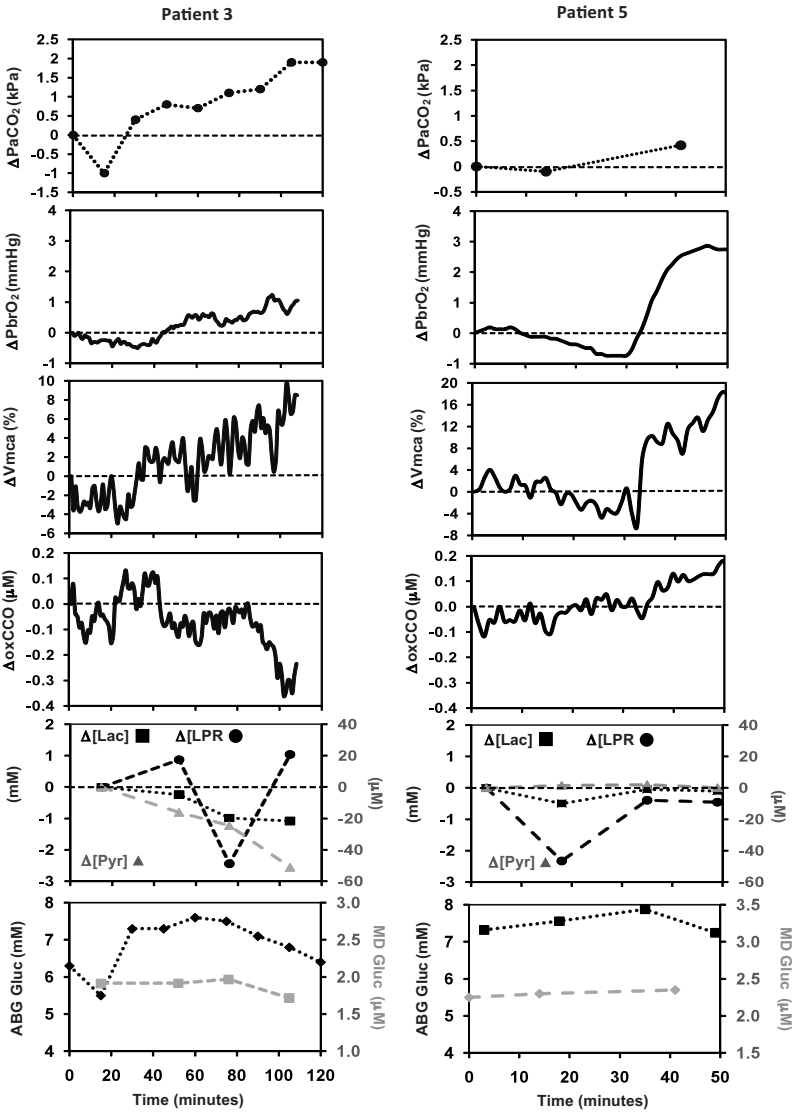

Fig. 2.2 In patient 3 intracerebral lactate and pyruvate concentrations dropped and a significant reduction in oxCCO was also observed. In patient 5 there were no changes in lactate and pyruvate and a significant oxidation in oxCCO was seen. Even though the intracerebral oxygenation levels increased in both patients, as seen by the measured $PbrO_2$, significant differences were observed in the metabolic variables suggesting a possible decrease in aerobic metabolism in patient 3.

two distinct patterns of change in response to increased cerebral oxygen delivery after hypercapnoea), and the noncontinuous MD variables lactate and pyruvate. To investigate this we have recently developed a mathematical model to interpret and

predict cerebral physiological and biochemical variables [11]. It is possible that, through the use of a combination of multimodal data collection and model informed data interpretation, we will be able to increase our understanding of our measurements, characterize pathophysiological changes after TBI and potentially identify monitor-based, individualized treatment strategies.

Acknowledgments

The authors would like to thank the EPSRC (EP/D060982/1) for the financial support of this work. This work was undertaken at University College London Hospitals and partially funded by the Department of Health's National Institute for Health Research Centres funding scheme.

References

1. Bouma GJ, Muizelaar JP, Stringer WA et al. (1992) Ultra-early evaluation of regional cerebral blood flow in severely head-injured patients using xenon-enhanced computerized tomography. J.Neurosurg. 77:360–368.
2. Vannucci RC, Brucklacher RM, Vannucci SJ, (1997) Effect of carbon dioxide on cerebral metabolism during hypoxia-ischemia in the immature rat. Pediatr.Res. 42:24–29.
3. Tachtsidis I, Tisdall MM, Leung TS et al. (2009) Relationship between brain tissue haemodynamics, oxygenation and metabolism in the healthy human adult brain during hyperoxia and hypercapnea. Adv.Exp.Med.Biol. 645:315–320.
4. Tisdall MM, Tachtsidis I, Leung TS et al. (2008) Increase in cerebral aerobic metabolism by normobaric hyperoxia after traumatic brain injury. J.Neurosurg. 109:424–432.
5. Valdueza JM, Balzer JO, Villringer A et al. (1997) Changes in blood flow velocity and diameter of the middle cerebral artery during hyperventilation: assessment with MR and transcranial Doppler sonography. AJNR Am.J.Neuroradiol. 18:1929–1934.
6. Tisdall MM, Tachtsidis I, Leung TS et al. (2007) Near-infrared spectroscopic quantification of changes in the concentration of oxidized cytochrome c oxidase in the healthy human brain during hypoxemia. J.Biomed.Opt. 12:024002.
7. Matcher SJ, Cope MDelpy DT, (1994) Use of the water absorption spectrum to quantify tissue chromophore concentration changes in near-infrared spectroscopy. Phys.Med.Biol. 39:177–196.
8. Schulz MK, Wang LP, Tange M et al. (2000) Cerebral microdialysis monitoring: determination of normal and ischemic cerebral metabolisms in patients with aneurysmal subarachnoid hemorrhage. J.Neurosurg. 93:808–814.
9. Brian JE, Jr., (1998) Carbon dioxide and the cerebral circulation. Anesthesiology 88:1365–1386
10. Vespa P, McArthur DL, Alger J et al. (2004) Regional heterogeneity of post-traumatic brain metabolism as studied by microdialysis, magnetic resonance spectroscopy and positron emission tomography. Brain Pathol. 14:210–214.
11. Banaji M, Mallet A, Elwell CE et al. (2008) A model of brain circulation and metabolism: NIRS signal changes during physiological challenges. PLoS.Comput.Biol. 4:e1000212.

Chapter 3
Effects of Assuming Constant Optical Scattering on Haemoglobin Concentration Measurements Using NIRS during a Valsalva Manoeuvre

Lei Gao, Clare E. Elwell, Matthias Kohl-Bareis, Marcus Gramer, Chris E. Cooper, Terence S. Leung, and Ilias Tachtsidis

Abstract Resolving for changes in concentration of tissue chromophores in the human adult brain with near-infrared spectroscopy has generally been based on the assumption that optical scattering and pathlength remain constant. We have used a novel hybrid optical spectrometer that combines multi-distance frequency and broadband systems to investigate the changes in scattering and pathlength during a Valsalva manoeuvre in 8 adult volunteers. Results show a significant increase in the reduced scattering coefficient of 17% at 790nm and 850nm in 4 volunteers during the peak of the Valsalva. However, these scattering changes do not appear to significantly affect the differential pathlength factor and the tissue haemoglobin concentration measurements.

3.1 Introduction

In near-infrared spectroscopy (NIRS) of biological tissue, the mean optical pathlength depends on the differential pathlength factor (DPF), a parameter that takes into account the increased photon pathlength caused by multiple light scattering in the illuminated tissue. From the diffusion theory, the relationship between the DPF and absorption coefficient (μ_a) and reduced scattering coefficient (μ_s') in an infinite turbid medium has been shown to be [1]:

Lei Gao, Clare E. Elwell, Terence S. Leung, and Ilias Tachtsidis
Biomedical Optics Research Laboratory, Department of Medical Physics and Bioengineering, University College London, Gower Street, London WC1E 6BT
e-mail: iliastacmedphys.ucl.ac.uk

Matthias Kohl-Bareis, and Marcus Gramer
University of Applied Sciences Koblenz, RheinAhrCampus Remagen, Remagen, Germany

Chris E. Cooper
Department of Biological Sciences, University of Essex, Colchester Essex, UK

J.C. LaManna et al. (eds.), *Oxygen Transport to Tissue XXXII*, Advances in Experimental Medicine and Biology 701, DOI 10.1007/978-1-4419-7756-4_3,

$$DPF = \frac{\sqrt{3\mu_s'}}{2\sqrt{\mu_a}} \tag{3.1}$$

In differential continuous-wave NIRS, the assumption is made that changes in concentration are due only to changes in absorption, and that the DPF remains constant, enabling the quantification of chromophore concentration changes from an arbitrary baseline, using the modified Beer-Lambert law [2]:

$$\Delta A = \varepsilon \cdot \Delta C \cdot d \cdot DPF \tag{3.2}$$

where ΔA is change in attenuation, ε is the extinction coefficient, ΔC is the change in chromophore concentration, d is the source-detector spacing.

However, there is experimental evidence to suggest reduced scattering coefficient (μ_s') is altered in animal brains during asphyxia and death [3], as well as in exercising human muscle [4]. The aims of this study were to monitor the μ_s' changes during increases in total cerebral haemoglobin concentration (Δ[HbT]) in adult volunteers during a Valsalva manoeuvre, and to investigate the influence of changes in DPF on the measurement of Δ[HbT].

3.2 Methods

Following ethical approval, 8 adult volunteers (4 females and 4 males) with a mean age of 26 years (range 21–31 years) were studied. To monitor the brain, we used the hybrid optical spectrometer, details of which have been described elsewhere [5]. Briefly, the instrument consists of a multi-distance broadband spectrometer (MDBBS) and a multi-distance frequency domain (110 MHz) spectrometer (MDFD). The MDBBS measures changes in light attenuation across a broadband spectrum (504-1068nm) at optode distances of 2, 2.5, 3 and 3.5cm. The MDFD measures absolute values for μ_a and μ_s' at four discrete wavelengths (690, 750, 790 and 850nm) at 3 and 3.5cm. The optodes from each system were fused together and attached to the left temporal region of the head. Ambient light was minimised with black cloth. All volunteers were seated throughout the experiment. After 2 minutes of baseline measurements, the Valsalva was performed (forced expiration against a closed glottis) for 40s followed by 2 minutes of recovery.

3.3 Analysis

Data were filtered to remove obvious movement artefacts and 6 seconds time-averaging was employed. We calculated a time-variant DPF (calculate DPF for each data point every 6s), and a time-invariant DPF (calculate mean DPF over the first 10 data points from 0-60s) using the MDFD μ_a and μ_s' at 690, 750, 790 and 850nm from

Eq. (2.1). The modified Beer-Lambert law (MBL) (Eq. (2.2)) was used to derive oxyhaemoglobin ($\Delta[HbO_2]$), and deoxyhaemoglobin concentration changes ($\Delta[HHb]$) from the MDBBS multi-wavelength data from the furthest detector (3.5cm) using both the time-variant DPF and the time-invariant DPF for the 790nm. In addition, correction factors for the wavelength dependency of optical pathlength were applied to the chromophore absorption coefficient [6]. Separately, using the MDFD μ_a and assuming a brain tissue water percentage concentration of 70%, we estimated $\Delta[HbO_2]$ and $\Delta[HHb]$. $\Delta[HbT]$ could then be derived from the sum of $\Delta[HbO_2]$ and $\Delta[HHb]$. The peak change in $\Delta[HbT]$ during the Valsalva was used to identify the maximum response in all subjects. Using the 'Student t-test' (significance at $p < 0.05$) within subjects, we compared the differences for μ_s' and time-variant DPF at all four MDFD wavelengths between their value during Valsalva (maximum response) versus baseline (the first 10 data points). For group analysis, we calculated the percentage change in μ_s' and time-variant DPF from baseline to Valsalva.

3.4 Results

Analysis of the $\Delta[HbT]$ mean response for all 8 volunteers as calculated using the time-variant DPF, time-invariant DPF and the MDFD four wavelengths μ_a show no significant differences at Valsalva (see Fig. 1). Analysis of changes in μ_s' for all 8 subjects reveal 4 volunteers with no change (Group A), and 4 volunteers showing a significant increase (Group B) during Valsalva. Figures 2(a) and 3(a) show an example from each group. In Group B, significant increases in μ_s' (up to 30% in one subject) were seen across all four MDFD wavelengths. Table 1.1 and Table 1.2

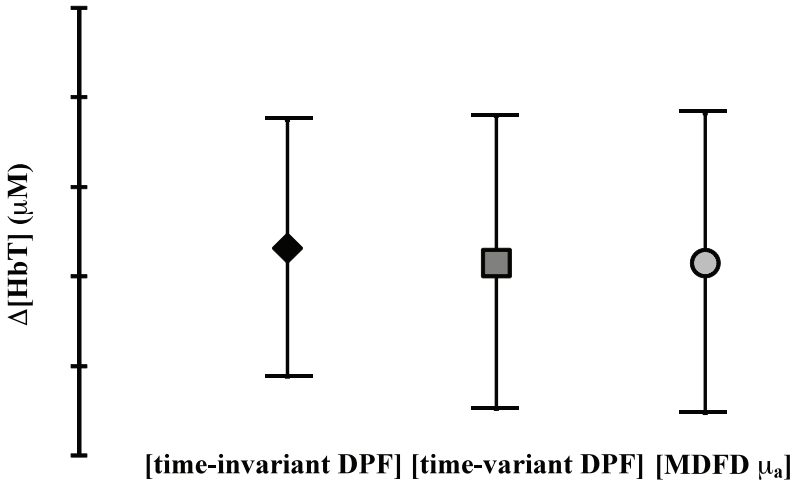

Fig. 3.1 Group $\Delta[HbT]$ mean changes $\pm$SD during Valsalva using the time-invariant DPF, the time-variant DPF and the MDFD four wavelengths μ_a.

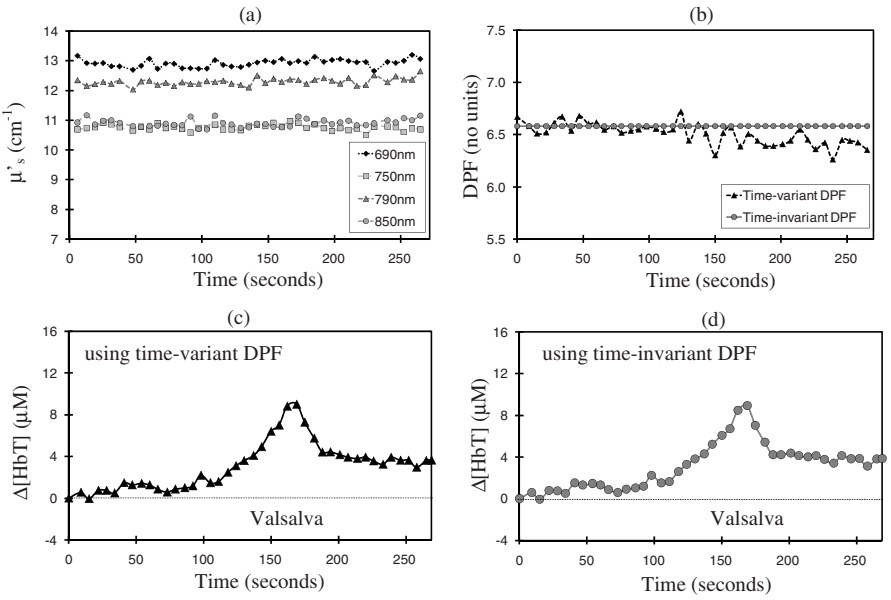

Fig. 3.2 Group A, Subject 4 (a) change in μ_s'; (b) Time-variant DPF versus Time-invariant DPF at 790nm; (c) Δ[HbT] using time-variant DPF; (d) Δ[HbT] using time-invariant DPF .

Table 3.1 Group A, μ_s' and time-variant DPF (mean ±SD) at baseline and Valsalva.

	Group A - μ_s'(cm^{-1})			Group A - DPF (no units)		
λ(nm)	Baseline	Valsalva	change	Baseline	Valsalva	change
690	11.7 ± 3.1	11.9 ± 3.2	+2%	7.6 ± 1.1	7.5 ± 1.3	−1%
750	9.4 ± 2.0	9.4 ± 1.9	0%	6.3 ± 0.8	6.3 ± 0.9	0%
790	10.5 ± 3.1	10.6 ± 3.3	+1%	7.4 ± 1.0	7.2 ± 1.1	−3%
850	9.7 ± 2.4	9.5 ± 2.6	−2%	6.4 ± 0.9	6.4 ± 0.9	0%

Table 3.2 Group B, μ_s' and time-variant DPF (mean ±SD) at baseline and Valsalva.

	Group B - μ_s'(cm^{-1})			Group B – DPF (no units)		
λ(nm)	Baseline	Valsalva	change	Baseline	Valsalva	change
690	10.5 ± 1.1	11.8 ± 1.6	+12%	7.1 ± 0.5	7.2 ± 0.7	+1%
750	9.1 ± 0.8	10.3 ± 1.3	+13%	6.1 ± 0.2	6.0 ± 0.5	-1%
790	9.0 ± 1.2	10.5 ± 1.3	+17%*	6.5 ± 0.6	6.5 ± 0.9	0%
850	9.0 ± 1.0	10.5 ± 1.1	+17%*	6.1 ± 0.2	6.1 ± 0.4	0%

*Student's t-test significance $p < 0.05$.

show the results for μ_s' and time-variant DPF (group mean ±SD) for Group A and B, respectively.

In Group B, μ_s' summary analysis shows a significant mean increase of 17% at 790nm and 850nm; no significant increases were seen in the other wavelengths. In both groups there was no significant change in the time-variant DPF during the

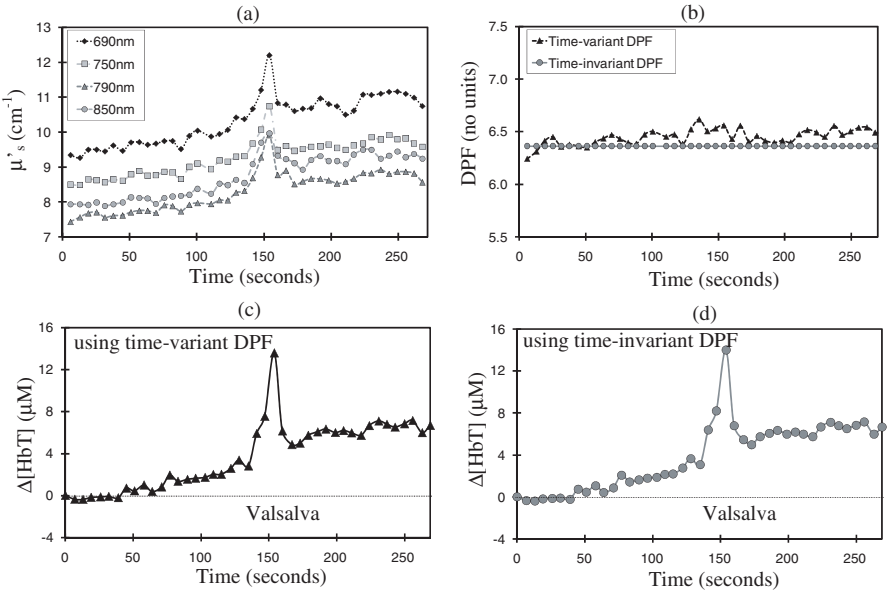

Fig. 3.3 Group B, Subject 1 (a) change in μ'_S; (b) Time-variant DPF versus Time-invariant DPF at 790nm; (c) Δ[HbT] using time-variant DPF; (d) Δ[HbT] using time-invariant DPF .

Valsalva at any of the four wavelengths. Figures 2(b) and 3(b) show an example from each group. Since Δ[HbT] is inversely proportional to DPF (Eq. 1.2) there was no significant effect on measured Δ[HbT], whether a time-variant (see Fig. 2(c) and 3(c)) or a time-invariant DPF was used (see Fig. 2(d) and 3(d)).

3.5 Discussion

Studies with our hybrid optical spectrometer have allowed measurement of optical scattering and absorption on the adult head during a Valsalva manoeuvre. A statistically significant increase in μ'_s that corresponded well to the Valsalva peak was seen in half of the subjects studied.

The general physiological response during the Valsalva is an increase in intra-abdominal and thoracic pressure, resulting in a decrease in venous return which causes pooling of blood within the brain [7]. The increases in measured μ'_s during the Valsalva are unlikely to be due to structural changes in tissue cellular level. However, the effects of changes in blood flow [8] and cerebrospinal fluid volume [9] within the optical field of view are potential explanations. There was no correlation between measured Δ[HbT] and μ'_s change (data not shown) as was also the case in exercising human muscle [3]. Thus, it is unlikely the consistent increase in total haemoglobin is solely responsible for the large μ'_s increases seen in some subjects.

Although μ_s' did show significant changes in some subjects, time-variant DPF remained relatively stable in all subjects during the Valsalva and hence, the effects on measured Δ[HbT] were not significant whether a time-variant or time-invariant DPF was used in the calculation. In addition, no differences were seen in the calculation of Δ[HbT] using the MDFD μ_a and using the MDBBS measurements with either the time-variant or the time-invariant DPF.

Further work is needed to determine the origin of the observed changes in μ_s' to establish whether similar changes may occur in other physiological (e.g., functional activation), or pathophysiological (e.g. sleep apnoea) states. Further algorithm development may be necessary to correct for measured changes in μ_s' in the calculation of changes in NIRS chromophores.

Acknowledgments

The authors would like to thank the EPSRC (EP/D060982/1) and the Department of Health's National Institute for Health Research Centres funding scheme for the financial support of this work.

References

1. Fantini S, Hueber D, Franceschini MA et al (1999) Non-invasive optical monitoring of the newborn piglet brain using continuous-wave and frequency-domain spectroscopy. Phys. Med. Biol. 44:1543-1563.
2. Delpy DT and Cope M (1997) Quantification in tissue near-infrared spectroscopy. Phil. Trans. Roy. Soc. Lond. Series B-Biological Sciences 352(1354):649-659
3. Zhang G, Katz A, Alfano RR et al (2000) Brain perfusion monitoring with frequency-domain and continuous-wave near-infrared spectroscopy: a cross-correlation study in newborn piglets. Phys. Med. Bio. 45:3143-3158.
4. Ferreira L, Hueber D, Barstow TJ et al (2007) Effects of assuming constant optical scattering on measurements of muscle oxygenation by near-infrared spectroscopy during exercise. J. Appl. Physiol. 102:358-367.
5. Tachtsidis I, Kohl-Bareis M, Leung TS et al (2008) A hybrid multi-distance phase and broadband spatially resolved algorithm for resolving absolute concentrations of chromophores in the near-infrared light spectrum: application on to dynamic phantoms. Biomedical Topical Meetings (The Optical Society of America), BSuE76, Florida, USA.
6. Essenpreis M, Elwell CE, Cope M et al (1993) Spectral dependence of temporal point spread functions in human tissues. Applied Optics 32(4):418-425.
7. Matta B, Lam J, Smielewiski P et al (1996) The Effect of the VM on Cerebral Haemodynamics: A Near Infrared Spectroscopy Study. J. Neuro. Anesthes.: 8(4):336.
8. Tomita M, Ohtomo M, Suzuki N et al (2006) Contribution of the flow effect caused by shear-dependent RBC aggregation to NIR spectroscopic signals. NeuroImage 33:1-10.
9. Okada E and Delpy DT (2003) Near-infrared light propagation in an adult head model. I. Modeling of low-level scattering in the cerebrospinal fluid layer. Applied Optics 42(16): 2906-2914.

Chapter 4
Speech Therapy Changes Blood Circulation and Oxygenation in the Brain and Muscle
A Near-Infrared Spectrophotometry Study

Martin Wolf, Dietrich von Bonin, and Ursula Wolf

Abstract Recently it has been shown that artistic speech therapy (AST) has effects on heart rate variability. The aim of this pilot study was to investigate whether AST also affects hemodynamics and tissue oxygenation in the brain and skeletal muscle measured by near infrared spectrophotometry (NIRS). The results show that ATS has effects on important physiological parameters, i.e., it leads to a decrease in cerebral blood flow during recitation and to brain activation thereafter.

4.1 Introduction

Artistic speech therapy (AST) consists of guided speaking exercises by using epic, lyric and dramatic poetry and thereby employs rhythmic speech. AST is applied in various indications such as respiratory, cardiovascular and psychosomatic diseases. It has been shown that recitation of hexameter verses has effects on heart rate variability and leads to a strong cardiorespiratory synchronization, while synchronization during a controlled breathing exercise was less pronounced and during spontaneous breathing minimal [1]. Effects of AST on hemodynamics and tissue oxygenation have not yet been investigated. However, studying physiological parameters may help to improve objectivity in arts therapy research since they have the potential to demonstrate the stimulation of self-regulatory processes or the psycho- physiological balance due to therapeutic interventions.

The aim of this pilot study was to investigate whether ATS also affects hemodynamics and tissue oxygenation in the brain and skeletal muscle measured by near infrared spectrophotometry (NIRS).

Martin Wolf
Clinic of Neonatology, University Hospital Zurich, Switzerland
e-mail: Martin.Wolf@usz.ch

Dietrich von Bonin and Ursula Wolf
Institute for Complementary Medicine KIKOM, University of Bern, Switzerland

J.C. LaManna et al. (eds.), *Oxygen Transport to Tissue XXXII*, Advances in Experimental Medicine and Biology 701, DOI 10.1007/978-1-4419-7756-4_4,

4.2 Methods

Seven subjects (3 male, 4 female, age range 29 to 49 years) were measured while performing an ATS exercise. All subjects included were professional ATS-therapists. The protocol consisted of 10min pre-baseline measurement, 10min reciting a hexameter, followed by 10min post-baseline measurement.

An ISS OxiplexTS NIRS instrument was used which is described in detail in [2]. One sensor was placed on the left forehead, the other on the lateral calf muscle approximately 12cm below the knee cap. Sensors were fixed with elastic bandages. This instrument modulates the intensity of the laserdiodes (692nm and 834nm), employs a multidistance geometry and, consequently, is able to quantify the time the light needs to travel through tissue, the light scattering and absorption coefficients, which enables to non-invasively measure absolute concentration values of the following parameters: oxy- and deoxyhemoglobin (O_2Hb and HHb in μM), total hemoglobin (tHb in μM) and tissue oxygen saturation (StO_2 in %). The multidistance geometry reduces the effect of superficial tissue layers, such as skin and skull (brain) and adipose tissue (muscle).

By a paired t-test the last 5min of pre-baseline were compared to the first and last 5min of the hexameter recitation, and the first and last 5min of the post-baseline. For the significances * indicates $p < 0.05$ and ** $p < 0.01$.

4.3 Results

During the first 4min of the 10min pre-baseline initial changes in the measured parameters were observed. After this period the measurements were stable, i.e., no significant changes between the period of 240s to 420s compared to 420s to 600s in any of the parameters were observed. Thus, all other values were compared to the 5min of the pre-baseline period.

In the brain (Fig. 1) during the first 5min of hexameter reciting, tHb, O_2Hb and StO_2 decreased by (mean $\pm$ standard error of mean (SEM)) $1.01\pm0.36\mu$M*, $1.16\pm0.32\mu$M* and $1.22\pm0.30\%$**, respectively and continued decreasing during the second 5min of recitation (tHb: $1.29\pm0.49\mu$M*; O_2Hb: $1.75\pm0.54\mu$M*; StO_2: $2.29\pm0.67\%$*). HHb did not change significantly during recitation.

In the brain, during the post-baseline period tHb returned to and was not significantly different from the pre-baseline level. However, O_2Hb and StO_2 remained reduced during post-baseline measurement for the first 5min by $1.55\pm0.48\mu$M* and $2.83\pm0.53\%$** and the second 5min by $1.19\pm0.44\mu$M* and $2.77\pm0.55\%$**, while HHb increased by $0.94\pm0.08\mu$M** during the first 5min and $1.08\pm0.15\mu$M** during the second 5min of post-baseline measurement.

In the leg (Fig. 2), the tHb and HHb concentration decreased by (mean $\pm$ SEM) $1.23\pm0.49\mu$M* and $0.76\pm0.25\mu$M*, respectively during the first 5min of hexameter recitation and tHb increased by $0.75\pm0.29\mu$M* during the last 5min of post-baseline measurement. All other parameters did not change significantly.

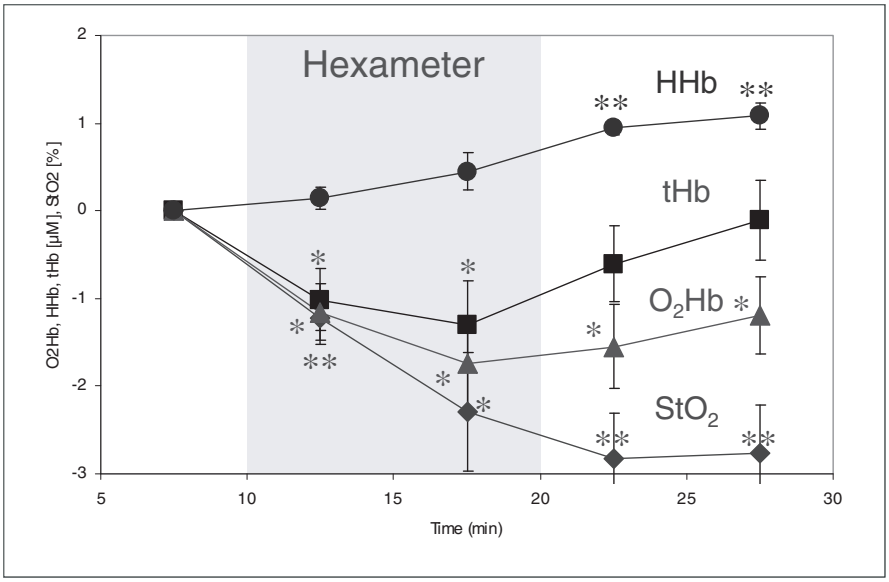

Fig. 4.1 Mean difference compared to baseline (± SEM) in oxy-, deoxy and total haemoglobin concentration (O_2Hb, HHb, tHb) and tissue oxygen saturation (StO_2) in the brain during and after reciting a hexameter. For the significances * indicates $p < 0.05$ and ** $p < 0.01$.

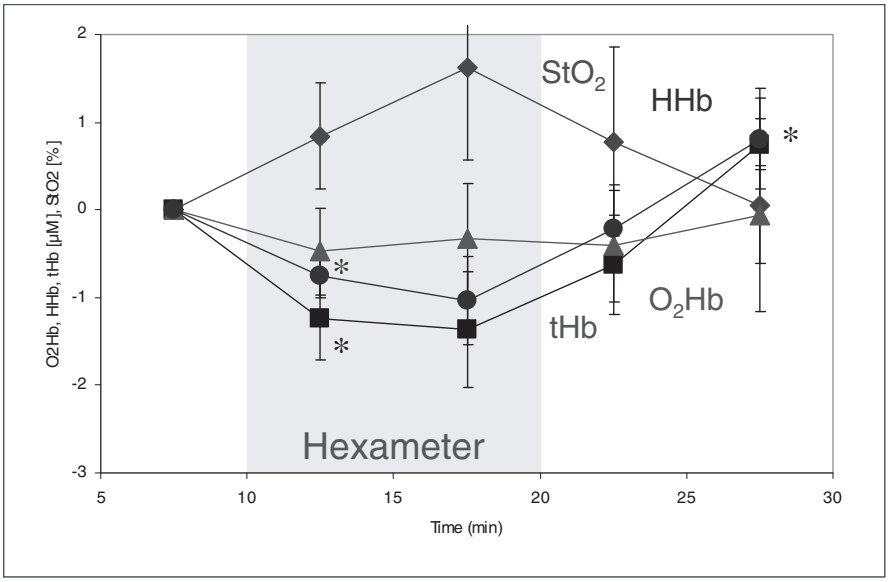

Fig. 4.2 Mean difference compared to baseline (± SEM) in oxy-, deoxy and total haemoglobin concentration (O_2Hb, HHb, tHb) and tissue oxygen saturation (StO_2) in the leg during and after reciting a hexameter. For the significances * indicates $p < 0.05$ and ** $p < 0.01$.

4.4 Discussion

The findings in the brain can be interpreted as a decrease in cerebral blood flow during recitation and a return of cerebral blood flow to baseline levels with increased O_2 consumption after recitation.

During recitation, the reason for the decrease in cerebral blood flow could be a change in partial pressure of carbon dioxide (pCO_2). pCO_2 is affected by breathing. In particular a higher breathing frequency (hyperventilation) can be induced by the rhythmic breathing associated with a hexameter. Hyperventilation leads to a lower pCO_2, which reduces cerebral blood flow and volume (tHb). A reduced blood flow is associated with an increase in HHb concentration and a decrease in O_2Hb concentration and StO_2.

After recitation tHb increased and returned to baseline levels, which also indicates a return to baseline of cerebral blood flow and volume. However, HHb further increased and O_2Hb and StO_2 remained decreased. This finding is unlikely to be associated with a change in pCO_2. It indicates an increase in O_2 consumption due to an activation of the brain. This long-term effect of recitation is an interesting finding because it is different from the effects observed during visual stimulation and motor tasks [3]. The interpretation of this finding is yet unclear. It is however, based on the data of this pilot study, it is too early to draw general conclusions with respect to therapeutic effects of AST.

The findings in the leg muscle are characterized by a significant decrease in tHb and an increase in StO_2 (not significant) during recitation. A lower tHb either indicates a lower blood flow or an increased venous return due to the movement of the leg muscles. Since StO_2 is likely to be increased, we presume that the latter has occurred. The subjects may very well have moved more during recitation than before or after this exercise, even though they were asked to stand completely still. Venous return is naturally maintained while standing still through minor muscle activity. However, this activity increases while moving and so does the venous return. After recitation the StO_2 returned to baseline level, while tHb significantly increased. This finding may be due to an increase in the venous blood volume, while the subjects were standing still again after recitation. The findings could also be interpreted as a lower O_2 consumption during recitation and the opposite after recitation.

4.5 Conclusion

The results show that AST has effects on important physiological parameters, i.e., it leads to a decrease in cerebral blood flow during recitation and to brain activation thereafter. The research is being continued.

Acknowledgments

We gratefully acknowledge the financial support of the Asta Blumfeldt Foundation. We also thank the speech therapists who took part in this study.

References

1. Cysarz D, von Bonin D, Lackner H, et al (2004) Oscillations of heart rate and respiration synchronize during poetry recitation. Am J Physiol Heart Circ Physiol. 287:H579-87
2. Fantini S, Franceschini MA, Maier JS, et al (1995): Frequency-domain multichannel optical detector for noninvasive tissue spectroscopy and oximetry. Optical Engineering 34:32-42.
3. Wolf M, Wolf U, Toronov V, et al (2002) Different time evolution of oxyhemoglobin and deoxyhemoglobin concentration changes in the visual and motor cortices during functional stimulation: a near-infrared spectroscopy study. Neuroimage. 2002 Jul;16(3 Pt 1):704-12.

Part II
Oxygen Sensors and Measurement

Chapter 5
Evaluation of Lithium Naphthalocyanine (LiNc) Microcrystals for Biological EPR Oximetry

Ramasamy P. Pandian, Simi M. Chacko, M. Lakshmi Kuppusamy, Brian K. Rivera, and Periannan Kuppusamy

Abstract A new paramagnetic crystalline material, namely, lithium naphthalocyanine (LiNc), whose electron-paramagnetic-resonance (EPR) line width is highly sensitive to oxygen content, has been evaluated for use as oximetry probe in cells and tissues. Previously, we reported on the synthesis, structural framework, magnetic and oxygen-sensing properties of LiNc microcrystalline powder (*Pandian et al, J. Mater. Chem. 19, 4138, 2009*). The material exhibited a single, sharp EPR line that showed a highly linear response of its width to surrounding molecular oxygen (pO_2) with a sensitivity of 31.2 mG/mmHg. In the present study, we evaluated the suitability of this material for *in vivo* oximetry in biological systems. We observed that the probe was stable in tissues for more than two months without any adverse effect on its oxygen-sensing properties. We further demonstrated that the probe can be prepared in sub-micron sizes for uptake by stem cells. Thus, the high oxygen sensitivity, biocompatibility, and long-term stability in tissues may be useful for high-resolution EPR oximetry.

5.1 Introduction

Abnormal variations in the supply and use of oxygen is closely linked to many major types of pathological abnormalities such as ischemic heart disease, reperfusion injury, oxygen toxicity, peripheral vascular disease, and wound healing [1]. Furthermore, the success of therapeutic regimens such as chemo- or radiotherapy for cancer treatment is highly dependent upon the concentration of oxygen in the targeted tumor tissues. *In vivo* measurement of molecular oxygen is crucial for effective diagnosis and treatment of multiple disease states [2]. Therefore, an accurate and reliable method to determine its concentration in biological systems is highly critical.

Ramasamy P. Pandian, Simi M. Chacko, M. Lakshmi Kuppusamy, Brian K. Rivera and Periannan Kuppusamy
Davis Heart and Lung Research Institute, Department of Internal Medicine, The Ohio State University, Columbus, OH 43210, USA
e-mail: kuppusamy.1@osu.edu

J.C. LaManna et al. (eds.), *Oxygen Transport to Tissue XXXII*, Advances in Experimental Medicine and Biology 701, DOI 10.1007/978-1-4419-7756-4_5,

In recent years, electron paramagnetic resonance (EPR) spectroscopy has been shown to be useful for *in situ* or *in vivo* measurements of oxygen (oximetry) in many biological systems. EPR oximetry can provide real-time, non-invasive and nonperturbing measurements of oxygen. Although EPR oximetry is unique in its potential for high-sensitivity oxygen measurements, the success of EPR oximetry relies heavily on the nature of the oxygen-sensing paramagnetic probe. The challenge is to develop favorable oximetry spin probes that are highly oxygen-sensitive, biocompatible, and capable of providing repetitive measurements noninvasively. Biomedical EPR oximetry has been limited by the difficulties associated with developing suitable probes that are capable of providing high resolution oxygen data over a wide range of oxygen concentrations. We have thus far made several variants of promising lithium phthalocyanine-based synthetic molecules for possible use as a suitable oximetry probe in a variety of biological applications [3-6]. However, a highly-sensitive oxygen-sensing probe for use in EPR oximetry has not yet been identified in phthalocyanine-based crystalline materials. We have previously reported upon lithium naphthalocyanine-based materials as an aggregate combination of Li_2Nc and LiNc. This combination showed marked advantages over other EPR probes, especially with respect to sensitivity and linear response to pO_2 over a wide range of concentrations. However, the oxygen-sensing properties of the aggregate revealed limited stability and responsiveness in biological tissues [7]. Recently, we reported on the synthesis, structural framework, magnetic and oxygen-sensing properties of a pure form of LiNc microcrystalline powder [8]. The material exhibited a single, sharp EPR line that showed a highly linear response of its width to surrounding molecular oxygen (pO_2). In the present study, we evaluated the suitability of this material for *in vivo* oximetry in biological systems.

5.2 Materials and Methods

Lithium naphthalocyanine (LiNc) was synthesized as reported [8]. Cryopreserved, primary rat mesenchymal stem cells (MSCs), isolated from the bone marrow of adult Fisher-344 rats, were procured from Chemicon (Billerica, MA). The cells were characterized by the supplier to be positive for CD29 (integrin β_1) and CD54. The primary cells were thawed and cultured using Dulbecco's Modified Eagle Medium (DMEM + GlutaMAX-1; low glucose, 1x) containing 10% heat-inactivated FBS and penicillin/streptomycin (GIBCO). Accutase (Chemicon), a cell-detachment solution containing proteolytic and collagenolytic enzymes, was used for separation of adherent cells upon passage. MSCs of passage three were used for all experiments. The cells were grown at 37˚C in a humidified environment at 5% CO_2 in air.

5.2.1 Preparation of particulates for cell culture studies

Microcrystalline particulates of LiNc were suspended in culture medium (10 mg/0.5 ml) and sonicated at 22.5 kHz using a horn with a tip diameter of 3 mm (Sonic Dismembrator model 100, Fisher Scientific). The ultrasound power was set to a

value of 3 (out of a possible value of 9) on the generator for a total of 10 times with 1 min gap for cooling. At the end of sonication, the suspension was placed on ice for 2 min to allow the heavier particulates to settle to the bottom of the tube. The solution contained fine particulates of LiNc with a mean particulate size of ∼300 nm. All preparations were carried out under sterile conditions.

5.2.2 Z-stack localization studies of nanocrystalline LiNc in cells

MSCs at passage 3 were cultured on sterile cover slips in six-well plates at a seed density of 3×10^4cells/dish in the presence of 100 μg/ml of LiNc nanocrystalline probes for 48 h. The cells attached to cover slips were washed twice with PBS. Following the removal of excess LiNc probe, the cells were permeabilized and fixed with 0.25% Triton X-100 and 4% paraformaldehyde for 10 min at room temperature and blocked for 30 min with 1% BSA in 0.01% TBS-Tween. The cells were stained with 5 μM DiI (Invitrogen/Molecular Probes) to identify the membrane and 10 μM Draq5 (Alexis) to identify the nucleus. The cover slips with cells were then fixed to a glass slide with mounting medium (Gel Mount Aqueous mounting medium) and viewed using a confocal fluorescence microscope (LSM 510; Zeiss, Thornwood, NY). Images were overlaid using LSM Image Browser software to generate a merged image for each specimen. Z-stacks were created by obtaining images at 0.32-μm intervals.

5.2.3 Preparation of mice

Female C3H mice were obtained from the Frederick Cancer Research Center Animal Production Facility (Frederick, MD). The animals were housed five per cage in a climate- and light-controlled room. Food and water were allowed *ad libitum*. The animals were 50-days old and weighed about 25 g at the time of the experiment. The mice were anesthetized with ketamine (200 mg/kg b.w.) and xylazine (4 mg/kg b.w.) by intraperitoneal injection during the time of EPR measurements. A thermistor rectal probe was used to monitor body temperature. The body temperature was maintained at 37±1°C using an infrared lamp. All animals were used according to the Public Health Services Policy, the Federal Welfare Act, and ILACUC procedures and guidelines.

5.2.4 pO_2 measurements in gastrocnemius muscle tissue of mice

About 20 μg of LiNc microcrystalline powder was implanted in the gastrocnemius muscle of the right leg of C3H mice (n = 6). The EPR spectrum of the particulate in the leg was recorded periodically up to 60 days after the implantation of particulate. In order to verify the response of the particulate to oxygen, blood flow to the leg was constricted by gently tying down the upper leg for 10 min with an elastic band and the EPR measurement was repeated. The EPR measurements were carried

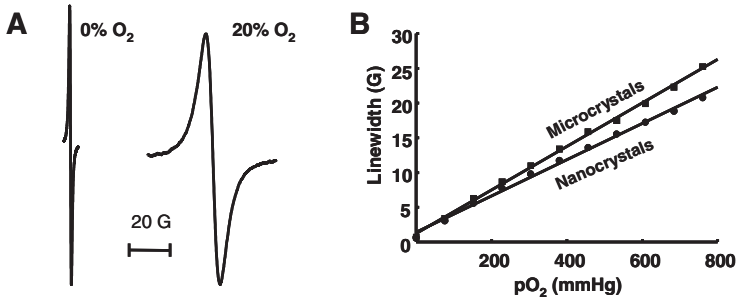

(a) (b)

Fig. 5.1 Oxygen sensitivity of LiNc crystals. (A) EPR spectra of LiNc microcrystals under anoxic (0% O_2) and 20% O_2 environments. The spectra were acquired using an X-band (9.78 GHz) EPR spectrometer at room temperature. (B) Effect of molecular oxygen on the EPR linewidth of LiNc micro- and nanocrystals. A linear variation of line width with the pO_2 is observed. The probe sensitivity (as measured by the slope) is 31.2 mG/mmHg for the microcrystals and 27.2 mG/mmHg for the nanocrystals.

out on anesthetized mice using an L-band (1.32 GHz) spectrometer (Magnettech, Germany) equipped with automatic coupling and tuning controls for tissue oxygen measurements. The animal was oriented on the bedplate so that the observation spot was centered at the slot. The animal was secured to the bedplate with adhesive tape and placed under the resonator such that the normal muscle was in direct contact with the active surface of the resonator. The value of pO_2 in tissue was obtained from a standard curve of the EPR line width versus the oxygen concentration.

5.3 Results

5.3.1 Oxygen-sensitivity of LiNc probes

The effect of molecular oxygen on the EPR line shape of LiNc micro- and nanocrystals is shown in Figure 1. The peak-to-peak line width was dependent on pO_2. The line width increased linearly with pO_2 over the entire 0-760 mmHg range. The slope of the line width *versus* pO_2 calibration curve, which reflects the sensitivity of the probe to oxygen concentration, was higher for raw microcrystals (31.2 mG/mmHg) than that of sonicated nanocrystals (27.2 mG/mmHg). However, in both cases the calibration was linear through 760 mmHg of oxygen.

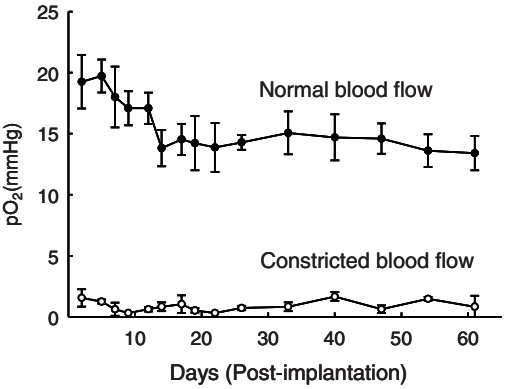

Fig. 5.2 Long-term stability and response to oxygen, in vivo. The stability of LiNc microcrystals implanted in the gastrocnemius muscle (upper hind leg) of C3H mice was evaluated for 60 days. The plot shows repeated measurements of pO_2 from mice ($n = 6$). The response of particulates to oxygen was checked by temporarily constricting blood flow to the leg. The data show that the particulates are stable and responsive in live tissues for 2 months.

5.3.2 Evaluation of LiNc for in vivo oximetry

In order to evaluate the long-term stability of this new probe in biological tissues, we implanted the particulates in the gastrocnemius muscle tissue of mice and performed repeated measurements of pO_2 in the same animals over a period of time. Sharpening of the EPR line width during interruption of blood flow to the leg was used as an indication of reduced tissue oxygenation and responsiveness of the particulate to change in tissue pO_2. The pO_2 of the tissue under normal blood flow conditions was 15.55 ± 1.59 mmHg, whereas that of constricted tissue was 0.87 ± 0.34 mmHg during the 60-day period (Figure 2). The non-zero pO_2 values in the flow-constricted tissue suggest that the constrictions were not totally effective. This was due to our efforts to make the measurements for at least 2 months. Because of this, we took great care to avoid causing injury to the animal during the period of constriction.

Mice were periodically euthanized through the 60-day study period and tissue pO_2 values were assessed to verify the registration of anoxic pO_2 in the dead animal. The pO_2 values in these tissues were close to zero. We also observed that the oxygen sensitivity of the recovered particulates from these tissues was not changed and were similar to that of the original, unimplanted particulates. The LiNc probes were stable in tissues for longer times than the previously reported aggregate of LiNc and Li_2Nc [7]. The high sensitivity (31.2 mG/mmHg) of the newly-developed LiNc could be useful, especially in oximetry applications requiring a higher resolution in hypoxic cells and tissues, where it is difficult to obtain good resolution using other probes.

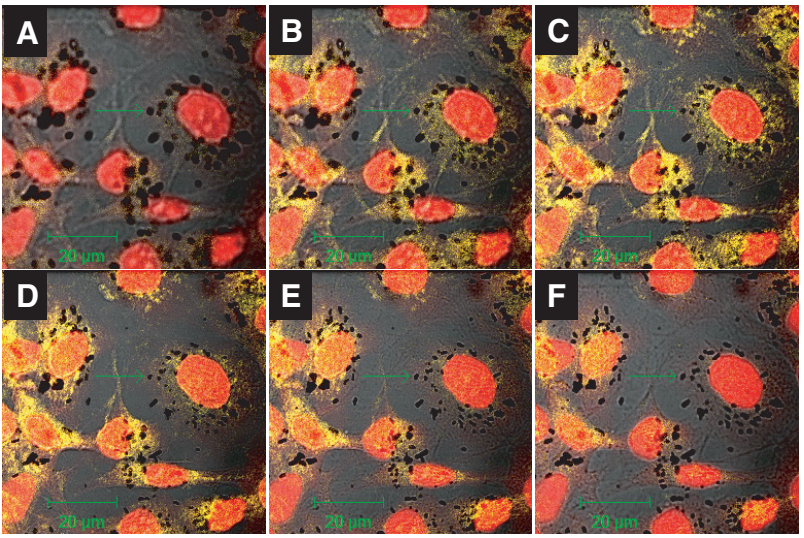

Fig. 5.3 Representative Z-stack confocal images of LiNc nanocrystal localization in MSCs. A–F: Confocal Z-stack images. The cell membrane was stained using DiI (yellow), and the nucleus was labeled with Draq5 (red). Arrows point to the dark crystalline LiNc localized around the nuclear membrane inside the cytoplasm.

5.3.3 Endocytosis of LiNc by MSCs

Incubation of MSCs (at 70% confluence) with LiNc nanocrystals resulted in substantial endocytosis of the probe by the cells. After incubation, the extracellular LiNc nanoparticles were removed by repeated washings. The cells showed an intense EPR spectrum that was highly sensitive to oxygen concentration in the medium, confirming the presence of intracellular LiNc nanocrystals. Previously, we have reported the uptake of LiNc-BuO probes for different cell lines, including smooth muscle cells, ovarian cancer cells, and skeletal myoblasts [6,9,10]. We observed for the first time that the highly oxygen-sensitive LiNc spin probe could likewise be easily internalized by endocytosis in MSCs. Confocal microscopy analysis showed the presence of the LiNc nanocrystals localized around the perinuclear membrane of MSCs (Figure 3). The unique stability and paramagnetic property of nanoparticulate LiNc crystalline probes internalized within MSCs could be used to visualize cell proliferation, migration, and trafficking in specific tissues using EPR spectroscopy.

5.4 Discussion

The LiNc oximetry probe, which we have demonstrated in the present work, has many advantages when compared to other particulate probes reported previously [7]. The most important advantage with this probe is the non-saturation of EPR spectra at typical incident microwave powers used during measurements of biological samples.

Since the EPR line is non-saturable, the signal-to-noise ratio can be substantially improved by increasing the microwave power levels. This is very desirable and indeed much needed, particularly for *in vivo* measurement of pO_2 in live animals, where animal movement or breathing can cause disturbances during measurement at low microwave power settings. Another advantage is that the probe has high sensitivity to oxygen concentration (31.2 mG/mmHg). This means that any small change in pO_2 can be measured with reasonable resolution. This sensitivity is approximately 4-5-fold higher than that of LiPc and LiNc-BuO crystals [3-6].

5.4.1 Conclusions

The LiNc microcrystals exhibit stability in tissues for more than two months and possibly longer. Thus, the LiNc probe may enable accurate and reliable measurements of pO_2 in a wide range of applications, including determination of hypoxic tissue oxygenation in myocardial infarction and tumor therapy.

Acknowledgments

We acknowledge the financial support from the NIH grant EB 004031. The authors thank Dr. S. Varadharaj for her help in the confocal microscopy studies.

References

1. Kulkarni AC, Kuppusamy P, Parinandi NL (2007) Oxygen, the lead actor in the pathophysiologic drama: enactment of the trinity of normoxia, hypoxia, and hyperoxia in disease and therapy. Antiox Redox Signal 9:1717-1730.
2. Tatum JL, Kelloff GJ, Gillies RJ et al (2006) Hypoxia: importance in tumor biology, noninvasive measurement by imaging, and value of its measurement in the management of cancer therapy. Int J Radiat Biol 82:699-757.
3. Ilangovan G, Zweier JL, Kuppusamy P (2000) Electrochemical preparation and EPR studies of lithium phthalocyanine: Evaluation of the nucleation and growth mechanism and evidence for potential-dependent phase formation. J Phys Chem B 104:4047-4059.
4. Pandian RP, Dolgos M, Dang V et al (2007) Structure and oxygen-sensing paramagnetic properties of a new lithium 1,8,15,22-tetraphenoxyphthalocyanine radical probe for biological oximetry. Chem Mater 19:3545-3552.
5. Pandian RP, Kim Y, Woodward PM et al (2006) The open molecular framework of paramagnetic lithium octabutoxy-naphthalocyanine: implications for the detection of oxygen and nitric oxide using EPR spectroscopy. J Mater Chem 16:3609-3618.
6. Pandian RP, Parinandi NL, Ilangovan G et al (2003) Novel particulate spin probe for targeted determination of oxygen in cells and tissues. Free Radic Biol Med 35:1138-1148.
7. Ilangovan G, Manivannan A, Li H et al (2002) A naphthalocyanine-based epr probe for localized measurements of tissue oxygenation. Free Rad Biol Med 32:139-147.
8. Pandian RP, Dolgos M, Marginean C et al (2009) Molecular packing and magnetic properties of lithium naphthalocyanine crystal: hollow channels enabling permeability and paramagnetic sensitivity to molecular oxygen J Mater Chem 19:4138-4147.
9. Bratasz A, Pandian RP, Deng Y et al (2007) In vivo imaging of changes in tumor oxygenation during growth and after treatment. Magn Reson Med 57:950-959.

10. Wisel S, Chacko SM, Kuppusamy ML et al (2007) Labeling of skeletal myoblasts with a novel oxygen-sensing spin probe for noninvasive monitoring of in situ oxygenation and cell therapy in heart. Am J Physiol Heart Circ Physiol 292:H1254-1261.

Chapter 6
Challenges to Intestinal pO_2 Measurement Using EPR

Elaine Fisher, Mahmood Khan, Richard Steiner, and Periannan Kuppusamy

Abstract Acute and chronic intestinal ischemia has been linked to the development of gastrointestinal symptoms such as abdominal pain, nausea and vomiting, bowel dysfunction and more seriously, the complications of sepsis, shock and death. Advances in electron paramagnetic resonance (EPR) oximetry have resulted in accurate and reliable in vivo measurement of the partial pressure of oxygen (pO_2) in solid organs (e.g., muscle, heart) [1], but has yet to be tested in thin walled organs such as intestine. Our ultimate goal is to noninvasively monitor intestinal pO_2 during acute and chronic intestinal ischemia in a rat model. A series of experiments to deliver oxygen-sensitive indicator probes to the small/large intestine by intravenous, luminal and wall injection, as well as direct placement of a solid probe against the outer intestinal wall were attempted. Only the LiNc:BuO:PDMS chip sutured to the peritoneal wall and in direct contact with the intestine allowed for noninvasive pO_2 measurement by EPR. However, the validity of site-specific intestinal pO_2 measurement could not be confirmed and the obtained pO_2 value likely reflected peritoneal cavity oxygenation. Developing methods for probe placement on or inside the intestinal wall are needed for noninvasive, site-specific intestinal pO_2 measurement by EPR to track changes during acute and chronic intestinal ischemia.

6.1 Introduction

Oxygen plays a fundamental role in the pathophysiology of disease [2]. The gut is susceptible to reductions in whole body oxygen as blood flow is shunted from this

Elaine Fisher and Richard Steiner
The University of Akron, College of Nursing & Dept. of Statistics, Akron, OH 44325
e-mail: efisher@uakron.edu

Mahmood Khan and Periannan Kuppusamy
Center for Biomedical EPR Spectroscopy and Imaging, Davis Heart and Lung Research Institute, The Ohio State University, Columbus, OH 43210

J.C. LaManna et al. (eds.), *Oxygen Transport to Tissue XXXII*, Advances in Experimental Medicine and Biology 701, DOI 10.1007/978-1-4419-7756-4_6,

nonvital organ to meet the oxygen demand of vital organs, i.e., the brain, heart, and lungs. Local reductions in blood flow similarly trigger a cascade of responses leading to alterations in intestinal permeability and function [5, 7]. Oxygen deficits in the gut often go undetected until late stage and crisis occurs. Tracking intestinal oxygenation and prompt intervention may be key to preventing or limiting intestinal symptoms and dysfunction.

Electron paramagnetic resonance spectroscopy (EPR) directly detects the pO_2 via oxygen-sensing probes. Three probes for intestinal pO_2 measurement were selected. Given the thin wall of the small intestine, a trityl probe, administered intravenously into the internal jugular vein was chosen to distribute oxygen-sensing probes via the bloodstream to the intestine. We also chose to use the nontoxic, particulate oxygen-sensing probe lithium octa-n-butoxynaphthalocyanine (LiNc-BuO) which has been extensively studied in animal models [1, 6]. LiNc-BuO has several advantages over other particulate probes namely, it has a very high spin density (7.2×10^{20} spins/g), produces a single, sharp EPR absorption peak characterized by a 100% Lorentzian shape, and demonstrates long-term stability maintaining its line shape and oxygen sensitivity for 6 months or more in vivo. The final selected probe was composed of LiNc BuO microcrystals embedded in the oxygen permeable material polydimethyl siloxane (PDMS) by cast-molding and polymerization and referred to by Kuppusamy et al. as the LiNc-BuO:PDMS chip [3]. In vivo the LiNc-BuO:PDMS chip produced reliable, reproducible measures of rat muscle pO_2 under hypoxic and ischemic conditions [4]. These three probes were selected for our experiments based on their success in producing accurate and reliable measures of pO_2 when tested in animal models of ischemia. The experiments reported in this manuscript focus on the method of probe placement and the ability to noninvasively measure pO_2 by EPR post-surgical placement in a rat model of intestinal ischemia.

6.2 Methods

6.2.1 Animal Preparation

The animals used in each experiment were humanely treated and the experiments were conducted in accordance with the guiding Principles for the Care and Use of Laboratory Animals and IACUC approved protocol. (The Ohio State University, Columbus, OH). For survival surgeries sterile conditions were maintained. All rats were anesthetized by intraperitoneal injection (IP) of ketamine (200 mg/kg) and xylazine (4 mg/kg). Anesthesia was maintained using 0.5 - 1% isoflurane via nose cone and supplemented with ketamine/xylazine IP as needed. The internal jugular vein was cannulated to allow access for the IV administration of the trityl probe. A 10-cm midline abdominal incision was made to expose the intestine. The superior mesenteric artery (SMA) was isolated and a vascular occluder or suture was placed around the vessel to achieve varying degrees of occlusion as dictated by the experimental

protocol. Temperature was maintained at 37°C ± 1°C using an infrared heat lamp. At the end of protocols involving acute ischemia, rats were euthanized by inducing a state of deep anesthesia with 4% isoflurane and the diaphragm and heart punctured. For survival experiments involving chronic intestinal ischemia, the abdomen was sutured closed in two layers. Post-operatively temperature was maintained using a warming lamp. Once recovered, a one-time dose of buprenex (0.6 mL; 0.015 mg/mL) was administered subcutaneously and rats were returned to the animal care facility.

Two models of intestinal ischemia, an *acute model of ischemia* and a *chronic model of ischemia*, were used to evaluate changes in intestinal oxygenation. For the *acute ischemic model*, the superior mesenteric artery (SMA) was isolated and a vascular occluder (Fine Science Tools, Foster, CA) was positioned around the artery at its origin off the abdominal aorta. The vascular occluder balloon was maximally inflated and the intestine was assessed for color change (pink → pale) to ensure correct placement. Blood flow was evaluated using the Transonic Flowprobe (T 206 - Transonic Systems Inc., Ithica, NY) at baseline, 100% SMA occlusion, and during reperfusion.

We developed a *model of chronic intestinal ischemia* by banding the SMA to create varying degrees of flow restriction. The SMA was isolated and a 5-0 silk suture was placed loosely around the artery. A blunt tipped 25- or 29-gauge needle was placed parallel to the artery and beneath the suture. The suture was securely tied around the needle and the needle was removed. Blood flow was measured post-banding.

6.2.2 Probe Placement and EPR Measurement

LiNc-BuO microcrystals were sonicated to 1-10 micron size and suspended in solution. For luminal placement, LiNc-BuO (0.1 mL) was injected via a 29-gauge needle through the small intestinal wall into the lumen approximately 2.5 cm above the cecum.

For intestinal wall probe placement, a 29-gauge needle was positioned parallel to the intestine and the needle gently threaded between the intestinal wall to create a track prior to injecting 0.1 mL of LiNc-BuO. The needle exit site was gently massaged to seal the track to prevent oxygen sensing outside the wall.

Finally, a 1 mm × 2 mm piece of LiNc-BuO:PDMS chip was sutured to the inner peritoneal muscle wall. When the abdomen was closed, the chip was in direct contact with the outer wall of the intestine. A permanent marker was used to mark the probe location on the external skin for subsequent pO_2 measurement.

For experiments using LiNc-BuO, calibration was performed prior to probe insertion using X-band (9.8 GHz) and L-band (1.2 GHz) spectroscopy. Spectra obtained from the different gas mixtures (0-40%) were recorded. The peak-to-peak linewidth was measured and a calibration curve of linewidth versus pO_2 was constructed. Linearity of the calibration curve was assessed and the sensitivity determined from the slope.

For in vivo experiments, EPR pO_2 measurement was obtained using L-band (1.2 GHz) at baseline, SMA occlusion, and reperfusion for the acute model and at 3-days and weekly for rats in the chronic ischemia group. The intestinal pO_2 was also measured 5-minutes after the animal was deceased for an anoxic tissue value. The pO_2 was calculated as (tissue mG – anoxic tissue mG)/sensitivity.

6.2.3 Statistical Methods

Preliminary data analysis included the identification of measures of central tendency, plotting of residuals to detect nonlinear patterns, determining whether statistical assumptions were met, and individual plotting of variables according to time for the purpose of identifying trends. Variability of the data led to statistical comparison using percent of baseline values in milligause (mG) rather than actual milligause values. The level of significance was defined as $p \leq 0.05$.

6.3 Results

Baseline SMA blood flow was 8.8 mL/minute, 0.55 mL/minute during 100% SMA occlusion, and 13 mL/minute at 1-minute reperfusion, with a return to baseline by 3-minutes ($n = 2$). Average baseline flow was 21.7 mL/min./kg. A 60-70% reduction in blood flow from baseline resulted when SMA banding was done using a 25-gauge needle. This level of obstruction produced a significant change in intestinal pO_2 (9.4, 4.4, 2.4 mm Hg; baseline, 100% occlusion, dead respectively) and survival rates greater than 1-week. SMA banding using a 29-gauge needle produced a 72-75% flow reduction from baseline and rats died within 24-hours (n=2). Necropsy revealed a foul fecal odor on opening the cavity and extensive bloating and mottling of the intestine, particularly the small intestine.

No EPR spectrum was detected in the small intestine post-intravenous administration of the trityl probe (2 mL of 0.5 mm/mL; $n = 1$). Increasing the probe concentration to 20 mm/mL (2 mL) produced spectra of poor quality with decay in less than 5 minutes. We suspected the probe was being rapidly removed from the bloodstream by the liver or kidney however, no spectra were detectable when the resonator was placed directly over either organ.

LiNc-BuO microcrystals were injected into the lumen of the small intestine with a 29-gauge needle. Luminal pO_2 was 7.7 and 3.9 mm Hg for baseline and ischemia, respectively ($n = 1$). EPR pO_2 measurement was only possible when the abdomen remained open. Intestinal motility prevented the site-specific monitoring of pO_2. Needle puncture likewise posed the risk of leaking luminal contents and bacteria into the cavity and the development of peritonitis, sepsis, and death.

Thinness of the small intestine wall prohibited probe placement by injection. However, we were able to inject LiNc-BuO into the wall of the large intestine ($n = 4$).

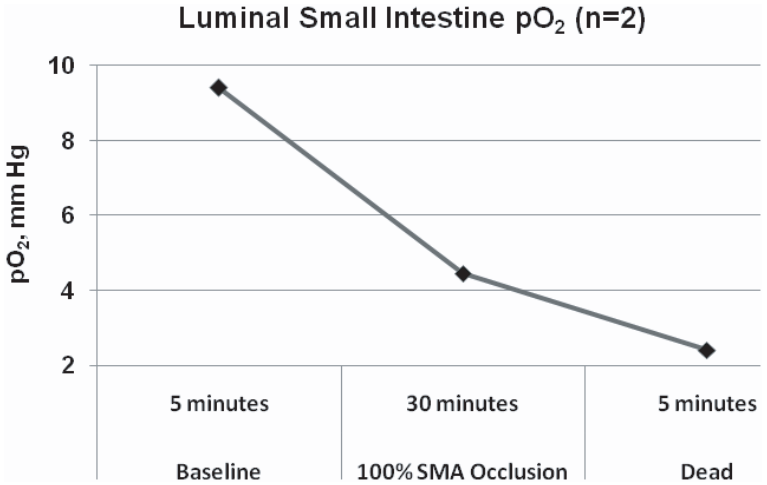

Fig. 6.1 SMA occlusion between 60 and 70% produced a 53% reduction in luminal pO_2.

EPR spectra were detectable only when the cavity was open and the intestine with the LiNc-BuO probe placed directly beneath the resonator. Varying the level of SMA occlusion resulted in reproducible changes in pO_2 (Figure 2A). Because of variability in the individual rat data, we used percent comparisons from baseline. The t-test revealed a significant decline in pO_2 from baseline to 100% SMA occlusion ($p = 0.002$). A slight overshoot of baseline occurred with reperfusion but did not differ from baseline ($p = 0.43$).

For LiNc-BuO injected into the large intestine wall, the pO_2 was measured over time in four SMA banded rats (60-80% occlusion). Spectral acquisition was not possible through the closed abdomen and thus, was surgically opened during pO_2 measurement. On average, a 51% reduction in pO_2 occurred between baseline and SMA banding (19.6 ± 10.3mm Hg; 9.6 ± 2.6 mm Hg). Rat 1 had a 74% reduction in pO_2 from baseline and died within 24-hours of banding. The second rat became morbidly ill after 1-week and was euthanized. The remaining two rats (3 & 4), both experienced an increase in pO_2 1-week post-banding. For Rat 3 pO_2 continued to decline at week 3 and 4 while Rat 4 demonstrated an increase in pO_2 at week 4 similar to baseline. Banding was not evident in Rat 4 on necropsy.

The 1 × 2 mm LiNc-BuO:PDMS chip was sutured to the inner peritoneal wall to lay against the intestine when the abdominal cavity was closed. EPR spectra were obtained through the closed abdominal wall. Rats were placed in control ($n = 2$) or SMA banded groups ($n = 2$) (Figure 3). Because the chip senses all oxygen in its environment, post-banding readings were similar to baseline despite closure of the abdomen. The pO_2 values for all rats were reduced by post-operative week 1. For Rat 2, the EPR signal was lost at week 2. Rat 4 became morbidly ill at week 4 and was euthanized. Necropsy revealed blue-black intestinal tissue. At week 7 animals were euthanized and the chip retrieved. In 3 of the 4 rats, a thick fat pad completely covered the probe.

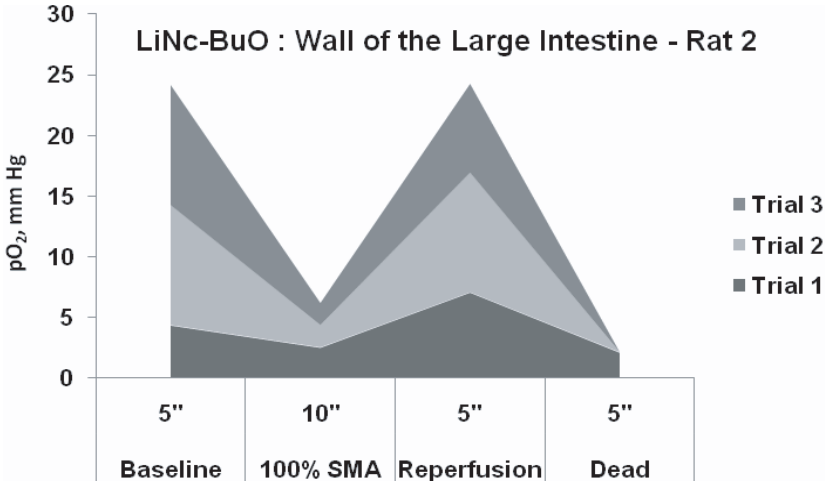

(a)

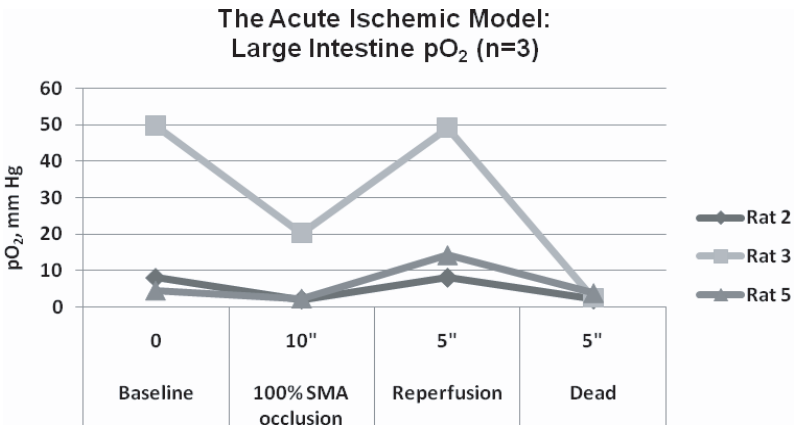

(b)

Fig. 6.2 Figure 2A. Reproducible trends in pO_2 were found when flow was varied in a cycle of three trials from baseline to 100% SMA occlusion to reperfusion in Rat 2. Figure 2B. The three trials were averaged for each rat (n=3) and pO_2 values were plotted against condition, with the final condition being tissue anoxia. We suspect the increased pO_2 values obtained for Rat 3 occurred in response to the probe being in direct contact with a blood vessel.

6.4 Discussion and Conclusions

The major challenge we faced for small intestine pO_2 measurement by EPR was probe placement. Thinness of the small intestine wall prevented the injection of LiNc-BuO. The injection of probe between the wall of the large intestine carried

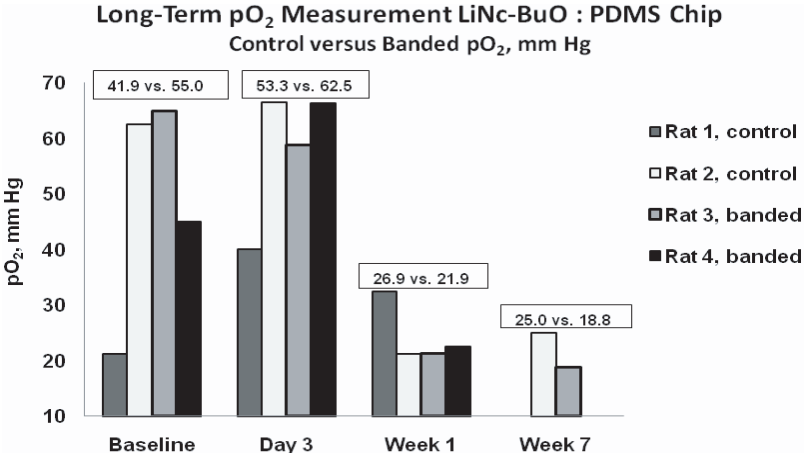

Fig. 6.3 Above the bars, means values of pO_2 (mm Hg) are reported for the control ($n = 2$) versus banded ($n = 2$) group by time. Rats in both the control and banded group had an increase in pO_2 at day-3 which may represent a hyperemic response to surgical insult and for the banded group, an attempt to compensate for the reduction in blood flow. Normalization of pO_2 occurred for weeks 1-7.

the risk of intestinal perforation and leakage of stool and bacteria into the cavity and may have contributed to rat mortality. Sufficient quantities of LiNc-BuO could not be injection into the intestinal wall to allow for noninvasive pO_2 measurement. Only the LiNc:BuO:PDMS chip met our criteria for noninvasive measurement of pO_2. However, since LiNc-BuO microcrystals are sensitive to oxygen within the surrounding environment, it is likely we obtained pO_2 values using the LiNc:BuO:PDMS chip reflective of oxygen in the fat pad and peritoneal muscle wall.

The *ideal* oxygen-sensing probe would allow for noninvasive monitoring, be flexible to conform to the intestinal wall for site-specific monitoring, be shielded from other oxygen sources within the environment, and be biocompatible and sensitive to track trend changes in pO_2 over time. Tracking variations in oxygen related to pathophysiological processes in animals and ultimately in patients with acute and chronic intestinal ischemia, will add to our knowledge of oxidative stress and assist with defining and tracking symptom complexes with the goal of tailoring interventions to eliminate, reduce or stabilize symptoms.

Acknowledgments

This work was supported by a NIH:NINR Mentored Scientist Award - KO1 NR009787-01 to the first author. Special thanks are extended to Sarath Meduru for assistance with long-term EPR pO_2 measurement and tissue retrieval.

References

1. Khan, M., Kutala, V.K., Wisel, S. et al (2008) Measurement of oxygenation at the site of stem cell therapy in a murine model of myocardial infarction. Adv.Exp.Med.Biol. 614, 45-52.
2. Kulkarni, A.C., Kuppusamy, P. and Parinandi, N. (2007) Oxygen, the lead actor in the pathophysiologic drama: enactment of the trinity of normoxia, hypoxia, and hyperoxia in disease and therapy. Antioxid.Redox.Signal. 9, 1717-1730.
3. Meenakshisundaram,G., Eteshola,E., Pandian,R.P., et al (2009) Fabrication and physical evaluation of a polymer-encapsulated paramagnetic probe for biomedical oximetry. Biomed.Microdevices. 11,773-782.
4. Meenakshisundaram,G., Eteshola,E., Pandian,R.P. et al (2009) Oxygen sensitivity and biocompatibility of an implantable paramagnetic probe for repeated measurements of tissue oxygenation. Biomed.Microdevices. 11, 817-826.
5. Niebauer,J., Volk,H.D., Kemp,M. et al (1999) Endotoxin and immune activation in chronic heartfailure: a prospective cohort study. Lancet 353, 1838-1842.
6. Pandian,R.P., Parinandi,N.L., Ilangovan,G., et al (2003) Novel particulate spin probe for targeted determination of oxygen in cells and tissues. Free Radic.Biol.Med. 35, 1138-1148.
7. Sandek,A., Bauditz,J., Swidsinski,A. et al (2007) Altered intestinal function in patients with chronic heart failure. J.Am.Coll.Cardiol. 50, 1561-1569.

Chapter 7
Quantification of Systemic Interference in Optical Topography Data during Frontal Lobe and Motor Cortex Activation: An Independent Component Analysis

Sundeep Patel, Takusige Katura, Atsushi Maki, and Ilias Tachtsidis

Abstract Functional near-infrared optical topography (OT) is used to non-invasively measure the changes in oxygenated and deoxygenated haemoglobin ($\Delta[HbO_2]$, $\Delta[HHb]$) and hence investigate the brain haemodynamic changes, which occur in response to functional activation at specific regions of the cerebral cortex. However, when analysing functional OT data the task-related systemic changes should be taken into account. Here we used an independent component analysis (ICA) method on the OT $[HbO_2]$ signal, to determine the task-related independent components and then compared them with the systemic measurements (blood pressure, heart rate, scalp blood flow) to assess whether the components are due to systemic noise or neuronal activation. This analysis can therefore extract the true OT haemodynamic neuronal response and hence discriminate between regional activated cortical areas and global haemodynamic changes.

7.1 Introduction

Functional optical topography (OT) uses near-infrared light to non-invasively measure the changes in oxygenated and deoxygenated haemoglobin ($\Delta[HbO_2]$, $\Delta[HHb]$) across multiple brain sites during brain neuronal activation. The OT functional haemodynamic changes should occur at specific locations that overlay the cortical activated areas and should be closely coupled to the task-related timing periods. This assumes that the functional haemodynamic task-related changes are occurring on top of an unchanged global systemic and brain resting state. However in certain

Sundeep Patel and Ilias Tachtsidis
Biomedical Optics Research Laboratory, Department of Medical Physics and Bioengineering, University College London, Gower Street, London WC1E 6BT, UK
e-mail: iliastac@medphys.ucl.ac.uk

Takusige Katura and Atsushi Maki
Advanced Research Laboratory, Hitachi Ltd, 2520 Akanuma, Hatoyama, Saitama 350-0395, Japan

J.C. LaManna et al. (eds.), *Oxygen Transport to Tissue XXXII*, Advances in Experimental Medicine and Biology 701, DOI 10.1007/978-1-4419-7756-4_7,

functional OT experiments these assumptions are not accurate. Using two channels near-infrared spectroscopy (NIRS) Leung and colleagues found a relatively high correlation between $\Delta[HbO_2]$ signals over the frontal cortex (FC) and motor cortex (MC) during finger tapping while also observing a significant increase in heart rate (HR) [1]. In a study in 2008, we have observed significant task-related changes in mean blood pressure (MBP) and HR during anagram solving and in some volunteers the $\Delta[HbO_2]$ and $\Delta[HHb]$ signals measured over the activated FC were correlated with the MBP signal [2]. In a subsequent study we have observed significant changes in the NIRS signals over the FC and a control area, the MC; we also observed task-related changes in MBP and scalp blood flow (scalp flux) that appear to contribute to the changes in the NIRS signals over both the activated and control regions of the cortex [3]. Finally, recently in a study on 22 adult subjects using OT to produce maps of the haemodynamic response of both FC and MC during anagram solving, while simultaneously monitoring the systemic physiology (HR, MBP, scalp flux), we observed that during the task, half of the subjects demonstrated a significant change in at least one systemic variable and certain OT channels were highly correlated with these systemic changes [4]. These systemic changes are thus 'global noise components' and any analysis of functional OT signals must take this effect into account.

Recent work using independent component analysis (ICA) allowed extraction of the task-related independent components (TR-IC) from OT signals and separation of these signals into activation-related and noise-related components [5]. Here we use the same ICA methodology and expanded it to assess whether the TR-ICs is due to systemic noise (TR-NIC) or neuronal activation (TR-AIC) by carrying out correlation analysis with measured systemic variables.

7.2 Methods

We studied a 20-year-old right-handed female, with English as her first language (this study was approved by the UCL Research Ethics Committee). NIRS measurements were conducted with the ETG-100 Optical Topography System (Hitachi Medical Co., Japan) using two 12-channel arrays. Each optode array consisted of 5 source optodes (each delivering light at 780 and 830 nm) and 4 detector optodes. The source-detector interoptode spacing was 30mm and data was acquired at 10Hz. The optodes were placed over the subject's left frontal cortex and positioned according to the International 10-20 system of electrode placement so that channels 1-12 were centred approximately over the frontopolar region (Fp) and channels 13-24 were centred approximately over the left motor cortex (C3) (see Figure 1(a)). A Portapres® system (TNO Institute of Applied Physics) was used to continuously and non-invasively measure MBP and HR from the finger. A laser Doppler probe (FloLab, Moore Instruments) was placed over the forehead to monitor the changes in scalp blood flow (scalp flux).

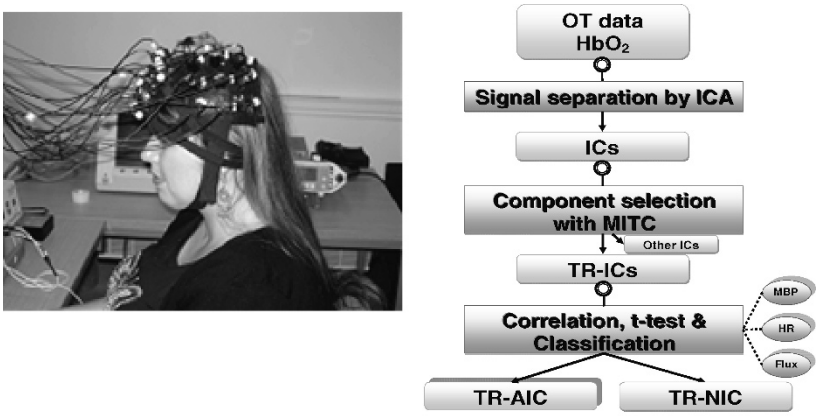

Fig. 7.1 (a) Picture of a volunteer with the OT system showing channels 1-12 placed over the frontal lobe and channels 13-24 placed over the motor cortex. (b) Block diagram of analysis steps.

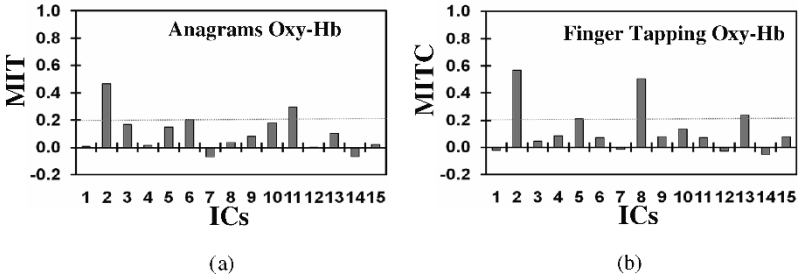

Fig. 7.2 Bar graphs show MITC distributions for [HbO_2] for (a) anagrams and (b) finger tapping.

Data were recorded during 1 minute of the subject at rest (baseline), followed by 45 seconds of the subject solving anagrams (a mixture of 4-letter, 6-letter and 8-letter anagrams), followed by 30 seconds of rest, followed by 30 seconds of finger tapping. In this study, solving an anagram was defined as producing one coherent word using only the letters from another word (e.g., kitchen – thicken). Each anagram-solving and finger-tapping period was repeated a total of eight times, with the study ending after a 60 second rest period (total study time 19.5 minutes). During this functional paradigm the participants were asked to be still and silent; and no response to anagram solving was requested.

Pre-processing of the OT signals and the ICA for the Δ[HbO_2] was done with a software platform developed by Hitachi called Platform for Optical Topography Analysis Tools or POTATo (ver P3_UCL0810, Hitachi 2009). This involved a moving average with a period of 3s to filter the data followed by a polyfit difference function of 8 degrees to reduce the effect of low frequency noise. The method of ICA used is similar to that carried out by Katura and colleagues [5] and involves

using principle component analysis (PCA) to reduce the noise in the data and reduce the number of components. Whether a component is used or discarded is determined by the component's contribution to the total energy. In this analysis, the threshold for truncation was set at 99% such that components contributing less than 1% of the total energy were not used. The next step was using a 'time-delayed decorrelation algorithm (TDD) to separate the different independent components [6,7,8]. The TDD was based on the assumption that the various components that make up the [HbO_2] data are independent and if these components are independent of each other, their cross-correlations will be zero with any time delays; so any dependence is removed by the time delay. The time delay used in this procedure was between 0 and 15s with steps of 1.5s. To find the components of the signal that were due to the activation tasks or TR-ICs (see Fig. 1(b)) we selected them from the separated ICs based on mean inter-trial cross-correlation (MITC), which is a measure of reproducibility of a given IC over repeated trials, those that are equal or larger than 0.2. To assess whether the TR-IC is due to systemic noise or neuronal activation, we carried out correlation analysis with the systemic measurements and a t-test between the baseline and activation period. The TR-AIC is identified as the TR-IC with the lowest correlation with the systemic variables and a positive significant ($p < 0.05$) increase during the activation period.

7.3 Results

Figure 2 shows the MITC distribution and Table 1 shows the correlation coefficients between the systemic measurements and the ICs with MITC $\geq$ 0.2 for both anagrams and finger tapping. During the anagram activation ICs 2, 6 and 11 had an MITC of 0.2 or higher (see Figure 3(d)). IC 2 was identified as the TR-AIC as it demonstrated a significant positive increase during the activation ($p= 0.008$) and it was not correlated with any of the systemic variables. ICs 6 and 11 were identified as TR-NICs as they did not demonstrate a positive increase during activation and also IC 11 demonstrated a positive correlation with HR.

During the finger tapping activation ICs 2, 5, 8 and 13 had an MITC of 0.2 or higher (see Figure 4(d)). ICs 2 and 13 demonstrated a significant positive increase during the activation (p=0.038 and p=0.034); however IC 13 was identified as the TR-AIC as it was not positively correlated with any of the systemic variables. ICs 2, 5 and 8 were identified as TR-NICs; IC 2 was correlated with the scalp flux and ICs 5 and 8 did not demonstrate an increase during the finger tapping.

7.4 Discussion

It is often necessary when analysing functional OT signals to use appropriate methods and statistical tests that incorporate the systemic changes that can occur during

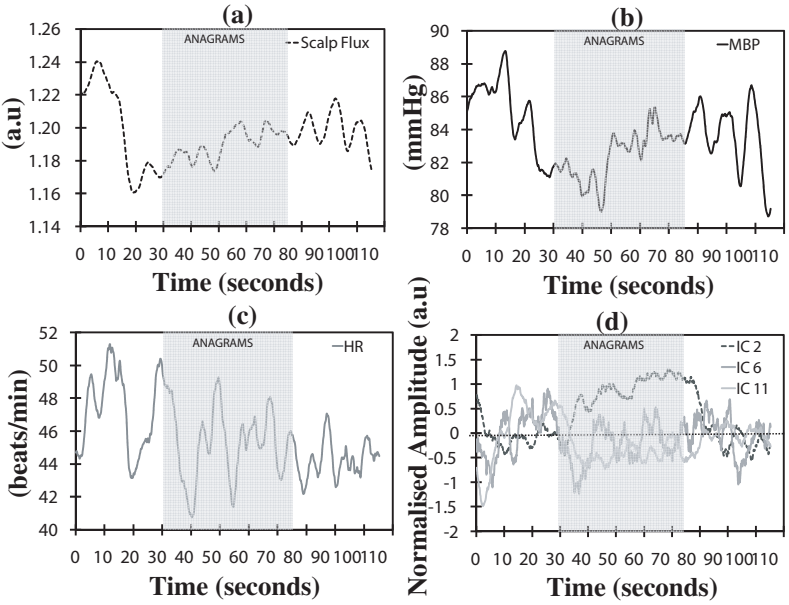

Fig. 7.3 Traces are the block averaged time courses during the anagram activation for the (a) scalp flux; (b) MBP; (c) HR; and (d) the independent components with MITC ≥ 0.2.

Table 7.1 Correlations values between systemic variables and ICs with MITC$\geq$0.2 for † Anagrams and * Finger Tapping.

	Anagrams			Finger Tapping		
ICs	Scalp Flux	MBP	HR	Scalp Flux	MBP	HR
$2^{\dagger *}$	−0.10	−0.23	−0.21	0.39	0.26	0.06
5^{*}	−0.33	−0.45	0.09	−0.40	−0.40	−0.06
$6^{\dagger}$	−0.26	0.04	0.01	−0.28	0.01	−0.29
$8^{¤}$	−0.59	−0.46	−0.17	−0.36	−0.05	−0.08
$11^{\dagger}$	−0.28	0.10	0.31	−0.30	−0.08	−0.02
$13^{¤}$	−0.07	−0.04	−0.03	−0.37	−0.31	−0.23

brain activation. Here, we describe a methodology based on ICA that allows for the identification of both the neuronal haemodynamic signal and the systemic interference in the functional OT data. This analysis can therefore extract the true OT haemodynamic neuronal response from the systemic haemodynamic changes and hence discriminate between regional activated cortical areas and global changes.

In order to account for the systemic physiological noise, we have previously used Statistical Parametric Mapping (SPM) [4]; while others have used Principal Component Analysis [9,10] and Independent Component Analysis [5,8]. Therefore, we detail an ICA based method for OT data that expands on previous work [5] by incorporating systemic measurements in the identification process of the TR-AIC.

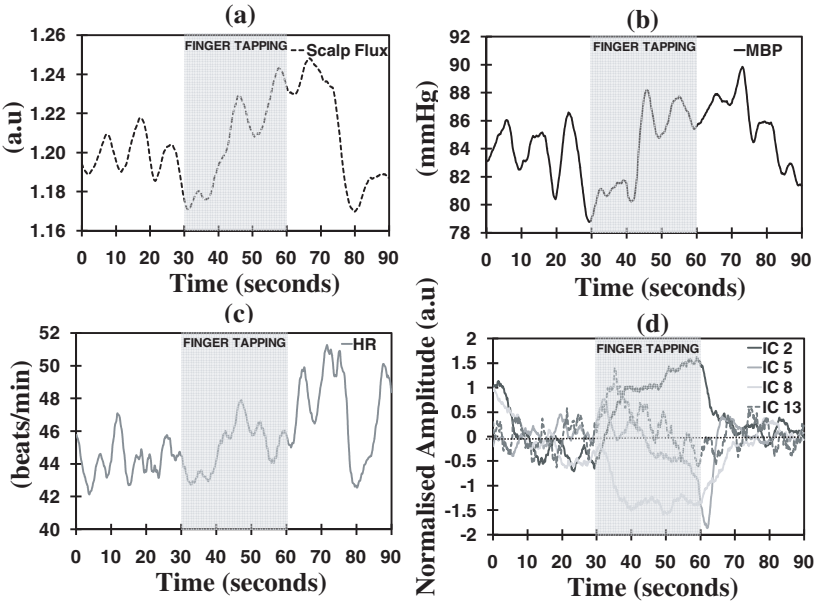

Fig. 7.4 Traces are the block averaged time courses during the finger tapping activation for the (a) scalp flux; (b) MBP; (c) HR; and (d) the independent components with MITC ≥ 0.2.

This method can be used both at the intra- and inter-subject level and can possibly enhance the interpretation of the task-related OT response.

Acknowledgments

The authors would like to thank the EPSRC (EP/D060982/1).

References

1. Leung TS, Elwell CE, Henty JR et al (2003) Simultaneous measurement of cerebral tissue oxygenation over the adult frontal and motor cortex during rest and functional activation. Adv.Exp.Med.Biol. 510:385-389
2. Tachtsidis I, Leung TS, Devoto L et al (2008) Measurement of frontal lobe functional activation and related systemic effects: a near-infrared spectroscopy investigation. Adv.Exp.Med.Biol. 614:397-403
3. Tachtsidis I, Leung TS, Tisdall MM et al (2008) Investigation of frontal cortex, motor cortex and systemic haemodynamic changes during anagram solving. Adv.Exp.Med.Biol. 614:21-28
4. Tachtsidis I, Leung TS, Chopra A et al. (2009) False positives in functional near-infrared topography. Adv.Exp.Med.Biol. 645:307-314
5. Katura T, Sato H, Fuchino Y et al (2008) Extracting task-related activation components from optical topography measurement using independent components analysis. J.Biomed.Opt. 13:054008-
6. Cardoso JF and Souloumiac A, (1996) Jacobi angles for simultaneous diagonalization. SIAM J.Matrix Anal.Appl. 17:161-164

7. Ziehe A and Muller KR, (1998) TDSEP an efficient algorithm for blind separation using time structure. Proc.ICANN98, Springer, Berlin 675-680
8. Hirosaka R, Katura T, Kawaguchi H et al (15-7-2004) Noisy time-delayed decorrelation and its application to extraction of neural activity from single optical recordings in guinea pigs. Physica D.: Nonlinear.Phenomena. 194:320-332
9. Huppert TJ, Diamond SG, Franceschini MA et al (1-4-2009) HomER: a review of time-series analysis methods for near-infrared spectroscopy of the brain. Appl.Opt. 48:D280-D298
10. Franceschini MA, Joseph DK, Huppert TJ et al. (2006) Diffuse optical imaging of the whole head. J.Biomed.Opt. 11:054007

Chapter 8
Measuring Oxygen in Living Tissue: Intravascular, Interstitial, and "Tissue" Oxygen Measurements

David F. Wilson, Olga S. Finikova, Artem Y. Lebedev, Sophia Apreleva, Anna Pastuszko, William M.F. Lee, and Sergei A. Vinogradov

Abstract Oxygen dependent quenching of phosphorescence has been used to measure the oxygen pressure in both the vasculature of the microcirculation and the interstitial spaces of resting muscle tissue. Oxygen sensitive molecules were either dissolved in the blood (intravascular space) or micro-injected into the interstitial space and the distributions, histograms, of the oxygen pressure were measured. The mean oxygen pressures are higher in the blood than in the interstitial space but the oxygen pressures in the lowest 10% of the two spaces were not significantly different, indicating there is minimal (< 1 mm Hg) oxygen gradient between the two spaces in the capillary bed.

8.1 Introduction

Oxygen is bound to hemoglobin when it is transported from the lung to other tissues; but upon reaching those tissues, only diffusion is responsible for the movement of oxygen molecules from the blood plasma through the walls of the micro-vessels into the interstitial (pericellular) space, and finally into the cells to the mitochondria where oxygen is consumed. Quantitative measurements of oxygen pressures within different compartments of tissue are necessary in order to understand how oxygen diffusion affects oxygen delivery and the role of cellular oxygen pressure in tissue biochemistry and physiology.

Oxygen measurement methods, however, are typically either specific for one tissue compartment, such as the intravascular space (e.g., oxy/deoxy-hemoglobin-based

David F. Wilson, Olga S. Finikova, Artem Y. Lebedev, Sophia Apreleva, Anna Pastuszko, and Sergei A. Vinogradov
Department of Biochemistry and Biophysics, University of Pennsylvania, Philadelphia, PA 19104
e-mail: wilsondf@mail.med.upenn.edu

William M.F. Lee
Department of Medicine, University of Pennsylvania, Philadelphia, PA 19104

J.C. LaManna et al. (eds.), *Oxygen Transport to Tissue XXXII*, Advances in Experimental Medicine and Biology 701, DOI 10.1007/978-1-4419-7756-4_8,

measurements), or are non-specific, such as for oxygen electrodes inserted into the tissue. One method, oxygen dependent quenching phosphorescence, is unique in that it can be used for measuring oxygen in different tissue compartments.

In this paper, we compare oxygen measurements in the blood plasma of the microcirculation (vascular space) and interstitial space within tissue. The vascular wall is the only physical barrier between the blood plasma and the interstitial space, and oxygen consumption within the interstitial space is very small. The difference in oxygen pressure between the compartments is a function of the diffusion distance and the rate of oxygen consumption by the cells. Oxygen measurements have been made in both awake and anesthetized mice in order to control for the possibility of stress and/or anesthetic induced changes in blood pressure and vascular resistance.

8.2 Materials and Methods

Oxygen dependent quenching of phosphorescence provides a non-invasive optical method for determining oxygen pressures in biological and other samples (1-6,8,9,13-17,21,18,21,25-27). The available oxygen sensitive phosphors, such as Oxyphors R0, R2 and G2, contain Pd-porphyrin cores that are at least partially exposed to the medium, where they readily bind to biological macromolecules, particularly albumin. Albumin plays an important role, both limiting access of oxygen to the porphyrin core, thereby facilitating oxygen measurements in the physiological range (0-120 mm Hg), and providing a relatively homogeneous microenvironment for the porphyrin core.

For measurements of oxygen in the system containing no albumin, we have recently developed a new family of dendritic phosphors (10-12,19,22). The performance of the new probes is illustrated in Figure 1, where the Stern-Volmer plots are shown for Pt-porphyrin-based dendrimers generations 0 (no dendrimer added)-3 (for details, see ref. [12]).

With increase in the dendrimer generation, the oxygen sensitivity decreases. The oxygen sensitivity of the original core (G0) is very high, with a quenching constant of nearly 4000 mm $Hg^{-1}sec^{-1}$, - too high to be useful for measuring oxygen pressures in the physiological range. By generation 2 the quenching constant has decreased to less than 200 mm $Hg^{-1}sec^{-1}$, a value well suited for tissue oxygen measurements. Adding a coat of polyethylene glycol results in an oxygen sensor that is highly soluble in aqueous media and for which the oxygen sensitivity is the same whether it is dissolved in simple phosphate buffer or blood serum. Graph B of the figure shows that the PEG coated sensors are insensitive to the biological agents, including albumin, in blood serum. There was no difference in the Stern-Volmer plot for oxygen quenching whether this particular Oxyphor was dissolved in a simple phosphate buffer or blood serum from a rat.

Measurements of the distribution of oxygen (histograms) were carried out as described earlier (20,23,24). The excitation light of a frequency-domain phosphorometer was modulated as the sum of 37 different frequencies ranging from 100 Hz

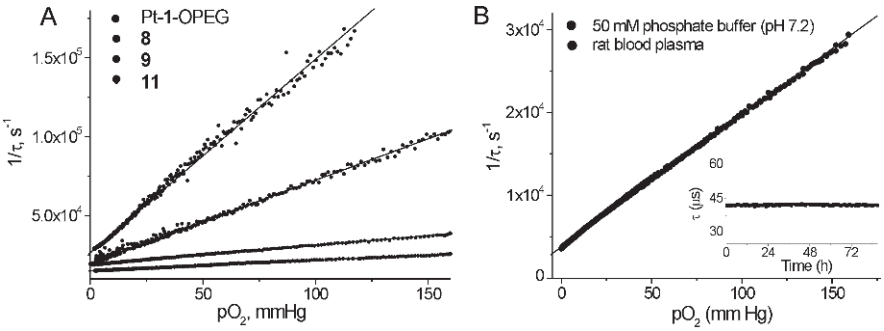

Fig. 8.1 A) Stern-Volmer plots of Pt porphyrin oxygen probes of different dendritic generations. The periphery of the dendrimers is modified with oligoethyleneglycol residues, which makes the probes insensitive to the presence of biological macromolecules, which is illustrated by the experiment shown in graph B), where the dendritic probe was titrated in the aqueous buffer and in the rat blood plasma, rendering identical Stern-Volmer plots. The inset shows signal stability evaluation for the same probe.

to 38,000 Hz. The collected data were used to calculate the distribution of phosphorescence lifetimes and the amount of the phosphor corresponding to each lifetime. The histograms have been normalized by setting the sum (integral) of the Y axis values for each histogram to 1.0. This procedure removes the dependence on the excitation light intensity and phosphorescence collection efficiency. Both the intensities (amplitudes) and lifetimes of phosphorescent signals decrease with increasing oxygen pressures. The decrease in signal strength with increasing oxygen pressure (decreasing the signal to noise) results in the "tail" effect on the high oxygen end of the histogram. This asymmetric broadening is intrinsic to distribution analysis, where the uncertainty in determination of phosphorescence lifetimes increases with decreasing signal-to-noise ratio (S/N).

There is no evidence of toxicity of the Oxyphors, either alone or when illuminated. Injection of the Oxyphor into the blood has no effect on the measured physiological parameters in 2-5 day old pigs or when added to cell culture media had no effect on growth of the cells in culture.

8.3 Results and Discussion

Oxygen pressures in the intravascular and interstitial spaces have been measured using Pd-tetrabenzoporphyrin encapsulated inside generation 2 poly-arylglycine (AG) dendrimer covered with oligoethylene glycol residues (Av. MW 350). This sensor, Oxyphor G3, is biologically inert and can be loaded into the interstitial space by injection into tissue using a 30 guage or smaller needle. Either Oxyphor G3 or Oxyphor G2 can be injected into the blood for measuring the intravascular oxygen pressure. Measurements of the oxygen distribution in the interstitial space have been com-

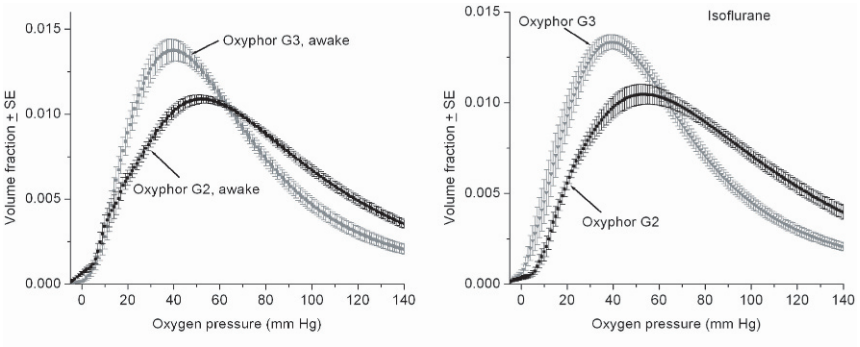

Fig. 8.2 Comparison of the oxygen histograms measured for the interstitial space (Oxyphor G3) and intravascular space (Oxyphor G2) of skeletal muscle in awake (A) and isoflurane anesthetized (B) mice. The histograms are the means for 11 (Oxyphor G3) or 10 (Oxyphor G2) independent experiments with error bars indicating the Standard Error of the Mean (±SE).

pared with those for the intravascular (blood plasma) space in normal and tumor tissue in awake and anesthetized animals. For normal resting muscle in awake mice (Fig. 2), the lowest 10% of oxygen pressures in normal muscle for the interstitial and intravascular spaces were not different (< 1 mm diffusion gradient) whereas in isoflurane anesthetized mice there was a small but significant ($p = 0.01$) difference. In both cases, however, the intravascular oxygen histograms were "skewed" to higher oxygen values compared to the interstitial space, consistent with a population of larger vessels with oxygen pressures significantly higher than in the surrounding interstitial space.

The oxygen pressures in K1735 tumor tissue were very low in both the intravascular and interstitial spaces when measured in awake mice but these increased dramatically when the mice were anesthetized with isoflurane. This was in contrast to resting muscle where the histograms for awake and anesthetized mice were not significantly different. The increase in oxygen pressure in the tumor is consistent with the isoflurane lowering the resistance of the tumor vessels relative to normal muscle, increasing blood flow to the tumor tissue. Tumor tissue also differs from muscle in that the lowest 10% of the oxygen distribution in the interstitial space was significantly lower than for the intravascular space. The presence of an increased oxygen gradient is consistent with tumor tissue having regions with significantly greater distances from the vessels to the cells than does muscle.

8.4 Conclusions

1. In normal resting muscle the oxygen pressure difference from the vascular space of the capillaries to the interstitial space is less than 1 mm Hg. Thus, the vascular

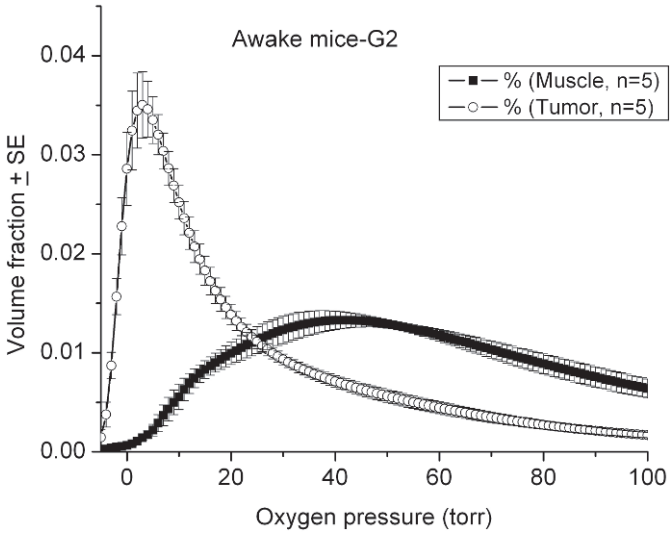

Fig. 8.3 Comparison of the oxygen histograms for the blood in the microcirculation (Oxyphor G2) of K1735 tumors (open squares) and normal muscle (solid squares) in awake mice.

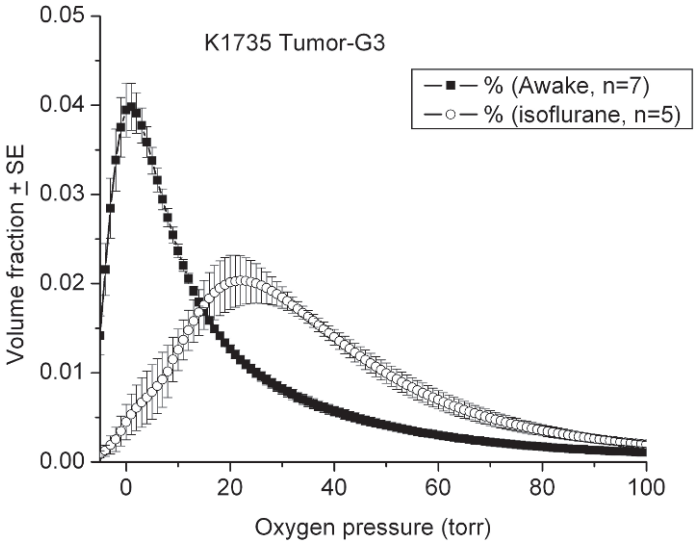

Fig. 8.4 Histograms of the oxygen distributions in the interstitial space (Oxyphor G3) of K1735 tumors in awake (solid squares) and isoflurane anesthetized (open squares) mice.

wall does not cause a significant diffusion/metabolism induced decrease in oxygen pressure between the blood plasma and the pericellular space.

2. In K1735 tumors of awake animals, the oxygen pressures in both the vascular and interstitial spaces of the tumor are much lower than in normal muscle. There

is also a substantial intravascular/interstitial space oxygen difference, consistent with substantially increased distances from the capillary walls to the cells.
3. The oxygen levels in K1735 tumors greatly increase when mice are given isofluorane anesthesia, rising nearly to those of normal tissue. This suggests an anesthetic induced decrease in vascular resistance in the tumors relative to the surrounding tissue.

Acknowledgments

Supported by Grants HL058669, NS031465, and HL081273.

References

1. Behnke BJ, Kindig CA, Musch TI, Koga S, and Poole DC (2001) Dynamics of microvascular oxygen pressure across the rest-exercise transition in rat skeletal muscle. *Resp. Physiol*. 126(1): 53-63.
2. Dewhirst MW, Ong ET, Braun RD, Smith B, Klitzman B, Evans SM, and Wilson DF (1999) Quantification of longitudinal tissue pO2 gradients in window chamber tumours: impact on tumour hypoxia, *Br. J. Cancer* 79: 1717-1722.
3. Buerk DG, Tsai AG, Intaglietta M, and Johnson PC (1998) Comparing tissue PO_2 measurements by recessed microelectrode and phosphorescence quenching. *Adv. Exp. Biol. Med*. 454: 367-374.
4. Dunphy I, Vinogradov SA, and Wilson DF(2002) Oxyphor R2 and G2: Phosphors for measuring oxygen by oxygen dependent quenching of phosphorescence. *Analy. Biochem*. 310: 191-198.
5. Huang Ch-Ch, Lejevadi NS, Tammela O, Pastuszko A, Delivoria-Papadopoulos M, and Wilson DF. (1994) Relationship of extracellular dopamine in striatum of newborn piglets to cortical oxygen pressure. *Neurochem. Res*. 19: 640-655.
6. Johnson PC, Vandegriff K, Tsai AG, and Intaglietta M (2005) Effect of acute hypoxia on microcirculatory and tissue oxygen levels in rat cremaster muscle. *J. Appl. Physiol*. 98: 1177-1184.
7. Kripke ML. (1979) Speculations on the role of ultraviolet radiation in the development of malignant melanoma. *J. Natl. Cancer Inst.* 63: 541-548.
8. Poole DC, Behnke BJ, McDonough P, McAllister RM, and Wilson DF. (2004) Measurement of muscle microvascular oxygen pressures: compartmentalization of phosphorescent probe. *Microcirculation*. 11(4): 317-326.
9. Richmond KN, Shonat RD, Lynch RM, and Johnson PC. (1999) Critical PO_2 of skeletal muscle in vivo. *Am. J. Physiol. Heart Circ. Physiol*. 277: H1831–H1840.
10. Rietveld IB, Kim E, and Vinogradov, SA. (2003) Dendrimers with tetrabenzoporphyrin cores: near infrared phosphors for in vivo oxygen imaging. *Tetrahedron* 59**:** 3821-3831.
11. Rozhkov V, Wilson DF, and Vinogradov SA. (2002) Phosphorescent Pd porphyrin-dendrimers: Tuning core accessibility by varying the hydrophobicity of the dendritic matrix. *Macromolecules* 35: 1991-1993.
12. Lebedev, AY. Cheprakov, AV. Sakadzic, S. Boas, DA. Wilson, DF. and Vinogradov, SA. (2009) Dendritic Phosphorescent Probes for Oxygen Imaging in Biological Systems. *ACS Appl. Mater. Interfaces*, 1, 1292-1304.
13. Rumsey WL, Pawlowski M, Lejavardi N, and Wilson DF. (1994) Oxygen pressure distribution in the heart in vivo and evaluation of the ischemic "border zone." *Am. J. Physiol.* 266(4 Pt 2): H1676-80.

14. Rumsey WL, Vanderkooi JM, and Wilson DF. (1988) Imaging of phosphorescence: A novel method for measuring the distribution of oxygen in perfused tissue. *Science 241*: 1649-1651.
15. Shonat RD and Johnson PC. (1997) Oxygen tension gradients and heterogeneity in venous microcirculation: a phosphorescence quenching study. *Am. J. Physiol. Heart Circ. Physiol*. 272: H2233–H2240.
16. Shonat, RD, Wilson DF, Riva CE, and Pawlowski M. (1992) Oxygen distribution in the retinal and choroidal vessels of the cat as measured by a new phosphorescence imaging method. *Appl. Optics* 31: 3711-3718.
17. Sinaasappel M, Donkersloot C, van Bommel J, and Ince C. (1999) PO_2 measurements in the rat intestinal microcirculation. *Am. J. Physiol*. 276: G1515-20.
18. Vanderkooi JM, Maniara G, Green TJ, and Wilson DF. (1987) An optical method for measurement of dioxygen concentration based on quenching of phosphorescence, *J. Biol. Chem.* 262: 5476-5482.
19. Vinogradov SA, Fernandez-Seara MA, Dugan BW, and Wilson DF (2001) Frequency domain instrument for measuring phosphorescence lifetime distributions in heterogeneous samples, *Rev. Sci. Instruments* **72**, 3396-3406.
20. Vinogradov SA, Lo L-W, Jenkins WT, Evans SM, Koch C, and Wilson DF. (1996) Noninvasive imaging of the distribution of oxygen in tissue in vivo using near infra-red phosphors, *Biophys. J*. 70: 1609-1617.
21. Vinogradov SA and Wilson DF. (1994) Metallotetrabenzoporphyrins. New phosphorescent probes for oxygen measurements. *J. Chem. Soc., Perkin Trans. II***,** 103-111.
22. Vinogradov SA and Wilson DF. (1994) Phosphorescence lifetime analysis with a quadratic programming algorithm for determining quencher distributions in heterogeneous systems. *Biophys. J*. 67: 2048-2059.
23. Vinogradov SA and Wilson DF (2000) Recursive maximum entropy algorithm and its application to the luminescence lifetime distribution recovery. *Appl. Spectroscopy* **54:** 849-855.
24. Wilson DF, Rumsey WL, Green TJ, and Vanderkooi JM. (1988) The oxygen dependence of mitochondrial oxidative phosphorylation measured by a new optical method for measuring oxygen. *J. Biol. Chem.* 263: 2712-2718.
25. Wilson DF Vinogradov SA Grosul P Vaccarezza MN Kuroki A and Bennett J. (2005) Oxygen distribution and vascular injury in the mouse eye measured by phosphorescence lifetime imaging. *Appl. Optics* 44: 1-10.
26. Ziemer L Lee WMF Vinogradov SA Sehgal C and Wilson DF. (2005) Oxygen distribution in murine tumors: characterization using oxygen-dependent quenching of phosphorescence. *J. Appl. Physiol*. 98: 1503-1510.

Chapter 9
Cerebral Oxygenation of the Cortex and Striatum Following Normobaric Hyperoxia and Mild Hypoxia in Rats by EPR Oximetry Using Multi-Probe Implantable Resonators

Huagang Hou, Hongbin Li, Ruhong Dong, Sriram Mupparaju, Nadeem Khan, and Harold Swartz

Abstract Multi-site electron paramagnetic resonance (EPR) oximetry, using multi-probe implantable resonators, was used to measure the partial pressure of oxygen (pO_2) in the brains of rats following normobaric hyperoxia and mild hypoxia. The cerebral tissue pO_2 was measured simultaneously in the cerebral cortex and striatum in the same rats before, during, and after normobaric hyperoxia and mild hypoxia challenges. The mean baseline tissue pO_2 values were not significantly different between the cortex and striatum. During 30 min of 100% O_2 inhalation, a statistically significant increase in tissue pO_2 of all four sites was observed, however, the tissue pO_2 of the striatum area was significantly higher than in the forelimb area of the cortex. Brain pO_2 significantly decreased from the baseline value during 15 min of 15% O_2 challenge. No differences in the recovery of the cerebral cortex and striatum pO_2 were observed when the rats were allowed to breathe 30% O_2. It appears that EPR oximetry using implantable resonators can provide information on pO_2 under the experimental conditions needed for such a study. The levels of pO_2 that occurred in these experiments are readily resolvable by multi-site EPR oximetry with multi-probe resonators. In addition, the ability to simultaneously measure the pO_2 in several areas of the brain provides important information that could potentially help differentiate the pO_2 changes that can occur due to global or local mechanisms.

9.1 Introduction

The cerebral tissue is the critical site for pO_2-dependent physiological and pathophysiological processes in the brain. Therefore, tissue pO_2 is the pertinent parameter for following these processes. In the past, surrogates had to be used for these values, such as the pO_2 available in the vascular system. Recently, more direct measurements

EPR Center for Viable Systems, Department of Diagnostic Radiology, Dartmouth Medical School, Hanover, NH 03755, USA
e-mail: huagang.hou@Dartmouth.edu

J.C. LaManna et al. (eds.), *Oxygen Transport to Tissue XXXII*, Advances in Experimental Medicine and Biology 701, DOI 10.1007/978-1-4419-7756-4_9,

have been made using oxygen electrodes. However, these methods have limitations due to the trauma associated with the introduction of the probe and are difficult to use for repeated pO_2 measurements. Electron paramagnetic resonance (EPR) oximetry has the potential to provide repeated non-invasive measurements of tissue pO_2 at specific sites. This methodology has been successfully used to study the effects of various anesthetics, a hemoglobin modifier, brain tumors, and ischemia/reperfusion on brain oxygenation [1-3]. With the recent development of multi-site capability using multi-probe implantable resonators, it is now possible to gain insight into tissue pO_2 in specific areas of the brain with excellent sensitivity and precise localization [4].

This paper summarizes the results obtained using four multi-probe implantable resonators in the brains of rats subjected to normobaric hyperoxia and mild hypoxia. We have also investigated the response of different regions of the brain to these challenges.

9.2 Materials and Methods

9.2.1 Multi-probe implantable resonators

Oxygen sensitive lithium phthalocyanine (LiPc) crystals and implantable resonators were synthesized and fabricated in our laboratory. The properties of LiPc have been reported earlier [5]. The resonator has two sets of loops, a larger loop on one end and four small loops on the other end. The large loop is used to couple inductively to the L-band EPR spectrometer. The small loops contain LiPc aggregates which are coated with a highly gas permeable biocompatible Teflon AF 2400® (Aldrich, Steinheim, Germany). The small loops are implanted in the sites of interest and the larger loop is placed on the skull below the skin for coupling with the external loop resonator of the EPR spectrometer. The high density of the unpaired spins, combined with a narrow intrinsic line width of embedded LiPc crystals, allows measurements of pO_2 in the brain with an area of $\sim$ 0.1-0.12 mm^2. Implantable resonators were calibrated before implantation into the brain and the EPR spectra reflect the average pO_2 on the surface of each probe. The response to oxygen of the probes (EPR line width as a function of pO_2) remained unchanged after implantation in the rats' brains, which allowed the monitoring of oxygen for several weeks [4].

9.2.2 Animal preparation

All animal procedures were conducted in strict accordance with the NIH Guide for the Care and Use of Laboratory Animals, and were approved by the Institutional Animal Care and Use Committee of Dartmouth Medical School.

Eleven male Sprague-Dawley rats, 250-330 g (Charles River Laboratories, Wilmington, MA) were used. One week prior to the pO_2 measurement, the rats were anesthetized with 2-2.5% isoflurane in 30% O_2 through a nose cone and 4-probe implantable resonators were placed directly into the brain at a depth of 3.0 and 5.5 mm from the surface of the skull, through 1.0 mm drill holes located 3.0 and 4.5 mm from the midline (left and right) and 0.5 mm behind the bregma (Figure 1).

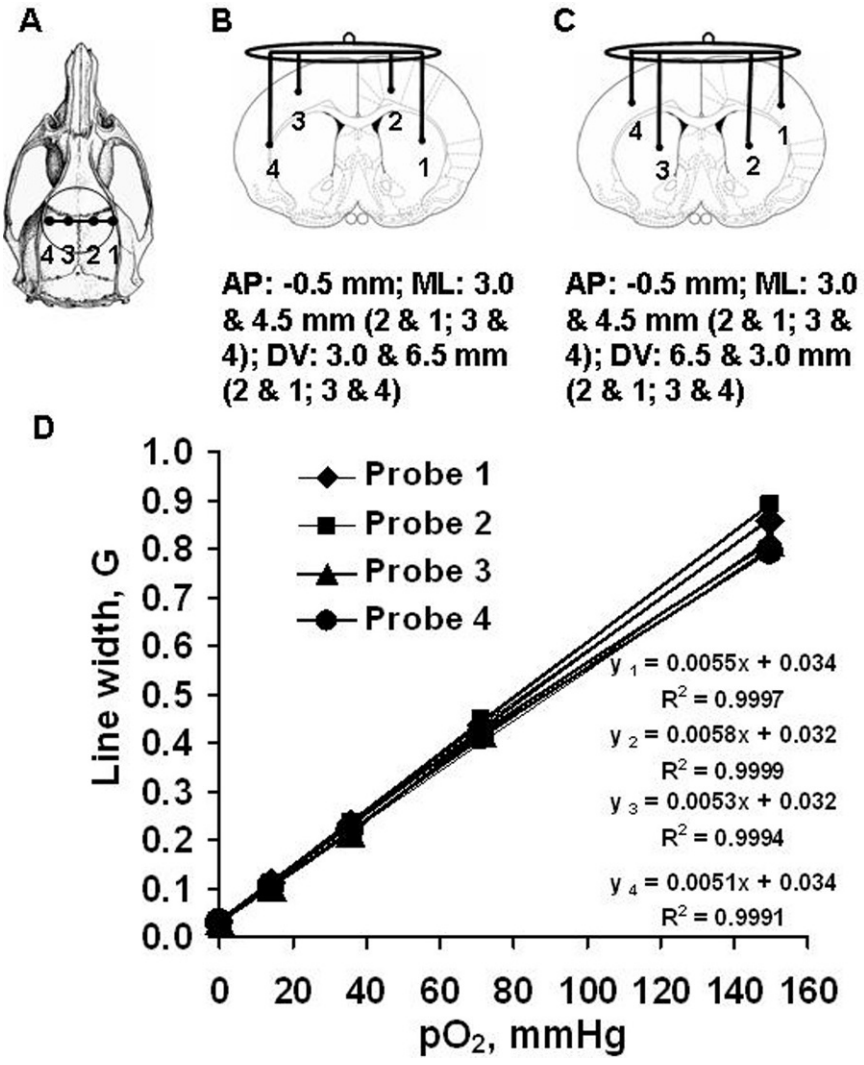

Fig. 9.1 (A) Axial view of the rat skull with trephination positions of the implantable resonator; (B) Schematic of cross-section of a rat brain showing the implantable resonator in the forelimb area of the cortex (probe 2 & 3) and striatum area (probe 1 & 4); (C) Parietal cortex area (probe 1 & 4) and striatum area (probe 2 & 3); and (D) Typical calibration curves of a 4-probe implantable resonator.

The study has two groups of rats: (1) forelimb area of the cortex (site 2 & 3) and striatum (site 1 & 4) on each hemisphere, n = 6; (2) the parietal cortex area (site 2 & 3) and striatum (site 1 & 4) on each hemisphere, n = 5. The rats were anesthetized with 1.5% isoflurane and 30% oxygen and a baseline pO_2 was measured for 30 min using multi-site EPR oximetry as described below. After the baseline pO_2 measurements, animals were subjected sequentially to normobaric hyperoxia (FiO_2 100% O_2 for 30 min), normoxia (FiO_2 30% O_2 for 25 min), mild hypoxia (FiO_2 15% O_2 for 15 min) and normoxia (FiO_2 30% O_2 for 20 min). During EPR measurements, the temperature of the animals was monitored using a rectal probe and maintained at 37±0.5˚C using a thermostatically-controlled heated pad and a flow of warm air.

9.2.3 Multi-site EPR oximetry

EPR oximetry was performed with an L-band (1.2 GHz) EPR spectrometer with an external loop resonator specifically designed for *in vivo* experiments [6]. The rat was placed between the poles of the EPR magnet and the head positioned under the extended loop resonator and adjusted to obtain the maximum signal from the implanted probe. A set of coils capable of generating a magnetic field gradient in the direction of the magnetic field with a magnitude of up to 3.0 G/cm was used to separate the EPR spectra from the probes of the implanted resonator [7]. Cerebral pO_2 was determined by measuring the peak-to-peak line widths of the EPR spectra, which was then converted to pO_2 by using appropriate calibration of the implantable resonator used in the study. The spectrometer parameters were: incident microwave power of 1-2 mW: modulation frequency 24 kHz, magnetic field 430 G, scan time 10 sec and modulation amplitude not exceeding one third of the peak-to-peak line width (typically 0.3-0.5 G).

9.2.4 Statistical analysis

Data were analyzed by Student's "T" test. A paired "T" test was used to compare 30% O_2 with the other interventions (100% O_2 and 15% O_2 inhalation) within the same group. Comparisons between the cerebral cortex and striatum in the same hemisphere at the same time point were made using Student's "T" test for unpaired samples. The tests were two-sided, and a change with a p-value < 0.05 was considered statistically significant. All data are expressed as mean ± SE, n is the number of animals used in each group.

9.3 Results

Several features of these results are pertinent for the purpose of this report, which is to demonstrate the feasibility of this technique. One important advantage of this new technique is the feasibility of carrying out oximetry at any depth. This considerably extends the application of EPR oximetry to almost any site where the resonator can

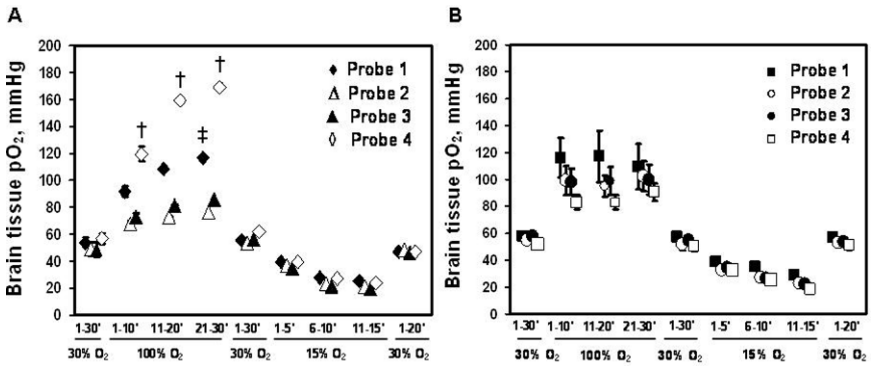

Fig. 9.2 The time course of mean brain tissue pO_2 (mean ± SE) measured by multi-site EPR oximetry with a 4-probe implantable resonator in rats during normobaric hyperoxia (100% O_2) and mild hypoxia (15% O_2) challenges. A: Group1; $n = 6$; B: Group 2; $n = 5$. ‡$p < 0.05$ compared with pO_2 in site 2; †$p < 0.05$ compared with pO_2 in site 3 (unpaired Student's "T" test).

be implanted. Secondly, the signal-to-noise ratios of the EPR spectra obtained with implantable resonators in the present study are significantly better than the spectra recorded from the LiPc crystals implanted directly at a similar, or even shallower depth, in the brain in previous studies [2, 3].

The average tissue pO_2 of the cerebral cortex and striatum are summarized in Figure 2. The baseline tissue pO_2 values of the cerebral cortex and striatum are in the expected range, and were similar and stable during the baseline measurements. During the 30 min of 100% O_2 inhalation, a statistically significant increase in the pO_2 of the four sites was observed ($p < 0.05$), but the responses of the cerebral cortex and striatum to this challenge were different. The tissue pO_2 was significantly higher in the striatum area than in the forelimb area of the cortex ($p < 0.05$). The tissue pO_2 of the four sites decreased significantly from baseline during 15 min of mild hypoxia ($p < 0.05$ and $p < 0.01$). The tissue pO_2 recovered in a similar manner in the cerebral cortex and striatum when the rats were allowed to breathe 30% O_2.

9.4 Discussion

Multi-site EPR oximetry with multi-probe implantable resonators make it feasible to measure acute changes of the pO_2 at several sites of the brain simultaneously and repeatedly over the entire experimental period. Furthermore, due to the immediate response of the LiPc embedded in the sensor loops to changes in pO_2, this approach could potentially be used to measure the dynamics of pO_2 changes over time .[4]. Spatial resolution between sites in the range of 1.5 mm (site 1 and site 2; site 3 and site 4, Figure 1 B and C) can easily be achieved by applying minimal gradient power without significant distortion of the EPR signals. This is a particularly useful feature of multi-site EPR oximetry because the measurement from one region can be used as

an internal control while the signals from other regions in the same or contralateral hemisphere could be monitored as indicators of the experimental procedures.

As summarized in Figure 2, the pO_2 values at the four different sites in brain were stable over 30 min of baseline measurements and are similar to our recently reported values [4], but are higher than those reported earlier [2, 3]. This is likely due to the differences in breathing (ventilated vs. spontaneous procedure), level of FiO_2, PaO_2 and the concentration of anesthetics used in these studies. A significant difference in pO_2 between the forelimb area of the cortex and striatum during normobaric hyperoxia challenge in group 1, may reflect anatomical differences, possibly accentuated by the differences in response of blood flow in these two areas under 30% O_2 and 100% O_2 inhalation. Further studies are needed to assess the effect of normobaric hyperoxia on blood flow between the forelimb area of the cortex and striatum. There are some technical aspects and precautions necessary in using this approach. Due to some variation in the calibration observed at higher oxygen concentrations (Figure 1D), it is advised to calibrate each resonator before it is implanted, so that the EPR line width recorded from each probe (site) could be converted to pO_2 by using its own calibration. In addition, it is essential that the multi-probe implantable resonators are implanted into tissue a few days in advance of the experiments to allow any tissue damage to heal that might occur due to the implantation of the probes.

In conclusion, the present results suggest that 1) normobaric hyperoxia and mild hypoxia significantly enhances and decreases cerebral oxygenation, respectively, 2) the responses of the forelimb area of the cortex and striatum to normobaric hyperoxia are different, and 3) the ability to simultaneously measure the pO_2 in several areas of the brain provides a unique possibility to investigate pO_2 changes at different sites that might occur due to global or local mechanisms.

Acknowledgments

This work was supported by NIH grants PO1EB2180, and used the facilities of the EPR Center for Viable Systems (P41EB002032).

References

1. Hou, H., Grinberg, O, Williams, B, Grinberg, S, Yu, H, Alvarenga, DL, Wallach, H, Buckey, J, Swartz, HM. (2007) Effect of oxygen therapy on brain damage and cerebral pO2 in transient focal cerebral ischemia in the rat. . Physiol Meas 28:963-76
2. Hou, H., Grinberg, O.Y., Grinberg, S.A., et al. (2005) Cerebral tissue oxygenation in reversible focal ischemia in rats: multi-site EPR oximetry measurements. Physiol Meas 26:131-41
3. Hou, H., Khan, N., O'Hara, J.A., et al. (2005) Increased oxygenation of intracranial tumors by efaproxyn (efaproxiral), an allosteric hemoglobin modifier: In vivo EPR oximetry study. Int J Radiat Oncol Biol Phys 61:1503-9
4. Li, H., Hou, H., Sucheta, A., et al. (2010) Implantable resonators - a technique for repeated measurements of oxygen at multiple deep sites with in vivo EPR Adv Exp Med Biol 662:265-72

5. Liu, K., Gast P, and Moussavi, M. (1993) Lithium phthalocyanine: A probe for electron paramagnetic resonance oximetry in viable biological systems. Proc Natl Acad Sci USA 90:5438-42
6. Swartz, H.M., Clarkson, R.B. . (1998) The measurement of oxygen in vivo using EPR techniques. . Physics in Medicine & Biology 43:1957-75
7. Smirnov, A.I., Norby, S.W., Clarkson, R.B., et al. (1993) Simultaneous multi-site EPR spectroscopy in vivo. Magn Reson Med 30:213-20

Chapter 10
^{31}P-MRS Studies of Melanoma Xenografts with Different Metastatic Potential

Lin Z. Li, Rong Zhou, Dennis B. Leeper, and Jerry D. Glickson

Abstract Previously we reported that three imaging methods, dynamic contrast enhanced magnetic resonance imaging (DCE-MRI), $T_{1\rho}$-MRI, and ultralow temperature NADH/flavoprotein fluorescence imaging (redox scanning), could differentiate the less metastatic human melanoma cell line A375P from a more metastatic line C8161 growing as mouse xenografts in nude mice (Li LZ *et al.* Adv. Exp. Med. Biol., 2007, 599:67-78; PNAS, 2009, 106:6608-6613). The more metastatic C8161 tumor was characterized by less blood perfusion/permeability, a more oxidized mitochondrial redox state in the tumor core, and a smaller $T_{1\rho}$ relaxation time constant averaged across the entire tumor section. In the current study, we have further probed the bioenergetic status and tissue microenvironment of these tumors by applying whole tumor phosphorous magnetic resonance spectroscopy (^{31}P-MRS) to these two xenografts in a vertical bore 9.4-T Varian magnet. The phosphomonoester (PME)/βNTP ratio and intracellular pH value (pH_i) were determined. The phosphomonoester (PME)/βNTP was higher in the more metastatic C8161 tumors (n=4) than in the less metastatic A375P tumors (n=4) ($p < 0.1$). No significant difference between the pH_i of C8161 and A375P was observed.

10.1 Introduction

Identification of imaging biomarkers of tumor metastatic potential would facilitate treatment planning and aid in the design of agents that modify the tumor phenotype.

Lin Z. Li, Rong Zhou, and Jerry D. Glickson
Department of Radiology, School of Medicine, University of Pennsylvania, Philadelphia, PA19104, USA
e-mail: linli@mail.med.upenn.edu

Dennis B. Leeper
Department of Radiation Oncology, School of Medicine, Thomas Jefferson University, Philadelphia, PA 19107, USA

J.C. LaManna et al. (eds.), *Oxygen Transport to Tissue XXXII*, Advances in Experimental Medicine and Biology 701, DOI 10.1007/978-1-4419-7756-4_10,

For this purpose, we have used MRI and optical imaging to compare xenografts in athymic nude mice of the most metastatic melanoma cell line (C8161) and the least metastatic cell line (A375P) in a panel of five human melanoma cell lines obtained from Dr. Mary Hendrix at Northwestern University. Three lines exhibiting intermediate levels of aggressiveness (A375M, A375P10, A375P5) were included in some of the optical and $T_{1\rho}$-MRI experiments. DCE-MRI, $T_{1\rho}$-MRI, and mitochondrial redox imaging (ultralow temperature NADH/flavoprotein fluorescence imaging) provided sensitive imaging biomarkers for differentiation of the two extreme phenotypes, i.e., most metastatic C8161 versus least metastatic A375P [1, 2]. In particular, the mitochondrial redox ratio (Fp/(Fp+NADH)) reflected the relative aggressiveness of all five human melanoma cell lines based on their *in vitro* ability to penetrate a Matrigel barrier in a Boyden chamber and the number of lung metastases measured *in vivo*. These data support the conclusion that the tumor microenvironment, including blood perfusion, oxygen/nutrition supply, as well as mitochondrial bioenergetic status of cancer cells, plays a key role in cancer progression to metastasis, which has also been supported by a number of studies in the literature [3-7]. The mitochondrion is the cellular power plant that generates ATP, the major high-energy fuel that drives many physiological processes including lipid metabolism and biosynthesis. Abnormalities in metabolic states and lipid metabolism have been associated with cancer progression to metastasis.

^{31}P-MRS, which measures the relative levels of Pi (inorganic phosphate), NTP (nucleoside tri-phosphate) and phospholipid metabolites such as PCr (phosphocreatine), PME (phosphomonester) and PDE (phosphodiester), is useful for cancer diagnosis and prediction of treatment response in animal models and patients. For example, in patients with soft tissue sarcomas both PME/Pi and PDE/Pi ratios correlated inversely with the rate of pathological complete response, and the pretreatment PDE/PME ratio correlated directly with metastasis-free survival and overall survival [7]. In addition, ^{31}P-MRS measures intracellular pH on the basis of the relative chemical shift of inorganic phosphate referenced to α-NTP or PCr [8, 9].

The goal of the present study is to identify potential ^{31}P-MRS biomarkers of human melanoma metastatic potential. Our hypothesis is that the two human melanoma mouse xenografts (A375P and C8161), with widely different metastatic potential, will exhibit distinct differences that can be detected by ^{31}P-MRS. Our data demonstrate that the PME/βNTP ratio can differentiate between these two tumor models ($p < 0.1$) while intracellular pH can not.

10.2 Materials and Methods

Melanoma cells (2×10^6) were subcutaneously implanted on the back, shoulders or in the thighs of 7-9 week old male athymic nude mice (NCI strain NCr-nu/nu). After 1-2 months, the tumors reached approximately 7-18 mm in the longest dimension, and the volumes ranged from 0.16 to 1.0 cm^3, calculated by the tumor length L, width W and height H as measured by the calliper, i.e., Vol$= 1/6\pi$ L$\times$W$\times$H. These tumors

were then examined by ^{31}P-MRS in a vertical bore (89 mm) 9.4-T Varian NMR spectrometer. The mice were maintained under anaesthesia with 1% isofluorane in oxygen delivered through a nose cone. ^{31}P-MR spectra of two A375P and four C8161 tumors were obtained with a radiofrequency slotted tube resonator (diameter ~13 mm) double-tuned to ^{1}H and ^{31}P. The phosphorous spectra of another two A375P tumors were obtained using a surface coil (diameter ~8 mm) also double-tuned to ^{1}H and ^{31}P to improve signal sensitivity for relatively smaller tumors. The magnetic field inhomogeneity was below 0.5 ppm following shimming on the proton signals. ^{31}P-MR spectra were acquired with a single pulse excitation with a TR (time of repetition) of 2 s and a bandwidth of 8000 Hz. Depending on the signal to noise ratio (SNR), the number of excitations ranged from 256-1028. The chemical shifts and relative intensities (peak areas) of PME, Pi, PCr, γNTP, αNTP, βNTP peaks were determined with NMR spectrum analysis software (NUTS) following proper phase adjustment and baseline correction. The intracellular pH values, pH_i, were quantified based on the shift of the Pi peak from the PCr peak using the Henderson-Hasselbalch equation.

10.3 Results and Discussion

Figure 1 shows typical phosphorous NMR spectra obtained for a C8161 and an A375P tumor. PME, Pi, PCr, γNTP, αNTP, βNTP peaks were clearly discernable in the spectra. Although field inhomogeneity could have been further improved by single voxel shimming to better resolve phosphorous peaks, we did not attempt to do this because significant tissue heterogeneity observed by MRI in the aggressive tumors [1] would keep the ^{31}P-MR peaks broad even with single voxel shimming. Table 1 includes means and standard deviations of the pH_i, the PME/βNTP ratio, and the volume for the two melanomas (n=4 for each).

There was no statistically significant difference in the tumor volume between the two lines ($p > 0.1$). The average PME/βNTP ratio was 0.9 ± 0.4 and 2.6 ± 1.4 for A375P melanoma and C8161 melanoma, respectively. The difference between the two lines had a moderate statistical significance ($p < 0.1$). Although more mice are needed to establish greater significance, the trend to higher PME/βNTP ratios in the more aggressive C8161 tumors is in agreement with previous clinical [10] and non-Hodgkin's lymphoma patients evaluated by Arias-Mendoza *et al.* [11], which showed that these ratios increased with tumor grade.

The average pH_i of the more metastatic C8161 melanoma was less than that of the less metastatic A375P melanoma by about 0.2 pH units, which corresponds to a factor of 60% higher H^+ concentration in the more aggressive tumor. An acidic tissue microenvironment has been linked to malignancy and is believed to be one of the driving forces for cancer progression to metastasis [12-14]. However, the difference observed between the two lines here was not statistically significant. This could be due to the small number of tumors and/or possibly to contamination of NMR signals from muscles since the ^{31}P-MRS method used here was not volume selective. Still,

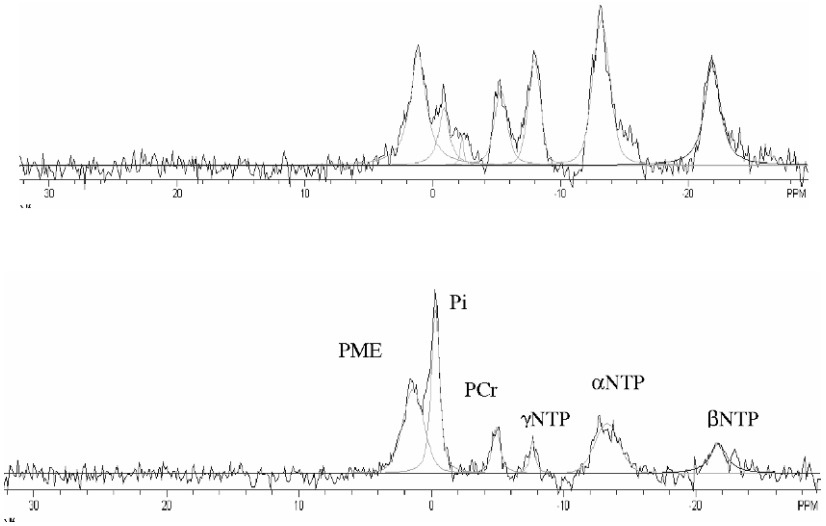

Fig. 10.1 Typical ^{31}P-MRS spectra of an A375P (upper panel) and a C8161 tumor (lower panel). PME: phosphomonoester, Pi: phosphate; PCr: phosphocreatine; NTP: nucleotide triphosphate.

this lack of significant difference could be explained by the fact that tumor acidity mainly exists in the extracellular space, and the pH measured on the basis of ^{31}P-MRS may mainly result from the contribution from the intracellular space. It is known that the pH in the extracellular space (6.3∼7.0) of tumors in animal models is maintained acidic relative to the pH in the intracellular space (6.9∼7.4), whereas, this pH gradient is reversed in normal tissues [14]. In the future, an extracellular pH indicator 3-aminopropylphosphonate (3-APP) will be injected to measure the extracellular pH by ^{31}P-MRS in order to test differences in the extracellular pH between these two melanoma xenografts.

Table 10.1 Mean ± standard deviation of the tumor volume, PME/βNTP and pH_i in two melanoma lines differing in metastatic potential.

	Volume (cm^3)	PME/βNTP	pHi
A375P (n=4)	0.37±0.05	0.90±0.36	7.22±0.36
C8161 (n=4)	0.63±0.35	2.65±1.41	7.01±0.21
t-test p value	0.2	0.09	0.4

One shortcoming of this preliminary study is that ^{31}P-MRS was conducted without volume selection. It is possible to have signal contamination from non-tumor tissues for relatively small tumors; although the contamination should be small and negligible for rather large tumors since the effective coil space for signal acquisition will be mainly filled up by tumor tissues.

In summary, this study has shown that ^{31}P-MRS should be able to differentiate between the metastatic and the indolent human melanoma mouse xenografts. In the

future, volume selective ^{31}P-MRS with 3-APP can be used to probe the difference between tumors with different metastatic potential. The pH imaging using MR contrast agents could also be utilized to investigate the pH heterogeneity in tumor tissues [14].

Acknowledgement

The authors thank Dr. Mary Hendrix and Dr. Elisabeth Seftor at Northwestern University for providing melanoma cell lines. This study is supported in part by NIH Grant P01-CA56690-08 & 08S1 (PI: D.B. Leeper, Project Leader: J.D. Glickson) and P50-CA093372-04 (PI: M. Herlyn).

References

1. Li, L.Z., et al Predicting melanoma metastatic potential by optical and magnetic resonance imaging. Adv Exp Med Biol, 2007. **599**: p. 67-78.
2. Li, L.Z., et al Quantitative magnetic resonance and optical imaging biomarkers of melanoma metastatic potential. Proceedings of the National Academy of Sciences of the United States of America, 2009. **106**(16): p. 6608-6613.
3. Rofstad, E.K. Microenvironment-induced cancer metastasis. Int J Radiat Biol, 2000. **76**(5): p. 589-605.
4. Subarsky, P. and R.P. Hill The hypoxic tumour microenvironment and metastatic progression. Clin Exp Metastasis, 2003. **20**(3): p. 237-250.
5. Gillies, R.J., et al MRI of the tumor microenvironment. J Magn Reson Imaging, 2002. **16**(4): p. 430-450.
6. Vaupel, P. and A. Mayer Hypoxia in cancer: significance and impact on clinical outcome. Cancer and Metastasis Reviews, 2007. **26**(2): p. 225-239.
7. Dewhirst, M.W., et al Relation between pO(2), P-31 magnetic resonance spectroscopy parameters and treatment outcome in patients with high-grade soft tissue sarcomas treated with thermoradiotherapy. International Journal of Radiation Oncology Biology Physics, 2005. **61**(2): p. 480-491.
8. Bhujwalla, Z.M., et al Estimations of intra- and extracellular volume and pH by P-31 magnetic resonance spectroscopy: effect of therapy on RIF-1 tumours. British Journal of Cancer, 1998. **78**(5): p. 606-611.
9. Zhou, R., et al Intracellular acidification of human melanoma xenografts by the respiratory inhibitor m-iodobenzylguanidine plus hyperglycemia: A P-31 magnetic resonance spectroscopy study. Cancer Research, 2000. **60**(13): p. 3532-3536.
10. Shukla-Dave, A., et al Prediction of treatment response of head and neck cancers with P-31 MR spectroscopy from pretreatment relative phosphomonoester levels. Academic Radiology, 2002. **9**(6): p. 688-694.
11. Arias-Mendoza, F., M.R. Smith, and T.R. Brown, Predicting treatment response in non-Hodgkin's lymphoma from the pretreatment tumor content of phosphoethanolamine plus phosphocholine. Academic Radiology, 2004. **11**(4): p. 368-376.
12. Gatenby, R.A. and R.J. Gillies Why do cancers have high aerobic glycolysis? Nature Reviews Cancer, 2004. **4**(11): p. 891-899.
13. Gatenby, R.A., et al Acid-mediated tumor invasion: a multidisciplinary study. Cancer Research, 2006. **66**(10): p. 5216-5223.
14. Gillies, R.J., et al PH imaging. IEEE Engineering in Medicine and Biology Magazine, 2004. **23**(5): p. 57-64.

Chapter 11
Modulation of Tumor Hypoxia by Topical Formulations with Vasodilators for Enhancing Therapy

Zrinka Abramovic, Huagang Hou, Kristl Julijana, Marjeta Sentjurc, Jean P. Lariviere, Harold M. Swartz, and Nadeem Khan

Abstract Tumor hypoxia is a well known therapeutic problem which contributes to radioresistance and aggressive tumor characteristics. Lack of techniques for repeated measurements of tumor oxygenation (pO_2, partial pressure of oxygen) has restricted the optimization of hypoxia modifying methods and their efficacious application with radiotherapy. We have investigated a non-invasive method to enhance tissue pO_2 of peripheral tumors using topical application of formulations with BN (Benzyl Nicotinate), a vasodilator, and have used EPR (Electron Paramagnetic Resonance) oximetry to follow its effect on tumor oxygenation.

We incorporated 2.5% BN in both hydrogel and microemulsions and investigated the effects on pO_2 of subcutaneous RIF-1 (Radiation Induced Fibrosarcoma) tumors in C3H mice. The experiments were repeated for five consecutive days. The topical application of BN in hydrogel led to a significant increase from a pre-treatment pO_2 of 9.3 mmHg to 11 - 16 mmHg at 30 - 50 min on day 1. However, the magnitude and the time of significant increase in pO_2 decreased with repeated topical applications. The BN in a microemulsion resulted in a significant increase from a baseline pO_2 of 8.8 mmHg to 13 - 18 mmHg at 10 - 50 min on day 1. Experiments repeated on subsequent days showed a decline in the magnitude of pO_2 increase on repeated applications. No significant change in tumor pO_2 was observed in experiments with formulations without BN (vehicle only).

EPR oximetry was successfully used to follow the temporal changes in tumor pO_2 during repeated applications for five consecutive days. This approach can be potentially used to enhance radiotherapeutic outcome by scheduling radiation doses when an increase in tumor pO_2 is observed after topical applications of BN formulations.

Zrinka Abramovic, Kristl Julijana, and Marjeta Sentjurc
Jozef Stefan Institute, Laboratory of Biophysics, Jamova 39, 1000 Ljubljana, Slovenia
e-mail: nadeem@dartmouth.edu

Huagang Hou, Jean P. Lariviere, Harold M. Swartz, and Nadeem Khan
EPR Center for Viable Systems, Department of Diagnostic Radiology, Dartmouth Medical School, Hanover, NH 03755 and Norris Cotton Cancer Center, Dartmouth Hitchcock Medical Center, Lebanon, NH 03756, USA

J.C. LaManna et al. (eds.), *Oxygen Transport to Tissue XXXII*, Advances in Experimental Medicine and Biology 701, DOI 10.1007/978-1-4419-7756-4_11,

11.1 Introduction

Hypoxia influences treatment outcome not only through treatment resistance, but also by promoting more aggressive tumor behaviors [1, 2]. As a result, several new treatment strategies to improve tumor oxygenation are being investigated to improve the efficacy of therapeutic modalities; these include systemic application of blood flow modifying agents, drugs that can change oxygen consumption, and by increasing the oxygen content in the breathing gas such as by using carbogen (95% O_2 + 5% CO_2) [3-5].

We believe that the measurement of tumor pO_2 during such treatments could be used as a guide to optimize these methods and this information could be used to schedule therapies to enhance therapeutic outcome. Some very useful information has been obtained by invasive methods (e.g., the polarographic oxygen electrode, or a luminescence optical sensor based on oxygen-quenching) even though they can not be repeated frequently or indirectly by monitoring oxygen availability in the circulatory system (NIR spectroscopy and NMR methods) [6, 7]. With the recent development of *in vivo* EPR oximetry, it is now possible to obtain accurate and repetitive measures of tissue oxygen from the same locations in the tissue [8, 9]. After initial insertion of the paramagnetic oxygen-sensitive probe into the tissue, the oximetry measurements are completely non-invasive and can be performed repeatedly for longer periods of time (days, weeks and even years) [8].

We have focused on the development of formulations that could be applied topically on peripheral tumors to enhance tumor oxygenation. We report the effect of the formulations prepared by using a vasoactive compound, Benzyl Nicotinate (BN), on tissue pO_2 of subcutaneously grown RIF-1 tumors using EPR oximetry. The BN was incorporated in two different delivery systems (i) a hydrogel formulation and (ii) a water-in-oil microemulsion, and the changes in tumor pO_2 were followed with repeated applications of the BN formulations for five consecutive days.

11.2 Materials and Methods

11.2.1 Animals and tumor models

All animal procedures were conducted in strict accordance with the NIH Guide for the Care and Use of Laboratory Animals and were approved by the Institutional Animal Care and Use Committee of Dartmouth Medical School. The radiation-induced fibrosarcoma (RIF-1) cells were provided by Dr. J. B. Mitchell, National Cancer Institute. The cells were cultured in RPMI 1640 medium supplemented with 10 % FBS, and antibiotics. The procedure for tumor inoculation in female C3H mice (Charles River Laboratories, MA), and the methods to prepare the BN formulations have been reported previously [4, 10, 11].

11.2.2 Experiment design

The mice were divided into 4 groups: (i) BN-Hydrogel (n = 7) (ii) Hydrogel alone (n = 7) (iii) BN in the microemulsion (BN-ME) (n = 8) and (iv) the microemulsion (ME) alone (n = 5). The mice were anesthetized with 1.5 % isoflurane and 100% oxygen delivered through a nose cone, and a baseline (pre-treatment) tumor pO_2 was measured for 25 min using EPR oximetry described below. After baseline pO_2 measurements, a 0.2 ml of the formulation was gently applied on the tumor for 1 min without moving the mouse from the spectrometer, and the pO_2 measurements were continued for 60 min to determine the effect of the BN formulations on tumor pO_2. The experiments were repeated for five consecutive days. In the control group, the formulations without BN (i.e., hydrogel alone or microemulsion alone) were applied and the same protocol was followed.

11.2.3 EPR oximetry

EPR oximetry was performed with an L-band (1.2 GHz) EPR spectrometer equipped with an external loop resonator specifically designed for *in vivo* experiments [8, 9]. The lithium phthalocyanine (LiPc) crystals used for pO_2 measurements were synthesized in our laboratory; its physicochemical properties and use for measuring tissue pO_2 have been described previously [12]. Once the tumors reached a volume of 70 - 90 mm^3, the LiPc (40 μg) crystals were loaded in 25 gauge needles and injected into the tumors at a depth of 1 - 2 mm from the surface. The EPR spectra obtained from these deposits reflect the average partial pressure of oxygen on the surface of the crystals. Tumor pO_2 was determined by measuring the peak-to-peak line-widths of the EPR spectra, which was then converted to pO_2 by using appropriate calibrations for the LiPc crystals used in this study.

For pO_2 measurements, the anesthetized mice (1.5% Isoflurane, 100% O_2) were placed between the poles of the EPR magnet and the resonator loop was placed gently over the tumor. The spectrometer parameters were: incident microwave power of 4 - 6 mW: modulation frequency 27 kHz; magnetic field 430 G; scan time 10 sec (usually 6 scans were averaged to increase signal to noise ratio), and modulation amplitude not exceeding one third of the peak-to-peak line-width (typically 0.02 - 0.05 G). During EPR measurements, the temperature of the animals was monitored using a rectal probe and maintained at $37 \pm 0.5^{\circ}C$ using a thermostatically controlled heated pad and a flow of warm air.

11.2.4 Data analysis

The baseline tumor pO_2 was averaged for 25 min (shown at time 0) and the pO_2 data obtained after topical application of the formulations were averaged for 10 min each

to assess temporal changes in tumor pO_2. A paired t-test was used to determine the statistical significance of the changes in pO_2 within the group. The tests were two-sided, and a change with a p value < 0.05 was considered statistically significant. All data are expressed as mean $\pm$ SE; n is the number of animals in each group.

11.3 Results

11.3.1 Effect of the BN in hydrogel formulation on RIF-1 tumor pO_2

The RIF-1 tumors were hypoxic with a baseline pO_2 of 9.3 ± 0.8 mmHg and tumor volume of 71 ± 6 mm^3 on day 1, Figure 1. The tumor pO_2 increased significantly to 11 ± 2 mmHg at 30 min after topical application of BN in hydrogel, and the pO_2 remained at a significantly higher level during 60 min of measurements. Experiments repeated on day 2 led to a significant increase in pO_2 at 20 - 30 min only. Similar results were obtained on days 3 - 5, but the magnitude and the time of a significant increase in tumor pO_2 declined over days. The baseline tumor pO_2 in the hydrogel alone group was 9.5 ± 0.8 mmHg, and no significant increase in tumor pO_2 was observed after topical application of hydrogel alone, Figure 2.

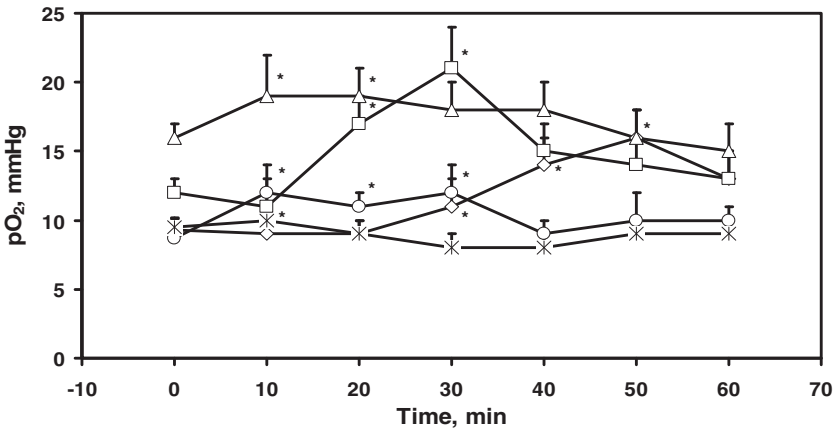

Fig. 11.1 Tissue pO_2 of RIF-1 tumors measured before (time = 0 min) and after the topical applications of the BN formulation in hydrogel. ◇ day 1; day 2; day 3; day 4; ? day 5. *p < 0.05 compared with baseline pO_2, mean + SE, n = 7.

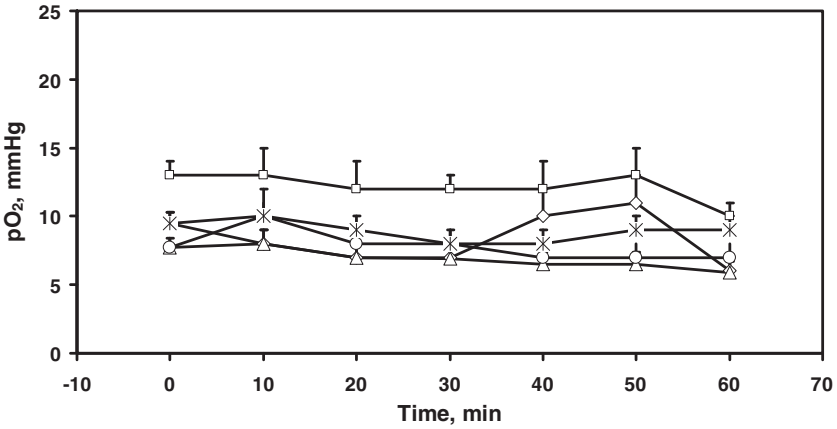

Fig. 11.2 Tissue pO_2 of RIF-1 tumors measured before (time = 0 min) and after the topical applications of the hydrogel alone (control group). ◇ day 1; day 2; day 3; day 4; ? day 5. *$p < 0.05$ compared with baseline pO_2, mean + SE, n = 7.

11.3.2 Effect of the BN in microemulsion formulation on RIF-1 tumor pO_2

The RIF-1 tumors were hypoxic with a baseline pO_2 of 8.8 ± 0.3 mmHg and tumor volume of 80 ± 8 mm^3 on day 1. The tumor pO_2 increased significantly within 10 min after topical application of the BN formulation, Figure 3. A maximal increase in tumor pO_2 to 18.5 ± 0.9 mmHg was observed at 20 min, and the tumors remained at a significantly oxygenated level during 60 min of measurements. Experiments repeated on day 2 also resulted in a significant increase in tumor pO_2, which declined after 30 min of topical application. Similar results were obtained on day 3 and day 4, but no significant increase in tumor pO_2 was observed on day 5. The baseline tumor pO_2 of the control group was 8.2 ± 0.7 mmHg on day 1, and no significant increase was observed after the topical application of microemulsion alone during 5 days of experiments, Figure 4.

11.4 Discussion

The goal of this study was to enhance tissue oxygenation of peripheral tumors by an innovative approach, i.e., by topical application of a vasoactive compound onto the tumors. The topical application of drugs has many potential advantages including high patient compliance, sustained and controlled delivery over time as desired, and less toxicity as compared to systemic treatments. Benzyl Nicotinate was selected as a vasoactive drug on the basis of its lipophilicity which makes it a good can-

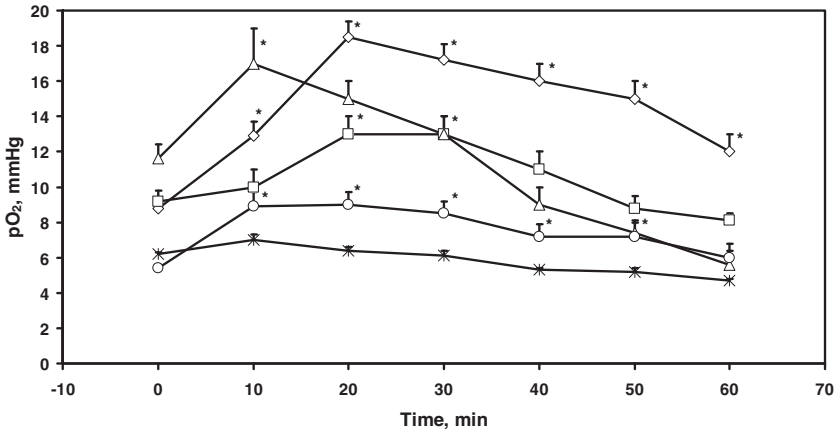

Fig. 11.3 Tissue pO_2 of RIF-1 tumors measured before (time = 0 min) and after the topical applications of the BN formulation in microemulsion. ◇ day 1; day 2; day 3; day 4; ? day 5. *$p < 0.05$ compared with baseline pO_2, mean + SE, n = 8.

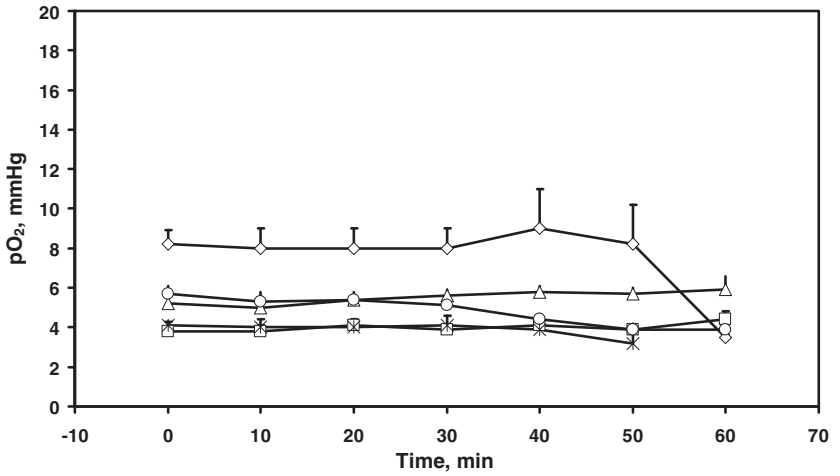

Fig. 11.4 Tissue pO_2 of RIF-1 tumors measured before (time = 0 min) and after the topical applications of the microemulsion alone (control group). ◇ day 1; day 2; day 3; day 4; ? day 5. *$p < 0.05$ compared with baseline pO_2, mean + SE, n = 5.

didate for skin penetration. Enzymatic hydrolysis of BN results in nicotinic acid, which increases cutaneous blood flow locally and, as a consequence, increases tissue oxygenation [10, 11].

The results indicate a significant increase in tumor pO_2 after BN application in both of the formulations tested. The magnitude and the time of maximal increase in tumor pO_2 declined over days, and by day 5, little or no change was observed. In the

control groups (formulations without BN), no increase in tumor pO_2 was observed as compared to the baseline pO_2, which confirms that the increase in tumor pO_2 is likely due to the vasodilating effect of Benzyl Nicotinate. However, a variation in the baseline tumor pO_2 over days was observed in these experiments. A significant increase in the skin pO_2 of Balb C mice after a topical application of 2.5% BN incorporated in hydrogel or microemulsion was reported by Abramovic et al. [10]. The magnitude of an increase in skin pO_2 was relatively higher then that observed with RIF-1 tumors in this study. These differences in response are likely due to a better vascularization of healthy skin dermis and subcutis compared to hypoxic RIF-1 tumors. An increase in the pre-treatment skin pO_2 of Balb C mice on each day and a subsequent increase in skin pO_2 during repeated applications of liposome-entrapped BN were observed by Kristl et al [11]. However, the magnitude of an increase in skin pO_2 varied over days with a maximal increase on day 3 followed by a decline on subsequent days. A decrease in the effect of repeated BN applications on tumor pO_2 is likely due to several factors. We speculate that a saturation of the enzymes that hydrolyze BN to active nicotinic acid has occurred during repeated applications. It is also likely that with tumor growth, an increase in the depth of the oximetry probes from the surface occurred, resulting in a lack of sensitivity to vasodilation by BN formulation.

We plan to carry out a systematic study to determine the effect of different anesthetics, breathing gases and the factors that lead to the variations in an increase in tumor pO_2 observed during repeated applications of BN formulation. Nevertheless, the increase in tumor pO_2 observed in this study potentially could be used to enhance the radiotherapeutic outcome of peripheral tumors if irradiated at the time of a significant increase in tumor pO_2 observed after the topical application of BN formulations.

In conclusion, these results provide temporal information on the effectiveness of BN formulations in enhancing tumor oxygenation and the potential of EPR oximetry to monitor these changes repeatedly during such treatments. Further modifications are being carried out to optimize these formulations for their potential application with radiotherapy to improve radiotherapeutic outcome.

Acknowledgments

NIH grants CA118069 and CA120919 to NK, and P01EB2180 to HMS.

References

1. Overgaard, J. (2007) Hypoxic radiosensitization: adored and ignored. J Clin Oncol 25:4066-74
2. Vaupel, P. (2008) Hypoxia and aggressive tumor phenotype: implications for therapy and prognosis. Oncologist 13 Suppl 3:21-6

3. Bache, M., Kappler, M., Said, H.M., et al (2008) Detection and specific targeting of hypoxic regions within solid tumors: current preclinical and clinical strategies. Curr Med Chem 15:322-38
4. Hou, H., Khan, N., Grinberg, O.Y., et al (2007) The effects of Efaproxyn (efaproxiral) on subcutaneous RIF-1 tumor oxygenation and enhancement of radiotherapy-mediated inhibition of tumor growth in mice. Radiat Res 168:218-25
5. Wardman, P. (2007) Chemical radiosensitizers for use in radiotherapy. Clin Oncol (R Coll Radiol) 19:397-417
6. Padhani, A.R., Krohn, K.A., Lewis, J.S., et al (2007) Imaging oxygenation of human tumours. Eur Radiol 17:861-72
7. Vikram, D.S., Zweier, J.L., and Kuppusamy, P. (2007) Methods for noninvasive imaging of tissue hypoxia. Antioxid Redox Signal 9:1745-56
8. Khan, N., Williams, B.B., Hou, H., et al (2007) Repetitive tissue pO_2 measurements by electron paramagnetic resonance oximetry: current status and future potential for experimental and clinical studies. Antioxid Redox Signal 9:1169-82
9. Swartz, H.M. and Clarkson, R.B. (1998) The measurement of oxygen *in vivo* using EPR techniques. Phys Med Biol 43:1957-75
10. Abramovic, Z., Sustarsic, U., Teskac, K., et al (2008) Influence of nanosized delivery systems with benzyl nicotinate and penetration enhancers on skin oxygenation. Int J Pharm 359:220-7
11. Kristl, J., Abramovic, Z., and Sentjurc, M. (2003) Skin oxygenation after topical application of liposome-entrapped benzyl nicotinate as measured by EPR oximetry *in vivo*: influence of composition and size. AAPS PharmSci 5:E2
12. Liu, K.J., Gast, P., Moussavi, M., et al (1993) Lithium phthalocyanine: a probe for electron paramagnetic resonance oximetry in viable biological systems. Proc Natl Acad Sci USA 90:5438-42

Part III
Blood and Blood Substitutes

Chapter 12
MP4, a Vasodilatory PEGylated Hemoglobin

Russell H. Cole and Kim D. Vandegriff

Abstract A vasodilatory hemoglobin (Hb)-based O_2 carrier (HBOC) has been developed by surface conjugation polyethylene glycol to tetrameric human Hb (MP4, Sangart, San Diego). Because the NO-binding kinetics of MP4 are similar to vasoconstrictive HBOCs, we propose that the decoupling of NO scavenging from vascular response is a consequence of MP4's high O_2 affinity ($p50 = 5$ mmHg) and unique surface chemistry. The release of ATP from erythrocytes is vasodilatory and the application of a high O_2 affinity HBOC minimizes ATP interference with intravascular ATP signaling. [1] A second potential mechanism of action for MP4 involves the surface conjugation of polyethylene glycol (PEG) to tetrameric human Hb. It has been shown that the addition of unconjugated high molecular weight (M_w) PEG to cultured lung endothelial cells causes an immediate and significant reduction in endothelial permeability; an effect opposite to that of endothelial agonists such as cell-free Hb. [2] It appears that some of the benefits of the PEG-endothelium interaction are carried onto molecules such as PEGylated Hb and PEGylated albumin, as demonstrated by favorable hemodynamic responses *in vivo*. PEGylation of $\beta 93$ cysteine residues, as in MP4, has also been reported to increase the nitrite reductase activity of Hb and enhance conversion of endogenous nitrite to bioactive NO. [3]

12.1 Introduction

Scientists have been searching for a viable oxygen-carrying resuscitation fluid for the better part of the past century. [4] Hemoglobin is the obvious choice as the functional compound because of its high O_2-carrying capacity, however, the creation of a cell-free hemoglobin derivative with appropriate properties has been a formidable task. [4] The first-generation of HBOCs were based on chemical modifications to stabilize tetrameric Hb and reduce renal toxicity. These products included

Sangart Inc., 6175 Lusk Blvd., San Diego, CA 92121
e-mail: russell.cole@gmail.com

J.C. LaManna et al. (eds.), *Oxygen Transport to Tissue XXXII*, Advances in Experimental Medicine and Biology 701, DOI 10.1007/978-1-4419-7756-4_12,

tetrameric human Hb cross-linked between subunits ($\alpha\alpha$Hb, $p50 = 33$ mmHg, M_w = 64 kDa), produced by Baxter, and heterogeneous polymers of bovine Hb (PBH, $p50 = 54$ mmHg, $M_w \sim 200$ kDa), produced by Biopure. These products cause adverse physiological phenomena, namely vasoconstriction and decreased capillary perfusion. A second-generation product, polyethylene glycol (PEG)-conjugated human Hb (MP4, $p50 = 5$ mmHg, $M_w = 95$ kDa) was developed by Sangart to eliminate the undesirable hemodynamic properties of earlier HBOCs.

Figure 1 shows the hemodynamic responses of 1^{st}- and 2^{nd}-generation products after a 10% topload of 4 g/dl HBOC in a hamster skin-fold model as a generalized representation of HBOC infusion. [5] The infusion of each HBOC leads to a similar increase in mean arterial pressure (MAP). The 1^{st}-generation products caused decreased cardiac index (CI), while MP4 did not, indicating increased peripheral vascular resistance (PVR) with $\alpha\alpha$Hb and PBH, but not MP4. This correlates with arteriolar vasoconstriction, with an observed reduction in arteriolar diameter with $\alpha\alpha$Hb and PBH, and an unchanged (or increased) arteriolar diameter observed with MP4. Although the vasoconstriction caused by 1^{st}-generation products is consistent with decreased bioavailability of nitric oxide (NO) to the vascular smooth muscle, the NO-binding kinetics of all three HBOCs are similar, and the measured arteriolar wall [NO] are not significantly different. [5] The advantageous hemodynamic response brought about by MP4 is a function of the high O_2 affinity and unique surface chemistry (PEGylation). This paper is intended to give a basic outline of the function of MP4, and is divided into O_2 affinity and PEGylation effects.

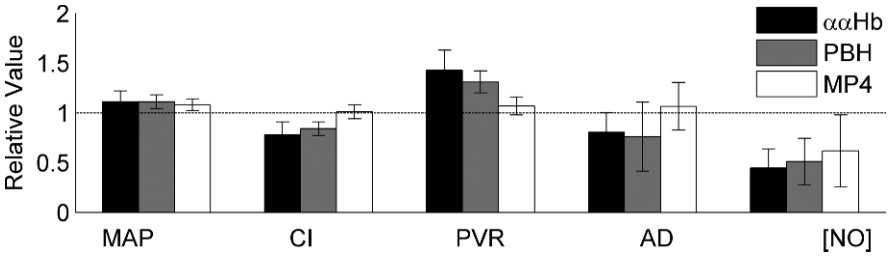

Fig. 12.1 Changes relative to baseline in mean arterial pressure (MAP), cardiac index (CI), peripheral vascular resistance (PVR), arteriolar diameter (AD), and arteriolar wall [NO] in hamster model after 10% topload of HBOC. All values are relative to baseline, except [NO], which is relative to a 10% topload of saline. $P < 0.05$ relative to MP4 (*). $n = 6$ for baseline, $n = 5$ for $\alpha\alpha$Hb, MP4, PBH. [5]

12.2 Oxygen Affinity Mediated Vasoactivity

Local regulation of microvascular flow is a complex process evolved to match intravascular O_2 supply to metabolic demand. The vasoconstrictive activity of infused HBOCs is well publicized and often linked to the efficient scavenging of endothelial-

derived nitric oxide (NO) and the consequent interruption of signaling processes within the vascular smooth muscle. [6] Our coworkers have noted that among HBOCs with similar NO-binding kinetics, vasopressor response in rats correlated with HBOC $p50$ [7], leading to the theory that HBOC vasoconstriction is due in part to an excessive supply of O_2 to the arterioles. [8] Because O_2 transport is also enhanced by the facilitated diffusion of cell-free Hb-bound O_2, MP4 was formulated with increased molecular volume and low $p50$ HBOC. [9]

The ability of the vasculature to directly sense the O_2 content of blood has long been hypothesized, yet the search for a direct O_2 sensor in the vascular wall has been difficult. Ellsworth and coworkers have proposed that the RBC itself serves as an O_2 sensor through the release of intracellular ATP as RBCs desaturate. [1] According to this theory, ATP released from RBCs diffuses to the vessel wall, binds purinergic receptors, and induces a vasodilatory response that is conducted upstream through the microcirculation (Fig. 2).

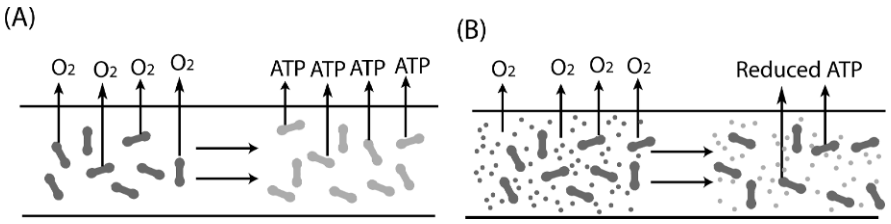

Fig. 12.2 Schematic of ATP-mediated vascular control. (A) RBCs offload O_2 and release ATP as they desaturate, causing vasodilation. (B) RBC/low-affinity HBOC suspensions release O_2 from both RBCs and HBOC, allowing RBCs to maintain a higher level of fractional saturation and reducing ATP release.

Because of their lack of erythrocytic encapsulation, HBOCs deliver O_2 earlier than similar $p50$ RBC suspensions. [10] We have hypothesized that the release of O_2 from low O_2 affinity HBOCs infused into the bloodstream will increase intravascular pO_2 and keep RBCs saturated. According to the Ellsworth et al. data, this will be accompanied by a reduction in erythrocytic release of ATP, which should reduce the magnitude of ATP-induced vasodilation. To study the interaction between HBOCs and RBC ATP release, we performed *in vitro* experiments by desaturating RBCs in the presence of either high- or low-$p50$ HBOCs. [11]. These studies mixed equal amounts of oxygenated RBCs and deoxygenated HBOC ($p50$ = 8 mmHg or $p50$ = 33 mmHg) to mimic the effects of removing half of the total O_2 content from a flowing RBC/HBOC suspension. We found that RBC ATP release was reduced more in the presence of a high-$p50$ HBOC (Fig. 3) and that increases in ATP release above baseline correlated strongly with the amount of O_2 released from RBCs. These results indicate a potential role of HBOC $p50$ in O_2 sensing.

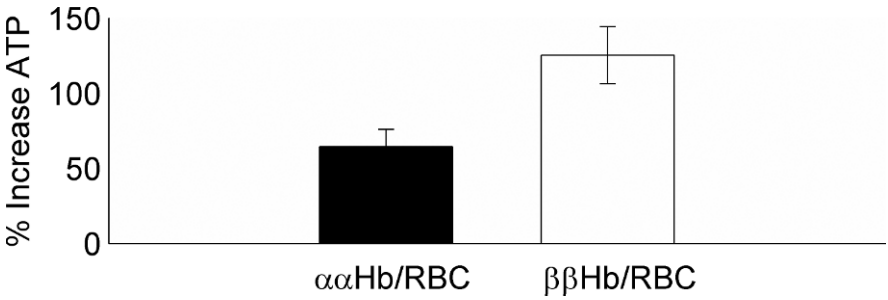

Fig. 12.3 Increase in erythrocytic ATP release when 1 g/dl oxygenated RBCs were mixed with 1 g/dl deoxygenated HBOCs. The HBOCs $\alpha\alpha$Hb (p50 = 33 mmHg) and $\beta\beta$Hb ($p50 = 8$ mmHg) are cross-linked tetrameric human Hbs prepared in our laboratory. ($P < 0.02$, $n = 3$)

12.3 PEGylation

When Hb is removed from antioxidant systems that exist within the erythrocyte, Hb readily participates in oxidative side reactions, producing reactive oxygen species (ROS) such as superoxide radical ($O_2^{\cdot -}$) and hydrogen peroxide (H_2O_2). Oxidative stress by HBOCs on endothelial cells is known to increase microvascular permeability, altering the fluid balance between the blood and the tissue and allowing plasma components, including ROS, to extravasate. [12] The rate of HBOC extravasation can be reduced by increasing the size of HBOC molecules, thereby reducing the speed of molecular diffusion. [13] *In vivo* experiments on the rat mesentery have shown that HBOC-induced endothelial dysfunction is often accompanied by indications of inflammatory activity, such as mast cell degranulation. [12]

Although the original intent in conjugating PEG to Hb was to increase intravascular residence times and decrease renal toxicity, a number of recent reports indicate that PEG has additional beneficial effects in the vasculature. Unconjugated high M_W PEG has been shown to tighten endothelial junctions and mitigate the effects of various agonists on cultured endothelial monolayers. [2] High M_W PEG also has been shown to reduce ischemia/reperfusion injury in pig and rat kidney models. [14] It is not clear how these positive effects of PEG on the vasculature may be altered by conjugation of the polymer to circulating proteins, but some effort has been made to study the effects of PEG size with varied sites of attachment. [15] In a hemodiluted hamster model, PEG conjugation to two proteins (albumin and hemoglobin) improved hemodynamic parameters, such as cardiac index, functional capillary density, and O_2 extraction as compared to animals infused with unmodified human serum albumin (Fig. 4). [16] The infusion of 1 g/dl MP4 to the bloodstream returned O_2 extraction to near-baseline levels. The authors suggested that the favorable hemodynamic response to PEGylated proteins is due to vascular refilling, caused by their high colloid osmotic pressure (40-50 mmHg).

Additional evidence points to direct involvement of PEG-Hb in NO signaling processes. Gladwin has shown that the reduction of endogenous nitrite by Hb can be a significant source of bioactive NO.....[17] The proposed reaction scheme is

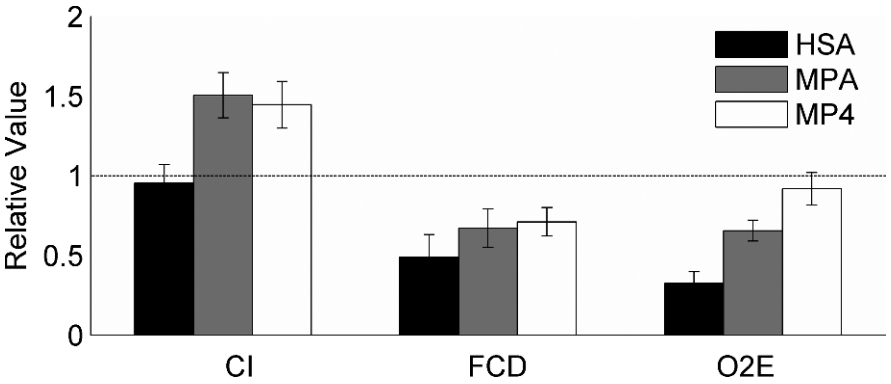

Fig. 12.4 Cardiac index (CI), functional capillary density (FCD), and O_2 extraction (O2E) in hemodiluted hamster model (Hct = 11%) after infusion with human serum albumin (HSA), PEGylated albumin (MPA), and PEGylated Hb (MP4). Values are relative to baseline (Hct = 49%). Data from experiments performed by Cabrales et al. [16]. $P < 0.05$ relative to HSA (*), $P < 0.05$ relative to MPA (+). $n = 5$ for all groups.

nitrite (NO_2^-) reaction with ferrous deoxyHb ($HbFe^{+2}$) to form NO and ferric metHb ($HbFe^{+3}$) (Eq. (1)). It is postulated that a temporary $HbFe^{+3}NO_2^-$ complex then reacts with NO to recycle ferrous deoxyHb with the formation of dinitrogen trioxide (N_2O_3), a stable, bioavailable form of NO that may diffuse to the vessel walls, subsequently degrading to form NO and NO_2^- (Eq. (2)).

$$NO_2^- + HbFe^{+2} + H^+ \rightarrow NO + HbFe^{+3} + OH^-, \tag{12.1}$$

$$HbFe^{+3}NO_2^- + NO \rightarrow HbFe^{+2} + N_2O_3. \tag{12.2}$$

Recently, Lui et al. found that the nitrite reductase activity of a PEGylated Hb MP4-analog is 10-times greater than the activity of native Hb, 5-times greater than $\alpha\alpha$HB, and 3-times greater than Hb with N-ethylmaleimide conjugated to the β93 cysteines. These differences are due to conformational changes induced by attachment of PEG at the β93 cysteines and PEG interactions with the Hb molecule. [3] The nitrite reductase pathway provides another possible mechanism for MP4 to counteract the effects of HBOC NO scavenging.

12.4 Conclusion

The vasodilatory activity of MP4 does not fit with the prevailing dogma of HBOC NO scavenging as the primary effector of microvascular tone. This paper summarizes three possible mechanisms for the observed effects of MP4. The effects of MP4's low $p50$ and enhanced nitrite reductase activity are straight forward because ATP and NO are known vasodilators that fit into the existing scientific framework. The *in vivo*

response to a PEGylated, non-O_2 carrying molecule suggests that PEG conjugation itself is advantageous, either due to an increase in blood volume from the high oncotic pressure of PEG or because of PEG conjugated to a molecular surface maintains some of the same properties induced by the infusion of free PEG into the bloodstream.

References

1. M.L.Ellsworth, T.Forrester, C.G.Ellis, and H.H.Dietrich, Am.J.Physiol 269 (1995) H2155-H2161.
2. E.T.Chiang, S.M.Camp, S.M.Dudek, M.E.Brown, P.V.Usatyuk, O.Zaborina, J.C.Alverdy, and J.G.Garcia, Microvasc.Res. 77 (2009) 174-186.
3. F.E.Lui, P.Dong, and R.Kluger, Biochemistry 47 (2008) 10773-10780.
4. R.M.Winslow, Blood substitutes (Elsevier, Inc., London, 2006).
5. A.Tsai, P.Cabrales, B.Manjula, S.Acharya, R.Winslow, and M.Intaglietta (2006) Blood 108 3603-3610.
6. J.S.Olson, E.W.Foley, C.Rogge, A.L.Tsai, M.P.Doyle, and D.D.Lemon (2004)Free Radic.Biol.Med. 36 685-697.
7. R.J.Rohlfs, E.Bruner, A.Chiu, A.Gonzales, M.Gonzales, D.Magde, M.D.Magde, K.D.Vandegriff, and R.M.Winslow (1998) J.Biol.Chem. 273 12128-12134.
8. M.McCarthy, K.Vandegriff, and R.Winslow, Biophys.Chem. (2001) 92 103-117.
9. K.D.Vandegriff, A.Malavalli, J.Wooldridge, J.Lohman, and R.M.Winslow, Transfusion 43 (2003) 509-516.
10. R.H.Cole, K.D.Vandegriff, A.J.Szeri, O.Savas, D.A.Baker, and R.M.Winslow (2007)Biophys.Chem. 128 63-74.
11. Cole R, Malavalli A, and Vandegriff K.D.(2009) Biophys.Chem. 144119-122.
12. A.L.Baldwin, Antioxid.Redox.Signal. (2004)6 1019-1030.
13. R.O.Dull, B.J.DeWitt, R.Dinavahi, L.Schwartz, C.Hubert, N.Pace, and C.Fronticelli (2004)J.Appl.Physiol 97 1930-1937.
14. J.P.Faure, T.Hauet, Z.Han, J.M.Goujon, I.Petit, G.Mauco, M.Eugene, M.Carretier, and V.Papadopoulos (2002) J.Pharmacol.Exp.Ther. 302 861-870.
15. P.Cabrales, N.D.Kanika, B.N.Manjula, A.G.Tsai, S.A.Acharya, and M.Intaglietta (2004) Am.J.Physiol Heart Circ.Physiol 287 H1609-H1617.
16. P.Cabrales, A.G.Tsai, R.M.Winslow, and M.Intaglietta (2005) Am.J.Physiol Heart Circ.Physiol 289 H2392-H2400.
17. M.T.Gladwin and D.B.Kim-Shapiro (2008) Blood 112 2636-2647.

Chapter 13
Zymogen Protein C to Prevent Clotting without Bleeding during Invasive Medical Procedures

Duane F. Bruley, Sanjay B. Jagannath, and Micheal B. Streiff

Abstract Thrombophilic disorders that predispose patients to develop blood clots can be life-threatening and result in a large economic burden on healthcare expenditures. Venous Thromboembolism (VTE) (deep vein thrombosis and pulmonary embolism) are the third leading cause of death in the United States. Protein C deficiency is a common thrombophilic condition that affects an estimated 1 in 400 Americans. Zymogen Protein C (ZPC) is the precursor to Activated Protein C (APC), a pivotal endogenous anticoagulant in human blood. Patients with protein C deficiency who have roughly half the normal level of protein C are estimated to be at 10-fold increased risk of VTE. We describe the use of protein C concentrate (Ceprotin®, Baxter, Deerfield, IL) in a patient with protein C deficiency and with a previous pulmonary embolism who developed a life-threatening gastrointestinal bleed after polypectomy. The patient is a 75-year-old male at very high risk for deep vein thrombosis and possible lung emboli. He has heterozygous Protein C deficiency (50%) and heterozygosity for the prothrombin gene G20210A mutation. During a routine colonoscopy, a large 3 cm cecal polyp was identified and resected. Eight days post-procedure while performing abdominal exercise he developed a life-threatening GI bleed originating from the polypectomy site as his warfarin was becoming therapeutic on a Low Molecular Weight Heparin (LMWH) periprocedural bridge. The patient's warfarin was reversed with vitamin K, and LMWH and warfarin were discontinued. To prevent thrombosis, he was started on ZPC until anticoagulation could be safely restarted.

Duane F. Bruley
Synthesizer, Inc., 2773 Westminster Road, Ellicott City, MD 21043, USA
e-mail: bruley@umbc.edu

Sanjay B. Jagannath
Associate Professor of Medicine, Director, Pancreatitis Center, Division of Gastroenterology, Johns Hopkins Hospital, 600 Wolfe Street, Blalock 465, Baltimore, MD 21205, USA

Micheal B. Streiff
Associate Professor of Medicine, Medical Director, Anticoagulation Management Service, Division of Hematology, Department of Medicine, Johns Hopkins Medical Institutions, 1830 E. Monument Street, Suite 7300, Baltimore, MD 21205-2196, USA

J.C. LaManna et al. (eds.), *Oxygen Transport to Tissue XXXII*, Advances in Experimental Medicine and Biology 701, DOI 10.1007/978-1-4419-7756-4_13,

During endoscopy, the bleeding site was treated with an injection of 1:10,000 dilution of epinephrine, followed by cauterization and placement of endoclips (4 metal staples). Three days after endoscopic repair LMWH was restarted with warfarin. Sixteen months post-bleed, the patient remains on life-long warfarin without further episodes of bleeding or thrombosis. Zymogen Protein C concentrate (Ceprotin®, Baxter Deerfield, IL) should be strongly considered for peri-procedural management of any patient with protein C deficiency and previous thromboembolism.

13.1 Introduction

As with many scientific findings, Protein C was discovered in a serendipitous way. In 1960 an inhibitory to blood coagulation was found and named autoprothrombin II [16]. Originally it was thought to be derived from prothrombin, however in 1972 it was shown that the precursor protein was not prothrombin [17]. It was determined in 1974 that rabbits generated anticoagulant activity in response to intravenous injection of thrombin and the inhibitory activity appeared to be similar to autoprothrombin II A [14]. In 1976, a new vitamin K-dependent protein was purified from bovine plasma and named Protein C because it was the third peak in an ion-exchange column elution [25]. Protein C was shown to be the proenzyme of a serine protease which could be activated by thrombin. Activated Protein C (APC) was then confirmed to be autoprothrombin II A [24] and human Protein C was first purified in 1979 [15].

Zymogen Protein C (ZPC) can be activated by thrombin alone but a more efficient activation process involves a thrombin/thrombomodulin complex bound to endothelial membrane and to the surface of platelets [9, 12]. This process takes place where and when APC is needed, thus preventing clotting with little or no bleeding.

The coagulation cascade includes at least three pathways that regulate coagulants: the antithrombin III inhibition of coagulation proteases, which is accelerated by vascular heparin-like molecules [23], the lipoprotein associated coagulation inhibitor (LACI) that blocks the activity of the factor VIIa-tissue factor complex [22], and, finally, the pivitol pathway which includes activated protein C (APC) that deactivates factors Va and VIIIa [11]. These three inhibitory pathways function together to inhibit both the proteases and their cofactors in the coagulation system. Clinical data suggest that patients with antithrombin III or Protein C deficiency are subject to thrombotic complications [23, 8].

Thrombophilic disorders that predispose patients to develop blood clots can be life-threatening and result in a large economic burden on healthcare expenditures. Venous thromboembolism (VTE) (deep vein thrombosis/DVT, and pulmonary embolism) are the third leading cause of death in the United States. Protein C deficiency (hereditary and acquired) is a condition that can result in patient mortality.

The endogenous anticoagulants and their cofactors play an important role in normal blood hemostasis and tissue health via oxygenation and metabolic waste product removal. Protein C deficiency is a hidden disease that affects 1 in 400 Americans. Approximately 1 in 16,000 are symptomatic, but all are prone to developing DVT

and lung emboli. Zymogen Protein C has a host of beneficial in-vivo characteristics. When activated it not only acts as a natural anti-coagulant but has also been found to have antithrombotic, anti-inflammatory and anti-apoptotic properties. Most importantly APC inhibits red cell coagulation and platelet-dependent thrombosis formation [13].

References giving detailed information on Protein C, it's biochemistry and production are Bertina, 1988; and Bruley and Drohan, 1990 [1, 6]. Earlier work on anticoagulants [2] pre-dated Protein C however the many attributes of ZPC [4] started a focused research effort on the low- cost production of this pivotal trace blood protein.

An important previous clinical research effort, the peri-operative use of ZPC for the left hip replacement of the same patient [5, 7, 26] was a very successful procedure. That work and the present case should lead the way to many safer surgeries in the future.

13.2 Emergency Procedure

The patient, a 75–year-old male with a medical history notable for protein C deficiency (protein C activity level of approximately 50%), had experienced DVT and bilateral pulmonary embolism at age 65. Subsequently, he was noted to be heterozygous for the prothrombin 20210 gene mutation by DNA analysis, had been prescribed life-long warfarin therapy targeted to an international normalized ratio (INR) range 2 to 3, and has not suffered any additional episodes of VTE.

The protein C deficiency was diagnosed in the summer of 1981 during testing suggested by Dr. Rene Bourgain (ISOTT member) [3] via laboratory assays conducted by Dr. Richard Marlar [18, 19], after the patients middle son sustained an idiopathic pulmonary embolism. At the same time, other family members were diagnosed with protein C deficiency: father, brother and two of three sons at approximate protein C activity levels of 48%, 38%, 48%, and 50%, respectively.

On Thursday, September 4, 2008 the patient underwent a routine colonoscopy. During the procedure a large 3 cm diameter cecal polyp was identified and resected. The wound was double cauterized and on the next day warfarin therapy was started using a Low Molecular Weight Heparin (LMWH) bridge to prevent clotting during the recovery to therapeutic INR levels of 2 to 3. Eight days after the polyectomy the patient reached INR of 2.0 and was approved to start exercise (Thursday, September 11, 2008). About one hour after abdominal exercise a strong urge to evacuate created an excessive rectal bleed from the wound site. The patient stopped LMWH shots and warfarin treatment simultaneously to attempt slowing the bleed. He was admitted to the Emergency Room that evening at the Johns Hopkins Hospital, Baltimore, MD and was managed while waiting for the bleed to stop. Sunday, September 14, 2008, vitamin K was administered and later that evening a Go-Lytely prep was taken by the patient to prepare for an emergency colonoscopy, scheduled for early Monday morning, September 15, 2008. Since there was a 10/20 fold increased risk of VTE the patient was bridged during the procedure with ZPC to prevent clotting without

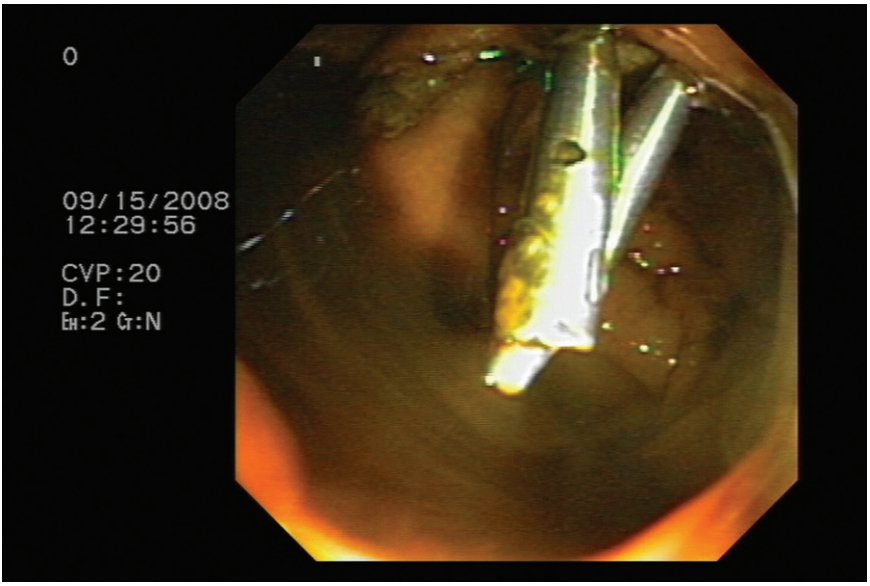

Fig. 13.1 Post polypectomy bleeding controlled with placement of endoclips.

increased bleeding. The initial doses were calculated at 60 units per kilogram twice a day. When Protein C activity peaks reached 205% of normal, the dose was reduced to prevent increasing the supraphysiologic levels of Protein C and using excessive ZPC.

During the endoscopy, the bleeding site was treated with an injection of l:10,000 dilution of epinephrine, followed by cauterization and placement of four metal staples (see Figure 1). Three days after endoscopic repair, while on ZPC protection, warfarin (7 mg/day) was restarted with a LMWH bridge (70 mg two times/day) to prevent thrombosis. Sixteen months post-bleed, the patient remains on life-long warfarin without further episodes of bleeding or thrombosis.

13.3 Discussion/Results

When natural and man-made anticoagulants are used in medical procedures, it is necessary to consider at least three things, first, the safety of the patient, second, the efficacy of the drug used and third, the additional cost involved. For the case of Protein C deficient patients it is very wise to consider the use of ZPC because it is effective against thrombosis and does not cause significant bleeding (if any) because of its activation process. As with the patient cited in this paper, the Protein C activity was assayed at 205% of normal levels without complications. Since this procedure was completed successfully it suggests the ZPC bridging be considered for PC deficient patients whenever invasive medical procedures are required. This

might also be true for patients with normal PC levels for highly invasive orthopedic surgery, brain surgery, etc.

An important unknown is what is the optimal ZPC level sufficient for different medical problems? Therefore, more data must be generated for a spectrum of potential uses. The use of ZPC products beg for refinement of peri-procedural ZPC levels, development of economic production technologies and patient compliant administration technologies.

Because of the unknown pharmacokinetics of the blood factors [27] while returning to accepted INR level, bridging with LMWH is necessary for at least protein C deficient patients. Therefore, there is a need for further studies regarding LMWH dosing levels to enhance patient safety. Presently, there is little or no data regarding dose level interaction during the return period to accepted INR levels while using a combination therapy of warfarin and LMWH. It is possible that using full-dose warfarin along with full-dose LMWH until therapeutic values of INR are reached, could contribute to unnecessary bleeds and possible patient death.

13.4 Product Cost/Production

For wider use of ZPC and APC it is necessary to explore technologies to produce less expensive products. At the present time, Eli Lilly is producing activated Protein C (Xigris) employing human cell culture and Baxter International is using Immunoaffinity Chromatography to recover ZPC (Ceprotin) from human blood plasma. Both processes are extremely expensive which limits the use of Protein C products to only very special medical emergencies. Past work [28, 29] is being continued to research the application of immobilized metal affinity chromatography, IMAC [20, 21] to replace Immuno-affinity Chromatography, using the best combination of absorption and elution buffers for optimal bio-downstream processing to achieve low cost production of Protein C products. The use of transgenic animals might also be a viable alternative [10] for high volume, lower cost bio-processing. With low cost products and the development of novel administration techniques it might be possible to use prophylactic ZPC to treat Protein C deficiency.

13.5 Conclusion

Based on the success of this case, Zymogen Protein C concentrate (Ceprotin, Baxter, Deerfield, IL) should be strongly considered for invasive peri-procedural management of any patient with protein C deficiency and previous thromboembolism.

Clinical medicine should be aware of other medical procedures that would be safer using ZPC. In all cases, dosing studies should be done to ensure optimal safety, efficacy and cost.

Acknowledgments

We want to thank Suzanne B. Bruley for her dedicated effort in the typing and proofing of this manuscript.

References

1. Bertina, R.M. (1988) Protein C and Related Proteins. Churchill Livingstone, New York
2. Bicher, H. I., Bruley, D. F., and Knisely, M. H (1973) Anti-adhesive drugs and tissue oxygenation, Advances in Experimental Medicine and Biology. Plenum Press, 37B:657-667.
3. Bourgain,R.H. (1978) The Effect of indomethacin and ASA on in-vivo induced white platlet thrombus formation, Thromb. Res., 12: 1079-1086.
4. Bruley, D.F. (1998) Protein C-the ultimate anticoagulant/antithrombotic?, : anticoagulant, antithrombotic, and thrombolytic thearapeutics II, edited by C.A.Thibeault and L.M. Savage ,IBC Library Series-Boston: 129-161.
5. Bruley, D. F. (2009) Zymogen protein c concentrate for safer heterozygote surgery, i am a guinea pig!", Advances In Experimental Medicine and Biology, Oxygen Transport To Tissue XXX, Springer, Vol.645, : 115-121.
6. Bruley, D.F., Drohan, W.N. (1990) Advances in applied biotechnology series, protein c and related anticoagulants. 11, Gulf Publications, Houston, TX.
7. Bruley, D.F., Mears, S.C.and Streiff, M.B. (2010) Safer surgery using zymogen protein c concentrate, advances in experimental medicine and biology, oxygen transport to tissue XXXI, Springer, Vol. 662,:439-445.
8. Clouse, L.H., Comp, P.C. (1986) The regulation of hemostasis: the protein c system. N. Engl. J. Med 314:1298-1304.
9. Comp, P. Esmon, C. (1981) Generation of fibrinolytic activity by infusion of activated protein c into dogs. J. Clin. Invest. 68:1221-1228.
10. Dave,A.,Bruley,D.F.,Kang,K.A. (1999) Preliminary studies in the separation of human protein c from transgenic milk using immobilized metal affinity chromatography, oxygen transport to tissue XXI, Advances in Experimental Medicine and Biology, Kluwer Academic/Plenum Publishers,NY, Vol.471,639-647.
11. Esmon, C. T. (1989) The roles of protein C and thrombomodulin in the regulation of blood coagulation. J Biol Chem 264:4743.
12. Esmon C.T. (1990) Regulation of coagulation the nature of the problem, protein c and related anticoagulants, Advances In Biotechnology Series, Vol II. Editors, Duane F. Bruley and William N. Drohan, Gulf Publishing Company, Houston.
13. Gruber, A., Griffin, J.H. Harker, L.A., Hanson, S.R. (1989) Inhibition of platelet-dependent thrombosis formation by human activated protein c in a primate model, Blood. 73:639-642.
14. Hyde E., Wetmore R., Gurewich V. (1974) Isolation and characterization of an in-vivo thrombin-induced anticoagulant activity, Scandinavian Journal of Haematology 13: 121-128.
15. Kisiel W. (1979) Human plasma protein c., isolation, characterization and mechanism of activation by a-thrombin, Journal of Clinical Investigation 64: 761-769.
16. Mammen E.F., et.al (1960) Handbook of proteolytic enzymes, Edited by Alan J Barrett, Neil D Rawlings and Fred J. Woessneer, CLAN SA-SI, 56 Protein C, pp 174, Academic Press.
17. Marciniak, E. (1972) Inhibitor of human blood coagulation elicited by thrombin, Journal of Laboratory and Clinical Medicine 79: 924-934.
18. Marlar, R.A. (1981) Records, The Milwaukee Blood Center, Milwaukee, WI, USA.
19. Marlar, R. A., Montgomery, R. R., Broakman, A. W. (1989) Diagnosis and treatment of homozygous protein c deficiency. Report of the working party on homozygous protein C deficiency of the subcommittee on protein C and protein S, International Committee on Thrombosis and Haemostasis, J. Paediatrics. 114:528-534.

20. Porath, J. (1992) Immobilized metal ion affinity chromatography, Prot. Express. Purif. 3:263-281.
21. Porath, J., Carlsson, J., Olsson, I., Belfrage, G. (1975) Metal chelate affinity chromatography, a new approach to protein fractionation, Nature. 258:598-599.
22. Rapaport, S. I. (1989) Blood 73,359.
23. Rosenberg, R. and Marcum, J. A. (1985) ASAIO J. 8, 215.
24. Seegers W. H., Novea E., Henry R.L., Hassouna H. I. (1976) Relationship of 'new' vitamin k-dependent protein c and 'old' autoprothrombin II-a, Thrombosis Research 8:543-552.
25. Stenflo J.(1976) A new vitamin K-dependent protein, Journal of Biological Chemistry 25: 355-363.
26. Thakkar,S.C., Streiff,M.B., Bruley,D.F., Mears,S.C., Case report: perioperative use of protein c concentrate for protein c deficiency in tha, Clinical Orthopaedics and Related Research, Springer, N.Y. (accepted for publication).
27. Weiss, P., Soff,G.A., Halkin,H., Seligsohn,U. (1987) Decline of protein c and s and factors II, VII, IX and X during the initiation of warfarin therapy, Thrombosis Research 45, 783-790.
28. Wu, H., Bruley, D. F. (1999) Homologous blood protein separation using immobilized metal affinity chromatography – protein c separation from prothrombin with application to the separation of factor IX and prothrombin, Biotechnol. Prog. 15:928-931.
29. Wu, H., Bruley, D. F. (2002) Chelator, metal ion and buffer studies for protein c separation, Comparative Biochemistry and Physiology, Part A. 132:213-220.

Part IV
Tumor Biology

Chapter 14
Oxygenation Status of Urogenital Tumors

Peter Vaupel, Michael Hoeckel, and Arnulf Mayer

Abstract In malignant urogenital tumors, tissue oxygenation is compromised and very heterogeneous, with steep and fluctuating spatio-temporal oxygen gradients signaling a complex instability in tumor oxygenation (complex "4D-heterogeneity"). Tumor hypoxia is highly dynamic, and rapidly changing pO_2 gradients may be key factors driving hypoxia-dependent adaptive processes leading to malignant progression. The grand median oxygen tension in malignant urogenital tumors is 7–11 mmHg. In contrast, benign leiomyomas of the uterus are severely, but uniformly, hypoxic with only shallow oxygen gradients ("static hypoxia"). In these benign tumors, the median pO_2 is 1 mmHg and signs of hypoxia-driven processes are missing.

14.1 Introduction

Tumor hypoxia has been recognized as an important driving force for malignant progression since it can promote local invasion of cancer cells, intravasation, and finally metastatic spread to distant sites. This promotion occurs in a co-operative manner (a) at the *transcriptome level* leading to hypoxia-induced changes in gene expression coordinated by a special set of transcription factors, such as HIFs, NFκB and AP-1, indicating redundancy in biological mechanisms in malignant tumors (below 1% O_2 or < 7 mmHg), (b) at the *proteome and metabolome level*, e.g., via posttranscriptional and posttranslational modifications (below 1% O_2 or < 7 mmHg), (c) at the *genome/epigenome level* by increasing genomic and epigenomic instability

Peter Vaupel and Arnulf Mayer
Department of Radiooncology and Radiotherapy, University Medical Center, Langenbeckstrasse 1, 55131 Mainz, Germany
e-mail: vaupel@uni-mainz.de

Michael Hoeckel
Department of Gynaecology, Liebigstrasse 20a, 04103 Leipzig, Germany

J.C. LaManna et al. (eds.), *Oxygen Transport to Tissue XXXII*, Advances in Experimental Medicine and Biology 701, DOI 10.1007/978-1-4419-7756-4_14,

(below 0.1% O_2 or < 0.7 mmHg), and finally (d) at the *cell population level* by clonal selection and clonal expansion according to phenotype fitness [1-10].

Redundancy in biological mechanisms in malignant tumors—as mentioned above—seems to be widespread as evidenced by the fact that there are several pathways responsible for the regulation of given individual processes (e.g., angiogenesis, invasion [9]). Redundancy, in the sense that many biological mechanisms in malignant tumors are complementary/compensatory, should therefore be recognized as a further hallmark of cancer.

Tumor hypoxia also plays a pivotal role in acquired treatment resistance since it is capable of directly and/or indirectly conferring resistance to therapy (e.g., [11-17]). As a result, hypoxia has been shown to act as an independent, adverse prognostic factor [18-25].

Due to the seminal role tumor hypoxia plays in malignant progression and acquired treatment resistance, information concerning the oxygenation statuses of tumors in terms of oxygen partial pressure distributions is indispensable in the clinical setting. For this reason, the respective oxygenation status for urogenital tumors has been compiled in this review, together with blood flow data, a major determinant of the O_2 status.

14.2 Oxygenation status of urogenital tumors

The incidence of urogenital cancers in Central Europe in 2004 (of all newly diagnosed cancer cases) was 42% in men (leading cancer: prostate, 25%), and 20% in women (leading malignancy: cancer of the body of the uterus, 6%). Due to the major role of tumor hypoxia in malignant progression and acquired treatment resistance, knowledge of the oxygenation status of urogenital tumors is of great importance. For this reason, data which have been collected over the past 20 years using a computerized pO_2 histography system (as described in [26,27]) are presented, indicating that hypoxia is a characteristic feature of solid tumors and heterogeneity of tumor oxygenation is a typical finding in these malignancies.

14.2.1 Oxygenation status of solid tumors

Current knowledge of the pretherapeutic oxygenation status of urogenital cancers is summarized in Table 1. As a rule, most tumors (of all types) exhibit hypoxic/anoxic areas which are heterogeneously distributed within the tissue.

There may be some overlap in patients reported from the same institution. Empty boxes indicate lack of suitable information.

In general, tumor oxygenation is compromised as compared to the respective normal tissues (see Table 2), independent of clinical characteristics and patient de-

Table 14.1 Pretherapeutic oxygenation status of locally advanced urogenital cancers (HF 2.5 = hypoxic fraction with pO_2 readings $\leq$ 2.5 mmHg, HF 5 = hypoxic fraction with pO_2 readings $\leq$ 5 mmHg). n = number of patients.

Tumor type	[References]	n	Median pO_2 (mmHg)	HF 2.5 (%)	HF 5 (%)
Cervix cancer	(reviewed in [27])	730	9	28	44
Prostate cancer	[27,28]	438	7		38
Vulvar cancer	[29-31]	54	11	25	40
Renal cell cancer	[32]	3	10		

Table 14.2 Oxygenation status of normal tissues (selection)

Tissue	Median pO_2 (mmHg)	HF 2.5 (%)	HF 5 (%)	HF 10 (%)	References
Cervix	42	8	13	20	[33]
Myometrium	9	4	23	51	[39]
Prostate			58		[34]
	26*		9*	22*	[35]
Subcutis (pubic mount)	56	0	0	5	[29]
Kidney	31	0	3	8	[32]

*Data from two "normal" prostates. For further explanation see Table 1.

mographics. Besides intra-tumor variability, tumors exhibit pronounced inter-patient variability.

As previously described [e.g., 9], tumor hypoxia predominantly results from an inadequate perfusion due to severe structural and functional abnormalities of the tumor microcirculation, an increase in diffusion distances for O_2, and tumor-associated or therapy-induced anemia. Since blood flow as a major determinant of the O_2 supply plays a critical role in the development of tumor hypoxia, perfusion data are relevant in this context. In cervix cancers, blood flow (data obtained from dynamic CT-derived parameters) is inconsistent with mean values ranging from 0.08 ml/g/min (range: 0.02–0.29) [36] to 0.99 ($\pm$ 0.17) ml/g/min [37]. Blood flow measured with quantitative MRI was 0.34 (0.19–0.52) ml/g/min in prostate cancer and 0.13 (0.10-0.19) ml/g/min in the normal prostate (values are median pre-treatment data with their interquartile ranges) [38].

14.2.2 Oxygenation status of benign leiomyomas

An investigation of the oxygenation status of 17 leiomyomas of the uterus using polarographic needle electrodes and the expression of hypoxia-related markers in biopsy specimens of the same tumor areas has shown that these benign tumors are severely hypoxic, with median oxygen partial pressures ranging from 0-5 mmHg (grand median: 1 mmHg, see Table 3). The hypoxic fraction HF 2.5 was 73% and HF 5 was 90% [39]. For normal myometria the grand median pO_2 was 9 mmHg

Table 14.3 Oxygenation status and expression of hypoxia-related markers in normal myometrium and uterine tumors [9, 39].

	Myometrium (normal)	Leiomyoma (benign)	Leiomyosarcoma (malignant)	Cervix Ca (malignant)
Median pO_2 (mmHg)[range]	9 [5-20]	1 [0-5]	2	10 [2-34]
HF 2.5 (%)	4	73	55	23
pO_2 variability	high	low	high	high
pO_2 gradients	steep	shallow	steep	steep
HIF-1α	none	none	low → high	low → high
GLUT-1	none	none	low → high	low → high
CA IX	none	none	low → high	low → high

which was significantly higher than that of the leiomyomas. In contrast to malignant uterus tumors (cervix cancers, leiomyosarcomas), none of the hypoxia-related markers (hypoxia-inducible factors, HIFs, glucose transporter-1, GLUT-1, or carbonic anhydrase IX, CA IX) were expressed in any leiomyomas [39-42].

14.3 Conclusions

In malignant urogenital tumors, tissue oxygenation is compromised and very heterogeneous (complex 4D-heterogeneity). Tumor hypoxia is highly dynamic with rapidly changing steep pO_2 gradients (see Table 3). In contrast, benign leiomyomas are severely and uniformly hypoxic with only shallow pO_2 gradients. Despite this hypoxic/anoxic microenvironment, leiomyomas do not show a measurable expression of HIF-1α, HIF-2α, CA IX and GLUT-1. From these data it is concluded that fluctuating spatial and temporal pO_2 gradients signaling a complex instability in oxygenation ("4D-heterogeneity") may be seminal factors driving adaptive processes and malignant progression.

Acknowledgments

This work was supported by grant #106758 from the Deutsche Krebshilfe. We thank Dr. Debra Kelleher and Mrs. Anne Deutschmann-Fleck for their excellent editorial assistance.

References

1. Hoeckel M, Vaupel P (2001) Tumor hypoxia: Definitions and current clinical, biologic, and molecular aspects. J Natl Cancer Inst 93:266-276
2. Semenza GL (2000) Hypoxia, clonal selection, and the role of HIF-1 in tumor progression. Crit Rev Biochem Mol Biol 35:71-103
3. Giaccia AJ (1996) Hypoxic stress proteins: Survival of the fittest. Semin Radiat Oncol 6:46-58

4. Denko NC, Fontana LA, Hudson KM et al (2003) Investigating hypoxic tumor physiology through gene expression patterns. Oncogene 22:5907-5914
5. Vaupel P (2004) The role of hypoxia-induced factors in tumor progression. The Oncologist 9:10-17
6. Hoeckel M, Vaupel P (2001) Biological consequences of tumor hypoxia. Semin Oncol 28:36-41
7. Vaupel P, Mayer A, Hoeckel M (2004) Tumor hypoxia and malignant progression. Methods Enzymol 381:335-354
8. Vaupel P, Mayer A (2007) Hypoxia in cancer: Significance and impact on clinical outcome. Cancer Metastasis Rev 26:225-239
9. Vaupel P (2005) Pathophysiology of solid tumors. In: The Impact of Tumor Biology on Cancer Treatment and Multidisciplinary Strategies: (Eds.: Molls M, Vaupel P, Nieder C et al), pp 51-92, Springer, Heidelberg, New York
10. Bristow RG, Hill RP (2008) Hypoxia, DNA repair and genetic instability. Nat Rev Cancer 8:180-192
11. Vaupel P (2009) Physiological mechanisms of treatment resistance. In: The Impact of Tumor Biology on Cancer Treatment and Multidisciplinary Strategies: (Eds.: Molls M, Vaupel P, Nieder C et al), pp 273-290, Springer, Heidelberg, New York
12. Brown JM (2007) Tumor hypoxia in cancer therapy. Methods Enzymol 435:297-321
13. Harrison L, Blackwell K (2004) Hypoxia and anemia: Factors in decreased sensitivity to radiation therapy and chemotherapy? The Oncologist 9:31-40
14. Tannock IF (2001) Tumor physiology and drug resistance. Cancer Metastasis Rev 20:123-132
15. Vaupel P, Thews O, Hoeckel M (2001) Treatment resistance of solid tumors: Role of hypoxia and anemia. Med Oncol 18:243-259
16. Vaupel P, Hoeckel M (2008) Tumor hypoxia and therapeutic resistance. In: Nowrousian MR (ed) Recombinant Human Erythropoietin (rhEPO) in Clinical Oncology. 2nd edit, Springer, Wien, New York, pp 283-306
17. Vaupel P (2008) Hypoxia and aggressive tumor phenotype: Implications for therapy and prognosis. The Oncologist 13 (Suppl 3):21-36
18. Hoeckel M, Knoop C, Schlenger K et al (1993) Intra-tumoral pO_2 predicts survival in advanced cancer of the uterine cervix. Radiother Oncol 26:45-50
19. Hoeckel M, Schlenger K, Aral B et al (1996) Association between tumor hypoxia and malignant progression in advanced cancer of the uterine cervix. Cancer Res 56:4509-4515
20. Gatenby RA, Kessler HB, Rosenblum JS et al (1988) Oxygen distribution in squamous cell carcinoma metastases and its relationship to outcome of radiation therapy. Int J Radiat Oncol Biol Phys 14:831-838
21. Brizel DM, Scully SP, Harrelson JM et al (1996) Tumor oxygenation predicts for the likelihood of distant metastases in human soft tissue sarcoma. Cancer Res 56:941-943
22. Fyles A, Milosevic M, Wong R et al (1998) Oxygenation predicts radiation response and survival in patients with cervix cancer. Radiother Oncol 48:149-156
23. Nordsmark M, Overgaard M, Overgaard J (1996) Pretreatment oxygenation predicts radiation response in advanced squamous cell carcinoma of the head and neck. Radiother Oncol 41:31-39
24. Vaupel P, Hoeckel M (2003) Tumor oxygenation and its relevance to tumor physiology and treatment. Adv Exp Med Biol 510:45-49
25. Vaupel P (2004) Tumor microenvironmental physiology and its implications for radiation oncology. Semin Radiat Oncol 14:198-206
26. Vaupel P, Schlenger K, Knoop M et al (1991) Oxygenation of human tumors: Evaluation of tissue oxygen distribution in breast cancers by computerized O_2 tension measurements. Cancer Res 51:3316-3322
27. Vaupel P, Hoeckel M, Mayer A (2007) Detection and characterization of tumor hypoxia using pO_2 histography. Antiox Redox Signal 9:1221-1235
28. Milosevic M, Chung P, Parker C et al (2007) Androgen withdrawal in patients reduces prostate cancer hypoxia: Implications for disease progression and radiation response. Cancer Res 67:6022-6025
29. Vaupel P, Mayer A, Hoeckel M (2006) Oxygenation status of primary and recurrent squamous cell carcinomas of the vulva. Eur J Gynaecol Oncol 27:142-146

30. Vaupel P, Thews O, Mayer A et al (2002) Oxygenation status of gynecologic tumors: What is the optimal hemoglobin level? Strahlenther Onkol 178:727-731
31. Stone JE, Parker R, Gilks CB et al (2005) Intratumoral oxygenation of invasive squamous cell carcinoma of the vulva is not correlated with regional lymph node metastasis. Eur J Gynaecol Oncol 26:31-35
32. Lawrentschuk N, Poon AMT, Foo SS et al (2005) Assessing regional hypoxia in human renal tumours using ^{18}F-fluoromisonidazole positron emission tomography. BJU International 96:540-546
33. Hoeckel M, Schlenger K, Knoop C et al (1991) Oxygenation of carcinomas of the uterine cervix: Evaluation of computerized O_2 tension measurements. Cancer Res 51:6098-6102
34. Parker C, Milosevic M, Toi A et al (2004) Polarographic electrode study of tumor oxygenation in clinically localized prostate cancer. Int J Radiat Oncol Biol Phys 58:750-757
35. Movsas B, Chapman JD, Horwitz EM et al (1999) Hypoxic regions exist in human prostate carcinoma. Urology 53:11-18
36. Lyng H, Vorren AO, Sundfor K et al (2001) Intra- and intertumor heterogeneity in blood perfusion of human cervical cancer before treatment and after radiotherapy. Int J Cancer 96:182-190
37. Haider MA, Milosevic M, Fyles A et al (2005) Assessment of the tumor microenvironment in cervix cancer using dynamic contrast enhanced CT, interstitial fluid pressure and oxygen measurements. Int J Radiat Oncol Biol Phys 62:1100-1107
38. Kershaw LE, Logue JP, Hutchinson CE et al (2008) Late tissue effects following radiotherapy and neoadjuvant hormone therapy of the prostate measured with quantitative magnetic resonance imaging. Radiother Oncol 88:127-134
39. Mayer A, Hoeckel M, Wree A et al (2008) Lack of hypoxic response in uterine leiomyomas despite severe tissue hypoxia. Cancer Res 68:4719-4726
40. Mayer A, Wree A, Hoeckel M et al (2004) Lack of correlation between expression of HIF-1.α protein and oxygenation status in identical tissue areas of squamous cell carcinomas of the uterine cervix. Cancer Res 64:5876-5881
41. Mayer A, Hoeckel M, Wree A et al (2005) Microregional expression of glucose transporter-1 and oxygenation status: Lack of correlation in locally advanced cervical cancers. Clin Cancer Res 11:2768-2773
42. Mayer A, Hoeckel M, Vaupel P (2005) Carbonic anhydrase IX expression and tumor oxygenation status do not correlate at the microregional level in locally advanced cancers of the uterine cervix. Clin Cancer Res 11:7220-7225

Chapter 15

Tumor pO_2 as a Surrogate Marker to Identify Therapeutic Window during Metronomic Chemotherapy of 9L Gliomas

Sriram Mupparaju, Huagang Hou, Jean P. Lariviere, Harold M. Swartz, and Nadeem Khan

Abstract Glioblastomas are aggressive and highly vascularized primary brain tumors with a 5-year survival rate of less than 10%. Approaches targeting tumor vasculature are currently being investigated to achieve therapeutic benefits for this fatal malignancy. However, lack of suitable markers that can be used to monitor therapeutic effects during such treatments has restricted their optimization. We have focused on the development of tumor pO_2 as a surrogate marker to identify the therapeutic window during metronomic chemotherapy. We report the effect of four weekly administrations of cyclophosphamide (140 mg/Kg, i.p), a chemo drug, on tumor pO_2 and growth of subcutaneous 9L tumors in SCID mice. The repeated measurement of tumor pO_2 was carried out using *in vivo* EPR oximetry. The subcutaneous 9L tumors were hypoxic with a pre-treatment tumor pO_2 of 5.1 ± 1 mmHg and a tumor volume of 236 ± 45 mm^3 on day 0. The tumor pO_2 increased significantly to 26.2 $\pm$ 2 mmHg on day 10, and remained at an elevated level till day 31 during weekly treatments with cyclophosphamide. The tumor pO_2 then declined to 20 ± 9 mmHg on day 43. The tumor volume of the control group increased significantly with no change in tumor pO_2 over days.

Results indicate a transient increase in tumor pO_2 during metronomic chemotherapy of 9L gliomas and could be potentially used as a marker to identify vessel normalization during metronomic chemotherapy. The ability to identify therapeutic window non-invasively using EPR oximetry can have a significant impact on the optimization of clinical protocols. *In vivo* EPR oximetry is currently being tested for repeated pO_2 measurements in patients with superficial tumors.

Sriram Mupparaju, Huagang Hou, Jean P. Lariviere, Harold M. Swartz, and Nadeem Khan
EPR Center for Viable Systems, Dartmouth Medical School, Hanover, NH 03755, USA
e-mail: nadeem@dartmouth.edu

Sriram Mupparaju, Huagang Hou, and Nadeem Khan
Norris Cotton Cancer Center, Dartmouth-Hitchcock Medical Center, Lebanon, NH 03756, USA

J.C. LaManna et al. (eds.), *Oxygen Transport to Tissue XXXII*, Advances in Experimental Medicine and Biology 701, DOI 10.1007/978-1-4419-7756-4_15,

15.1 Introduction

Glioblastomas are malignant brain tumors with a poor prognosis. The median survival is less than one year from the time of diagnosis and, even in the most favorable situations, most patients do not survive beyond two years despite aggressive treatment protocols (1-3). Multimodality approaches with systemic chemotherapy administered concurrently and as an adjuvant with radiotherapy have shown only modest survival advantages and are usually accompanied with acute or late toxicity.

New therapeutic approaches, based on tumor genetics or physiology, are urgently needed that can improve the outcome for patients with this highly malignant tumor. Metronomic chemotherapy is a recently developed approach which involves a repetitive administration of small doses of chemo drugs. This approach targets tumor endothelium, which results in the pruning of the immature and inefficient tumor blood vessels. This process leads to an initial remodeling of the remaining vasculature, resulting in a transiently improved tumor microenvironment and normalized tumor vasculature (4, 7). The normalized tumor vasculatures are characterized by less leaky, less dilated and less tortuous vessels with a more normal basement membrane. This should enhance drug delivery and oxygen into the tumors, thereby providing a therapeutic window which, if exploited, could improve the outcome of chemo and/or radiotherapy (10, 13). However, the effect of metronomic regimens is likely to vary with the dose and the interval between doses and therefore may significantly alter the therapeutic outcome. Unfortunately, the currently used read-outs, namely, time to progression, progression-free survival, and median survival, can be assessed only at the end of the treatment and are not suitable markers to guide dose optimization, identify non-responders, and assess efficacy during treatment. Therefore, reliable markers that are indicative of the efficacy and can identify non-responders early during the course of therapy are vital to achieve the best therapeutic results.

We hypothesize that metronomic chemotherapy will lead to an increase in tumor pO_2 (partial pressure of oxygen) associated with changes in the tumor vasculature. These changes in tumor pO_2 could be used as a potential surrogate marker to optimize dose regimens, identify non-responders, and predict outcome. We report the results of our ongoing study on the effect of metronomic chemotherapy using 4 weekly treatments with cyclophosphamide on tissue pO_2 and growth of subcutaneous 9L gliomas in SCID mice.

15.2 Methods

15.2.1 Animal and tumor models

All animal-use procedures were in strict accordance with the NIH Guide for the Care and Use of Laboratory Animals and were approved by the Institutional Animal Care and Use Committee of Dartmouth Medical School. The 9L cells were grown *in vitro*

in DMEM medium with 10% FBS and 1% penicillin-streptomycin. For injection, the cells were trypsinized and suspended in DMEM, without serum or additives. The tumors of 6-8 mm in length were obtained in 14-16 days by subcutaneous injection of 100 μl cell suspension (4×10^5 cells) with a 25-gauge needle in the left flank of anesthetized (2-2.5% isoflurane with 30% O_2) SCID mice (Charles River Laboratories, MA).

15.2.2 Implantation of oximetry probe (LiPc) for pO_2 measurements using multi-site EPR oximetry

Once the tumors reached a size of 6-8 mm in length, the mice were anesthetized (2-2.5% isoflurane with 30% O_2), and two aggregates of LiPc crystals (40-50 μg each) were injected into the tumors (4 mm apart, 2 mm depth) using 25 gauge needles. Once injected, these LiPc deposits provided repeated tissue pO_2 measurements at two sites of each tumor simultaneously using multi-site Electron Paramagnetic Resonance (EPR) oximetry (8, 9, 12).

For pO_2 measurements, the mice were anesthetized (1.5% isoflurane, 30% O_2) and positioned between the poles of the EPR magnet. The external loop resonator was placed close to the surface of the tumor and pre-treatment (baseline) EPR measurements were acquired for 30 minutes on day 0. The EPR spectra were averaged for 1 minute each to improve the signal to noise ratio. Typical settings for the spectrometer were incident microwave power, 4-6 mW; magnetic field center, 400 gauss; scan range, 2 gauss; modulation frequency, 27 kHz. Modulation amplitude was set at less than one-third of the EPR line width. During EPR measurements, the temperature of the animals was monitored using a rectal probe and maintained at $37 \pm 0.5^{\circ}$C using a thermostatically controlled heated pad and a flow of warm air. Cyclophosphamide was prepared in phosphate buffered saline (PBS, Mediatech Inc. VA) and the mice received single doses (140 mg/kg, i.p) on days 0, 7, 14 and 21. The tumor pO_2 and volume measurements were continued for approximately seven weeks. A similar protocol was used for the control group and the mice were treated with the vehicle (PBS) only.

15.2.3 Tumor volume measurements

The tumor volumes were measured using the formula: $\pi/6 \times \text{length} \times \text{width}^2$. This is a well-established procedure for tumor volume measurement of peripheral tumors and has been used routinely in our experiments (5, 6). The mice of the control group were euthanized on day 14 in accordance with the IACUC guidelines on the maximal allowed tumor load on each mouse.

15.2.4 Data analysis

The tumor pO_2 from the two LiPc implants of each tumor was measured simultaneously for 30 minutes and the data were pooled to obtain an average tumor pO_2 on each day of measurements. A paired t-test was used to determine the statistical significance of the changes in pO_2 within the group and an unpaired t-test was used to determine the statistical significance between groups at the same time points. The tests were two-sided, and a change with a p-value < 0.05 was considered statistically significant. All data are expressed as mean $\pm$ SE; $n = 3 - 4$.

15.3 Results

15.3.1 Effect of metronomic cyclophosphamide on 9L tumor pO_2

The baseline tumor pO_2 of the cyclophosphamide (CPA) and the control group were 5 ± 1 mmHg and 8.5 ± 2 mmHg, respectively, and no significant difference was observed between groups, Figure 1. In the CPA treated group, a significant increase in the tumor pO_2 was observed from day 10 when compared with the baseline and the control group. The tumor pO_2 remained at a significantly oxygenated level till day 31 and then slowly declined on day 43 after the last CPA treatment on day 21. On the other hand, no significant change in the tumor pO_2 of the control group was observed during two weeks of repeated measurements.

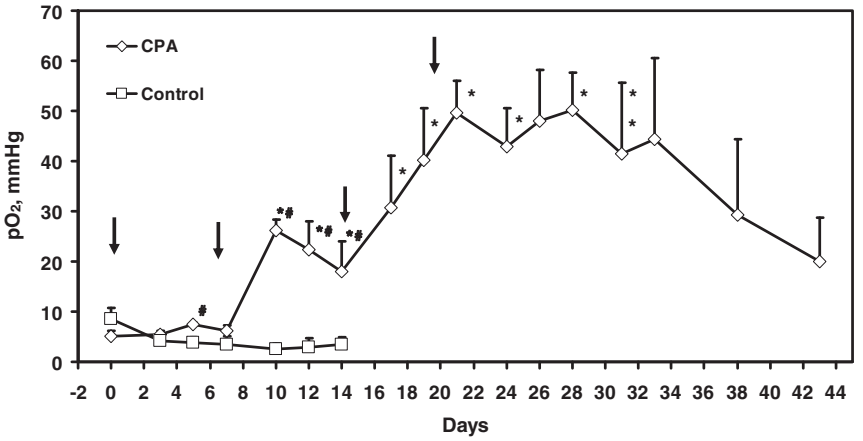

Fig. 15.1 Tumor pO_2 of subcutaneous 9L tumors in the control () and CPA (◇) treated groups. The mice were administered metronomic CPA (140 mg/Kg, i.p) on day 0, day 7, day 14 and day 21 (indicated by arrows). Mean + SE, $n = 3 - 4$. * $p < 0.05$, compared with the baseline; # $p < 0.05$, compared with the control group.

15.3.2 Effect of metronomic cyclophosphamide on 9L tumor growth

The tumor volumes of the CPA and the control groups were 236 ± 45 and 181 ± 36 mm^3 and were not significantly different, Figure 2. A significant increase in tumor volume was observed from day 6 to day 10 in the CPA treated group as compared to the pre-treatment volume. However, the tumor volume decreased and remained at the baseline level during subsequent measurements. A significant increase in the tumor volume of the control group was observed from day 7 during 2 weeks of measurements. The tumor volume of the CPA treated group was significantly smaller than the control group on days 10 - 14.

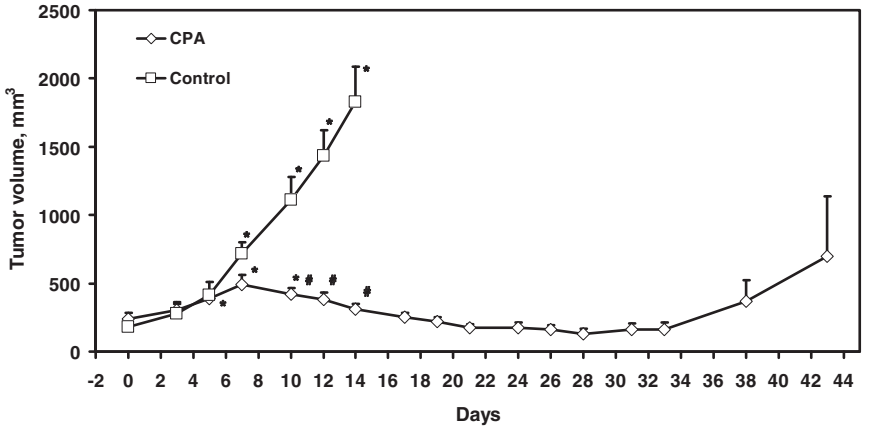

Fig. 15.2 The tumor volume of subcutaneous 9L tumors in the control () and CPA (◇) treated groups. The mice were administered metronomic CPA (140 mg/kg, i.p) on day 0, day 7, day 14 and day 21. Mean + SE, $n = 3 - 4$. * $p < 0.05$, compared with baseline; # $p < 0.05$, compared with the control group.

15.4 Discussion

The effect of metronomic chemotherapy is likely to vary with the dose and the interval between doses, and may therefore significantly alter the therapeutic outcome. Unfortunately, lack of an appropriate marker to identify vascular changes during metronomic chemotherapy has restricted therapeutic optimization.

Our results confirm an increase in tumor pO_2 during metronomic CPA treatment of 9L gliomas. This is likely due to the normalization of the tumor vasculature during metronomic CPA treatments (11). These findings support our hypothesis that an increase in tumor oxygenation will occur during metronomic chemotherapy and

repeated tumor pO_2 measurements by EPR oximetry can provide crucial information on vessel normalization during such treatments. Tumor pO_2 could be potentially used to predict outcome, identify non-responders and efficiently combine this approach with radiotherapy to enhance therapeutic outcome. EPR oximetry is currently being tested for repeated pO_2 measurements in patients with peripheral tumors undergoing chemo and/or radiotherapy. We are currently investigating the changes in microvessel density, and vascular endothelial growth factor levels and how these relate to the changes in tumor pO_2 observed during the treatments. Nevertheless, these results are promising and provide insight on the effect of metronomic chemotherapy on tumor oxygenation.

Acknowledgments

NIH grants CA118069 and CA120919 to NK, and P01EB2180 to HMS.

References

1. Buckner JC. Factors influencing survival in high-grade gliomas. Semin Oncol 30:10-14, 2003.
2. Buckner JC, Brown PD, O'Neill BP, Meyer FB, Wetmore CJ, Uhm JH. (2007) Central nervous system tumors. Mayo Clin Proc 82:1271-1286.
3. DeAngelis LM. (2001) Brain tumors. N Engl J Med 344:114-123.
4. Fukumura D, Jain RK. (2007)Tumor microvasculature and microenvironment: targets for anti-angiogenesis and normalization. Microvasc Res 74:72-84.
5. Hou H, Khan N, Grinberg OY, Yu H, Grinberg SA, Lu S, Demidenko E, Steffen RP, Swartz HM. (2007)The effects of Efaproxyn (efaproxiral) on subcutaneous RIF-1 tumor oxygenation and enhancement of radiotherapy-mediated inhibition of tumor growth in mice. Radiat Res 168:218-225.
6. Hou H, Lariviere JP, Demidenko E, Gladstone D, Swartz H, Khan N. (2009) Repeated tumor pO(2) measurements by multi-site EPR oximetry as a prognostic marker for enhanced therapeutic efficacy of fractionated radiotherapy. Radiother Oncol 91:126-131.
7. Jain RK. (2005) Normalization of tumor vasculature: an emerging concept in antiangiogenic therapy. Science 307:58-62.
8. Khan N, Williams B, Swartz H. (2006) Clinical applications of in vivo EPR: rationale and initial results. Applied Magn Reson 30:185-199,.
9. Khan N, Williams BB, Hou H, Li H, Swartz HM. (2007)Repetitive tissue pO_2 measurements by electron paramagnetic resonance oximetry: current status and future potential for experimental and clinical studies. Antioxid Redox Signal 9:1169-1182.
10. Kim JT, Kim JS, Ko KW, Kong DS, Kang CM, Kim MH, Son MJ, Song HS, Shin HJ, Lee DS, Eoh W, Nam DH. (2006) Metronomic treatment of temozolomide inhibits tumor cell growth through reduction of angiogenesis and augmentation of apoptosis in orthotopic models of gliomas. Oncol Rep 16:33-39.
11. Ma J, Waxman DJ (2007). Collaboration between hepatic and intratumoral prodrug activation in a P450 prodrug-activation gene therapy model for cancer treatment. Mol Cancer Ther 6:2879-2890.
12. Swartz HM, Clarkson RB. (1998) The measurement of oxygen in vivo using EPR techniques. Phys Med Biol 43:1957-1975.

13. Zhou Q, Guo P, Wang X, Nuthalapati S, Gallo JM. (2007) Preclinical pharmacokinetic and pharmacodynamic evaluation of metronomic and conventional temozolomide dosing regimens. J Pharmacol Exp Ther 321:265-275.

Chapter 16

Hypoxia-Induced Extracellular Acidosis Increases p-Glycoprotein Activity and Chemoresistance in Tumors *in Vivo* via p38 Signaling Pathway

Oliver Thews, Martin Nowak, Christoph Sauvant, and Michael Gekle

Abstract Due to inadequate perfusion, tumors develop hypoxia and extracellular acidosis. *In vitro*, this acidic environment (pH=6.6) has a strong impact on the acitvity of the p-glycoprotein (pGP) drug transporter responsible for multidrug resistance. This effect is most probably mediated via p38 and/or ERK1/2 signalling pathways. The aim of the study was to analyze whether these findings also play a role for chemosensitivity in solid growing tumors *in vivo*. Therefore, experimental R3327-AT1 tumors of the rat were exposed to an acidifying treatment leading to forced glycolysis. The intratumoral pO_2 was determined polarographically and the extracellular pH was measured with needle electrodes. In addition the cytotoxicity of daunorubicin chemotherapy was assessed. Tumor oxygenation was markedly worsened by the acidosis treatment leading to a mean tumor pO_2 of 1 mmHg. This hypoxia resulted in a pronounced acidification of the tumor tissue from pH 7.04 down to 6.65. Extracellular acidosis *in vivo* decreased caspase 3-activity after daunorubicin treatment by 30% indicating a reduced chemosensitivity. Inhibition of the p38 signalling pathway restored the reduced chemosensitivity at least partially. However, in contrast to the *in vitro* findings inhibition of ERK1/2 had practically no impact *in vivo*.

Oliver Thews and Martin Nowak*
Institute of Physiology and Pathophysiology, University of Mainz, 55099 Mainz, Germany
e-mail: olthews@uni-mainz.edu

Christoph Sauvant
Institute of Physiology, University of Würzburg, 97070 Würzburg, Gemany

Michael Gekle
Institute of Physiology, University of Halle, 06097 Halle (Saale), Germany

*This study forms part of the doctoral thesis of Martin Nowak.

J.C. LaManna et al. (eds.), *Oxygen Transport to Tissue XXXII*, Advances in Experimental Medicine and Biology 701, DOI 10.1007/978-1-4419-7756-4_16,

16.1 Introduction

Multidrug resistance is a phenomenon commonly found in numerous human tumor entities. Tumor cell lines (as well as various normal tissues) express the p-glycoprotein (pGP; belonging to the ATP-binding cassette ABC-family) which is able to export xenobiotics actively and thereby reduce the cytotoxicity of chemotherapeutic drugs resulting in a multidrug resistant phenotype [1]. Modulation of the pGP-activity (e.g., by inhibitors) can modify the cytotoxic efficacy of chemotherapy [2]. On the other hand, human tumors show several key differences compared to normal tissues with respect to morphological and histopathological features and also in terms of physiological characteristics at the cellular and tissue level. When compared to normal tissues, solid-growing tumors exhibit structural and functional abnormalities of the vascular network with inadequate perfusion that does not follow a regular pattern thus leading to an insufficient O_2 supply [3]. As a consequence of tumor hypoxia, tumor cells switch their metabolism to glycolysis leading to pronounced extracellular acidosis with pH below 6.5 whereas the intracellular pH stays at 6.8 to 7.2 [4,5].

It has been shown that hypoxia [6], glucose depletion [7] and reactive oxygen species [8] regulate the MDR1 gene and thereby possibly affect pGP expression. In addition, in cell culture experiments it was demonstrated that extracellular acidosis with a pH of 6.6 increases the functional activity of the p-glycoprotein leading to a reduced cytotoxicity of chemotherapeutic drugs [9,10]. These data reveal that lowering the extracellular pH increases the pGP-mediated drug efflux rate without changing the expression whereby activation of MAP kinases (p38, ERK1/2) seem to play a key role in signal transduction. However, it is unclear whether these mechanisms play a role in the *in vivo* situation in solid growing tumors.

Therefore, in the present study *in vivo* experiments, in which the tumor extracellular pH was artificially decreased, should elucidate whether the acidosis reduces the cytotoxic efficacy of daunorubicin treatment in these tumors. It should also be analyzed whether the signal cascades found *in vitro* are relevant for the situation in solid tumors.

16.2 Methods

16.2.1 Animals and tumors

For all studies, solid carcinomas of the R3327-AT1 cell line were heterotopically subcutaneously induced by injection of AT1 cells (0.4 ml approx. 10^4 cells/μl) into the dorsum of the hind foot of male Copenhagen rats. Experiments were performed when tumors reached a target volume of 0.5-3.0 mL, approx. 10-14 days after inoculation of tumor cells. Studies were approved by the regional ethics committee and

conducted according to UKCCCR guidelines [11] and the German Law for Animal Protection.

16.2.2 Acidosis treatment

In order to induce a pronounced extracellular acidosis in the tumors, animals were treated with a combination of inspiratory hypoxia (inspiratory O_2-fraction 8%, starting 15 prior to measurements), hyperglycemia (3 g/kg b.w., i.v., 30 min prior to the measurements) and an injection of meta-iodo-benzylguanidine (MIBG, 20 mg/kg b.w., i.v. 4 h prior to the measurements) in order to increase anaerobic glycolysis in the tumor cells.

16.2.3 pO_2 and pH measurements

The distribution of tumor oxygen partial pressure (pO_2) was measured polarographically using steel-shafted microelectrodes (outer diameter: 300 μm) and the pO_2 histography system (Eppendorf, Hamburg, Germany; for more details of this method see [12]). The oxygenation status of each tumor was described by the mean pO_2 as well as by the fraction of pO_2 values $\leq$ 2.5 mmHg.

The extracellular pH was measured with steel-shafted pH glass electrodes (type MI-418B, Microelectrodes Inc, Bedford NH, USA) with an outer diameter of 800 μm. The electrode was inserted into the tumor and stepwise moved through the tissue (step width 1 mm). 20 to 30 individual pH measurements were obtained from 3 to 4 parallel electrode tracks in each tumor.

16.2.4 Daunorubicin and kinase inhibitor treatments

In order to assess the cytotoxicity of daunorubicin (DNR), tumor bearing animals received a single dose of DNR (50 mg/kg b.w., i.p., dissolved in isotonic saline). Three hours after chemotherapy the caspase 3 activity was measured in the tumor tissue. The MAP kinase signaling pathways were blocked by specific inhibitors (SB203580 for p38 and U0126 for ERK1/2) by direct intratumoral injection (volume $\sim$20 μL) 30 min prior to the daunorubicin treatment. The tumor on the contralateral hind foot served as intra-individual control.

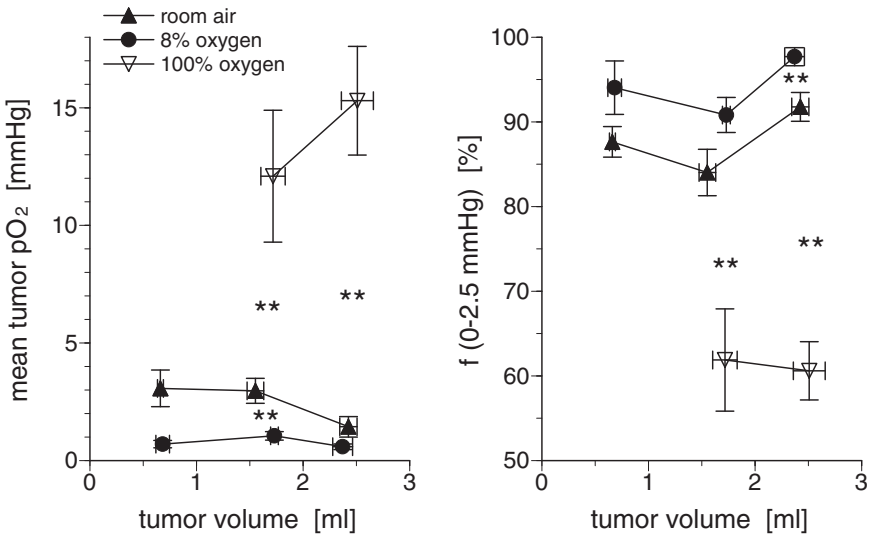

Fig. 16.1 Oxygenation (described by the mean tumor pO_2 and the fraction of hypoxic pO_2 values $.\leq 2.5$ mmHg) of AT1 tumors with different volumes in control animals, animals breathing hypoxic (8% O_2) and hyperoxic (100%) gas mixtures. Values are expressed as means±SEM of at least 6 tumors. (**) $p < 0.01$.

16.3 Results

AT 1 tumors show pronounced hypoxia even under control conditions (Fig. 1) with negligible dependency on the tumor volume. Breathing a hypoxic gas mixture containing only 8% oxygen further worsened the oxygenation status. The mean tumor pO_2 was reduced to only 1 mmHg, and more than 90% of the measured pO_2 values were below 2.5 mmHg. By comparison, breathing of pure oxgen improved oxygenation resulting in a mean pO_2 of ∼15 mmHg.

Combination of inspiratory hypoxia with i.v. injection of high dose glucose and application of MIBG (an inhibitor of complex I of the respiratory chain) induced glycolytic metabolism in the tumors as indicated by an acidification of the tissue (Fig. 2). In small tumors (volume < 1 mL) the extracellular tumor pH decreased from 7.04±0.05 down to 6.65±0.04. In these acidified tumors the cytotoxicity of a daunorubicin chemotherapy was reduced as indicated by a significant reduction of caspase 3 activity by ∼30% compared to pH 7.04 (Fig. 3).

Inhibiting the p38 MAP kinase pathway was able to reverse the acidosis-induced chemoresistance at least partially (Fig. 4). During p38 inhibition, the daunorubicin cytotoxicity was not significantly different between tumors at 7.0 and 6.6. Inhibiting the ERK1/2 pathway had no impact on cytotoxicity (Fig. 4).

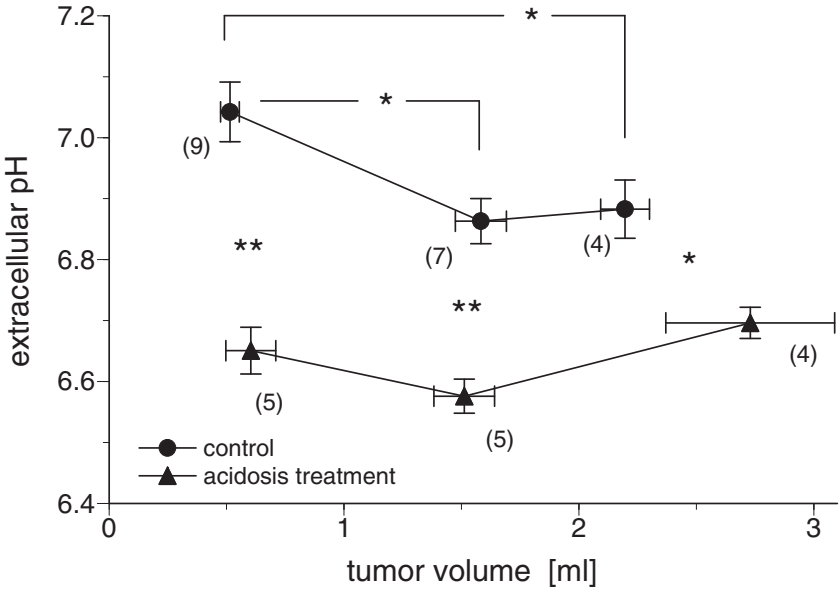

Fig. 16.2 Extracellular pH in control tumors (of different volumes) and in tumors underwent an acidosis treatment (combination of inspiratory hypoxia, hyperglycemia and MIBG). Values are expressed as means±SEM. Number of tumors in brackets; (*) $p < 0.05$; (**) $p < 0.01$.

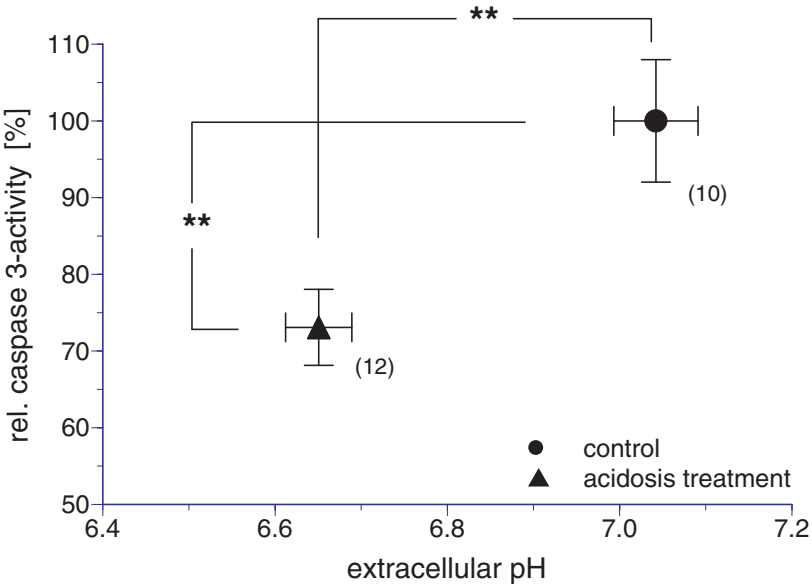

Fig. 16.3 Cytotoxicity of daunorubicin treatment *in vivo* (determined by the relative caspase 3-activity) in control tumors and tumors which underwent induced acidosis. (**) $p < 0.01$.

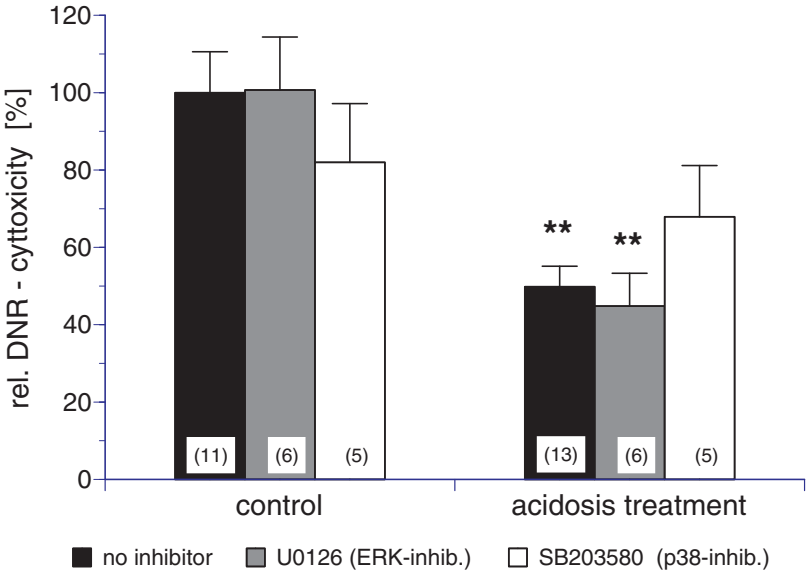

Fig. 16.4 Daunorubicin cytotoxicity in control (pH 7.0) and acidic (pH 6.6) tumors. In addition, p38 and ERK1/2 MAP kinase pathway was blocked by intratumoral injection of specific inhibitors. Values are expressed as means±SEM. Number of tumors in brackets; (**) $p < 0.01$ *vs.* control.

16.4 Discussion

Compared to other experimental tumor models [13], AT1 tumors are poorly oxygenated showing a mean pO_2 of only 2 to 3 mmHg. Breathing a gas mixture containing only 8% O_2 worsens tumor oxygenation especially in the group of small tumors (< 1 mL). Inspiratory hyperoxia in turn increased the mean tumor pO_2 and reduced the fraction of hypoxic measurements, which was also the case in other tumor entities [14].

Kalliomäki and Hill [15] proposed a procedure by which the extracellular pH can be lowered in solid growing tumors. They suggested increasing glycolytic metabolism in tumor cells by inducing tumor hypoxia (by reduced inspiratory O_2 fraction), the inhibition of the respiratory chain, and pronounced increase in glucose supply. This procedure is based on the results of Zhou et al. [16] who introduced the use of MIBG + hyperglycemia to reduce tumor pH. Following this protocol the extracellular pH was markedly reduced by approximately 0.5 (Fig. 2), which is comparable to results with other tumor lines [15] even though it has to be noted that the potentiometric pH measurement destroys some cells which may affect the pH measurement. This drop was in the same range as in the cell culture experiments in which a marked increase of the pGP activity was found [10]. In the same experimental setting, inspiratory hyperoxia (100% O_2) was able to slightly increase tumor pH by 0.1 (data not shown).

Analyzing the cytotoxicity of a daunorubicin treatment in acidotic and control tumors confirmed the *in vitro* results that extracellular acidosis increases pGP activity and, as a result, reduces chemosensitivity [9,10] (Fig. 3). However, the present results do not prove that the reduced pH increases the pGP transport rate *in vivo*, which has to be demonstrated in further studies. In principle, it may also be possible that the extracellular acidosis reduces the uptake of daunorubicin which might be the case since daunorubicin is a weak base (pK_a=8.46) [17]. However, cell culture experiments measuring the kinetics of daunorubicin uptake after change of pH showed no difference between pH 7.4 and 6.6 [9]. Zhou et al. [16] demonstrated that the combination of MIBG and hyperglycemia reduced the cellular ATP content which, on the one hand, can reduce daunorubicin-induced apoptosis but, on the other hand, would decrease the pGP activity and result in an increase of the cellular daunorubicin concentration. Further studies are needed to measure the ATP content and the intracellular pH *in vivo*.

In contrast to the *in vitro* results, the ERK1/2 inhibitor U0126 has virtually no impact on the daunorubicin cytotoxicity *in vivo* (Fig. 4) whereas, inhibition of p38 restored chemosensitivity, at least in part. However, the different effect of ERK1/2 *in vitro* and *in vivo* still remains unclear.

Acknowledgments

This study was supported by the Deutsche Krebshilfe (grants 106774/106906).

References

1. Higgins CF (2001) ABC transporters: physiology, structure and mechanism - an overview. Res Microbiol 152: 205-210
2. Fojo T, Bates S (2003) Strategies for reversing drug resistance. Oncogene 22: 7512-7523
3. Höckel M, Vaupel P (2001) Tumor hypoxia: definitions and current clinical, biological, and molecular aspects. J Natl Cancer Inst 93: 266-276
4. Vaupel P, Kallinowski F, Okunieff P (1989) Blood flow, oxygen and nutrient supply, and metabolic microenvironment of human tumors: a review. Cancer Res 49: 6449-6465
5. Rofstad EK, DeMuth P, Sutherland RM (1988) ^{31}P NMR spectroscopy measurements of human ovarian carcinoma xenografts: relationship to tumour volume, growth rate, necrotic fraction and differentiation status. Radiother Oncol. 12: 315-26
6. Comerford KM, Wallace TJ, Karhausen J et al (2002) Hypoxia-inducible factor-1-dependent regulation of the multidrug resistance (MDR1) gene. Cancer Res 62: 3387-3394
7. Ledoux S, Yang R, Friedlander G et al (2003) Glucose depletion enhances P-glycoprotein expression in hepatoma cells: role of endoplasmic reticulum stress response. Cancer Res 63: 7284-7290
8. Wartenberg M, Gronczynska S, Bekhite MM et al (2005) Regulation of the multidrug resistance transporter P-glycoprotein in multicellular prostate tumor spheroids by hyperthermia and reactive oxygen species. Int J Cancer 113: 229-240

9. Sauvant C, Nowak M, Wirth C et al (2008) Acidosis induces multi-drug resistance in rat prostate cancer cells (AT1) in vitro and in vivo by increasing the activity of the p-glycoprotein via activation of p38. Int J Cancer 123: 2532-2542
10. Thews O, Gassner B, Kelleher DK et al (2006) Impact of extracellular acidity on the activity of p-glycoprotein and the cytotoxicity of chemotherapeutic drugs. Neoplasia 8: 143-152
11. Workman P, Twentyman P, Balkwill F et al (1998) United Kingdom Co-ordinating Committee on Cancer Research (UKCCCR) Guidelines for the Welfare of Animals in Experimental Neoplasia (2nd edit.). Br J Cancer 77: 1-10
12. Vaupel P, Schlenger K, Knoop C et al (1991) Oxygenation of human tumors: evaluation of tissue oxygen distribution in breast cancers by computerized O_2 tension measurements. Cancer Res 51: 3316-3322
13. Thews O, Kelleher DK, Lecher B et al (1997) Effect of cell line and differentiation on the oxygenation status of experimental sarcomas. Adv Exp Med Biol 428: 123-128
14. Thews O, Kelleher DK, Vaupel P (1997) Tumor oxygenation under normobaric and hyperbaric hyperoxia: Impact of various inspiratory CO_2 concentrations. Adv Exp Med Biol 428: 79-87
15. Kalliomäki T, Hill RP (2004) Effects of tumour acidification with glucose+MIBG on the spontaneous metastatic potential of two murine cell lines. Br J Cancer 90: 1842-1849
16. Zhou R, Bansal N, Leeper DB, Glickson JD (2000) Intracellular acidification of human melanoma xenografts by the respiratory inhibitor *m*-iodobenzylguanidine plus hyperglycemia: a ^{31}P magnetic resonance spectroscopy study. Cancer Res 60: 3532-6
17. Chaplin DJ, Horsman MR, Trotter MJ et al (1998) Therapeutic significance of microenvironmental factors. In Blood Perfusion and Microenvironment of Human Tumors, Molls M, Vaupel P, eds., Springer, Berlin, 131-143

Chapter 17
Evidence against a Major Role for TKTL-1 in Hypoxic and Normoxic Cancer Cells

Arnulf Mayer, Angelika von Wallbrunn, and Peter Vaupel

Abstract Based on studies performed with a selected mouse monoclonal anti-transketolase-like (TKTL)-1 antibody (clone JFC12T10), overexpression of TKTL-1 has been shown to be correlated with poor survival and increased metastatic spread in several human tumor entities. Since the clinical aggressiveness mediated by TKTL-1 has been partially related to resistance to hypoxia, we originally aimed to explore the influence of hypoxia on the expression of TKTL-1. Unexpectedly, results of our experiments indicated that the antibody clone JFC12T10 lacks target specificity. Since the majority of data on the role of TKTL-1 in human cancer is based upon studies performed with this antibody clone, we subsequently re-evaluated the expression of TKTL-1 in six different cancer cell lines (HeLa, MCF-7, A549, HT-1080, M21 and TF-1). Using RT-PCR and consecutive sequence analysis, we show that transketolase (TKT), not TKTL-1, is the dominant isoform of transketolases in the cell lines analyzed. Our data argue against a major role of TKTL-1 for the metabolism of cancer cells.

17.1 Introduction

A series of recent publications has suggested that overexpression of the TKT isoenzyme TKTL-1 is correlated with metastasis formation and poor patient survival [1-9]. It has been speculated that TKTL-1 represents a critical element of the elusive "Warburg effect" in cancer cells [2, 10]. According to this hypothesis, enzymatic reactions

Arnulf Mayer and Peter Vaupel
Department of Radiooncology and Radiotherapy, University Medical Center, Langenbeckstrasse 1, 55131 Mainz, Germany
e-mail: arnmayer@uni-mainz.de

Angelika von Wallbrunn
Institute of Physiology and Pathophysiology, University Medical Center, Duesbergweg 6, 55099 Mainz, Germany

J.C. LaManna et al. (eds.), *Oxygen Transport to Tissue XXXII*, Advances in Experimental Medicine and Biology 701, DOI 10.1007/978-1-4419-7756-4_17,

catalyzed by TKTL-1 are rate-limiting for energy production due to glucose degradation via the non-oxidative part of the pentose-phosphate pathway (PPP). Cancer cells which are thus believed to be rendered partially oxygen-independent in terms of their metabolic activity are expected to have an increased capability for proliferation in the oxygen-depleted microenvironments frequently found in solid malignant tumors.

The mechanism by which overexpression of TKTL-1 in malignant cells occurs has not been investigated. Tong et al. [11] speculated that HIF-1α may be involved in the upregulation of TKT to compensate for a HIF-1α-mediated inhibition of the oxidative part of the PPP. In an analogous manner, we considered the possibility that TKTL-1 overexpression in human cancers is related to hypoxia or HIF-1α expression.

17.2 Methods

Cells were cultured in MEM (1 g/L glucose), Ham's F12 (1.8 g/L glucose) or RPMI 1640 (2 g/L glucose) supplemented with 10% fetal calf serum, 5% glutamine and 5% penicillin/streptomycin (PAA laboratories) at 37˚C in a humidified atmosphere containing 5% CO_2. TF-1 culture medium was additionally supplemented with 3 ng/mL GM-CSF (Biomol). Hypoxic treatment of cells was performed in an incubator with oxygen control (Labotect) flushed with premixed gas (1% O_2, 5% CO_2 and 94% N_2) for 12 h.

Differential protein extraction of cytoplasmic, nuclear and membranous fractions was performed using NE-PER and MEM-PER kits (Pierce), respectively. 25 μg of lysates were separated by SDS-PAGE and electroblotted to PVDF membranes. Primary antibodies (TKTL-1, Linaris; HIF-1α, BD Transduction Lab.; CA IX, Abcam; ß-actin, Santa Cruz) were detected using appropriate secondary antibodies conjugated to horseradish peroxidase (Santa Cruz). Bands were developed using ECL (GE Healthcare) and images were captured with a CCD camera (LAS-3000, Fuji). ß-actin was used as a loading control (lower panels in Fig. 1).

Immunohistochemistry was carried out according to standard protocols including antigen retrieval by heating specimens in 10 mM sodium citrate (pH 6.0) in a steamer (FS 10, Braun) for 40 min. The primary antibody was detected using the micropolymer-based, biotin-free Impress^{TM} detection system (Vector). DAB was used as the peroxidase substrate.

Total RNA was isolated using the peqGold Total RNA-Kit (Peqlab) according to the manufacturer's instructions. To eliminate residual genomic DNA, RNA samples were subjected to DNAse I digestion (MBI Fermentas). For each reverse transcription (RT) reaction to synthesize single stranded complementary DNA (cDNA), total RNA (2 μg) was used in a 20 μl reaction (RevertAid^{TM} First Strand cDNA Synthesis Kit, MBI Fermentas). For PCR amplification, 1 μg of cDNA was used in a 50 μl reaction containing 10 mM Tris-HCl, 1.5 mM $MgCl_2$, 50 mM KCl, pH 8.3, 200 μM each dNTP and 1U Taq (Peqlab) or Pfu (MBI Fermentas) DNA Polymerase with 0.4 μM of each oligonucleotide primer. PCR was performed using a Mastercycler ep

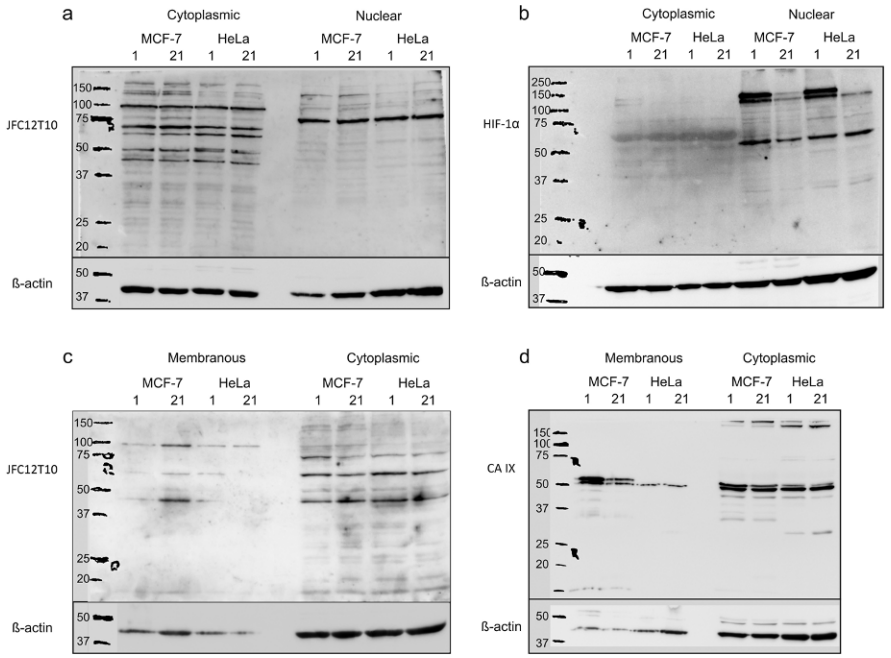

Fig. 17.1 Western blots of hypoxic (1% O_2) and normoxic (21% O_2) MCF-7 and HeLa cells. Cytoplasmic and nuclear fractions (**panels a & b**, NE-PER extraction protocol) were probed with the antibody clones JFC12T10 against TKTL-1 **(a)** and BD clone 54 against HIF-1α **(b)**. Membranous and cytoplasmic fractions (**panels c & d**, MEM-PER extraction protocol) were incubated with the antibody clones JFC12T10 against TKTL-1 **(c)** and ab15086 against CA IX **(d)**. See text for details.

(Eppendorf). In each PCR experiment, following an initial incubation at 95˚C for 5 min, the denaturation step was performed at 95˚C for 30 sec, annealing step at 60˚C for 1 min, and the extension step was 72˚C for 1 min for 35 cycles. A final extension step was performed at 72˚C for 10 min after the last cycle. Products were analyzed by electrophoresis in 2.5% agarose gels and the specificity of the amplified PCR products was confirmed by sequencing (GATC Biotech). The sequences of primers were designed using the software Prime3 [10]. Real-time polymerase chain reaction was performed by using SYBR green I dye with ROX according to the manufacturer's protocol (ABgene, Thermo Fisher Scientific) in a total volume of 25 μl. Real-time PCR was conducted on an ABI 7300 (Applied Biosystems) system by using the following parameters: denaturing at 95˚C for 15 s, 40 cycles at 95˚C for 15 s and at 60˚C for 1 min. ß-actin was used as an internal control and each assay included probes and calibration samples in triplicates. Data analysis was carried out by using ABI data analysis software. To control the specificity of amplification products, primer inhibition plots and melting curve analyses were performed. Primer efficiencies were found to be above 90% in all cases and inspection of dissociation curves confirmed negligible levels of primer self-hybridization. The expression amount of the target sample was expressed as the relative fold change according to the $\Delta\Delta$Ct method [12].

17.3 Results

17.3.1 Lack of target specificity of anti-TKTL1 mAb clone JFC 12T10

To assess the modulation of the protein expression levels of TKTL-1 by oxygen, we performed western blotting analyses of normoxic (21% O_2) and hypoxic (1% O_2) HeLa and MCF-7 cells. Lysates were prepared according to differential extraction protocols yielding both cytoplasmic and nuclear (NE-PER protocol, see methods) fractions. According to the description of Coy et al. [10], who generated and characterized the antibody clone JFC12T10, bands corresponding to TKTL-1 were expected at approx. 75 kDa. However, as depicted in Fig. 1a, 75 kDa bands are faint in cytoplasmic fractions of both cell types with HeLa cells showing hardly any expression. Instead, several distinct bands of higher and lower molecular weight are seen in both cell types (95, 66, 59, 49, and 44 kDa, respectively). Surprisingly, a 75 kDa band clearly dominates in the nuclear extracts of both MCF-7 and HeLa cells. None of these bands showed regulation by hypoxia. Conversely, detection of HIF-1α (Fig. 1b) in the same extracts showed the expected absence of bands in the cytoplasmic fractions and two closely adjacent, clearly hypoxia-inducible bands of a molecular weight of approx. 120 kDa. Additional bands are present around 60 kDa, which may correspond to products of proteasomal degradation of HIF-1α.

To further characterize the binding properties of the anti-TKTL-1 antibody clone JFC12T10, we next probed membranous and cytoplasmic extracts generated with the MEM-PER protocol and reagents (Fig. 1c). 90 kDa-bands were seen in the membranous fractions, while cytoplasmic fractions showed bands slightly below 75 kDa. The former may correspond to the respective bands seen in the cytoplasmic and nuclear fractions obtained with the NE-PER kit. MEM-PER extraction again yielded bands at 59 and 44 kDa in the cytoplasm, respectively. Validity of the MEM-PER extraction protocol was confirmed by probing the same extracts with an antibody against CA IX (Fig. 1d). As expected, the 55 kDa membrane isoform of this HIF-1α-dependent protein is strongly induced in hypoxic MCF-7 cells compared with their normoxic counterparts. No induction was seen in hypoxic HeLa cells, however. Contrary to the band pattern obtained with clone JFC12T10, the anti-CA IX antibody showed few additional bands, indicating high target specificity. ß-actin (lower panels) confirms the separation of subcellular compartments.

17.3.2 Clone JFC12T10 yields implausible immunohistochemical staining results

Since TKTL-1 overexpression (using this antibody) has been related to malignant progression and metastatic behavior, we next examined benign uterine leiomyomas ($n = 3$), an entity that exhibits neither of these traits. Surprisingly, we find cyto-

plasmic and nuclear expression identical to that observed in solid malignant tumors.

17.3.3 Analysis of TKT, TKTL-1, and TKTL-2 expression in six cancer cell lines

These results cast doubt upon the concept of cancer-specific up-regulation of TKTL-1. Therefore, we next investigated the expression of TKT, TKTL-1 and TKTL-2 (yet another TKT isoform) at the mRNA level by RT-PCR in normoxic and hypoxic HeLa, MCF-7, A549, HT1080, M21 and TF-1 cells. We used three different sets of primers for each gene, including those published by Coy et al. [10]. TKT is the dominant isoform in all cell types analyzed. Significant expression of TKT-1 is found only in HT-1080 fibrosarcoma and M21 melanoma cells. Expression of TKTL-1 in HeLa, MCF-7 and A549 cells is very weak. TKTL-2 expression is also negligible. Induction of TKT isoforms under hypoxia was then further analyzed in the same set of cells by quantitative realtime PCR. Except for a minor down-regulation of TKTL-2 under hypoxic conditions, no obvious pattern of oxygen dependence of these genes emerged (data not shown).

17.4 Conclusions

Published data regarding the binding specificity of the anti-TKTL-1 antibody clone JFC12T10 could not be confirmed. Instead, our results show that clone JFC12T10 detects multiple proteins in cytosolic, nuclear and membrane-associated compartments, as assessed by differential protein extraction and western blotting. A 75 kDa band identified by Coy et al. as TKTL-1 corresponds to a nuclear protein. Not surprisingly, this antibody also stains nuclei in immunohistochemistry. Although this finding is questionable for a PPP enzyme located in the cytoplasm, this staining pattern has been published repeatedly [2, 6, 10], but a lack of antibody specificity has not been considered. Clinical data obtained with this antibody clone should be interpreted with great caution. Furthermore, our PCR data indicate that TKT, universally and unequivocally, is the dominant isoform of transketolases in the cell lines analyzed. Additionally, none of these genes were significantly up- or downregulated under hypoxic conditions. These data do not support a major role for TKTL-1 in the metabolism of cancer cells under either normoxic or hypoxic conditions. Thus, convincing evidence for the effectiveness of an “anticancer” diet aimed at circumventing the PPP [10] is not available.

Acknowledgments

This work was supported by grant #106758 from the Deutsche Krebshilfe. We thank Dr. Debra Kelleher and Mrs. Anne Deutschmann-Fleck for their excellent editorial assistance.

Note

A detailed presentation of these data has been published in *Internat. J. Oncol.* 37(2):265-71 (2010).

References

1. Staiger WI, Coy JF, Grobholz R, et al (2006) Expression of the mutated transketolase TKTL1, a molecular marker in gastric cancer. Oncol Rep 16:657-61
2. Langbein S, Zerilli M, zur Hausen A, et al (2006) Expression of transketolase TKTL1 predicts colon and urothelial cancer patient survival: Warburg effect reinterpreted. Br J Cancer 94:578-85
3. Foldi M, Stickeler E, Bau L, et al (2007) Transketolase protein TKTL1 overexpression: A potential biomarker and therapeutic target in breast cancer. Oncol Rep 17:841-5
4. Krockenberger M, Honig A, Rieger L, et al (2007) Transketolase-like 1 expression correlates with subtypes of ovarian cancer and the presence of distant metastases. Int J Gynecol Cancer 17:101-6
5. Volker HU, Scheich M, Schmausser B, et al (2007) Overexpression of transketolase TKTL1 is associated with shorter survival in laryngeal squamous cell carcinomas. Eur Arch Otorhinolaryngol 264:1431-6
6. Langbein S, Frederiks WM, zur Hausen A, et al (2008) Metastasis is promoted by a bioenergetic switch: New targets for progressive renal cell cancer. Int J Cancer 122:2422-8
7. Zerilli M, Amato MC, Martorana A, et al (2008) Increased expression of transketolase-like-1 in papillary thyroid carcinomas smaller than 1.5 cm in diameter is associated with lymph-node metastases. Cancer 113:936-44
8. Zhang S, Yue JX, Yang JH, et al (2008) Overexpression of transketolase protein TKTL1 is associated with occurrence and progression in nasopharyngeal carcinoma: a potential therapeutic target in nasopharyngeal carcinoma. Cancer Biol Ther 7:517-22
9. Chen H, Yue JX, Yang SH, et al (2009) Overexpression of transketolase-like gene 1 is associated with cell proliferation in uterine cervix cancer. J Exp Clin Cancer Res 28:43
10. Coy JF, Dressler D, Wilde J, et al (2005) Mutations in the transketolase-like gene TKTL1: clinical implications for neurodegenerative diseases, diabetes and cancer. Clin Lab 51:257-73
11. Tong X, Zhao F, Thompson CB (2009) The molecular determinants of de novo nucleotide biosynthesis in cancer cells. Curr Opin Genet Dev 19:32-7
12. Livak KJ, Schmittgen TD (2001) Analysis of relative gene expression data using real-time quantitative PCR and the $2^{-??Ct}$ Method. Methods 25:402-8

Chapter 18
NMR Metabolic and Physiological Markers of Therapeutic Response

Seung-Cheol Lee, Harish Poptani, E. James Delikatny, Stephen Pickup, David S. Nelson, Stephen J. Schuster, Sunita D. Nasta, Jakub Svoboda, Steven C. Goldstein, Stephen G. Wallace, Laurie A. Loevner, Eric A. Mellon, Ravinder Reddy, and Jerry D. Glickson

Abstract Identification of reliable metabolic and physiological NMR detectable markers for prediction and early detection of therapeutic response is essential to enabling NMR guided individualized therapy for cancer. Because non-Hodgkin's lymphoma (NHL) is a prevalent form of cancer that exhibits ~50% response to therapy and often presents with large superficial lesions easily accessible to multinuclear magnetic resonance spectroscopy (MRS) measurements, it is an ideal test bed for development of NMR methods for prediction and early detection of response. A multicenter study, in which we have participated, has already shown that pre-treatment ^{31}P MRS measurement of the phosphate monoester (PME) to nucleoside triphosphate (NTP) ratio can identify about 2/3 of the patients who are destined not to exhibit a complete clinical response to a variety of therapeutic agents. Because ^{31}P MRS is limited to relatively large superficial tumors, we have been exploring ^{1}H MRS and MRI methods for early detection of therapeutic response. Using xenografts of the most common form of human NHL, diffuse large B-cell lymphoma (DLBCL), we have

Seung-Cheol Lee, Harish Poptani, E. James Delikatny, Stephen Pickup, David S. Nelson, and Jerry D. Glickson
Laboratory of Molecular Imaging, Department of Radiology, University of Pennsylvania School of Medicine, Philadelphia, PA 19104, USA
e-mail: seungch@mail.med.upenn.edu

Stephen J. Schuster, Sunita D. Nasta, Jakub Svoboda, and Steven C. Goldstein
Abramson Cancer Center, University of Pennsylvania School of Medicine, Philadelphia, PA 19104, USA

Stephen G. Wallace
Virtua Fox Chase Cancer Program, Mount Holly, NJ 08060, USA

Laurie A. Loevner
Department of Radiology, University of Pennsylvania School of Medicine, Philadelphia, PA 19104, USA

Eric A. Mellon and Ravinder Reddy
Center for Magnetic Resonance and Optical Imaging, Department of Radiology, University of Pennsylvania School of Medicine, Philadelphia, PA 19104, USA

J.C. LaManna et al. (eds.), *Oxygen Transport to Tissue XXXII*, Advances in Experimental Medicine and Biology 701, DOI 10.1007/978-1-4419-7756-4_18,

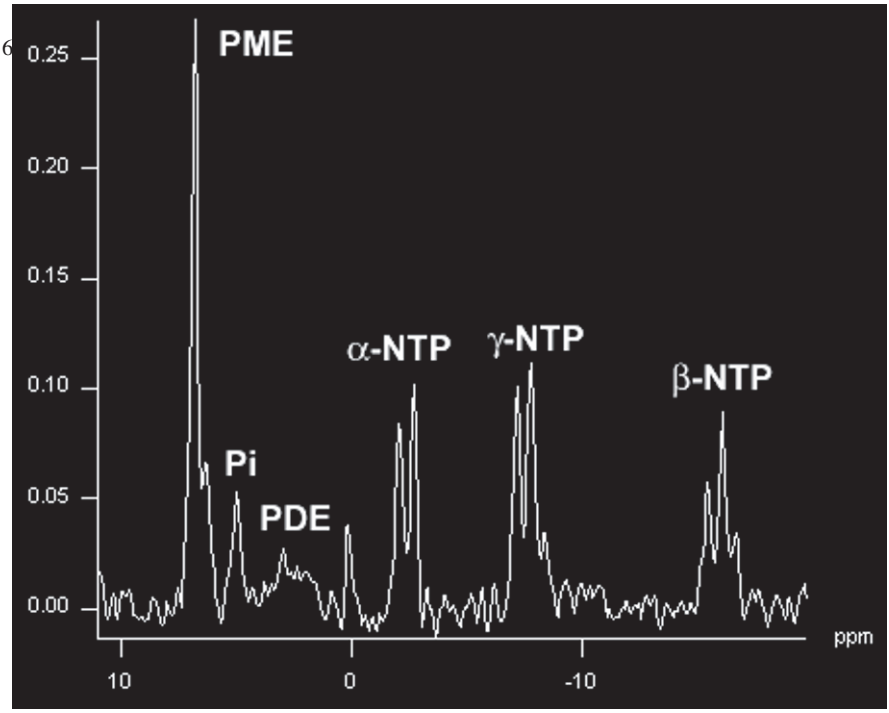

Fig. 18.1 A ^{31}P spectrum from a lymphoma patient measured using a 1.5 T clinical scanner in the Hospital of the University of Pennsylvania. Various phosphorus metabolite peaks including PME and three NTPs were observed.

detected therapeutic response within one cycle of therapy with CHOP (cyclophosphamide, doxorubicin, vincristine, prednisone), rituximab plus CHOP (RCHOP) or radiation (15 Gy) through detection of a decrease in lactic acid (Lac) or total choline (tCho) and an increase of apparent diffusion coefficients (ADC). We have also performed ^{1}H MRS of NHL patients in a clinical scanner. One of the patients exhibited a 70% decrease in Lac within 48 h of treatment with RCHOP.

18.1 Introduction

Nuclear magnetic resonance (NMR) can provide *in vivo* non-invasive measures of therapeutic response in cancer patients and cancer animal models. By detecting metabolic or physiological changes of cancer following treatment by MRS and MRI, respectively, therapeutic responses that precede tumor volumetric changes can be detected non-invasively. *In vivo* MRS and physiologically sensitive MRI are already playing important roles in the clinic for patients who have cancer in the brain, breast, or prostate. However, for NHL, clinical NMR is only being used

in the form of anatomical MRI to complement computerized tomography (CT) and [^{18}F]fluorodeoxyglucose positron emission tomography (FDG PET). Providing physicians with biochemical and biophysical information obtainable by NMR can benefit the patient by predicting or observing early therapeutic response, thereby facilitating timely modification of treatment regimens. Development of this capability is the underlying rationale for this study.

18.2 NMR Therapeutic Response Markers in Non-Hodgkin's Lymphoma

18.2.1 ^{31}P MRS of non-Hodgkin's lymphoma patients

A multi-institutional group consisting of Columbia University (T. Brown), University of Pennsylvania (J.D. Glickson), Memorial Sloan Kettering Cancer Center (J. Koutcher), St. George's Hospital in UK (J. Griffiths), Royal Marsden Hospital and Institute of Cancer Research in UK (M.O. Leach), and Radboud University Nijmegen Medical Centre in Netherlands (A. Heerschap) has been measuring pretreatment ^{31}P MRS of non-Hodgkin's lymphoma patients for prediction of therapeutic response. Patients failed to show a complete response (CR, i.e., complete disappearance of the local tumor) if their pretreatment PME/NTP level fell above a threshold level that was defined with the help of the International Prognostic Index (a purely clinically determined classification of the stage of NHLs). Those with PME/NTP ratios below this threshold level exhibited roughly a 50% rate of CRs [1,2].

18.2.2 ^{1}H MRS/MRI of NHL xenografts

We have performed ^{1}H NMR studies of therapeutic response of an NHL xenograft model to CHOP (cyclophosphaamide, doxorubicin, vincristine, prednisone) chemotherapy, rituximab plus CHOP immunochemotherapy, and radiation therapy. ^{1}H MRS measured lactate and total choline levels of the tumor. Lactate was detected using the selective multiple quantum coherence (SelMQC) or the Hadamard-encoded SelMQC (Had-SelMQC) sequence [3], and total choline was detected using the stimulated echo acquisition mode (STEAM) sequence. ^{1}H MRI measured T_2 and apparent diffusion coefficients (ADC) of tumor water. T_2 was measured using a spin echo sequence with varied echo times, and ADC was measured using a diffusion-weighted sequence by the trace of the diffusion tensor. Fig. 2A shows representative SelMQC spectra from a lymphoma xenograft at various time points during CHOP chemotherapy. The Lac/water ratio is displayed as a function of time following drug administration. Control tumors did not exhibit a change in the Lac/water ratio while treated tumors showed a decrease of this ratio. Fig. 2B shows a representative STEAM spectrum

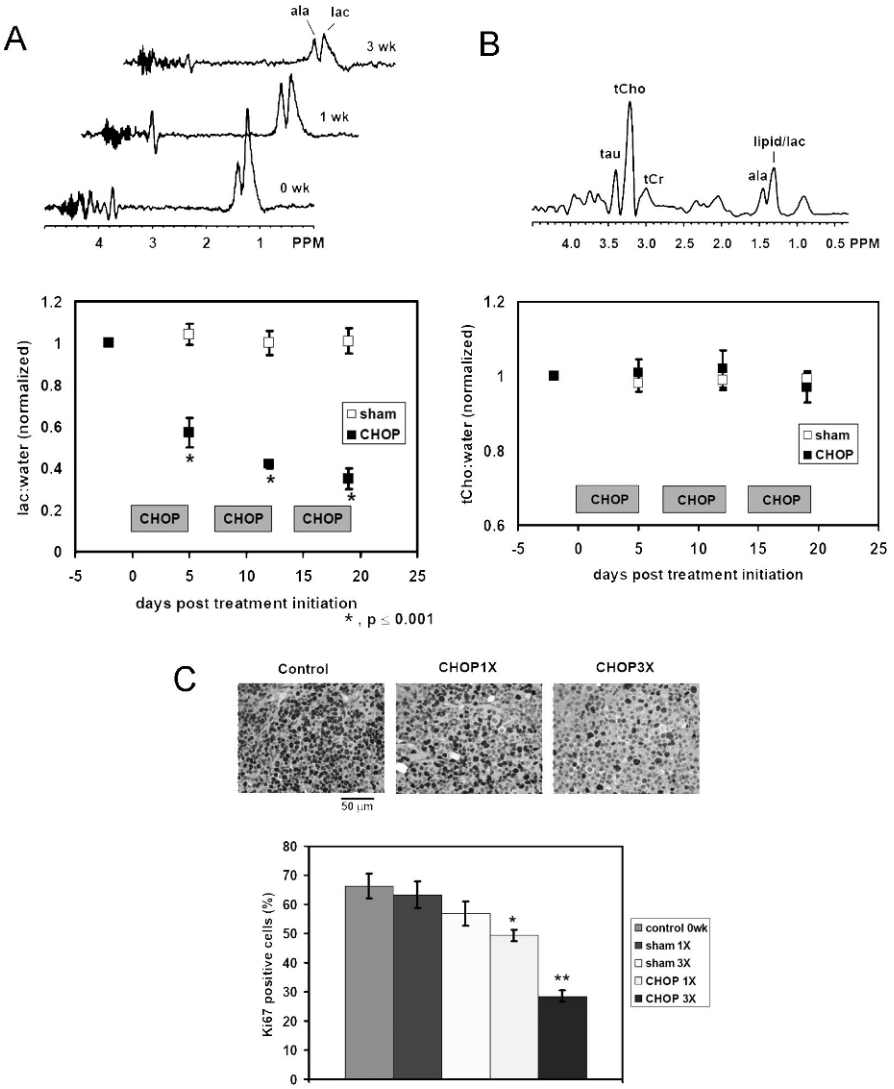

Fig. 18.2 NMR metabolic changes upon CHOP chemotherapy in an NHL xenograft model. Extracted and rearranged from: In vivo MRS markers of response to chemotherapy in a non- Hodgkin's lymphoma xenograft, Lee et al, NMR in Biomedicine 21:7, Copyright © 2008, Wiley-Blackwell.

from the xenograft and the time course of the tCho/water ratio, which did not change following CHOP chemotherapy. These studies demonstrate that Lac is a very early indicator of response to CHOP chemotherapy in this NHL model. Fig. 2C shows Ki67 staining of tumor tissues following chemotherapy. The Ki67 index decreased after treatment in parallel with the Lac/water changes. The *in vivo* lactate levels correlate with the proliferation of tumor cells [4]. This is consistent with the hypothesis

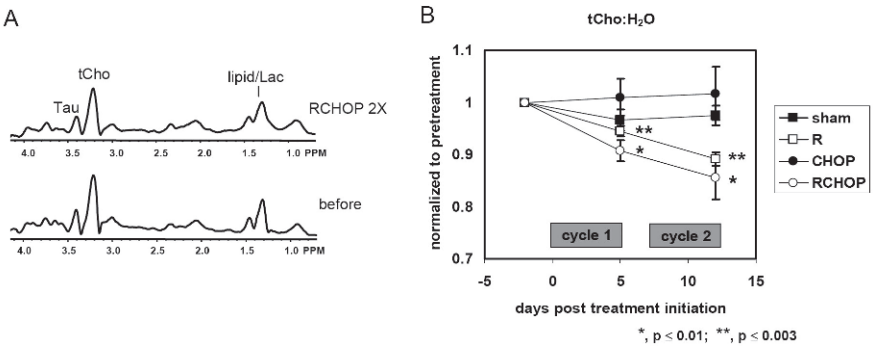

Fig. 18.3 NMR metabolic response upon rituximab plus CHOP immunochemotherapy. Extracted from: In vivo ^{1}H MRS of WSU-DLCL2 human non-Hodgkin's lymphoma xenografts: response to rituximab and rituximab plus CHOP, Lee et al., NMR in Biomedicine 22:3, Copyright © 2009, Wiley-Blackwell.

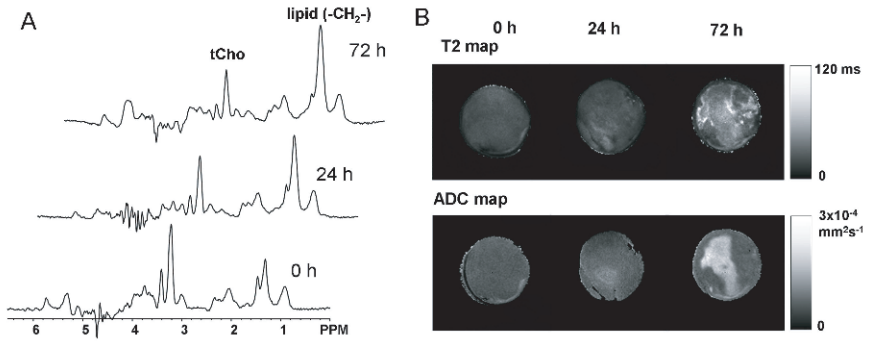

Fig. 18.4 NMR metabolic and physiological responses to a 15 Gy radiation in an NHL xenograft. Extracted from: Early detection of radiation therapy response in non-Hodgkin's lymphoma xenografts by *in vivo* ^{1}H magnetic resonance spectroscopy and imaging, Lee et al., NMR in Biomedicine 23:6, Copyright © 2010, Wiley-Blackwell.

that increased glycolysis of tumor cells serves mainly to provide building blocks for cellular replication rather than to compensate for energy deficits resulting from diminished mitochondrial activity [5].

We next applied the same ^{1}H MRS methods to rituximab immunotherapy and rituximab plus CHOP immunochemotherapy of the NHL xenograft. Lac/H_2O did not change with rituximab, while tCho/H_2O decreased after inclusion of rituximab in the therapy. This suggests that *in vivo* tCho/H_2O is an indicator of response to rituximab [6].

We then applied the ^{1}H MRS and T_2- and diffusion-weighted MRI methods to radiation therapy of the NHL xenograft. Lac/H_2O and tCho/H_2O decreased and lipid (-CH_2-)/H_2O increased within 24 h after 15 Gy radiation. The apparent diffusion coefficient (ADC) increased at 72 h after radiation, while overall T_2 did not change until 72 h [7].

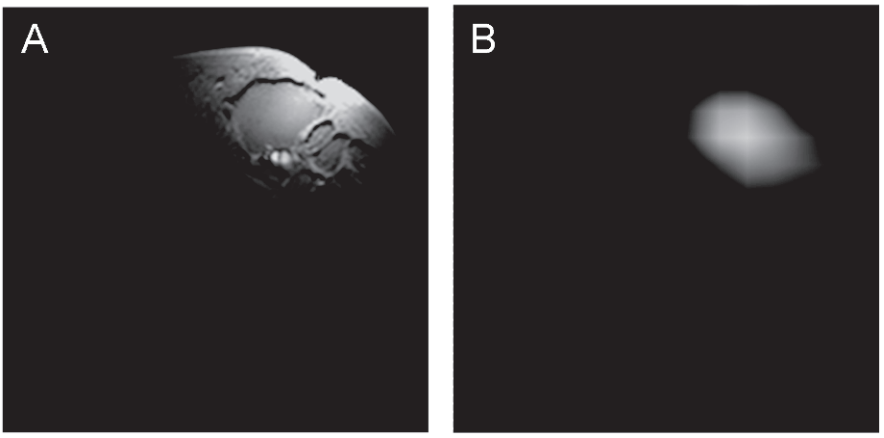

Fig. 18.5 An NHL patient with diffuse large B-cell lymphoma in the inguinal node. A proton T_2-weighted water image (A), and a proton lactate image (B).

18.2.3 ^{1}H MRS of non-Hodgkin's lymphoma patients

Success in the study of animal models of NHL prompted us to translate the HadSelMQC sequence to a standard 3T scanner (Siemens, Trio) [8]. Lactate levels from NHL patients as well as a normal volunteer subjected to tourniquet-induced vascular occlusion of the leg were successfully imaged *in vivo*. In one of several preliminary studies of NHL patients, a 63 yr old male patient with an inguinal diffuse large B-cell lymphoma exhibited a 70% decrease in Lac, 15% increase in tCho and 25% decrease in tumor volume within 48 hr of treatment with one cycle of RCHOP. This patient then went on to show a CR and is still in remission at one year from treatment. This early clinical study demonstrates that Lac is a very early indicator of response, and the increase in tCho suggests that the patient may be refractive to rituximab therapy; this will have to be confirmed in future studies of confirmed R-refractive patients.

18.3 Discussion

Lactate is the end product of glycolysis. Phosphocholine, a major constituent of tCho, is a precursor of the synthesis of the membrane phosphopolipid, phosphatidylcholine. The importance of aerobic glycolysis to the metabolism of the cancer cell has been noted since Warburg's classical work [9]. The significance of phospholipid metabolism in tumor growth has only recently begun to be appreciated [10]. We are actively investigating the mechanism(s) underlying the role of these pathways as indices of tumor therapeutic response. Lactate imaging monitors the same metabolic pathway, glycolysis, as does FDG PET, the currently accepted standard for evaluating therapeutic response of NHL. The NMR methods offer a number of

advantages: 1) cheaper, 2) no radiation exposure, and 3) they may detect and predict response sooner. Comparative studies of the utility of ^{1}H MRS/MRI vs. FDG PET as indicators of therapeutic response are planned for the future.

18.4 Conclusions

NMR provides noninvasive markers of early therapeutic response to various therapies in non-Hodgkin's lymphoma, which is expected to play important roles in follow-up and modification of treatments of NHL patients in the clinic.

Acknowledgments

This research was performed with the support of NIH grants R01-CA101700, 1R01CA118559, 2U24-CA083105, 5P41RR002305.

References

1. Arias-Mendoza F, Smith MR, Brown TR. (2004) Predicting treatment response in non-Hodgkin's lymphoma from the pretreatment tumor content of phosphoethanolamine plus phosphocholine. Acad Radiol 11:368-376.
2. Arias-Mendoza F, Payne GS, Zakian K et al (2008) Treatment response predictor using 31P MRS for CHOP and R-CHOP Therapy in Diffuse Large B-Cell Lymphoma. Proc Intl Soc Mag Reson Med 16:768.
3. Pickup S, Lee SC, Mancuso A et al (2008) Lactate imaging with Hadamard-encoded slice-selective multiple quantum coherence chemical-shift imaging. Magn Reson Med 60:299-305.
4. Lee SC, Huang MQ, Nelson DS et al (2008) In vivo MRS markers of response to chop chemotherapy in the WSU-DLCL2 human diffuse large B-cell lymphoma xenograft. NMR Biomed 21:723-733.
5. Bui T, Thompson CB. (2006) Cancer's sweet tooth. Cancer Cell 9:419-420.
6. Lee SC, Delikatny EJ, Poptani H et al (2009) In vivo ^{1}H MRS of WSU-DLCL2 human non-Hodgkin's lymphoma xenografts: response to rituximab and rituximab plus CHOP. NMR Biomed 22:259-266.
7. Lee SC, Poptani H, Pickup S et al (2010) Early detection of radiation therapy response in non-Hodgkin's lymphoma xenografts by *in vivo* ^{1}H magnetic resonance spectroscopy and imaging. NMR Biomed 23:624-632.
8. Mellon EA, Lee SC, Pickup S et al (2009) Detection of lactate with a hadamard slice selected, selective multiple quantum coherence, chemical shift imaging sequence (HDMD-SelMQC-CSI) on a clinical MRI scanner: application to tumors and muscle ischemia. Magn Reson Med 62:1404-1413.
9. Warburg O. (1956) On the origin of cancer cells. Science 123:309-314.
10. Podo F. (1999) Tumour phospholipid metabolism. NMR Biomed 12:413-439.

Chapter 19
Characterizing Breast Cancer Mouse Xenografts with $T_{1\rho}$-MRI
A Preliminary Study

Lin Z. Li, He N. Xu, and Ravinder Reddy

Abstract Previously three imaging methods, dynamic contrast enhanced magnetic resonance imaging (DCE-MRI), $T_{1\rho}$-MRI, and low temperature NADH/Fp (reduced nicotinamide adenine dinucleotide/oxidized flavoprotein) fluorescence imaging (redox scanning) were reported to differentiate the mouse xenografts of a less metastatic human melanoma cell line A375P and a more metastatic line C8161. The more metastatic melanoma is characterized by less blood perfusion/permeability and more oxidized mitochondrial redox state in the tumor core and lower $T_{1\rho}$ relaxation time averaged across the tumor section. These features may be useful for identifying imaging biomarkers for cancer metastatic potential. Here, we have employed $T_{1\rho}$- and T_2-weighted MRI to image mouse xenografts of two human breast cancer lines (more metastatic MDA-MB-231 and less metastatic MDA-MB-468) on a vertical bore 9.4-T Varian MR system. The preliminary results indicated that the more metastatic MDA-MB-231 tumors had shorter $T_{x\rho}$ relaxation constants on average than the less metastatic MDA-MB-468 tumors, and $T_{x\rho}$ relaxation might be a potential biomarker of breast tumor metastatic potential. Distinct ring-like structures were observed on $T_{x\rho}$-weighted MR images of the breast tumors, indicating tumor core and rim difference. This observation appears to be consistent with the tumor core-rim difference previously observed by DCE-MRI and redox scanning on aggressive melanoma xenografts.

19.1 Introduction

A biomarker of tumor aggressiveness or metastatic potential may help physicians to select proper treatment strategies and evaluate treatment response for cancer patients. Imaging biomarkers have the advantage of providing spatial and/or temporal distribution information about biological or physiological indices and have been increasingly utilized in the translational cancer research and clinical practice. The long-term objective of this study is to identify imaging biomarkers for tumor metastatic potential.

Department of Radiology, School of Medicine, University of Pennsylvania, Philadelphia, PA, USA
e-mail: linli@mail.med.upenn.edu

J.C. LaManna et al. (eds.), *Oxygen Transport to Tissue XXXII*, Advances in Experimental Medicine and Biology 701, DOI 10.1007/978-1-4419-7756-4_19,

Previously, proton magnetic resonance imaging (MRI) and optical imaging techniques have been employed to characterize mouse xenografts of human melanoma cell lines with different levels of aggressiveness [1]. The aggressiveness of these lines had been characterized by the clinical data, the measurement of the tumor metastatic potential in mouse models, and the invasive potential of cell lines *in vitro* by the Boyden chamber method. DCE-MRI observation and histological assay of the vascular structure of tumor tissue indicated that a highly metastatic melanoma had lower blood perfusion in the tumor core compared to a poorly metastatic melanoma. $T_{1\rho}$-MR indicated that the average $T_{x\rho}$ value in metastatic melanoma was shorter than in indolent melanoma. Although $T_{x\rho}$-MRI is sensitive to pH, oxygenations, and protein concentrations, the underlying mechanism for this difference between the aggressive and indolent tumors awaits further investigation. Distinct tumor core-rim difference was also observed by low temperature NADH/Fp fluorescence imaging [2], which provides not only images of the relative intensity of NADH (reduced nicotinamide adenine dinucleotide) and Fp (oxidized flavoprotein) fluorescence in tissue, but also images of redox ratio. Higher Fp redox ratio, Fp/(Fp+NADH), indicates a more oxidized mitochondrial redox state. The melanoma tumor core exhibited more oxidized mitochondrial redox status compared to the tumor rim as indicated by the Fp redox ratio. The Fp redox ratios in the oxidized tumor regions were also found to correlate linearly with the aggressiveness of five melanoma xenografts spanning the full range of tumor progression to metastasis.

The low temperature NADH/Fp fluorescence imaging has also been applied to mouse xenografts of human breast cancer cell lines MCF-7 (poorly metastatic) and MDA-MB-231 (highly metastatic) [3]. The preliminary redox imaging data obtained were consistent with those of melanoma mouse xenografts, i.e., the more metastatic breast tumors exhibit more oxidized tumor cores with higher Fp redox ratios than those of indolent tumors. Several redox imaging biomarkers including Fp redox ratio, NADH, and Fp nominal concentrations have been shown to differentiate between MCF-7 and MDA-MB-231 tumors. Therefore, it would be interesting to explore whether DCE-MRI and $T_{x\rho}$-MRI can distinguish between the poorly metastatic and highly metastatic breast tumors xenografted in mice, and whether the similar results consistent with those obtained on melanoma models can be obtained on breast tumor models as well.

In this paper, we report the preliminary $T_{x\rho}$-MRI data obtained on a highly metastatic breast tumor xenograft MDA-MB-231 and a less metastatic breast tumor xenograft MDA-MB-468 [4]. Our data indicate that $T_{x\rho}$-MRI can differentiate between these two lines with different metastatic potential and MDA-MB-231 breast tumors exhibited core-rim difference on $T_{x\rho}$-MRI. Our study suggests that clinically translatable $T_{x\rho}$-MRI may be a possible imaging biomarker for breast cancer metastatic potential.

19.2 Methods

Human breast cancer cell lines (MDA-MB-231 and MDA-MB-468) were grown in PRMI culture medium reaching about 100% confluency and then harvested to be

subcutaneously implanted into the flanks or the upper parts of legs of athymic nude mice (NCI strain 01B74 NCr-nu/nu). Each inoculation consists of about 10 million breast cancer cells in 100 μl PBS buffer (pH=7). When tumors reached the size of 6∼9 mm in diameter, the mice were subject to MRI scans under anaesthesia with continuous O_2 flow doped with 1-2% isofluorane. Three MDA-MB-231 tumors and two MDA-MB-468 tumors were imaged by $T_{x\rho}$- and T_y-weighted MRI.

$T_{x\rho}$-MRI of mouse tumors were conducted on a 9.4-T vertical bore Varian MR spectrometer. $T_{x\rho}$-MR sequence [5] started with a spin-locking three pulse cluster (time of spin locking denoted as TSL and spin-locking frequency as SLF) to lock the proton magnetization in the transverse plane and then followed with a regular spin-echo data acquisition. A single slice spin echo $T_{x\rho}$-MRI sequence (TR 3s, TE, 4 TSLs ranging from 15-125 ms, field of view (FOV) 2.0 cm) was used to acquire images of a plane sectioning the central portion of a tumor. Customized IDL (Interactive Data Language) programs were used to fit the data to a single exponential component decay to obtain the $T_{x\rho}$gelaxation time and $T_{x\rho}$ maps. Regular T_y-MRI (TR 1.5s, 5 equal spaced TEs varying from 12-67 ms, thickness 1-2 mm, FOV 2 cm) was also conducted to obtain T_y-weighted MR images of tumor slices and generate T_2 maps with a single exponential fit of the signal changes versus TEs. For some tumors, a multi-slice $T_{x\rho}$-MRI sequence (TR 3s, TE 12ms, 4 equally-spaced TSLs starting from 15-30 ms to about 120 ms, thickness 2 mm, matrix 64x64) and T_y-MRI sequence were used to acquire $T_{x\rho}$- and T_2-weighted images, respectively, across the entire tumor volume.

19.3 Results and Discussion

Figure 1 shows preliminary results from single slice MRI. The mean $T_{1\rho}$ and T_2 relaxation times of each tumor group were plotted in the graph. The more metastatic

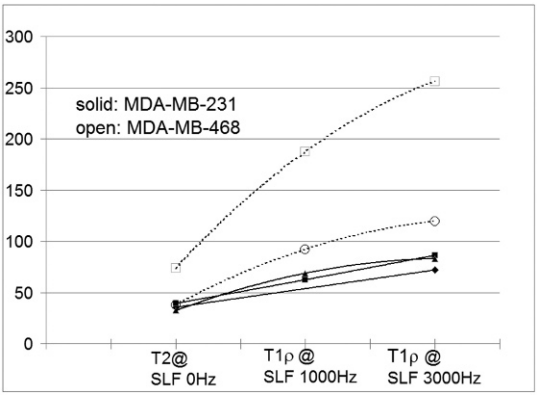

Fig. 19.1 Comparison of the average T_2 and $T_{1\rho}$ relaxation time constants (in ms) between MDA-MB-468 (N=2, open symbols and dashed lines) and more metastatic MDA-MB-231 tumors (N=3, solid symbols and solid lines).

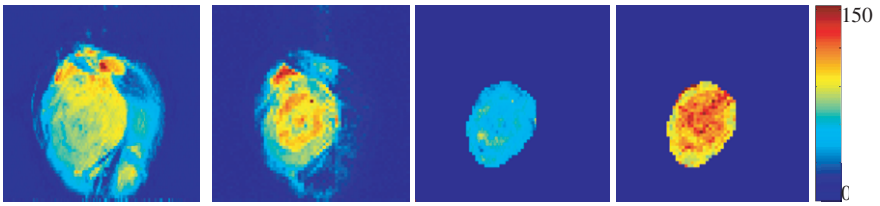

Fig. 19.2 Representative images of a slice sectioning the center of a MDA-MB-231 tumor. (a) T_2-weighted image; (b) $T_{1\rho}$-weighted image; (c) T_2 map; (d) $T_{1\rho}$ map. The range of T_2 or $T_{1\rho}$ relaxation time constants in ms is indicated by the colorbar.

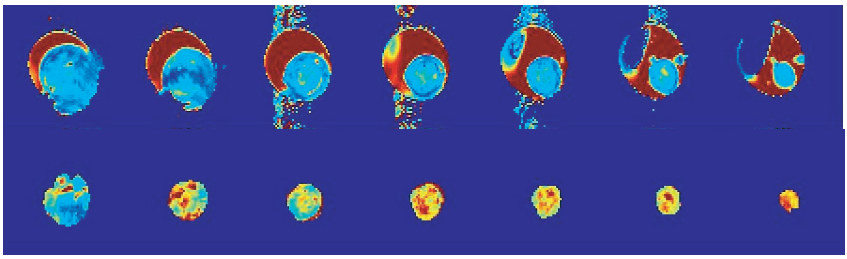

Fig. 19.3 Multi-slice T_2 (upper row) and $T_{1\rho}$ (lower row) maps for a typical MAD-MB-231 tumor. Image orientation was in parallel with the body surface and the top of the tumor. The depth of the image slices (1mm thickness) ranged from about 1 mm (right) to 7mm (left). Field of view = 2.5 cm. The dark red regions in the 1^{st} row were not tumors but gels used for enhancing B_1 field homogeneity for more effective $T_{1\rho}$-MR.

MDA-MB-231 tumors had shorter average $T_{1\rho}$ relaxation constants than the less metastatic MDA-MB-468 tumors, whereas T_2 does not differentiate well between these two lines.

A distinct ring-like structure was observed on $T_{1\rho}$ weighted MR images of breast tumors, indicating tumor core and rim difference in MDA-MB-231 (Fig. 2). The tumor core-rim difference was also observed on T_2-weighted images but appeared to be less distinct. Thus, $T_{1\rho}$ maps appear to show higher heterogeneity than T_2 maps. This is further supported by multi-slice $T_{1\rho}$ and T_2 maps indicating hot regions (higher relaxation values) in the tumor core areas, whereas T_2 maps did not show a distinct difference (Fig. 3). This observation appears to be consistent with the tumor core-rim difference previously observed by DCE-MRI and redox scanning on aggressive melanoma xenografts.

19.4 Discussion

Our studies on melanoma and breast cancer mouse xenografts support that $T_{1\rho}$ relaxation time constant can be a potential biomarker for cancer aggressiveness in the clinic. $T_{x\rho}$ relaxation rates reflect the interaction between water protons and macromolecules, and $T_{1\rho}$ relaxation is sensitive to macromolecular concentration and pH,

oxygen saturation and cell death. Further study is needed to explore the underlying mechanism for the $T_{x\rho}$ differences.

Heterogeneities in relaxation constants were also observed for some MDA-MB-468 tumors. Work is in progress to characterize these heterogeneities in more tumors and compare with those of MDA-MB-231. Work is also in progress to study more breast tumors with MRI followed by redox scanning, and compare the MR images with the redox scanning images of the same breast tumor at various depths from the tumor surface. Since the higher Fp redox ratio in the tumor core but not in the rim has been shown as a potential biomarker for tumor metastatic potential, it will be interesting to test if $T_{1\rho}$ value in the tumor core and rim may differ in their power to predict tumor aggressiveness as well.

19.5 Conclusions

Clinically translatable $T_{1\rho}$- and T_2-MR imaging has been applied to mouse xenografts of two human breast tumor lines MDA-MB-231 (more metastatic) and MDA-MB-468 (less metastatic). Our preliminary data indicated that the average $T_{1\rho}$ value might distinguish between these two tumor lines but the average value of T_2 did not. Multislice $T_{1\rho}$ images showed a distinct tumor core-rim difference with some core regions having higher $T_{1\rho}$ values. Our studies on melanoma and breast cancer mouse xenografts support that $T_{1\rho}$ relaxation time constant can be a potential biomarker for cancer aggressiveness in the clinic.

Acknowledgments

This work is supported by the Susan G. Komen Foundation Career Catalyst Research Grant (Lin Z. Li, KG080169) and Center for Magnetic Resonance and Optical Imaging, an NIH-supported research resource (Ravinder Reddy, RR02305). We would also like to acknowledge the technical assistance received from Dr. Steve Pickup and valuable discussions with Dr. Jerry Glickson.

References

1. Li LZ, Zhou R, Xu HN et al (2009) Quantitative magnetic resonance and optical imaging biomarkers of melanoma metastatic potential. Proceedings of the National Academy of Sciences of the USA 106:6608-6613
2. Li LZ, Xu HN, Ranji M et al (2009) Mitochondrial redox imaging for cancer diagnostic and therapeutic studies. Journal of Innovative Optical Health Sciences 2:325-341
3. Xu HN, Nioka S, Glickson JD et al (2010) Quantitative mitochondrial redox imaging of breast cancer metastatic potential. Journal of Biomedical Optics, 15:036010

4. Sieuwerts AM, Klijn JG and Foekens JA (1997) Assessment of the invasive potential of human gynecological tumor cell lines with the in vitro Boyden chamber assay: influences of the ability of cells to migrate through the filter membrane. Clinical & Experimental Metastasis 15:53-62
5. Wheaton AJ et al (2004) Pulse sequence for multislice $T_{1\rho}$-weighted MRI. Magnetic Resonance in Medicine 51:362-369

Chapter 20
Effect of AEM Energy Applicator Configuration on Magnetic Nanoparticle Mediated Hyperthermia for Breast Cancer

Krishna K. Sanapala, Kapila Hewaparakrama, and Kyung A. Kang

Abstract Magnetic nanoparticle mediated low heat hyperthermia (42∼45^{o}C) *via* alternating electromagnetic (AEM) energy is a promising, cancer specific and minimally-invasive cancer therapy. Iron oxide particles frequently used for this therapy are non-toxic and already used as a contrast agent for magnetic resonance imaging. One important issue in the hyperthermia is applying an appropriate amount of energy to the tumor at various sizes and depths, with a minimal damage to normal tissue. For the therapy to be desirable, the AEM energy applicator needs to be non-invasive and user-friendly. To better understand the effect of the probe on the magnetic field distribution, computer simulation was performed for the field distribution by probes with various configurations. In a solenoid-type probe, the field is mainly inside the probe and, therefore, is difficult to use on body. A pancake-shaped probe is easy to use but the field penetration is shallow and, thus, may better serve surface tumor treatment. A sandwich probe, composed of two pancake probes, has a penetration depth deeper than a pancake probe. The results also showed that the spacing between two adjacent coils and the number of coil turns are very important for controlling the field penetration depth and strength. Experiments were also performed to study the effects of the size and concentration of iron oxide nanoparticles on heating. Among the tested particle sizes of 10∼50 nm, 30 nm particles showed the best heating for the same mass.

20.1 Introduction

Current cancer hyperthermia is performed mainly in two ways: ablation of tissue area containing tumor at a very high temperature and the low-heat (∼42^{o}C) hyperthermia[1]. For the thermal ablation, radio-, micro- or ultrasound waves are often used either externally or with an internal applicator. Its potential side effects can be pain, infection, bleeding, blood clots, swelling, burns and blistering at the site, and damage to the skin, muscles, and nerves near the treated area[1,2,3]. Recently, magnetic

Department of Chemical Engineering, University of Louisville, Louisville, KY 40292, USA
e-mail: kyung.kang@louisville.edu

J.C. LaManna et al. (eds.), *Oxygen Transport to Tissue XXXII*, Advances in Experimental Medicine and Biology 701, DOI 10.1007/978-1-4419-7756-4_20,

nanoparticle (MNP) mediated, low-heat hyperthermia has attracted considerable attention. Neel and Brownian relaxations appear to be the two main mechanisms contributing to heating[4,5]. When conjugated with cancer-targeting biomolecules, these particles can deliver heat selectively to the tumors[5,6,7].

The main operational parameter for heating the tumor containing MNPs is the magnetic field strength generated by the AEM field generator. The field strength depends on the AEM application-probe configuration, the spacing between the two adjacent coils, and the number of coil turns[7,8]. Currently, solenoid-type AEM probes are used, which is uncomfortable for patients and not very efficient in delivering AEM fields to the tumor site inside the breast tissue. The heating performance depends also on the MNP size and concentration[7,9]. The size should be appropriate for generating a large amount of heat, minimizing the amount of MNPs required for efficient treatment.[7] In addition, the MNPs need to be small enough to avoid accumulation in excretory organs, but big enough to increase the blood circulation time and cellular uptake. Although more studies are needed, a reasonable size may be larger than biomolecules (> 5 nm) but smaller than 100 nm[10,11] . In the present work, the effects of the probe configuration and the particle size and concentration of MNPs on heating performance were studied.

20.2 Materials, Instruments, and Methods

The AEM field generator [frequency, 135-400 kHz; maximum power, 12.5 kW] was purchased from Taylor Winfield (Brook Field, OH). The three probe configurations tested were solenoid [3 turn probe of 3 cm outer diameter made of 5 (W) x 5 (H) mm coil with 3 mm spacing between adjacent turns], pancake [3 turn, 3 cm diameter, 5 (W) x 5 (H) mm, 2 mm spacing] and sandwich [two, 3 turn pancake probes (5 cm diameter), 5 (W) x 5 (H) mm, 2 mm]. Iron oxide nanoparticles at sizes of 10, 20, 30, 40 and 50 nm were supplied by Ocean Nanotech (Springdale, AR). For the nanoparticle heating experiment, the sample was placed in a glass test tube, wrapped with aerogel insulation (Cabot Aerogel; Billerica, MA) and subjected to AEM field for a predetermined time. Digital thermometer (Fisher Scientific; Pittsburg, PA) and infra-red thermometer (Fluke Corporation; Beijing, China) were used for sample temperature measurements before and after heating. MAT Lab and Simulink (MathWorks; Natick, MA) were used for computer simulation[8] of magnetic field distribution generated by various probes.

20.3 Results and Discussion

20.3.1 Effect of probe configuration on magnetic field distribution

To better understand the magnetic field distribution generated by the probes with various configurations, computer simulations[8] were performed for a solenoid, a pancake, and a sandwich probe with an outer diameter of 4.5 cm, 3 coil turns and 0.75 cm spacing between two adjacent turns. In the simulation, the coil was assumed to be a line. For this study, a current of 1A was applied to the probe.

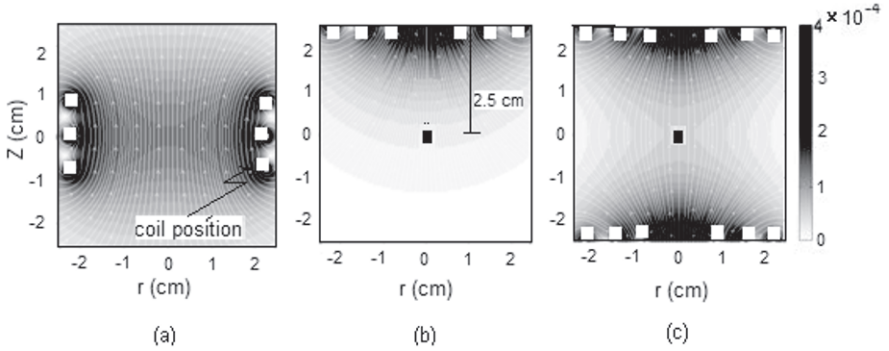

Fig. 20.1 Magnetic field distributions for (a) a solenoid, (b) a pancake, and (c) a sand-wich probes.

For the solenoid probe, the magnetic field is concentrated mainly inside the probe (Figure 1(a)). Therefore, the sample or tissue containing tumor may have to be placed in the core of the probe. Among the three probes, at the same dimension, magnetic field strength at the center of the solenoid probe is highest. However, if this probe is to be used for humans, the diameter of the probe needs to be much larger than 3 cm, which will reduce the field strength extensively. In addition, the probe shape is not user-friendly for the patients because, during the treatment, the coil needs to wrap around the organ or body parts. A flat pancake-shaped probe is user-friendly. The magnetic field is strong around the probe but the field penetration depth is rather shallow (Figure 1(b)). Therefore, this probe will be good for shallow tumor treatment. The sandwich-shaped probe had a better field penetration and also higher field strength than the pancake probe (Figure 1(c)). When the field strengths at 2.5 cm away from the pancake and sandwich probes were compared, assuming the cancer tumor is in the middle of the breast tissue (Figure 1(b) and (c)), a sandwich probe was found to generate a field strength twice that of a pancake probe.

At a constant power level, the field intensity can change by changing the number of turns of the coil. Figure 2(a) and (b) show the field distributions of sandwich probes with 2 and 4 turns, respectively. In the entire field, the field of the 4-turn probe shows greater strength than that of the 2-turn one. When the field strength at a point 2.5 cm (in the middle of the two probes) was compared, the 4-turn probe was found to generate twice the strength generated by the 2-turn probe. The intensity in the middle of the probe linearly increases with the number of the turns and the depth of field penetration increases (Figure 2(c)). When the spacing between two adjacent coil turns decreases, the field strength around the probe increases with less penetration depth (data not presented). In practice, the spacing may be reduced only up to a certain limit because the coil is air-cooled through it.

20.3.2 Effect of MNP concentration on heating

Figure 3(a) shows heating of the MNPs using a solenoid probe with the change in concentration between 0.01 and 0.1 wt%, at a constant power of 3,850W (70V and

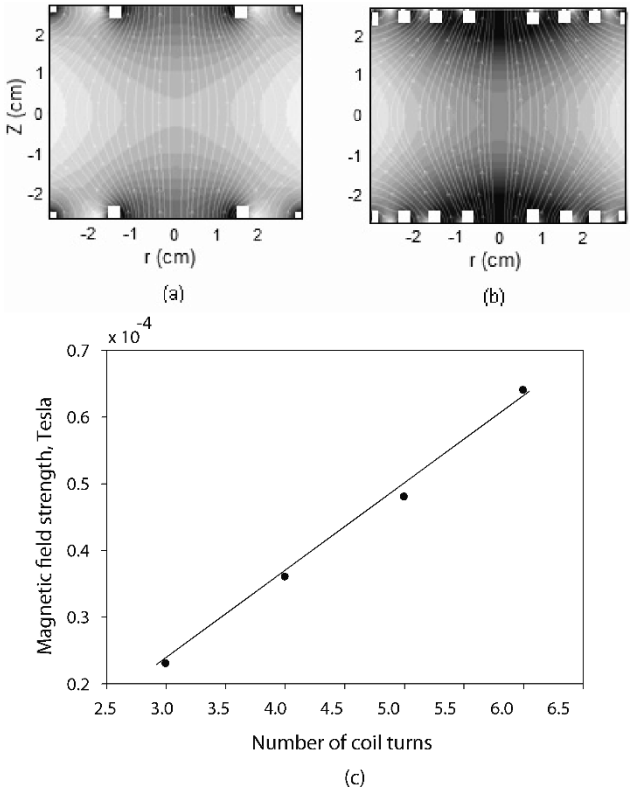

Fig. 20.2 Magnetic field distribution of a sandwich probe with (a) 2 and (b) 4 coil turns. (c) Effect of the number of coil turns on magnetic field strength at 2.5 cm away from the probe [current, 1A].

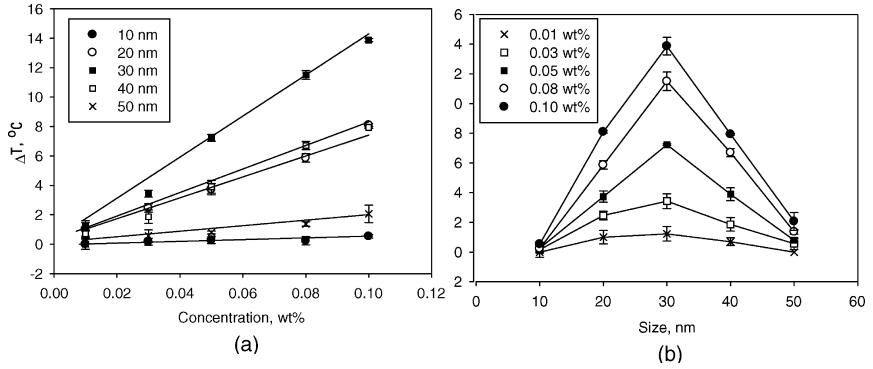

Fig. 20.3 Effects of the particle (a) concentration and (b) size on heating. [probe type, solenoid; power, 3,850W; AEM application time, 5 mins]

55A). For all sizes, temperature rise linearly increased with the increase in particle concentration.

20.3.3 Effect of nanoparticle size on heating

To understand the effect of the MNPs size dependence on heating, nanoparticles of 10, 20, 30, 40 and 50 nm were subjected to an AEM field generated by a solenoid probe at a constant power of 3,850W. Of the nanoparticle sizes studied, at a constant wt%, 30 nm particles showed the greatest heating and 10 nm and 50 nm particles showed the lowest heating (Figure 3(b)).

20.4 Conclusions

For the effect of the probe configuration on heating at a constant diameter and number of turns, a solenoid probe generates a higher magnetic field than other configurations. However, for human use, the diameter of the solenoid probe needs to be much greater than the pancake or sandwich probes but this configuration is not user-friendly for the subjects and clinicians. The pancake probe generates a high field strength close to the probe and may be suitable for shallow tumor treatment. The sandwich probe, by a two-dimensional approach, can penetrate the magnetic field into a greater depth, and may be useful for the treatment of deep seated tumors. In all of the probes, increasing the number of turns increases the magnetic field strength.

Of the iron oxide nanoparticle sizes tested (10 to 50 nm), 30 nm has shown the highest heating at the same concentration. The particle heating linearly increases with increasing concentration.

With thorough understanding of the operational and system parameters in AEM field generation, and well-heating MNPs conjugated with appropriate cancer targeting biomolecules (e.g., monoclonal antibodies, aptamers, folate, etc.), MNP mediated hyperthermia may become a minimally invasive, highly cancer specific cancer therapy with minimal negative side effects.

References

1. Falk MH and Issels RD (2001), Hyperthermia in oncology, International Journal of Hyperthermia, 17, 1-18
2. Livraghi T, Lazzaroni S, and Meloni F (2001) Radiofrequency thermal ablation of hepatocellular carcinoma, European Journal of Ultrasound, 13, 159-166
3. Scoggins CR, Gleason JF, Martin RC, Kehdy FJ, Hutchinson JR, and McMasters KM (2004) Thermal ablation of liver tumors, Cancer Therapy, 2, 455-462

4. Kalambur VS, Han B, Hammer BE, Shield TW, Bischof JC (2005) In vitro characterization of movement, heating and visualization of magnetic nanoparticles for biomedical applications, Nanotechnology, 16, 1221–1233
5. Kotitz, R, Weitschies W, Trahms L, Semmler W (1999) Investigation of brownian and neel relaxation in magnetic fluids, Journal of Magnetism and Magnetic Materials, 201, 102-104
6. Jin H, Kang KA. (2007) Application of novel metal nanoparticles as optical/thermal agents in optical mammography and hyperthermic treatment for breast cancer, advances in experimental medicine and biology, 599, Oxygen Transport to Tissue XXVIII , 45-52
7. Jin H, Hong B, Kakar SS, Kang KA (2008) Tumor-specific nano-entities for optical detection and hyperthermic treatment of breast cancer, Advances in Experimental Medicine and Biology, 614 (31), Oxygen Transport to Tissue XXIX, 275-284
8. Smythe, WR (1950) Static and dynamic electricity, McGraw Hill publishers, New York
9. Hergt R, Andra W, D'ambly CG, Hilger I, Kaiser WA, Richter Uwe, Schmidt HG (1998)Physical limits of hyperthermia using magnetite fine particles, IEEE Transactions on Magnetics, 34(5), 3745-3754
10. Mornet S, Vasseur S, Grasset F, Veverka P, Goglio G, Demourgues A, Portier J, Pollert E, Duguet E (2004) Magnetic nano particle design for medical diagnosis and therapy, Journal of Materials Chemistry, 14, 2161–2175
11. Zhang SL, Li J, Lykotrafitis G, Bao G, Suresh S (2008) Size-dependant endocytosis of nanoparticles, Advanced Materials, 20, 1-6

Chapter 21
Highly Specific, NIR Fluorescent Contrast Agent with Emission Controlled by Gold Nanoparticle

Jianting Wang, Martin O'Toole, Archna Massey, Souvik Biswas, Michael Nantz, Samuel Achilefu, and Kyung A. Kang

Abstract Nanoparticles are currently being intensively studied for *in vivo* molecular imaging because of their unique and beneficial properties. Among these particles, some metal particles possess strong surface plasmon fields that can effectively alter fluorescence. Using this fluorescence alteration, an NIR fluorophore based, nano-sized contrast agent for breast cancer diagnosis is being developed. The fluorophore is conjugated to gold nanoparticles (GNP) *via* a short spacer whose length was specially adjusted to have the strong plasmon field to quench the fluorescence. The spacer also has a special molecular sequence that can be cleaved by an enzyme secreted by targeted cancer cells. Normally, the entity does not fluoresce. If it is delivered to the cancer site, the short spacer would be cleaved by the enzyme secreted by the cancer cell at which point the fluorescence would be restored. This entity can incorporate a cancer targeting molecule for a cancer specific delivery. The entity specifically targets cancer cells and fluoresce only when the spacer is cleaved by a specific cancer secreting biomolecule, providing dual specificity for cancer diagnosis. In the future, this entity will be combined with cancer drugs for seamless detection and personalized therapy.

21.1 Introduction

Fluorescence contrast agents have been extensively used in clinical diagnosis. Naturally, the agents providing high specificity are highly desirable for molecular imaging. Recently, nanoparticles have been intensively studied as candidates for image contrast agents and drug delivery because their small size allows interactions with

Jianting Wang, Martin O'Toole, and Kyung A. Kang
Department of Chemical Engineering, University of Louisville, Louisville, KY 40292, USA
e-mail: kyung.kang@louisville.edu

Archna Massey, Souvik Biswas, and Michael Nantz
Department of Chemistry, University of Louisville, Louisville, KY 40292, USA

Samuel Achilefu
Department of Radiology, Washington University School of Medicine, St. Louis, MO 63110, USA

J.C. LaManna et al. (eds.), *Oxygen Transport to Tissue XXXII*, Advances in Experimental Medicine and Biology 701, DOI 10.1007/978-1-4419-7756-4_21,

biological systems at a molecular level and they provide longer circulation time in the body[1]. Some metal nanoparticles, such as gold and silver, with the application of light, generate a strong surface plasmon field by oscillating electrons around the metal surface. The field strength may depend upon the metal type, particle size, and the wavelength of light[2,3]. If any fluorophore is within the field, the field may alter the fluorescence output. For the selected metal particle and fluorophore, the level of fluorescence alteration depends mainly on the distance between them. The surface plasmon field very close to the particle is so strong that, if a fluorophore is placed within it, the field attracts electrons associated with fluorescence emission resulting in fluorescence quenching[4]. If a fluorophore is placed at a particular distance from the particle, the fluorescence can be enhanced, because the plasmon field enhances the excitation decay rate of the fluorophore[2,3,4,5,6]. Gold is a metal of our interest because of its chemically inert nature and its ability to generate an intense surface plasmon field[2,7].

Utilizing the distance-dependent fluorescence alteration, we have been designing a near-infrared (NIR), nano-fluorescent contrast agent for highly specific cancer diagnosis. In this agent, the fluorophore is conjugated to a gold nanoparticle (GNP) *via* a short spacer so that the fluorescence is quenched. The short spacer is designed in such a way that it can be cleaved by a biomolecule secreted by the target cancer cells. Our nano-entity can also include a receptor mediated target, immobilized on the GNP surface. When this contrast agent is administered to a human, the targeting molecule leads the entity to the cancer site. At the cancer site, the short spacer is cleaved and fluorescence is emitted. This specific targeted delivery and disease-conditional fluorescence emission together provide dual-specificity for cancer site localization and diagnosis.

The model system to test the feasibility of our nano-entity is: For fluorophore, an FDA-approved, Indocyanine Green (ICG; Fig. 1(a))-based NIR fluorophore, Cypate (Fig. 1(b)), is used. Cypate, unlike ICG, has two functional groups for conjugation to other molecules[8]. A peptide containing a G-G-R motif is used in the short spacer (Fig. 1(c)), which can be cleaved by a breast cancer secreted enzyme, urokinase-type plaminogen activator (uPA)[9]. To improve the solubility and stability of the agent,

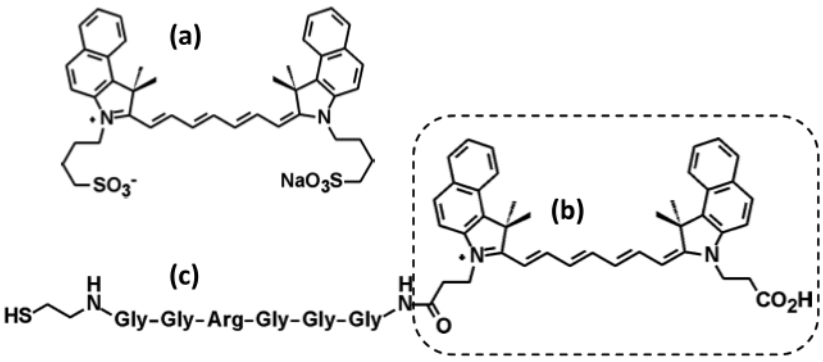

Fig. 21.1 Molecular structure of (a) ICG, (b) Cypate, and (c) Short spacer

a short PEG molecule HS-$(CH_2)_{11}$-$(C_2H_4O)_4$-OH was coated on the GNP surface. Here, the fluorescence quenching by attaching Cypate to GNP *via* the short peptide spacer and fluorescence de-quenching upon uPA addition was investigated. Although not yet studied, tamoxifen is our breast cancer targeting molecule which will guide our entity to the cancer site.

21.2 Materials and Methods

21.2.1 Synthesis of short spacer and Cypate Conjugation

The short-spacer $HSCH_2CH_2NH$–G–G–R–G–G–G-NH_2 (SL) was synthesized using standard solid-phase peptide synthesis techniques[10]. Cysteamine-loaded polystyrene resin and all amino acids were purchased from Novabiochem (San Diego, CA). 3-(diethoxyphosphoryloxy)-1,2,3-benzotriazin-4(3H)-one (DEPBT), Hydroxybenzotriazole (HOBt), N, N-Diisopropylethylamine (DIPEA), CH_2Cl_2, trifluoroacetic acid and triethylsilane were obtained from Aldrich (St. Louis, MO). Synthesized SL was analyzed by HPLC and high resolution mass spectrometry (HRMS). HPLC analysis and purifications were conducted on a Waters Corporation Delta 600 instrument (Waters corp.; Milford, MA). Fourier transform ion cyclotron resonance (FTCIR) measurements were performed on a Thermo LTQ-FT instrument (7 tesla; Thermo scientific, Waltham, MA). The length of the SL was estimated using the Hyperchem 7.5 software (Hypercube Inc.; Gainesville, FL).

The synthesis of Cypate has been previously reported[8]. Cypate (140 mg, 0.227 mmol) was added to the $HSCH_2CH_2NH$-G-G-R-G-G-G-NH_2-loaded resin (65 mg, 0.045 mmol peptide) in DMF at room temperature. DEPBT (68 mg, 0.227 mmol), HOBt (30 mg, 0.227 mmol), and DIPEA (0.08 mL, 0.45 mmol) were added as coupling agents. After shaking overnight, the resin was filtered and thoroughly washed with CH_2Cl_2 7 times. The resin then was dried under vacuum.

To the $HSCH_2CH_2NH$-G-G-R-G-G-G-NHC(O)-Cypate resin prepared above (15 mg, 0.01 mmol) in CH_2Cl_2 (0.3 mL), at room temperature, triethylsilane (0.06 mL) was added. After shaking for 15 min, trifluoroacetic acid (0.04 mL) was added and the resin suspension was shaken for 1 hr, allowed to stand for 1 hr, and then shaken for 3 hrs. The resin was filtered and the filtrate was concentrated by rotary evaporation. The residue was washed with diethylether 5 times and dried under vacuum to obtain the target cysteamine-hexapeptide-cypate (SL-Cy) conjugate (7 mg, 62% based on resin loading, 12% based on Cypate consumption). The conjugates were characterized with HRMS (FTCIR): $C_{59}H_{73}N_{12}O_9S$ $[M]^+$, calcd 1125.5338, found 1053.5114 (loss of acrylic acid $[M^+ - HO_2CCH = CH_2]$, calcd for $C_{56}H_{69}N_{12}O_7S$, 1053.5127.

21.2.2 Conjugation of SL-Cy to GNP and fluorescence measurement

Gold nanoparticle colloids (5 and 10 nm in citric and tannic acids) were purchased from Ted Pella (Redding, CA). (1-Mercapto-11-undecyl) tetra(ethylene gly-

col) (sPEG; MW, 380.58) was from Asemblon (Redmond, WA). Human urokinase from human (uPA) was purchased from Innovative Research (Novi, MI)

SL-Cy and sPEG were conjugated to 5 nm GNP with sPEG by the following steps: 16 μL SL-Cy (5 mg/mL in ethanol) was mixed with 30 μL sPEG (3.36 mg/ml) (molar ratio of SL-Cy/sPEG = 1:4), and the mixture was diluted in 5 mL ethanol; 5 mL of 5 nm GNP colloid (83 nM) was drop-wise added into the SL-Cy/sPEG solution with stirring. The same protocol was used for 10 nm GNP. For both 5 and 10 nm GNP, per unit GNP surface area was reacted to the same amount of SL-Cy/sPEG. The mixture of GNP, SL-Cy and sPEG was incubated with stirring for 4 hrs at room temperature. The solution was dialyzed in 2 L of DI H_2O overnight, and the dialyzed solution was centrifuged (11000 RPM, 45 min), and re-dispersed in 1.5 mL of H_2O. To quantify GNP and conjugated Cypate, absorption spectra were taken for the re-dispersed conjugates on a Beckman DU520 spectrometer (Beckman Instruments Inc.; Fullerton, CA).

Fluorescence was measured (all samples in 0.001M PBS buffer) in a 96-well Uniplate (Whatman; Florham Park, NJ) using a Spectra Gemini XPS fluorometer (Molecular Devices Corp.; Sunnyvale, CA). The excitation and emission wavelengths were 780 and 830 nm, respectively.

21.3 Results and Discussion

21.3.1 Fluorescence quenching

This novel, nano-contrast agent is to be minimally fluorescing in a non-reacted condition, minimizing the non-specific signal. For fluorescence silencing, Cypate needs to be placed very close to the GNP so that the strong surface plasmon field of the GNP quenches the fluorescence. The molecular spacer linking Cypate and GNP was, therefore, designed to be as short as possible. The spacer length estimated by computer simulation was 2.5 nm.

SL-Cy was reacted with GNPs (5 and 10 nm) and the SL-Cy conjugated GNPs (GNP-SL-Cy) were purified by dialysis and centrifugation. Assuming that conjugating Cy-SL to GNP minimally changes the extinction coeficient of Cy-SL at 780 nm, Cypate in the conjugates was quantified by the absorption at 780 nm. Then, the concentration of Cypate in the sample was adjusted to the level of 5 μM SL-Cy. The fluorescence of the GNP-SL-Cy was measured and compared to free SL-Cy at a Cypate concentration of 5 μM. As can be seen in Fig. 2, conjugating SL-Cy to 5 and 10 nm GNP quenched the fluorescence by 83% and 97%, respectively. The 10 nm GNP quenched more fluorescence than the 5 nm, possibly because 10 nm GNP has higher plasmon field intensity at SL length than 5 nm GNP, in agreement with our previous experimental findings[11].

21.3.2 Fluorescence de-quenching

When the contrast agent is delivered to the cancer site, the fluorescence is expected to be de-quenched by uPA cleaving the short spacer. To test this de-quenching design,

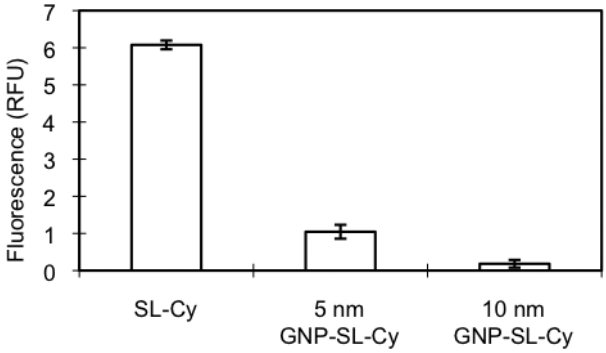

Fig. 21.2 Fluorescence of SL-Cy (5 μM) and GNP-SL-Cy, for GNP size 5 and 10 nm

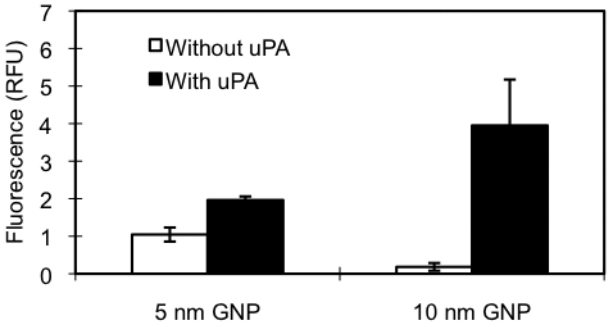

Fig. 21.3 Fluorescence of GNP-SL-Cy before and after uPA addition, for GNP size 5 and 10 nm

uPA was added to the solutions of 5 and 10 nm GNP-SL-Cy, and fluorescence change was monitored (Fig. 3). For 5 nm GNP, the initial fluorescence was 1.045 RFU, and immediately after adding uPA it increased to 1.963 RFU (32% restoration). For 10 nm GNP-SL-Cy, the fluorescence was as low as 0.183 RFU. After adding uPA, the fluorescence increased to 3.95 RFU (65% restoration). The restored fluorescence by 10 nm GNP-SL-Cy conjugates was 2 times higher than that of 5 nm GNP-SL-Cy. This may be because the fluorescence of cleaved Cypate could still be affected by nearby GNPs, and the mean distances between the Cypate and the GNP and the plasmon field of the GNP were different for the solution of 5 and 10 nm GNP.

21.4 Conclusions and Future Study

We have designed a molecular, beacon-like, NIR fluorescent contrast agent for the application to breast cancer detection. A safe NIR fluorophore, Cypate was conjugated to GNP at 5 and 10 nm *via* a short molecular spacer (~2.5 nm) containing a GGR peptide sequence which can be cleaved by uPA. By linking GNP to Cypate, fluorescence was quenched by up to 97%, giving out very little fluorescence. Once the conjugates were exposed to uPA, the fluorescence was restored. For this partic-

ular system, 10 nm GNPs appeared to be more effective for the contrast agent than 5 nm GNPs. Further studies will be performed to confirm the results.

The agent can be further modified to emit fluorescence at an enhanced level by placing another, non-cleavable spacer between the fluorophore and the GNP. We have previously shown that GNP can also enhance the fluorescence at a particular distance from the fluorophore[2,3]. When the short spacer is cleaved, the distance between the fluorophore and the GNP will be determined by the long spacer and the fluorescence will be enhanced, thereby providing higher contrast. The agent can also be incorporated with cancer therapy functionalities, for example, chemotherapy agents, enabling both specific diagnosis and site specific drug delivery. Because of the cancer specific fluorescence emission of our contrast agent, it also has a potential to be used with photodynamic therapy to provide highly specific therapy with minimal side effects.

Acknowledgments

Authors acknowledge U.S. Army (DoD) Breast Cancer Program (BC074387) for the financial support.

References

1. Singh R and Lillard JW (2009) Nanoparticle-based targeted drug delivery. Journal/Experimental and Molecular Pathology 102:38
2. Hong B and Kang KA (2006) Biocompatible, nanogold-particle fluorescence enhancer for fluorophore mediated, optical immunosensor. Journal/Biosensors and Bioelectronics 21:1333-1338
3. Hong B and Kang KA (2006) Fluorescence Enhancers for Fluorophore Mediated Biosensors for Cardiovascular Disease Diagnosis. Journal/Advances in experimental medicine and biology 578:179-184
4. Anger P, Bharadwaj P and Novotny L (2006) Enhancement and quenching of single-molecule fluorescence. Journal/Physical review letters 96:113002
5. Bharadwaj P, Anger P and Novotny L (2007) Nanoplasmonic enhancement of single-molecule fluorescence. Journal/Nanotechnology 18:044017
6. Stranik O, McEvoy HM, McDonagh C and MacCraith BD (2005) Plasmonic enhancement of fluorescence for sensor application. Journal/Sensors and actuators B 107:148-153
7. Connor EE, Mwamuka J, Gole A, Murphy CJ and Wyatt MD (2005) Gold nanoparticles are taken up by human cells but do not cause acute cytotoxicity. Journal/Small 1:325-327
8. Achilefu S, Dorshow R, Bugaj J and Rajagopalan R (2000) Novel receptor-targeted fluorescent contrast agents for in vivo tumor imaging. Journal/Invest Radiol 35:479-485
9. Pakneshan P, Szyf M, Farias-Eisner R and Rabbani S (2004) Reversal of the hypomethylation status of urokinase (uPA) promoter blocks breast cancer gr. Journal/J Biol Chem 279:31735-44.
10. Merrifield RB (1963) Solid Phase Peptide Synthesis. I. The Synthesis of a Tetrapeptide. Journal/J. Am. Chem. Soc. 84:2149-2154
11. Wang J, Nantz MH, Achilefu S and Kang KA (2008) FRET-Like Fluorophore-Nanoparticle Complex for Highly Specific Cancer Localization. Journal/Advances in experimental medicine and biology

Part V
Presidential Symposium

Chapter 22
Oral Pioglitazone Reduces Infarction Volume and Improves Neurologic Function Following MCAO in Rats

D'Arbra Blankenship, Jon Niemi, Elizabeth Hilow, Molly Karl, and Sophia Sundararajan

Abstract Thiazolidinediones (TZDs) are neuroprotective in rodent stroke models using intra-peritoneal, intra-venous and inter-ventricular routes of administration. We tested if oral pioglitazone at doses similar to those used by humans to treat diabetes reduces infarction volume following middle cerebral artery occlusion (MCAO) in the rat. Rats were fed DMSO or pioglitazone (0.65mg/kg equivalent to a 45mg dose in a 70kg man, 0.40mg/kg equivalent to a 30mg dose or 0.20mg/kg to a15mg dose) dissolved in DMSO daily for five days prior to 2 hour MCAO. Animals underwent serial functional analysis using the modified neurologic stroke scale (mNSS), the adhesive sticker test and the inclined plane, all of which test motor sensory function. Twenty one days later, MCAO rats were sacrificed and infarct volumes determined. We found significant reductions in the infarct volume using the 0.65 and 0.40mg/kg dose. Furthermore, these rats had improved performance on behavioural assays. The 0.20mg/kg dose did not significantly reduce infarction volume or improve behaviour.

22.1 Introduction

Stroke is a devastating disease with limited treatment available. Although neuroprotective agents have been identified in rodent ischemia models, these successes have yet to be replicated in human trials. It is widely believed that the rapid progression of irreversible injury limits our ability to prevent cell death and disability in humans [1]. If neuroprotective agents could be administered prior to vessel occlusion, the chances for neuroprotection in humans would be increased. The idea of pretreatment

D'Arbra Blankenship, Jon Niemi, Elizabeth Hilow, Molly Karl, and Sophia Sundararajan
Department of Neurology University Hospitals of Cleveland and Case Western Reserve University, 11100 Euclid Ave., Cleveland, OH 44106, USA
e-mail: sophia.sundararajan@case.edu

Sophia Sundararajan
Department of Neurosciences University Hospitals of Cleveland and Case Western Reserve University, 11100 Euclid Ave., Cleveland, OH 44106, USA

J.C. LaManna et al. (eds.), *Oxygen Transport to Tissue XXXII*, Advances in Experimental Medicine and Biology 701, DOI 10.1007/978-1-4419-7756-4_22,

is usually thought of as impractical, but if a putative neuroprotective agent was also used to treat a chronic medical condition, then pretreatment would be a viable and immensely practical option.

Thiazolidinediones (TZDs) are excellent candidates for pretreatment of cerebral ischemia. TZDs are FDA approved for the treatment of type 2 diabetes, a major risk factor for stroke. TZDs are agonists for peroxisome proliferator-activated receptor gamma (PPARγ), a nuclear transcription factor that regulates adipocyte differentiation and lipid metabolism. It has been reported that PPARγ agonists are anti-inflammatory and ameliorate injury in inflammatory disease models [2]. TZDs reduce proinflammatory cytokine expression, limit leukocyte infiltration and macrophage differentiation, all of which exacerbate injury following ischemic stroke. Additionally, TZDs increase superoxide dismutase and catalase levels enhancing free radical scavenging [3,4].

We previously hypothesized and found that TZDs are neuroprotective in a rodent transient cerebral ischemia model using intraperitoneal injections [5,6]. These findings have subsequently been validated by other laboratories using intra-peritoneal, intra-venous and intra-ventricular administration of PPARγ agonists [7-12]. One TZD, pioglitazone, has been found to reduce infarction volume when given orally. However, the dose tested, 20mg/kg, is dramatically higher than that used in humans [4]. We were interested in knowing if patients who take TZDs for diabetes might be protected if they suffer a stroke. In this study, we hypothesize that doses similar to those used to treat patients would be neuroprotective and improve neurologic function in a rat middle cerebral artery occlusion (MCAO) model.

22.2 Methods

Male Wistar rats, 250-300g, were obtained from Charles River (Wilmington, MA). Animals were housed and cared for in the Animal Resource Center with free access to food and water. All procedures were approved by the Institutional Animal Care and Use Committee for Case Western Reserve University. Pioglitazone was obtained from Takeda Pharmaceuticals North America (Chicago, IL) and dissolved in DMSO. Rats were fed DMSO, 0.65, 0.40 or 0.20mg/kg pioglitazone in 10 microliters from a pipette daily for five days.

On the fifth day of drug treatment, rats underwent MCAO by the suture method as described previously [5]. A 4.0 nylon suture with a flame rounded tip was advanced through the internal carotid artery to occlude the MCA while cerebral blood flow was monitored using laser Doppler (Perimed AB, Jarfalla, Sweden). At the time of the reperfusion, rats were again anesthetized and the suture removed with cerebral blood flow monitoring to ensure reperfusion. Arterial blood pressure, arterial blood gases and temperature were all monitored and controlled during the length of the procedure.

All animals were trained for at least three days prior to MCAO by an investigator blinded to treatment assignment. This familiarized the animals with the examiner,

the individual tests, and ensured that all animals performed well prior to MCAO. Behaviour was assessed one, four, seven, 15 and 21 days after MCAO using the mNSS, which tests a combination of motor and sensory tests including the balance beam, and the absence or presence of seizures and reflexes [13], the adhesive sticker test, which tests the rat's ability to sense and remove an adhesive sticker from the forepaw [14], and the inclined plane in which the rat's ability to stay on an incline without slipping or falling is determined [15].

Twenty two days later, MCAO rats were euthanized by exposure to 5% isoflurane until breathing ceased and underwent intracardiac perfusion with 4% paraformaldehyde. Following removal, the brains were immersion fixed in 4% paraformaldehyde overnight. Tissue was cryoprotected in 30% sucrose in PBS and 20 micron frozen sections collected every 1000 micrometers beginning at the level of the forceps minor corpus callosum and extending through the hippocampus. Sections were stained with Thionin and the area of infarction measured using Bioquant computer software (R&M Biometrics, Nashville, TN) by subtracting the uninfarcted tissue in the ischemic hemisphere from the volume of the contralateral hemisphere. This method corrects for post-ischemic edema.

22.3 Results

We found that both 0.65 and 0.40mg/kg pioglitazone significantly reduce infarct volume following MCAO in the rat while a dose of 0.20mg/kg pioglitazone does not significantly reduce infarct volume (Fig. 1). Importantly, there was no difference in cerebral flow reduction in any of the groups tested (data not shown).

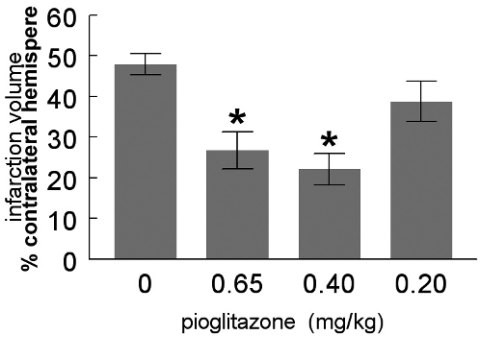

Fig. 22.1 *Oral Pioglitazone reduces infarction volume.* Rats fed pioglitazone, 0.65 or 0.40mg/kg pioglitazone dissolved in DMSO had significantly smaller infarcts than rats fed DMSO alone for five days prior to 2 hour MCAO. Rats fed 0.20mg/kg pioglitazone had infarct volumes which were not significantly different from rats fed DMSO alone. Animals were sacrificed 22 days after MCAO and infarction volume determined from thionine stained frozen sections of the brain (n=12 for control; n=10 for 0.65 and 0.40mg/kg pioglitazone; n=8 for 0.20mg/kg pioglitazone; Student's t-test: p=0.001 for 0.65mg/kg pioglitazone; $p < 0.001$ for 0.40mg/kg pioglitazone).

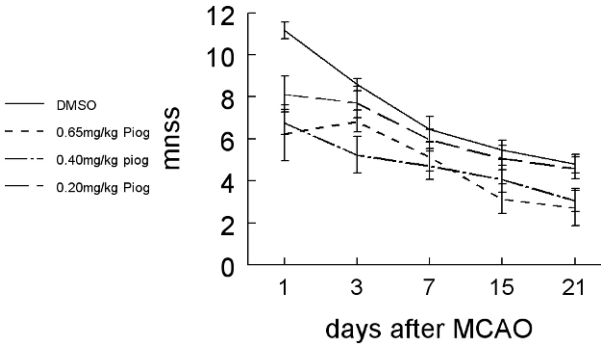

Fig. 22.2 *Oral pioglitazone improves mNS*. mNSS is improved in animals fed 0.65 or 0.40mg/kg for 5 days prior to MCAO and assessed serially over a 3-week period (n=12 for DMSO; n=7 for 0.65mg/kg; n=10 for 0.40mg/kg; n=8 for 0.20mg/kg; one-way ANOVA $p < 0.001$).

Reductions in infarct volume are associated with improved neurologic function as measured over a three-week period. Animals were assessed using the mNSS which includes motor and sensory measures as well as performance on the balance beam, and the presence and absence of seizures and reflexes by an examiner blinded to treatment assignment. Rats fed 0.65 or 0.40mg/kg pioglitazone had lower mNSS scores than animals fed DMSO. mNSS for animals fed the 0.20mg/kg dose was not significantly different from the DMSO fed animals (Fig. 2).

Function was also assessed using the adhesive sticker test, which tests the ability of the animal to sense and remove a sticker from the affected forepaw. Animals treated with 0.40mg/kg pioglitazone had significantly improved performance compared to the DMSO fed animals (one-way ANOVA $p < 0.01$), while animals treated with 0.65mg/kg and 0.20mg/kg did not show improved behaviour (one-way ANOVA $p > 0.05$). Animals were also tested on the inclined plane in which the angle of incline is gradually increased until the degree angle at which the animal begins to slip and then the angle at which the animal falls off the incline are recorded. Rats treated with 0.65 and 0.40mg/kg pioglitazone were able to tolerate higher inclines without slipping or falling off than DMSO treated rats (Fig. 3; one-way ANOVA $p < 0.001$). Rats treated with 0.20 mg/kg began to slip at a steeper incline than control rats (one-way ANOVA $p < 0.05$) but the incline at which they fell was not significantly different from control animals (one-way ANOVA $p > 0.05$).

22.4 Discussion

These data show that pioglitazone at doses similar to those used clinically reduces injury in animals undergoing MCAO. Metabolism of thiazolidinediones is similar in primates and rodents [16] suggesting that diabetics taking TZDs may be protected if they suffer a stroke.

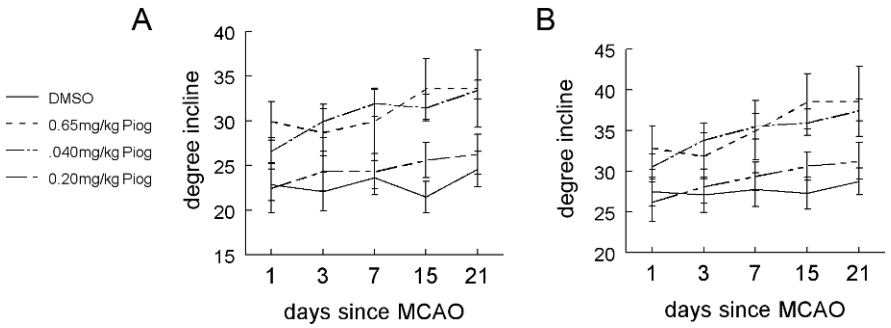

Fig. 22.3 *Oral pioglitazone improves performance on an inclined plane*. Rats treated with 0.65mg/kg or 0.40mg/kg were able to tolerate significantly steeper inclines without slipping (A) or falling (B) than DMSO treated rats following MCAO. Rats treated with 0.20mg/kg began to slip at a steeper incline than control rats (n=12 for DMSO; n=7 for 0.65 mg/kg; n=10 for 0.40mg/kg; n=8 for 0.20mg/kg; one-way ANOVA $p < 0.001$ for 0.65mg/kg and 0.40mg/kg compared to control; $p > 0.05$ for 0.20mg/kg slip and fall compared to DMSO).

The interval between the onset of ischemia and the initiation of therapy is widely viewed to be the primary explanation for the failure to translate neuroprotection in animal models to human therapy [1]. Using a "pretreatment" model, this barrier is eliminated and the chances for successful neuroprotection enhanced. "Pretreatment" has widely been dismissed as impractical because of the difficulty predicting when a stroke will occur. However, several agents used to treat stroke risk factors have been proposed as neuroprotective agents, including TZDs. Pioglitazone is currently being tested as a secondary stroke preventative agent in patients with insulin resistance without diabetes in the Insulin Resistance Intervention after Stroke (IRIS) trial which, if positive, would be expected to further increase the number of patients taking pioglitazone on a daily basis.

Unfortunately, clinical trials involving "pretreatment" would be extremely challenging. Given the heterogeneity of stroke, both with respect to subtype and severity, it would be necessary to have a large number of events to analyze, as these factors could not be controlled for in a pretreatment study. Furthermore, since only a fraction of the patients in the trial would have a stroke, the number of patients that would need to be enrolled would be extremely large. Therefore, it seems unlikely that "pretreatment" will be tested clinically. On the other hand, if TZDs are found to be protective in a "post-ischemia" model, then those findings may be extrapolated to a "pretreatment" model and guide therapy for conditions such as diabetes.

Acknowledgments

The authors would like to acknowledge the many helpful discussions with Gary Landreth, Joseph LaManna and David Lust who have provided not only expertise

but encouragement throughout the duration of this project. Support for this work was generously provided by Takeda Pharmaceuticals, North America, Inc.

References

1. Ginsberg M (2008) Neuroprotection for ischemic stroke: past, present and future. Neuropharm 55: 363-389.
2. Daynes RA, Jones DC (2002) Emerging roles of PPARs in inflammation and immunity. Nat Rev Immunol 2: 748-759.
3. Girnun GD, Domann FE, Moore SA et al. (2002) Identification of a functional peroxisome proliferator-activated receptor response element in the rat catalase promoter. Mol Endocrinol 16: 2793-801.
4. Shimazu T, Inoue I, Araki N et al. (2005) A peroxisome proliferator-activated receptor-g agonist reduces infarct size in transient but not in permanent ischemia. Stroke 36: 353-359.
5. Sundararajan S, Gamboa JL, Victor NA, et al. (2005) PPARg ligands reduce inflammation and infarction size in transient focal ischemia. Neurosci 130: 685-696.
6. Victor NA, Wanderi EW, Gamboa JL et al. (2006) Altered PPARgamma expression and activation after transient focal ischemia in rats. Eur J Neurosci 24: 1653-1663.
7. Allahtavokoli M, Shabanzadeh AP, Sadr SS et al. (2006) Rosiglitazone, a peroxisome proliferator-activated receptor-gamma ligand, reduces infarction volume and neurological deficits in an embolic model of stroke. Clin Exp Pharmacol Physiol 33: 1052-1058.
8. Lin T-N, Cheung W-M, Wu J-S et al. (2006) 15D-prostaglandin J2 protects brain from ischemia-reperfusion injury. Arterioscler Thromb Vasc Biol 26: 481-487.
9. Lou Y, Yin W, Signore AP et al. (2006) Neuroprotection against focal ischemic brain injury by the peroxisome proliferator-activated receptor-gamma agonist rosiglitazone. J Neurochem 97: 435-448.
10. Ou Z, Zhao X, Labiche L et al. (2006) Neuronal expression of peroxisome proliferator-activated receptor-gamma (PPARgamma) and 15D—prostaglandin J2-mediated protection after experimental cerebral ischemia in the rat. Brain Res 1096: 196-203.
11. Pereira MP, Hurtado O, Cardenas A et al. (2006) Rosiglitazone and 15D-deoxy-delta 12, 14-prostaglandin J2 cause potent neuroprotection after experimental stroke through noncompletely overlapping mechanisms. J Cereb Blood Flow Metab 26: 218-229.
12. Tureyen K, Kapadia R, Bowen KK et al (2007) Peroxisome proliferator-activated receptor-g agonists induce neuroprotection following transient focal ischemia in normotensive, normoglycemic as well as hypertensive and type-2 diabetic rodents. J Neurochem 101: 41-56.
13. Chen J, Sanberg P, Li Y (2001) Intravenous administration of human umbilical cord blood reduces behavioral deficits after stroke in rats. Stroke 32: 2682-2688.
14. Zhang L, Chen J, Li Y (2000) Quantitative measurement of motor and somatosensory impairments after mild (30min) and severe (2h) transient middle cerebral artery occlusion in rats. J Neurol Sci 174: 141-146.
15. Yonemori F, Yamaguchi T, Yamada H (1998) Evaluation of motor deficit after chronic focal ischemia in rats. J Cereb Blood Flow Metab 18: 1099-1106.
16. Maeshiba Y, Yutaka Y, Yamashita K (1997) Disposition of the new antidiabetic agent pioglitazone in rats, dogs and monkeys. Arzneim-Forsch/Drug Res 47: 29-35.

Part VI
Angiogenesis

Chapter 23
Chronic Mild Hypoxia Ameliorates Chronic Inflammatory Activity in Myelin Oligodendrocyte Glycoprotein (MOG) Peptide Induced Experimental Autoimmune Encephalomyelitis (EAE)

Paula Dore-Duffy, Marie Wencel, Vladimir Katyshev, and Kristen Cleary

Abstract While the pathologic events associated with multiple sclerosis (MS), diffuse axonal injury, cognitive damage, and white matter plaques, have been known for some time, the etiology of MS is still unknown and therapeutic efforts are somewhat disappointing. This may be due to a lack of fundamental knowledge on how to buffer the brain from secondary injury following immune attack. Maintenance of central nervous system (CNS) homeostasis is a complex set of regulatory adjustments by the neurovascular unit that includes induction of adaptive angiogenesis. Although aspects of adaptive angiogenesis are induced in MS and experimental autoimmune encephalomyelitis (EAE), vascular remodeling is ineffective and the balance between metabolic need and oxygen (O_2) and glucose availability is disrupted. We hypothesized that restoration of metabolic homeostasis in the CNS would ameliorate tissue damage and promote repair in myelin oligodendrocyte glycoprotein (MOG)-induced EAE in mice. Exposure of animals to chronic mild hypoxia (10% O_2) increased vascular density and significantly delayed onset and severity of clinical EAE. When animals were exposed to hypoxia after the onset of clinical symptoms, the severity of chronic inflammatory disease was reduced or even inhibited. In addition, spinal cord pathology was decreased. While the mechanism of protection is unclear, results suggest that hypoxia has therapeutic potential in EAE.

23.1 Introduction

The maintenance of CNS homeostasis is the result of a coordinated effort of the cellular constituents of the blood brain barrier (BBB) and parenchymal cell composing the neurovascular unit [1]. Together, these cells make fine tuned regulatory adjustments that maintain the balance between O_2 availability, bioenergetics and tissue

Department of Neurology, Division of Immunology, Wayne State University School of Medicine, Detroit, Michigan, 48201
e-mail: pdduffy@med.wayne.edu

J.C. LaManna et al. (eds.), *Oxygen Transport to Tissue XXXII*, Advances in Experimental Medicine and Biology 701, DOI 10.1007/978-1-4419-7756-4_23,

metabolic demand [2-4]. In the brain there is a direct relationship between local capillary density, cerebral blood flow, and metabolic homeostasis. In the adult, there is a continuous matching of tissue O_2 with capillary density. As such, structural adaptations that result in increased vascular density have been shown to underlie adaptive angiogenesis [3, 4]. Dysregulation could lead to pathological conditions associated with neuronal/axonal loss. Such a situation may be involved in axonal injury as seen in multiple sclerosis (MS).

MS is a chronic progressive demyelinating disease of the CNS characterized by multifocal leukocyte infiltration into the CNS with demyelination [5, 6]. For decades, the scientific world defined MS as an autoimmune disease. Recently, however, our thoughts regarding the etiology of MS have shifted [7], particularly in an effort to explain the lack of remyelination associated with remission of disease [8]. At the vascular level, infiltration of leukocytes may result in disruption and dissolution of the endothelium with loss of focal bioenergetic homeostasis and axonal degradation. Focal loss of metabolic homeostasis has been likened to the hypoxia observed during focal ischemic injury [9]. We examined the effect of therapeutic angiogenesis on MOG-induced EAE in mice. Results indicate the exposure to chronic mild normobaric hypoxia attenuated the development and chronic expression of clinical symptoms in MOG-induced EAE.

23.2 Methods

23.2.1 Immunization protocol for MOG-induced chronic EAE

Female C57BL/6 mice (6-8wk) were immunized with MOG_{35-55}, (MEVGWYRSPFSRVVHLYRNGK) [100μl] (final concentration=200 μg) emulsified with complete Freund's adjuvant (CFA) containing 4 mg/ml M. tuberculosis in a single subcutaneous injection at the base of the tail. Control animals were immunized with an equivalent volume of CFA emulsion that did not contain MOG peptide. All mice were injected intraperitoneally with 200μl of pertussis toxin (400 ng) immediately after immunization and 2 days later. Mice were evaluated on a daily basis for changes in body weight, overt signs of illness, and clinical signs of EAE using a 5-point scoring system: 0-no symptoms; 1-flaccid tail; 2-paresis of hind limbs; 3-paralysis of hind limbs; 4-quadriplegia; 5-death.

23.2.2 Determination of capillary density

Sections (5μm) were fixed with 4% paraformaldehyde, permeabilized with 0.1% Triton X-100, quenched with 0.3% H_2O_2 (in 30% methanol), and incubated with 5% blocking serum. Sections were incubated with goat polyclonal anti-glucose trans-

porter protein (Glut-1) Ab (1:100, SCBT, CA) and a biotinylated secondary antibody (Vector Laboratories, CA). Color detection was performed with avidin-biotin horseradish peroxidase solution, ABC kit, and the diaminobenzidine peroxidase substrate kit (Vector Laboratories, CA, USA). The number of vessels per field, 20-30 fields per sample, was determined and the mean $\pm$ SD calculated.

23.2.3 Exposure to normobaric hypoxia

Animals were housed in a Biospherix Hypoxia chamber calibrated to administer 10% O_2 for varying periods of time (0, 3, 5, 7, 10, 12, 14, 16, 18 p.i. for up to three weeks).

23.2.4 Immunocytochemistry

Coronal sections (4 μm thick) through the smCx and hipp were cut on a cryostat and collected in 1% PBS as free-floating sections. Tissue was permeabilized with 0.6% Triton X. *Banderiaes simplicifolia*-FITC (1:100; Sigma) was used to visualize endothelial membranes. Analyses were conducted using 4 to 6 sections per animal with 3 to 6 areas per section. Between-group analyses were determined by one-way analysis of variance (ANOVA). Data are reported as mean $\pm$ SD. Significance is at p-value < 0.05 [10, 11] 95% power. For hematoxylin and eosin stains, brain tissue was sectioned at 10μm and mounted onto gelatin-coated slides. After air-drying, the slides were prepared according to the following order: hematoxylin 3 mins, wash 2X, eosin Y 15 secs, dip 2X in 95% EtOH 1 min each, dip in 100% EtOH 1 min each, 50% EtOH/50% xylene 1 min, dip in xylene 1 min each.

23.3 Results

23.3.1 Normobaric hypoxia induced adaptive angiogenesis in C57BL/6 mice

Mice were exposed to 10% O_2 or normoxia for varying periods of time up to three weeks. Animals were weighed daily and blood samples taken for determination of hematocrit levels. Animals were sacrificed at 4, 7, 14, and 21 days and samples were taken from the spinal cord and brain. Capillary density was determined by immunocytochemistry for expression of glut-1. Results are shown in Figure 1a, b.

Hypoxia induced a significant increase in the density of glut-1+ capillaries in both the cortex and spinal cord of C57BL/6 mice. Maximum increase in density

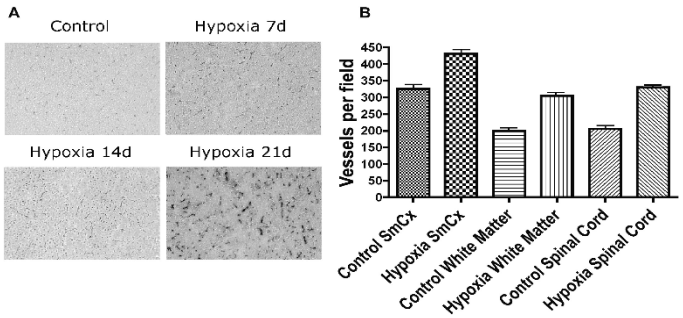

Fig. 23.1 Effect of hypoxia on CNS capillary density: Animals were exposed to hypoxia for varying periods of time. Normoxic animals were housed in the same room directly outside the chambers. The brain and spinal cord were harvested and random samples were taken. A minimum of four random sites was taken per area. Frozen sections were stained with the antibody directed toward glut-1. The number of glut-1-positive capillaries was counted.

was observed by two weeks exposure to low O_2. Structural changes in the vascular density were associated with moderate reduction in animal weight and increased hematocrit (data not shown).

23.3.2 MOG-induced EAE

Female 8-week-old mice were immunized using MOG_{35-55} peptide as detailed in methods. Animals were examined daily and scored using a 5-point scoring system. An average of three out of four animals developed clinical symptoms by day 12-18 p.i. Clinical score was graphed as shown in Figure 2.

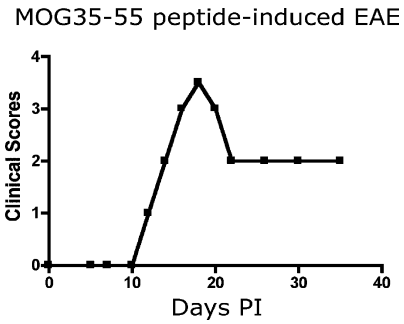

Fig. 23.2 MOG-induced EAE in C57BL/6 mice. Six to eight week old animals were immunized with MOG_{35-55} peptide. Clinical scores were determined daily and graphed. The figure shows a classic clinical pattern of chronic MOG-induced EAE.

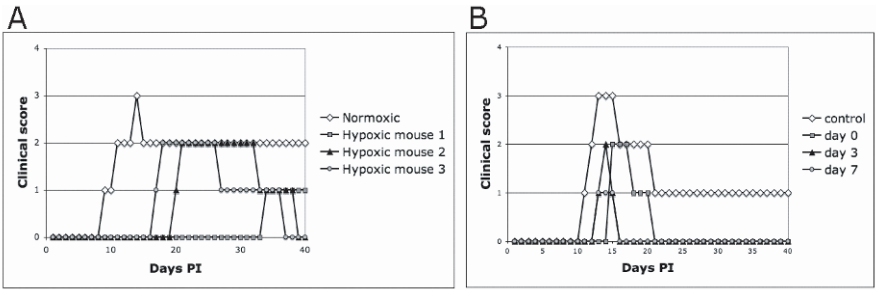

Fig. 23.3 A - Effect of normobaric hypoxia on EAE. Mice were immunized with MOG35-55 peptide. Immediately following immunization, the animals were placed in the normobaric hypoxia chambers. Control animals were exposed to normoxic environments at day 0. Clinical score was determined on daily examination. Exposure to moderately low levels of oxygen (10%) significantly decreased severity and delayed onset of neurological symptoms. (Figure depicts results from a representative experiment; N = 3.) **B - Effect of normobaric hypoxia administered after the development of clinical symptoms.** Mice were immunized on day 0. Clinical scores were determined daily. Animals were entered in the normobaric chambers when clinical scores reached 2 or above. Mice were exposed to 10% oxygen for at least 20 days. Clinical scores were determined daily.

Samples of brain and spinal cord were also taken to determine the effect of immunization on vascular density. Results indicate that there was a modest reduction in capillary density during chronic phases of MOG EAE.

23.3.3 Effect of hypoxia on MOG-induced EAE

MOG-immunized mice were housed in the hypoxia chambers on the same day as immunization. Animals were scored daily for 40 days. Results in Figure 3 indicate that the rate of development and the severity of EAE were attenuated by exposure to mild chronic hypoxia.

In a second set of experiments, animals were immunized on day zero and transferred to the normobaric chambers when animals exhibited a clinical neurological score of at least 2.0. Animals were kept in the hypoxic environment for 21 days. Controls were immunized and housed in a similar chamber under normoxic conditions. Results in Figure 3b indicate that exposure to normobaric hypoxia ameliorated clinical symptoms. During exposure to chronic mild hypoxia the animals remained free of clinical symptoms.

Samples of the brain and spinal cord were taken and evaluated for capillary density and for histology. Results in Figure 4 indicate that exposure to chronic mild hypoxia reduced the evidence of inflammation in the spinal cord.

Although the number and size of perivascular cuff formation were decreased, a few small plaques were still seen in the spinal cord. Exposure to normobaric hypoxia induced a significant increase in capillary density suggesting that physiological angiogenesis could be induced in EAE mice (Figure 5a, b).

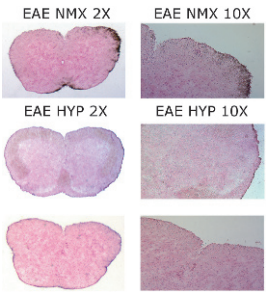

Fig. 23.4 Effect of normobaric hypoxia on histological evidence of EAE in the spinal cord of immunized animals. Mice were immunized with MOG peptide on day 0 and housed in normobaric chambers following onset of clinical signs of disease (score at least 2). Animals were sacrificed at varying times. Sections were stained for evidence of inflammatory activity using H+E.

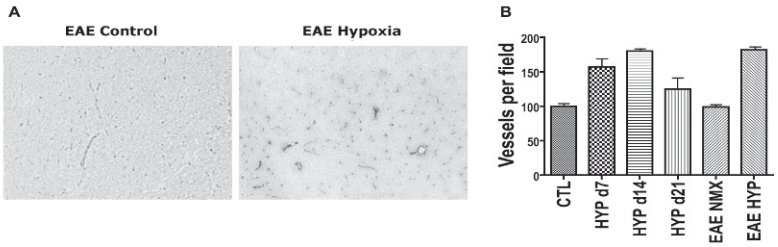

Fig. 23.5 Normobaric hypoxia induces an increase in capillary density in MOG-induced EAE. Random sections of spinal cord were stained for the expression of glut-1. Representative sections are shown in the figure.

Reduction in inflammatory activity in EAE mice exposed to hypoxia correlated with the appearance of hypoxia-inducible factor-1 alpha (HIF-1α) positive nuclei throughout the spinal cord of immunized mice (data not shown). That exposure to normobaric hypoxia, administered after the onset of clinical symptoms inhibited the development of chronic inflammatory disease, indirectly suggests that peripheral sensitization of leukocytes was not altered.

23.4 Conclusions

In MS, the availability of O_2 and glucose to the brain is compromised in demyelinated zones due to plaque formation and destruction of the endothelium concomitant with leukocyte infiltration and cuff formation [9]. The formation of a focal state of hypoxia may result in decreased energy sources leading to neuronal degeneration [9, 11]. Increased availability of O_2 and glucose to the CNS may restore bioenergetics. Therapeutic angiogenesis has not been tested in MS.

Physiological angiogenesis may be induced by a number of therapeutic strategies: **1)** Direct use of proangiogenic growth factors known to induce angiogenesis;

2) Specific growth factors that are being investigated for their pro-angiogenic effects are basic fibroblast growth factor (bFGF), fibroblast growth factor (FGF), platelet derived growth factor (PDGF) and vascular endothelial cell growth factor (VEGF). FGF and VEGF have been studied the most widely [12-14]; **3)** The use of growth factor mimetics or gene therapy to promote expression of pro-angiogenic factors [15, 16], or protein therapy using proangiogenic peptides [17, 18]; and **4)** The induction of endogenous/adaptive angiogenesis [18-20]. Adaptive/physiological angiogenesis can be induced by exercise conditioning [21-24], memory and learning and exposure to chronic mild hypoxia [3, 4]. Induction of physiological angiogenesis as a therapeutic paradigm results in stabilization of hypoxia-inducible factor-1 alpha (HIF-1α) [3, 4, 25]. HIF-1α stimulates the production of the HIF-responsive genes such as VEGF and erythropoietin (EPO) [26]; both of which have been shown to be neuroprotective [27-30].

Hypoxia ameliorated chronic inflammatory symptoms in MOG-induced EAE in mice. That low O_2 had therapeutic efficacy even when initiated after the development of clinical symptoms, which suggests that amelioration of disease did not involve inhibition of MOG-specific T-cells. This is supported by the ability to detect sensitized T-cells in the spleen following immunization with MOG peptide (data not shown). Results also suggested that the transmigration of leukocytes across the BBB into the CNS was decreased following exposure to low O_2. Of particular note, is the fact that the number of inflammatory lesions and evidence of mesangial involvement was decreased. This suggests that may have altered the state of vascular permissiveness essential for leukocyte transmigration.

We have shown that microvessels in white matter and gray matter in MS brain and the CNS of animals with EAE express activation markers [31, 32]. While chronic mild hypoxia induces transient expression of endothelial activation markers [33, 34], there is no evidence of leukocyte transmigration. Normobaric hypoxia may ultimately restore vascular quiescence and may involve a number of indirect mechanisms that involve induction of growth factors, cytokines, and regulatory elements that are neuroprotective.

References

1. Hawkins BT, Davis TP (2005) The blood-brain barrier/neurovascular unit in health and disease. Pharmacol Rev 57:173-85.
2. Chávez JC, Agani F, Pichiule P, et al. (2000) Expression of hypoxia-inducible factor-1alpha in the brain of rats during chronic hypoxia. J Appl Physiol 89:1937-42.
3. Xu K, Lamanna JC (2006) Chronic hypoxia and the cerebral circulation. J Appl Phys 100:725-30.
4. Dore-Duffy P, LaManna JC (2007) Physiologic angiodynamics in the brain. Antioxid Redox Signal 9:1363-71.
5. Charcot JM (1868) Histologie de la sclérose en plaques. Gazette des Hôpitaux civils et militaires 41: 554, 557–558, 566.
6. Sospedra M, Martin R (2005) Immunology of multiple sclerosis. Annu Rev Immuno 23:683-747.

7. Barnett MH, Sutton I (2006) The pathology of multiple sclerosis: a paradigm shift. Curr Opin Neurol 19:242-7.
8. Franklin RJ (2002) Why does remyelination fail in multiple sclerosis? Nat Rev Neurosci 3:705-14.
9. Trapp BD, Stys PK (2009) Virtual hypoxia and chronic necrosis of demyelinated axons in multiple sclerosis. Lancet Neurol 8:280-91.
10. LaManna JC, Chavez JC, Pichiule P (2004) Structural and functional adaptation to hypoxia in the rat brain. J Exp Biol 207:3163-9.
11. Puchowicz MA, Koppaka SS, LaManna JC (2009) Brain metabolic adaptations to hypoxia. In: McCandless DW (ed) Metabolic Encephalopathy, Springer, US.
12. Henry TD (1999) Therapeutic angiogenesis. BMJ 318:1536-9.
13. Ye L, Haider HK, Jiang SJ, et al. (2004) Therapeutic angiogenesis using vascular endothelial growth factor. Asian Cardiovasc Thorac Ann 12:173-81.
14. Waltenberger J (1998) Therapeutic angiogenesis in the heart using peptide growth factors: Angiogenesis research entering clinical trials. Angiogenesis 2:115-117.
15. Ylä-Herttuala S, Rissanen TT, Vajanto I, et al. (2007) Vascular endothelial growth factors: biology and current status of clinical applications in cardiovascular medicine. J Am Coll Cardiol 49:1015-26.
16. Bouïs D, Kusumanto Y, Meijer C, et al. (2006) A review on pro- and anti-angiogenic factors as targets of clinical intervention. Pharmacol Res 53:89-103.
17. Santulli G, Ciccarelli M, Palumbo G, et al. (2009) In vivo properties of the proangiogenic peptide QK. J Transl Med 7:41.
18. Humar R, Zimmerli L, Battegay E (2009) Angiogenesis and hypertension: an update. J Hum Hypertens. doi: 10.1038/jhh.2009.63.
19. Benarroch EE (2009) Hypoxia-induced mediators and neurologic disease. Neurology 73:560-5.
20. Serebrovskaya TV, Manukhina EB, Smith ML, et al. (2008) Intermittent hypoxia: cause of or therapy for systemic hypertension? Exp Biol Med (Maywood) 233:627-50.
21. Gustafsson T, Puntschart A, Kaijser L, et al. (1999) Exercise-induced expression of angiogenesis-related transcription and growth factors in human skeletal muscle. Am J Physiol 276:H679-85.
22. Ding Y, Li J, Luan X, et al.(2004) Exercise pre-conditioning reduces brain damage in ischemic rats that may be associated with regional angiogenesis and cellular overexpression of neurotrophin. Neuroscience 124:583-91.
23. Ding YH, Ding Y, Li J, et al. (2006) Exercise pre-conditioning strengthens brain microvascular integrity in a rat stroke model. Neurol Res 28:184-9.
24. Kreipke CW, Morgan R, Kallakuri S, et al. (2007) Behavioral pre-conditioning enhances angiogenesis and cognitive outcome after brain trauma. Neurol Res 29:388-94.
25. Schroedl C, McClintock DS, Budinger GR, et al. (2002) Hypoxic but not anoxic stabilization of HIF-1alpha requires mitochondrial reactive oxygen species. Am J Physiol Lung Cell Mol Physiol 283:L922-31.
26. Post DE, Van Meir EG (2001) Generation of bidirectional hypoxia/HIF-responsive expression vectors to target gene expression to hypoxic cells. Gene Ther 8:1801-7.
27. Grimm C, Wenzel A, Stanescu D, et al. (2004) Constitutive overexpression of human erythropoietin protects the mouse retina against induced but not inherited retinal degeneration. J Neurosci 24:5651-8.
28. Grimm C, Hermann DM, Bogdanova A, et al. (2005) Neuroprotection by hypoxic preconditioning: HIF-1 and erythropoietin protect from retinal degeneration. Semin Cell Dev Biol 16:531-8.
29. Anderson J, Sandhir R, Hamilton ES, et al. (2009) Impaired Expression of Neuroprotective Molecules in the HIF-1-alpha Pathway following Traumatic Brain Injury in Aged Mice. Journal of Neurotrauma. doi:10.1089/neu.2008-0765
30. Harten SK, Ashcroft M, Maxwell PH (2009) Prolyl Hydroxlase Domain (PHD) inhibitors: a route to HIF activation & neuroprotection. Antioxidants & Redox Signaling. doi:10.1089/ars.2009.2870.

31. Dore-Duffy P, Washington R, Dragovic L (1993) Expression of endothelial cell activation antigens in microvessels from patients with multiple sclerosis. Adv Exp Med Biol 331:243-8.
32. Dore-Duffy P, Balabanov R, Rafols J, et al. (1996) Recovery phase of acute experimental autoimmune encephalomyelitis in rats corresponds to development of endothelial cell unresponsiveness to interferon gamma activation. J Neurosci Res 44:223-34.
33. Dore-Duffy P, Balabanov R, Beaumont T, et al. (1999) Endothelial activation following prolonged hypobaric hypoxia. Microvasc Res 57:75-85.
34. Milner R, Hung S, Erokwu B, et al. (2008) Increased expression of fibronectin and the alpha 5 beta 1 integrin in angiogenic cerebral blood vessels of mice subject to hypobaric hypoxia. Mol Cell Neurosci 38:43-52.

Chapter 24
Effect of Oxygenation on Stem-Cell Therapy for Myocardial Infarction

Mahmood Khan, Sarath Meduru, Ramasamy P. Pandian, Brian K. Rivera, and Periannan Kuppusamy

Abstract Stem-cell transplantation to treat acute myocardial infarction (MI) is gaining importance as a minimally invasive and potent therapy to replace akinetic scar tissue by viable myocardium. Our recent studies have shown that stem-cell transplantation marginally improves myocardial oxygenation in the infarct tissue leading to improvement in cardiac function. The aim of the present study was to determine the effect of hyperbaric oxygen (HBO) treatment on myocardial oxygenation and recovery of function in MI hearts. Fisher-344 rats were subjected to MI by permanently ligating the left-anterior-descending (LAD) coronary artery. The rats were then exposed to 100% O_2 at a pressure of 2 atmospheres for 90 minutes, and the exposure was repeated for 5 days a week for 2 weeks. Adult bone-marrow-derived rat mesenchymal stem cells (MSC, $5x10^5$ cells) were mixed with OxySpin (LiNc-BuO, oxygen sensor) and implanted in the infarct and peri-infarct regions of the heart. M-mode ultrasound echocardiography was performed at baseline and at 2 weeks post-transplantation. The myocardial pO_2 in the MSC+HBO group (16.2±2.2 mmHg) was significantly higher when compared to untreated MI (3.8±1.9 mmHg) or MSC (9.8±2.3 mmHg) groups. In addition, there was a significant improvement in cardiac function, increased vessel density, and VEGF expression in MSC+HBO group compared to MSC group ($p < 0.05$). In conclusion, the results suggested a beneficial effect of HBO administration on stem-cell therapy for MI.

24.1 Introduction

Any therapeutic intervention that could attenuate myocardial remodeling and reduce the incidence or severity of congestive heart failure (CHF) following acute myocardial infarction (MI) would provide a significant benefit in an area of unmet medical need. One of the most promising interventions is cell-based therapy (cell therapy, cellular transplantation, or cellular cardiomyoplasty) for repair and regeneration of

Davis Heart and Lung Research Institute, Department of Internal Medicine, The Ohio State University, Columbus, OH 43210, USA
e-mail: Mahmood.Khan@osumc.edu

J.C. LaManna et al. (eds.), *Oxygen Transport to Tissue XXXII*, Advances in Experimental Medicine and Biology 701, DOI 10.1007/978-1-4419-7756-4_24,

the infarct myocardium [1,2]. A major impediment in the successful application of cellular cardiomyoplasty is the limited survival of the transplanted cells in the infarct tissue presumably due to low oxygen levels in the ischemic myocardium [3]. Therefore, there is a pressing need to oxygenate the infarct myocardium for improved survival of the transplanted stem cells.

Hyperbaric oxygen (HBO) therapy has been used in several disease modalities as a pharmacological adjuvant. The HBO treatment protocol usually involves repeated administration (by breathing) of 100% oxygen at a pressure of 2-3 atmospheres for 1-2 hours. One of the earliest studies to examine the effects of HBO on ischemia-reperfusion (I/R) injury was reported by Sterling et al. [4]. This study showed that animals exposed to HBO during ischemia only, reperfusion only, or ischemia and reperfusion periods had significantly smaller infarcts when compared to control animals, indicating that HBO had a protective effect against I/R injury. The goal of the present study was to see whether stem-cell transplantation along with HBO administration could improve the oxygenation and functional recovery of the infarct heart.

24.2 Materials and Methods

24.2.1 Reagents

Dulbecco's Modified Eagle medium (DMEM), fetal bovine serum, penicillin, streptomycin, trypsin, sodium pyruvate, and phosphate-buffered saline (PBS) were purchased from Gibco BRL (Grand Island, NY). MTT (3-(4,5-dimethylthiazol-2-yl)-5-(3-carboxymethoxyphenyl)-2-(4-sulfophenyl)-2H-tetrazolium) colorimetric assay kit, lactate dehydrogenase (LDH) assay kit, Nuclear Fast Red solution were obtained from Sigma (St. Louis, MO). DAPI (4, 6-diamino-2-phenylindole) was from Invitrogen (Carlsbad, CA). OxySpin was synthesized as reported [5].

24.2.2 Bone marrow-derived mesenchymal stem cells

Mesenchymal stem cells (MSC), isolated from bone-marrow of Fisher-344 rats, were procured from Chemicon (Billerica, MA). The cells were thawed and cultured using DMEM with GlutaMax (4500-mg/l glucose) supplemented with 10% heat-inactivated fetal bovine serum, 100-U/ml penicillin, and 100-μg/ml streptomycin. Accutase (Chemicon, Billerica, MA), a cell-detachment solution containing proteolytic and collagenolytic enzymes, was used for separation of adherent cells. MSCs of passage 3 were used for experiments. The cells were grown at 37˚C in a humidified environment of 5% CO_2 / 95% air.

24.2.3 Induction of MI and MSC transplantation

The study was divided into 3 groups of rats with 4 rats/group: (i) MI only, where the animals received medium only; (ii) MSC, where the MI animals received MSCs (iii)

MSC+HBO, where the MI animals received MSCs followed by HBO treatment. MI was induced in Fisher-344 rats as reported earlier [6,7]. MSCs were transplanted in the rat hearts after 30 min of LAD coronary artery ligation. Three intramyocardial injections (one in the infarct and two in the peri-infarct regions) of MSCs, a total of 5×10^5 cells in 100 μl of serum-free medium, were given to the hearts 30 min after LAD artery ligation.

24.3 Echocardiography and Myocardial pO_2 Measurements

M-mode transthoracic echocardiography was performed in rats as reported[6]. Myocardial oxygenation was measured in the closed-chest rat hearts using *in vivo* EPR oximetry as described [6-8]. Measurements were done at least 3 days after placement of the oximetry probe in the tissue to allow time for the animal to recover from the thoracic surgical procedures. The pO_2 measurements were done before as well as immediately after HBO treatment in control (non-infarct) and infarct (MI) hearts.

24.3.1 Immunohistological staining of cardiac tissue

Cardiac tissue sections were fixed in formalin and embedded in paraffin. Six-micron sections of the fixed tissue sections were serially rehydrated in 100%, 95%, and 80% ethanol after deparaffinization with xylene. Slides were kept in steam for 30 min and then washed in PBS (pH 7.4) three times for 5 min each. The tissue sections were then incubated with 2% goat serum and 5% bovine-serum albumin in PBS to reduce nonspecific binding. The sections were then incubated for 4 hours with mouse anti-CD29, anti-α-smooth muscle actin (α-SMA) or anti-VEGF. The sections were then incubated with appropriate anti-mouse secondary antibodies (1:1000 dilution) conjugated to Texas red (CD29, α-SMA) or FITC (VEGF). Nuclei were counterstained with hardset DAPI. The tissue slides were visualized using an inverted Nikon fluorescence microscope.

24.3.2 Data analysis

Statistical significance of the results was evaluated using a Student's t-test. A p value of < 0.05 was considered to be significant.

24.4 Results

24.4.1 Hyperbaric oxygenation and myocardial pO_2

Myocardial pO_2 measurements were done at the end of 2 weeks at the baseline and after transplantation of MSCs and HBO therapy in the infarct heart. The mean baseline pO_2 in healthy hearts before the induction of MI was 21.3±2.0 mmHg (Figure 1). The myocardial pO_2 in MSC group of hearts was significantly improved when compared to MI (9.8±2.3 mmHg *versus* 3.8±1.2 mmHg; $p < 0.05$). In addition,

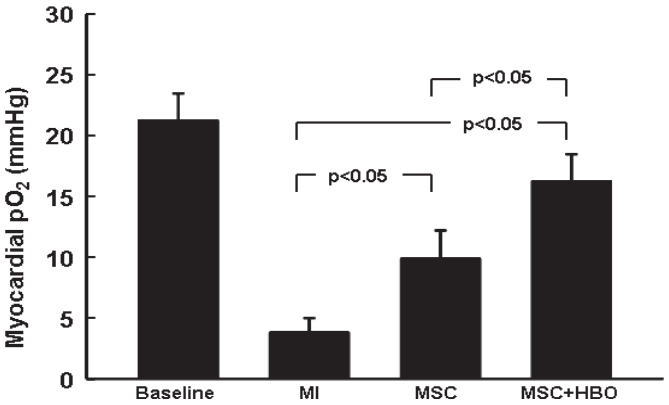

Fig. 24.1 Myocardial pO2 in rat hearts transplanted with stem cells at 2 weeks. The results (mean±SD; N=4 rats) show an increase in myocardial oxygenation in hearts treated with MSC and further enhancement in pO2 was observed in hearts treated with HBO.

MSC+HBO group showed a further significant ($p < 0.05$) enhancement in myocardial oxygenation (16.2±2.2 mmHg) when compared to MSC group. The results suggested that HBO treatment restored the myocardial oxygenation to near-normal levels in the infarcted heart transplanted with MSCs.

24.4.2 HBO enhances the recovery of cardiac function

Ultrasound echocardiography (M-mode, short-axis) was performed in rats at 2 weeks after treatment of infarct (MI) hearts with MSC alone, or MSC followed by HBO exposure. The results showed a significant improvement in cardiac function in MSC+HBO group when compared to MSC group (Figure 2).

24.4.3 Immunostaining for angiogenesis and VEGF expression

Immunostainings for α-smooth muscle actin (SMA, for blood vessels), CD29 (marker for MSC), and VEGF expression (marker for angiogenesis) were performed in heart sections at 2 weeks post-MSC transplantation. There was an increase in CD29-positive cells, α-SMA, and VEGF expression in MSC+HBO group when compared to the MI or MSC group. These results indicated increased stem-cell retention and vasculogenesis in the MSC+HBO group, when compared to the MSC group (Figure 3).

24.5 Discussion

The results indicated the beneficial effects of HBO treatment in enhancing the engraftment of MSCs transplanted into an ischemic heart, leading to significant improvements in cardiac function, and angiogenesis. HBO treatment showed a significantly

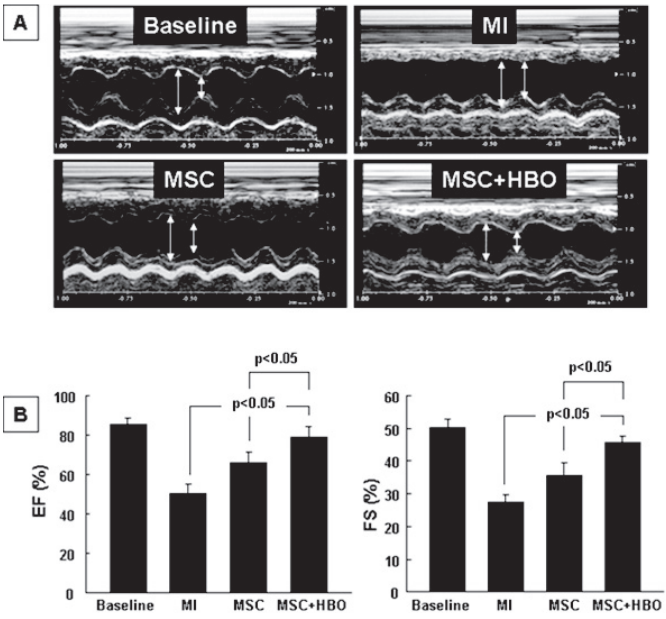

Fig. 24.2 Effect of MSC and HBO treatment on the recovery of cardiac function in MI hearts. Echocardiography (M-mode) was used to measure cardiac function in hearts 2 weeks after transplanted with MSCs. A. Representative echocardiograms obtained from hearts at baseline, infarction (MI), MSC transplantation (MSC), and MSC+HBO treatment (MSC+HBO). B. Mean±SD values (N=4) of left ventricular ejection fraction (EF) and fractional shortening (FS). The MSC+HBO group shows a significant improvement in functional recovery when compared to MSC group.

greater recovery in heart function than that provided by MSCs alone. The beneficial effect of HBO could stem from an increase in CD29-positive graft survival, leading to an increase in VEGF production, and angiogenesis. In our previous studies we demonstrated that transplantation of skeletal myoblast enhanced the myocardial oxygenation [3,9]. However, there was only a marginal improvement in cardiac function. The findings of the present study clearly indicated that oxygenating the infarct tissue by HBO exposure leads to substantial increase in myocardial oxygenation and thereby leading to significant improvement in cardiac function. Therefore, the present study demonstrated that HBO could serve as an effective adjuvant to MSC-based cardiomyoplasty.

24.6 Conclusion

Overall, mesenchymal stem-cell transplantation along with hyperbaric oxygen therapy enhanced the myocardial oxygenation and recovery of heart function possibly leading to improved angiogenesis and VEGF expression in the infarct heart. HBO therapy seems to be a possible adjuvant for stem-cell therapy in the clinical settings.

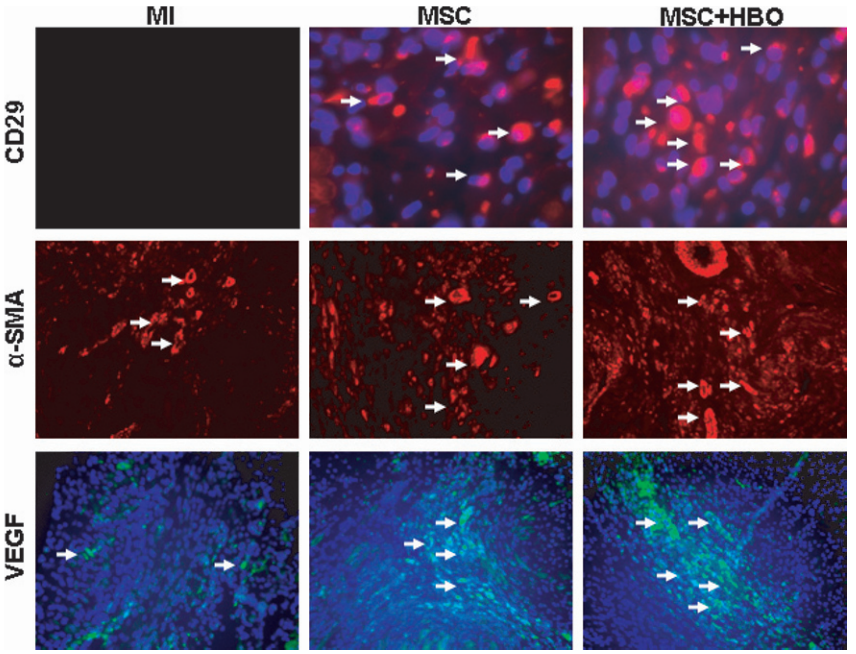

Fig. 24.3 Representative immunofluorescence images of tissue sections stained with antibodies against CD29 (red) superimposed with DAPI (blue) nuclear staining, a-SMA (red) and VEGF (green). White arrows indicate CD29 positive/vessels/VEGF expression in the cardiac section treated with or without stem cells. The images show an increasing number of CD29 positive, increased vessel and VEGF expression in MSC+HBO group when compared to MSC-alone group.

Acknowledgments

This study was supported by grant funding from AHA (SDG 0930181N to MK) and NIH (R01 EB006153 to PK).

References

1. Guarita-Souza LC, Carvalho KA, Rebelatto C et al (2006) Cell transplantation: differential effects of myoblasts and mesenchymal stem cells. Int J Cardiol 111:423-429.
2. Kuramochi Y, Fukazawa R, Migita M et al (2003) Cardiomyocyte regeneration from circulating bone marrow cells in mice. Pediatr Res 54:319-325.
3. Khan M, Kutala VK, Vikram DS et al (2007) Skeletal myoblasts transplanted in the ischemic myocardium enhance in situ oxygenation and recovery of contractile function. Am J Physiol Heart Circ Physiol 293:H2129-2139.
4. Sterling DL, Thornton JD, Swafford A et al (1993) Hyperbaric oxygen limits infarct size in ischemic rabbit myocardium in vivo. Circulation 88:1931-1936.
5. Pandian RP, Parinandi NL, Ilangovan G et al (2003) Novel particulate spin probe for targeted determination of oxygen in cells and tissues. Free Radic Biol Med 35:1138-1148.

6. Khan M, Meduru S, Mohan IK et al (2009) Hyperbaric oxygenation enhances transplanted cell graft and functional recovery in the infarct heart. J Mol Cell Cardiol 47:275-287.
7. Wisel S, Khan M, Kuppusamy ML et al (2009) Pharmacological preconditioning of mesenchymal stem cells with trimetazidine (1-[2,3,4-trimethoxybenzyl]piperazine) protects hypoxic cells against oxidative stress and enhances recovery of myocardial function in infarcted heart through Bcl-2 expression. J Pharmacol Exp Ther 329:543-550.
8. Chacko SM, Khan M, Kuppusamy ML et al (2009) Myocardial oxygenation and functional recovery in infarct rat hearts transplanted with mesenchymal stem cells. Am J Physiol Heart Circ Physiol 296:H1263-1273.
9. Khan M, Kutala VK, Wisel S et al (2008) Measurement of oxygenation at the site of stem cell therapy in a murine model of myocardial infarction. Adv Exp Med Biol 614:45-52.

Part VII
Mitochondrial Metabolism

Chapter 25

Regulation of Cytosolic and Mitochondrial Oxidation via Malate-Aspartate Shuttle: An Observation Using Dynamic ^{13}C NMR Spectroscopy

Ming Lu, Suhanti Banerjee, Gerald M. Saidel, and Xin Yu

Abstract The malate-aspartate (M-A) shuttle provides an important mechanism of metabolic communication between the cytosol and the mitochondria. In this study, dynamic ^{13}C NMR spectroscopy was combined with a multi-domain model of cardiac metabolism for direct quantification of metabolic fluxes through the tricarboxylic acid (TCA) cycle (V_{TCA}) and the M-A shuttle (V_{M-A}) in intact heart. The sensitivity of this approach to altered M-A shuttle activity was examined at different cytosolic redox states. Dynamic ^{13}C NMR spectra were acquired from isolated rat hearts perfused with ^{13}C labeled fatty acid at either low (fatty acid only) or high cytosolic redox state induced by exogenous glucose and lactate. V_{TCA} and V_{M-A} were determined by least-square fitting of the model to NMR data. Our results showed that while V_{TCA} was similar, V_{M-A} increased by 75% at high cytosolic redox state. Therefore, our proposed method provides the opportunity for direct quantification of metabolic communication between subcellular compartments via the M-A shuttle.

Ming Lu, Suhanti Banerjee, Gerald M. Saidel, and Xin Yu
Department of Biomedical Engineering, Case Western Reserve University, Cleveland, OH, USA
e-mail: xin.yu@case.edu

Xin Yu
Department of Radiology, Case Western Reserve University, Cleveland, OH, USA

Xin Yu
Department of Physiology and Biophysics, Case Western Reserve University, Cleveland, Ohio, USA

Ming Lu and Xin Yu
Case Center for Imaging Research, Case Western Reserve University, Cleveland, OH, USA

Ming Lu, Gerald M. Saidel, and Xin Yu
Center for Modeling Integrated Metabolic Systems, Case Western Reserve University, Cleveland, OH, USA

J.C. LaManna et al. (eds.), *Oxygen Transport to Tissue XXXII*, Advances in Experimental Medicine and Biology 701, DOI 10.1007/978-1-4419-7756-4_25,

25.1 Introduction

The malate-aspartate (M-A) shuttle plays an important role in regulating cardiac energy metabolism by transporting cytosolic ATP-yielding reducing equivalents, i.e., NADH, indirectly into the mitochondria via a transport-transamination-redox cycle that spans the cytosolic and mitochondrial domains (1). Changes in M-A shuttle activity and shuttle-associated protein expression have been indicated at altered pathophysiological conditions. However, experimental measurements of the M-A shuttle activity have been challenging. It has not been possible to directly measure the M-A shuttle activity in intact tissues due to limitations in quantifying cytosolic and mitochondrial metabolites experimentally. To date, most investigations on M-A shuttle have employed the isolated mitochondrion system. However, such an approach has the inherent limitation of an artificial cytosolic environment.

In the last twenty years, ^{13}C NMR spectroscopy has become a valuable tool for the evaluation of cardiac metabolism (2). The utilization of ^{13}C-enriched substrates provides unique observation about tracer distribution in intermediary metabolites (3). Dynamic ^{13}C NMR observation of glutamate labeling in intact hearts has been demonstrated to be sensitive to both tricarboxylic acid (TCA) cycle flux and the M-A shuttle activity (4). Kinetic analysis methods have also been developed for quantification of metabolic fluxes from dynamic ^{13}C NMR spectroscopy data (4). Previous models have used a lumped parameter to represent the interconversion rate between glutamate and α-ketoglutarate as an index of the M-A shuttle activity (4). However, these single domain models do not provide direct quantification of the M-A shuttle flux and the distribution of shuttle-associated metabolites between the cytosol and the mitochondria.

In the present study, a novel approach that combines dynamic ^{13}C NMR spectroscopy with a multi-domain kinetic model of cardiac metabolism was developed to elucidate the role of M-A shuttle in regulating myocardial energetics. The responses of TCA cycle flux (V_{TCA}) and M-A shuttle activity (V_{M-A}) to augmented cytosolic redox state (NADH/NAD$^+$) induced by exogenous lactate and glucose were examined. Our findings indicate that such an approach allows direct assessment of metabolic communication between the cytosolic and mitochondrial compartments via the M-A shuttle.

25.2 Methods

25.2.1 Isolated heart perfusion

Hearts were excised from 2-month-old male Sprague-Dawley rats and retrogradely perfused at 100 cm hydrostatic pressure with a modified Krebs-Henseleit buffer equilibrated with 95% O_2/5% CO_2 (pH 7.4). Perfusate was maintained at 37˚C. A water-filled latex balloon was inserted into the left ventricle to monitor the contractile parameters of the heart. Left ventricular developed pressure (LVDP) and heart rate (HR) were continuously recorded. Rate pressure product (RPP=LVDP$\times$HR) was used as an index of mechanical work. Myocardial O_2 consumption rate (MVO_2)

was calculated from the coronary flow and the difference in O_2 tension between the arterial supply line and the coronary effluent.

Isolated hearts were perfused with either short-chain (2.5 mM [2-^{13}C] acetate, group 1, $n = 8$) or long-chain (0.32 mM [U-^{13}C] palmitate with 3% albumin, group 2, n=6) fatty acids. A 3^{rd} group comprised of hearts perfused with 2.5 mM [2-^{13}C] acetate with additional unlabeled glucose (5.0 mM) and lactate (1.0 mM) to induce high cytosolic redox state (n=8). At the start of the perfusion protocol, the heart was perfused with unlabeled substrates for 15 min to establish metabolic equilibrium. A ^{31}P spectrum and a natural abundance ^{13}C spectrum were collected. Once the perfusate was switched to ^{13}C-enriched buffer, acquisition of dynamic ^{13}C NMR spectra began immediately for over 40 min until steady-state enrichment was reached. At the end of the perfusion protocol, hearts were freeze-clamped and extracted by 7% perchloric acid for quantification of substrate utilization and anaplerosis by high-resolution ^{13}C NMR spectroscopy as previously described (4). Glutamate content was measured by spectrophotometric assays.

25.2.2 NMR spectroscopy

NMR spectra of isolated perfused hearts were acquired on a Bruker 9.4T vertical-bore spectrometer with hearts situated in a 20 mm broadband NMR probe. ^{31}P spectra were acquired at 161.9 MHz with a 90° pulse angle, 1.3 s acquisition, 1 s relaxation delay, and 32 averages. Proton-decoupled ^{13}C NMR spectra were acquired at 101 MHz with 45° rf pulses, 0.58 s acquisition, 1 s relaxation delay, and 8k data points. For the acetate (group 1 and 3) and palmitate (group 2) groups, ^{13}C spectra were collected over 32 and 100 scans, respectively. Natural abundance ^{13}C signal was digitally subtracted, and the raw NMR signal was processed by exponential filtering with a line broadening of 20Hz to enhance the signal-to-noise ratio, followed by Fourier transformation. Peak assignments were referenced to the known resonance of 2-carbon acetate at 24.1ppm (groups 1 and 3) or triglyceride at 30ppm (group 2). Signal intensity, representative of metabolite content, was determined by the integration of the peak areas. The time courses of fractional enrichment of glutamate at 4- (C4) and 2-carbon (C2) positions were obtained by normalizing signal intensity to steady-state enrichment of glutamate C4 measured from high-resolution ^{13}C NMR analysis of tissue extracts described below.

High-resolution ^{13}C spectra of heart extracts were acquired on a Bruker 900MHz spectrometer with a 5 mm ^{13}C/^{1}H probe. Proton-decoupled spectra were collected over 1024 scans with 90° rf pulses, 4.26 s repetition time and 8k data set. Fractional enrichment of acetyl-CoA (F_c), i.e., the steady-state enrichment level of glutamate C4, and the ratio of anaplerotic flux to V_{TCA} (y) were determined from the multiplet structure of glutamate resonance peaks (2).

25.2.3 Kinetic analysis and statistical evaluation

In the current study, a previous multi-domain model of cardiac metabolism (5) was expanded to incorporate the dynamic labeling of major metabolite pools with ^{13}C

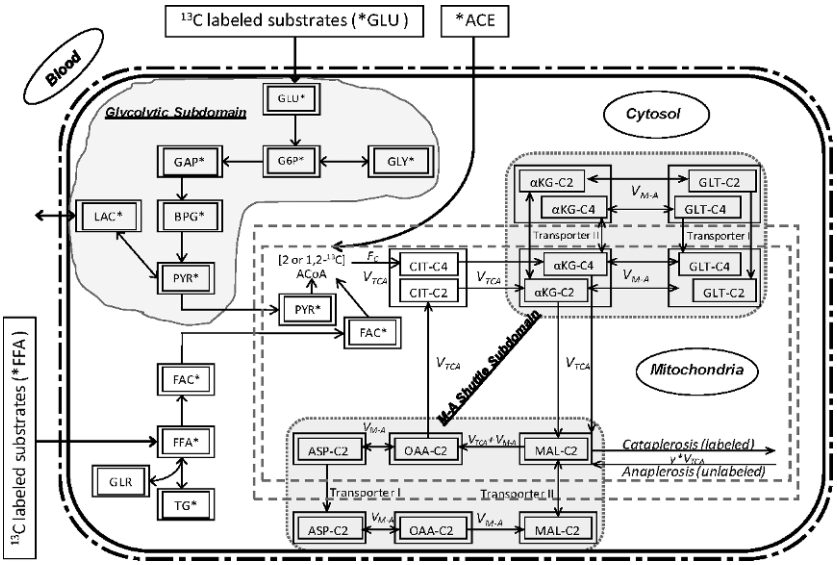

Fig. 25.1 Compartmental model of cardiac metabolism. *, ^{13}C labeled species. Large boxes represent metabolite pools. Small boxes represent isotopic compartments for modeling.

for quantification of V_{TCA} and V_{M-A} (Figure 1). With the exception of glutamate, metabolite concentrations were taken from literature on hearts perfused with similar substrates (4; 5). V_{TCA} and V_{M-A} were determined from the least-square fitting of the model to the ^{13}C enrichment curves of glutamate C4 and C2, with the standard deviation calculated from the Jacobian matrix of the model. Simulations and parameter optimization were performed by solving the model equations using DLSODE, a robust implicit integrator for stiff and sparse systems, and NL2SOL, a solver for nonlinear least-square problems.

All measurements of this study are presented as mean $\pm$ SD. Mean values from different groups were compared by one-way analysis of variance. If there were statistical differences, multiple pairwise comparisons were performed using Tukey's test. P values less than 0.05 were considered statistically significant.

25.3 Results

25.3.1 Physiological function, glutamate content

As shown in Table 1, there were no statistical differences between the three groups in heart weight, RPP and MVO_2. Compared to the other groups, tissue glutamate content from hearts oxidizing palmitate was significantly lower.

Table 25.1 Physiological function and tissue glutamate content

	Low cytosolic redox state		High cytosolic redox state
	Group 1	Group 2	Group 3
Perfusate	^{13}C-acetate	^{13}C-palmitate	^{13}C-acetate+glucose+lactate
Heart Weight (g)	1.42±0.23	1.33±0.18	1.48±0.17
RPP$\times 10^3$ (mmHg/min)	20.9±5.3	16.6±3.8	18.8±5.0
MVO_2 (μmol/min/g wt)	2.5±0.5	2.4±0.5	2.6±0.6
Glutamate (μmol/g wt)	3.4±0.5	2.5±0.4*	3.2±0.7

*: significant difference, $p < 0.05$.

25.3.2 Fatty acid utilization

At low cytosolic redox state, acetate (group 1) and palmitate (group 2) contributed to 92±3% and 88±5% of oxidative metabolism, respectively (p=n.s.). At high cytosolic redox state (group 3), the contribution of acetate to oxidative metabolism was significantly reduced to 78±5% due to the oxidation of exogenous unlabeled glucose and lactate via pyruvate dehydrogenase.

25.3.3 Dynamic ^{13}C NMR spectra

Representative dynamic ^{13}C NMR spectra from each group are shown in Figure 2. Compared to the high cytosolic redox state (Figure 2C), hearts at a low redox state showed delayed incorporation of ^{13}C into the glutamate pool (Figure 2A&B). ^{13}C

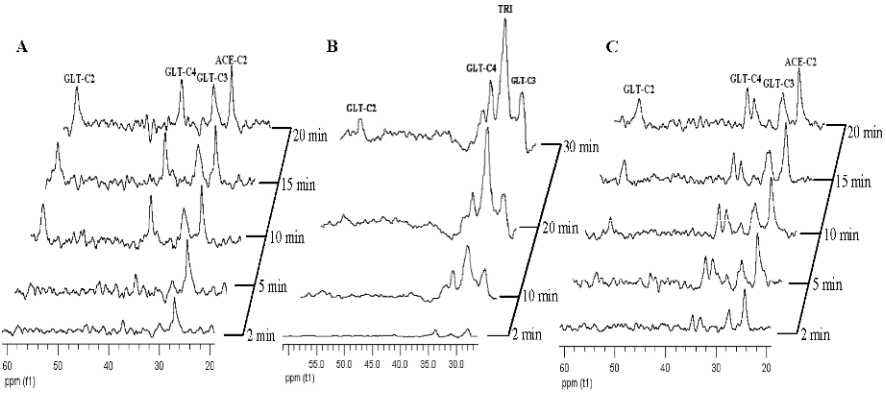

Fig. 25.2 Dynamic ^{13}C NMR spectra of isolated rat hearts perfused with 2.5 mM [2-^{13}C] acetate (A), 0.32 mM [U-^{13}C] palmitate (B), and 2.5 mM [2-^{13}C] acetate plus unlabeled 5.0 mM glucose and 1.0 mM lactate (C). Peak assignments: GLT-C2, glutamate C2; GLT-C4, glutamate C4; GLT-C3, glutamate C3; ACE-C2, acetate C2; TRI, triglycerides.

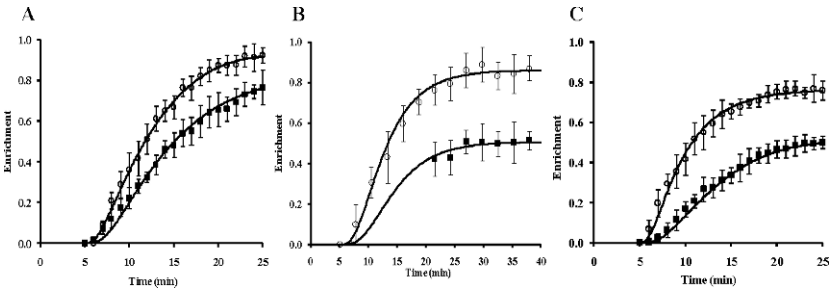

Fig. 25.3 Time course and model fitting of glutamate ^{13}C enrichment. A. group 1; B. group 2; C. group 3. Open circles: GLT-C4; closed squares: GLT-C2. Solid lines were the model simulations with optimal V_{TCA} and V_{M-A}.

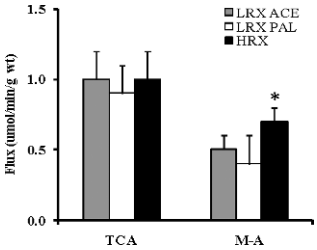

Fig. 25.4 V_{TCA} and V_{M-A}. LRX ACE: low cytosolic redox state, acetate perfusion; LRX PAL: low cytosolic redox state, palmitate perfusion; HRX: high cytosolic redox state. *: p <0.05.

enrichment curves of glutamate and the results of kinetic analysis are shown in Figure 3. The average half time, i.e., the time to 50% steady-state enrichment, for glutamate C4 was 6.5 min for group 1, 7.6 min for group 2, and 4 min for group 3, indicating a faster labeling kinetics for group 3.

25.3.4 Determinations of TCA cycle flux and M-A shuttle activity

Least-square fitting of the kinetic model to the glutamate labeling data is shown in Figure 3 for all three groups. At low cytosolic redox state, both V_{TCA} and V_{M-A} were similar between group 1 and 2 (Figure 4). At high cytosolic redox state (group 3), V_{TCA} was unaltered compared to the other two groups. However, V_{M-A} (0.7 ± 0.1 μmol/min/g wt, p <0.05) increased by 40% and 75% compared to group 1 and 2, respectively. As a result, this suggests enhanced M-A shuttle flux associated with elevated cytosolic redox state (Figure 4).

To test whether the changes in glutamate labeling kinetics in group 3 were due to lower fractional enrichment of acetyl-CoA, model simulation of glutamate enrichment in group 3 was performed by increasing the acetyl-CoA enrichment to that of group 1 using the same flux parameters obtained from group 3. With a hypothetical

acetyl-CoA enrichment of 92%, simulated glutamate enrichment curves reached a steady-state level similar to that of group 1. However, glutamate labeling kinetics was faster than that of group 1. Therefore, the kinetics of ^{13}C enrichment in glutamate is determined by V_{TCA} and V_{M-A} instead of the fractional acetyl-CoA enrichment level.

25.4 Discussion

Previous kinetic analysis methods used a lumped parameter as an index of the interconversion rate between glutamate and α-ketoglutarate (4). Distribution of metabolites between mitochondria and cytosol was not considered in these earlier studies. Therefore, quantification of M-A shuttle activity was not complete. In this study, we developed a multi-domain ^{13}C labeling model of cardiac metabolism with detailed representation of the M-A shuttle. By least-square fitting of the model to the dynamic NMR-measured glutamate enrichment, we found an increase in M-A shuttle activity induced by elevated cytosolic redox state in intact hearts. Thus, we show here the first approach that allows the direct assessment of metabolic communication between cytosol and mitochondria via the M-A shuttle.

Compared with hearts perfused with fatty acid only (group 1 and 2), high cytosolic redox state (group 3) induced a shift of oxidative metabolism, i.e., oxidation of glucose and lactate reduced the contribution of acetate to the total oxidative metabolism. Like in the brain (6), ATP production in the heart is also tightly coupled to energy demand, i.e., the workload. Since high cytosolic redox state did not induce an increase in workload, both oxygen consumption and the TCA cycle flux were unaltered. However, exogenous lactate and glucose led to an accelerated incorporation of ^{13}C into the glutamate pool, suggesting an enhanced M-A shuttle activity.

In conclusion, kinetic analysis of ^{13}C incorporation into the glutamate pool showed that TCA cycle flux is unaltered with changes in cytosolic redox state, whereas the M-A shuttle activity is more sensitive to alterations in cytosolic NADH/NAD^+. Our proposed method provides the opportunity to directly quantify metabolic communication between subcellular compartments via the M-A shuttle in intact, functioning hearts.

Acknowledgments

Supported by R01HL73315 and R01HL86935 from NHLBI

References

1. LaNoue, K. F. and Williamson, J. R. (1971) Interrelationships between malate-aspartate shuttle and citric acid cycle in rat heart mitochondria, *Metabolism* 20, 119-140.
2. Malloy, C. R., Sherry, A. D., and Jeffrey, F. M. (1988) Evaluation of carbon flux and substrate selection through alternate pathways involving the citric acid cycle of the heart by $_{13}C$ NMR spectroscopy, *J Biol Chem.* 263, 6964-6971.

3. Chance, E. M., Seeholzer, S. H., Kobayashi, K., and Williamson, J. R. (1983) Mathematical analysis of isotope labeling in the citric acid cycle with applications to $_{13}$C NMR studies in perfused rat hearts, *J Biol Chem.* 258, 13785-13794.
4. Yu, X., White, L. T., Doumen, C., Damico, L. A., LaNoue, K. F., Alpert, N. M., and Lewandowski, E. D. (1995) Kinetic analysis of dynamic $_{13}$C NMR spectra: metabolic flux, regulation, and compartmentation in hearts, *Biophys. J.* 69, 2090-2102.
5. Lu, M., Zhou, L., Stanley, W. C., Cabrera, M. E., Saidel, G. M., and Yu, X. (2008) Role of the malate-aspartate shuttle on the metabolic response to myocardial ischemia, *J Theor. Biol* 254, 466-475.
6. Shulman, R. G., Rothman, D. L., Behar, K. L., and Hyder, F. (2004) Energetic basis of brain activity: implications for neuroimaging, *Trends Neurosci.* 27, 489-495.

Chapter 26
In Vivo Assessment of Oxygen Consumption via Deuterium Magnetic Resonance

Gheorghe D. Mateescu, Allen Ye, Chris A. Flask, Bernadette Erokwu, and Jeffrey L. Duerk

Abstract We present a novel approach to simultaneously measure, *in vivo, non-invasively*, glucose and oxygen consumption *via* Deuterium Magnetic Resonance (DMR). Mice are administered deuteriated glucose by intravenous injection. The rate of formation of nascent (deuteriated) mitochondrial water is then measured *via* DMR. The rate of glucose metabolism and oxygen utilization is assessed by tracking their separate peaks in DMR spectra during dynamic scanning. Further studies will aim to validate these results by comparison with *in vivo* ^{17}O-MRI (mitochondrial function), ^{13}C-MRI and ^{19}FDG-PET (glucose metabolism) and *ex vivo* ^{1}H- and ^{2}H-MR, as well as mass spectrometry.[1]

26.1 Introduction

Essential knowledge of mitochondrial function has been initially obtained in experiments on isolated mitochondria and tissue preparations [1-4]. Nuclear magnetic resonance (NMR) and more recently magnetic resonance imaging (MRI) and spectroscopy (MRS) greatly expanded this knowledge, making it possible to perform *in vivo*, *noninvasive* measurements. Based on research conducted in the early 1970s [5], tissue oxygenation could be estimated from paramagnetically shifted histidyl proton signals of deoxyhemoglobin and deoxymyoglobin [6]. The investigation of oxidative phosphorylation by ^{31}P MR began at about the same time [7, 8] and later on ^{13}C MR

Allen Ye and Jeffrey L. Duerk
Department of Biomedical Engineering, Case Western Reserve University, Cleveland, OH 44106
e-mail: gdm2@case.edu

Gheorghe D. Mateescu, Chris A. Flask, Bernadette Erokwu, and Jeffrey L. Duerk
Case Center for Imaging Research, Case Western Reserve University, Cleveland, OH 44106

Gheorghe D. Mateescu
Department of Chemistry, Case Western Reserve University, Cleveland, OH 44106

[1] Dedicated to the memory of George Emil Palade and Marco Cabrera.

J.C. LaManna et al. (eds.), *Oxygen Transport to Tissue XXXII*, Advances in Experimental Medicine and Biology 701, DOI 10.1007/978-1-4419-7756-4_26,

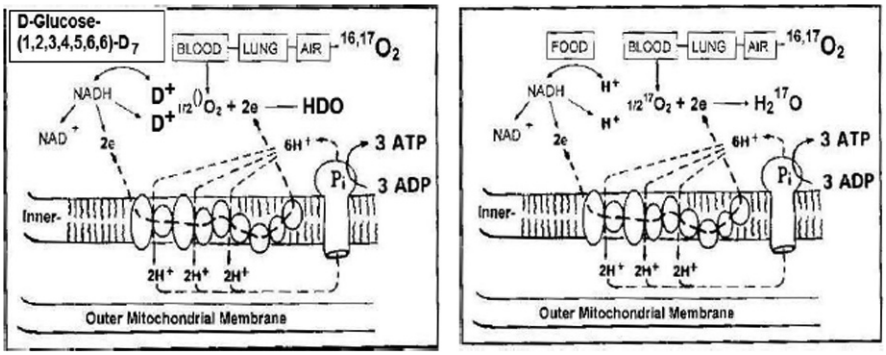

Fig. 26.1 Illustration of multinuclear MRS assessment of mitochondrial metabolism. The left panel shows the basic principle for the simultaneous DMR determination of glucose metabolism and mitochondrial water (HDO) formation. The right panel describes the employment of ^{17}O-enriched air that yields ^{17}O-enriched water.

[9, 10] contributed substantially to the understanding of mitochondrial metabolism. The first ^{17}O MRI and MRS experiments [11-13] were reported in the late 1980s and direct and indirect determination of the rate of formation of nascent mitochondrial water (MRO_2) *via* ^{17}O MR were reported in the early 1990s [14-22]. In spite of considerable technological progress, ^{17}O MR is slow in reaching the clinical phase [23]. This is primarily due to the high cost of the MR-sensitive isotope.

Use of DMR has been made for the elucidation of metabolic pathways in gluconeogenesis [24] and in fermentation [25, 26]. However, no DMR investigation of mitochondrial respiration is known to date. Such investigations are highly desirable in order to develop a better understanding of the relationship between glucose and oxygen consumption [27] and the impairment of mitochondrial function in a wide variety of diseases.

As seen in Figure 1, the particular advantage of this novel approach results from the fact that it offers a new avenue to simultaneously investigate both sides of the mitochondrial "coin" – glucose *and* oxygen consumption.

In this communication we present preliminary data that demonstrate the feasibility of DMR and its incorporation into a multinuclear approach in cell bioenergetics research.

26.2 Materials and Methods

All animal procedures were approved by the Institutional Animal Care and Use Committee of Case Western Reserve University. A 4-month-old male nude mouse (AA7, Charles River Laboratories) weighing 26.7 g was rapidly anesthetized using 3% isoflurane in oxygen. A tail vein catheter (Abbocath, Abbott Labs, Abbott Park, IL) was applied prior to placing the animal within a Bruker Biospec 9.4 Tesla

MRI scanner (Bruker Biospin, Billerica, MA). The animal's respiration rate (40-60 breaths/minute) and core body temperature (35±1°C) were maintained throughout the imaging procedures with manual anesthesia adjustments and controlled warm air, respectively. Dynamic ^{2}H-NMR spectroscopy was performed using the following parameters: 90^o pulse = 100 μs, TR = 1 s, NS = 16, ADC Time = 680 ms, 240 repetitions, exponential line broadening = 15 Hz). At the beginning of the scanning process, three baseline spectra were recorded, then the animal was infused with 16 mg D-Glucose-1,2,3,4,5,6,6-d$_7$ (Cambridge Isotope Laboratories) dissolved in 200 μL sterile saline solution.

26.3 Results

Figure 2 represents the *in vitro* DMR spectrum of a 4.6 mM perdeuteriated glucose (G-d7) in saline solution made with natural abundance water (0.015% ^{2}H). A relatively small (15 Hz) line broadening was applied in order to anticipate the appearance of the spectrum expected *in vivo* (much broader lines, due to longer correlation times), but to also be able to distinguish the groups of resonances of individual deuterons in the molecule. It is seen that absorptions due to deuterons in the anomeric positions 1α and 1β overlap with the natural abundance peak of residual water (4.8 ppm), while the resonances of deuterons in positions 2, 3, 4, 5, and 6 coalesce in two overlapping groups of resonances at higher field, that are well separated from the "water group."

In vivo dynamic DMR spectra of nascent mitochondrial water formation (HDO) and glucose metabolism are shown in Figure 3. Since there was considerable overlap

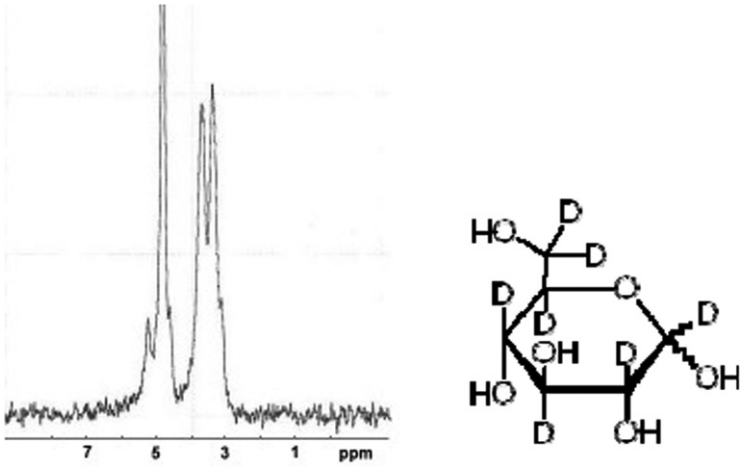

Fig. 26.2 DMR spectrum of D-Glucose-(1, 2, 3, 4, 5, 6, 6)-D$_7$). Carbon numbering starts clockwise after the oxygen in the pyranose ring. The sharp, tallest peak at 4.8 ppm is the resonance of water (HDO). The peaks at 5.23 ppm (to the left of the water peak) and the shoulder at 4.63 ppm (on the right of water) belong to the anomeric deuterons (alpha and beta). Overlapping peaks of D in positions 2-6 are situated into two groups between 3 and 4 ppm.

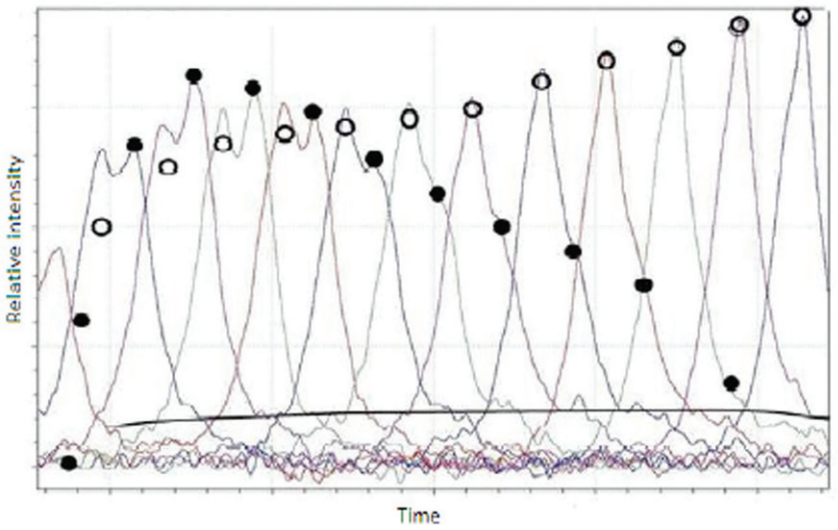

Fig. 26.3 *In vivo* dynamic DMR of glucose-D_7 (black) and of HDO (open circles) on a nonlinear time scale. The baseline (first spectrum on left) was measured just before tail *iv* infusion of perdeuteroglucose; the subsequent 12 spectra were taken at 96, 128, 160, 256, 416, 544, 944, 1104, 1424, 2844, 3324, and 3804 s.

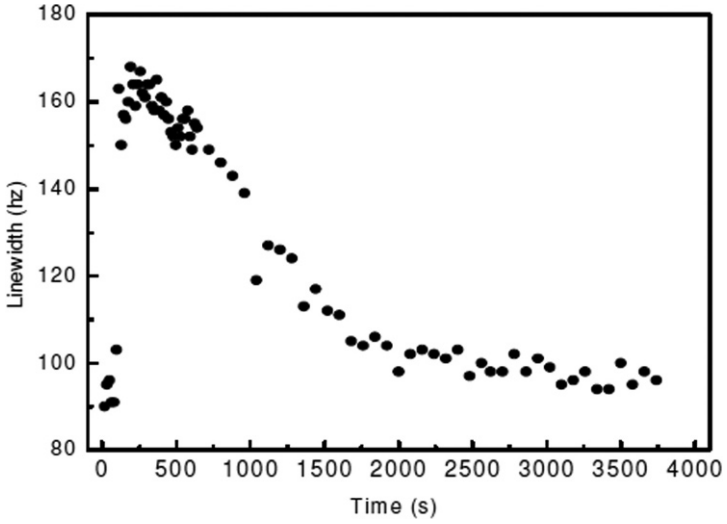

Fig. 26.4 Line width evolution during the experiment illustrated in Figure 3 (see text).

of the HDO and D-glucose peaks in vivo, we also measured the line width of the combined peaks as a preliminary assessment of glucose metabolism. The evolution of the line width is shown in Figure 4.

26.4 Discussion

Results shown in Figures 3 and 4 demonstrate the feasibility of *simultaneous in vivo*, *noninvasive* determination of glucose and oxygen consumption *via* Deuterium Magnetic Resonance performed on animals fed or injected deuteriated glucose. An important precedent has been established in fermentation studies on bacteria [25]. Interestingly, the authors of that study were justifiably considering the formation of HDO as a (label) loss; the essential difference in our approach is that, in the very first seconds of the experiment, the observed HDO originates overwhelmingly in mitochondria and it represents *nascent mitochondrial water*.

Initially we chose to employ glucose deuteriated at all carbon atoms (hydroxyl protons are rapidly exchanging) in order to obtain high intensity deuterium signals. Comparing spectra in Figures 2 and 3 it is seen that, in spite of the overlap of the two anomeric deuteron absorptions with that of HDO and in spite of the fact that severe line broadening in tissues causes the merging of the peaks belonging to deuterons 2, 3, 4, 5, and 6 (see Fig. 1), one can readily obtain at least a semi-quantitative, simultaneous evaluation of glucose and oxygen consumption.

Work in progress is aiming at a quantitative approach with a mathematical model that combines peak intensities, integrals, and the apparent FWHM (Full Width at Half Maximum). In order to avoid the peak overlapping described above, the glucose to be used is deuteriated only at either carbon 1 or carbon 6. The latter will yield spectra with greatly increased separation between water and glucose signals, making it possible to obtain quantitative results. The former will constitute a test of the validity of results derived exclusively from the evolution of absorption line widths.

Of particular importance of DMR is its potential to trace the exogenous deuterium label in the network of anaplerotic/cataplerotic processes [28] (signals under the curved line in Fig. 3). Monitoring deviations from mitochondrial homeostasis will be useful for diagnostic and monitoring the treatment of mitochondrial diseases [29]. Moreover, we believe a definite possibility exists that the kinetic isotope effect (^{2}D/^{1}H) may slow *in vivo* enzymatic reactions [30] to a sufficient extent to affect the growth of diseased cells. Indications exist in the literature that diseased (e.g., malignant) cells are more susceptible to this effect than normal cells [31]. The authors mention, however, that high (generally toxic) concentrations would be needed. Since the overwhelming majority of glucose is known to be metabolized in mitochondria, employing deuteriated glucose may constitute an excellent means to concentrate the heavy isotope at sites of high enzymatic activity for targeted treatment. Current plans include cell cultures to verify this hypothesis.

26.5 Conclusion

A complete picture of mitochondrial chemistry and function is yet to emerge. Owing to its two-sided nature (simultaneous probing of both “ingredients” of the highly exergonic reaction that yields the metabolic water) and to its potential integration in

a multinuclear MR analysis, the DMR approach described here clearly opens new avenues towards the ultimate understanding of mitochondrial function. Considering the good results obtained on small animals, it becomes evident that in the much larger volumes of human tissues and organs this approach will yield even better, more refined and more useful information. Potential validation studies will include *in vivo* ^{17}O-, ^{31}P-, and ^{13}C-MR as well as *ex vivo* ^{1}H- and ^{2}H-MR, ^{19}FDG PET [32-34] and Mass Spectrometry [35].

Acknowledgments

We are grateful for the valuable assistance of Mark Griswold, Jeremy Heilman, Matt Riffe and Natalia Gudino in the process of building the DMR coil, Joe Molter for animal preparation and handling, and James Basillion and Ann-Marie Broome for providing the nude mice.

References

1. Hogeboom GH, Schneider WC, Palade GE (1948) Cytochemical studies of mammalian tissues I. Isolation of intact mitochondria from rat liver; some biochemical properties of mitochondria and submicroscopic particulate material. J Biol Chem 172:619–628 and references cited therein
2. Kennedy EP and Lehninger AL (1949) Oxidation of fatty acids and tricarboxilic acid cycle intermediates by isolated rat liver mitochondria. J Biol Chem 179:957–972
3. Chance B and Williams GR (1955) Respiratory enzymes in oxidative phosphorylation IV. The respiratory chain. J Biol Chem 172:429–438 and references cited therein
4. Hoppel C and Cooper C (1968) The action of digitonin on rat liver mitochondria: the effects on enzyme content. Biochem J 107:367–375
5. Goff H and La Mar GN (1977) High-spin ferrous porphyrin complexes as models for deoxymyoglobin and hemoglobin. **A** proton nuclear magnetic resonance study. J Am Chem Soc 99:6599–6606
6. Tevald MA, Lanza IR, Befroy DE, Kent-Brown JA (2009) Intramyocellular oxygenation during ischemic muscle contraction in vivo. Eur J Appl Physiol 106:333–343
7. Chance B, Im J, Nioka S, Kushmerick M (2006) Skeletal muscle energetics with PMR: personal views and historic perspectives. NMR Biomed 19:904–926 and literature cited therein
8. Arias-Mendoza F, Payne GS, Zakian KL et al (2006) In vivo ^{31}P MR spectral patterns and reproducibility in cancer patients studied in a multi-institutional trial. NMR Biomed 19:504–512
9. Golman K. in 't Zandt R, Thaning M (2006) Real-time metabolic imaging. PNAS 103:11270–11275 and literature cited therein
10. Yu X, White LT, Doumen C et al (1995) Kinetic analysis of dynamic ^{13}C NMR spectra: metabolic flux, regulation, and compartmentation in hearts. Biophys J 69:20902102
11. Mateescu GD, Yvars GM, Dular T (1987) Oxygen-17 magnetic resonance imaging. Proc Soc Magn Reson Med 6:929
12. Mateescu GD, Yvars GM, Dular T (1988) Water, ions, and O-17/proton magnetic resonance imaging. In: Läuger P, Packer L, Vasilescu V (eds) Water and Ions in Biological Systems. Birkhauser, Boston, 239-250.
13. Mateescu GD, Yvars GM, Pazara DI, Alldridge NA, LaManna JC, Lust DW, Mattingly M, Kuhn W (1989) Combined ^{17}O-^{1}H magnetic resonance imaging in plants, animals, and materials.

In: Baillie TA, Jones JR (eds) Synthesis and applications of isotopically labeled compounds. Elsevier, 499-508.
14. Arai T, Nakao S, Mori K, Ishimori K, Morishima I, Miyazawa T, Fritz-Zieroth B (1990) Cerebral oxygen utilization analyzed by the use of O-17 and its MR. Biochem Biophys Res Comm 169:153-158
15. Mateescu GD (1991) From materials testing to brain-function testing. Spectroscopy International 3:14-18
16. Mateescu GD, LaManna JC, Lust DW, Mars L, Tseng J (1991) Oxygen-17 magnetic resonance: *in vivo* detection of nascent mitochondrial water in animals breathing ^{17}O-enriched air. Proc Soc Magn Reson Med 10:1031
17. Pekar J, Ligetti L, Ruttner Z, Lyon R, Sinnwell T, van Gelderen P, Fiat D, Moonen CT, McLaughlin A (1991) *In vivo* measurement of cerebral oxygen consumption and blood flow using ^{17}O magnetic resonance Imaging. Magn Reson Med **21**:313–319
18. Mateescu GD, Fercu D (1993) Interleave ^{17}O/^{31}P MRS: novel approach for in vivo determination of defects in oxidative phosphorylation (mitochondrial metabolism). Proc Soc Magn Reson Med 12:110
19. Fiat D, Kang S (1993) Determination of the rate of cerebral oxygen consumption and regional blood flow by non-invasive ^{17}O in vivo NMR spectroscopy and MRI. Neurol Res 15:7–22
20. Mateescu GD, Cabrera ME (1997) *In vivo* ^{17}O magnetic resonance spectroscopy: determination of temperature effects on metabolic rates (Q_{10} factor). Adv Exp Med Biol 411**:**585–590
21. Kwong KK, Hopkins AL, Belliveau JW et al (1991) Proton NMR Imaging of cerebral blood flow using $H_2^{17}O$. Magn Reson Med 2:154–158 and references cited therein
22. Mateescu GD, Cabrera M, Fercu D (1998) ^{17}O and ^{31}P magnetic resonance imaging and spectroscopy: *in vivo* investigations of cell bioenergetics. In: Bluemler P, Bluemich B, Botto R, Fukushima E (eds) Spatially Resolved Magnetic Resonance. Wiley-VCH, Weinheim, New York, 421-429
23. Zhu X-H, Zhang N, Zhang Y et al (2005) In vivo ^{17}O NMR approaches for brain study at high field. NMR Biomed 18:83–103
24. Weiss BC, Margolis D, Burgess SC et al (2004) Glucose production pathways by ^{2}H and ^{13}C NMR in patients with HIV-associated lipoatrophy Magn Reson Med 51:649–654, and references cited therein
25. Aguayo JB, Gamesik MP, Dick JD (1988) High resolution deuterium NMR studies of bacterial metabolism. J Biol Chem 263**:**19552–19557
26. Roger O, Lavigne R, Mahmoud M et al (2004 Quantitatve ^{2}H NMR at natural abundance can distinguish the pathway used for glucose fermentation by lactic acid bacteria. J Biol Chem 279**:**24923–24928
27. Gjedde A (2009) Variable ATP yield and uncoupling of oxygen consumption in human brain, this volume
28. Owen OE, Kalhan SC, Hanson RW (2002) The key role of anaplerosis and cataplerosis for citric acid cycle function. J Biol Chem 263**:**30409–30412
29. Wallace DC (1999) Mitochondrial Diseases in Man and Mouse. *Science,* 283:1482-1488
30. Pedersen LG, Bartolotti L, Li L (2006) Deuterium and its role in the machinery of evolution. J Theor Biol 238:914-918 and references cited therein
31. Kushner DJ, Baker A, Dunstall TG (1999) Pharmacological uses and perspectives of heavy water and deuteriated compounds. Can J Physiol Pharmacol 77:79–88
32. Landau BR, Spring-Robinson CL, Muzic RF Jr, et al (2007) 6-Fluoro-6-deoxy-D-glucose as a tracer of glucose transport. Am J Physiol Endocrinol Metab 293(1):E237-45. Epub 2007 Apr 3.PMID: 17405828
33. Gjedde A (1995) Glucose metabolism. In: Wagner HN Jr, Szabo Z, Buchanan JW (eds) Principles of Nuclear Medicine, 2nd edn. Saunders, Philadelphia: 54-71
34. Vafaee M, Gjedde A (2004) Spatially dissociated flow-metabolism coupling in brain activation. NeuroImage 21:507-515
35. Burgess SC, Nuss M, Chandramouli V et al (2003) Analysis of gluconeogenic pathways in vivo by distribution of ^{2}H in plasma glucose: comparison of nuclear magnetic resonance and mass spectrometry. Analytical Biochemistry. doi:10.1016/S0003-2697(03)00158-1

Chapter 27
Elevated Mitochondrial DNA Copy Number and POL-γ Expression but Decreased Expression of TFAM in Murine Intestine Following Therapeutic Dose Irradiation

Hengshan Zhang, David J. Maguire, Mei Zhang, Lurong Zhang, and Paul Okunieff

Abstract Mitochondria play pivotal roles in cellular handling of oxygen and in apoptosis, the ordered suicide response of cells to irradiation. The involvement of expression products from the 16.5 kb human mitochondrial genome in these activities has been studied widely. However, little is known about effects of irradiation on mammalian mitochondrial DNA (mtDNA). The relative lack of mtDNA repair mechanisms compared with nuclear DNA (nDNA) predicts particular vulnerability to irradiation. Using a technique developed to ascertain mtDNA:nDNA ratios, we previously showed that this ratio increases dramatically in murine small bowel within 48 hours following whole body irradiation . We now report that those levels continue to rise for four days and remain elevated at close to that level beyond 30 days after 5 Gy of irradiation. We further demonstrate that levels of the mtDNA-specific DNA polymerase-γ (Pol-γ) also show a sharp and sustained increase during this time course after a 2-Gy dose. Paradoxically, transcription factor A (TFAM), exhibited the directly opposite response.

27.1 Introduction

DNA strand breakage is the hallmark of ionizing irradiation. In mammals, there are thousands of single strand, and dozens of double strand breaks in nDNA for every Gy of irradiation, with well over 95% rapidly repaired [1]. mtDNA sustains a

Hengshan Zhang
Department of Radiation Oncology, University of Florida, 2033 Mowry Road, Box 103633, Gainesville, FL 32610, USA
e-mail: pokunieff@ufl.edu

David J. Maguire
Department of Radiation Oncology, University of Rochester Medical Center, 601 Elmwood Avenue, Rochester, NY 14642, USA

Mei Zhang, Lurong Zhang, and Paul Okunieff
Department of Molecular Genetics and Microbiology, Duke University Medical Center, Durham, NC 27710, USA

J.C. LaManna et al. (eds.), *Oxygen Transport to Tissue XXXII*, Advances in Experimental Medicine and Biology 701, DOI 10.1007/978-1-4419-7756-4_27,

higher level of DNA damage, and only 30% is repaired [2]. After irradiation, nDNA also has a number of advantages over mtDNA in terms of repair mechanisms [3, 4], and continued mitochondrial function would be expected to depend upon rapid replication of the circular mitochondrial genome instead, which is present in high copy number.

Increases in mtDNA:nDNA ratio were previously reported in murine brain and spleen [5] over a 120-minute period, in murine gut [6] over a 24-hour period, and in murine bone marrow over a 48-hour period [6]. It has been suggested [5] that this mechanism provides new mtDNA copies on undamaged or slightly compromised templates. Increased levels of enzymes involved in DNA synthesis would also be expected to be found in irradiated tissues.

In the present investigation, the mtDNA:nDNA ratio was studied over an extended period up to 30 days post-irradiation using a real-time PCR directed toward the amplification of a stable region of murine mtDNA and the murine 18S ribosomal RNA gene. We also investigated the levels of two important enzymes involved in the synthesis and expression of mtDNA.

27.2 Materials and Methods

Male Balb/c mice, 6 to 8 weeks old, were divided into groups of 5 animals each. Control mice were not irradiated, while other groups received total body irradiation (TBI) with the aid of a plastic restrainer at 2 Gy or 5 Gy via a J. L. Shepherd Irradiator with a ^{137}Cs γ-ray source. The dose rate was 1.84 Gy/minute. The mice were then sacrificed at four days, 21 days, or 30 days post-irradiation. Mice were housed in a pathogen-free barrier facility in a 12-hour light/12-hour dark cycle and fed an autoclaved standard rodent chow. All protocols were approved by the University of Rochester Committee on Animal Research, and all experiments were carried out in accordance with USPHS guidelines. Small bowel tissues were collected and frozen immediately at -70˚C until use. Total DNA was extracted from these tissues by standard proteolytic digestion followed by phenol/chloroform/isoamyl alcohol purification. Absorbance at 260 nm was used for quantification of the extracted DNA. Two PCR primers and a probe for directing the mouse mtDNA were designed on the basis of the GeneBank mitochondrial genome sequence (NC_006914, *Mus musculus domesticus* mitochondrion) using RealTimeDesign™ (Biosearch Technologies, Inc.). These sequences are 5'-GCC CAC ATA GGA TGA ATA-3' (forward primer), 5'-TGA GGT TGA GTA GAG TGA-3' (reverse primer) and 5'-CAL Fluor Red 610-AGC AAT TCT TCC TTA CAA CCC ATC-CC-BHQ2-3' (probe). They direct the synthesis of a 64-bp mtDNA fragment from a mtDNA region in which deletions are rare. As such, alterations in mitochondrial DNA content or copy number in cells can be detected quantitatively by comparing them to a nuclear encoded housekeeping gene. The housekeeping gene used in this study was mouse 18S rRNA gene. Two primers and a probe amplifying this housekeeping gene were designed based on GeneBank sequence (NC_003278, *Mus musculus* 18S rRNA) using the same pro-

gram, and their sequences are 5' ACG *TCT* GCC CTA TCA AC-3' (forward primer), 5'-GGT AGC CGT TTC TCA G-3' (reverse primer) and 5'-FAM-TTT CGA TGG TAG TCG CCG TGC-BHQ-1 3' (probe). The synthesis of primers and probes was performed at Biosearch Technologies, Inc. Amplification of two targets, including one from mtDNA and one from 18S rRNA described above, were performed in a single reaction tube. Total reaction volume per sample was 20 μl, containing 2 x iQ^{TM} Supermix (1 x final), two pairs of the primers directing either mtDNA or nDNA, 0.5 μM each, two corresponding probes, 0.5 μM each, and 30 ng of total DNA purified from murine intestine. Since amplification of any one target can influence the amplification of the other targets in the same tube, the multiplex reaction was optimized by adding additional $MgCl_2$, dNTP, and Taq DNA polymerase. Each reaction was subjected to an initial denaturation of 3 minutes at 95˚C followed by 50 amplification cycles of denaturation at 95˚C for 10 seconds, 55˚C to anneal and extension for 1 minute on a Bio-Rad iQ5 multicolor real-time PCR detection system. Conventional PCR was first run to develop cycling conditions using the same primers. PCR assays were performed in duplicate or triplicate for each DNA sample. The cycle number (Ct) at which the fluorescent signal of a given reaction well crossed the threshold value was used to estimate mtDNA:nDNA ratios, using $2_T^{-\Delta\Delta C}$ and assuming equal efficiencies [7].

Intestinal tissues dissected from mice from the groups described above were sonicated in NP-40 cell lysis buffer (pH 8.0) containing 0.15 M NaCl, 50 mM Tris-HCl, 1% NP-40, and protease inhibitor cocktail (containing PMSF, leupeptin, aprotinin, and pepstatin, 10 μg/ml each) with a Vibra Cell sonicator (Sonics & Materials, Inc. CT). Supernatants were collected by centrifugation at 600 $\times$ g for 15 minutes at 4 ˚C. Samples (45 μg of protein) containing equal volumes of supernatant derived from each animal in the same group after adjustment to equivalent protein content, were subjected to 8% SDS-PAGE gel electrophoresis, as per Laemmli [8]. After electrophoresis, proteins were transferred to Supported Nitrocellulose membranes (0.2 μM) (*Bio-Rad* Laboratories, CA) using PS 500 XT DC power supply (Hoefer Scientific Instruments, San Francisco). The filter was blocked with 5% non-fat dried milk in TBS-T (20 mM Tris-HCl, 140 mM NaCl, 0.25% Tween 20, pH 7.6) and treated with polyclonal rabbit anti-DNA polymerase gamma antibody (ab2969, Abcam, Inc., MA) or polyclonal rabbit anti-TFAM antibody (ARP31400_P050, Aviva System Biology, CA) as primary antibody, and then with horseradish peroxidase-conjugated goat antibody against rabbit IgG (Bio-Rad) as a secondary antibody. Signals were visualized using Immobilon Western HRP Substrate Luminol Reagent (Millipore Corporation, MA).

27.3 Results and Discussion

Small bowel mucosa is a rapidly renewing tissue. Within a few days of irradiation, the entire luminal epithelium is completely replaced [9]. Thus, loss of mtDNA could seriously impact recovery given the potential for hemi-depletion with each cell division. Therefore, it was interesting to see how mtDNA might respond to low-dose

irradiation. To test this, irradiation doses that have no obvious histological effects were used. The small bowel ti ssues were collected from mice 4, 21, and 30 days following 2 Gy or 5 Gy of irradiation. Total DNA extracted from each sample was subjected to real-time PCR. Since each cycle of PCR leads to almost a doubling in DNA copies, the cycle numbers measured at the threshold can be used to estimate mtDNA:nDNA ratios [7].

At 4 days after irradiation, mtDNA:nDNA ratios increased compared with non-irradiated tissues, and were still elevated as long as 30 days after exposure (Figure 1a). The effect was seen consistently in the three mouse strains tested. Previous work found that tissues irradiated to 4 Gy indicated a clear increase in copy ratio compared with 2 Gy, which was consistent with a dose-dependent response [6]. This result is consistent with a compensatory replication of mtDNA to replace lost or damaged mtDNA. Other explanations include a lowering of the copy number of chromosomes per cell by redistribution of the cell cycle However, this is very unlikely since the proportion of cells in S-phase at 24 hours and subsequently after irradiation is stable or moderately increased, which would lead to a decrease rather than the observed increase in mtDNA:nDNA ratio.

Pol-γ is the nuclear-encoded enzyme responsible for the replication of mtDNA. In keeping with the observed nDNA:mtDNA ratios, Pol-γ intensity increases significantly within 4 days after irradiation and is seen to remain elevated throughout the time course of the experiment (Figure 1b). This result is consistent with a mechanism whereby there is active synthesis of mtDNA and has been observed previously in a range of tissue culture cells and specialized tissues.

TFAM, an important nuclear-encoded initiator in the events leading to expression of mtDNA-encoded genes, induces structural changes of the promoter required for POLRMT-dependent promoter recognition. Decreased levels of TFAM following irradiation (Figure 1b) would indicate down-regulation of the nuclear gene for this protein. This may reflect a cellular mechanism that limits excessive transcription of the vastly increased number of broken copies of mtDNA present after irradiation. This finding contrasts with results of numerous experiments on cultured cells and suggests a fundamental difference in the way tissues, as opposed to single cells, respond to irradiation.

The extended elevation in mtDNA:nDNA ratio in total DNA extracted from whole tissues infers a mechanism of information retrieval after irradiation damage in which the first step is synthesis of multiple copies of mtDNA. For this to occur, levels of Pol-γ increase after irradiation. To prevent replication of damaged copies of mitochondrial genomes, TFAM is down-regulated. This limits the expression of 'crippled' protein species such as those mutated at active sites, binding sites, or electron-transfer sites, as well as those in which truncation, missense, or frame shift variants would lead to inappropriate protein location or misaligned and erroneous inter-subunit binding within mitochondria. After an appropriate interval, multiple fragmented copies of regions of mtDNA may recombine, thus re-creating intact, replicable copies of the mitochondrial genome. Limited mtDNA repair may also contribute to this process. The results of this tissue-based investigation differ from experiments reported using cell culture. In tissue culture, it can be inferred that

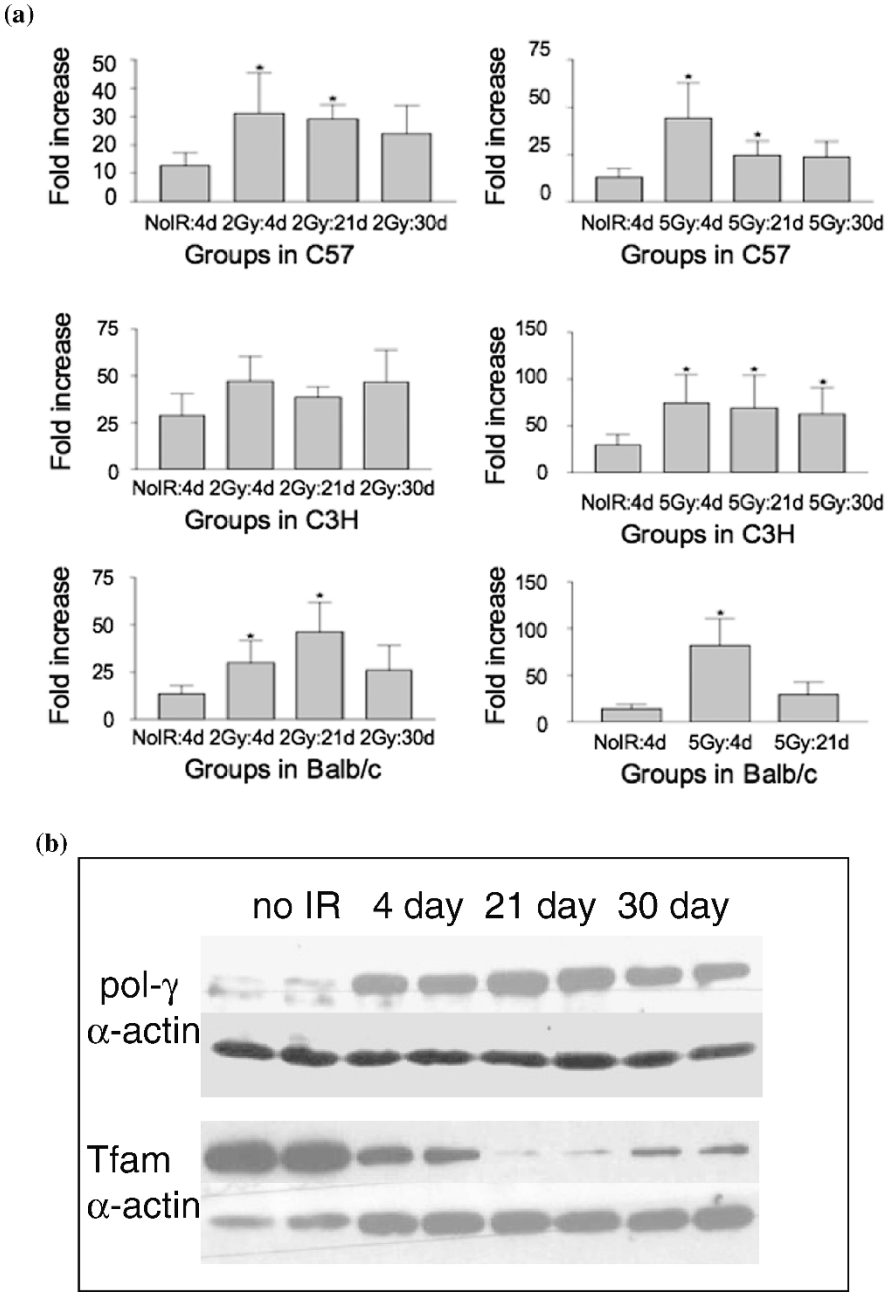

Fig. 27.1 Time course of gut mucosa response to irradiation: (a) mtDNA/nDNA ratio in three murine strains before irradiation and at 4, 21, and 30 days after 2 Gy or 5 Gy of irradiation (Mean $\pm$ Standard Deviation); (b) western blots of gut extracts probed for pol-γs TFAM, and the housekeeping gene α-actin over the time period described in the figure for 5 Gy.

replication and expression of IR-damaged genomes continue post-irradiation. In that environment, respiration-competent cells would be expected to out-compete cells with limited oxidative capacity.

27.4 Conclusions

After whole body irradiation at 2 or 5 Gy, elevated mtDNA:nDNA ratios seen in three mouse strains within four days post-irradiation were maintained for up to 30 days. These changes reflect increased levels of mtDNA, rather than decreased nDNA levels. Elevations in pol-γ, the enzyme responsible for mtDNA synthesis, were also observed during this period, but TFAM levels fell dramatically during this same period of elevated mtDNA and pol-γ levels. These results provide the basis for a possible mechanism for retrieval of mtDNA in essentially closed systems in which tissue integrity must be maintained, while avoiding potential damage from compromised electron flow through the electron transport chain. A further study is planned to investigate maintenance of these effects up to 12 months post-irradiation.

Acknowledgments

This research was supported in part by the Center for Medical Countermeasures against Radiation Program, U19-AI067733, National Institute of Allergy and Infectious Diseases. We thank Amy K. Huser for excellent technical editing.

References

1. Purkayastha SJ, Milligan R, and Bernhard WA (2007) On the chemical yield of base lesions, strand breaks, and clustered damage generated in plasmid DNA by the direct effect of x rays. Radiat Res 168:357-366
2. Yakes FM, and Van Houten B (1997) Mitochondrial DNA damage is more extensive and persists longer than nuclear DNA damage in human cells following oxidative stress. Proc Natl Acad Sci USA 94:514-519
3. Iliakis G, Wang H, Perrault AR, et al. (2004) Mechanisms of DNA double strand break repair and chromosome aberration formation. Cytogenet Genome Res 104:14-20
4. Larsen NB, Rasmussen M, and Rasmussen LJ (2005) Nuclear and mitochondrial DNA repair: similar pathways? Mitochondrion 5:89-108
5. Malakhova L, Bezlepkin VG, Antipova V, et al. (2005) The increase in mitochondrial DNA copy number in the tissues of γ-irradiated mice. Cell Mol Biol Lett 10:721–732
6. Zhang H, Maguire D, Swarts S, et al. (2009) Replication of murine mitochondrial DNA following irradiation. Adv Exp Med Biol 645:43-48
7. Pfaffl MW (2001) A new mathematical model for relative quantification in real time RT-PCR. Nuc Acids Res 29:e45
8. Laemmli, UK (1970) Cleavage of structural proteins during the assembly of the head of bacteriophage T4. Nature 227:680-685
9. Denham JW, Hauer-Jensen M, Kron T, et al. (2000) Treatment-time-dependence models of early and delayed radiation injury in rat small intestine. Int J Radiat Biol Phys 48:871-887

Chapter 28
Heterogeneity of Mitochondrial Redox State in Premalignant Pancreas in a PTEN Null Transgenic Mouse Model

He N. Xu, Shoko Nioka, Britton Chance, and Lin Z. Li

Abstract Pancreas-specific deletion of PTEN in mice revealed progressive premalignant lesions such as ductal metaplasia with infrequent malignant transformation. In this study, we aimed at evaluating the mitochondrial redox state of the metaplastic pancreas in a pancreas-specific PTEN null transgenic mouse model. The two intrinsic fluorophores, reduced nicotinamide adenine dinucleotide (NADH) and oxidized flavoproteins (Fp) such as flavin adenine dinucleotide (FAD), in the respiratory chain in mitochondria are sensitive indicators of mitochondrial redox states and have been applied to the studies of mitochondrial function with energy-linked processes. The redox ratio, Fp/(Fp+NADH) provides a sensitive index of mitochondrial redox state. We have obtained optical images of the *in vivo* mitochondrial redox states of the snap-frozen pancreases from pancreas-specific PTEN null mice (Pdx1-Cre;PTEN$^{lox/lox}$, N=3) and the controls (PTEN$^{lox/lox}$, N=3) using the redox scanner at low temperature. The results showed high spatial heterogeneity of mitochondrial redox state in the mutated pancreases with hot spots of much higher Fp redox ratios whereas the normal ones, were relatively homogenous. The cystic dilation regions in the metaplastic pancreases showed little to no NADH or Fp signal. Histological analysis confirmed no cells existed in these regions. It is the first time that the *in vivo* mitochondrial redox states of the metaplastic mouse pancreas were optically imaged. Our previous results on human melanoma and breast cancer mouse xenografts have shown that mitochondrial redox state quantitatively correlates with cancer metastatic potential. The more oxidative mitochondrial redox state (higher Fp redox ratio) corresponded to the higher metastatic potential of the tumors. As mitochondrial redox state imbalance is associated with abnormal mitochondrial function, and redox state mediates the generation of reactive oxygen species and many signal transduction pathways,

He N. Xu and Lin Z. Li
Department of Radiology, School of Medicine, University of Pennsylvania, Philadelphia, PA, USA
e-mail: linli@mail.med.upenn.edu

Shoko Nioka and Britton Chance
Johnson Research Foundation, Department of Biochemistry and Molecular Biophysics, School of Medicine, University of Pennsylvania, Philadelphia, PA, USA

J.C. LaManna et al. (eds.), *Oxygen Transport to Tissue XXXII*, Advances in Experimental Medicine and Biology 701, DOI 10.1007/978-1-4419-7756-4_28,

this research may provide insights for studying basic biology and developing early diagnostic imaging biomarkers for pancreatic cancer.

28.1 Introduction

Early detection of pancreatic cancer demands reproducible imaging biomarkers. Pancreas-specific deletion of PTEN in mouse revealed progressive premalignant lesions such as ductal metaplasia with infrequent malignant transformation [1]. PTEN is a tumor suppressor gene inhibiting the activity of PI3K/Akt signaling pathway, which plays a key role in cancer progression. This premalignant pancreatic cancer model provides an excellent tool for searching for biomarkers in early pancreatic cancer detection. In mitochondria, the two intrinsic fluorophores, reduced nicotinamide adenine dinucleotide (NADH) and oxidized flavoproteins (Fp) such as flavin adenine dinucleotide (FAD), in the respiratory chain are sensitive indicators of mitochondrial redox states and have been applied to the studies of mitochondrial function with energy-linked processes. The redox ratio, Fp/(Fp+NADH) provides a sensitive index of mitochondrial redox [2-6].

Previously, by using the low-temperature redox scanning technique [6-9] we discovered that *in vivo* mitochondrial redox state is a sensitive marker distinguishing between normal tissue and human melanoma xenografted in mice [10] and differentiating tumor aggressiveness among five human melanoma tumor lines spanning a wide range of metastatic potential in mouse xenografts [11]. In the present investigation, we report the preliminary results of quantitative mitochondrial redox imaging of mouse pancreases using the pancreas-specific PTEN knockout mice as the model system. The possible link between the premalignant lesions in the pancreas and the *in vivo* mitochondrial redox state, provides insights for basic biology studies and may aid the development of early diagnostic imaging biomarkers for pancreatic cancer.

28.2 Methods

Three PTEN null mice (Pdx-1-Cre;PTEN$^{lox/lox}$) and three control mice (PTEN$^{lox/lox}$) were prepared in the Stanger laboratory [1]. All mice were about 8 months old. The pancreases of the anesthetized mice were quickly resected and dipped into liquid nitrogen within 2 seconds after removal. The samples for redox scan were prepared as previously described [12, 13]. Briefly, a snap-frozen pancreas was carefully placed into the chilled mounting medium composed of ethanol-glycerol-water (10:30:60) contained in a plastic screw closure of 24 mm diameter. Frozen reference standards (one NADH and one Fp with known concentrations) were quickly mounted adjacent to the tissue. The screw closure containing the tissue and reference standards was then maintained in liquid nitrogen awaiting redox scanning.

The above prepared samples were redox-imaged under liquid nitrogen temperature using the redox scanner [6-9]. Briefly, the sample surface was first milled flat under liquid nitrogen by the grinder equipped with the scanner for redox scanning. A bifurcated fiberoptic probe driven by a stepper motor transmits the excitation photons from a mercury lamp and collects the emission photons from samples. The Fp excitation and emission filters are 430 ± 25 nm and 525 ± 32 nm, respectively; and those of NADH are 360 ± 26 nm and 430 ± 25 nm, respectively. The emission signals were transmitted to the photomultiplier tube and further processed by a personal computer to construct the NADH and Fp fluorescence images. The scanning matrix was 128×128 with a step size of 100 μm. Multiple sections at different milling depths spacing 100-400 μm were scanned for each pancreas (9 and 14 sections from the control group and the PTEN null group, respectively).

The acquired raw data were analyzed using MatLab® software to generate NADH and Fp and concentration-based Fp redox ratio (Fp/(Fp+NADH)) images. The inner area of each reference tube section was selected as the region of interest (ROI) for reference standards. The NADH signal from the Fp standard serves as the background signal for NADH channel and vice versa. The mean value of the signal intensities from each standard's image was computed with background signal subtraction. For tissue samples, ROIs were carefully drawn along the pancreas tissue rim. The NADH and Fp nominal concentrations in the tissue samples were obtained by comparing the fluorescence from tissue with that from the reference standards. Pixels having signals within 3-fold standard variations of the background signals were excluded from the analysis.

The mean value of Fp redox ratio, the standard deviation (SD) of the Fp redox ratio, the nominal concentrations of NADH and Fp, and the SD of these concentrations were obtained for the tissue ROI for each section subjected to redox scan, and then averaged across multiple sections for each pancreas to obtain the Fp redox ratio, SD of Fp redox ratio, NADH, Fp, SD of NADH, and SD of Fp for each individual pancreas. The group average values of these parameters from 3 pancreases in each group were also calculated to obtain the ^{g}Fp redox ratio, ^{g}SD of Fp redox ratio, ^{g}NADH, ^{g}Fp, ^{g}SD of NADH, and ^{g}SD of Fp. The statistical significance of the difference of these parameters between the two mouse groups was analyzed using unpaired t-tests.

28.3 Results

Figure 1 shows the typical images and their corresponding histograms of Fp redox ratio, Fp/(Fp+NADH), nominal concentration of Fp and NADH of two PTEN null pancreases in coronal and transversal section, respectively. Figure 2 shows the typical images and their corresponding histograms of Fp redox ratio, Fp/(Fp+NADH), nominal concentration of Fp and NADH of a normal pancreas. As clearly seen in Figure 1, the PTEN null pancreases are highly heterogeneous in their mitochondrial redox ratios. The cystic dilation area showed no fluorescent signal, indicating few

or no cells in the regions. H&E staining of the adjacent sections revealed no cells in these regions (data not shown).

The average Fp redox ratio is 0.35 and 0.38 for the control and pre-malignant group, respectively (Table 1). The unpaired t-test shows that there is no significant difference in Fp redox ratio between the two groups. However, the average standard deviations of the Fp redox ratios are significantly different between the two groups (p=0.02) with the control group having 0.06 and the pre-malignant group having 0.11, almost twice as large. The higher SD in the premalignant group is consistent with the wider peaks in the histograms of Fp redox ratio, indicating much higher heterogeneity in the distribution of mitochondrial redox states. Significant difference also exists in nominal concentration of NADH with the pre-malignant group having much lower NADH level. Additionally, a marginal difference (p=0.07) is seen in nominal concentration of Fp with the premalignant group having lower Fp level. The differences in the standard deviations of the fluorophore concentrations between the two groups are not significant.

28.4 Discussion

The redox images obtained in the present study revealed that significantly higher heterogeneity in the mitochondrial redox state was observed in PTEN knockout mice pancreases which were presumably undergoing metaplastic process. Studies suggested that the cellular basis of tumor progression was variability among subpopulations of tumor cells and such heterogeneity was associated with malignancy [14, 15]. Our previous studies on human melanoma and breast cancer mouse xenografts indicated that higher intratumor heterogeneity and higher Fp redox ratio were associated with more metastatic tumors as compared with indolent tumors [11, 16]. However, we did not observe a significant difference in the average value of Fp redox ratio between the PTEN null group and the control group. This may be partially explained by the fact that pancreas specific PTEN knockout only caused infrequent malignancy and premalignant lesions may only occupy a relatively small portion of the tissue distribution [1].

Therefore, the low average of Fp redox ratio of PTEN null pancreas may indicate that most of the cells were not yet cancerous, the "hot" spots of much higher Fp redox ratio might indicate premalignant transformation. The in-plane resolution in the redox images is 100 μm, not capable of fully resolving the pancreas premalignant lesions involving the ductal formations (size $\sim$200 μm or more). Ideally, if we could co-register our redox scanned section with the histology of the section, we may be able to tell if the hot spots correspond to premalignant lesions such as ductal metaplasia. However, such co-registration is practically difficult because the snap-frozen sample preparation has frozen the tissue at such a low temperature using liquid nitrogen, that it is not possible to slice the tissue, whereas raising the temperature for the tissue to melt distorts the tissue shape and histology. It may be worth developing tissue redox imaging *ex vivo* at a higher resolution so that morphological information

Table 28.1 Group (^{g}) average values of Fp, NADH and Fp redox ratio and standard deviations (SD) for 3 pancreases in each group.

	^{g}Fp redox ratio	^{g}SD of Fp ratio	^{g}NADH	^{g}SD of NADH	^{g}Fp	^{g}SD of Fp
Control	0.35±0.04	0.06±0.02	558±64	144±46	299±75	79±45
Pre-malignant	0.38±0.06	0.11±0.01	293±56	158±49	163±45	79±17
Unpaired t-test	0.49	0.02	0.01	0.73	0.07	0.98

on premalignant lesions might be obtained and correlated with mitochondrial redox state.

28.5 Conclusions

In this paper we reported our current progress in imaging the mitochondrial redox state in premalignant pancreas in the PTEN null transgenic mouse model. Compared to the control group, characteristically wider distribution of the mitochondrial redox states in the premalignant pancreases was delineated by the standard deviation of Fp redox ratio and by the wide peaks in the histograms of Fp redox ratio, indicating higher heterogeneity in their mitochondrial redox states. Our preliminary results suggested possible roles of mitochondrial redox states in pancreatic cancer transformation.

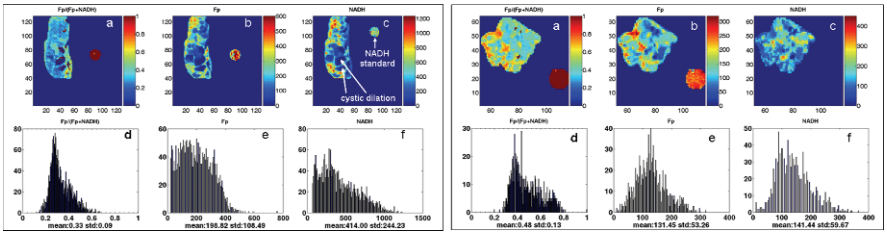

Fig. 28.1 Typical pseudo-color redox images (top row) and their corresponding histograms (bottom row) of PTEN null pancreases (left panel: coronal section, milling depth 1340 μm; right panel: transversal section, milling depth 100 μm). From left to right: Fp redox ratio (0-1); Fp nominal concentration (μM); NADH nominal concentration (μM). The color bar of Fp redox ratio image indicates the ratio range from 0-1. The color bars of Fp and NADH images indicate the nominal concentrations in μM. The x axes of the corresponding histograms represent the Fp or NADH concentration or redox ratio. The y axes represent the number of pixels in the tissue section having a specific value of redox ratio or fluorophore concentration. The round spots outside the tissue area are Fp or NADH reference standards; image matrix: 128×128 (left panel) and 64×128 (right panel); resolution: 100 μm.

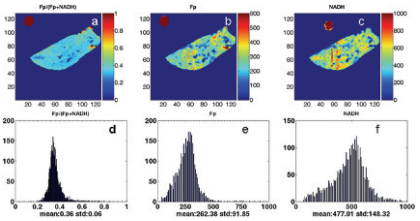

Fig. 28.2 Typical pseudo-color redox images (top row) and their corresponding histograms (bottom row) of the control group (coronal section, milling depth 0 μm). Image matrix: 128×128, resolution: 100 μm.

Acknowledgments

This work was supported by the Susan G. Komen Foundation Grant KG081069 (PI: L.Z. Li) and National Institutes of Health-supported Research Resource Grant P41-RR002305 (PI: R. Reddy). We would like to thank Dr. Ben Z. Stanger for providing the transgenic mice for this study and his valuable discussions. We also appreciate Dr. Q.C. Yu for his valuable discussions on the histological analysis and Mr. Baohua Wu for his assistance, particularly in software development for data analysis.

References

1. Stanger BZ, Stiles B, Lauwers GY et al (2005) PTEN constrains centroacinar cell expansion and malignant transformation in the pancreas. Cancer Cell 8:185-95
2. Chance B, Williams GR (1955) Method for the localization of sites for oxidative phosphorylation. Nature 176:250-254
3. Chance B, Baltscheffsky H (1958) Respiratory Enzymes in Oxidative Phosphorylation. J Biol Chem 233:736-739
4. Chance, B. & Schoener, B (1966) Fluorometric studies of flavin component of the respiratory chain in Flavins and Flavoproteins. Slater, E. C. eds. pp 510-519. Elsevier, Amsterdam.
5. Chance B, Schoener B, Oshino R et al. (1979) Oxidation-reduction ratio studies of mitochondria in freeze-trapped samples. NADH and flavoprotein fluorescence signals. J Biol Chem 254:4764-4771
6. Chance B (1991) Optical Method. Annu Rev Biophys Biophys Chem 20:1-28
7. Quistorff B, Haselgrove JC, Chance B (1985) High spatial resolution readout of 3-D metabolic organ structure: An automated, low-temperature redox ratio-scanning instrument. Anal Biochem 148:389-400
8. Gu Y, Qian Z, Chen J et al (2002) High-resolution three-dimensional scanning optical image system for intrinsic and extrinsic contrast agents in tissue. Rev Sci Instrum 73:172-178
9. Li LZ, Xu HN, Ranji M et al (2009) Mitochondrial redox imaging for cancer diagnostic and therapeutic studies. Journal of Innovative Optical Health Sciences **2**, 325-341
10. Li LZ, Zhou R, Zhong T et al (2007) Predicting melanoma metastatic potential by optical and magnetic resonance imaging. Adv Exp Med Biol 599:67-78
11. Li LZ, Zhou R, Xu HN et al. (2009) Quantitative magnetic resonance and optical imaging biomarkers of melanoma metastatic potential. Proc Natl Acad Sci U S A 106:6608-13
12. Xu HN, Wu B, Nioka S et al. (2009) Calibration of redox scanning for tissue samples, *Proceedings of Biomedical Optics* in San Jose, CA, Jan. 24, Ed. SPIE 7174:71742F

13. Xu HN, Wu B, Nioka S et al. (2009) Quantitative redox scanning of tissue samples using a calibration procedure. Journal of Innovative Optical Health Sciences 2:375-385
14. Heppner GH, Miller FR (1998) The cellular basis of tumor progression. Int Rev Cytol 177:1-56
15. Fidler IJ, Hart IR (1982) Biological diversity in metastatic neoplasms: origins and implications. Science 217:998-1003
16. Xu HN, Nioka S, Glickson JD et al. (2010) Quantitative mitochondrial redox imaging of breast cancer metastatic potential. Journal of Biomedical optics 15:036010

Chapter 29

Potential Application of ^{17}O MRI to Human Ischemic Stroke

Robert DeLaPaz and Pradeep Gupte

Abstract In cerebral ischemia, measurement of cerebral blood flow (CBF) alone is not a sensitive or specific predictor of tissue survival. Measurements of oxygen metabolism, which are directly related to cellular energy metabolism, are better predictors of tissue survival and the best of these is the "oxygen extraction fraction" (OEF). Elevation of OEF in Stage 2 hemodynamic failure, or "misery" perfusion, indicates that prolongation of this state or further reduction in blood flow will lead to failure of oxygen metabolism and cellular necrosis, making it a sensitive and specific biomarker for the "ischemic penumbra" and a predictor of impending cerebral infarction. The methods now used to measure *in vivo* human cerebral metabolic rate of oxygen ($CMRO_2$) and OEF include ^{15}O-PET and MRI deoxyhemoglobin sensitive techniques (Blood Oxygen Level Dependent, BOLD methods). These methods have practical and fundamental limitations for use in the clinical stroke setting. ^{17}O-MRI is a method of imaging oxygen metabolism by detecting the tissue water ($H_2^{17}O$) produced by oxidative metabolism of $^{17}O_2$ gas that can be performed on conventional, clinical MRI scanners using a chemically stable, non-radioactive, MR-detectable isotope of oxygen. It is more logistically applicable to clinical stroke than ^{15}O-PET and more directly quantitative than BOLD MRI. ^{17}O-MRI promises to provide a direct, quantitative, widely available and clinically practical method for assessing $CMRO_2$ and OEF for evaluation of human cerebral ischemia.

Robert DeLaPaz
Neuroradiology, Columbia University, New York, NY, USA
e-mail: rld17@columbia.edu

Pradeep Gupte
Rockland Technimed, Ltd., Airmont, NY, USA

J.C. LaManna et al. (eds.), *Oxygen Transport to Tissue XXXII*, Advances in Experimental Medicine and Biology 701, DOI 10.1007/978-1-4419-7756-4_29,

29.1 Limitations of Hemodynamic Imaging of Cerebral Ischemia

When reduced tissue perfusion pressure produces cerebral hemodynamic compromise, reflex autoregulatory vasodilation occurs in order to maintain blood flow by reducing arteriolar vascular resistance and increasing vascular blood volume (CBF=CBV/MTT). This compensatory mechanism can maintain normal or minimally reduced levels of cerebral blood flow (CBF) in regions of cerebral ischemia and mask hemodynamically compromised tissue from methods that measure CBF alone. Methods that also measure the increase in cerebral blood volume (CBV) and prolongation of the mean transit time (MTT) are more sensitive to hemodynamic compromise. However, vascular flow methods do not directly reflect the metabolic or morphological integrity of cerebral tissue and are relatively insensitive predictors of ischemic energy failure and cellular necrosis. A wide, overlapping range of severity and duration of hemodynamic changes may be seen with cerebral tissue that is either reversibly ischemic or irreversibly injured (1).

MRI methods that combine hemodynamic parameters with water diffusion imaging (perfusion-diffusion or PWI-DWI imaging) have improved the predictive value of blood flow methods by using diffusion restriction as a marker for the ischemic infarct "core" and reduced flow without diffusion restriction as a marker for ischemic but viable tissue. These methods typically use gadolinium bolus dynamic susceptibility contrast (DSC) MR perfusion weighted imaging (PWI) to measure tissue blood flow parameters (CBF, CBV, MTT and TTP) which are compared to the volume of presumed infarcted tissue indicated by restricted water diffusion (reduced ADC on DWI). When the low blood flow volume is larger than the restricted diffusion volume by 20% or more, a perfusion-diffusion (PWI-DWI) "mismatch" is said to exist. A key limitation of the MRI mismatch approach is that it may overestimate the true "ischemic penumbra" and not specifically identify tissue at risk of infarction. The low blood flow in the mismatch zone may include both underperfused but metabolically stable "oligemic" tissue which is likely to survive at the existing perfusion level as well as unstable "penumbral" tissue that is likely to become infarcted if reperfusion therapy is delayed or ineffective. In addition, all regions of diffusion restriction may not indicate completed infarction but may include recoverable "penumbral" tissue (2,3).

29.2 Hemodynamic Failure and Oxygen Metabolism in Cerebral Ischemia

Because the brain is an obligate aerobic tissue (oxygen is essential for preservation of energy metabolism) measurements of oxygen metabolism are directly related to cellular energy metabolism and are better predictors of ischemic tissue survival than blood flow measurements alone. Although delivery of oxygen decreases with decreasing blood flow, brain tissue can increase the relative amount of oxygen it

"extracts" from a unit volume of blood, ranging from a normal of 40% to a high of 70-80%. This ratio between oxygen delivery and consumption is called the "oxygen extraction fraction" or OEF. In the minimal state of cerebral ischemia, called Stage 1 hemodynamic failure, or "oligemic" perfusion, blood flow is largely maintained by vasodilation (increased CBV, with prolonged mean transit time, MTT) and oxygen metabolism ($CMRO_2$) is maintained with normal or only slightly elevated OEF. Cerebral tissue in this oligemic state may survive for prolonged periods or recover normal function without structural injury when normal blood flow returns. As perfusion pressure continues to decrease, the capacity of autoregulatory vasodilation to maintain normal blood flow is exceeded and blood flow decreases substantially. This produces a state of reduced blood flow with markedly increased OEF called Stage 2 hemodynamic failure, or "misery perfusion" and is considered the true "ischemic penumbra" (4,5). When oxygen extraction becomes maximal, prolonged low blood flow or further decreases in blood flow lead to failure of oxidative energy metabolism and ultimately to infarction (necrosis). In human cerebral ischemia the region of reduced blood flow and the MRI perfusion-diffusion mismatch typically include both Stage 1 oligemic perfusion and Stage 2 misery perfusion. Therefore, measurement of oxygen metabolism is needed to discriminate between these potentially recoverable and unrecoverable states. OEF has been shown to be the most sensitive and specific metabolic predictor of tissue survival and impending cerebral infarction (4-9).

29.3 Limitations of PET and BOLD MRI Measurement of $CMRO_2$ and OEF

The imaging methods now used to measure *in vivo* human $CMRO_2$ and OEF include ^{15}O-PET and deoxyhemoglobin sensitive techniques (Blood Oxygen Level Dependent, BOLD methods). Direct *in vivo* measurement of oxygen metabolism is available using the radioactive oxygen isotope, ^{15}O, with Positron Emission Tomography (PET) detection methods. ^{15}O-PET is currently considered the "gold standard" for measurement of $CMRO_2$ and OEF in human brain and has been used to study acute ischemia, clearly demonstrating the changes in oxygen metabolism described above in acute Stage 1 and Stage 2 hemodynamic failure (2,3,9). ^{15}O-PET has also been used to study chronic vascular stenosis, showing elevated cerebral OEF as an indication of reduced cerebrovascular reserve and marginal oxygen metabolism in patients with large vessel stenosis at high risk of ischemic stroke (9,10). Comparisons with MRI PWI-DWI mismatch methods have demonstrated the greater specificity and sensitivity of ^{15}O-PET $CMRO_2$ and OEF in the evaluation of acute and chronic hemodynamic failure. However, the clinical usefulness of ^{15}O-PET is limited by the need for an on-site cyclotron for isotope production (^{15}O $T_{1/2}$ = 2 minutes), sparse availability of PET imaging equipment, long duration and complexity of the scanning technique, radiation exposure, the need for arterial blood sampling and the high cost of the imaging equipment and infrastructure.

BOLD MRI methods are not ideal for measurement of $CMRO_2$ and OEF because they are dependent on complex, indirect effects of oxygen metabolism on intravascular deoxyhemoglobin concentrations which are also dependent on cerebral blood flow (CBF) and blood volume (CBV) changes. BOLD MRI signal is derived from intravascular and extravascular T2 and T2* relaxation effects which vary with field strength, vessel size and perivascular water diffusion. BOLD MRI $CMRO_2$ calculations also require assumptions about unmeasurable variables within the image voxel, including local hematocrit, relative volumes of arterial and venous blood, vessel geometry, tissue oxygen diffusion rates and oxygen concentration gradients adjacent to blood vessels. These multiple variables and assumptions result in a high level of complexity and inherent uncertainty of BOLD MRI methods, making precise quantification of tissue $CMRO_2$ and OEF difficult (11). Attempts have been made to simplify the BOLD MRI approach by directly imaging T_2, T_2*, and T_2' (T_2-prime) changes in acute stroke patients, based on the assumption that reductions in these relaxation times are directly correlated with increased deoxyhemoglobin which, in turn, is an indicator of increased OEF. Applications of these approaches in clinical stroke have shown reduced relaxation values in a minority of cases and mixed results when correlated with clinical outcome and final infarct volume (12,13,14). Direct comparison of T_2* images with ^{15}O-PET has shown no correlation with measured OEF (15). Current BOLD MRI methods lack the sensitivity, specificity and accuracy needed for clinical prediction of tissue injury in human cerebral ischemia.

29.4 ^{17}O-MRI Measurement of $CMRO_2$ and OEF in Human Cerebra Ischemia

Oxygen-17 ($^{17}O_2$) is a naturally occurring, chemically stable, non-radioactive isotope of oxygen that comprises a small fraction of normal air (0.037% of atmospheric oxygen). Unlike the predominant isotope of atmospheric oxygen (^{16}O), the ^{17}O nucleus has non-integer spin (5/2), making it MR visible and detectable directly using MR spectroscopic techniques and indirectly with proton MRI methods. The low MR sensitivity of the ^{17}O nucleus relative to the hydrogen nucleus (gyromagnetic ratio 1/7 that of the ^{1}H proton) requires specialized coils to generate natural abundance images using direct detection techniques and, although demonstrated at 1.5T (16), are improved at high magnetic fields (7T and 9.4T) (17,18,19). High spatial resolution proton MRI on clinical systems at 1.5T or 3.0T can be used to indirectly detect ^{17}O by utilizing its effect on proton relaxation when it is metabolized to water ($H_2^{17}O$). The ^{17}O nucleus in the water molecule interacts with the ^{1}H protons via scalar coupling and shortens water T2, T2* and T1p (T1rho, the rotating frame spin-lattice relaxation time). Proton images of brain $H_2^{17}O$ have been obtained using T2-weighted (20,21,22), ^{17}O-decoupled (23,24,25) and spin-locked T1p (T1rho) techniques. (26,27) Water T2-weighted signal change can be confounded with other causes (e.g., deoxyhemoglobin) and ^{17}O-decoupling requires specialized hardware, making the T1p techniques the most favorable for quantitative ^{17}O metabolic imaging

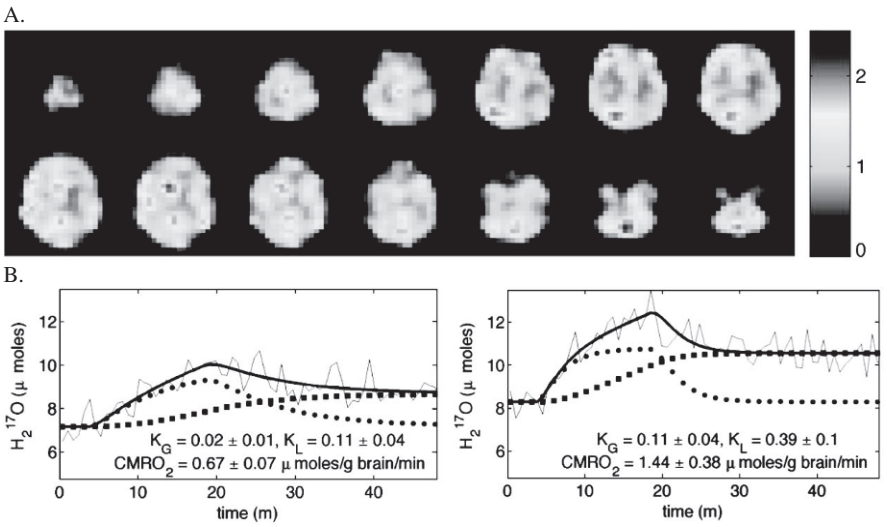

Fig. 29.1 A.^{17}O-MRI $CMRO_2$ maps of a healthy 54 y.o. male volunteer corrected for brain tissue mass (umol/g brain/min). B. Representative ^{17}O time-courses for single voxels corresponding to low (left, white matter) and high (right, gray matter) metabolic rates. The three-phase metabolic model of water production (thick line) accurately describes the ^{17}O MR data (thin line) to yield $CMRO_2$ values with K_G and K_L constants shown. The signal contribution (squares) from $H_2^{17}O$ generated throughout the body, transported by the blood, and diffusing into the tissue reaches a plateau when the $H_2^{17}O$ gain from wash-in and $H_2^{17}O$ loss from wash-out and chemical conversion are balanced. The signal contribution (dots) from local oxygen metabolism reaches a maximum during inhalation and returns to baseline as $H_2^{17}O$ loss due to wash-out and chemical conversion occurs. The exact formulas for $CMRO_2$ calculation are in equations 6 and 9 of reference 19. (reproduced with permission from ref. 19)

on unmodified clinical MRI systems. Signal to noise of direct and indirect methods is improved by isotope enrichment and quantitative dynamic $CMRO_2$ images have been obtained in animal and human brain using delivery of $^{17}O_2$ gas via inhalation, extracorporeal autologous blood enrichment or synthetic oxygen carriers (e.g., perfluorocarbons) (17-27) (Figure 1).

The concept underlying ^{17}O-MRI of $CMRO_2$ and OEF in cerebral ischemia is similar to ^{15}O-PET with the radioactive ^{15}O tracer replaced by the non-radioactive ^{17}O tracer. Although PET with radiolabeled oxygen gas ($^{15}O_2$) is the current "gold standard" for quantitative assessment of cerebral oxygen metabolism, the measurement is not straightforward. Both the $^{15}O_2$ gas and the metabolic water, $H_2^{15}O$ produced by oxidative metabolism, contribute to the signal detected by PET, so additional measurements of cerebral blood volume (CBV) and blood flow (CBF) using controlled delivery of $C^{15}O$ and $H_2^{15}O$ with arterial sampling of blood $^{15}O_2$ and $H_2^{15}O$ have traditionally been performed. (29) However, the bolus $^{15}O_2$ inhalation "one step" method, that assumes total conversion of oxygen to tissue water, has reduced the need for multiple invasive arterial sampling in clinical applications by eliminating two of the three tracers in the "three step" method. (30) A fundamental advantage

of ^{17}O-MRI for imaging oxygen metabolism is that the $^{17}O_2$ gas (either in blood or tissue) is MR invisible and only the ^{17}O that is metabolized to $H_2^{17}O$ is detected and imaged. This unique feature allows a noninvasive or minimally invasive approach and significantly simplifies measurement and quantification of $CMRO_2$ and OEF compared to traditional ^{15}O-PET by eliminating the need for invasive monitoring of the arterial oxygen input function and multiple radiotracer assessments. $CMRO_2$ is calculated by knowing the rate of tissue $H_2^{17}O$ production, the CBF and the concentration of delivered arterial $^{17}O_2$gas (17). CBF can be determined non-invasively with MRI arterial spin labeling (ASL) or by gadolinium DSC or $H_2^{17}O$ injection methods. Arterial $^{17}O_2$ concentration (Ca) can be determined by the linear relationship to the inhalation rate, by the known quantity delivered with an autologous or exogenous oxygen carrier or by the change in tissue O_2 gas concentration imaged with longitudinal relaxation rate methods ($R_1 = 1/T_1$) (28). OEF can then be determined from the ratio of $CMRO_2$ to Ca and CBF (EOF = $CMRO_2$ / (Ca * CBF)). Application of this quantitative $CMRO_2$ and OEF imaging is likely to have the same advantages over BOLD MRI in cerebral ischemia as have been demonstrated with ^{15}O-PET. Implementation of indirect ^{17}O-MRI imaging techniques on existing clinical MRI systems and delivery of $^{17}O_2$ gas in the clinical setting by inhalation or injection will also likely lead to shorter acquisition times and a much wider application of quantitative $CMRO_2$ and OEF imaging to clinical stroke evaluation than is currently practical with ^{15}O-PET.

In addition to the changes in oxygen metabolism associated with cerebral ischemia, it is well known that reduced tissue oxygen levels are also associated with "oxidative stress" that triggers irreversible cellular processes and mitochondrial biochemical cascades leading to excitotoxic, necrotic and apoptotic cell death (31,32). These processes are responsible for ischemic injury that does not respond to, or may be worsened by, the return of normal blood flow. Although there is a large body of experimental literature describing these mechanisms, there has been no study in human cerebral ischemia that identifies levels of $CMRO_2$ reduction or OEF elevation that may correlate with the onset of these irreversible processes. It is anticipated that ^{17}O-MRI will allow more extensive study of oxidative metabolism in clinical cerebral ischemia and help define "trigger" levels of compromised oxygen metabolism that lead to irreversible mechanisms of injury.

29.5 Summary and Conclusion

A widely available, clinically practical method is needed for quantitative imaging of oxygen metabolism in human cerebral to improve upon the current blood flow and diffusion based imaging approaches. ^{17}O-MRI can provide imaging of $CMRO_2$ and OEF that is more directly quantitative than BOLD MRI and more logistically applicable to clinical cerebral ischemia than ^{15}O-PET. Implementation of ^{17}O-MRI on the existing installed base of diagnostic MRI systems can provide a widely avail-

able and clinically practical method for quantitative imaging of oxygen metabolism in human cerebral ischemia.

References

1. Latchaw RE, Yonas H, Hunter GJ, et al(2003) Guidelines and recommendations for perfusion imaging in cerebral ischemia: A scientific statement by the American Heart Association. Stroke; 34(4):1084-1104.
2. Sobesky J, et.al (2005) Does the mismatch match the penumbra? MRI and PET in stroke. Stroke.;36(5):980-985.
3. Heiss W-D, Sobesky J, (2008) Comparison of PET and DW/PW-MRI in Acute Ischemic Stroke, Keio J Med; 57 (3): 125-131
4. Baron JC, Bousser MG, Comar D, et. al (1981) Noninvasive tomographic study of CBF and oxygen metabolism *in vivo*. Potentials, limitations, and clinical applications in cerebral ischemic disorders. Eur Neurol; 20: 273-284.
5. Kastrup J, Siesjö BK, Symon L (1981) The ischemic penumbra. Stroke; 12: 723-725
6. Sette G, et. al (1989) Brain haemodynamics and oxygen metabolism in cerebrovascular disease. Brain;113:931.
7. Heiss WD, Graf R (1994) The ischemic penumbra. Curr Opin Neurol; 7: 11-19
8. Hossmann KA (1994) Viability thresholds and the penumbra of focal ischemia. Ann Neurol; 36:557-565
9. Derdeyn CP, Videen TO, Yundt KD, et al (2002) Variability of cerebral blood volume and oxygen extraction: stages of cerebral haemodynamic impairment revisited. Brain; 125(Pt 3):595-607.
10. Kuroda S, Shiga T, Houkin K, et al (2006) Cerebral oxygen metabolism and neuronal integrity in patients with impaired vasoreactivity attributable to occlusive carotid artery disease. Stroke ; 37(2):393-398.
11. Van Zijl PCM, Measurement of Oxygen Metabolism with MRI: What Can and Cannot be Done? *ISMRM 2006:48*
12. Geisler BS, Brandhoff F, Fiehler J, Saager C, et al. (2006) Blood-oxygen-level-dependent MRI allows metabolic description of tissue at risk in acute stroke patients. Stroke; 37: 1778-1784.
13. Wardlaw JM, von Heijne A (2006) Increased oxygen extraction demonstrated on gradient echo (T2*) imaging in a patient with acute ischaemic stroke. Cerebrovasc Dis ; 22:456-458.
14. Morita N, Harada M, Uno M, Matsubara S, et al (2008) Ischemic findings of T2 * -weighted 3-tesla MRI in acute stroke patients. Cerebrovasc Dis; 26: 367-375.
15. Donswijk ML, Jones PS, Guadagno JV, etal (2009) T2*-weighted MRI versus oxygen extraction fraction PET in acute stroke. Cerebrovasc Dis. ;28(3):306-13
16. Fiat D, Hankiewicz J, Liu S, Trbovic S, Brint S. (2004) 17O magnetic resonance imaging of the human brain. *Neurol Res.* ;26(8):803-808.
17. Zhu XH, etal (2005) In vivo ^{17}O NMR approaches for brain at high field. *NMR Biomed.* ;18(2):83-103.
18. Zhu XH, Du F, Zhang N, etAl (2009) Advanced In Vivo Heteronuclear MRS Approaches for Studying Brain Bioenergetics Driven by Mitochondria. Methods Mol Biol. ;489:317-57.
19. Atkinson, I.C., Thulborn, K.R. Feasibility of mapping the tissue mass corrected bioscale of cerebral metabolic rate of oxygen consumption using 17-oxygen and 23-sodium MR imaging, NeuroImage (2010), doi:10.1016/j.neuroimage.2010.02.056 (Epub Feb 24, 2010)
20. Hopkins AL, Haacke EM, Barr, et al (1988) Oxygen-17 contrast agents. Fast imaging techniques. Invest Radiol ;23(suppl 1):S240–2.
21. Arai T, Nakao S, Morikawa S, et al (1998) Measurement of local cerebral blood flow by magnetic resonance imaging: in vivo auto radiographic strategy using ^{17}O-labeled water. Brain Res Bull;45:451-456

22. DeLaPaz RL, Gupte P, Connolly S, Wu E, Brown T. (1939) Oxygen-17 Uptake in Mouse Cerebral Ischemia. *ISMRM* 2003;.
23. Ronen I, Merkle H, Ugurbil K, Navon G. (1998) Imaging of H217O distribution in the brain of a live rat by using proton-detected 17O MRI. *Proc Natl Acad Sci U S A.*; 95 (22):12934-12939.
24. Reddy R, Stolpen AH, Charagundla SR, Insko EK, Leigh JS. (1996)17O-decoupled 1H detection using a double-tuned coil. Magn Reson Imaging.;14(9):1073-1078.
25. de Crespigny AJ, D'Arceuil HE, Engelhorn T, et al (2000) MRI of focal cerebral ischemia using (17)O-labeled water. Magn Reson Med ;43:876–83.
26. Tailor DR, Baumgardner JE, Regatte RR, Leigh JS, Reddy R. (2004) Proton MRI of metabolically produced H2 17O using an efficient 17O2 delivery system. Neuroimage.;22(2):611-618.
27. Mellon EA, et al (2009) Single shot T1rho MRI of metabolically generated water in vivo. Adv Exp Med Biol. 2009;645:279-86.
28. O'Conner JPB, Naish JH, Jackson A, Waterton JC, et al (2009)Comparison of Normal Tissue $R1$and $R*2$Modulation by Oxygen and Carbogen. Magn Reson Med 61:75-83
29. Okazawa H, Kudo T. (2009) Clinical impact of hemodynamic parameter measurement for cerebrovascular disease using positron emission tomography and (15)O-labeled tracers. Ann Nucl Med. ;23(3):217-27.
30. Ohta S, Meyer E, Thompson CJ, Gjedde A. (1992)Oxygen consumption of the living human brain measured after a single inhalation of positron emitting oxygen. J Cereb Blood Flow Metab. ;12:179–92.
31. Brouns R, De Deyn PP, (2009) The complexity of neurobiological processes in acute ischemic stroke. Clin Neurol Neurosurg. ;111(6):483-95
32. Niizuma K, Endo H, Chan PH. (2009)Oxidative stress and mitochondrial dysfunction as determinants of ischemic neuronal death and survival. J Neurochem.;109 Suppl 1:133-8

Part VIII
Development

Chapter 30
Fetal Cerebral Oxygenation: The Homeostatic Role of Vascular Adaptations to Hypoxic Stress

William J. Pearce, Stacy M. Butler, Jenna M. Abrassart, and James M. Williams

Abstract The mammalian fetus is highly adapted for growth in a low-O_2 environment in which arterial O_2 tensions average near 30 mm Hg. Acute decreases in O_2 tension below this value elicit vasodilatation, but the responses are blunted compared to those observed in adults. Chronic hypoxia in the fetus stimulates a pattern of cerebrovascular remodeling that results in an increased wall thickness and decreased overall contractility and also depresses the capacity for cerebral vasodilatation through decreases in NO release, soluble guanylate cyclase activity, and expression of PKG substrates. Many of these hypoxic effects appear to be homeostatic and may be mediated by VEGFs, which increase in direct response to hypoxia and, in turn, can dramatically alter the expression and function of multiple contractile proteins in cerebrovascular smooth muscle through both endothelium-dependent and endothelium-independent effects on large artery smooth muscle.

30.1 Introduction

The near universal importance of O_2 as an electron acceptor has given rise to a remarkable diversity of mechanisms that mediate homeostatic adaptation to limited O_2 availability. Adaptation to hypoxia is essential for many pathophysiological processes, such as ischemia and wound repair, but one of the best examples is the developing mammalian fetus. Normally, arterial O_2 tensions in a healthy fetus average near 30 mm Hg, a situation which Eastman described more than 50 years ago as "Mount Everest *in utero*" [1]. To thrive in this environment, the fetus is equipped with a unique isoform of hemoglobin that has a higher O_2 affinity than adult hemoglobin, and thus can "extract" O_2 from maternal hemoglobin in the placenta [2]. Owing to this and other adaptations, the fetal cardiovascular system exhibits a clear ability to

Center for Perinatal Biology, Divisions of Physiology, Pharmacology, and Biochemistry, Loma Linda University School of Medicine, Loma Linda, CA 92350
e-mail: wpearce@llu.edu

J.C. LaManna et al. (eds.), *Oxygen Transport to Tissue XXXII*, Advances in Experimental Medicine and Biology 701, DOI 10.1007/978-1-4419-7756-4_30,

match tissue blood flow, and cerebral perfusion in particular, to metabolic activity under a broad variety of physiological conditions [3, 4].

30.2 Responses to Acute Hypoxia

Acute hypoxic stress can elicit a compensatory cerebral vasodilatation in the healthy fetus, but the magnitude of this response is significantly smaller than observed in adults [3, 4]. This attenuation is due not only to a reduced release of tissue vasodilator metabolites in response to hypoxia, but also to a reduced direct effect of hypoxia on fetal cerebrovascular smooth muscle [5]. Whereas the release of vasoactive molecules from the vascular endothelium typically contributes to hypoxic vasodilatation in adult cerebral arteries [6], this contribution is also diminished in immature cerebral arteries [7]. Supplementing these reduced fetal hypoxic cerebrovascular responses, however, are powerful systemic fetal reflexes known as "brain sparing" responses, which redistribute cardiac output in favor of the brain in response to hypoxia [8]. Fetal tissues also typically exhibit a lower metabolic rate for oxygen and contain mitochondria more resistant to hypoxic damage than those of adult tissues [9]. Thus, the fetal cardiovascular system is well adapted to maintain cerebral oxygen homeostatis, even during episodes of acute systemic hypoxia.

30.3 Responses to Chronic Hypoxia

In contrast to acute fetal hypoxia, which is typically caused by either maternal hypoxia or abrupt reductions in placental perfusion, chronic fetal hypoxia is clinically more common and has a wider variety of causes. Placental insufficiency, placentia abruptia, maternal infection or inflammation, maternal hypertension, undernutrition, alcohol abuse, and smoking all can contribute to chronic fetal hypoxia [10]. In response to chronic hypoxia, fetal cerebral arteries undergo dramatic remodeling responses that enlarge both the endothelial and smooth muscle cells of fetal cerebral arteries [11]. Functionally, chronic hypoxia enhances agonist-induced calcium mobilization, but reduces overall cerebrovascular contractility though significant changes in myofilament calcium sensitivity [12, 13] (Figure 1). The capacity for vasodilatation is also reduced by chronic hypoxia and this effect involves decreases in endothelial NO production and vascular soluble guanylate cyclase activity [11, 14]. Interestingly, chronic hypoxia has little effect on the abundance or activity of protein kinase G (PKG), the downstream effector for NO-induced changes in vascular cGMP. Even so, chronic hypoxia ablates the ability of PKG to inhibit contractility (Figure 2), suggesting that chronic hypoxia decreases the availability of substrates that mediate the effects of PKG on cerebrovascular contractility. The identities of these substrates are currently unknown, but remain the topic of active investigation. Confocal immunohistochemistry studies further suggest that decreased PKG substrate availability may

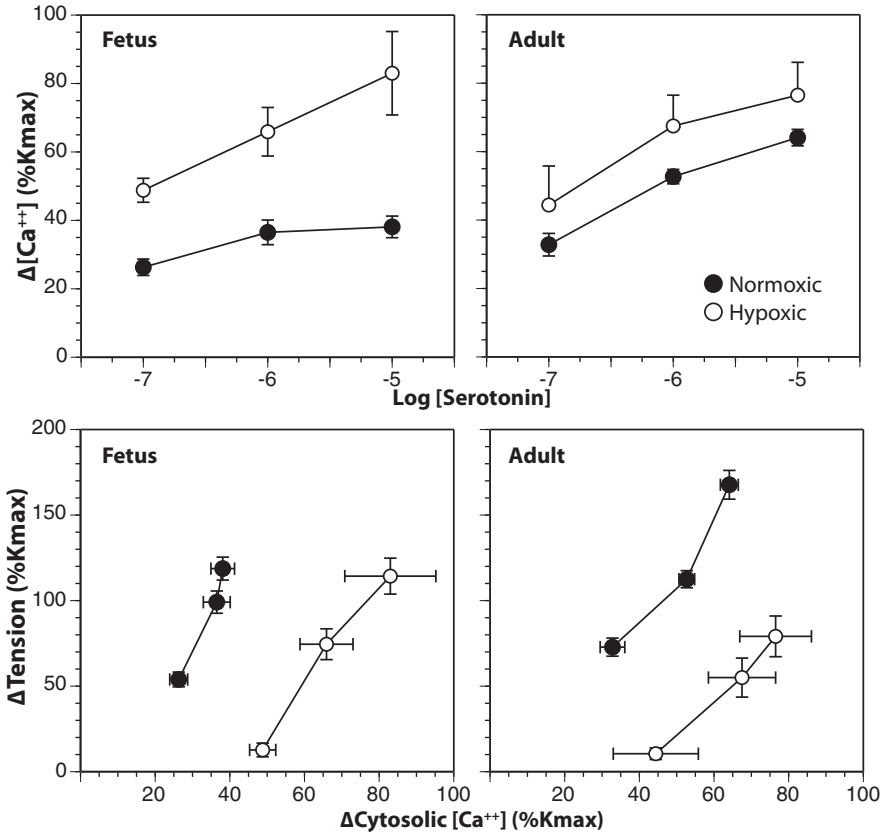

Fig. 30.1 Effects of chronic hypoxia on Ca^{++} mobilization and myofilament Ca^{++} sensitivity in fetal and adult cerebral arteries. Acclimatization to chronic hypoxia for 110 days at an altitude of 3820 m enhanced serotonin-induced increases in cytosolic Ca^{++} (upper panels) but depressed myofilament sensitivity to Ca^{++} (lower panels) in main branch middle cerebral arteries taken from term (140 d) fetal and non-pregnant adult sheep (18-24 mo old). Cytosolic Ca^{++} and contractile force were measured simultaneously in fura-2 loaded artery segments mounted in a Jacso CAF-110 photometer. Ca^{++} sensitivity was indicated by the slopes of the relations between the changes in tension (expressed relative to the maximum contractile response to 120 mM K^+) and cytosolic Ca^{++} produced in response to serotonin. Error bars indicate SEM for $N \geq 6$.

also involve a more heterogeneous distribution of PKG expression throughout the artery wall.

30.4 VEGF and Hypoxic Vascular Adaptation

Despite the many well-documented effects of chronic hypoxia on fetal cerebral artery structure and function, the main molecular mechanisms driving these changes remain

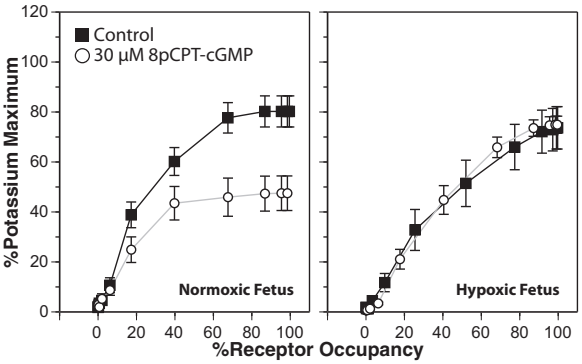

Fig. 30.2 Chronic hypoxia ablates the ability of Protein Kinase G to inhibit serotonergic contractile tone (expressed relative to the maximum contractile tone produced in response to 120 mM K^+) in ovine fetal middle cerebral arteries. Concentration-response determinations for serotonin were determined in vitro in the presence and absence of a cell permeant and non-metabolizable activator of Protein Kinase G, and then converted to occupancy-response curves using parallel measurements of agonist binding affinity. PKG activation potently inhibited serotonergic tone independent of changes in serotonergic receptor density or affinity in arteries from normoxic, but not chronically hypoxic, term fetuses. Chronic hypoxia was imposed on the fetuses by maintaining pregnant ewes at 3820m for the final 110 days of gestation. Error bars indicate SEM for N≥6.

largely unidentified. Among the many growth factors that could potentially mediate the cerebrovascular effects of chronic hypoxia, the most promising candidates are the Vascular Endothelial Growth Factors (VEGFs). This family of peptide growth factors has close similarity to the Platelet Derived Growth Factor family and arises from multiple genes with numerous splicing variants [15]. Most importantly, the main member of the VEGF family, VEGF-A_{165}, is upregulated in response to increases in Hypoxia-Inducible Factor, a transcription factor that increases in direct response to hypoxia [16]. Uncertainty about the ability of VEGFs to mediate hypoxic remodeling arises mainly from the view that VEGF acts primarily on endothelial cells to stimulate angiogenesis [15]. However, recent evidence suggests that VEGF may also exert trophic effects on non-endothelial cell types including neurons of both the central [17] and peripheral [18] nervous systems. Most importantly, VEGF has recently been shown to influence vascular differentiation through a direct effect on VEGF receptors in smooth muscle cells [19]. These findings support the novel hypothesis that hypoxic changes in the structure and function of large artery smooth muscle may involve direct effects of VEGF.

To assess the potential of VEGF as a trophic factor in large artery smooth muscle, ovine carotid arteries harvested under sterile conditions from term fetal (140 d) and non-pregnant adult sheep were denuded of endothelium, then organ cultured (37 ^oC, 95% O_2, 5% CO_2) under serum starvation conditions in DMEM to align the cell cycle status of all cells in the artery wall. The 24-hour period of starvation also facilitated diffusional extraction of endogenous trophic factors present in the tissue at the time of harvest. Following starvation, the arteries then were maintained in organ culture for an additional 24 hours in the presence or absence of a low physiological

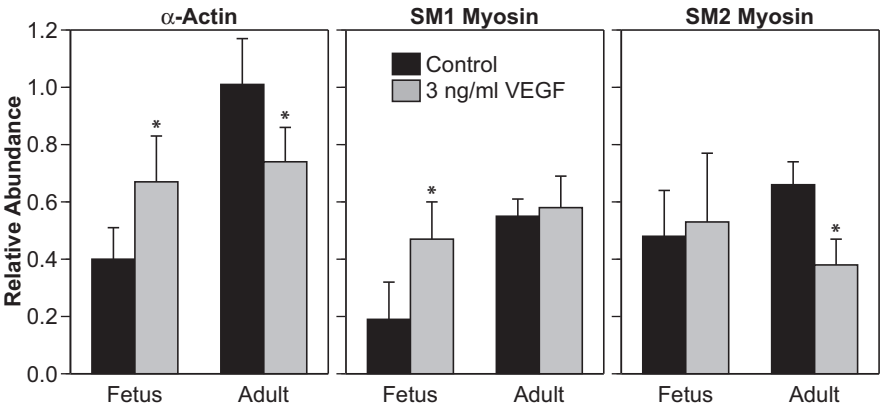

Fig. 30.3 VEGF alters contractile protein expression in ovine arteries in an age-dependent manner. In endothelium-denuded ovine carotids, 24 hours of organ culture with VEGF enhanced expression of α-actin and the SM1 myosin isoform in fetal arteries, but decreased α-actin and SM2 myosin in adult arteries. Error bars indicate SEM for n$\geq$4. Asterisks indicate VEGF values significantly different than control at $P < 0.05$.

concentration (3 ng/ml) of VEGF-A_{165}. This 3 ng/ml concentration was 10-30 fold less than used in many cell culture studies and was selected because it approximated the endogenous concentrations present in adult ovine arteries, as revealed by Western blotting. Organ culture for 24 hours with 3 ng/ml VEGF-A_{165} clearly upregulated expression of certain contractile proteins in the fetal arteries, but decreased other proteins in adult arteries (Figure 3), thus demonstrating the vasotrophic potential of VEGF-A_{165} in large artery smooth muscle. Most interestingly, organ culture with VEGF-A_{165}influenced protein distribution most prominently in the smooth muscle immediately adjacent to the basal lamina, as indicated by fluorescent immunohistochemistry. The reasons why reactivity to VEGF-A_{165} were dependent on age and location are unclear but most probably arise from differences in either the types or densities of VEGF receptors expressed, and/or the coupling of VEGF receptors to gene expression; many of the kinases that mediate the nuclear effects of VEGF exhibit major age-related changes that occur gradually throughout postnatal maturation [15].

To assess the functional impact of organ culture with VEGF-A_{165}, active stress-strain relations were determined in wire-mounted fetal middle cerebral arteries that had been cultured with VEGF-A_{165}. Artery strain was calculated as the ratio of working diameter divided by unstressed diameter where unstressed diameter was measured at a near-zero initial tension (30 mg). Artery stresses were calculated as the contractile tensions in dynes divided by cross-sectional areas in mm^2, which were measured as the products of artery wall thicknesses and segment lengths measured via microscope. Working wall thicknesses were corrected for stretch at each strain level examined. Myogenic stresses were calculated as the differences in total artery stresses measured at rest in normal sodium Krebs solution (37 ^oC, pH 7.4) before and after freezing the arteries in liquid N_2 and equilibration in 3 mM EGTA. These in vitro measurements of stretch-induced contractile stresses revealed that serum starvation

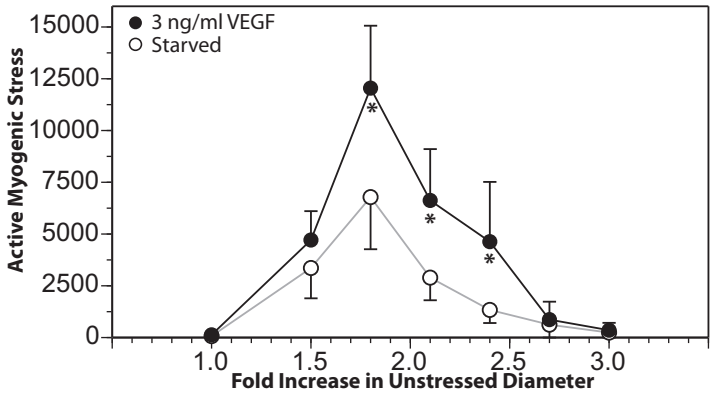

Fig. 30.4 Organ culture with VEGF enhanced myogenic tone in fetal middle cerebral arteries. Term fetal ovine middle cerebral arteries denuded of endothelium were organ cultured for 24 hours with a low concentration of VEGF-A_{165}. Treatment with VEGF significantly enhanced peak myogenic tone compared to serum starvation alone. This effect was not observed in adult middle cerebral arteries. Error bars indicate SEM for $n \geq 7$. Asterisks indicate VEGF values significantly greater than Starved at $P < 0.05$.

for 48 hours significantly reduced myogenic reactivity to progressive stretch and peak myogenic stress compared to fresh arteries. More importantly, these measurements also demonstrated that 24 hours of serum starvation followed by 24 hours of organ culture in a low physiological concentration (3 ng/ml) of VEGF can enhance fetal cerebrovascular contractility through direct effects on smooth muscle (Figure 4). Because the extent of strain required to produce maximum myogenic stress was identical in serum starved and VEGF treated arteries, the results also suggest that the effects of VEGF on the structure and orientation of the extracellular matrix were not as prominent as effects on the contractile apparatus. Consistent with this interpretation, organ culture with VEGF-A_{165} significantly increased the relative abundance of both smooth muscle α-actin and SM1 myosin in fetal, but not adult, cerebral arteries (Figure 3). These findings strongly support the hypothesis that VEGF helps mediate the remodeling effect of chronic hypoxia on fetal cerebral arteries.

30.5 Summary and Conclusions

The fetus is highly adapted for growth in a low-O_2 environment. As a consequence of this adaptation, cerebral vasodilator responses to acute hypoxia are dampened in both fetal vascular smooth muscle and endothelium. Chronic hypoxia stimulates extensive cerebrovascular remodeling that increases wall thickness but decreases overall contractility, largely through depressed myofilament Ca^{++} sensitivity. Chronic hypoxia also depresses endothelium-dependent vasodilatation through decreases in NO release, soluble guanylate cyclase activity, and expression of PKG substrates.

Many of the cerebrovascular effects of chronic hypoxia appear to be homeostatic and may be mediated by VEGFs, which increase in direct response to hypoxia and, in turn, can directly influence cerebrovascular smooth muscle through endothelium-independent effects to alter the expression and function of multiple contractile proteins. Taken together, these findings demonstrate that the fetal cerebral vasculature is highly adapted to thrive in the hypoxic environment characteristic of *in utero* life, and suggest that further study of the molecular mechanisms mediating fetal adaptation to both physiological and pathophysiological perturbations hold great promise for improvements in strategies for management of the at-risk fetus and neonate.index[sub]hypoxia!induced stress@-induced stress|)

References

1. Eastman NJ (1954) Mount everest in utero. Am J Obstet Gynecol 67:701-11.
2. Bank A (2006) Regulation of human fetal hemoglobin: new players, new complexities. Blood 107:435-43.
3. Blood AB, Hunter CJ, Power GG (2003) Adenosine mediates decreased cerebral metabolic rate and increased cerebral blood flow during acute moderate hypoxia in the near-term fetal sheep. J Physiol 553:935-45.
4. Nishida N, Blood AB, Hunter CJ, Bragg S, Williams J, Pearce WJ, Power GG (2006) Role of prostanoids in the regulation of cerebral blood flow during normoxia and hypoxia in the fetal sheep. Pediatr Res 60:524-9.
5. Pearce WJ, Ashwal S (1987) Developmental changes in thickness, contractility, and hypoxic sensitivity of newborn lamb cerebral arteries. Pediatr Res 22:192-6.
6. Pearce WJ, Ashwal S, Cuevas J (1989) Direct effects of graded hypoxia on intact and denuded rabbit cranial arteries. Am J Physiol 257:H824-33.
7. Zurcher SD, Ong-Veloso GL, Akopov SE, Pearce WJ (1998) Maturational modification of hypoxic relaxation in ovine carotid and cerebral arteries: role of endothelium. Biol Neonate 74:222-32.
8. Salihagic-Kadic A, Medic M, Jugovic D, Kos M, Latin V, Kusan Jukic M, Arbeille P (2006) Fetal cerebrovascular response to chronic hypoxia–implications for the prevention of brain damage. J Matern Fetal Neonatal Med 19:387-96.
9. Larsen GA, Skjellegrind HK, Vinje ML, Berg-Johnsen J (2008) Mitochondria are more resistant to hypoxic depolarization in the newborn than in the adult brain. Neurochem Res 33:1894-900.
10. Rees S, Harding R, Walker D (2008) An adverse intrauterine environment: implications for injury and altered development of the brain. Int J Dev Neurosci 26:3-11.
11. Williams JM, Pearce WJ (2006) Age-dependent modulation of endothelium-dependent vasodilatation by chronic hypoxia in ovine cranial arteries. J Appl Physiol 100:225-32.
12. Teng GQ, Williams J, Zhang L, Purdy R, Pearce WJ (1998 Sep) Effects of maturation, artery size, and chronic hypoxia on 5-HT receptor type in ovine cranial arteries. Am J Physiol 275:R742-53.
13. Nauli SM, Williams JM, Gerthoffer WT, Pearce WJ (2005) Chronic hypoxia modulates relations among calcium, myosin light chain phosphorylation, and force differently in fetal and adult ovine basilar arteries. J Appl Physiol 99:120-7.
14. Pearce WJ, Williams JM, White CR, Lincoln TM (2009) Effects of chronic hypoxia on soluble guanylate cyclase activity in fetal and adult ovine cerebral arteries. J Appl Physiol 107:192-9.
15. Hoeben A, Landuyt B, Highley MS, Wildiers H, Van Oosterom AT, De Bruijn EA (2004) Vascular endothelial growth factor and angiogenesis. Pharmacol Rev 56:549-80.
16. Nilsson I, Shibuya M, Wennstrom S (2004) Differential activation of vascular genes by hypoxia in primary endothelial cells. Exp Cell Res 299:476-85.

17. Storkebaum E, Lambrechts D, Carmeliet P (2004) VEGF: once regarded as a specific angiogenic factor, now implicated in neuroprotection. Bioessays 26:943-54.
18. Marko SB, Damon DH (2008) VEGF promotes vascular sympathetic innervation. Am J Physiol Heart Circ Physiol 294:H2646-52.
19. Osada-Oka M, Ikeda T, Imaoka S, Akiba S, Sato T (2008) VEGF-enhanced proliferation under hypoxia by an autocrine mechanism in human vascular smooth muscle cells. J Atheroscler Thromb 15:26-33.

Chapter 31

Impaired Cerebral Autoregulation Using Near-Infrared Spectroscopy and Its Relation to Clinical Outcomes in Premature Infants

Alexander Caicedo, Dominique De Smet, Joke Vanderhaegen, Gunnar Naulaers, Martin Wolf, Petra Lemmers, Frank Van Bel, Lieveke Ameye, and Sabine Van Huffel

Abstract The concordance between the change in the Mean Arterial Blood Pressure (MABP) and the Cerebral Blood Flow (CBF) is studied using the Correlation, Coherence and Partial Coherence methods in order to detect Impaired Cerebral Autoregulation in Neonates. The presence of impaired autoregulation is assessed by the use of the Critical Percentage of Recording Time (CPRT). The changes in CBF are reflected by the measurement of changes in cerebral intravascular oxygenation (HbD), regional cerebral oxygen saturation (rSO_2), and cerebral tissue oxygenation (TOI), as measured by Near-Infrared Spectroscopy (NIRS) (INVOS4100 and NIRO300). The relation between impaired autoregulation and long term clinical outcomes in premature infants is studied.

31.1 Introduction

Cerebral autoregulation refers to the maintenance of a constant CBF over a broad range of arterial blood pressures. This process avoids damage in the brain due to hemorrhagic brain injury and ischemia. Evidence of impaired cerebral autoregulation

Alexander Caicedo, Dominique De Smet, Lieveke Ameye, and Sabine Van Huffel
ESAT/SCD, Dept. of Electrical Engineering, Katholieke Universiteit Leuven, Belgium
e-mail: Alexander.CaicedoDorado@esat.kuleuven.be

Joke Vanderhaegen and Gunnar Naulaers
Neonatal Intensive Care Unit, University Hospital Gasthuisberg, Katholieke Universiteit Leuven, Belgium

Martin Wolf
Clinic of Neonatology, University Hospital Zurich, Switzerland

Petra Lemmers and Frank Van Bel
Department of Neonatology, University Medical Center, Wilhelmina Children's Hospital, Utrecht, The Netherlands

J.C. LaManna et al. (eds.), *Oxygen Transport to Tissue XXXII*, Advances in Experimental Medicine and Biology 701, DOI 10.1007/978-1-4419-7756-4_31,

in preterm infants has been found in the literature [1]; however, its relation with clinical outcomes is uncertain [2].

Cerebral autoregulation can be assessed by analyzing the relation between Mean Arterial Blood Pressure (MABP) and Cerebral Blood Flow (CBF), which can be measured continuously. The similarity in the dynamics of both signals has been quantified so far by means of correlation, (partial) coherence [1] [3], among other methods. Intervals with a correlation, (partial) coherence coefficient > 0.5 are considered to present impaired autoregulation. In order to include all this information in a single value, two scores have been used: the Pressure Passive Index (PPI) [4], defined as the percentage of 10-min epochs with impaired autoregulation, and the Critical Percentage of Recording Time (CPRT), which represents the percentage of the total measuring time during which impaired cerebral autoregulation is detected [5].

MABP can be measured continuously by classical clinical monitors. Cerebral blood flow, however, is difficult to measure continuously. By means of Near-Infrared Spectroscopy (NIRS), changes in hemoglobin difference (HbD) can be measured, which reflect changes in CBF [6] [7] in case of constant arterial oxygen saturation (SaO_2). The CBF also correlates with the Tissue Oxygenation Index (TOI) and the regional Arterial Oxygen Saturation (rSO_2) [8].

Clinical outcomes in preterm infants are normally assessed by the use of birth weight and gestational age. However, other variables have been proven to be more sensitive to the prediction of the clinical outcomes in the neonates such as the CRIB score [9]. Moreover, long-term development of infants with regard to mental and psychomotor development is assessed by the Bayley and the Griffith scores.

In this paper we examine, by means of a multicentric study, how well cerebral autoregulation as quantified by correlation, (partial) coherence and derived measures, is related to the long-term clinical outcomes of premature infants, as quantified by the above-mentioned scores.

31.2 Data

The study was performed in 33 infants, admitted at the University Medical Center Utrecht (The Netherlands), mean gestational age of 28.9 ± 1.8 weeks and a birth weight of 1120 ± 509 grams. Another 20 infants from the University Hospital Leuven (Belgium), with a gestational age of 28.4 ± 3.5 weeks and a birth weight of 1113 ± 499 grams were included. In all infants the peripheral oxygen saturation SaO2 was measured continuously by pulse oximetry, and MABP by an indwelling arterial catheter. With NIRS, the HbD and the tissue oxygenation index (TOI) were continuously and non-invasively recorded using the NIRO 300 (Hamamatsu) (Leuven data), and in Utrecht the regional cerebral oxygen saturation (rSO_2) was recorded using the INVOS4100 (Somanetics). MABP, SaO_2 and NIRS signals were simultaneously measured during the first three days of life and downsampled at 0.333Hz. The total length of the recordings was 50-70 hours for the Utrecht data and 6-9 hours for the Leuven data.

31.3 Methods

31.3.1 Signal Analysis

In the data preprocessing artifacts < 1.5 seconds were removed and corrected by interpolation. Artifacts > 1.5 seconds were truncated. Hence, a single continuous measurement was replaced by a set of continuous artifact-free segments. Then, the signals were filtered and downsampled to 0.333Hz in order to obtain a common sampling frequency. Assessment of autoregulation was done by analysis of MABP-HbD and MABP-TOI signals (Leuven data) and analysis of MABP-rSO_2 signals (Utrecht data). After preprocessing, the signals were divided into segments of 20 minutes. For each segment, the correlation (CORR), coherence (COH) and partial coherence (PACOH) coefficients were calculated. For the (partial) coherence, the Welch method was used for the assessment of the respective cross-power and auto-power spectra densities. This method involves a further segmentation of the signals into 10-minute epochs with an overlap of 7.5 minutes. The average of the coefficients in the frequency range 0.003Hz-0.1 Hz is then calculated [7]. This procedure was applied to all 20-minute length segments and a time series with the corresponding coefficients was obtained. This time series, together with a Critical Score Value (CSV) of 0.5, were used to derive the CPRT score for the corresponding infant.

With respect to clinical outcomes, infants were classified as normal, suspicious or abnormal according to their clinical scores. The CRIB score was measured in the first 12 hours after birth. Infants with score < 3 or > 3 were classified as normal or abnormal, respectively. The Bayley score was calculated at the age of 12 and 24 months for infants with a gestational age < 30 weeks for Leuven and Utrecht respectively. The Bayley score is based upon the Mental Developmental Index (MDI) and the Psychomotor Developmental Index (PDI) and is 100 ± 15 in case of good outcome. Hence, patients were classified as normal if MDI and PDI > 85, as suspicious if MDI or PDI < 85 or as abnormal if MDI and PDI < 85. The Griffith score is similar to the Bayley score but is used only for babies with a gestational age > 30 weeks.

31.3.2 Statistical Analysis

This was performed using the SAS System, version 9.1, SAS Institute Inc., Cary, NC, USA. The concordance scores computed from TOI versus MABP and from HbD versus MABP, using the recordings from Leuven, can be considered as two measurements from the same underlying process. Therefore, the paired t-test was applied in order to test the difference between these concordance scores computed in two ways as mentioned above: mean as well as CPRT values derived from the COR, COH and PACOH concordance scores. To assess whether the concordance scores were predictive for outcome (normal, 'suspicious', abnormal) in the Utrecht data, the non-parametric Kruskal-Wallis test was applied. Least squares regression analysis was applied to investigate the relation between the concordance scores and the CRIB score. All reported p-values were two-tailed and a nominal p-value < 0.05 was considered as statistically significant.

Table 31.1 Comparison between TOI-MABP and HbD-MABP in Leuven (N=20)

Score	Method	Mean TOI-MABP	Mean HbD-MABP	p-value
Mean	COR			
	mean ± st dev	23.5±8.8	27.9±10.3	0.06
	median (min-max)	23.8 (10.7 – 51.5)	25.1 (16.0 – 49.0)	
	COH			
	mean ± st dev	36.2±3.7	41.1±6.3	< 0.01
	median (min-max)	35.3 (31.6 – 43.2)	40.6 (33.6 – 61.8)	
	PCOH			
	mean ± stdev	36.4±3.7	40.8±4.8	< 0.01
	median (min-max)	36.2 (32.7 – 47.7)	39.9 (35.1 – 43.7)	
CPRT	COR			
	mean ± stdev	5.8±10.9	12.2±18	0.04
	median (min-max)	0.4 (0 – 48)	1.4 (0 – 59.0)	
	COH			
	mean ± st dev	4.0±6.12	14.0±22.9	0.06
	median (min-max)	3.5 (0 – 19.8)	6.3 (0 – 100)	
	PCOH			
	mean ± st dev	4.6±6.6	13.9±20.4	0.05
	median (min-max)	1.2 (0 – 24)	6.3 (0 – 85)	

31.4 Results

Table 1 presents the difference in concordance scores for the Leuven data, i.e., HbD versus MABP compared to TOI versus MABP. The difference in the mean COR scores did not reach statistical significance, implying that both methods might be used interchangeably. Similarly the CPRT COH and PACOH scores from TOI-MABP were not statistically significantly different from those obtained with HbD-MABP. Nevertheless, the mean COH or mean PACOH scores computed from TOI-MABP were significantly smaller than mean COH or mean PACOH based on HbD-MABP, although these differences are relatively small, e.g., mean COH: 36.2% TOI-MABP compared to 41.1% HbD-MABP (p-value < 0.01) or in other words an absolute difference of 4.9%.

In Leuven, 30% (6/20) of the infants had an abnormal outcome. Nevertheless no statistical evidence could be found for the predictive value of the concordance scores with respect to clinical outcome (normal/abnormal). However, CPRT CORR seemed to be predictive for the CRIB score: higher values of CPRT CORR were associated with higher values of the CRIB score (R-square of 0.27) (Figure 1).

Of the 33 babies from Utrecht, 20 (61%) had normal outcome, 9 (27%) 'suspicious' and 4 (12%) abnormal. Table 2 shows the COR, COH and PACOH stratified by the baby's outcome. No trend reached statistical significance, likely related to the underpowered sample size as we have only 4 cases with an abnormal outcome. Nevertheless, the obtained values are encouraging, e.g. median CPRT COH is 3.5% in the normal cases, 6.0% in the 'suspicious' cases and 17.2% in the abnormal cases (p-value 0.08).

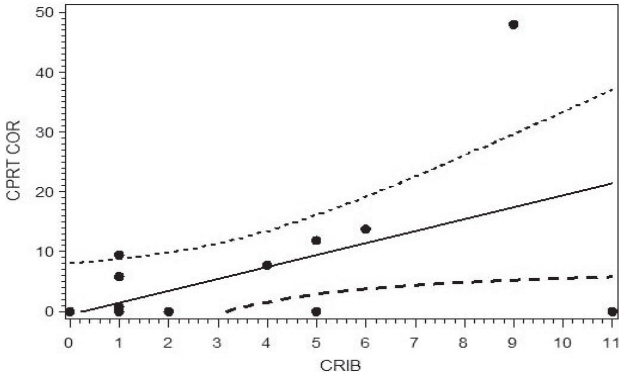

Fig. 31.1 Regression plot of CPRT CORR versus the CRIB score (the solid line presents the regression line, the dashed lines present the 95% confidence bounds).

Table 31.2 Concordance score stratified by the baby's outcome: normal, suspicious or abnormal

Score	Method	Normal (N=20)	Suspicious (N=9)	Abnormal (N=4)	p-value
Mean	COR				
	mean ± st dev	24.3±8.6	22.7±6.4	23.8±8.1	0.95
	median (min-max)	24.4 (11.9-46.4)	20.7 (12.0-31.1)	22.8 (15.0-34.7)	
	COH				
	mean ± st dev	37.3±3.4	38.8±2.6	40.1±5.0	0.27
	median (min-max)	36.7(32.4-47.2)	38.4 (34.2-42.7)	39.9 (34.8-45.7)	
	PCOH				
	mean ± st dev	37.0±3.5	39.7±2.4	39.1±5.1	0.09
	median (min-max)	36.2(32.7-47.7)	39.9 (35.1-43.7)	38.3 (34.6-45.1)	
CPRT	COR				
	mean ± st dev	8.1±10.4	5.2±6.3	9.7±8.7	0.5
	median (min-max)	4.0(0-38)	3.0 (0-18)	7.4 (2-22)	
	COH				
	mean ± st dev	5.3±7.4	8.8±7.0	19.4±18.3	0.08
	median (min-max)	3.5 (0-29)	6.0 (0-21)	17.2 (0-43)	
	PCOH				
	mean ± st dev	5.2±8.1	10.3±8.4	12.3±14.6	0.23
	median (min-max)	3 (0-34)	11.0 (0-27)	1. (0-29)	

31.5 Discussion

Cerebral autoregulation is a dynamic process that refers to the maintenance of a constant CBF over a broad range of perfusion pressures (MABP). Impaired cerebral autoregulation is considered a risk factor for brain injury in the sick, premature infant [1] [6] [7]. Continuous measurements of MABP and CBF are thus of interest to assess cerebral autoregulation. With NIRS, changes in HbD can be continuously measured, which represent changes in CBF [1] [6]. For the analysis of cerebral autoregulation,

the relation between MABP and CBF or HbD can then be assessed by the correlation, coherence and partial coherence method.

The COH method has been applied to continuous measurements of MABP and HbD to detect impaired cerebral autoregulation [1] [6] and [10]. HbD however is an unstable parameter which is strongly affected by movement artefacts. Wong et al. [7] first described the use of TOI instead of HbD for measuring autoregulation in a clinical setting.

We found similar scores for the mean COR, the CPRT COH and the CPRT PACOH, between MABP-HbD and MABP-TOI. However, the mean COH and PACOH scores for MABP-TOI were statistically smaller than those obtained for MABP-HbD. However these differences are small and within the normal variation of these parameters, therefore they are considered as clinically not relevant. From these important findings we infer that HbD and TOI are interchangeable parameters for the assessment of (impaired) cerebral autoregulation.

Impaired autoregulation has been associated with mortality in sick infants, although a correlation with clinical outcomes that are based upon mental and psychomotor development, such as the CRIB score, Bayley score or Griffith score, could not yet be proven. Because of our small study population, we were not able to prove a statistically significant association between these clinical scores and the mean or CPRT of the CORR/COH/PACOH scores computed from MABP-versus NIRS-measured TOI or rSO_2, although the CPRT index, calculated using the CORR methods, seems to be predictive for the CRIB score: a trend of higher CPRT values with higher CRIB scores (i.e., worse clinical outcome) was observed. In order to statistically prove this, further research is recommended, based upon a larger study population, including more infants with a bad clinical outcome and infants with higher variations in MABP. Our results imply that by means of NIRS and optimal signal processing, dynamic autoregulation and its relation to clinical outcome can be assessed.

Acknowledgments

Research supported by the Research Council KUL: GOA-AMBioRICS, GOA-MANET, CoE EF/05/006 Optimization in Engineering (OPTEC), by FWO projects G.0519.06 (Noninvasive brain oxygenation) and the Belgian Federal Science Policy Office IUAP P6/04 (DYSCO, ‘Dynamical systems, control and optimization’, 2007-2011).

References

1. Tsuji M, Saul J, du Plessis A et al (2000)Cerebral intravascular oxygenation correlates with mean arterial pressure in critically ill premature infants. Pediatric Review 106(4):625-632.

2. Greisen G (2005) Autoregulation of cerebral blood flow in newborn babies. Early Human Development, 81:423-428.
3. De Smet D, Jacobs J., Ameye L., Vanderhaegen J, Naulaers G et al (2008) The Partial coherence method for assessment of impaired cerebral autoregulation using Near-Infrared Spectroscopy: potential and limitations. Proceedings ISOTT 2008, August 3-7, Sapporo, Japan, to appear.
4. Soul J, Hammer P, Tsuji M et al (2007) Fluctuating pressure-passivity is common in the cerebral circulation of sick premature infants. Pediatric Research 61: 467-473.
5. De Smet D, Vanderhaegen J, Naulaers G et al (2009) New measurements for assessment of impaired cerebral autoregulation using near-infrared spectroscopy. Advances in Experimental Medicine and Biology; 645:273-278.
6. Soul J, Taylor G A, Wypij D et al (2000) Noninvasive detection of changes in cerebral blood flow by near-infrared spectroscopy in a piglet model of hydrocephalus. Pediatric Research 48(4):445-449.
7. Wong F, Leung T, Austin T et al (2008) Impaired autoregulation in preterm infants identified by using spatially resolved spectroscopy. Pediatrics 121:604-611.
8. Tachtsidis I, Tisdall M. et al (2008) Measurement of cerebral tissue oxygenation in young healthy volunteers during acetazolamide provocation: a transcranial Doppler and near-infrared spectroscopy investigation, Advances in Experimental Medicine and Biology 614: 389-396.
9. Lago P, Freato F, Betio T et al (1999) Is the crib score (clinical risk for babies) a valid tool in predicting neuro developmental outcome in extremely low birth weight infants? Biology of the Neonate 76:220-227.
10. Morren G, Lemmerling P, Van Huffel S et al (2001) Detection of autoregulation in the brain of premature infants using a novel subspace-based technique. Proceedings of 23rd International IEEE-EMBS Conference 2:2064-2067.

Part IX
Systems Modeling

Chapter 32
Variable ATP Yields and Uncoupling of Oxygen Consumption in Human Brain

Albert Gjedde, Joel Aanerud, Ericka Peterson, Mahmoud Ashkanian, Peter Iversen, Manoucher Vafaee, Arne Møller, and Per Borghammer

Abstract The distribution of brain oxidative metabolism values among healthy humans is astoundingly wide for a measure that reflects normal brain function and is known to change very little with most changes of brain function. It is possible that the part of the oxygen consumption rate that is coupled to ATP turnover is the same in all healthy human brains, with different degrees of uncoupling explaining the variability of total oxygen consumption among people. To test the hypothesis that about 75% of the average total oxygen consumption of human brains is common to all individuals, we determined the variability in a large group of normal healthy adults. To establish the degree of variability in different regions of the brain, we measured the regional cerebral metabolic rate for oxygen in 50 healthy volunteers aged 21-66 and projected the values to a common age of 25. Within each subject and region, we normalized the metabolic rate to the population average of that region. Coefficients of variation ranged from 10 to 15% in the different regions of the human brain and the normalized regional metabolic rates ranged from 70% to 140% of the population average for each region, equal to a two-fold variation. Thus the hypothetical threshold of oxygen metabolism coupled to ATP turnover in all subjects is no more than 70% of the average oxygen consumption of that population.

32.1 Introduction

The cerebral metabolic rate for oxygen ($CMRO_2$) is the most accurate measure of brain energy turnover. As much as 95% of the oxygen is consumed in mitochondria and this consumption most accurately reflects the adenosine triphosphate (ATP) turnover. The exact coupling ratio in human brain is, however, unknown.

The distribution of brain oxidative metabolism values among healthy humans is astoundingly wide for a measure that is presumed to reflect normal brain function and is purported to change only minimally with changes of brain function. Under normal

Pathophysiology and Experimental Tomography Center, University of Aarhus, Aarhus
Dept of Neuroscience & Pharmacology, University of Copenhagen, Copenhagen, Denmark
e-mail: gjedde@sund.ku.dk

J.C. LaManna et al. (eds.), *Oxygen Transport to Tissue XXXII*, Advances in Experimental Medicine and Biology 701, DOI 10.1007/978-1-4419-7756-4_32,

circumstances, as much as 90% of the glucose consumed undergoes oxidation to CO_2 but only about 75% of the total glucose consumption on average is coupled to oxidative rephosphorylation of ATP, according to recent estimates of ATP-turnover by means of *in vivo* 31P MR spectroscopy and magnetization transfer [3]. The remaining 15% of the glucose consumption is believed to be uncoupled from the resynthesis of ATP in mitochondria by means of pores in the inner membrane that dissipate the hydrogen ion gradient and thus help maintain the electron flux independently of the ATP turnover. The estimates of oxidative metabolism in human brain raise the possibility that the oxygen consumption rate coupled to ATP turnover is similar in all healthy brains. The additional oxygen consumption then reflects varying degrees of uncoupling in different individuals. To test the hypothesis that a lower threshold of about 70-80% of the oxygen consumption by the human brain is common to all normally functioning individuals, we determined the variability in a large group of normal healthy adults.

32.2 Methods

To establish the degree of variability of brain oxidative metabolism in different regions of the human brain, we measured the regional cerebral metabolic rate for oxygen ($CMRO_2$) in 49 healthy volunteers aged 21-66 and intrapolated the values to a common age of 25 years. The Research Ethics Committee of County Aarhus approved the study and the subjects gave informed consent.

32.2.1 PET/MRI Methods

The full details of the PET and MRI methods were published by Borghammer et al. [1]. Each subject underwent $[^{15}O]O_2$ emission recording that lasted 3 minutes (21 frames) from the onset of inhalation of 1 GBq $[^{15}O]O_2$. The PET recordings were acquired in 3D mode with the ECAT EXACT HR 47 (CTI/Siemens) whole-body tomograph with transverse resolution of 3.6–7.4 mm and axial resolution of 4.0–6.7 mm [8]. The reconstructed images were corrected for random and scattered events, detector efficiency variations, and dead time. Catheters were inserted in the left radial artery and right cubital vein, and arterial blood radioactivity determined with automated blood sampling, cross-calibrated to the tomograph and corrected for external delay and dispersion. Anatomical MR images were used to co-register MR and PET images.

32.2.2 Image pre-processing

Summed images of the individual emission recordings were co-registered and then transformed into common stereotaxic coordinate space, using a combination of linear and non-linear transformations. With the decay-corrected arterial inputs, parametric maps of $CMRO_2$ were calculated with single step, two-compartment, weighted-integration [6].

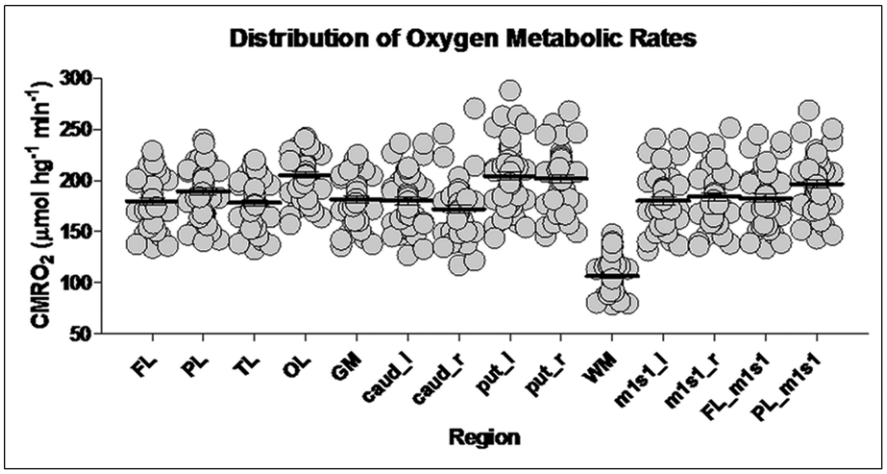

Fig. 32.1 $CMRO_2$ estimates of 49 healthy volunteers, adjusted to age 25 years. Regions are frontal (FL), parietal (PL), temporal (TL) and occipital (OL) lobes, gray and white matter (GM, WM), left and right caudate nuclei (caud_l, caud_r) and putamina (put_l, put_r), and left and right sensorimotor (m1s1_l, m1s1_r), precentral frontal (FL_m1s1) and postcentral parietal (PL_m1s1) cortices.

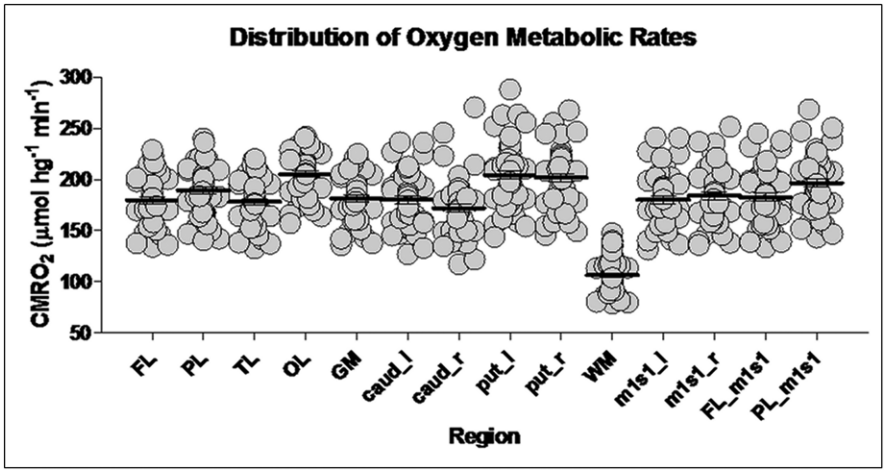

Fig. 32.2 $CMRO_2$ values normalized to population mean of every region.

32.3 Results

Coefficients of variation ranged from 10 to 15% in the different regions listed in the abscissa of Figure 1. The normalized regional metabolic rates ranged from 70% to 140% of the population average for each region, the two-fold variation shown in Figure 2. In this figure, the hypothetical threshold of oxygen metabolism coupled

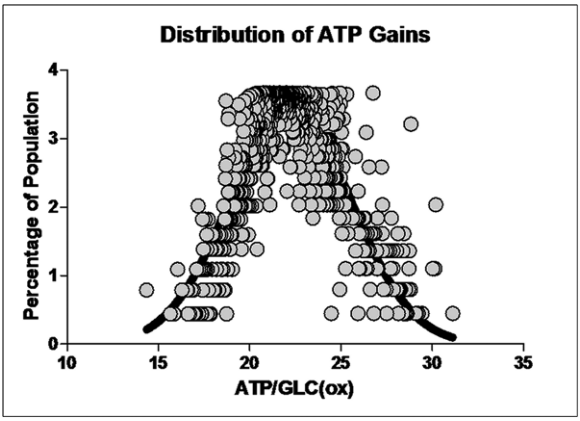

Fig. 32.3 Distribution of ATP gains (mol/mol glucose oxidized to CO_2).

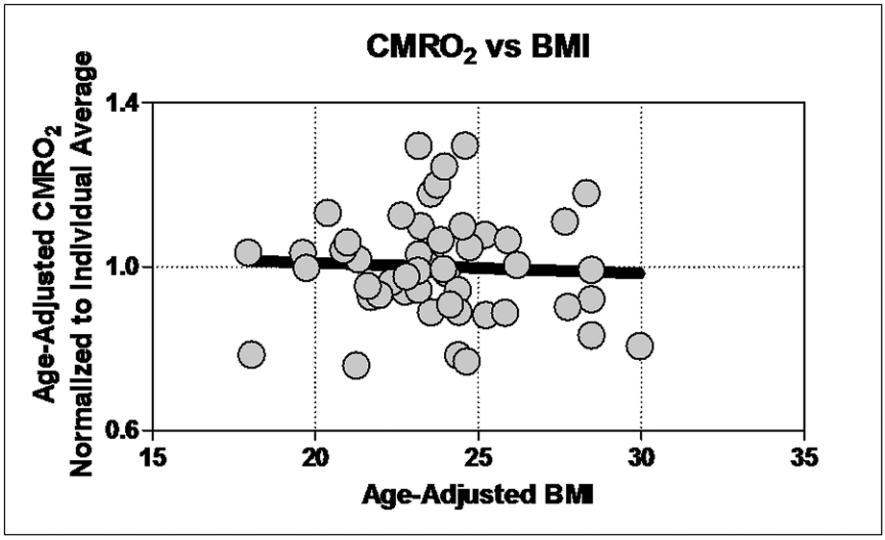

Fig. 32.4 Absent relation between age-adjusted BMI values and individual averages of $CMRO_2$ values normalized to regional population averages.

to ATP turnover, presumed to be common to all subjects, was close to 75% of the average oxygen consumption of the population.

We estimated the average ATP gain of the human brain by introducing the value of 29 mol per mol of glucose, argued by Brand [2] to be the absolute maximum gain from oxidation of glucose, to which we added 2 mol/mol from glycolysis for a total of 31 mol/mol glucose. We then determined the probability distribution of ATP gains from the variable $CMRO_2$ values among individual subjects, as shown in Figure 3. The average ATP gain was then 24±3 (SD) mol/mol glucose, or about 75% of the

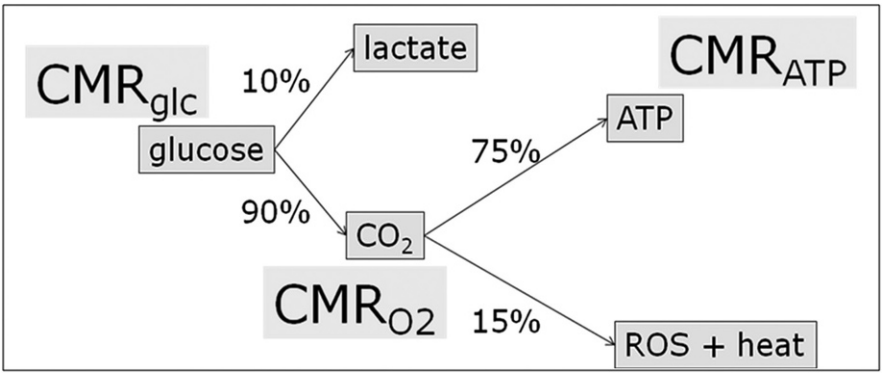

Fig. 32.5 Average energy dispersal of glucose molecules in brain metabolism, where CMR_{ATP} refers to the rate of oxidative phosphorylation, and ROS refers to reactive oxygen species.

maximum. Interestingly, the variability and range of $CMRO_2$ values was similar to the range and variability of body-mass indices of the present subjects (24±3 (SD) kg/m^2, adjusted to a common age of 25 years), as shown in Figure 4, although no correlation was found between the two measures, as the figure shows.

32.4 Discussion

According to the hypothesis, uncoupled and heat-generating idling could account for the variability from 70% to 140% of the population average, as shown in Figure 5, which summarizes this hypothesis. The distribution of oxidative brain metabolic rates in this large group of normal healthy adults therefore is consistent with the claim that 70% of the oxygen consumption is common to all normal healthy adult brains, while the remainder of the total reflects different degrees of uncoupling.

Genetically controlled differences of the degrees of uncoupling are now held to play roles in obesity and the onset of diabetes II [4,7,9]. It is tempting to claim that the variability of $CMRO_2$ values in healthy adult human beings may have a similar explanation, although the mechanism relating the two is speculative. Among the uncoupling pores in the inner mitochondrial membranes responsible for hydrogen-ion gradient dissipating leaks, are the uncoupling proteins (UCP1-5), of which some operate in brain. These proteins could act as clutches that would cause mitochondria to idle without changing the total oxygen consumption. However, the distribution of BMI values in the present subjects had no correlation to the distribution of oxygen metabolism values.

Higher degrees of uncoupling are held to be beneficial and neuroprotective because they prevent excessive reduction of cytochromes and the accompanying generation of reactive oxygen species that occurs when the electron flux is not maintained. In parallel with different degrees of uncoupling known to operate in other parts of the

body, such as the thyroid gland and brown fat where uncoupling is a factor involved in thermogenesis, the uncoupling proteinsindex[sub]uncoupling proteins may contribute to individual differences of body-mass index, as well as to the variability of cerebral oxygen consumption rates in healthy human beings.

The averages presented in Figure 5 are meant to reflect whole-brain or average gray matter. It is of interest that recent evaluations of energy turnover mechanisms in different cellular compartments of the mammalian brain suggest that the oxygen-glucose index (OGI) of 5.5, which reflects the 10% of glucose that leads to lactate production, actually varies greatly among cell types as well as within cells of the same type. Some evaluations suggest that the OGI in astrocytes may be as low as 1, and the corresponding OGI in neurons as high as 20 [5].

References

1. Borghammer P, Jonsdottir KY, Cumming P, Ostergaard K, Vang K, Ashkanian M, Vafaee M, Iversen P, Gjedde A. (2008) Normalization in PET group comparison studies—the importance of a valid reference region. *Neuroimage.* ;**40(2):**529-40. Epub 2008 Jan 12.
2. Brand MD. (2005)The efficiency and plasticity of mitochondrial energy transduction. *Biochem Soc Trans*.;**33(Pt 5):**897-904.
3. Du F, Zhu XH, Qiao H, Zhang X, Chen W. (2007) Efficient in vivo 31P magnetization transfer approach for noninvasively determining multiple kinetic parameters and metabolic fluxes of ATP metabolism in the human brain. *Magn Reson Med.* ;**57(1):**103-14.
4. Fisler JS, Warden CH. (2006) Uncoupling proteins, dietary fat and the metabolic syndrome. *Nutr Metab (Lond).* 12;**3:**38.
5. Hyder F, Patel AB, Gjedde A, Rothman DL, Behar KL, Shulman RG. (2006)Neuronal-glial glucose oxidation and glutamatergic-GABAergic function. *J Cereb Blood Flow Metab.*;**26(7):**865-77. Epub 2006 Jan 11. Review.
6. Ohta S, Meyer E, Thompson CJ, Gjedde A. (1992) Oxygen consumption of the living human brain measured after a single inhalation of positron emitting oxygen. *J Cereb Blood Flow Metab*. ;**12(2):**179-92.
7. Rabøl R, Højberg PM, Almdal T, Boushel R, Haugaard SB, Madsbad S, Dela F. (2009) Improved glycaemic control decreases inner mitochondrial membrane leak in type 2 diabetes. *Diabetes Obes Metab.* ;**11(4)**:355-60
8. Wienhard K, Dahlbom M, Eriksson L, Michel C, Bruckbauer T, Pietrzyk U, Heiss WD. (1994) The ECAT EXACT HR: performance of a new high resolution positron scanner. *J Comput Assist Tomogr.* ;**18(1):**110-8.
9. Wortmann SB, Zweers-van Essen H, Rodenburg RJ, van den Heuvel LP, de Vries MC, Rasmussen-Conrad E, Smeitink JA, Morava E. (2009) Mitochondrial energy production correlates with the age-related BMI. *Pediatr Res.* ;**65(1):**103-8

Chapter 33
Interpretation of NMR Spectroscopy Human Brain Data with a Multi-Compartment Computational Model of Cerebral Metabolism

Rossana Occhipinti, Erkki Somersalo, and Daniela Calvetti

Abstract One of the main difficulties in studying human brain metabolism at rest and during neuronal stimulation is that direct quantitative information of metabolite and intermediate concentrations in real time from *in vivo* and *in situ* brain cells is extremely difficult to obtain. We present a new six compartment dynamic computational model of the astrocyte-glutamatergic neuron cellular complex, previously used and validated for steady state investigations [1], which utilizes Michaelis-Menten type kinetic expressions for the reaction fluxes and transport rates. The model is employed to interpret experimental data (total tissue concentrations of glucose, lactate, aspartate, and glutamate) collected via NMR spectroscopy [2] in terms of compartmentalized metabolism. By integrating numerical methods with Bayesian statistics, we obtain an ensemble of models in statistical agreement with the data. Moreover, our preliminary results seem to suggest that NMR spectroscopy detects the time profile of the concentrations of glucose, lactate and aspartate in glutamatergic neuron.

33.1 Introduction

Although numerous advancements in improving the temporal and spatial resolution and reliability of several experimental modalities, such as magnetic resonance spectroscopy (MRS) and functional magnetic resonance imaging (fMRI), these techniques are incapable of providing direct quantitative information about the details of cellular metabolism. Multi-compartment mathematical models of brain energetics, which distinguish between astrocytes and neurons, can help analyzing and interpreting experimental data in terms of compartmentalized metabolism.

Rossana Occhipinti, Erkki Somersalo, and Daniela Calvetti
Department of Mathematics, Case Western Reserve University, Cleveland, OH 44106, USA
e-mail: daniella.calvetti@case.edu

Daniela Calvetti
Cognitive Science, Case Western Reserve University, Cleveland, OH 44106, USA

J.C. LaManna et al. (eds.), *Oxygen Transport to Tissue XXXII*, Advances in Experimental Medicine and Biology 701, DOI 10.1007/978-1-4419-7756-4_33,

Several mathematical models of cellular brain metabolism have been proposed and utilized to provide theoretical data [3, 4] or to interpret isotopic labeling data [5]. One feature of these models is that, to reduce their complexity and the number of unknown parameters, several metabolic pathways have been lumped together, thus reducing the resolution of the models and their predictive abilities. In this study, we propose a new detailed dynamic computational model of the astrocyte-glutamatergic cellular complex, previously utilized for steady state investigations [1], where each cell type is compartmentalized into cytosol and mitochondria and several key metabolic pathways, which have been detected or hypothesized in brain cells, have been included. We employ Bayesian statistics and numerical techniques to estimate an ensemble of kinetic parameters and to produce a collection of dynamic responses capable of explaining the experimental human data collected by ^{1}H NMR spectroscopy during prolonged visual stimulation [2]. The detailed multi-compartment model of brain energetics proposed here allows the interpretation of this data in terms of compartmentalized metabolism.

33.2 Methods

The multi-compartment mathematical model employed in this study is a dynamic extension of the steady state computational model of the astrocyte-glutamatergic cellular complex proposed in [1]. Since we are concerned with dynamic situations, the model is modified to account for kinetic expression for the reaction fluxes and transport rates and for separate compartments for the blood and the extracellular space. Thus the fully dynamic model of the astrocyte-glutamatergic cellular complex comprises a total of six compartments: cytosol and mitochondria in astrocyte, cytosol and mitochondria in glutamatergic neuron, blood domain and extracellular space (ECS). The biochemical pathways considered in this model are the same as those included in our steady state model. The transport of a biochemical species from a compartment to another can be facilitated by a carrier medium or occur by passive diffusion. The reaction fluxes and transport rates are modeled following the Michaelis-Menten form as done in [6]. The kinetic expression of the transport rate of glutamate from the cytosol of neuron to the ECS is modeled using a different kinetic form which encodes the information that membrane permeability in presynaptic neurons changes in correspondence of neuronal depolarization and neuronal activity. Since the transport rate of glutamate, $J^N_{cyt\to ECS,GLU}$, is low when neurons are at rest and rapidly increases in conjunction with an action potential u, we write

$$J^N_{cyt\to ECS,GLU} = T\frac{(C^N_{c,\,GLU})^n}{(C^N_{c,\,GLU})^n + M(u)},$$

where $C^N_{c,\,GLU}$ is the concentration of glutamate in the cytosol of presynaptic neuron, u is a time dependent function describing the integrated action potential and the M(u) is the affinity coefficient which depends on u through

$$M(u) = M_0 \left(1 - \alpha \frac{u^m}{u^m + u_0^m}\right),$$

with m and α parameters controlling the shape of this saturation curve.

The changes in the concentrations of the biochemical species included in the model are described by a system of 95 nonlinear coupled ordinary differential equations which can be written compactly in the form

$$V\frac{dC}{dt} = G(C,\Theta, t) \in \mathbb{R}^{95},$$

where $G(C,\Theta, t):\mathbb{R}^{95} \times \mathbb{R}^{250} \times \mathbb{R} \rightarrow \mathbb{R}^{95}$ is a nonlinear function describing the combined effects of reactions, transports and convection, $C(t) \in R^{95}$is the state vector containing the metabolite concentrations and Θ is the vector of the 250 kinetic parameters associated with the reaction fluxes and transport rates. In order to fully identify a forward dynamic model, we need to specify the 250 system parameters and the 95 initial concentrations C_0, thus accounting for all the unknowns together we need to estimate 345 model parameters $x = [C_0, \Theta]$.

Following the methodological approach introduced in [6], which integrates numerical methods with Bayesian statistics, we infer the posterior distribution of the unknown parameters using experimental data and prior belief. The posterior probability density is explored via adaptive Metropolis-Hastings (AM) algorithms [7]. The experimental data used to construct the likelihood density are the total tissue concentration of glucose, lactate, aspartate and glutamate collected via ^{1}H NMR spectroscopy during sustained visual stimulation [2]. In Fig. 1 we illustrate the simulation protocol. We assume that the experiment starts at time $t_0 = 5$ min and that the system is near a steady state before the onset of the visual stimulation, which

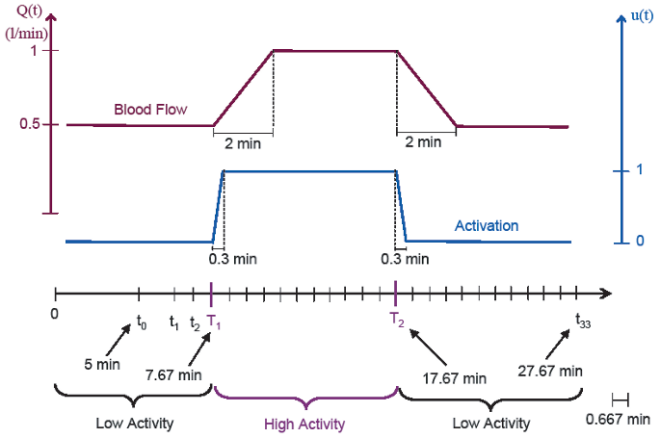

Fig. 33.1 Schematic description of the simulation protocol and data collection. Experimental data are collected at time $t = t_j$, $1 \leq j \leq 33$. The times T_1 and T_2 are the starting and final times of the visual stimulation.

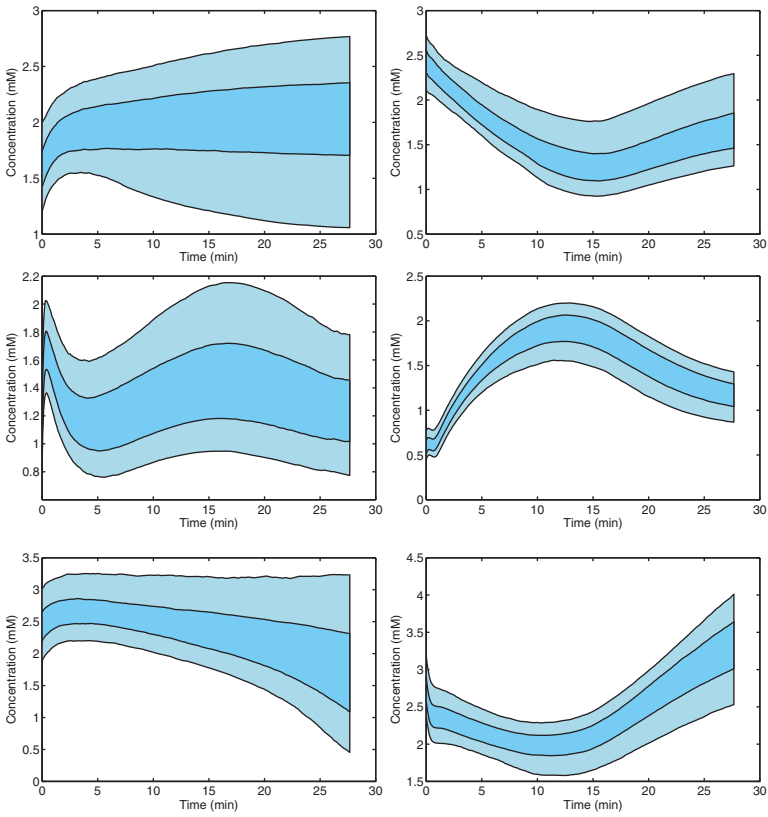

Fig. 33.2 The 50% (darker) and 90% (lighter) pointwise predictive envelopes of the time profiles of the concentration of glucose (first row), lactate (second row) and aspartate (third row) in the cytosol of astrocyte (first column) and in the cytosol of glutamatergic neuron (second column).

starts at time $T_1 = 7.67$ min and ends at time $T_2 = 17.67$ min. The application of the visual stimulus is simulated by ramping the activation function u(t) linearly from u = 0 (low activity) to u = 1(high activity). During the application of the visual stimulus, the cerebral blood flow (CBF) Q is changed linearly from the resting value Q = 0.5 l/min to Q = 1 l/min. The end of the visual stimulus is modeled by decreasing the CBF and the activation function back to the resting values.

33.3 Results

Using state-of-the art Markov Chain Monte Carlo method we generate a sample of 30,000 points, $x_k = [C_{0,k} \;\; \Theta_k]$, $1 \leq k \leq 30{,}000$, each one corresponding to a set of parameters which specifies one forward model $C_k(t) = C(t, x_k)$. We run the simulation for each model and analyze this ensemble of dynamic responses by calculating the time course predictive envelopes which contain, at each time instant t, a given

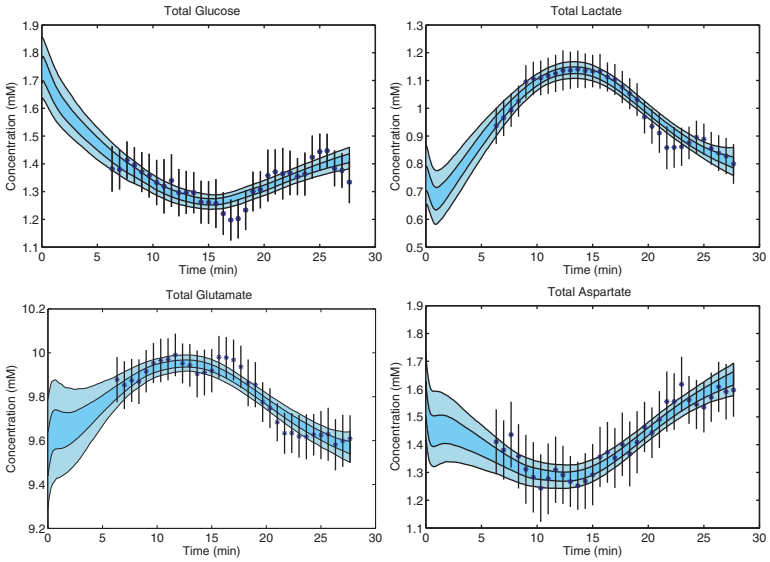

Fig. 33.3 The 50% (darker) and 90% (lighter) pointwise predictive envelopes of the total glucose, lactate, glutamate and aspartate concentrations in brain tissue calculated from the posterior sample. The experimental data and corresponding standard errors are indicated by the blue stars and by superimposed line segments.

percentage of the responses of the forward models [6]. In Fig. 3 we display the 50% (darker) and 90% (lighter) predictive envelopes for the four measured metabolites obtained from this sample. Additional analyses of the sample will be needed before drawing more definitive conclusions. The ensemble of dynamic responses can explain the data quite well. In Fig. 2 we illustrate our model prediction in terms of compartmentalized metabolism. In particular, we show the predictive envelopes of the time profiles of glucose, lactate and aspartate in the cytosol of astrocyte (first column) and in the cytosol of glutamatergic neuron (second column). The time profiles of the concentrations of these three metabolites in the cytosol of glutamatergic neuron follow the trend of the corresponding measured total tissue concentrations shown in Fig. 3. This suggests that NMR spectroscopy detects the time profiles of the concentrations of glucose, lactate and aspartate in glutamatergic neuron. We also observe that our preliminary results show that glutamatergic neurons always have greater oxidative activity and astrocytes utilize about 35% of the total oxygen consumption, in agreement with emerging evidence of higher rate of oxidative metabolism in astrocytes [8].

33.4 Discussion

In this study we have shown how a multi-compartment computational model of brain energetics can be used to interpret experimental data in terms of compartmentalized

metabolism and make predictions that may help our understanding of the complex metabolic interplay between the different types of cells in the brain. The Bayesian approach to the parameter estimation problem has allowed the estimation of a collection of parameters that are able to explain the experimental data and whose associated forward models can be in statistical agreement. In fact, pointwise predictive envelopes provide a measure of the reliability of the model predictions at different time instances. Our results are promising and will be further analyzed to study their sensitivity to the estimated parameter values.

References

1. Occhipinti R, Somersalo E, Calvetti D (2009) Astrocytes as the glucose shunt for glutamatergic neurons at high activity: an in silico study. J Neurophysiol 101:2528-2538
2. Mangia S, Tak I, Gruetter R et al (2007) Sustained neuronal activation raises oxidative metabolism to a new steady-state level: evidence from ^{1}H NMR spectroscopy in the human visual cortex. J Cereb Blood Flow Metab 27:1055-1063
3. Aubert A, Costalat R (2005) Interaction between astrocytes and neurons studied using a mathematical model of compartmentalized energy metabolism. J Cereb Blood Flow Metab 25:1476-1490
4. Simpson IA, Carruthers A, Vannucci SJ (2007) Supply and demand in cerebral energy metabolism: the role of nutrient transporters. J Cereb Blood Flow Metab 27:1766-1791
5. Gruetter R, Seaquist ER, Ugurbil K (2001) A mathematical model of compartmentalized neurotransmitter metabolism in the human brain. Am J Physiol Endocrinol Metab 281:E100-112
6. Calvetti D, Somersalo E (2006) Large scale statistical parameter estimation in complex systems with an application to metabolic models. Multiscale Model Simul 5:1333-1366
7. Haario H, Saksman E, Tamminen J (2001) An adaptive Metropolic algorithm. Bernoulli 7:223-242
8. Hertz L, Peng L, Dienel GA (2007) Energy metabolism in astrocytes: high rate of oxidative metabolism and spatiotemporal dependence on glycolysis/glycogenolysis. J Cereb Blood Flow Metab 27:219-249.

Chapter 34

Regional Brain Blood Flow in Mouse: Quantitative Measurement Using a Single-Pass Radio-Tracer Method and a Mathematical Algorithm

K. Xu, K. Radhakrishnan, A. Serhal, F. Allen, J. C. LaManna, and M. A. Puchowicz

Abstract We[1] have developed a reliable experimental method for measuring local regional cerebral blood flows in anesthetized mice. This method is an extension of the well-established single-pass dual-label indicator method for simultaneously measuring blood flow and glucose influx in rat brains. C57BL6J mice ($n = 10$) were anesthetized and regional blood flows (ml/min/g) were measured using the radio-tracer method. To test the sensitivity of this method we used a mathematical algorithm to predict the blood flows and compared the two sets of results. Measured regional blood flows between 0.7 and 1.7 ml/min/g were similar to those we have previously reported in the rat. The predicted blood flows using an assumed linearly increasing arterial tracer concentration-versus-time profile (that is, a ramp) were similar to the values measured in the physiological experiments (R^2 0.99; slope 0.91). Thus, measurements of local regional cerebral blood flow in anesthetized mice using a single-pass radio-tracer method appear to be reliable.

K. Xu
Department of Neurology, Case Western Reserve University, 10900 Euclid Avenue, Cleveland, OH 44106, USA

A. Serhal and J.C. LaManna
Department of Physiology and Biophysics, Case Western Reserve University, 10900 Euclid Avenue, Cleveland, OH 44106, USA

M.A. Puchowicz
Department of Nutrition, Case Western Reserve University, 10900 Euclid Avenue, Cleveland, OH 44106, USA
e-mail: michelle.puchowicz@case.edu

K. Radhakrishnan
Department of Pathology and Cancer Center, University of New Mexico School of Medicine, Albuquerque, New Mexico 87131, USA

[1] The first and second authors contributed equally to this work.

J.C. LaManna et al. (eds.), *Oxygen Transport to Tissue XXXII*, Advances in Experimental Medicine and Biology 701, DOI 10.1007/978-1-4419-7756-4_34,

34.1 Introduction

Local cerebral blood flows have been measured in animal models using radio-tracer techniques over the past 50 years [1,2]. The recent development of mutant mice makes the mouse a useful model for studying neurological diseases by combining local cerebral blood flow measurements [3,4] and molecular mechanisms associated with brain disease and injury. We previously [5] described a modified iodoantipyrine (IAP) method for measuring local cerebral blood flow in mice. This approach required quantification of both local tissue and arterial concentrations of [^{14}C]IAP at a single point in time, as well as use of a mathematical algorithm, and included sensitivity analysis. The modeling study revealed that the calculated blood flow was sensitive to the assumed arterial [^{14}C]tracer concentration profile. Greater sensitivity with the input profile increases the possibility of error, thus resulting in erroneous blood flow values. Sensitivity analysis provides information on the effects of uncertainties or changes in the input parameters of the problem on the solution [6,7]. We have recently developed a quantitative experimental method for measuring local regional cerebral blood flows in anesthetized mice that results in theoretically computed predictions that are less sensitive to the assumed arterial [^{14}C]tracer concentration profile. This method is an extension of the well-established single-pass, dual-label indicator method for simultaneously measuring blood flow and glucose influx in rat brains [2,8]. To test the sensitivity, we used the previous mathematical algorithm and three different tracer concentration-versus-time profiles to predict blood flows [5] and compared them with the experimentally deduced values.

34.2 Methods

34.2.1 Animal preparations and surgical procedures

All procedures were approved by the Institutional Animal Care and Use Committee of Case Western Reserve University. Adult C57BL6J mice (n=10; 6 male, 4 female; age 14 weeks) were anesthetized with Avertin injection (intraperitoneal, 0.06 mg/kg) prior to surgical placement of the catheters and for the duration of the experiment. Briefly, the surgical procedure involved placement of a right atrial silastic catheter (0.03 cm i.d., 0.063 cm o.d.) into the external jugular vein and insertion into the right atrium. A second catheter (polyethylene tubing; PE-10, 0.028 cm i.d., 0.06 cm o.d.) was placed in the femoral artery, to obtain blood samples for hematocrit and radioisotope tracer content.

34.2.2 Regional blood flow measurements

Regional brain blood flows were measured by using a single-pass blood flow indicator uptake method [9]. The femoral artery cannula was connected to a syringe pump calibrated to withdraw at a rate of 0.30 ml/min and started 6 sec before injection of the tracers. A bolus containing the radioisotope of $n-$[^{14}C]butanol tracer (0.01 mL

of 0.10 mCi/mL, American Radiolabeled Chemicals, St. Louis, Missouri, USA, into 0.04 ml saline) was given via jugular-vein catheter 8 sec prior to decapitation. The withdrawn blood was collected in pre-weighed vials, and 0.10 ml aliquots were measured for their radioisotope content. To correct for the residual vascular radioactive content, samples of venous blood oozing from the foramen magnum were collected at decapitation in heparinized tubes, and aliquots of the venous plasma were counted to estimate the intravascular compartment volumes [10]. The brain was rapidly removed and bilateral frontal, parietal, hippocampal, cerebellar and brain stem samples were weighed in pre-weighed scintillation vials containing 0.60 ml Soluene (tissue solubilizer). The tissue radioisotope content (dpm) was determined by β-scintillation spectroscopy (1600 TR Packard, Packard Instrument, Downers Grove, IL, USA). The experimental regional brain blood flow (BF; ml/g/min) was determined from the measured radioisotope content in each of the brain tissue and femoral artery blood samples using the following equation:

$$\mathrm{BF} = \frac{\mathrm{DPM}_{\mathrm{tissue}}}{\mathrm{DPM}_{\mathrm{blood}}} \times \frac{F_{\mathrm{s}}}{m}, \tag{34.1}$$

where DPM_{tissue} = brain tissue sample radioactivity count corrected for intravascular compartment volumes, F_s = syringe pump withdrawal rate (ml/min), DPM_{blood} = radioactivity count in the blood, and m = brain tissue sample mass (g).

34.2.3 Mathematical algorithm for regional blood flows

The experimental blood flows calculated with equation (2.1) were evaluated by comparisons with predictions of a modified mathematical model that we previously developed for computing blood flows in mice using the single-point method [5]. This method required arterial and tissue tracer concentrations at a single point in time(T), an assumed arterial [^{14}C] tracer concentration-versus-time profile, and the convolution integral described by Sakurada et al. [2]:

$$C^*(T) = \lambda K \int_0^T C_a^*(t) e^{-K(T-t)} dt, \tag{34.2}$$

where $C^*(T)$ is the local tissue radioactivity per unit mass (dpm/g) at the sampling time T (=t_3; Fig. 1),$C_a^*(t)$the arterial blood radioactivity per unit volume (dpm/ml) at any time t, and $K = (fD)/(\lambda m)$, where f = blood flow rate (ml/min), D = diffusion coefficient of the tracer across the blood-brain barrier, λ = tissue:blood partition coefficient, and m = mass of brain tissue sample.

As in our previous work [5], three specific arterial [^{14}C]tracer concentration-versus-time profiles were used to calculate the predicted regional brain blood flows in the mice (Fig. 1): (a) a ramp (linear rise) over the time interval [t_1, t_2], followed by a constant value over the time interval [t_2, t_3]; (b) ramp over the time interval [t_1, t_3]; and (c) step function (constant value) over the time interval [t_1, t_3]. In this study, these profiles were constructed from the experimentally measured average

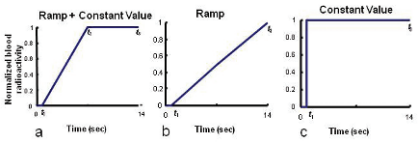

Fig. 34.1 Three assumed arterial tracer concentration-versus-time profiles over a 3-14 sec period with 0.5 sec lag time: a) ramp (linear rise) over the time interval $[t_1, t_2]$, followed by a constant value over the time interval $[t_2, t_3]$; b) ramp over the time interval $[t_1, t_3]$; c) step function (constant value) over the time interval $[t_1, t_3]$.

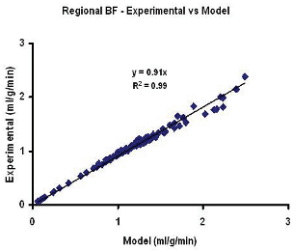

Fig. 34.2 Regional blood flows: experimental versus computational using the linear concentration-versus-time profile (ramp, Fig. 1b). Blood flow values represent five bilateral regions (frontal, parietal, hippocampal, cerebellar, brain stem).

femoral artery tracer concentration. The total experimental time (t_3) ranged from 3 to 14 sec. Each of the three profiles (Fig. 1) assumed a short time delay ($t_1 = 0.5$ sec) following tracer injection (at $t = 0$) and $t_2 = 1$ sec, based on experimental data of the arterial tracer concentration-versus-time profile (data not shown). An expression for the tissue [^{14}C] tracer concentration at the sampling time t_3 was then derived from the convolution integral, equation (2.2), and the blood flow computed by using an iterative method.

34.3 Results

Among the three arterial tracer concentration profiles considered in this study (Fig. 1) the linear concentration-versus-time profile, that is, a ramp (Fig. 1b), resulted in the best agreement between the experimental blood flows obtained from the physiological experiments and the predictions of the mathematical model. For this concentration profile, the correlation between experimental measurements and mathematical calculations of blood flow in various regions of the brain for all mice is shown in Fig. 2. The two sets of results are very similar to one another: linear regression analysis gave a slope of 0.91 and $R^2 = 0.99$. The correlation coefficient approaches 1.0 for blood flows in the physiological range (0.7-1.6 ml/g/min). The linear correlation analysis between the experimental measurements and modeling results showed similar slopes and R^2 values for all three arterial tracer concentration profiles (Table 1).

Table 34.1 Comparisons of experimental measurements of blood flow with calculated values using the three arterial tracer concentration-versus-time profiles examined (see Figs. 1 and 2)

Arterial Tracer Concentration Profile	Slope	R^2
a) Ramp + Constant	0.860	0.956
b) Ramp	0.911	0.985
c) Step Function (constant value)	0.856	0.955

34.4 Discussion

The single-pass radio-tracer method has been well developed in rats, but until recently was not widely practiced in smaller animals such as the mouse, because of the technical difficulties associated with small size [3]. Our experimental strategy enabled us to overcome the technical difficulties associated with using small animals involving surgical placement of catheters and frequent blood sampling. Regional blood flows measured in this study were comparable to those previously reported using the blood flow indicator method in rodents [2-4, 6]. These results were also consistent with our previously computed values using a mathematical model in conjunction with a modified IAP method, single time point arterial and tissue concentration measurements and an assumed arterial tracer concentration-versus-time profile [5]. The computed blood flow was found to be very sensitive to the assumed concentration profile, illustrating the importance of generating an accurate profile [5]. Serial measurements of the arterial tracer concentration can clearly produce a more accurate concentration profile than using a single-point measurement. In this study, we therefore used an average tracer concentration measured over several seconds of arterial sampling to construct the concentration profile. The blood flows calculated with the three concentration profiles were similar in magnitude to one another. However, the ramp, a linearly increasing arterial tracer concentration with time (Fig. 1b), resulted in the best agreement between experimental blood flows and mathematical predictions. We prefer this profile, because it is simpler and our previous work showed it to be less sensitive to the total experimental time than the ramp + constant [5]. Thus, the blood flows computed in this study were not as sensitive to the arterial tracer concentration-versus-time profile as the previously calculated results using the single-point measurements. Measurements of local regional cerebral blood flow in anesthetized mice using the single-pass radio-tracer method are reliable.

Acknowledgments

We would like to thank the Mouse Metabolic Phenotyping Center, Case Western Reserve University. These studies were supported by the National Institutes of Neurological Disorders and Stroke NS46074.

References

1. Kety SS and Schimidt CF (1948) The nitrous oxide method for the quantitative determination of cerebral blood flow in man. J Clin Invest 27:476-483
2. Sakurada O, Kennedy C, Jehle J, Brown JD, Carbin GL, and Sokoloff L (1978) Measurement of local cerebral blood flow with [^{14}C]iodoantipyrine. Am J Physiol 234:H59-66
3. Jay TM, Lucignani G, Crane AM, Jehle J, and Sokoloff L (1988) Measurement of local cerebral blood flow with [^{14}C]iodoantipyrine in the mouse. J Cereb Blood Flow Metab 8:121-129
4. Maeda K, Mies G, Olah L and Hossmann KA (2000) Quantitative measurement of local cerebral blood flow in the anesthetized mouse using intraperitoneal [^{14}C]iodoantipyrine injection and final arterial heart blood sampling. J Cereb Blood Flow Metab 20:10-14
5. Puchowicz MA, Radhakrishnan K, Xu K, Magness DL, and LaManna JC (2005) Computational study on use of single-point analysis method for quantitating local cerebral blood flow in mice. Adv Exp Med Biol 566:99-104
6. Radhakrishnan K (1991) Combustion Kinetics and Sensitivity Analysis Computations. In: Oran ES and Boris JP (eds) Numerical Approaches to Combustion Modeling. pp. 83-128, American Institute of Aeronautics and Astronautics, Inc., Washington, DC.
7. Radhakrishnan K (2003) LSENS: Multipurpose Kinetics and Sensitivity Analysis Code for Homogeneous Gas-Phase Reactions. AIAA J 41:848-855
8. Richards HK, Lovick AHJ, and Pickard JD (1987) A modification of the method for measurement of cerebral blood flow using [^{14}C]iodoantipyrine in small animals. J Cereb Blood Flow Metab 7:124-126
9. LaManna JC and Harik SI (1986) Regional studies of blood-brain barrier transport of glucose and leucine in awake and anesthetized rats. J Cereb Blood Flow Metab 6:717-723
10. Xu K, Puchowicz MA, and LaManna JC (2004) Renormalization of regional brain blood flow during prolonged mild hypoxic exposure in rats. Br Res 1027(1-2):188-191

Part X
Microcirculation and Wound Healing

Chapter 35

Wound Healing in Diabetes: Hemorheological and Microcirculatory Aspects

Giuseppe Cicco, Francesco Giorgino, and Sebastiano Cicco

Abstract Diabetes is associated with many hemorheological alterations. The decrease of RBC deformability, increase of aggregability, vasoconstriction, increase of blood viscosity and decrease of oxygen supply have a significant effect on wound healing, such as in foot ulcers. Basically, there is endothelial dysfunction and alteration of permeability; these impair wound healing in diabetic patients. Microcirculation still functions and there is blood flow, even when there is a decrease in vessel diameter, without anatomical lesions in vessel walls. It is necessary to maintain a good oxygen supply. Analyzing microcirculation and hemorheology in diabetes and considering methodologies to treat diabetic foot ulcers (e.g., hyperbaric oxygen therapy, laser, and vacuum) may help in the treatment of patient pathologies.

35.1 Introduction

In diabetic patients, long-term complications are related to the occurrence of vascular alterations which involve hemorheological and endothelium-dependent flow changes leading to possible tissue ischemia. The increased production of reactive oxygen species (ROS) is a key determinant of vascular changes. The duration and severity of diabetes can also cause the development of alterations in the skin and subcutaneous tissue, which may be the basis for more serious complications such as ulcers, foot infections and gangrene, leading to partial or more major amputations[1–2].

Giuseppe Cicco and Sebastiano Cicco
Hemorheology and Microcirculation Research Unit, University of Bari, Bari, Italy
e-mail: gcicco.emo@tiscali.it

Francesco Giorgino
Section of Internal Medicine, Endocrinology, Andrology and Metabolic Diseases, Department of Emergency and Organ Transplantation, University of Bari, Bari, Italy

J.C. LaManna et al. (eds.), *Oxygen Transport to Tissue XXXII*, Advances in Experimental Medicine and Biology 701, DOI 10.1007/978-1-4419-7756-4_35,

35.2 Hemorheology

Several factors may influence the hemorheological response and especially the red blood cell (RBC) deformability, which is necessary to allow the passage of RBCs (with a diameter of 3.5-7.0 microns) through the narrow arterial capillaries (with a diameter of 3.0-4.0 microns) in order to transport oxygen to tissues. This condition is only possible physiologically in the presence of deformable RBCs.

In vivo, the most important factors affecting RBC deformability are: a) the shear rate at the cell-fluid junction (mean shear rate, tube diameter, cell concentration or hematocrit); and b) the external fluid viscosity/plasma protein concentration.

Also, cell deformability is itself able to influence the stress deformation of RBC and many factors are involved in this response. One of these factors is the flexibility of the cell membrane, influenced by cell geometry, surface area and volume and by the elastic properties of the cell membrane (membrane composition and metabolic state). Another factor is the internal fluid viscosity, influenced by mean corpuscular hemoglobin concentration, physiochemical properties of hemoglobin, and intracellular structures.

Many other factors influence RBC aggregability, such as:

1. the influence of external environment (composition and concentration of plasma proteins and other macromolecules, shear rate and shear stress, cell concentration, geometric factors)
2. the aggregation tendency of RBC (cell deformability, electrical charge of cell surface, affinity of cell surface for macromolecules) [3–6].

The RBC deformability and hemorheology in the macrocirculation and microcirculation may influence blood flow and oxygen supply in tissues.

The factors influencing rheology of blood are hematocrit value, plasma composition, and properties of cellular elements. The internal homeostasis depends on an appropriate blood and oxygen supply[7]. Circulatory insufficiency can begin in a small local area leading immediately to local hypoxia, local acidosis, lack of required metabolites, and accumulation of metabolite wastes. This situation is followed by tissue injury, inflammation, leukocyte activation, decrease in RBC deformability, increase in RBC aggregation, increase in fibrinogen, increase in plasma viscosity (following dehydration) and hematocrit, increase in blood viscosity, decrease in blood flow and in oxygen supply, which form the basis for the circulatory insufficiency[8].

35.3 Hemorheological Alterations in Diabetes

Diabetes is characterized by increased generation of ROS, which is induced by hyperglycemia, hyperinsulinemia and insulin resistance. As noted above, this is an important factor initiating blood flow alterations, with the possibility of ischemia. In diabetes, there is a decreased production of nitric oxide (NO), associated with increased production of endothelin (ET-1), prostacyclin (PGI_2), angiotensin II, and

activation of angiotensin and endothelin. There is also fibrinogen oxidation with fibrin deposition. This condition leads to a functional vasoconstriction and possible thrombosis. Inflammation can often be present.

The increased ROS production can induce platelet activation [9–10]. In diabetes, there is a decrease in RBC deformability, due to the cytoskeleton alterations, and an increase in RBC aggregability[11]. The mechanisms proposed to explain these alterations in diabetes are: the influence of sorbitol plasma concentration on RBC volume/surface ratio, changes in internal viscosity influenced by calcium ion (Ca^{++}) concentrations and/or HbA_{1c} (glycated hemoglobin), abnormalities of the dynamic properties of RBC due to changes in cholesterol/phospholipids membrane ratio and by the degree of saturation of free fatty acids, and synthesis of advanced glycosylation end-products (AGEs).

These factors may decrease the RBC membrane fluidity by producing damage in the phospholipid structure and cytoskeleton. In addition, an increase of ROS in leukocytes may stimulate RBC aggregability[12–17].

Decreased blood flow leading to diminished tissue perfusion may also result from the action of neutrophils attached to the microvascular vessel walls, which affect endothelial cell function, through changes in integrin expression, ROS generation, and secretion of inflammatory cytokines[18–20].

Diabetes is also characterized by platelet alterations with a decrease in platelet membrane plasticity, and an increase in platelet aggregation and adhesion. The platelet activation is inversely linked to the degree of hyperglycemia[21–22].

35.4 Microcirculation and Wound Healing in Diabetes

In healthy subjects, the physiological wound healing process involves multiple factors simultaneously: *cellular factors* - platelets, neutrophils, macrophages, lymphocytes, fibroblasts; and *non-cellular factors* - proteins, extracellular matrix mucopolysaccharides (fibronectin, collagen, proteoglycans) and growth factors, including epidermal growth factor (EGF), platelet-derived growth factor (PDGF), fibroblast growth factor (FGF), and transforming growth factor (TGF). For a successful wound healing process, these factors need a normal tissue oxygenation and a normal blood flow. Indeed, decreased blood supply and/or decreased blood flow, such as occurs in diabetes, may impair the bringing together the elements needed to heal tissues. Oxygen is needed during the wound healing cascade. It has been reported that decreased pressure of transcutaneous oxygen is significantly related to the failure to heal and is a reliable indicator of local ischemia. Moreover, decreased oxygen availability in surrounding healthy tissues around the wound or ulcer can impair the migration of epithelial cells across the wound bed, thereby decreasing the hypoxic gradient in wounds and finally also impairing angiogenesis. Moreover, collagen metabolism is altered. Therefore, decreased oxidation induces a delay in the healing process with development of chronic ulcers with serious complications of infection including gangrene with pos-

sible amputation (diabetic foot), especially in patients with uncontrolled diabetes and poor education[23−24].

Many changes are present in microcirculation dysfunction in diabetes: vascular membrane thickening, peri- and intravascular fibrosis, increased vascular lumen diameter, decreased capillary density (capillary rarefaction), decreased exchange surface, slowing down of the transit of nutrients and O_2, increased arterial blood pressure, increased permeability to macromolecules, decreased permeability to micromolecules, shear stress and decreased tissue perfusion. There is also an interaction between endothelial and blood cells, endothelial dysfunction, thrombosis and plugging [25−26].

However, microcirculation blood flow in diabetes is present even if it is diminished. The changes are functionally and not anatomically-occlusive. The damage can lead to the development of an ulcer, occurring in these patients as a result of peripheral occlusive arterial disease (POAD) and neuropathy with the condition of ischemic foot and neuropathic foot without pain,. and can result in infections, both bacterial and purulent cysts. The result of this situation is the failure of vasodilation in the microcirculation to respond to several external stimuli (such as nervous, mechanical or thermic) when blood flow drops to a perfusion pressure of 20-30 mmHg. In other words, the diabetic foot develops an anatomic-functional change caused by POAD and/or diabetic neuropathy[27]. Ulcers are defined following the Leriche-Fontaine Classification[28] and the diabetic foot condition following the Wagner Classification[29] and the Texas University Wound Classification[30]. It is important to consider the level of the ulcer (superficial or deep, the presence or not of infection or ischemia or both). In the context of diabetic arteriopathy, high levels of glycemia are able to stop the replication of cultured human endothelial cells. Hyperglycemia can inhibit the repair of endothelial lesions repair encouraging the deposition of atherogenic substances in the subendothelial layers of the arterial walls. Fundamentally, there is endothelial dysfunction and there are alterations in permeability. These hinder wound healing in diabetes[31].

35.5 Hyperbaric Oxygen Therapy (HOT)

In the diabetic foot there is an important alteration of blood flow with peripheral hypoxia. In diabetic ulcers, only a small amount of oxygen linked to hemoglobin (in red blood cells) is available. Therefore, anemia does not delay wound healing in ulcers if the hematocrit is more than 15%. If the hematocrit is less than 15% and/or there is poor perfusion, HOT is the only approach able to maintain the tissue oxygen pressure at the levels useful for wound healing of these ulcers. HOT is used if the blood pressure at the ankle is about 40 mmHg and the transcutaneous oxygen pressure around the ulcer is about 20 mmHg. The target is that HOT with an oxygen pressure of about 2.5 atmospheres delivers the tissue oxygen needed even without the oxygen carried by the RBCs (as known, the oxygen supply to tissue for basal

functions is 5 ml O_2/100 ml of blood, this is possible to attain with oxygen physically dissolved in plasma through the use of HOT)[32].

All treatments comprise 30 sessions, but not continuously. It is useful to have 5-7 days of treatment per week including a rest period between treatments. Each treatment is performed once a day and lasts no more than 90 min per session. The oxygen pressure is at a maximum of 2.5 atmospheres. In fact, oxygen is very dangerous and toxic at pressures higher than 3 atmospheres.

The major risk is for the brain and lungs. It is necessary to avoid ROS production following hyperoxia which can damage the Red-Ox reactions in mitochondria and induce lipoperoxidation in cellular membranes. HOT can induce wound healing in the diabetic foot resolving hypoxia and infections. The collagen, neoangiogenesis, and lactate production are able to stimulate wound healing[33–34].

35.6 Laser and Negative Pressure Treatment (NPT)

Laser energy can help due to its characteristic transfer of energy at an ideal wavelength to stimulate collagen. Using an 808 nm diode laser connected to a rotating scanner it is possible to increase the vascularisation and to stimulate the bottom of the ulcer eliminating fibrinous layers[35].

Another methodology for the treatment of diabetic foot ulcers is the use of negative pressure at -125 mmHg, whereby blood flow increases immediately after application. At -500 mmHg blood flow increases 5 min after application. There is a positive effect in increasing wound perfusion[36] in chronic and diabetic wounds (i.e., foot ulcers) but topical negative pressure treatment did not accelerate complete wound healing. Many reviews on the usefulness of NPT have been published. There is a greater consensus in favor of Mendoca et al. (2006) and Pham et al. (2006), and less in favor of Wasiak et al. (2007), Nelson et al. (2007) and Ubbink et al. (2008); more studies are required to define the best application of these treatments[37–41].

35.7 Conclusions

In diabetes, neuropathy and vasculopathy are the main determinants of slow wound healing and the development of foot ulcers. Generally, the microcirculation is functioning normally. Blood flow is present, even when there is a decrease of vessel diameter following functional and not anatomical vasoconstriction, provided that the patient is atherosclerosis-free. It is important to maintain oxygen supply. New perspectives of treatment are laser and negative pressure, which are able to sustain wound healing. Additional studies are needed that focus on the clinical application of these modalities in the treatment of ulcers of the diabetic foot.

References

1. Forconi S. (2006) Il microcircolo nella malattia diabetica – Microangiologia. *Centro Scientif. Edr. Torino*;1:1-42.
2. Nathan DM, Cleary PA, Backlund JY. et al (2005) Intensive diabetes treatment and cardiovascular disease in patients with type 1 diabetes. *N Engl J Med* ;**353**:2643-53.
3. Chien Shu et al (1971) Present state of blood rheology in hemodilution, theoretical basis and clinical application *Int Symp Rottach-Egern*, ; Karger Basel 1972:1-45.
4. Goldsmith HL. (1968) The microrheology of red blood cell suspension *J Gen Physiol* :52-8.
5. Schmid-Schönbein H, Wells RE. (1971) Rheological properties of human erythrocytes. *Egern Physiol* : 63-146.
6. Di Perri T. et al (1981) Aspetti Fisiopatologici e Clinici delle Sindromi da iperviscosità ematica. *La Ric Clin Lab* ;1,11:73-84.
7. Dintenfass L. Hyperviscosity and hyperviscosaemia *MTP Press Lancaster*, 1985.
8. Baskurt OK. Mechanisms of Blood Rheology Alterations. *Handbook of Hemorheology. IOS Press* 2007;170-90.
9. Maritim AC, Sanders RA, Watkins JB. Diabetes, oxidative stress and antioxidants: a review. *J Biochem Mal Toxicol* 2003;**17**,24-38.
10. Nishikawa T, Edelstein D, Du XL. et al. Normalizing mitochondrial superoxide production blocks three pathways of hyperglycaemic damage. *Nature* 2000;**404**,787-90.
11. Neu B, Meiselman HJ. Red Blood Cell Aggregation. *Handbook of Hemorheology, IOS Press* 2007;114-36.
12. Caimi G, Lo Presti RL. Techniques to evaluate erythrocyte deformability in diabetes mellitus. *Acta Diabetologica* 2004;**41**,99-103.
13. Bryszewska M, Watala C, Torzecka W. Changes in fluidity and composition of erythrocyte membranes and in composition of plasma lipids in type 1 diabetes *Br J Haemat* 1986;**62**:111-6.
14. McMillan DE. Plasma protein changes, blood viscosity and diabetic microangiopathy. *Diabetes* 1976;**25**;858-64.
15. Volger E, Schmid-Schönbein H, Mehnert H. Microrheological changes of blood in diabetes mellitus. *Bibl Anat* 1975;**13**:97-8.
16. Schmid-Schönbein H, Volger E. Red cell aggregation and red cell deformability in diabetes. *Diabetes* 1976;**25**:897-902.
17. Baskurt OK,Temiz A, Meiselman HJ. Effect of superoxide anions on red blood cell rheologic properties. *Free Radic Biol Med* 1998;**24**:102-10.
18. Braun RD, Fisher TC, Meiselman HJ. et al. Decreased deformability of polymorphonuclear leukocytes in diabetic cats *Microcirculation* 1996;**3**:271-8.
19. Caimi G, Canino B, Montana M. et al., Polymorphonuclear leukocyte membrane fluidity and cytosolic calcium concentration in diabetes mellitus. *Acta Diabetol* 1998;**35**:158-60.
20. Sham SV, Wallin JD, Ellen SD. Chemiluminescence and superoxide anion production by leukocytes from diabetic patients. *J Clin Endocrinol Metab* 1983; **57**:402-9.
21. Sagel J, Colwell JA, Crock L. et. al., Increased platelet aggregation in early diabetes mellitus. *Ann Int Med* 1975;**82**:733-8.
22. Knobler H, Savion N, Shenkman B. et al., Adhesion and aggregation on sub-endothelium are increased in diabetic patients *Thromb Res* 1998;**90**:181-90.
23. Hunt TK. et al., The role of perfusion and oxygenation in wound healing. *Wound Care Textbook* 1998.
24. Laurie M. Rappl. Physiological changes in tissues denervated by SCI and possible effects on wound healing. *Int Wound J* 2008;**5**:435-44.
25. Kindig CA, Sexton Wl, Fedde MR. et al. Skeletal muscle microcirculatory structure and hemodynamics in diabetes. *Respir Physiol* 1998;**111**:163-75.
26. MacRury SM, Lowe GD. Blood rheology in diabetes mellitus. *Diab Med* 1990;**7**:285-91.
27. International Consensus on Diabetic Foot 2000 - *Mediserve Edr.* Naples, Italy.

28. Cicco G. et al. Peripheral perfusion and tissue oxygenation *AEMB Plenum Press New York USA* 1997;**31**:261-6.
29. Wagner FW. Foot Ankle Classification 1981 *In: "Int. Cons. on Diab. Foot" Mediserve* Naples, Italy 2000;13.
30. Lavery LA. Texas Wound Classification *In: "Int. Cons. Diab. Foot" Mediserve* Naples, Italy 2000,14.
31. Modena MG. et al. Diabetic arteriopathy *Min Med* 2004;**12**:81-9.
32. Nasole E. Ossigeno terapia Iperbarica in: *"Arteriopatia Diabetica degli arti inferiori" edr Stella A. Min. Medica* Torino 2004;**36**:245-54.
33. Niinikoski J. Oxygen and wound healing *Clin Plast Surg* 1997;**4**:361-4.
34. Niinikoski J, Hunt TK. Oxygen and wound healing. *In: Handbook of HOT. Springer edr.* 1996;485-507.
35. Marangoni O, Longo L. Laser in phlebology. Trieste 2006; 5-24.
36. Masahiro Shibata et al. Wound repair and regeneration. *Wound Rep Reg* 2008;**16**:460-5.
37. Mendoca DA, Papini R, Price PE. Negative pressure wound therapy: a snapshot of evidence. *Int Wound J* 2006;**3**:261-71.
38. Pham CT. et al., The safety and efficacy of topical negative pressure in non healing wounds: a systematic review. *J Wound Care* 2006;**15**:240-50.
39. Wasiak I, Cleveland H. Topical negative pressure (TNP) for partial thickness burns. *Cochrane Database System Review 2007*:3.
40. Nelson EA. Vacuum assisted closure for chronic wounds: a review of the evidence. *EWMA J* 2007;**7**:5-11.
41. Ubbink DT, Vermeulen H. A systemic review of topical negative pressure therapy for acute and chronic wounds. *Br J Surg* 2008;**95**:685-92.

Chapter 36
Modeling O_2-Dependent Effects of Nitrite Reductase Activity in Blood and Tissue on Coupled NO and O_2 Transport around Arterioles

Donald G. Buerk, Kenneth A. Barbee, and Dov Jaron

Abstract Recent evidence in the literature suggests that tissues play a greater role than blood in reducing nitrite to NO under ischemic or hypoxic conditions. Our previous mathematical model for coupled NO and O_2 transport around an arteriole, modified to include superoxide generation from dysfunctional endothelium, was developed further to include nitrite reductase activity in blood and tissue. Steady-state radial and axial NO and pO_2 profiles in the arteriole and surrounding tissue were simulated for different blood flow rates and arterial blood pO_2 values. The resulting computer simulations demonstrate that nitrite reductase activity in blood is not a very effective mechanism for conserving NO due to the strong scavenging of NO by hemoglobin. In contrast, nitrite reductase activity in tissue is much more effective in increasing NO bioavailability in the vascular wall and contributes progressively more NO as tissue hypoxia becomes more severe.

36.1 Introduction

Hypoxic vasodilation has been attributed to *S*-nitrosylated hemoglobin (Diesen et al. 2008), although this mechanism is questioned [10]. A role for nitrite (NO_2^-) in hypoxic vasodilationindex[sub]hypoxic vasodilation has received attention [9]. Reduction of NO_2^- to nitric oxide (NO) by hemoglobin appears to be maximal around the P_{50} of the oxyhemoglobin saturation curve [13]. However, recent evidence in the literature strongly suggests that tissues play a greater role than blood in reducing NO_2^- to NO under ischemic or hypoxic conditions when oxygen (O_2) is very low. Feelisch et al. [7] report a 3- to 5-fold lower rate for NO formation from nitrite reductase activity in red blood cells (rbcs) compared with NO formation from tissue homogenates. Li et al. [11] reported that maximum NO production from anoxic rbcs

School of Biomedical Engineering, Science and Health Systems, Drexel University, Philadelphia, PA, USA
e-mail: dgb28@drexel.edu

J.C. LaManna et al. (eds.), *Oxygen Transport to Tissue XXXII*, Advances in Experimental Medicine and Biology 701, DOI 10.1007/978-1-4419-7756-4_36,

is only 0.004 nM s^{-1} compared with rates > 0.5 nM s^{-1} for anoxic heart and liver tissue homogenates.

There has been limited mathematical modeling of these mechanisms. Buerk et al. [2] developed a steady-state mathematical model with coupled reactions for O_2, NO, superoxide ($O_2^{\bullet -}$), peroxynitrite ($ONOO^-$), hydrogen peroxide (H_2O_2), NO_2^- and nitrate (NO_3^-) for an arteriole to quantify mass transport through 5 concentric regions (blood, plasma layer, endothelium, vascular wall, perivascular tissue) for NO, pO_2, $O_2^{\bullet -}$, and $ONOO^-$, as well as production rates for H_2O_2, NO_2^-, and NO_3^- for varying $O_2^{\bullet -}$ production rates, superoxide dismutase (SOD) concentrations, carbon dioxide (CO_2) levels, pH, and other conditions. The model included reversible inhibition of mitochondrial O_2 consumption by NO, and predicted radial (r) and axial (z) variations in $ONOO^-$ due to competition between scavenging of $O_2^{\bullet -}$ by NO and inactivation of $O_2^{\bullet -}$ by SOD. A limitation of the model was that convective transport by blood flowing through the vessel was not included. Consequently, concentration profiles for H_2O_2, NO_2^-, and NO_3^- could not be predicted, although production rates for these species could be quantified. Our most recent NO and O_2 transport models include convective transport in the bloodstream [1, 4, 5]. We modified our previous models to include nitrite reductase activity in either blood or tissue.

36.2 Methods

The present model consists of 6 concentric radial layers: blood ($0 < r < 13\ \mu m$), rbc-free plasma layer ($13 < r < 14.5\ \mu m$), glycocalyx ($14.5 < r < 15\ \mu m$), endothelium ($15 < r < 16\ \mu m$), vascular wall ($16 < r < 19\ \mu m$), and surrounding avascular tissue ($19 < r < 120\ \mu m$). Blood flow through the lumen was assumed to have a parabolic shape, with maximum centerline (r=0) velocity of 1000 $\mu m\ s^{-1}$, for a blood flow rate of 33 nanoliters s^{-1} for the baseline simulation. All simulations were for a 300 μm axial length. Comparisons for different conditions were made for radial concentration profiles computed at the center of the segment (z=150 μm).

Convection-diffusion-reaction mass transport partial differential equations for concentrations C_i of multiple species were defined for each layer:

$$D_i \nabla^2 C_i - v \cdot \nabla C_i \pm \sum_{j=1}^{m} R_{i,j} = 0 \tag{36.1}$$

where i = O_2, $O_2^{\bullet -}$, NO, NO_2^-, NO_3^-, H_2O_2, and $ONOO^-$ with diffusion coefficient D_i for each species, convective velocity field v, sum of all (m) chemical reactions $R_{i,j}$ for each species (i) and their reactions with other chemical species (j).

For these simulations, the endothelial NO production rate was represented by O_2-dependent kinetics with a maximum rate of 25 $\mu M\ s^{-1}$ and K_m for O_2 of 4.7 Torr. O_2 consumption rates were 50, 1, and 17.5 $\mu M\ s^{-1}$ in the endothelium, vascular wall, and tissue, respectively, with $O_2^{\bullet -}$ production rates of 0.5, 0.02, and 0.35 $\mu M\ s^{-1}$ in the endothelium, vascular wall, and tissue, respectively. To simplify the model,

NO production from NO_2^- reduction by hemoglobin (R_{bNRA}) was assumed to be constant, equivalent to the maximum rate around the p_{50} of the oxyhemoglobin saturation curve. NO production from the reduction of NO_2^- in tissue (R_{tNRA}) was assumed to be an inverse function of tissue pO_2, given by

$$R_{tNRA} = R_{tNRAmax} / (1 + pO_2/k_t) \tag{36.2}$$

where k_t =12 Torr was estimated from O_2-dependent nitrite reductase activity data reported for tissue homogenates [11]. Other reaction rates used in the model were from the literature as described previously [1]. The resulting set of 7 coupled partial differential equations was written in cylindrical coordinates and solved numerically by finite element computational methods using commercial software (Flex-PDE, PDE Solutions, Inc., Antioch, CA, USA).

36.3 Results

Predicted radial NO profiles at the middle of the arteriole (z = 150μm) are shown in Fig. 1 for different rates of nitrite reductase activity in blood (Fig. 1A) or in tissue (Fig. 1B) with SOD = 1 μM and arterial blood PO_2 = 40 Torr at the entrance of the arteriole (z=0). NO profiles without nitrite reductase activity are shown by solid lines (bottom panels) with the additional amount of NO generated from nitrite reductase activity shown by dashed lines (ΔNO, top panels). Blood nitrite reductase activity (Fig. 1A) increases NO only by a few pM above the NO profile without nitrite reductase activity. NO profiles with nitrite reductase activity in blood overlap with the NO profile without nitrite reductase activity, and cannot be illustrated in the bottom panel. On the other hand, tissue nitrite reductase activity (Fig. 1B) has a greater impact on NO profiles (dashed lines). The additional NO (ΔNO, top panel) with nitrite reductase activity in tissue is several orders of magnitude (nM range) higher than that for the equivalent blood nitrite reductase activity.

The effect of SOD on model predictions due to inactivation of $O_2^{\bullet -}$ is shown in Fig. 2 for blood pO_2 = 70 (upper curves) or 40 (lower curves) Torr at the entrance of the arteriole. pO_2 increases (Fig. 2A) due to greater inhibition of tissue O_2 consumption as NO bioavailability increases with higher SOD, approaching the maximum pO_2 when there is zero $O_2^{\bullet -}$ production (dashed line). An example is shown for the increase in NO (Fig. 2B) with tissue nitrite reductase activity (dashed lines, maximum rate 1 nM s^{-1}, k_t = 12 Torr, SOD = 5 μM) compared with the NO profile without tissue nitrite reductase activity (solid lines). The peak NO in the endothelium decreases with more hypoxic conditions, although NO farther out in the tissue is higher since there is less $O_2^{\bullet -}$ production with lower tissue PO_2. The additional NO produced (top panel, Fig. 2B) is greater for lower blood PO_2 values at the entrance of the arteriole. Mean NO in the vascular wall (Fig. 2C) increases with higher SOD, and increases further when there is tissue nitrite reductase activity. Mean NO in the vascular wall with (dashed lines, open symbols) and without (solid lines, filled symbols) tissue

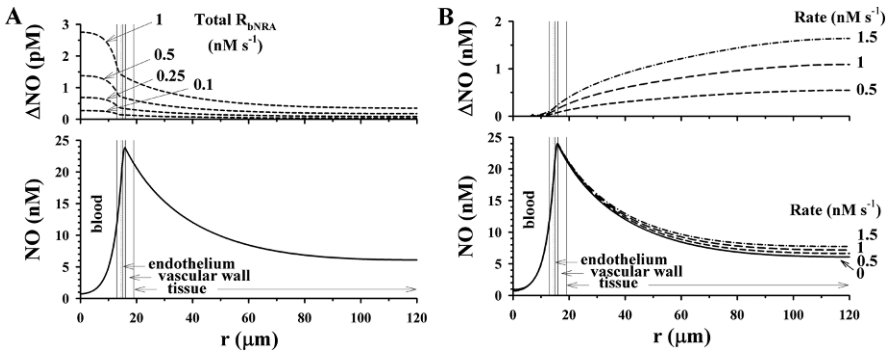

Fig. 36.1 Radial NO concentration profiles (bottom panels) with (dashed lines) and without (solid lines) nitrite reductase activity in blood (A) or in tissue (B). Additional amounts of NO generated with nitrite reductase activity compared with zero nitrite reductase activity are shown in top panels.

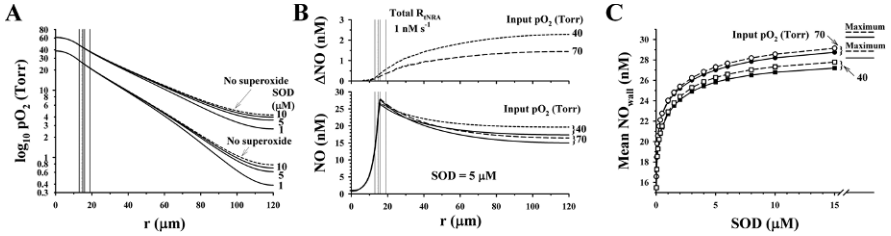

Fig. 36.2 Effects of SOD on pO_2 profiles (A), examples of NO profiles (bottom panel) with (dashed lines) and without (solid lines) tissue nitrite reductase activity and additional NO (ΔNO, top panel) produced (B), and mean NO in the vascular wall with (dashed lines, open symbols) and without (solid lines, filled symbols) tissue nitrite reductase activity (C).

nitrite reductase activity in the absence of $O_2^{\bullet-}$ production is shown for values of 70 and 40 Torr for arterial blood pO_2 at the entrance of the arteriole (upper right of Fig. 2C). While mean NO in the vascular wall is lower with decreased O_2 delivery and lower endothelial PO_2, for the parameters used in these simulations, nitrite reductase activity in tissue can partially compensate for the decrease in NO bioavailability with more hypoxic conditions.

The effect of varying blood flow relative to the baseline case (100%) is shown in Fig. 3 with SOD = 5 μM. pO_2 profiles (Fig. 3A) depend on the entrance pO_2 (70 Torr, upper curves; 40 Torr, lower curves) and decrease as flow is reduced. For this example, the maximum NO in the endothelium decreases due to lower endothelial pO_2 when blood flow is reduced to 25% of baseline (Fig. 3B). However, the NO profile farther out in the tissue is higher with the lower blood flow rate since tissue pO_2 falls and less $O_2^{\bullet-}$ is produced to scavenge NO. The NO profile is higher with nitrite reductase activity in tissue (dashed lines, for maximum rate 1 nM s^{-1}, k_t = 12 Torr) compared with the NO profile without nitrite reductase activity in tissue (solid lines). Mean NO in the vascular wall (Fig. 3C) decreases as flow is reduced (solid

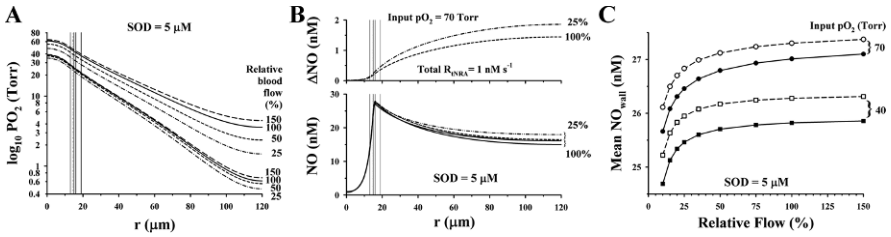

Fig. 36.3 Effects of blood flow and arterial blood pO_2 at the entrance of the arteriole on pO_2 profiles (A), NO profiles (B), and mean NO in the vascular wall (C) with (dashed lines, open symbols) and without (solid lines, filled symbols) nitrite reductase activity in tissue.

lines filled symbols) and NO bioavailability is partially restored when there is tissue nitrite reductase activity (dashed lines, open symbols).

36.4 Discussion

Our simulations demonstrate that nitrite reductase activity in blood has a minimal effect on NO profiles and is not an effective mechanism for conserving NO due to strong scavenging by hemoglobin. Our results are consistent with a diffusion model of blood nitrite reductase activity by Chen et al. [3] with zero NO generation by the endothelium which predicts NO profiles in the bloodstream that can supply the vascular wall with NO in the sub-pM range. In our model, none of the NO produced by reduction of NO_2^- in the rbc diffuses out of the bloodstream. Blood nitrite reductase activity slightly reduces the flux of NO from the endothelium to the bloodstream. Consequently, there is a very small elevation in the NO concentration profile in blood and tissue. In contrast, nitrite reductase activity in tissue is much more effective in increasing vascular wall NO, and even larger NO increases would be predicted with more severe tissue hypoxia. Radial and axial PO_2 profiles are also affected by tissue nitrite reductase activity with greater inhibition of O_2 consumption by higher NO levels.

There are limitations to our modeling approach. The model assumes homogenous properties in each radial layer for all of the parameters and reaction rates and does not include effects of shear stress on NO production by the endothelium. We used a maximum rate of nitrite reductase activity, independent of NO_2^-. Thus, the model is not valid under conditions where NO_2^- could become depleted. A more complete approach, albeit more complicated, would require a spatially heterogeneous model with first-order dependence on NO_2^-, since NO_2^- is twofold higher in rbcs than in blood plasma, and can be more concentrated in tissues compared with NO_2^- in the bloodstream [12]. We did not perform simulations where the endothelium becomes anoxic and endothelial NO synthase switches from the normal L-arginine pathway to covert NO_2^- to NO [8], and would add to the NO produced from tissue nitrite reductase activity through multiple enzymatic pathways [7, 11].

Acknowledgments

Supported in part by HL 068164 from NIH and BES0301496 from NSF.

References

1. Buerk DG (2009) Mathematical modeling of the interaction between oxygen, nitric oxide and superoxide. Adv Exp Med Biol 645:7-12
2. Buerk DG, Lamkin-Kennard K, Jaron D (2003) Modeling the influence of superoxide dismutase on superoxide and nitric oxide interactions, including reversible inhibition of oxygen consumption. Free Radic Biol Med 34:1488-1503
3. Chen K, Piknova B, Pittman RN et al (2008) Nitric oxide from nitrite reduction by hemoglobin in the plasma and erythrocytes. Nitric Oxide 18:47-60
4. Chen X, Buerk DG, Barbee KA et al (2007) A model of NO/O_2 transport in capillary-perfused tissue containing an arteriole and venule pair. Ann Biomed Eng 35:517-529.
5. Chen X, Jaron D, Barbee KA et al (2006) The influence of radial RBC distribution, blood velocity profiles, and glycocalyx on coupled NO/O_2 transport. J Appl Physiol 100:482-492
6. Deisen DL, Hess DT, Stamler JS (2008) Hypoxic vasodilation by red blood cells: evidence for an S-nitrosothiol based signal. Circ Res 103:545-553
7. Feelisch M, Fernandez BO, Bryan NS et al (2008) Tissue processing of nitrite in hypoxia: an intricate interplay of nitric oxide-generating and -scavenging systems. J Biol Chem 283: 33927-33934
8. Gautier C, van Faassen E, Mikula I et al (2006) Endothelial nitric oxide synthase reduces nitrite anions to NO under anoxia. Biochem Biophys Res Commun 341:816-821
9. Gladwin MT, Grubina R, Doyle MP (2009) The new chemical biology of nitrite reactions with hemoglobin: R-state catalysis, oxidative denitrosylation, and nitrite reductase/anhydrase. Acc Chem Res 42:157-167
10. Isbell TS, Sun C-W, Wu L-C et al (2008) SNO-hemoglobin is not essential for red blood cell-dependent hypoxic vasodilation. Nature Med 14:773-777
11. Li H, Cui H, Kundu TK et al (2008) Nitric oxide production from nitrite occurs primarily in tissues not in the blood: critical role of xanthine oxidase and aldehyde oxidase. J Biol Chem 283:17855-17863
12. van Faassen EE, Bahrami S, Feelisch M et al (2009) Nitrite as regulator of hypoxic signaling in mammalian physiology. Med Res Rev 29:683-741
13. Vitturi DA, Teng X, Toledo JC et al (2009) Regulation of nitrite transport in red blood cells by hemoglobin oxygen fractional saturation. Am J Physiol Heart Circ Physiol 296:H1398-H1407

Chapter 37

Skin SO_2 Measurement Using Visible Lightguide Spectrophotometry in a Black Population: A Feasibility Study

David K. Harrison, André R. Greenidge, and R. Clive Landis

Abstract The aim of the study was to investigate the influence of melanin content on the visible wavelength range spectrophotometric measurement of SO_2 in the skin of normal healthy black and white volunteers. The reactive hyperaemia induced by a 5-minute period of tourniquet occlusion of the brachial artery, as manifested in the change in skin SO_2, was compared with the reactive hyperaemia index (RHI) and arterial stiffness index (AI) as measured using the Endo-PAT2000® peripheral arterial tonometry device. Further measurements were carried out on a diabetic patient with critical ischaemia. The measurements in the normal volunteers and the patient showed that there that there was no correlation between SO_2 and melanin index ($r^2 = 0.02$). There was a poor correlation between the degree of reactive hyperaemia as assessed using tissue SO_2 measurement and the parameters derived using the Endo-PAT2000® device. Measurements on the critically ischaemic lower limb of the diabetic patient revealed a mean medial/lateral SO_2 of 26.3% and a degree of tissue hypoxia (the percentage of recordings with an SO_2 of 15% or less) of 16.2%. This pilot study demonstrated that the measurement of tissue SO_2 in the skin of black subjects is feasible, not only under conditions of normal perfusion, but also in critical limb ischaemia.

David K. Harrison
Regional Medical Physics Department, University Hospital of North Durham, Durham, UK, DH1 5TW
e-mail: d.k.harrison@ncl.ac.uk

André R. Greenidge and R. Clive Landis
Chronic Diseases Research Centre, Tropical Medicine Research Institute, University of West Indies, Bridgetown, Barbados, West Indies

J.C. LaManna et al. (eds.), *Oxygen Transport to Tissue XXXII*, Advances in Experimental Medicine and Biology 701, DOI 10.1007/978-1-4419-7756-4_37,

37.1 Introduction

The diabetic foot syndrome, including lower-extremity amputation (LEA) is a major contributor to morbidity and mortality from diabetes in developed countries [1]. In the developing world there is limited outcome data, but the available evidence suggests that all-cause mortality after diabetes-related LEA may be considerably higher than in developed countries [2-4]. High levels of type-2 diabetes are reported in the Caribbean [5], and the incidence of diabetes-related LEA in Barbados ranks among the highest reported in the world [3,6]. Affordable diagnostic scanning techniques to guide in early detection and surgical intervention of diabetic foot will play a critical role in improving clinical outcomes in this vulnerable group.

Peripheral arterial tonometry is a relatively new tool for the assessment of endothelial function and the Endo-PAT2000®(Itamar Medical, Israel) is one of the leading devices for measuring peripheral artery tone. It is a plethysmographic device that measures the blood volume changes in the fingertips resulting from the post-ischaemic reactive hyperaemia induced by a standard 5-minute period of tourniquet occlusion of the brachial artery [7]. The reactive hyperaemia also results in a transient increase in tissue oxygen saturation (SO_2), which can be measured in the skin using visible lightguide spectrophotometry (RM200 SO_2 Monitor, Whitland Research, Whitland, UK) [8].

The aim of the study was to investigate the influence of melanin content on the visible wavelength range SO_2 monitor used on the skin of normal healthy black and white volunteers. At the same time the reactive hyperaemia, as manifested in the change in skin SO_2 was compared with the reactive hyperaemia index (RHI) and arterial stiffness index (AI) as measured using the Endo-PAT2000® device. In order to investigate whether the techniques were applicable in conditions of severe occlusive arterial disease, further measurements were carried out on a diabetic patient who had already undergone amputation of the left toe due to critical limb ischaemia.

37.2 Methods

Eleven healthy volunteers (age range 21 – 57 yrs) with varying skin melanin contents were recruited for the study which was approved by the Research Ethics Committee of the University of the West Indies. Subjects were seated in a reclining chair in a quiet room at a temperature of approximately 25˚C. The Endo-PAT probes were attached to the index fingers of each hand and the SO_2 probe was attached to the volar forearm of each subject. After a stabilization period of 5 minutes, during which baseline measurements were recorded, an inflatable cuff was applied to the upper arm, at a pressure just above the subject's systolic blood pressure, for 5 minutes. After this time, the cuff was released and measurements continued for a further 5 minutes during recovery from the brachial artery occlusion.

In the diabetic patient, in addition to the reactive hyperaemia measurements, SO_2 measurements were carried out at approximately 1-cm intervals along the right leg from a point 3 cm medial to the tibial tuberosity down to the great toe. In addition, measurements were carried out at positions 3 cm medial and lateral, and 10 cm distal to the tibial tuberosity [8].

In addition to skin SO_2 measurements, the haemoglobin index (HbI) was derived from the absorption spectra [9] and used to calculate the relative oxygen delivery (HbO_2) from the formula:

$$HbO_2 = 100*HbI * SO_2 \tag{37.1}$$

A melanin concentration index was also derived from a sample absorption spectrum recorded on each individual. This was calculated from the slope of the line between the absorptions at 522.9 nm and 585.4 nm, these being the two isosbestic wavelengths between which there is only a small difference in absorption and thus where the difference between them is least sensitive to changes in Hb concentration.

37.3 Results

The relationship between SO_2 and melanin index is shown in Fig. 1(a). and it can be seen that there is no correlation between these parameters. However, Fig. 1(b) clearly shows a very high level of correlation between HbI and melanin index.

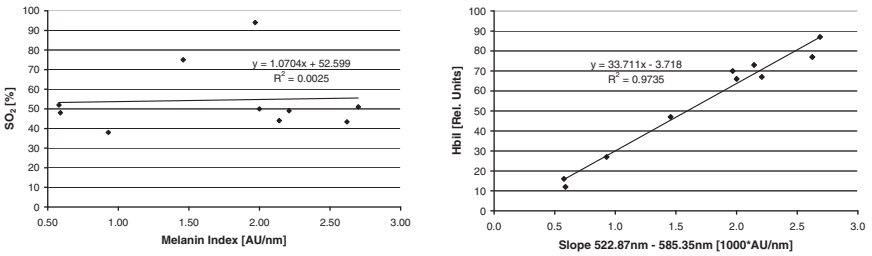

(a) (b)

Fig. 37.1 Relationship between **(a)** SO_2 and **(b)** HbI and melanin index.

Figures 2(a) and (b) show the relationship between the percentage increase in SO_2 (relative to the baseline value) and RHI and AI respectively. There is clearly no linear relationship between the parameters and the best fit polynomial is a quadratic function. Figure 3(a) shows the relationship between the increase in SO_2 and the baseline value. There is a very clear inverse linear relationship between the "starting point" SO_2 and the percentage increase during reactive hyperaemia.

Oxygen saturation has a maximum value of 100% and once this is reached, its value will no longer reflect the level of hyperaemia. A parameter that may reflect

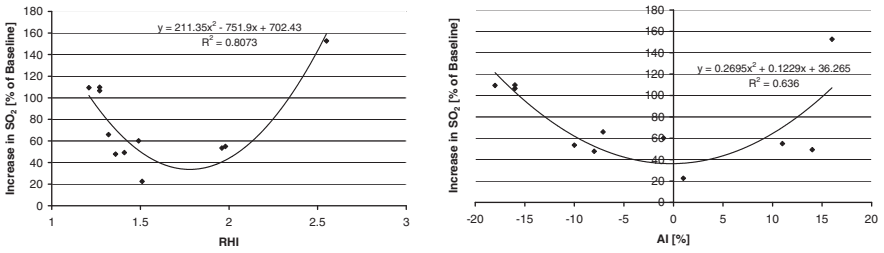

(a) (b)

Fig. 37.2 Relationship between the maximum hyperaemic increase in SO_2 (as percentage of baseline value) and **(a)** RHI and **(b)** AI.

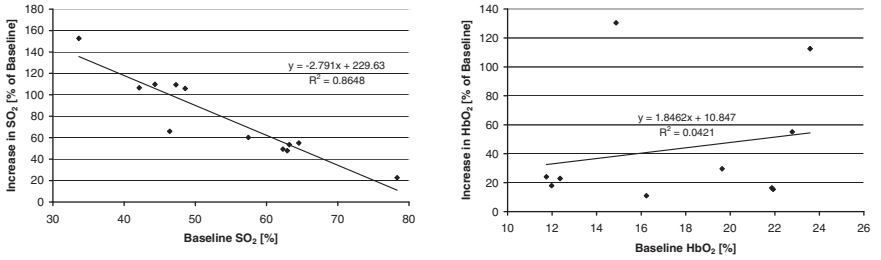

(a) (b)

Fig. 37.3 Relationship between the maximum hyperaemic increase in **(a)** SO_2 and **(b)** HbO_2 (as percentage of baseline value) and the mean pre-hyperaemic baseline value.

hyperaemia more reliably might be oxygen delivery as represented by HbO_2. In order to try and eliminate the melanin effect on the HbI values between subjects, the melanin index was used to normalize the calculated HbO_2 values. In contrast to Fig. 3(a), Fig. 3(b) shows that maximum hyperaemic HbO_2 is not related to the baseline value. Figure 4 shows the relationships between HbO_2 and RHI (a) and AI (b). Again, there is no clear linear relationship between them.

The histograms of the SO_2 measurements along the right forearm and the critically ischaemic right leg of the diabetic patient can be seen in Fig. 5 (a) and (b) respectively. The mean SO_2 along the forearm was 53.8% and the degree of tissue hypoxia was 0%. In contrast, in the right leg, the mean medial/lateral SO_2 was 26.3% and the degree of tissue hypoxia was 16.2%. The melanin index was 2.66 which was the second highest value recorded in these studies.

37.4 Discussion

One aim of this study was to determine to what extent SO_2 could be measured in skin with a high melanin content. Figure 1(a) demonstrates not only that it is possible to

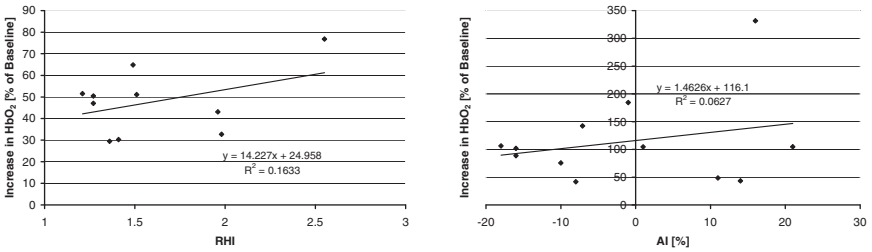

(a) (b)

Fig. 37.4 Relationship between the maximum hyperaemic increase in HbO_2 (as percentage of baseline value) and **(a)** RHI and **(b)** AI.

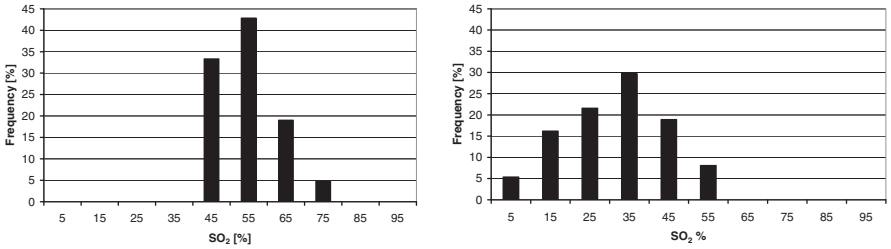

(a) (b)

Fig. 37.5 SO_2 histograms measured along (a) the right forearm and (b) the ischaemic right leg of the diabetic patient.

measure SO_2 in very dark skin, but also that the readings are independent of melanin content. However, the HbI values derived from the absorption spectra are clearly related to melanin content. This is probably due to the fact that the algorithm uses two isosbestic wavelengths to make the correction for melanin concentration, but the wavelength resolution may not be high enough to ensure that the influence of melanin is completely excluded. However, for the purpose of tissue viability assessment, HbI is not used and the independence of SO_2 from the influence of melanin is reassuring.

There was a poor correlation between the degree of reactive hyperaemia as assessed using tissue SO_2 measurement and the parameters derived using the Endo-PAT2000® device. This is due to the fact that oxygen saturation has a maximum value of 100% and once this is reached, its value will no longer reflect the level of hyperaemia. The parameter is very sensitive to changes in perfusion under low blood flow conditions. However, when perfusion is adequate to meet local demands, it changes very little with even quite large changes in perfusion (10). This is confirmed by the relationship shown in Fig. 3(a) where it is evident that the lower the initial baseline SO_2, the greater is the increase during reactive hyperaemia.

The above dependence of the response to reactive hyperaemia upon the baseline level seems to be absent with HbO_2 (Fig. 3(b)), but the relationships with RHI and AI are weak (Fig. 4). This may still be partly due to the fact that the SO_2 component of

Eq. 1 is limited to 100%. However, the different type of vascular control in the volar forearm skin compared with the index finger, where there are acral arterio-venous shunts, may also play a role.

A further aim of this exploratory study was that once the feasibility of measurement of tissue SO_2 had been established in normal dark-skinned individuals, the possibility should be investigated in cases where blood flow may be critically low and where low haemoglobin concentration causes difficulties even in white skin. The patient upon whom the measurements were made, had one of the highest melanin indices of the study. However, it was still possible to obtain recordings in the critically ischaemic limb. The results would indicate that, if the patient had required a lower limb amputation, healing at the below knee level would probably not have been viable [10].

In summary, it is clear from this study that the measurement of tissue SO_2 in the skin of black subjects is feasible, not only under conditions of normal perfusion, but also in critical limb ischaemia. The development of a low-cost SO_2 monitor is indicated for use in developing countries with a high incidence of diabetes and resultant lower limb amputations.

References

1. Bild DE, Selby JV, Sinnock P, Browner WS, Braveman P, Showstack JA (1989) Lower-extremity amputation in people with diabetes. Epidemiology and prevention. Diabetes Care 12:24-31
2. Chaturvedi N, Stevens LK, Fuller JH, Lee ET, Lu M (2001) Risk factors, ethnic differences and mortality associated with lower-extremity gangrene and amputation in diabetes. The WHO Multinational Study of Vascular Disease in Diabetes. Diabetologia 44 Suppl 2:S65-S71,
3. Kidmas AT, Nwadiaro CH, Igun GO (2004) Lower limb amputation in Jos, Nigeria. East Afr Med J 81:427-429,
4. Hambleton IR, Jonnalagadda R, Davis CR, Fraser HS, Chaturvedi N, Hennis AJ (2009) All-cause mortality after diabetes-related amputation in Barbados: a prospective case-control study: Diabetes Care 32:306-7,
5. Hennis A, Wu SY, Nemesure B, Li X, Leske MC (2002) Diabetes in a Caribbean population: epidemiological profile and implications. Int J Epidemiol 31:234-239,
6. Hennis AJ, Fraser HS, Jonnalagadda R, Fuller J, Chaturvedi N (2004) Explanations for the high risk of diabetes-related amputation in a Caribbean population of black African descent and potential for prevention. Diabetes Care 27:2636-2641
7. Kuvin JT, Patel AR, Sliney KA, Pandian NG, Sheffy J, Schnall RP, Karas RH and Udelson JE (2003) Assessment of peripheral vascular endothelial function with finger arterial pulse wave amplitude. Am Heart J 146: 168-748.
8. Harrison DK and Hawthorn IE (2005) Amputation level viability in critical limb ischaemia: Setting new standards. Adv Exp Med Biol: 566: 325-332
9. Harrison DK, Evans SD, Abbot NC, Swanson Beck J and McCollum PT (1992) Spectrophotometric measurements of haemoglobin saturation and concentration in skin during the tuberculin reaction in normal human subjects. Clin Phys & Physiol Meas 13: 349-363
10. Caddick J, Raine C, Harrison D and Erdmann M (2006) Lightguide spectrophotometry to monitor free TRAM flaps. Adv Exp Med Biol: 578: 351-356

Chapter 38
Antioxidant Properties of Quercetin

Mei Zhang, Steven G. Swarts, Liangjie Yin, Chaomei Liu, Yeping Tian, Yongbing Cao, Michael Swarts, Shanmin Yang, Steven B. Zhang, Kunzhong Zhang, Shaoqing Ju, David J. Olek, Jr., Lisa Schwartz, Peter C. Keng, Rob Howell, Lurong Zhang, and Paul Okunieff

Abstract Quercetin, a plant-derived aglycone form of flavonoid glycosides, has been used as a nutritional supplement and may be beneficial against a variety of diseases, including cancer. We examined the antioxidant properties of quercetin. The reduction potential of quercetin was measured at various pH values using voltammetric methods, and its total antioxidant capacity (TAC) was measured using the phosphomolybdenum method. The effect of quercetin on production of reactive oxygen species (ROS) and nitric oxide (NO) in LPS-stimulated human THP-1 acute monocytic leukemia cells was determined by flow cytometry using CM-H2DCFDA dye. The results were compared with curcumin, a natural product exhibiting a similar range of reported health benefits. Results: 1) Quercetin has a higher reduction potential compared with curcumin at three different pH settings and is comparable to Trolox at pH 7-9.5; 2) its TAC is 3.5 fold higher than curcumin; 3) it reduced LPS-induced ROS to near normal levels; 4) it reduced LPS-induced NO production. These data provide a physico-chemical basis for comparing antioxidants, with potential benefits individually or in combination.

38.1 Introduction

Quercetin, a plant-derived flavonoid commonly found in citrus fruit, buckwheat, and onions, has been used in traditional medicine to prevent or treat a variety of dis-

Mei Zhang, Steven G. Swarts, Liangjie Yin, Steven B. Zhang, Lurong Zhang, and Paul Okunieff
Department of Radiation Oncology, University of Florida, 2033 Mowry Road, Box 103633, Gainesville, FL 32610, USA
e-mail: pokunieff@ufl.edu

Chaomei Liu, Yeping Tian, Yongbing Cao, Michael Swarts, Shanmin Yang, Kunzhong Zhang, Shaoqing Ju, David J. Olek, Jr., Lisa Schwartz, Peter C. Keng, and Rob Howell
Department of Radiation Oncology, University of Rochester Medical Center, 601 Elmwood Avenue, Rochester, NY 14642, USA

J.C. LaManna et al. (eds.), *Oxygen Transport to Tissue XXXII*, Advances in Experimental Medicine and Biology 701, DOI 10.1007/978-1-4419-7756-4_38,

eases, such as cancer [1-2], cardiovascular and nervous disorders [3-4], obesity [5], and chronic inflammation [6-8]. Although the biological properties and underlying mechanism of action are largely unknown, the molecular structure of quercetin suggests that it is multi-functional and may act at least in part through a mitochondrial mechanism [9]. Some studies suggest that quercetin's key action is antioxidant [10], while others suggest an anti-inflammation effect. The latter is likely mediated by several mechanisms including inhibition of nuclear factor-kappaB (NF-kappaB) activation and modulation of nitric oxide synthase (iNOS), cyclooxygenase-2 (COX-2), and C-reactive protein (CRP) expression [6-8].

In this study, we used both physical and biological assays to determine the antioxidant capacity of quercetin and its effect on mitochondrial function and NO production under the insult of lipopolysaccharides (LPS).

38.2 Materials and Methods

38.2.1 Reagents, equipment, and cells

THP-1 cells (human acute monocytic leukemia cell line) and quercetin (purity ≥98%, HPLC) were used throughout this study. CM-H2DCFDA {5-(and-6)-chloromethyl-2',7'Œ-dichlorodihydro-fluorescein diacetate acetyl ester} and Calcein AM were purchased from Molecular Probes (Eugene, OR); $CoCl_2$, phosphomolybdenum, and other related chemicals for total antioxidant capacity (TAC) assay and lipopolysaccharides (endotoxin from Escherichia coli 055:B5) were purchased from Sigma-Aldrich (St. Louis, MO); Voltammetry and accessories were purchased from CH Instruments, Inc. (Austin, TX); SpectroMax M2 microplate reader was purchased from Molecular Devices (Sunnyvale, CA); FacStar flow cytometer was purchased from Becton Dickinson Company (San Jose, CA).

THP-1 cells were adjusted to 5 X 10^6/ml and treated with 100 ng/ml of endotoxin and then 50 or 100 μM of quercetin was added. Four hours later, the cells were divided into 100 μl per tube and stained with CM-H2DCFDA or Calcein AM, according to manufacturer's instructions.

38.2.2 Experimental methods and assays

Quercetin's oxidation potentials were measured using square wave voltammetric techniques. Quercetin (2 mg/ml in diemthylsulfoxide) was added to 1.0 ml phosphate buffered saline (pH 7.5). Oxidation potentials were acquired using a three electrode system: a glassy carbon working electrode, a platinum wire counter electrode, and an $Ag^{+2}/AgCl_2$ reference electrode, on an electrochemical analyzer (HCH Instruments, Inc). The anodic scan ranged from -0.9 to 1.0 V in 0.004 V increments (0.025 V

Table 38.1 Oxidation potentials as measured by square wave voltammetry.

Compound	pH 3	pH 7	pH 9.5
Curcumin	0.572 V	0.363 V	0.261 V
Quercetin	0.444 V	0.134 V	-0.017 V
Trolox	0.308 V	0.104 V	0.064 V

Table 38.2 Total antioxidant capacity as measured by phosphomolybdenum.

Compound	Assay 1	Assay 2	Assay 3	Mean	SD
Curcumin	1587.2	1589.2	1570.1	1582.2	10.5
Quercetin	5395.0	5868.5	5631.2	5631.6	236.8

amplitude) at 10-5 A/V sensitivity. Reference standards were Trolox and curcumin. Measurements were conducted at 25°C.

To assay TAC, the phosphomolybdenum method was used: reduction of Mo(VI)-Mo(V) by the test compound to form a green Mo(V) complex, measured at 695 nm. All determinations were performed in triplicate. Antioxidant capacities of curcumin were used as a reference compound for TAC.

For reactive oxygen species (ROS) assay, 100 μl of single cell suspension was incubated with CM-H2DCFDA. Fluorescence intensity was determined by flow cytometry at excitation of 480 nm and emission of 520 nm. Nitric Oxide (NO) concentration in conditioned media was measured with NO detection kits (Oxford Biomedical Research Inc., Oxford, MI) according to manufacturer's instructions. For the transition pore state of mitochondria assay, 5 μl of 2 μM Calcein AM was added to 100 μl of single cell suspension, then 5 μl of 80 mM $CoCl_2$ was added to the tubes, which quenched the cytosolic fluorescence and allowed the mitochondrial fluorescence to maintain, cells were then analyzed by flow cytometry for percentage of green fluorescent cells.

Student's *t* test was used to determine the significance between different treatment groups. P values < 0.05 were regarded as significant.

38.3 Results

Oxidation potentials (Epc) of quercetin were measured under three pH conditions: 3, 7, and 9.5. The potentials are shown in Table 1. Compared with those measured for curcumin and Trolox, the shift towards higher oxidation potentials with increases in pH is consistent with involvement of $^{+}H_3O$ in the oxidation reactions of phenoxy-containing antioxidants [11]. The Epc values for curcumin at pH 7 (0.363 V) and Trolox at pH 3 (0.308 V) differ from those reported elsewhere (0.63 V and 0.28 V, respectively), due to the high content of dimethylsulfoxide in the analysis buffer system that is necessary to dissolve quercetin [9, 10, 12].

Table 38.3 Quercetin reduces LPS-induced reactive oxygen species (ROS).

Agent group	%ROS positive cells	Mean of fluorescent intensity
DMSO alone 100 μM	0.82	14.01
LPS + DMSO 100 μM	11.81	26.55
LPS+Quercetin 100 μM	0.08	13.98
DMSO 50 μM	0.53	14.2
LPS + Vehicle alone 50 μM	7.03	23.09
LPS+Quercetin 50 μM	0.04	15.19

To determine quercetin's antioxidant capacity, the standard TAC assay was performed using a curcumin as reference control. In three independent assays, quercetin consistently demonstrated a higher antioxidant capacity than curcumin ($P < 0.05$) (Table 2).

To determine the antioxidant capacity of quercetin in inflammatory cells, LPS (100 ng/ml) was used to stimulate ROS generation in THP-1 cells. Quercetin or DMSO (vehicle control) was added with LPS. ROS generated was then measured via CM-H2DCFDA staining. LPS stimulated ROS production was reduced by quercetin to almost background level ($P < 0.05$, Table 3). There was no difference of inhibitory effect between 50 μM and 100 μM, indicating that these doses reach the plateau of capacity and a lower dose might still be effective.

Monocytes respond to pathogens or their products (such as LPS) with free radical surges intended to kill pathogens. NO production is one of the free radicals generated upon LPS stimulation. THP1 cells doubled NO production after LPS (Figure 1).

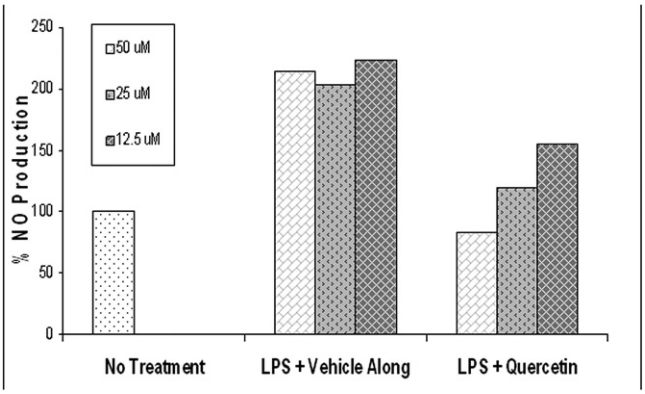

Fig. 38.1 NO production after LPS challenge. Quercetin reduced NO production to baseline levels in a dose-dependent manner.

THP1 cells were exposed to 100 ng/ml of LPS then treated immediately with quercetin or DMSO (vehicle control) for 4 hours. Cells were stained with Calcein AM and cytoplasmic fluorescence quenched with $CoCl_2$. $CoCl_2$ does not pass through

Table 38.4 Quercetin effects on Calcein AM fluorescence in mitochondria.

Treatment group	% positive cells	Mean of fluorescent intensity
DMSO 100 μM	57.46	62.81
LPS + DMSO 100 μM	66.16	69.25
LPS + Quercetin 100 μM	10.66	25.59
DMSO 50 μM	66.21	67.57
LPS + Vehicle 50 μM	70.43	72.14
LPS + Quercetin 50 μM	3.69	13.66

closed pores leading to preserved mitochondrial fluorescence. LPS slightly increased pore opening as evidenced by high positive cell staining, indicating no pore opening. Quercetin dramatically reduced Calcein AM positive stained cells (Table 4).

38.4 Discussion

Quercetin is a common component in many fruits and vegetables. Although the mechanism is not well-defined, high dietary intake of fruits and vegetables is associated with a reduction in cancer [1-2]. Antioxidant properties of quercetin confirmed by our data might partially explain the observed beneficial effect of quercetin. Bioavailability studies of quercetin indicate that after absorption, more than 96% of the ingested amount is excreted within 72 hours [13]. To reach this continuously high level as a food or nutritional supplement, it must have a very low toxicity profile [14-15].

ROS are an unavoidable toxic by-product of cellular energy production. To reduce the harmful impact, biological systems use two general processes: 1) enzymatic conversion of ROS to less toxic or non-active ROS, such as SOD; and 2) direct transfer of ROS to both endogenous antioxidant molecules, such as glutathione, and exogenous antioxidants, such as fruit and vegetable components. Quercetin and curcumin are in the second category. Different antioxidant combinations, with different redox potentials and organelle specificity, will likely be needed to maximally detoxify and export ROS to the extracellular space. For example, the use of quercetin with resveratrol results in a synergistic anti-obesity effect [5].

Voltammetric analysis at pH 7 confirms a high Epc for quercetin, indicating it is a better reducing agent than curcumin. In another assessment of the electron donating properties of quercetin, it was 3.5 fold more effective at reducing phosphomolybdenum from Mo(VI) to Mo(V) than curcumin. These antioxidant properties of quercetin are thought to contribute to the beneficial effect of the compound against LPS stress, as evidenced by the significant reduction in LPS-induced ROS and NO production. Perhaps unexpectedly, quercetin reduced fluorescence of mitochondria in macrophages after LPS. This generally indicates an opening of mitochondrial transition pores, but it can result from inhibition of p-glycoprotein [16].

38.5 Conclusions

In this study, both physical and biological methods were used to evaluate the antioxidant capacity of quercetin. Voltammetric analysis to estimate the electro-donation capacity and TAC are physical assays. Biological assays were performed with a THP-1 human monocytic leukemia cell line, due to its ROS and inflammatory relevance. We believe that these assays are useful and convenient for the study of antioxidant agents. This study shows that quercetin, compared with curcumin, has a very satisfactory antioxidant capacity and biological effects that include inhibition of inflammation and ROS. These properties can partially explain its reported health benefits.

Acknowledgments

This research was supported in part by the Center for Medical Countermeasures against Radiation Program, U19-AI067733, National Institute of Allergy and Infectious Diseases (NIH/NIAID). We thank Dr. David Maguire and Amy K. Huser for thoughtful editing contributions.

References

1. Neuhouser ML (2004) Dietary flavonoids and cancer risk: evidence from human population studies. Nutr Cancer 50(1):1-7
2. Murakami A, Ashida H, Terao J (2008) Multitargeted cancer prevention by quercetin. Cancer Lett 269(2): 315-325
3. Shankar S, Singh G, Srivastava RK (2007) Chemoprevention by resveratrol: molecular mechanisms and therapeutic potential. Front Biosci 12:4839-4854
4. Labinskyy N, Csiszar A, Veress G, et al (2006) Vascular dysfunction in aging: potential effects of resveratrol, an anti-inflammatory phytoestrogen. Curr Med Chem 13:989-996.
5. Yang JY, Della-Fera MA, Rayalam S, et al (2008) Enhanced inhibition of adipogenesis and induction of apoptosis in 3T3-L1 adipocytes with combinations of resveratrol and quercetin. Life Sci 82(19-20):1032-1039
6. Nam NH (2006) Naturally occurring NF-kappaB inhibitors. Med Chem 6:945-951
7. Teixeira S (2002) Bioflavonoids: proanthocyanidins and quercetin and their potential roles in treating musculoskeletal conditions. J Orthop Sports Phys Ther 32(7):357-363.
8. García-Mediavilla V, Crespo I, Collado PS, et al (2007) The anti-inflammatory flavones quercetin and kaempferol cause inhibition of inducible nitric oxide synthase, cyclooxygenase-2 and reactive C-protein, and down-regulation of the nuclear factor kappaB pathway in Chang Liver cells. Eur J Pharmacol 557(2-3):221-229
9. Karbarz M, Malyszko J (2008) Voltammetric behavior of trolox in methanol and ethanol solutions. Electroanalysis 20(17):1884-1890
10. Malyszko J, Karbarz M (2006) Electrochemical oxidation of trolox and a-tocopherol in acetic acid: A comparative study. J Electroanal Chem 595:136-144
11. Timbola AK, de Souza CD, Giacomelli C, et al (2006) Electrochemical oxidation of quercetin in hydroalcoholic solution. J Braz Chem Soc 17:139-148

12. Jovanovic SV, Steenken S, Boone CW, et al (1999) H-Atom Transfer Is A Preferred Antioxidant Mechanism of Curcumin. J Am Chem Soc 121:9677-9681
13. Mullen W, Rouanet JM, Auger C, et al (2008) Bioavailability of [2-(14)C]quercetin-4'-glucoside in rats. J Agric Food Chem 2456(24):12127-12137.
14. Verschoyle RD, Steward WP, Gescher AJ (2007) Putative cancer chemopreventive agents of dietary origin-how safe are they? Nutr Cancer 59(2):152-162.
15. van der Woude H, Alink GM, van Rossum BE, et al (2005) Formation of transient covalent protein and DNA adducts by quercetin in cells with and without oxidative enzyme activity. Chem Res Toxicol 18(12):1907-1916
16. Sun W, Wang W, Kim J, et al (2008) Anti-cancer effect of resveratrol is associated with induction of apoptosis via a mitochondrial pathway alignment. Adv Exp Med Biol 614:179-186

Chapter 39

Antioxidant Properties of Select Radiation Mitigators Based on Semicarbazone and Pyrazole Derivatives of Curcumin

Steven G. Swarts, Mei Zhang, Liangjie Yin, Chaomei Liu, Yeping Tian, Yongbing Cao, Michael Swarts, David J. Olek, Jr., Lisa Schwartz, Louie Zhang, Shanmin Yang, Steven B. Zhang, Kunzhong Zhang, Shaoqing Ju, Sadasivan Vidyasagar, Lurong Zhang, and Paul Okunieff

Abstract Fifty-eight semicarbazone and pyrazole derivatives of curcumin have been developed as potential mitigation agents to treat acute radiation syndrome (ARS). Pyridyl (D12, D13), furyl (D56), and phenyl (D68) derivatives of curcumin semicarbazones were found to provide the highest dose modifying factors (DMF) with respect to survival in sub-TBI (bone marrow sparing) exposures in mouse models. To investigate the basis for the mitigating effects of these agents on ARS, we examined their oxidation potentials and radical scavenging properties in comparison to other semicarbazone and pyrazole curcumin derivatives with less effective DMFs. Comparisons between D12, D13, D56, and D68 and other semicarbazone and pyrazole derivatives of curcumin did not show a sufficient difference in reducing properties and hydrogen atom donating properties for these properties to be the basis of the dose modifying activities of these compounds. Therefore, their DMFs likely reflect structure-activity relationship(s), wherein interaction with key receptors or alteration of enzyme expression result in modifications of cellular or tissue responses to radiation, rather than on the derivatives' ability to modify radiation-induced flux of free radicals through direct interaction with these radicals.

Steven G. Swarts, Mei Zhang, Liangjie Yin, Steven B. Zhang, Sadasivan Vidyasagar, Lurong Zhang, and Paul Okunieff
Department of Radiation Oncology, University of Florida, 2033 Mowry Road, Box 103633, Gainesville, FL 32610
e-mail: sgswarts@ufl.edu

Chaomei Liu, Yeping Tian, Yongbing Cao, Michael Swarts, David J. Olek, Jr., Lisa Schwartz, Louie Zhang, Shanmin Yang, Kunzhong Zhang, and Shaoqing Ju
Department of Radiation Oncology, University of Rochester Medical Center, 601 Elmwood Ave., Box 647, Rochester, NY 14642

J.C. LaManna et al. (eds.), *Oxygen Transport to Tissue XXXII*, Advances in Experimental Medicine and Biology 701, DOI 10.1007/978-1-4419-7756-4_39,

39.1 Introduction

Concern over potential mass casualties from deliberate radiation or nuclear events led to development of treatment strategies for acute radiation syndrome or ARS [1]. These include use of modified cytokines and novel anti-inflammatory agents to enhance preservation of function in radiation sensitive organ systems, e.g., gastrointestinal tract or hematopoietic systems. Curcumin is one potential radiation mitigation agent, due in part to its antioxidant and anti-inflammatory properties. This natural compound has been shown to reduce the acute and chronic effects of exposure to ionizing radiation [2, 3]. However, there are limits to the use of curcumin in this context given its susceptibility to hydrolysis at basic and neutral pH. Its half-life at neutral pH (phosphate buffer) is < 10 min) [4]. In an attempt to improve curcumin's radiation modifying properties, while increasing its stability to hydrolysis, synthetic derivatives of curcumin were made and tested for chemical and biological properties. Modification of curcumin's α,β-unsaturated 1,3-diketone moiety, as semicarbazone and pyrazole derivatives, improved the antioxidant and anti-inflammatory properties over curcumin [5, 6]. We refined the synthetic modifications of curcumin semicarbazone and pyrazole, adding substituted phenyl and heterocyclic aromatic groups to these base structures to further change the electron withdrawing and electron donating properties of curcumin derivatives.

Reducing and radical scavenging properties of curcumin derivatives are summarized and compared to their dose-modifying effects on survival in partial body (bone marrow sparing) irradiated mouse models, to test whether radiation mitigating effects of derivatives reflect reducing and/or radical scavenging properties.

39.2 Methods

Substituted curcumin semicarbazones were synthesized by reaction of curcumin and substituted hydrazides using a modification of the Furniss et al. [7] method. The R1 group in Figure 1 represents various aromatic substituents (i.e., phenyl, pyridyl, furyl, thiofuryl, imidazolinyl, etc.). Phenyl substituted curcumin semicarbazones are further substituted by addition of electron withdrawing (4-NO_2, 2-NO_2, and 4-CF_3) or donating (4-OH, 3-OH, 4-NH_2, 4-OCH_3-2-OH, 2-Cl, 4-Cl, 4-CH_3, 4-$C(CH_3)_3$) functional groups on the phenyl ring. In another approach, we synthesized substituted curcumin pyrazoles by reacting curcumin with substituted hydrazines using modifications to the Amolins et al. [8] method. The R2 group in Figure 1 represents various aromatic substituents (e.g., phenyl, benzyl, pyridyl, furyl, thiofuryl, imidazolinyl, etc.). Phenyl substituted curcumin pyrazoles are further substituted by addition of electron withdrawing (2-COOH, 4-COOH, 4-NO_2, 3-NO_2, 2-NO_2, 2,4-diNO_2, 2-CF_3, 3-CF_3, 4-CF_3) or donating (4-OCH_3, 4-CH_3, 2-CH_3, 3,5-diF, 4-I, 4-OCF_3) groups on the phenyl ring.

Oxidation potentials of curcumin derivatives were measured using square wave voltammetric techniques. Derivatives (2 mg/ml in diemthylsulfoxide) were added

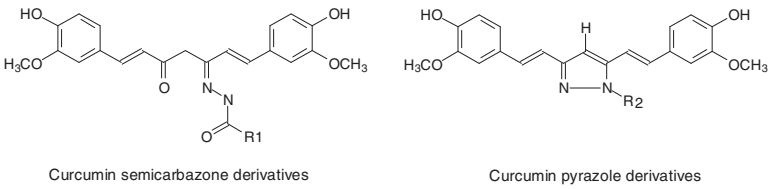

Fig. 39.1 Base structures of curcumin derivatives.

at volumes of 0.66 ml to 1.0 ml phosphate buffered saline (pH 7.5). Oxidation potentials were acquired using a 3-electrode system, glassy carbon working electrode, platinum wire counter electrode, and $Ag^{+2}/AgCl_2$ reference electrode, on an electrochemical analyzer (HCH Instruments). The anodic scan ranged from -0.9 to 1.0 V in 0.004 V increments. Trolox and curcumin were used as reference standards. Three independent measurements were conducted at 25^{o}C; relative standard deviation was $< 1\%$.

The curcumin derivatives were evaluated for their total antioxidant capacity (TAC) by reducing phosphomolybdenum from the Mo(IV) to Mo(V) oxidation states [9]. Curcumin and derivatives (0.3 mM) in DMF were combined with 0.7 ml of reagent solution (0.6 M sulfuric acid, 28 mM sodium phosphate and 4 mM ammonium molybdate). In separate tubes, 1000 μM ascorbic acid was added as a reference. Samples were heated to 95˚C for 90 minutes, cooled to room temperature, and absorbance of the Mo(V) oxidation state was measured at 695 nm. All determinations were done in triplicate. TAC values were calculated based on the ratio of the absorbances of the test compound to ascorbic acid and expressed as ascorbic acid equivalents (in μM).

Hydrogen donating or radical scavenging ability of curcumin and its derivatives were evaluated by measuring rates of reaction with the DPPH radical (2,2-diphenyl-1-picrylhydrazyl) relative to Trolox [10]. Briefly, curcumin and its derivatives were dissolved in methanol containing DPPH (500 μM) to concentrations ranging from 50 to 250 μM. After a 30-minute reaction in the dark at 37 ^{o}C, the absorbance was measured at 515 nm. Trolox was used as a reference standard. All determinations were performed in triplicate. Percentage inhibition (PI) was calculated following the equation: PI = [1-(Ab_{515} sample/Ab_{515} control)]*100. The IC_{50} value (inhibition concentration of sample at 50% fall in absorbance of DPPH) was used to compare DPPH scavenging activity. Results were expressed as ratios of IC_{50} values of derivatives relative to curcumin.

39.3 Results and Discussion

In an effort to find radiation mitigation agents that incorporate the antioxidant behaviors of curcumin, yet provide improved stability to hydrolysis, we designed a series of curcumin derivatives that are chemically modified at the α,β-unsaturated 1,3-diketone moiety. These derivatives are based on addition of a semicarbazone or

pyrazole function at this position. The semicarbazone derivative has shown improved antioxidant activity over curcumin [5]; whereas, the pyrazole derivative has similar antioxidant activity to curcumin but increased anti-inflammatory activity based on inhibition of the cyclooxygenase enzymes, COX-1 and COX-2 [6].

We further modified the curcumin semicarbazone and pyrazole derivatives through addition of aromatic functions that are expected to modify antioxidant properties of substituted derivatives by: 1) extending the pi system in the molecule, thereby increasing resonance stabilization of the free radical intermediates of these compounds; and 2) altering electron withdrawing or donating properties of the semicarbazone and pyrazole functions. One expected benefit of forming the semicarbazone and pyrazole derivatives is enhanced stability to hydrolysis at neutral pH, with half-lives typically > 72 hours at 37^{o}C, compared with < 10 minutes for curcumin at the same temperature [4].

When screened for ability to increase survival after partial body (bone marrow sparing) radiation exposures (8.5-12 Gy) in BALB/c mice, only four of 58 curcu-min derivatives provided dose modifying factors > 1 when the agents were given in daily oral doses post-irradiation. Structures of these four compounds are shown in Figure 2. In total body irradiation studies, DMF of > 1 was not achieved for curcumin or any derivatives.

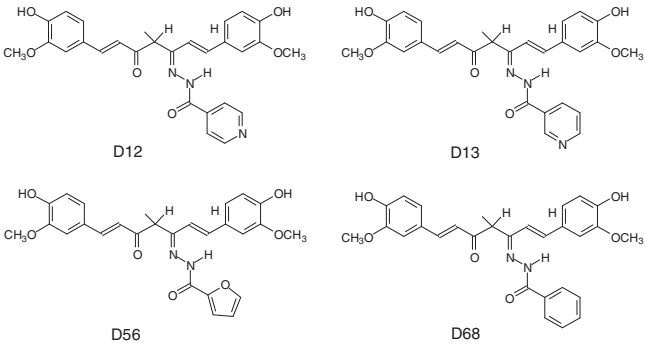

Fig. 39.2 Structures of bioactive curcumin derivatives.

To understand the basis for the mitigating effects of D12, D13, D56, and D68, we conducted a survey of the antioxidant properties of these four compounds in comparison to the other curcumin semicarbazone and pyrazole derivatives. Oxidation potentials (E_{pa}) for curcumin, its semicarbazone and pyrazole derivatives, and Trolox were measured at pH 7-7.5 (Table 1). The E_{pc} values did not differ significantly ($P > 0.05$) between substituted semicarbazone and pyrazole derivative classes, nor between various electron donating or electron withdrawing substituents in each class. However, average potentials for these two classes of derivatives were 60-90 mV lower than curcumin. Thus, chemical alteration of the 1,3-diketone function in curcumin to form electron-rich semicarbazone and pyrazole derivatives lowered the derivatives' oxidation potential relative to the parent (curcumin), but further modification of these

Table 39.1 Summary of reducing and radical scavenging properties of substituted curcumin semicarbazones and pyrazoles reported as mean with minimum and maximum values in parentheses.

Compound	Voltammetry (mV)	TAC[d]	DPPH[e]
Semicarbazones[a,c]			
e^- donating	272 (261-291)	2852 (1099-3380)	0.627 (0.570-0.677)
e^- withdrawing	272 (264-284)	2850 (1799-3362)	0.512 (0.401-0.584)
Pyrazoles[b,c]			
e^- donating	298 (260-358)	2326 (1290-3076)	0.812 (0.577-1.20)
e^- withdrawing	299 (232-394)	2093 (1476-4388)	0.877 (0.554-1.19)
D12[f]	308	1718	0.674
D13[f]	285	3177	0.600
D56[f]	269	3380	0.677
D68[f]	268	3240	0.595
Curcumin[f]	363	1582	1.00

a. Mean value from 5 (e^- donating) and 11 (e^- withdrawing) derivatives
b. Mean value from 6 (e^- donating) and 14 (e^- withdrawing) derivatives
c. Minimum and maximum values in parentheses
d. Expressed as ascorbic acid equivalents (in μM)
e. Expressed as the ratio of the IC_{50} values for the derivatives relative to curcumin
f. Mean value from triplicate measurements; relative standard deviations $< 5\%$

functions through addition of electron donating or withdrawing aromatic functions had a negligible affect on these potentials.

Further examination of reducing properties of curcumin derivatives involved assessing the relative ability of these compounds to reduce Mo(VI) to Mo(V) by reference to ascorbic acid through a TAC assay. Curcumin semicarbazones were found to be more effective than pyrazoles ($P < 0.05$) at reducing Mo(VI) to Mo(V) (Table 1). Also, both classes of derivatives were more effective ($P < 0.05$) than curcumin at reducing Mo(IV). As observed in the electrochemistry study, the substituent groups on the semicarbazone or pyrazole function did not significantly alter the ability of derivatives to reduce Mo(VI). In addition, only 3 of 4 potential radiation mitigation agents gave ascorbic acid equivalent values in the upper quartile of semicarbazone derivative values. This mirrors the measured oxidation potentials, where D13, D56, and D68 also had lower potentials than D12.

Another antioxidant property examined was the relative ability of curcumin derivatives to scavenge DPPH radicals. Semicarbazone derivatives showed, on average, higher reactivity toward DPPH radicals than pyrazole derivatives (Table 1). Unlike voltammetry and TAC analyses, significant differences were shown in reactivities between electron withdrawing and donating substituents within semicarbazone but not pyrazole derivatives. However, both derivative classes showed higher average reactivity with the DPPH radical than curcumin. This increased reactivity over curcumin is likely the result of increased resonance stabilization of resulting curcumin semicarbazone and pyrazole radicals. However, reactivities of D12, D13, D56, and D68 with DPPH were not significantly different from other curcumin derivatives, as

would be expected if radical scavenging properties of the four derivatives were the basis for their dose modification properties.

39.4 Conclusion

The reducing and radical scavenging properties of four curcumin derivatives (D12, D13, D56, and D68) were not significantly different from other curcumin derivatives. Thus, it is not expected that sufficient differences exist between them and other curcumin derivatives in their ability to directly modify radiation-induced radical levels, suggesting these antioxidant properties are not the basis for dose modifying activities of the four derivatives. These derivatives have yet to be assessed for ability to scavenge other radicals, such as superoxide radicals and the nitroxide radical. Since these four derivatives are formed from curcumin, it is likely that they have other effects that could indirectly influence radical levels, including increased antioxidant enzyme expression and/or decreased oxidant enzyme expression, as observed for curcumin [2, 3]. These derivatives could also have anti-inflammatory effects, as shown for curcumin pyrazoles, which are based on inhibition of COX 1 and COX 2 [6]. However, similar COX inhibition has yet to be shown for curcumin semicarbazone derivatives. Thus, additional radical scavenging and biological activities will need to be assessed for the curcumin semicarbazone and pyrazole derivatives in order to elucidate the basis of the dose modifying effects.

Acknowledgments

The authors gratefully acknowledge funding of this work by the Centers for Medical Countermeasures against Radiation Program (U19-AI067733) from the National Institute of Allergy and Infectious Diseases (NIAID/NIH). We also thank Dr. David Maguire and Amy K. Huser for thoughtful editing contributions.

References

1. Jarrett DG, Sedlak RG, Dickerson WE, Reeves GI (2007) Medical treatment of radiation injuries - Current US status. Radiat Meas 42:1063-1074
2. Jagetia GC (2007) Radioprotection and radiosensitization by curcumin. Adv Exp Med Biol 595:301-320
3. Venkatesan N, Punithavathi D, Babu M (2007) Protection from acute and chronic lung diseases by curcumin. Adv Exp Med Biol 595:379-405
4. Wang Y-J, Pan M-H, Cheng A-L, Lin L-I, Ho Y-S, Hsieh C-Y, Lin J-K (1997) Stability of curcumin in buffer solutions and characterization of its degradation products. J Pharm Biomed Anal 15:1867-1876

5. Dutta S, Padhye S, Priyadarsini KI, Newton C (2005) Antioxidant and antiproliferative activity of curcumin semicarbazone. Bioorg Med Chem Lett 15:2738-2744
6. Selvam C, Jachak SM, Thilagavathi R, Chakraborti AK (2005) Design, synthesis, biological evaluation and molecular docking of curcumin analogues as antioxidant, cyclooxygenase inhibitory and anti-inflammatory agents. Bioorg Med Chem Lett 15:1793-1797
7. Furniss BS, Hanneford AJ, Smith WG, Tatchell AR: Vogel's Text book of Practical Organic Chemistry, 5th Edition, Longman Publishers Pvt. Ltd.: 1989
8. Amolins MW, Peterson LB, Blagg BSJ (2009) Synthesis and evaluation of electron-rich curcumin analogues. Bioorg Med Chem 17:360-367
9. Prieto P, Pineda M, Aguilar M (1999) Spectrophotometric quantitation of antioxidant capacity through the formation of a Phosphomolybdenum Complex: Specific application to the determination of vitamin E. Analytical Biochem 269:337-341
10. Lamaism JI, Ptitjean-Freytet C, Carnet A (1991) DPPH scavenging activity. Pharm Acta Helv 66:185-188

Part XI
Gas Transport

Chapter 40
Impact of Intracellular Diffusion of Oxygen in Hypoxic Sensing

Eiji Takahashi and Michihiko Sato

Abstract Hypoxia-inducible factor 1 (HIF-1) is the key to genetic adaptations to hypoxia in eukaryotes. In vivo, capillary pO_2 and extracellular- and intracellular-O_2 gradients define pO_2 at the O_2 labile subunit HIF-1α. With a novel technique for subcellular imaging of O_2 heterogeneity using GFP, the present study was undertaken to examine the possibility that changes in mitochondrial respiration significantly affect intracellular O_2 gradients and thus, HIF-1 expression. We failed to demonstrate consistent changes in intracellular O_2 distributions in cultured cells with different metabolic and morphological properties (COS-7, Hep G2, and Hep3B cells) while mitochondrial O_2 consumption was widely changed at 1% O_2. Thus, we conclude that conductance for intracellular diffusion of O_2 is high in these cells and intracellular O_2 gradients might not be involved in the regulation of HIF-1 expression in vivo.

40.1 Introduction

Hypoxia-inducible factor 1 (HIF-1) is a ubiquitously expressed transcription factor. HIF-1 mediates reductions of cellular O_2 concentration and evokes a series of genetic responses, including erythropoiesis and angiogenesis, which enhance tissue O_2 supply by blood. In addition, HIF-1 appears to shift energy metabolism from oxidative phosphorylation to anaerobic glycolysis by upregulating the glucose transporter and glycolytic enzymes while actively suppressing oxidative phosphorylation (for recent review see [1]).

Oxygen deprivation at the cellular level stabilizes HIF-1's oxygen labile α-subunit. The putative oxygen-sensing molecule involved in this process is enzymes prolyl-

Eiji Takahashi
Department of Physiology, Yamagata University School of Medicine, Yamagata, Japan
e-mail: eiji@med.id.yamagata-u.ac.jp

Michihiko Sato
CLRE, Yamagata University School of Medicine, Yamagata, Japan

J.C. LaManna et al. (eds.), *Oxygen Transport to Tissue XXXII*, Advances in Experimental Medicine and Biology 701, DOI 10.1007/978-1-4419-7756-4_40,

4-hydroxylases (PHDs) that use oxygen as a cosubstrate. PHD2, probably the most active among PHDs in hypoxic regulation of HIF-1α, has been detected in the cytoplasm and nucleus [2]. Oxygen dependence (K_m) of PHD2 determined in vitro is in the range of 53-250 μM [2]. Thus, this molecule responds to changes in intracellular O_2 concentration in vivo.

In vivo, O_2 concentration at PHD2 is determined by capillary pO_2 and extracellular- and intracellular-O_2 gradients, the latter depending on O_2 flux to mitochondria. Inhibition of PHDs in neonatal cardiomyocytes [3] and in mouse skeletal muscle fibers [4] or induction of HIF-1α in cultured cells including cancer cell lines [5, 6] has been demonstrated to considerably suppress mitochondrial respiration. Elevation of intracellular pO_2 as a result of this down regulation of mitochondrial respiration may increase O_2 concentration at PHD2 and thus hydroxylation of HIF-1α. Therefore, in vivo induction of HIF-1α appears to be under the negative feedback regulation through diffusional O_2 gradients.

In the present study, using mitochondria specific GFP as an intracellular O_2 probe, we attempted to visualize heterogeneities of intracellular O_2 in cultured cells with different metabolic and morphological properties. We examined the possibility that the intracellular O_2 gradients might be involved in the regulation of HIF-1α.

40.2 Methods

Three cell lines, COS-7 (African green monkey kidney fibroblast-like cell), Hep3B (human hepatocellular carcinoma), and Hep G2 (human hepatocellular carcinoma), were separately cultured on a 13.5 mm diameter 0.1 mm thickness low-fluorescent polystyrene disk (Cell Disk LF, Sumilon) in 35 mm culture dishes. The shape of the cells was characterized using a phase contrast microscope ($\times$20 object lens, IX71, Olympus). In addition, thickness of the individual cell was determined using a confocal laser microscope (LSM5 Pascal, Zeiss) in GFP (AcGFP, Clontech) expressing cells.

Heterogeneities of O_2 concentration within a single cell were assessed using GFP as an O_2 probe [7]. A GFP expression vector with a mitochondria-targeting sequence (pAcGFP1-Mito, Clontech) was introduced in the cell using a linear polyethylenimine derivative (jetPEI, Polyplus-transfection). Before the experiment, cells on the cell disk were covered with 73 μl hepes-buffered DMEM without containing phenol red (PromoCell) and transferred to the airtight measuring cuvette. The medium was superfused at 3 ml/min with humidified gas containing 0-21% O_2 in N_2. Temperature was regulated at 37˚C. After equilibration to the superfusion gas for 20 min, cells were illuminated with a strong blue light (470-490 nm) using epifluorescence optics in the microscope ($\times$60 object lens, 75-W xenon arc lamp, neutral density filter removed) for 1 min (photo activation, PA). Cell images were captured before and immediately after a PA using a 16-bit CCD camera (SV512, PixelVision). Hypoxia-induced red shift of GFP fluorescence spectrum was evaluated by the ratio of the red fluorescence (F_{595}, excitation 525 nm, emission 595 nm, 0.6 sec exposure) and green

fluorescence (F_{510}, excitation 475 nm, emission 510 nm, 0.2 sec exposure). Before calculating the ratio image, haze in the fluorescence images was reduced using a mathematical filter. Mitochondria vigorously move and change position within the cell at each individual fluorescence measurement. To avoid such motion artifacts, a binarized mask image was generated using a pair of red and green fluorescence images that was subsequently applied to the ratio image. The red shift was related to O_2 concentration of the superfusion gas where cells were treated with 2 mM KCN to abolish O_2 gradients between the superfusion gas and mitochondrial matrix where GFP is expressed.

40.3 Results

The red fluorescence (F_{595}) was negligible (~4% of F_{510}) in GFP expressing cells. F_{595}/F_{510} of purified protein AcGFP1 in PBS did not change significantly when the buffer pH was varied from 6 to 8. In hypoxia, F_{595} was significantly increased after a one-minute photo activation while F_{510} was diminished (Fig. 1A). Figure 1B illustrates the relationship between superfusion O_2 and the red shift (F_{595}/F_{510}) in 2 mM KCN treated Hep3B and Hep G2 cells. The red shift was significant at $< 2\%$ O_2 and was progressively increased as O_2 concentration further decreased. Thus, the present technique allows detection of changes in intracellular O_2 at physiologically relevant O_2 levels.

Based on the sensitivity of the red shift to O_2 concentration changes (Fig. 1B), imaging of intracellular O_2 was conducted at 1% O_2. We also calculated the width of F_{595}/F_{510} histogram (W_{50}, Fig. 1C) and converted it in $\%O_2$ (W'_{50}) using the titration curve shown in Fig. 1B to quantitatively assess the heterogeneity.

Among the 3 cells studied, Hep G2 cell is the smallest in cross-section but the most thick (average thickness of COS-7, Hep G2, and Hep3B cells was 13.4 μm, 25.8 μm, and 19.6 μm, respectively, n=5). Figure 2 demonstrates red shift imaging in Hep G2 cells where F_{595}/F_{510} was indicated in shades of gray. Because of inherent variability in the ratio value, the histogram width (W'_{50}) in the KCN treated cell (with little heterogeneity of intracellular O_2) corresponded to 0.78% O_2. A normally respiring cell (left) showed a similar variability in F_{595}/F_{510} ($W'_{50} = 0.72\%$ O_2). We failed to consistently demonstrate spatial patterns in F_{595}/F_{510} that can be predicted from intracellular O_2 diffusion (i.e., increases in F_{595}/F_{510} toward the cell core). Finally, we used an uncoupler of oxidative phosphorylation (1 μM CCCP) to stimulate mitochondrial respiration, because increases in intracellular O_2 flux should augment O_2 heterogeneity in the cell. As shown in Fig. 2 (right), the distribution of F_{595}/F_{510} was unpredictable and the magnitude of variations appeared to be comparable to that of the KCN treated cell (left). W'_{50} in this CCCP treated cell was 0.68% O_2.

These results are similar in COS-7 and Hep3B cells in which treatment with CCCP did not consistently increase the variability in F_{595}/F_{510} compared to the KCN treated cells (data not shown). Thus, the present results are not compatible

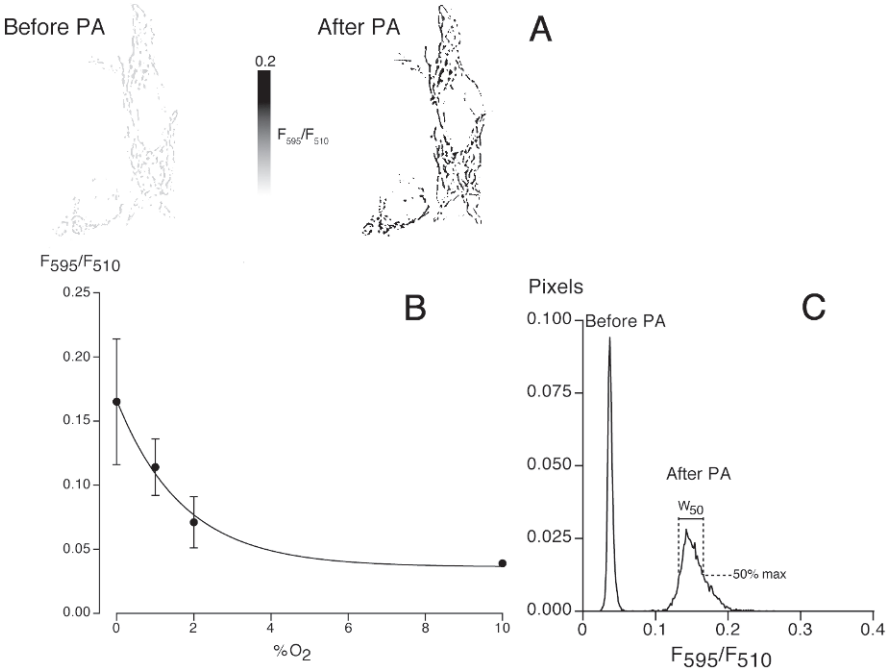

Fig. 40.1 A. Photo activation (PA) elevated red fluorescence (F_{595}) in GFP fluorescence in a COS-7 cell superfused with $< 0.001\%$ O_2. B. Titration curve indicating O_2 dependency of the red shift (F_{595}/F_{510}). Data were collected from Hep G2 and Hep3B cells and indicated in mean±SD. C. Heterogeneity of the red shift was evaluated by the width of F_{595}/F_{510} histogram.

with the hypothesis that mitochondrial respiration significantly affects intracellular O_2 through diffusional gradients within a cell.

40.4 Discussion

Several studies attempted to show the causal relationship between mitochondrial O_2 consumption and intracellular O_2/HIF-1 expression. In these studies, intracellular O_2 in cultured cells was assessed using pimonidazole [6, 8] or a near-infrared O_2 probe [9] while manipulating mitochondrial O_2 consumption. Because these O_2 measurements were conducted in cells cultured in conventional plastic dishes, the extracellular fluid layer appeared considerably thick (2.5-5 mm [8]) compared to in vivo tissues. Therefore, changes in intracellular O_2 level in these experiments most likely arose from changes in the extracellular O_2 gradients that also vary according to the experimental condition. To accurately define the role of diffusional O_2 transport in HIF-1 induction, O_2 gradients in the intracellular space must be specifically addressed.

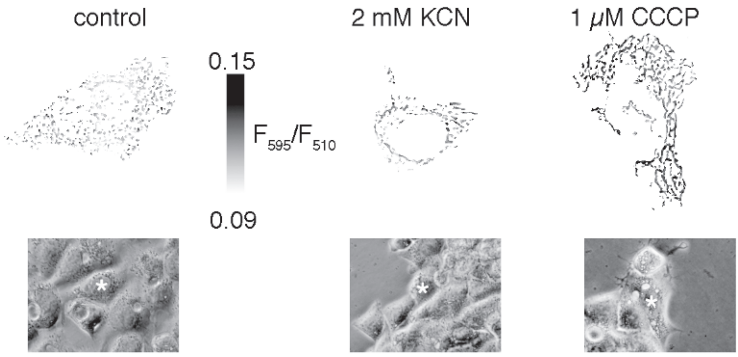

Fig. 40.2 Imaging of the red shift in Hep G2 cells superfused with 1% O_2 (upper panels). F_{595}/F_{510} is represented in shades of gray. Lower panels represent respective phase contrast images where the measured cell is indicated by an asterisk. Values for W'_{50} in % oxygen are 0.72, 0.78, and 0.68 for control, KCN, and CCCP cells, respectively.

Initially, we had expected gradients of F_{595}/F_{510} along the oxygen diffusion path in cells in which oxygen flux was significantly increased by 1 μM CCCP. We had also expected that the gradients might be detectable in Hep G2 cells, if not in COS-7 or Hep3B cells, because Hep G2 cells are thick (average thickness 25.8 μm) and the effect of vertical diffusion of O_2 from the culture medium through the top surface of cells may be ignored. However, we failed to demonstrate gradients of F_{595}/F_{510} consistent with the O_2 diffusion path that was predicted from spatial arrangements of the cell (see phase contrast images in bottom panels in Fig. 2). Variability of F_{595}/F_{510} was indistinguishable from those of the control and KCN treated cells.

In the present experimental model, the bottom of the cells firmly attaches to the O_2 impermeable cell disk and thus O_2 diffusion from the bottom surface of the cell can be ignored. On the other hand, the top surface of cells is exposed to culture medium and diffusional O_2 supply from the top surface cannot be ignored, particularly in thin cells such as COS-7 cell. The present results may indicate the possibility that vertical O_2 diffusion abolished the radial intracellular gradients of O_2 and, therefore, in the present experimental model, the conventional monolayer cell culture is inappropriate to address the intracellular gradients of O_2. However, unlike COS-7 cell, Hep G2 cell is very thick and the shape is nearly a cube. Thus, if there is a radial intracellular gradient of O_2 (parallel to the top/bottom surfaces), O_2 gradients should also be established in the direction from the top to the bottom.

Alternatively, the present results may indicate the possibility that resistance for intracellular diffusion of O_2 might be negligible in these cells. Oxygen concentration at O_2 sensor molecule, PHD, is determined in part by extracellular- and intracellular-O_2 gradients while magnitude of O_2 gradients is proportional to O_2 flux. Thus, remarkable downregulation of mitochondrial respiration as a consequence of hypoxic induction of HIF-1 may reduce O_2 gradients and elevate pO_2 at PHD [8-12]. However, the magnitude of O_2 gradients also depends upon the intracellular diffusion resistance to O_2. The present results appear to indicate that the conductance for O_2 diffusion

in the intracellular space of these cells is high and changes in mitochondrial O_2 consumption exert little effect on intracellular pO_2 gradients.

In most solid tumors, a significant portion of the tissue is hypoxic/anoxic. Vaupel [13] pointed out that one of the major mechanisms involved in emergence of hypoxic cells in solid tumors is perfusion-limited delivery of O_2. Mismatch of O_2 supply/consumption happens mainly due to disorganized formations of capillary network in tumor tissues. If so, HIF-1-induced downregulation of mitochondrial respiration would elevate O_2 concentration at PHD by restoring O_2 supply/consumption imbalance in the hypoxic loci. Although this mechanism is different from the initially hypothesized scheme of regulation, it certainly addresses the relevance of mitochondrial respiration in in vivo regulation of HIF-1 in perfusion-limited tissues.

References

1. Semenza GL (2009) Regulation of oxygen homeostasis by hypoxia-inducible factor 1. Physiology (Bethesda) 24:97-106
2. Berchner-Pfannschmidt U, Tug S, Trinidad B et al (2008) Nuclear oxygen sensing: induction of endogenous prolyl-hydroxylase 2 activity by hypoxia and nitric oxide. J Biol Chem 283:31745-31753
3. Sridharan V, Guichard J, Li CY et al (2008) O_2-sensing signal cascade: clamping of O_2 respiration, reduced ATP utilization, and inducible fumarate respiration. Am J Physiol Cell Physiol 295:C29-C37
4. Aragonés J, Schneider M, Van Geyte K et al (2008) Deficiency or inhibition of oxygen sensor Phd1 induces hypoxia tolerance by reprogramming basal metabolism. Nat Genet 40:170-180
5. Lu CW, Lin SC, Chen KF et al. (2008) Induction of pyruvate dehydrogenase kinase-3 by hypoxia-inducible factor-1 promotes metabolic switch and drug resistance. J Biol Chem 283: 28106-28114
6. Papandreou I, Cairns RA, Fontana L et al (2006) HIF-1 mediates adaptation to hypoxia by actively downregulating mitochondrial oxygen consumption. Cell Metab 3:187-197
7. Takahashi E, Takano T, Nomura Y et al (2006) In vivo oxygen imaging using green fluorescent protein. Am J Physiol Cell Physiol 291:C781-C787
8. Doege K, Heine S, Jensen I et al (2005) Inhibition of mitochondrial respiration elevates oxygen concentration but leaves regulation of hypoxia-inducible factor (HIF) intact. Blood 106:2311-2317
9. O'Hagan KA, Cocchiglia S, Zhdanov AV (2009) PGC-1α is coupled to HIF-1α-dependent gene expression by increasing mitochondrial oxygen consumption in skeletal muscle cells. Proc Natl Acad Sci USA 106:2188-2193
10. Brown ST, Nurse CA (2008) Induction of HIF-2α is dependent on mitochondrial O_2 consumption in an O_2-sensitive adrenomedullary chromaffin cell line. Am J Physiol Cell Physiol 294:C1305-C1312
11. Hagen T, Taylor CT, Lam F et al (2003) Redistribution of intracellular oxygen in hypoxia by nitric oxide: effect on HIF1α. Science 302:1975-1978
12. Taylor CT (2008) Mitochondria and cellular oxygen sensing in the HIF pathway. Biochem J 409:19-26
13. Vaupel P (2004) Tumor microenvironmental physiology and its implications for radiation oncology. Semin Radiat Oncol 14:198-206

Chapter 41
Micropores in the Vitteline Layer of the Eggs of the Dragonfly *Oligoaeshna pryeri*: A Preliminary Observation from the Viewpoint of Oxygen Uptake

Tomiyasu Koyama, Hiroko Takano, and Tohru. Yokoyama

Abstract In dragonfly eggs, oxygen diffusing in, and carbon dioxide diffusing out, encounter barriers in the shell. According to Tullett and Board, in avian eggs the most important of these barriers results from the geometry of the pores through the shells. As in birds, dragonfly egg shells consist of three layers: the exochorion, endochorion and the innermost vitelline membrane. Trueman has described pores and fine anchor-like structures in the endochorion but the vitelline membrane does not seem to have been studied. In the present work we have used scanning electron microscopy to examine the vitelline membrane in hatching eggs of *Oligoaeschna pryeri*. We have assumed that the numerous openings seen on the micrographs are pores through the membrane.

Results are expressed as means ± SD. The pore diameter, pore area and number per μm^2 of the vitelline membrane were 74.7 ± 61.3 nm, 4380 ± 3555 nm^2 and 4.16 ±1.3 pores/μm^2 (4.16 x10^8 pores/cm^2), respectively. The total pore area was calculated to be 18,222 $nm^2/\mu m^2$. In avian egg shells pore density depends on the weight of the egg. Results given by Tullett and Board suggest that an egg weighing 1 g may have a pore density of 300 pores/cm^2, which is much lower than the present result for dragonflies. It seems likely that the difference reflects the fact that in *Oligoaeshna pryeri* the eggs are immersed in water.

41.1 Introduction

Each animal species has developed a respiratory system appropriate to its needs. Avian eggs have calcified shells which are perforated to allow gas exchange between

Tomiyasu Koyama
Hokkaido University, Sapporo, Japan
e-mail: tomkoyamajp@yahoo.co.jp

Hiroko Takano
Hokkaido University, School of Medicine, Sapporo, Japan

Tohru. Yokoyama
Maruzen Publishing Co., Sapporo, Japan

J.C. LaManna et al. (eds.), *Oxygen Transport to Tissue XXXII*, Advances in Experimental Medicine and Biology 701, DOI 10.1007/978-1-4419-7756-4_41,

the embryo and the atmosphere. The eggs of domestic chickens, which weigh about 60g, have perforations in the shell with a diameter of 13.8 μm. The eggs of the much smaller sunbird (*Nectarinia osea*) weigh about 0.86g and have pores 6.5 μm in diameter [1,4]. These studies encouraged us to examine the respiratory strategy of smaller animals living in a more severe environment. Female dragonflies of the genus *Aeschnidae* have an ovipositor on the tail tip and insert their eggs one by one on to the stalks of grasses growing in water. The gas exchange between the embryo and water (which has an adsorption coefficient for oxygen at 20°C of only 0.031ml/ml/atm) occurs across the eggshell.

Some studies on dragonfly eggshells, made with the scanning electron microscope, revealed fine structures on the exo- and endochorion, while the innermost layer, the vitelline membrane, was described as "a dense layer without sub-structure" [3]. This suggests that the innermost membrane may inhibit gas exchange between the embryo and surrounding water. The present study investigated the fine structure of the vitelline membrane with a view to clarifying this point.

41.2 Methods

Live eggs of *Oligoaeschna pryeri* (a rare species) were obtained from a captured female. The tip of the tail was dipped in water and touched on a damp sheet of paper tissue. One hundred and fifty eggs were deposited by the female. They were maintained at about 20 $\sim$ 25 °C, and hatched over a period of 67 $\sim$ 100 days. The paper tissue bearing the sloughed eggshells was placed in a 70% ethanol:water mixture and the slough dehydrated through graded ethanol, then gold coated for observation by scanning electron microscopy (SEM).

41.3 Results

The intact eggshell was shaped like an elongated bamboo leaf; no protuberances were visible on the surface under light microscopy (Fig. 1). Its dimensions were $1.2 \times 0.4 \times 0.2$ mm.

As shown by SEM (Fig. 2) eggshells were partially ruptured during hatching. Numerous openings can be seen in Fig. 3. We assumed them to be pores through the vitelline membrane.

The pore diameter, pore area and pore number per μm^2 on the vitelline membrane surface were (means $\pm$ SD) 74.7 $\pm$ 61.3 nm and 4380 $\pm$3555 nm^2 and 4.16 $\pm$ 1.3 pores/μ m^2 (4.16 $\times$ 108 pores/cm^2), respectively. The total pore area per μ m^2 was calculated to be 18,222 nm^2/μ m^2 (18, 222 $\times$ 108μ m^2/cm^2) if pores are uniformly distributed over the whole surface of the shell.

41.4 Discussion

Pore density in avian eggshells depends on egg weight. The figure shown by Tullett and Board (Fig. 3) suggests that an egg weighing less than 1g may have a pore

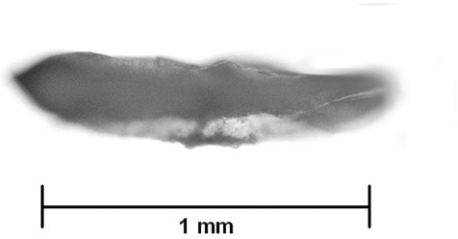

Fig. 41.1 A micrograph of a whole eggshell. Ruptured outgrowth of *Oligoaeschna pryeri.*

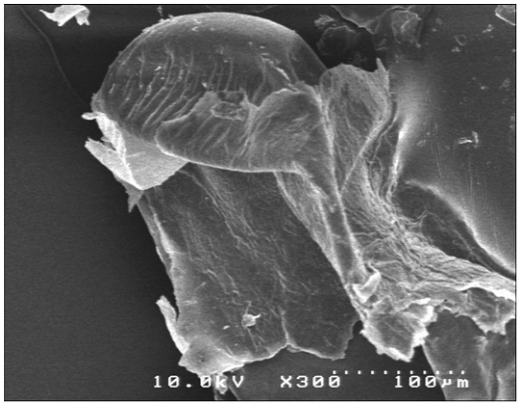

Fig. 41.2 A SEM micrograph of a localized portion ruptured by hatching. An external view.

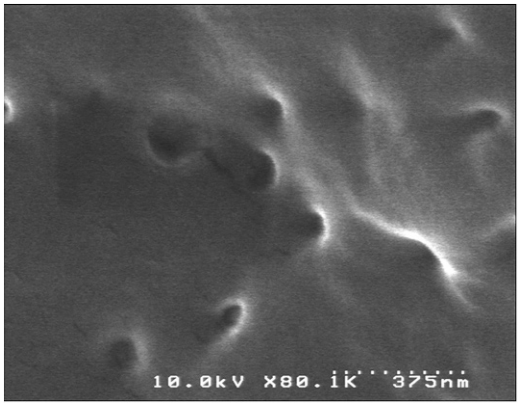

Fig. 41.3 A SEM micrograph of the surface of the vitelline layer. An inner view through the rupture.

density of 270 pores/cm^2 (total pore area per unit area is estimated at 1350μ m^2/cm^2) which is much smaller than the present result in the dragonfly. The difference in porosity between dragonfly and avian eggshells may arise because dragonfly eggs are submerged in water. The rate of diffusion of oxygen in water is about a million

times less than in air. Since the water surrounding the eggs will impede oxygen uptake [2], dragonfly eggshells will need this high pore density.

41.5 Conclusion

The vitelline layer of the eggshell of Oligoaeschna pryeri appears to have numerous micropores with a mean diameter of 74.7 ± 61.3 nm and a density of 4.16 ± 1.3 pores/μ m^2. It is suggested that the high degree of porosity is an adaptation to facilitate oxygen transport across the eggs which are submerged in water.

References

1. Ar A and Rahn H (1985) Pores in avian eggshells: gas conductance, gas exchange and embryonic growth rate, Respiration Physiology 61, 1-20.
2. Hinton HE (1981) Biology of insect eggs. Pergamon Press. vol.1 p.95
3. Trueman JWH (1991) Egg chorionic structures in cordulidae and libellulidae (anisoptera), Odonatologia 20(4), 441-452
4. Tullett SG and Board RG (1977) Determinants of avian eggshell porosity, J. Zool. London, 183, 203-211

Part XII
Hypoxic Adaptation

Chapter 42
A Heat-Shock Protein Co-Inducer Treatment Improves Behavioral Performance in Rats Exposed to Hypoxia

Kui Xu, Xiaoyan Sun, Bernadette O. Erokwu, Ibolja Cernak, and Joseph C. LaManna

Abstract We investigated the effect of a heat-shock protein co-inducer, arimoclomol (CytRx, LA, CA), on hypoxia-adaptive responses using a rat model of simulated altitude exposure (hypobaric hypoxia). Cognitive function was measured using a T-maze and an object recognition test. Motor function was measured using an inclined-screen test and an adhesion removal test. Immunohistochemical analyses were assessed in brain for heat-shock protein 70 (HSP 70), intercellular adhesion molecule 1 (ICAM-1) and apoptosis (TUNEL staining). Results show that both cognitive and motor performances were improved in rats treated with arimoclomol during hypoxic exposure; the hypoxia-induced expression of HSP70 and ICAM-1, and TUNEL-positive cells were reduced in brain with the treatment. Our data suggest that the arimoclomol treatment reduces the hypoxia-induced stress in brain tissue, and also improves the behavioral performance in rats during hypoxic adaptation.

42.1 Introduction

The brain is physiologically vulnerable to hypoxia due to its high demand for oxygen, thus, high altitude exposure (hypobaric hypoxia) may result in stress-related damage in the brain and lead to impaired behavioral performance. It has been suggested that the expression level of the heat-shock protein 70 (HSP 70) can be directly related to altitudinal clines of heat-stress resistance [1]. Because heat shock proteins (HSPs)

Kui Xu, Xiaoyan Sun, and Joseph C. LaManna
Departments of Physiology and Biophysics, , Case Western Reserve University, 10900 Euclid Avenue, Cleveland, OH 44106, USA
e-mail: kui.xu@case.edu

Bernadette O. Erokwu
Department of Anatomy, Case Western Reserve University, 10900 Euclid Avenue, Cleveland, OH 44106, USA

Ibolja Cernak
Johns Hopkins University Applied Physics Laboratory, 11100 Johns Hopkins Road, Laurel, MD 20773, USA

J.C. LaManna et al. (eds.), *Oxygen Transport to Tissue XXXII*, Advances in Experimental Medicine and Biology 701, DOI 10.1007/978-1-4419-7756-4_42,

protect the cells from a wide variety of physiological and pathological stresses including ischemia and hypoxia [2, 3], inducing HSPs may be a therapeutic approach to improve tolerance to high altitude [4, 5]. In this study, we hypothesize that induction of HSPs using an HSP co-inducer (arimoclomol) would improve behavioral performance by increasing tissue resistance toward mild hypoxia. The behavioral and immunocytohistochemical analyses (heat shock proteins, neurological inflammation marker and neuronal cell death) were assessed using a rat model of simulated altitude exposure.

42.2 Methods and Materials

42.2.1 Animals, simulated altitude exposure, and behavioral tests

Male Sprague-Dawley rats (~300 g) were purchased and allowed to acclimatize in the animal facility at Case Western Reserve University (CWRU) before being studied. Rats were randomly assigned to drug- and vehicle-treated groups, exposed to either normoxia or simulated altitude (hypobaric hypoxia) for 10 days. All drug-treated rats were administered arimoclomol (200 mg/kg, dissolved in PBS; Cytrx Corp., Los Angeles, CA) intraperitoneally daily; all vehicle-treated rats were given PBS instead. Hypoxic rats were kept in hypobaric chambers at a constant pressure of 380 mmHg (equivalent to 10% normobaric oxygen) except for about 3 hours daily being in atmosphere for maintenance and behavioral tests. The normoxic rats were housed in the same room to ensure identical ambient conditions [6]. Behavioral tests were performed by the Rodent Behavior Core of CWRU. Tests are: 1) The T-maze test is for general cognitive function. It is based on the innate preference of animals' spontaneous alternations. The sequence/latency of arm entries was recorded, and the alternation rate was calculated. 2) The Object Recognition test is based on the natural tendency of rodents to investigate a novel object instead of a familiar one. The frequency/duration of inspecting the objects was calculated. 3) The Inclined Screen (60- and 90-degree) test tests for balance, muscle strength and coordination. Latency to climb to the top and/or latency to fall was recorded, and the overall score was calculated. 4) The Adhesive (Sticky-tape) Removal test is for somatosensory deficits. The time to remove the sticky tape (18mm in diameter, placed bilaterally on the wrist) from both limbs was recorded.

42.2.2 Immunohistochemistry

As described previously [7, 8], immunohistochemistry of HSP 70 and ICAM-1 was performed on brain sections using corresponding primary antibodies (anti-heat-shock-protein-70 and anti-ICAM-1, Cell Signaling Technology). The apoptotic cell death was assessed by TUNEL staining using a detection kit (Promega).

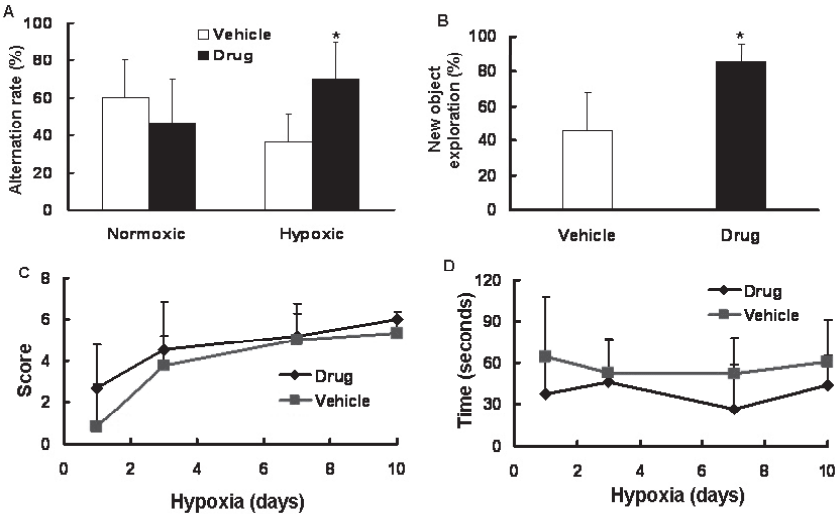

Fig. 42.1 Behavioral tests. **A:** T-maze test at 4 days of exposure. Alternation rate (%) = (numbers of alternation/total trials-1) × 100. **B:** Object recognition test at 9 days of hypoxic exposure. New object exploration (%) = (new object exploration time/total exploration time) × 100. **C:** Overall scores of the 90-degree inclined screen test during hypoxic exposure. The 60-degree inclined screen test has similar trends (data not shown). **D:** Time to remove sticky tapes in the adhesive removal test during hypoxic exposure. Values are mean ± SD, n = 6 each; * indicates significant difference compared to the vehicle-treated group with the same exposure condition.

42.2.3 Statistical analysis

Data are expressed as mean ± SD. Statistical analyses were performed using SPSS V13.0 for Windows. The comparison between any two groups was analyzed with a t-test. Significance was considered at the level of $p < 0.05$.

42.3 Results

42.3.1 Physiological variables

The body weights of normoxic rats were maintained while the body weights of hypoxic rats dropped about 15% at the end of the exposure. Consistent with a previous report [6], hematocrit increases with hypoxic exposure, in both drug- and vehicle-treated groups. At 10 days of hypoxic exposure, the hematocrit in hypoxic rats increased significantly (∼30%) compared to the normoxic controls. There were no significant differences in body weight or hematocrit between the drug-treated and the vehicle-treated groups in either normoxic or hypoxic conditions.

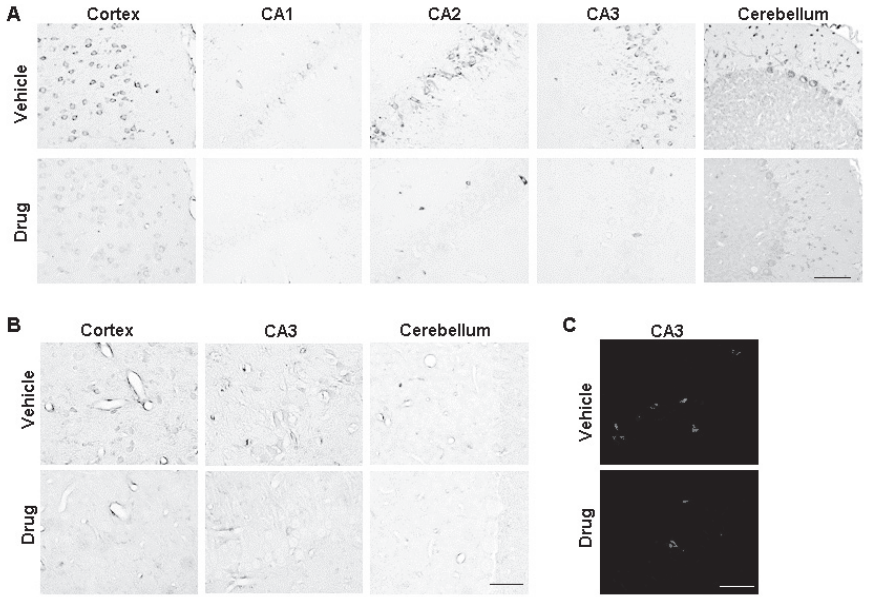

Fig. 42.2 Immunohistochemistry. **A:** HSP 70 in cortex, hippocampus (CA1-3) and cerebellum at 10 days of hypoxia. **B:** ICAM-1 in cortex, hippocampus (CA3) and cerebellum at 10 days of hypoxia. **C:** TUNEL staining in hippocampal CA3 region at 3 days of hypoxic exposure. The drug-treated brain has significantly less positive staining. Scale bar: 100μm.

42.3.2 Behavioral performance

For cognitive function, the T-maze test was measured on 2, 4, and 8 days of exposure. The drug-treated hypoxic group had a significantly higher alternation rate (indicative of sustained cognition) compared to the vehicle-treated hypoxic group (Fig. 1A). In the Object Recognition test, on the 9^{th} day of hypoxia, the new object exploration (%, is higher with good cognition) was significantly higher in the drug-treated rats compared to the vehicle-treated rats (Fig. 1B). The motor function was assessed on 1, 3, 7, and 10 days of exposure. The overall scores in the inclined screen test tended to be higher in the drug-treated group compared to the vehicle-treated group during hypoxia (Fig. 1C). In the Adhesive Removal test, during hypoxia, the drug-treated group used less time than the vehicle-treated group to remove the sticky tapes (Fig. 1D). There was no significant difference in either cognitive tests or motor tests between the drug-treated group and the vehicle-treated group under the normoxic condition.

42.3.3 Immunohistochemistry and TUNEL staining

Immunohistochemistry of HSP 70 and ICAM-1 and TUNEL staining was performed on sections of cortex, hippocampus and cerebellum. No positive staining was found

in any regions under normoxic condition (data not shown). In the vehicle-treated group, the positive staining of HSP 70 was visible as early as 1 day and was evident at 10 days of hypoxia; the HSP70 expression was markedly suppressed in the drug-treated group (Fig. 2A). Consistent with previously reported [9], the expression of ICAM-1, a marker of inflammation, was significantly elevated during hypoxic exposure compared to the normoxic controls (data not shown). Positive staining of ICAM-1 was found mostly at endothelium. The hypoxia-induced ICAM-1 elevation was noticeably reduced in the drug-treated group compared to the vehicle treated group (Fig. 2B). Signs of apoptosis (TUNEL staining) were evident in hippocampal CA3 region in the vehicle brain at 3 days of hypoxia but disappeared by 10 days of exposure. There was significantly less TUNEL-positive staining in the drug-treated brain (Fig. 2C).

42.4 Discussion

In this study, we found that arimoclomol, a heat-shock protein co-inducer, appears to improve both cognitive and motor performance during hypobaric hypoxic exposure (simulated high altitude). The hypoxia-induced inflammatory response, indicated by positive ICAM-1 staining, Fig. 2B) was suppressed by arimoclomol treatment. The signs of apoptosis in the hippocampus during hypoxic exposure (Fig. 2C) were also diminished by the treatment. Our data show that HSP-70 expression is highly induced in brain by hypoxia; however, the expression of HSP-70 was unexpectedly reduced by arimoclomol treatment (Fig. 2A). One explanation for this phenomenon might be that arimoclomol is acting primarily peripherally and this systemic effect results in amelioration of hypoxia-induced stress in brain. This is demonstrated by the suppression of hypoxia-induced inflammatory and apoptotic responses in the arimoclomol-treated group. In summary, the treatment with a heat-shock protein co-inducer, arimoclomol, improved the behavioral performance in rats exposed to hypoxia, and also reduced the hypoxia-induced stress in brain tissue.

Acknowledgments

This work is supported by DARPA (Defense Advanced Research Projects Agency), US Army ECBC, W911-NF-07-C-0053; Johns Hopkins University Applied Physics Laboratory subcontract 929408; HSP co-inducer (arimoclomol) was provided by CytRx Corporation, Los Angeles, CA, USA.

References

1. Sorensen JG, Norry FM, Scannapieco AC, and Loeschcke V (2005) Altitudinal variation for stress resistance traits and thermal adaptation in adult Drosophila buzzatii from the New World.J Evol Biol 18(4): 829-837

2. Zhong N, Zhang Y, Fang QZ, and Zhou ZN (2000) Intermittent hypoxia exposure-induced heat-shock protein 70 expression increases resistance of rat heart to ischemic injury. Acta Pharmacol Sin 21(5), 467-472
3. Murphy J, Song D, Welsh FA, Wilson DF, and Pastuszko A (1999) Regional expression of heat shock protein 72 mRNA following mild and severe hypoxia in neonatal piglet brain. Adv Exp Med Biol 471: 155-163
4. Soti C, Nagy E, Giricz Z, Vigh L, Csermely P, and Ferdinandy P (2005) Heat shock proteins as emerging therapeutic targets. Br J Pharmacol 146(6):769-780.
5. Snoeckx H, Cornelussen RN, van Nieuwenhoven FA, Reneman RS, and Van Der Vusse GJ (2001) Heat shock proteins and cardiovascular pathophysiology. Physiol Rev 81(4), 1461-1497
6. Xu K, Puchowicz MA, and LaManna JC (2004) Renormalization of regional brain blood flow during prolonged mild hypoxic exposure in rats. Brain Res 1027 (1-2):188-191
7. Pichiule P and LaManna JC (2002) Angiopoietin-2 and rat brain capillary remodeling during adaptation and deadaptation to prolonged mild hypoxia. J Appl Physiol 93 (3):1131-1139
8. Puchowicz MA, Xu K, Sun X, Ivy A, Emancipator D, and LaManna JC (2007) Diet-induced ketosis increases capillary density without altered blood flow in rat brain. Am J Physiol Endocrinol Metab 292 (6):E1607-E1615
9. Dore-Duffy P, Balabanov R, Beaumont T, Hritz MA, Harik SI, and LaManna JC (1988) Endothelial activation following prolonged hypobaric hypoxia. Microvasc Res 57 (2):75-85

Chapter 43
Chronic Intermittent Hypoxia-Induced Augmented Cardiorespiratory Outflow Mediated by Vasopressin-V_{1A} Receptor Signaling in the Medulla

Prabha Kc, Kannan V. Balan, Richard J. Martin, Joseph C. LaManna, Musa A. Haxhiu, and Thomas E. Dick

Abstract A co-morbidity of sleep-disordered breathing is hypertension associated with elevated sympathetic nerve activity, which may result from chronic intermittent hypoxia (CIH). CIH evokes plasticity in cardiorespiratory regulating sites, including the paraventricular nucleus (PVN), which acts to sustain increased sympathetic nerve activity. Our working hypothesis is that vasopressin neurons mediate the sustained increase in blood pressure and altered breathing associated with CIH. In a series of neuroanatomical experiments, we determined if vasopressin-containing PVN neurons innervate rostral ventrolateral medulla (RVLM), and altered cardiorespiratory responses induced by CIH conditioning (8h/day for 10 days) is mediated by vasopressin-V_{1A} receptor signaling in the medulla. In the first set of experiments, cholera toxin β subunit was microinjected into the RVLM to delineate innervation of the PVN. Immunohistochemistry data showed vasopressin-containing PVN neurons were double-labeled with cholera toxin β subunit, indicating vasopressin projection to the RVLM. In the second set, sections of the medulla were immunolabeled for vasopressin V_{1A} receptor, and its expression was significantly higher in the RVLM and in the neighboring rostral ventral respiratory column in CIH- than from RA-conditioned rats. In a series of physiological experiments, we determined if blocking the vasopressin V_{1A} receptor in the medulla would normalize blood pressure in CIH-conditioned rats and also attenuate the evoked responses to PVN disinhibition. Blood pressure, heart rate, diaphragmatic and genioglossus muscle activity were recorded in anesthetized, ventilated and vagotomized rats. The PVN was disinhibited by microinjecting bicuculline before and after blocking vasopressin V_{1A} receptors in the

Prabha Kc, Kannan V. Balan, Richard J. Martin, and Musa A. Haxhiu
Department of Pediatrics, Case Western Reserve University, Cleveland, OH 44106, USA
e-mail: prabha.kc@case.edu

Joseph C. LaManna
Department of Physiology and Biophysics, Case Western Reserve University, Cleveland, OH 44106, USA

Thomas E. Dick
Department of Medicine, Case Western Reserve University, Cleveland, OH 44106, USA

J.C. LaManna et al. (eds.), *Oxygen Transport to Tissue XXXII*, Advances in Experimental Medicine and Biology 701, DOI 10.1007/978-1-4419-7756-4_43,

RVLM/rostral ventral respiratory column. In RA-conditioned rats, PVN disinhibition increased blood pressure, heart rate, minute diaphragmatic and genioglossus muscle activity, and these increases were attenuated after blocking the vasopressin V_{1A} receptor. In CIH-conditioned rats, a significantly greater dose of blocker was required to blunt these physiological responses and it also normalized the baseline blood pressure. Our findings indicate that vasopressin is the neuropeptide released from PVN neurons that modulates cardiorespiratory output via the RVLM and rostral ventral respiratory column.

43.1 Introduction

Vasomotor tone depends primarily on the activity of neurons located in the rostral ventrolateral medulla (RVLM), but also in the hypothalamic paraventricular nucleus (PVN). Neurons in the PVN tonically influence vasomotor tone via efferent projections to the RVLM and the spinal cord, in particular the intermediolateral cell column [4, 9, 12, 13]. In addition, the PVN modulates respiration [5, 7, 8, 11]. Vasopressin is a neurotransmitter that defines one of the PVN sub-populations and regulates cardiovascular tone, water-electrolyte balance and other functions of the central nervous system including respiration [5, 6, 13].

Sleep-disordered breathing in obstructive sleep apnea is characterized by transient, repetitive cessation of breathing, which leads to several co-morbidities including sympathetic nerve activity and hypertension [3]. Repetitive intermittent hypoxia is a form of stress which is capable of evoking biochemical plasticity in the brain including the PVN which ultimately interferes with the balance between excitatory and inhibitory tone and disrupts cardiorespiratory homeostasis. Therefore, based on the known neuroanatomical connections between PVN and cardiorespiratory neurons in the medulla, namely the RVLM and the rostral ventral respiratory column neurons, and the role vasopressin in the cardiorespiratory system, we hypothesized that chronic intermittent hypoxia CIH)-conditioning augments vasopressin signaling in the RVLM and rostral ventral respiratory column, increasing pressor and respiratory activity.

43.2 Methods

Experiments were performed in adult Sprague Dawley rats which were exposed either to CIH (11 episodes/h, 8 h/day for 10 days) or to normoxia (RA). The animals were fed ad libitum. Subsequent neuroanatomical and physiological experiments were performed in the morning following the 10^{th} day of CIH exposure.

43.2.1 Neuroanatomical studies

43.2.1.1 Localization of vasopressin-containing PVN neurons that project to the RVLM

Cholera toxin β subunit, a retrograde tracer, was unilaterally microinjected into the RVLM. Five days following cholera toxin β subunit injections, the brains were

processed immunohistochemically for labeling of cholera toxin β subunit and vasopressin as described previously [5].

43.2.1.2 Localization of vasopressin V_{1A} receptors in the RVLM/rostral ventral respiratory column

Brain stem sections extending from Bregma 12.00 mm–13.60 mm of RA- and CIH-conditioned rats were stained for vasopressin V_{1A} receptor. Vasopressin V_{1A} receptor was chosen primarily because it is found throughout the brain and vasculature, whereas vasopressin V_{1b} and V_2 are localized in the anterior pituitary and kidneys respectively. In addition, following immunolabeling of vasopressin V_{1A} receptor, tissues were further processed for double labeling with parvalbumin to determine whether respiratory-related neurons express vasopressin V_{1A} receptor. Parvalbumin is used as a marker for neuroanatomical identification of respiratory neurons in the rostral ventral respiratory column [1].

43.2.2 Physiological studies

Rats were anesthetized, intubated, mechanically ventilated and vagotomized. A carotid artery was cannulated to monitor arterial blood pressure and a jugular vein to administer supplemental anesthetic and fluids. Small burr holes were made on the right side of the skull to reach the PVN and bilaterally to access the RVLM. Teflon-coated bipolar electrodes were inserted into the diaphragm and into the genioglossus muscle for recording electromyographic activity. Diaphragmatic and genioglossus muscle signals were amplified, filtered, and fed in parallel to an audio monitor and analog-to-digital computer-based data acquisition system with a sampling rate of 4 kHz per channel for offline analyses as described previously [5, 7, 8].

43.2.2.1 Disinhibition of PVN with $GABA_A$ receptor antagonist

Based on preliminary dose-response studies, PVN site was identified when $GABA_A$ receptor antagonist, bicuculline, (0.1 nmol, 100 nl) microinjected unilaterally into the PVN, produced a blood pressure change of $\geq$15 mmHg. Bicuculline inhibits membrane hyperpolarization and thereby increases the excitability of PVN neurons. Control studies were conducted by injecting the same volume (100 nl) of physiological saline into the PVN. Approximately 1 hour following bicuculline administration, vasopressin V_{1A} receptor antagonist (SR49059; 0.2 nmol, 200 nl/side), was microinjected bilaterally into the RVLM/rostral ventral respiratory column region. After reaching a steady-state condition at 7-10 min, the PVN was activated ipsilaterally with the same dose of bicuculline. In CIH conditioned animals, the dose of antagonist given to RA-conditioned rats did not significantly block the physiological responses (blood pressure, heart rate, minute diaphragmatic and genioglossus muscle activity), and hence the dose was increased (0.4 nmol, 200 nl/side).

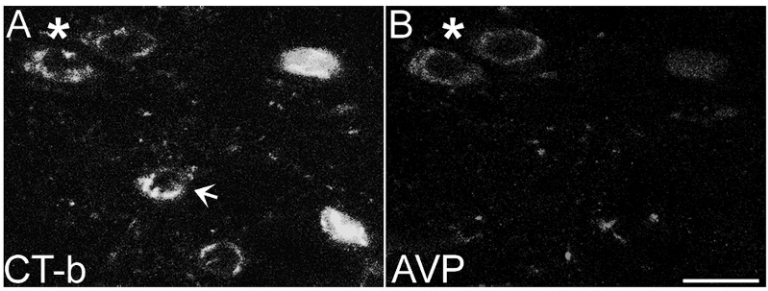

Fig. 43.1 Photomicrographs showing cholera toxin β subunit (CT-b)-labeled PVN neurons (A) and vasopressin (AVP)-immunolabeled neurons (B) following microinjection of CT-b into the RVLM. Asterisks represent a CT-b-labeled PVN neuron double-labeled with vasopressin and an arrow represents a CT-b-labeled neuron alone. Scale bar = 20 μm.

43.3 Results

43.3.1 Neuroanatomical studies

43.3.1.1 Localization of vasopressin-containing PVN neurons that project to the RVLM

Cholera toxin β subunit-labeled neurons were distributed bilaterally in the PVN with ipsilateral predominance to the site of cholera toxin β subunit injection. Analysis of bilaterally labeled cholera toxin β subunit neurons showed that 14.6% of cholera toxin β subunit-labeled PVN neurons were double-labeled with vasopressin (Fig. 1), indicating its influence on cardiorespiratory control.

43.3.1.2 Localization of vasopressin V_{1A} receptor in the RVLM/rostral ventral respiratory column

V_{1A} receptors were expressed throughout the rostrocaudal column of the RVLM. Data analysis indicated an up-regulation of vasopressin V_{1A} receptors in the CIH- as compared to RA-conditioned rats (110.8 $\pm$ 5.7 vs 85.8 $\pm$ per RVLM region; $p = 0.01$; Fig. 2). In addition, our data showed that parvalbumin-labeled neurons were double-labeled with V_{1A} receptor (Fig. 2) suggesting that vasopressin-V_{1A} receptor signaling in the medulla modulates cardiorespiratory activity and is enhanced by CIH.

43.3.2 Physiological studies

43.3.2.1 Effect of CIH-conditioning on mean arterial pressure

Blood pressure recording taken 30 min after the carotid artery cannulation in anesthetized rats showed mean arterial pressure was significantly higher in 10 day CIH-conditioned as compared to RA-conditioned animals (114.2 $\pm$ 5.9 vs 94.8 $\pm$ 3.1 mmHg; $p < 0.05$).

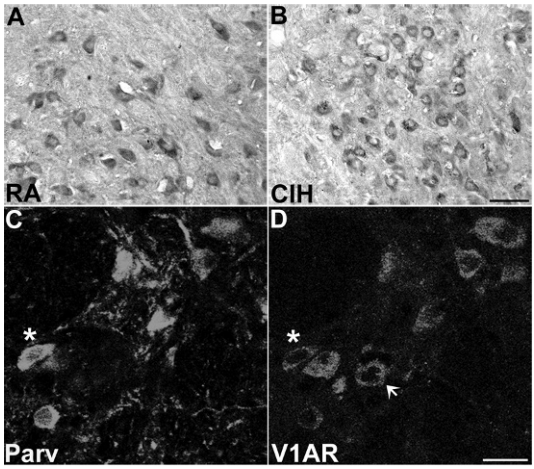

Fig. 43.2 Top panel: Photomicrographs showing the expression of vasopressin V_{1A} receptors in the RVLM region of a RA- (A) and CIH-challenged (B) rat. Bottom panel: Photomicrographs showing parvalbumin (Parv)-labeled neurons (C) and vasopressin V_{1A} receptor-immunolabeled neurons (D). Asterisks represent a parvalbumin-labeled rostral ventral respiratory column neuron double-labeled with vasopressin V_{1A} receptor and an arrow represents a vasopressin V_{1A} receptor-labeled neuron alone. Note, CIH-conditioning significantly up-regulated the expression of vasopressin V_{1A} receptors in the RVLM/rostral ventral respiratory column. Scale bar (A and B) = 100 μm; Scale bar (C – D) = 25 μm.

43.3.2.2 Effect of PVN disinhibition on mean arterial pressure and heart rate

In RA- and CIH-conditioned rats, following disinhibition of the PVN, mean arterial pressure and heart rate significantly increased from the baseline activity. However, the magnitude of mean arterial pressure increase in CIH-conditioned rats was significantly greater ($p < 0.05$; Table 1). There was no significant difference in the heart rate between RA- and CIH-conditioned rats following PVN disinhibition (Table 1). Vasopressin V_{1A} receptor antagonist microinjected bilaterally into the RVLM/rostral ventral respiratory column significantly attenuated the evoked increase in mean arterial pressure and heart rate (Table 1). However, in CIH-conditioned rats, the dose (0.2 nmol/side) of vasopressin V_{1A} receptor antagonist that blunted the evoked responses in RA-conditioned rats had no significant effect. A higher dose (0.4 nmol/side) of blocker was required to blunt the mean arterial pressure and heart rate to PVN disinhibition, and it also normalized the blood pressure.

43.3.2.3 Effect of PVN disinhibition on diaphragmatic and genioglossus muscle activity

In RA- and CIH-conditioned rats, disinhibition of the PVN increased minute diaphragmatic and genioglossus muscle activity significantly from the baseline activ-

Table 43.1 Mean arterial pressure, heart rate, minute diaphragmatic and genioglossus muscle activity in room air (RA)- and CIH-challenged rats before and after blockade of vasopressin V_{1A} receptors into the RVLM/rostral ventral respiratory column to PVN disinhibition with bicuculline. Data are expressed as percent change from the baseline activity. PVN disinhibition significantly increased mean arterial pressure, heart rate, minute diaphragmatic and genioglossus muscle activity from the baseline. When compared between these two groups, CIH-conditioned rats showed significantly higher mean arterial pressure, minute diaphragmatic and genioglossus muscle activity with no change in the heart rate (* = $p < 0.05$). Note, a higher dose of blocker was required to blunt these responses in CIH-conditioned rats.

RA			**CIH**	
Variables Measured	**Pre-blocker**	**Post blocker (0.2 nmol/side)**	**Pre-blocker**	**Post-Blocker (0.4 nmol/side)**
Mean Arterial Pressure (mmHg)	26.6±2.7	1.4±0.7	46.3±4.3*	4.3±2.0
Heart Rate (beats/min)	6.4±2.4	0.9±0.4	6.5±1.6	1.8±0.6
Diaphragmatic activity (Arbitrary units)	40.1±2.9	1.5±0.9	54.5±2.6*	5.7±2.1
Genioglossus activity (Arbitrary units)	46.0±2.8	4.2±1.6	62.1±3.6*	8.1±2.5

ity. Although disinhibition of the PVN increased the activity in both the groups, the magnitude of increase was significantly greater in CIH-conditioned rats ($p < 0.05$; Table 1). Microinjection of vasopressin V_{1A} receptor antagonist (0.2 nmol/side) into the RVLM/rostral ventral respiratory column blunted the PVN-evoked increase in minute diaphragmatic and genioglossus muscle activity from the baseline activity (Table 1). However, in CIH-conditioned rats, it required a higher dose (0.4 nmol/side) of blocker to blunt these responses.

43.4 Conclusions

The findings of the present study are consistent with our working hypothesis that vasopressin neurons are the specific sub-population of PVN neurons that mediate increases mean arterial pressure and heart rate, and blockade of vasopressin-V_{1A} receptors in the RVLM blunts these responses, indicating that the vasopressin-V_{1A} receptor signaling pathway modulates cardiovascular function via the RVLM. In addition to evoking sympathetic nerve activity, it also modulates respiratory output as indicated by increases in minute diaphragmatic and genioglossus muscleactivity to PVN disinhibition. The neuroanatomical studies establish that vasopressin-V_{1A} receptor signaling in the RVLM/rostral ventral respiratory column. Furthermore, CIH results in up-regulation of vasopressin V_{1A} receptors. The physiological studies showed that blocking vasopressin V_{1A} receptors attenuated the effect of PVN disinhibition. In the CIH-conditioned animals, the response to PVN disinhibition and the

requisite antagonist were greater than in RA-conditioned animals, and the blocker normalized the baseline blood pressure. In summary, the PVN controls sympathorespiratory activity through its connections and vasopressin V_{1A} receptor in the medulla and these activities are enhanced following CIH-conditioning.

Acknowledgments

This study was supported by a grant from the National Institutes of Health (grant K99HL087620 from the NHLBI).

References

1. Alheid, G. F., Gray, P. A., Jiang, M. C., Feldman, J. L., & McCrimmon, D. R. (2002). Parvalbumin in respiratory neurons of the ventrolateral medulla of the adult rat. J.Neurocytol. 31:693-71
2. Ciriello J, Calaresu FR (1980) Role of paraventricular and supraoptic nuclei in central cardiovascular regulation in the cat. Am J Physiol 239:R137-R142
3. Fletcher EC, Lesske J, Behm R, Miller CC, III, Stauss H, Unger T (1992) Carotid chemoreceptors, systemic blood pressure, and chronic episodic hypoxia mimicking sleep apnea. J Appl Physiol 72:1978-1984
4. Hardy SG (2001) Hypothalamic projections to cardiovascular centers of the medulla. Brain Res 894:233-240
5. Kc P, Haxhiu MA, Tolentino-Silva FP, Wu M, Trouth CO, Mack SO (2002) Paraventricular vasopressin-containing neurons project to brain stem and spinal cord respiratory-related sites. Respir Physiol Neurobiol 133:75-88
6. Kozniewska E, Romaniuk K (2008) Vasopressin in vascular regulation and water homeostasis in the brain. J Physiol Pharmacol 59 Suppl 8:109-116
7. Mack SO, Kc P, Wu M, Coleman BR, Tolentino-Silva FP, Haxhiu MA (2002) Paraventricular oxytocin neurons are involved in neural modulation of breathing. J Appl Physiol 92:826-834
8. Mack SO, Wu M, Kc P, Haxhiu MA (2007) Stimulation of the hypothalamic paraventricular nucleus modulates cardiorespiratory responses via oxytocinergic innervation of neurons in pre-Botzinger complex. J Appl Physiol 102:189-199
9. Pyner S, Coote JH (2000) Identification of branching paraventricular neurons of the hypothalamus that project to the rostroventrolateral medulla and spinal cord. Neuroscience 100:549-556
10. Reddy MK, Patel KP, Schultz HD (2005) Differential role of the paraventricular nucleus of the hypothalamus in modulating the sympathoexcitatory component of peripheral and central chemoreflexes. Am J Physiol Regul Integr Comp Physiol 289:R789-R797
11. Schlenker E, Barnes L, Hansen S, Martin D (2001) Cardiorespiratory and metabolic responses to injection of bicuculline into the hypothalamic paraventricular nucleus (PVN) of conscious rats. Brain Res 895:33-40
12. Shafton AD, Ryan A, Badoer E (1998) Neurons in the hypothalamic paraventricular nucleus send collaterals to the spinal cord and to the rostral ventrolateral medulla in the rat. Brain Res 801:239-243
13. Yang Z, Bertram D, Coote JH (2001) The role of glutamate and vasopressin in the excitation of RVL neurons by paraventricular neurons. Brain Res 908:99-103

Chapter 44

Effect of Inspiration of 12% O_2 (Balance N_2) on Cardiac Output, Respiration, Oxygen Saturation, and Oxygen Delivery

M. Bell, C. D. Thake, and C. B. Wolff

Abstract Low arterial oxygen saturation (SaO_2) will result in a reduced rate of arterial oxygen delivery to the tissues (DO_2), unless there is a compensatory increase in cardiac output (CO) or haemoglobin concentration (Hb). An adequate DO_2 can therefore be maintained by increasing ventilation, CO, or both. Sustaining a tissue specific oxygen extraction is thought to play an important part in overall compensation. The present study has examined responses to acute hypoxic exposure in 8 volunteers (breathing 12% oxygen, balance nitrogen) and describes changes in CO, ventilation and the SaO_2. Aims included: examination of the extent of inter-subject variations and seeing whether DO_2 was maintained. SaO_2, PCO_2, respiration (via stethograph) and Finapress (non-invasive) arterial blood pressure (BP) were recorded, firstly on air and then on 12% oxygen. CO was derived, off-line, from the BP record. CO was increased in 5 subjects (22%-45%) but was virtually unchanged in 3, and yet comparison for all 8 subjects showed that DO_2 on 12% oxygen was not significantly different from DO_2 on air (mean on air 1017 ml. min^{-1}; hypoxia 1080 ml. min^{-1}, $p = 0.27$). SaO_2 on 12% oxygen ranged between 85% and 93%. In conclusion, exposure to the same hypoxic gas mixture resulted in differing individual ventilatory and CO responses. However, DO_2 was well maintained.

M. Bell
St. Catherine's Hospital, Doncaster, UK
e-mail: chriswolff@doctors.org.uk

C. D. Thake
Faculty of Health and Life Sciences, Coventry University, UK

C. B. Wolff
William Harvey Research Institute, Anaesthetics Laboratory,38 Little Britain, St Bartholomew's Hospital, London University, London, EC1 7BE, UK

J.C. LaManna et al. (eds.), *Oxygen Transport to Tissue XXXII*, Advances in Experimental Medicine and Biology 701, DOI 10.1007/978-1-4419-7756-4_44,

44.1 Introduction

The rate of oxygen delivery in the arterial blood (DO_2) has to exceed the rate of tissue oxygen consumption (VO_2) by sufficient excess. For the steady-state, there is accurate regulation of DO_2 by tissue regulation of blood flow [1]. This works well for the normal state and for moderate hypoxia and anaemia. There are lower limits for arterial oxygen content (CaO_2) below which compensation breaks down. For skeletal muscle, $DO_2$is sustained down to 60% of normal CaO_2, while for the brain, the lower limit is around 90%. It is not clear, however, how much individual variation in CaO_2 occurs on exposure to the same degree of acute atmospheric hypoxia. For longer term exposure a recent study of high altitude hypoxia (at altitudes of 3000 to 5000 metres) showed a wide range of mean arterial oxygen saturation values (SaO_2, 81% to 93%). The heart rate (HR) showed a highly significant negative correlation with SaO_2 in 7 of their eight subjects consistent with cardiac output compensation for low CaO_2, supported by a near constant $HRxSaO_2$ product (surrogate DO_2) in all subjects [2].

The present study has examined the effect of inspiration of hypoxic inspirate (12% oxygen, balance nitrogen) in eight resting subjects. The idea was to see how well oxygen delivery was sustained in the face of individual variation in the resulting SaO_2.

44.2 Methods

Eight normal subjects (6 male, 2 female) were studied at rest with ethical permission from the Kings College Hospital Research Ethics Committee. The hypoxic inspirate was medical grade 12% oxygen (balance Nitrogen; supplier: BOC, Guildford, UK). The protocol included monitoring each subject firstly on air, breathing through a valve to allow collection of expired gas in a Douglas bag, for measurement of air breathing oxygen consumption (VO_2, derived from expired volume – Dry Gas Meter, Scientific and Research Instruments Ltd. Edenbridge, Kent, UK – and expired oxygen fraction – Oxygen Analyser, 580A Servomex Ltd., Crowborough, Sussex, UK). Four channels of information were then recorded firstly on air then on 12% oxygen: airway CO_2 (Datex Normocap, CD-102-22-00, Finland), respiration (non-linear, stethograph: Harvard Bioscience, Hollison MA, USA); SaO_2 (Pulse Oximeter, 515A, Novametrix, Medical Systems Inc., Wallingford CT, USA); non-invasive arterial blood pressure (BP, FINAPRESS^{TM} BP monitor, 6050-U000-593, BOC Health Care; Englewood CO, USA). Values were recorded at rest, first on air then on 12% oxygen inspirate, via an A-D converter (Cambridge Electronic Design, CED 1401, Cambridge, UK) on a personal computer using CED software (Spike2). Each subject's electrocardiogram (ECG) was recorded separately (MAC1200 digital, GE Medical Systems, Waukesha WI, USA). One millilitre (ml) of venous blood was drawn for haematocrit (Hct, Microcentrifuge and reader; Hawksley and Sons Ltd., Lancing, UK).

Table 44.1 Demography, ventilation, VO_2 and Hb during air breathing at rest.

	Weight (kg)	Height (cm)	BMI	VE (1 min^{-1})	VO_2 (ml min^{-1})	Hb (g/dl)
1CBW	62	175	20	8.56	213	11.4
2 CDT	88	175	29	5.52	206	13.6
3 M0B	63	180	19	7.10	182	14.4
4 D0B	60	161	23	7.42	223	12.9
5 S0G	74.2	169	26	12.78	231	12.5
6 R0S	80.1	182.5	24	6.97	158	13.7
7 C0S	66.6	164.5	25	7.66	239	12.4
8 D0F	80.5	173	27	10.25	232	15.6

BMI, body-mass index = Weight/metres squared;
VE is expired ventilation;
Hb = Hct × 0.33 [4].

Values proportional to cardiac output were derived offline from the recorded arterial blood pressure waveform. The method used is the commercial algorithm, PulseCO^{TM} (LiDCO^{TM}) a patented method [3]. The ratio of ventilation during hypoxia to ventilation on air was calculated as PCO_2, air/PCO_2, hypoxic.

Descriptive statistics (mean, etc), least squares regression line calculation and paired t testing have been used for analysis of data as appropriate.

44.3 Results

Height, weight and values of ventilation, oxygen consumption and Hb on air are given in Table 1.

The range of SaO_2 values on 12% oxygen was from around 85% to 93%. There were no ST changes on electrocardiographic (ECG) monitoring during hypoxia (7of 8 subjects recorded). The hypoxic SaO_2 was, reassuringly, 91% during the main experiment for the subject whose ECG was omitted; see Table 2.

Differences in time course of SaO_2 are illustrated for two subjects in Figure 1.

The ratio of hypoxic ventilation to that on air can be derived as the ratio of airway PCO_2 on air to airway PCO_2 on 12% oxygen (raw values in Table 2).

The cardiac output response has been calculated as the ratio of CO on 12% oxygen to the CO value on air. PCO_2, CO values are also shown in Table 2.

The ventilatory and CO responses are shown graphically in Figure 2 (by subject on the left) and in relation to hypoxic SaO_2 on the right. There is a clear relationship for the ventilatory response but not for the CO response.

The question then arises as to whether a compensatory response sustains DO_2 (the rate of oxygen delivery). This is examined in Figure 3.

DO_2 for the eight subjects is not significantly different in hypoxia than it is on air (see figure text).

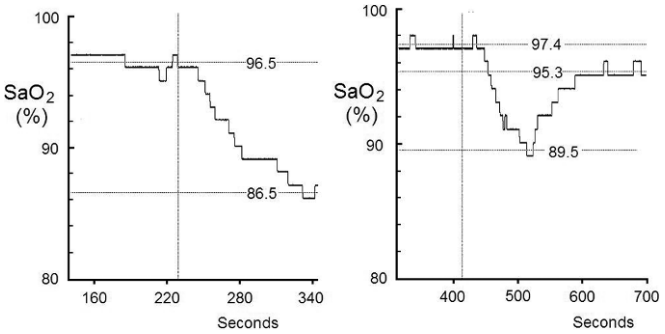

Fig. 44.1 Here arterial oxygen saturation is plotted against time, on the left for subject 1 with a fall to 86.5%. On the right (subject 2) SaO_2 initially fell to 89.5% then rose to a steady level of 95.3% due to a vigorous ventilatory response (PCO_2 fell from 45.5 to 34.3 mm Hg). For subject 1 the PCO_2 fall was much less (from 39.7 to 38.3 mm Hg) reflecting the much smaller ventilatory response.

Table 44.2 The main raw data including PCO_2, SaO_2 and CO on air and on 12% O_2.

	PCO_2 Air	PCO_2 12%O_2	SaO_2 Air	SaO_2 12%O_2	CO Air	CO 12%O_2
1CBW	40.8	38.5	97.7	84.9	8.93	10.99
2 CDT	40.9	33.4	98.3	92.5	3.39	4.46
3 M0B	40.5	38.2	97.5	85.0	7.11	10.3 a
4 D0B	31.9 b	26.5	96.8	92.9	5.46	5.25
5 S0G	34.1	30.4	96.0	90.7	5.99	5.86
6 R0S	40.7	37.0	98.5	87.4	4.52	5.94
7 C0S	30.6	29.9	97.3	87.1	5.88	7.19
8 D0F	39.9	36.6	96.2	87.4	5.33	5.25

a. CO here was based on only a small proportion of calculated values (because a large secondary BP wave confused computation in most cardiac cycles).
b. PCO_2 was not steady, rising to a level of 37.5 prior to hypoxic exposure.
Three subjects (4,5 and 8) were non-responders; CO did not increase on 12% oxygen exposure. PCO_2 units, mm Hg; CO units, l min^{-1}.

Oxygen delivery therefore appears to be well sustained in the hypoxic states which results from inspiration of 12% oxygen, though with considerable variation in the relative magnitude of the ventilatory and cardiac output changes in different individuals.

44.4 Discussion

The hypoxic ventilatory response seen here varies considerably, illustrated by the range of resulting SaO_2 values and the range of end-tidal PCO_2 changes. Inter-

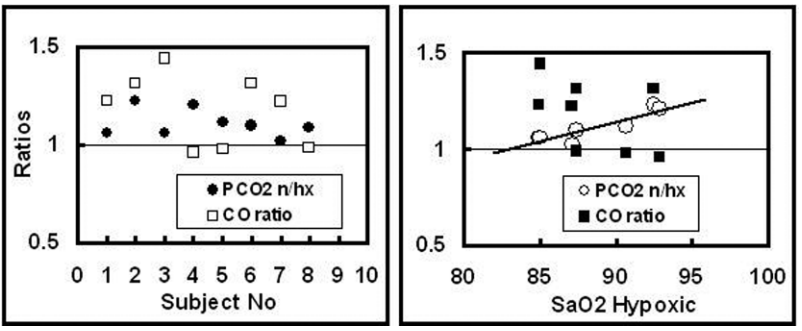

Fig. 44.2 The ventilatory responses here are shown as the ratio of normoxic to hypoxic PCO_2 (PCO_2 n/hx) and the cardiac output response as the ratio of CO on 12% oxygen (hypoxic) to CO on air (normoxic). The regression line for the ventilatory response (PCO_2 ratio) is: $y = 0.0203xSaO_2 - 0.682$, $r = 0.893$, $p = 0.0025$.

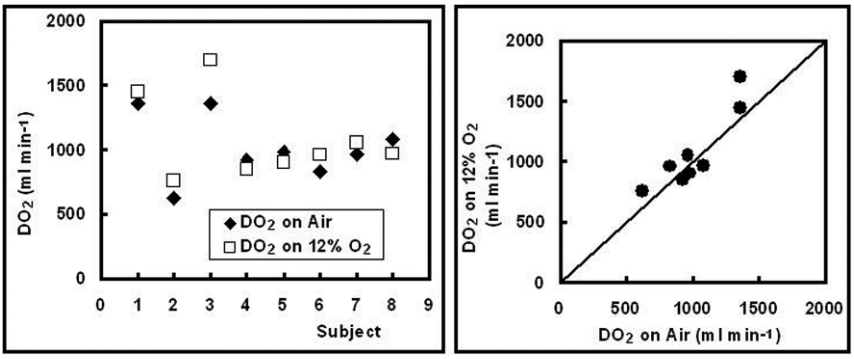

Fig. 44.3 Oxygen delivery values (DO_2) on air and on 12% oxygen (hypoxic) are shown on the left for each subject. On the right values of DO_2 are plotted one against the other with a line of identity, showing grouping largely close to the line. Hypoxic and normoxic values were not significantly different (paired $t = -1.188$, $p = 0.13$ one sided, 0.27 two sided; mean hypoxic DO_2 1080 ml min^{-1}, on air 1017 ml min^{-1}, mean difference 63 ml min^{-1}).

subject variation occurs despite all subjects breathing the same inspiratory oxygen concentration (12%). The strong correlation between the PCO_2 ratio (normoxic/ hypoxic) and the hypoxic SaO_2 (Figure 2) is due to the fact that the strongest ventilatory response results in the highest SaO_2. This raises the question as to whether the ventilatory response signifies sensitivity of the respiratory system. Although ventilation depends on SaO_2 similarly SaO_2 depends on ventilation. This illustrates the fact that a feedback loop is involved.

Since DO_2 is sustained in the eight subjects there is a compensatory increase in cardiac output where the respiratory response is low. The cardiac output response is peripheral and is thought to be from tissue control of vascular resistance in the tissue blood supply [1].

Cardiac output values have been derived here from the arterial blood pressure record (PulseCO^{TM} system) raising the question of the need or otherwise for calibration. Here, the default assumption is that the unscaled (uncalibrated) value can be used. This is based on the good correlation that has been found between PulseCO^{TM} derived CO and independent dye curve cardiac output values [5]. Values are proportional to cardiac output rather than absolute values but the comparisons have all been made within subject so scaling is likely to be sustained in hypoxia. Average DO_2 is close to the expected value (1000 ml min^{-1}) consistent with the uncalibrated values being close to the normal (Figure 3).

In conclusion, exposure to one specific hypoxic gas concentration (12% oxygen) evokes both ventilatory and cardiac output responses and the individual balance between these two varies between individuals.

Despite this variation oxygen delivery (over the range seen here, SaO_2 85% – 93%) is sustained at the same level in hypoxia as it is during air breathing.

There may well be implications from this study as regards clinical situations involving hypoxia and also regarding individual vulnerability to high altitude sickness.

Acknowledgments

Thanks are due to Professor CJ Hinds (anaesthetics) for providing the hypoxic gas mixture (William Harvey Institute, Queen Mary College, London). Also, A Tucker for loan of the ECG machine (Ernest Cooke Vascular & Microvascular Unit, St Bartholomew's Hospital). Also, Medical Expeditions – Medex, for the provision of Laboratory Facilities in collaboration with the Department of Health and Exercise Sciences, School of Sport, Bangor, Wales, UK.

References

1. Wolff CB (2007) Normal cardiac output, oxygen delivery and oxygen extraction. Adv. Exp. Med. Biol., 599: 169-182.
2. Parks T, Brierley G, Wilson C et al (2009) Arterial blood oxygen saturation and heart rate and their relationship to acute mountain sickness at altitude. A field study. (abstract) Proc Physiol Soc 14: PC2.
3. Band; DM, Linton NWF, Linton RAF et al (2000) Method and apparatus for the measurement of cardiac output. United States Patent 6,071,244: June 6.
4. Habibzadeh F, Yadollahie M, Roshanipoor M et al (2001) Derivation of blood hemoglobin concentration from hematocrit: a simple method for rural areas. M Arch. Irn. Med. **4**(3): 120-122.
5. Rhodes A and Sutherland R (2005) Arterial pulse power analysis: the LiDCO^{TM} Plus system. In, Functional Haemodynamic Monitoring Update in Intensive Care and Emergency Medicine 42. Eds., Pinsky MR and Payen D, Springer-Verlag, Berlin, Heidelberg, pp183-192.

Part XIII
Exercise Physiology

Chapter 45
Sufficient Oxygen Can Be Transported to Resting Skeletal Muscle via Arterialization of the Vein: Theoretical Considerations in a Rat Model

Tomiyasu Koyama and Tomiyasu Koyama

Abstract The blood supply to the lower limbs is often interrupted in patients suffering from arteriosclerosis obliterans (AO). In this condition, it is necessary to establish an oxygen supply via an alternative route. In the present theoretical study on rats, the possibility that adequate oxygen could be supplied through the venous system has been considered using simple calculations. The study was undertaken in the light of a report of a successful surgical approach in which the capillary bed is bypassed [1].

The total lengths of the collecting venules and of the arcade venules per mm^3 are reported to be 2.32 and 2.11 mm, respectively [2]. If these vessels were stretched out and connected to form a single, narrow venular tube, the total density would be 4.43 mm/mm^3. From the reciprocal of this value, the tissue cylinder surrounding the venule would have a radius of 268 μm. Taking an oxygen consumption rate for resting skeletal muscle of 0.16 ml/100g/min, and pO_2 value of 40 mmHg, the one-dimensional diffusion equation gives a maximal diffusion distance of 328 μm. This is larger than the radius of the tissue cylinder surrounding the venular tube. A calculation for Krogh's tissue cylinder gives an oxygen partial pressure gradient of 54 mmHg between the inflow and the outflow terminals. These calculations suggest the oxygen content of the venous blood is adequate to supply sufficient oxygen to resting skeletal muscle. This is consistent with the successful outcome in patients with direct A-V anastomoses and implies that the capillary network is not essential for oxygen transport to resting skeletal muscle.

45.1 Introduction

Arteriosclerosis obliterans (AO) is a disease of the blood vessels that leads to narrowing and hardening of the arteries and finally to loss of peripheral tissues. Calcium

Tomiyasu Koyama
Hokkaido University, Sapporo, Japan
e-mail: tomkoyamajp@yahoo.co.jp

Tomiyasu Koyama
Department of Vascular Surgery, Asahikawa Medical University, Asahikawa, Japan

J.C. LaManna et al. (eds.), *Oxygen Transport to Tissue XXXII*, Advances in Experimental Medicine and Biology 701, DOI 10.1007/978-1-4419-7756-4_45,

deposits in the walls of the arteries contribute to these vascular changes. Arteries become less elastic and cannot dilate, ultimately leading to total closure of the arteriolar vessels. Patients suffering from AO often have terrible pain in the limbs with extensive tissue loss in the periphery. In some patients where grafting to a distal artery is not possible the bypass is made to a distal vein [1]. With this technique the patent artery is connected to a vein so that the arterial blood to the muscle flows retrogradely through the vein. Since the microvessels on the arteriolar side are closed in such patients it is probable that the blood does not flow through the capillary network but reaches other veins via the venular anastomoses. This raises the question whether the short-circuited blood can supply the ischemic muscle with sufficient amount of oxygen.

Sasajima and colleagues [1] attempted to reduce the damage to the veins exposed to arterial pressure. After developing various techniques they succeeded in venous arterialization (DVA) of the vein in the ankle (vena plantaris). This was achieved by covering the vein, distal to the bypass, with healthy skin and a flap of the lateral rectus muscle. In some patients, whose feet appeared terminally damaged, this surgical technique saved them and the patient's quality of life was improved for up to 3 years.

Despite the apparent success of this bypass it is subject to the following serious criticisms.

1. The surgery costs too much without any financial merit.
2. There is no scientific evidence for the efficient oxygen supply to the ischemic limbs.

The present study is focused on this second criticism.

The specific question to be addressed is whether the retrograde arterial blood flow could supply sufficient oxygen to the foot muscles. With an artery-to-vein graft, arterial blood will not flow, as is normal, through the capillary net in the skeletal muscle, and then back into the vein via venular anastomoses. Tsai et al [6] have reviewed evidence suggesting the ability of venules to supply oxygen to tissue. It is known that in the rat spinotrapezius muscle [2] there is a dense network of venular anastomoses. We have assumed that there is a similarly dense venular network in human foot. We have further assumed the erythrocyte and capillary diameters to be broadly similar in rats and humans. With these assumptions, we have made a simple theoretical analysis of the capability of the rat venular network to supply oxygen to the peripheral tissues.

45.2 Methods

In our theoretical calculation, the venular network was considered as a single thin straight tube in a unit volume of tissue. It was assumed that oxygen can be delivered from venules to surrounding tissues when oxygen tension in the blood is higher that in the tissue [6]. Using the venular density in a rat skeletal muscle as reported by Schmid-Schönbein's laboratory [2], we treated all segments of venules in a unit volume of the tissue as a single thin venular tube. Furthermore, using the volume

of surrounding tissue cylinder, the gradient in partial pressure of oxgen could be estimated. Taking the reported rate of oxygen consumption in resting rat skeletal muscle [4] and the diffusion coefficient of oxygen in skeletal muscle, the diameter of the tissue cylinder supported by this venular tube could be calculated.

45.3 Results

Krogh's equation for the tissue cylinder model [4] was employed for the estimation of the partial pressure difference between the arterial inflow and venous outflow:

$$\Delta P = A \times K/4D, \tag{45.1}$$

where

$K = 760 \times R^2\{4.6 \times \log(R/r - 1) + r^2\}$,

$R =$ tissue cylinder radius $= 268\ \mu m$,

$\phi = 30\ \mu m$, the average diameter of venules,

$D = 1.64 \times 10^{-5}\ cm^2/\ min\ /760\ mmHg$, the diffusion coefficient of oxygen through tissue,

$A = 1.6 \times 10^{-3}\ ml/min/100\ g$, oxygen consumption rate of resting skeletal muscle.

A value of 54 mmHg for ΔP was obtained by using the above equations and values. This provides a probable venular pO_2 of 46 mmHg when pO_2 is assumed to be 100 mmHg in the arterial inflow. Confirmation of this result was obtained from a simple calculation using one-dimensional diffusion. The maximum distance, L, for oxygen to travel from the venular surface was estimated assuming boundary conditions dP/dx = 0 at x = L and a pO_2 of 40 mmHg (P_0) by simple diffusion

$$L = \sqrt{(2DP_0 / A)}. \tag{45.2}$$

Using the above values, L is calculated to be 320 μm, which is larger than the radius of the tissue cylinder.

The length of the arcade venules per mm^3 is reported to be 2.11 mm/mm^3. The values for the length of the collecting venules (CV) given by the number (z) of collecting venules per unit volume (mm^{-3}) and the mean distance (μm) between them, are 12.2 and 190, respectively (Table 3 of Ref. 2). Multiplied together these values give a density of 232 mm/mm^3. Figure 6 of Ref. 2 shows length histograms of collecting venules in the order 2, 3 and 4 to be 104, 272 and 279 μm, respectively. (Using the branching ratio shown in Table 1a of the same paper, we get a total length density of collecting venules to be $104 \times 3.15^2 + 272x3.15 + 279$ (μm) = $212.7mm/mm^3$, a similar value). If these vessels are stretched out and connected to form a single, thin venular tube the total density would be $4.43mm/mm^3$. From the reciprocal of this value, the tissue cylinder surrounding the venule would have

a radius of 268 μm. Putting these values and an oxygen consumption rate for the resting skeletal muscle of 0.16 ml/100g/min into the Krogh's tissue cylinder equation, we get a ΔP = 54mmHg. The A-V difference given is 46 mmHg, which is slightly higher than the normal measured venous oxygen tension, if PaO_2 is assumed to be 100 mmHg.

Taking P_0 to be a venous oxygen tension 40 mmHg at the outflow of the cylinder, the one-dimensional diffusion equation gives the maximal diffusion distance of 328 μm. This is larger than the radius of the tissue cylinder surrounding the venular tube, calculated above.

45.4 Discussion

The present estimation suggests an adequate oxygen supply to resting skeletal muscle, consistent with the successful vascular surgery in the patients. The capillary network is not essential for oxygen transport to resting muscle.

Takase et al. [5] reported that the application of arterial blood pressure to the femoral vein destroys the valves, causes inflammation, induces cytotoxic cytokines and produces apoptosis of cells in the venous walls within three weeks of surgery. In contrast, Sasajima and colleagues [1] showed that critically ischemic limbs, with extensive tissue loss or no graftable distal artery, could be rescued by venous arterialization together with the transfer of a flap of rectus muscle and skin and prior excision of the venous valves. A few days after completion of surgery the patients were walking

The theoretical considerations presented here suggest that adequate oxygen can be transported from venules to resting muscles of the surrounding tissue cylinder. This supports the idea that the arterial blood in the bypass flows through the richly developed venular network and can supply oxygen to the tissue. The blood finally reaches another branch of the vein flowing back to the vena cava. In other words, the results of the calculations presented here help to explain the successful clinical results. Finally, it should be mentioned that arterioles for the skeletal muscle are not always open but repeat intermittent closure [3]. The capillary network in the skeletal muscle has a remarkable reserve capacity. Moreover, oxygen diffuses through vascular walls of microvessels thicker than capillaries [6]. Now it can be said that the venular network is also a part of the safety network for the oxygen transport to the skeletal muscle.

45.5 Conclusion

The present estimation suggests an adequate oxygen supply to resting skeletal muscle by the arterial blood perfusion through the venular network, consistent with the successful vascular surgery in the patients.

Appendix

The surgical procedure described by Sasajima et al.[1]

The arteriovenous fistula was constructed in lower limbs of patients by the bypass surgery technique coupled with flap transfer and venous valve destruction. X-ray cineangiograms in patients who had received an arterio-venous bypass confirmed blood flow in venular vessels larger than 0.5mm in diameter. Blood may also flow into smaller vessels but could not be detected by the current method. The skin temperature rose at least by 5°. The pain disappeared from the muscles of the lower limbs. After a few days training patients could walk and enjoy a normal quality of life indicating a sufficient oxygen supply.

References

1. Azuma N, Inaba M, Haga NM, Uchida H, Asada H, Goh K and Sasajima T (2005) Jpn J Vasc Surg. **14**, 151-158
2. Engelson EL, Schmid-Schönbein GW and Zweifach BM (1985) The microvasculature in skeletal muscle, III. Venous network anatomy in normotensive and spontaneously hypertensive rats, Int J Microcirc: Clin. Exp **4,** 229-248.
3. Kamiya A, Ando J, Shibata M, Wakayama H (1990) The efficiency of the vascular tissue system for oxygen transport in the skeletal muscles. Microvasc Res **39,** 169-185
4. Opitz E and Schneider M (1950) Über die Sauerstoffversorgung des Gehirns und den Mechanismus von Mangelwirkungen. Ergebnisse Physiologie, Biologischen Chemie u. experimentellen Pharmakologie Bd.46, Springer-Verlag, Berlin, Göttingen, Heidelberg. Bd **46,** 127-260
5. Takase S, Pascarella L, Bergan JJ, and Schmid-Schönbein GW (2004) Hypertension-induced venous valve remodeling. J Vasc Surg. **39**, 1329-34
6. Tsai AG, Johnson PC , and M. Intaglietta,M (2003) Oxygen gradients in the microcirculation, Physiol Rev **83,** 933-963

Chapter 46
Skeletal Muscle Perfusion and Oxygenation Assessed by Dynamic NMR Imaging and Spectroscopy

P. G. Carlier

Abstract Muscle perfusion, and capillary and intramyocytic oxygenation can be probed non-invasively in vivo by functional NMR techniques, arterial spin labelling combined with imaging, BOLD imaging and deoxymyoglobin ^{1}H spectroscopy, respectively. After adequate adaptation of equipment, these measurements can be performed in parallel, together with ^{31}P spectroscopy and provide a comprehensive analysis of various facets of oxygen metabolism in dynamic protocols, in humans as well as in animal models.

46.1 NMR Determination of Skeletal Muscle Perfusion

In skeletal muscle, as in other organs, perfusion controls cell viability and tissue function. Muscle perfusion is characterized by a unique combination of kinetics. Resting blood flow is typically very low (only a few ml.min^{-1}.100g-^{1}tissue), but may increase by a factor of twenty during maximal exercise. The rate of change in muscle blood flow can also be quite rapid, as seen during reactive hyperemia. These properties impose particular constraints on the techniques that may be used.

Arterial spin labeling (ASL) combined with NMR imaging was first introduced by Detre et al. (1). Impressively, it fulfills all the basic characteristics one would expect from the ideal perfusion technique: a method that would be 1) totally non-invasive, 2) quantitative in absolute and not in relative terms, 3) spatially resolved and 4) temporally resolved. To our knowledge, only ASL NMR meets these four requirements. With ASL, the use of arterial water molecules as endogenous markers of perfusion alleviates the need for injections, making this method truly non-invasive. The ASL signal is proportional to the number of perfusing spins, providing quantitative mea-

Institute of Myology, NMR Laboratory, F-75651 Paris, France
CEA, I^{2}BM, MIRCen, IdM NMR Laboratory, F-75651 Paris, France
UPMC Univ Paris 06, F-75005 Paris, France
e-mail: p.carlier@institut-myologie.org

J.C. LaManna et al. (eds.), *Oxygen Transport to Tissue XXXII*, Advances in Experimental Medicine and Biology 701, DOI 10.1007/978-1-4419-7756-4_46,

surements of perfusion, expressed as a volume of blood per mass of tissue per unit of time, without requiring any further calibration or input function. The repetition of measurements on the order of seconds provides an adequate temporal resolution for dynamic studies. The encoding of tissue perfusion as an image generates a perfusion map of high spatial resolution.

The physics of ASL has been explained in detail in several theoretical reviews (2). In the pulsed ASL mode, the arterial spins are first magnetically tagged, typically positively or negatively, by a radio frequency (RF) pulse. There follows a delay, the evolution time (T), during which tagged perfusing spins enter the organ of interest and mix with the stationary spins. The arrival of the arterial spins into the tissue induces a modulation of tissue magnetization which is proportional to perfusion. This modulation is recorded by NMR imaging. In practice, at least two images with different arterial tag values are required to extract the perfusion information, and in most protocols these are acquired in pairs. This is the case with SATIR (for SATuration Inversion Recovery), the ASL variant developed in our laboratory (3), where the arterial spins are alternatively tagged positively by slice-selective (SS) inversion, and negatively by non-selective (NS) inversion. When possible differences between blood and tissue T1s are ignored, perfusion can be directly quantified using the following equation:

$$f = \frac{\lambda}{T} \times \ln\left[\frac{M_{SS}(T) - M_{ns}(T)}{M_{SS}(T) + M_{ns}(T)} \times (1 - \exp(r1.T)) + 1\right],$$

where f is the measurement of perfusion (ml. s^{-1}. ml $tissue^{-1}$), T is evolution time between inversion and acquisition, λ is the blood/tissue partition coefficient, r1 is the tissue spin-lattice relaxation rate, M is the tissue signal intensity in the tagged images.

In the skeletal muscle where perfusion can vary very rapidly over a wide range, the possibility that ASL techniques could monitor hyperemic responses almost indefinitely, over an extended period of time at a high sampling rate, is extremely appealing. This is a decisive advantage over other techniques. However, perfusion contrast of ASL is poor, which makes low perfusion states (such as muscle perfusion at rest) more difficult to quantify, though not impossible. Motion interferences are also an issue and limit the applicability of ASL methods during exercise. It has been proposed that velocity encoding ALS might be an interesting option to alleviate the condition of spatial congruence (4). Fast exchange is a prerequisite if simple processing of ASL data is to be used (5). Finite and non-instantaneous exchange times are to be taken into account when blood and tissue T1s are different, but the correction to be introduced is minor.

46.2 BOLD (Blood Oxygen Level Dependent) Effect in Muscle

As in most and perhaps all organs, capillary and venous blood oxygenation affects skeletal muscle NMR signal intensity. This is a well-known effect of BOLD due to the microscopic susceptibility changes induced by Hb desaturation (6).

A negative BOLD contrast develops within the first 2 min of an ischemic insult, and has unambiguously been assigned to early Hb desaturation (7). Cuff release after an ischemic period results in a strong positive BOLD contrast and there is a striking parallel between the time course of the BOLD signal and NIRS oxygenation curves during this reactive hyperemia (8). The slope of the ascending phase of the BOLD response and the early reperfusion peak has also been noted to be proportional (9). However, after a short ischemic period, typically of a few minutes, muscle perfusion quickly resumes baseline resting values, while BOLD signal decays at a much slower rate (9).

Several groups have suggested the possible use of BOLD contrast as a marker of muscle activation during contraction (10-13). One of the major advantages of this approach is to push the time-resolution to its limit of < 1 second. After a single contraction, a transient positive BOLD effect can be detected, with a time course that closely follows heme saturation monitored by NIRS (12). Physical activity modulates the intensity and duration of this response, independent of blood flow (10). Exposure to transient hyperoxia also results in a positive BOLD effect, of different amplitude in different muscles, possibly with relation to muscle type and fractional blood volume (11).

Blood volume changes, vascular network architecture, and tissue blood flow can, directly or indirectly, all modulate the BOLD response (9, 11, 14). In addition, particularly in skeletal muscle, the preferential alignment of capillaries along muscle fibers might render the BOLD effect dependent on the fiber angulation with respect to the main magnetic field. Indeed, preliminary experimental data suggest that this might indeed be the case. Additionally, during exercise, fluid shifts associated with osmotic changes in intracellular milieu induce an increase in muscle T2, which results in a positive contrast in T2-weighted images (13).

Quantitative analysis of BOLD images is challenging. Due to the multi-factorial nature of BOLD contrast, any attempt to precisely relate the intensity of the BOLD response to any one physiological variable would be elusive. Not only would the transformation of BOLD signal into a quantitative determination of blood oxygenation require a calibration procedure which would be hard to define, it would also imply either measurement or control of such additional variables as muscle blood volume, vascular architecture (and at least capillary density or mean intercapilllary distance) and orientation in the magnetic field (13). These requirements are virtually impossible to fulfill. For these reasons, BOLD contrast is unquestionably valuable but must not be considered as more than a relative and semi-quantitative indicator of blood oxygenation in muscle.

Because BOLD and perfusion bear a statistically significant relationship during post-ischemic hyperemia, the BOLD signal has also been proposed as an indirect marker of muscle perfusion (15). However, what may be valid in the particular ischemia-reperfusion paradigm will not be verified in other frequently encountered situations, such as moderate to heavy exercise, where muscle O_2 consumption is largely increased, and venous O_2 content is decreased.

46.3 Myoglobin (Mb) Spectroscopy as an Intracellular Probe of Muscle Oxygenation

Myoglobin (Mb), a small protein found exclusively in muscle, is a reversible O_2 carrier. In its deoxygenated form, the n-δ proton of F8 Histidine gives rise to an unambiguous, 100% NMR visible resonance, 75 ppm downfield from water (16), and thus this resonance can be used to quantify muscle oxygenation.

In the course of acute ischemia, Mb desaturation estimated from in vivo ^{1}H NMR shows a typical asymmetric sigmoid pattern over time ...(7, 16). The initial delay between the onset of ischemia and the rapid phase of Mb desaturation represents the period of time during which cell oxidative metabolism can be maintained through the release of O_2 bound to Hb in erythrocytes due to the high Hb P_{50}. Intracellular PO_2 then falls low enough to eventually induce O_2 release from Mb. This is the second phase, during which the residual oxidative metabolism depletes the Mb-bound O_2 stores. When the Mb reservoir is nearly empty, muscle enters the anaerobic state. During ischemic exercise, due to the high metabolic demand, the same succession of events occurs at an accelerated rate and Mb can become totally desaturated within a minute or so (17, 18).

During aerobic exercise, the deoxy-Mb resonance first increases roughly in proportion to the imposed workload. Maximum Mb desaturation plateaus at about 60% during quadriceps exercise (19), which is compatible with a diffusion facilitator role for Mb. During post-ischemic or post-exercise recovery, muscle reoxygenation can be monitored by the progressive disappearance of the deoxy-Mb resonance (17, 20).

Mb desaturation was measured in the leg of normal human volunteers at rest during different fractions of inspired O_2 (21). The demonstration of a significant level of Mb desaturation at rest in both normoxia (21% O_2) and hypoxia (10% O_2) is new evidence compatible with a permanent role of Mb as an intra-myocytic O_2 carrier. Molar Mb concentrations can be calculated very simply by normalizing the maximum deoxy-Mb signal to the water signal, which is measured with the same hardware. Muscle O_2 content can also be readily obtained by multiplying the measured percentage of Mb saturation by the Mb concentration and by Mb oxyphoric capacity, the former usually being derived from NMR data under ischemia and the latter being taken from physiological reference tables (17). Muscle de- or re-oxygenation rates are the first order derivative of muscle O_2 content measured in a series of spectra acquired with a high sampling rate. Muscle cytoplasmic PO_2 is determined using the classical Hill equation, where a measured percentage of Mb saturation is introduced (16).

46.4 Combining NMR Investigations of Perfusion, Oxygenation, and Energy Metabolism in the Skeletal Muscle

A further step, was to associate ^{31}P NMR spectroscopy of high energy phosphates, ^{1}H spectroscopy of Mb and perfusion NMR imaging (17, 18, 22) in a multi-parametric functional (mpf) NMR approach. A complete set of mpf-NMR data can be acquired

in 1.5-2s. This high data sampling rate allows detailed descriptions of dynamic processes such as post-exercise recovery. Collecting several NMR parameters at once not only saves time and reduces experimental variability, it also yields additional variables, such as maximum O_2 extraction by skeletal muscle calculated from the initial ones (17).

In elite athletes, the mpf-NMR acquisitions identified complex relationships between early reperfusion, myoglobin concentration and mitochondrial ATP production (18). When mitochondrial energy production is impaired, it is identified by an abnormally long creatine rephosphorylation time constant as calculated from post-exercise ^{31}P NMR spectra. Simultaneous evaluation of muscle reperfusion and reoxygenation can then help attribute the responsibilities for the defective ATP production. For instance, this approach may begin to address the etiology of direct impairment of mitochondrial function, as is the case in mitochondrial diabetes, or a consequence of impaired blood supply, as in atherosclerotic stenosis (23). In animal models, a similar confrontation of ASL perfusion and ^{31}P NMR spectroscopy data is possible (24).

Future development will take advantage of multi-channel RF transmit technology to collect mpf-NMR signals from individual muscles specifically. Collaborative efforts ought to be devoted to transferring this methodology to commercially available scanners and making this integrated approach widely available.

References

1. Detre JA, Leigh JS, Williams DS, Koretsky AP (1992) Perfusion imaging. Magn Reson Med. ;23:37-45.
2. Buxton RB.(2002) Arterial spin labelling techniques. Introduction to functional magnetic resonance imaging principles and techniques. New York: Cambridge University Press, :351-87.
3. Raynaud JS, Duteil S, Vaughan JT, Hennel F, Wary C, Leroy-Willig A, Carlier PG. (2001) Determination of skeletal muscle perfusion using arterial spin labeling NMRI: validation by comparison with venous occlusion plethysmography. Magn Reson Med. 46:305-11.
4. Duhamel G, de Bazelaire C, Alsop DC. (2003) Evaluation of systematic quantification errors in velocity-selective arterial spin labeling of the brain. Magn Reson Med. ;50:145-53.
5. St Lawrence KS, Frank JA, McLaughlin AC. (2000) Effect of restricted water exchange on cerebral blood flow values calculated with arterial spin tagging: a theoretical investigation. Magn Reson Med. ;44:440-9.
6. Ogawa S, Lee TM, Kay AR, Tank DW. (1990) Oxygenation sensitive contrast in magnetic resonance image of rodent brain at high magnetic fields. Proc. Natl. Acad. Sci. U.S.A. ;87:9868-9872.
7. Lebon V, Brillault-Salvat C, Bloch G, Leroy-Willig A, Carlier PG. (1998) Evidence of muscle BOLD effect revealed by simultaneous interleaved gradient-echo NMRI and myoglobin NMRS during leg ischemia. Magn Reson Med.;40:551-8.
8. De Blasi RA, Cope M, Ferrari M. (1992) Oxygen consumption of human skeletal muscle by near infrared spectroscopy during tourniquet-induced ischemia in maximal voluntary contraction. Adv Exp Med Biol. ;317:771-7.
9. Duteil S, Wary C, Raynaud JS, Lebon V, Lesage D, Leroy-Willig A, Carlier PG. (2006) Influence of vascular filling and perfusion on BOLD contrast during reactive hyperemia in human skeletal muscle. Magn Reson Med. 55:450-4.

10. Towse TF, Slade JM, Meyer RA. (2005) Effect of physical activity on MRI-measured blood-oxygen-level-dependent (BOLD) transients in skeletal muscle after brief contractions. J Appl Physiol. 2005;99:715-22.
11. Noseworthy MD, Bulte DP, Alfonsi J. (2003) BOLD magnetic resonance imaging of skeletal muscle. Semin Musculoskelet Radiol. ;7:307-15.
12. Meyer RA, Towse TF, Reid RW, Jayaraman RC, Wiseman RW, McCully KK. (2004) BOLD MRI mapping of transient hyperemia in skeletal muscle after single contractions. NMR Biomed. 17:392-8.
13. Damon BM, Gore JC. (2005)Physiological basis of muscle functional MRI: predictions using a computer model. J Appl Physiol. ;98:264-73.
14. Boxerman JL, Hamberg LM, Rosen BR, Weisskoff RM. (1995) MR contrast due to intravascular magnetic susceptibility perturbations. Magn Reson Med. ;34:555-66.
15. Ledermann HP, Steinbrich W, Heidecker HG, Schulte A, Aschwanden M, Jaeger K, Bilecen D-P. (2004) Calf muscle BOLD f-MRI: Comparison of healthy volunteers and Grade II PAOD Patients. Initial results. MAGMA. ;16:S58.
16. Wang Z, Noyszewski EA, Leigh JS. (1990) *In vivo* MRS measurement of deoxymyoglobin in human forearms. Magn Reson Med. ;14:562-7.
17. Carlier PG, Brillault-Salvat C, Giacomini E, Wary C, Bloch G. (2005) How to investigate oxygen supply, uptake, and utilization simultaneously by interleaved NMR imaging and spectroscopy of the skeletal muscle. Magn Reson Med. ;54:1010-3.
18. Duteil S, Bourrilhon C, Raynaud JS, Wary C, Richardson RS, Leroy-Willig A, Jouanin JC, Guezennec CY, Carlier PG. (2004) Metabolic and vascular support for the role of myoglobin in humans: a multiparametric NMR study. Am J Physiol Regul Integr Comp Physiol.;287:R1441-9.
19. Vanderthommen M, Duteil S, Wary C, Raynaud JS, Leroy-Willig A, Crielaard JM, Carlier PG. (2003) A comparison of voluntary and electrically induced contractions by interleaved 1H- and 31P-NMRS in humans. J Appl Physiol.;94:1012-24.
20. Brillault-Salvat C, Giacomini E, Jouvensal L, Wary C, Bloch G, Carlier PG. (1997) Simultaneous determination of muscle perfusion and oxygenation by interleaved NMR plethysmography and deoxymyoglobin spectroscopy. NMR Biomed.;10:315-23.
21. Richardson RS, Duteil S, Wary C, Wray DW, Hoff J, Carlier P. (2006)Muscle intracellular oxygenation: the impact of ambient oxygen availability. J Physiol. ;571:415-24.
22. Brillault-Salvat C, Giacomini E, Wary C, Peynsaert J, Jouvensal L, Bloch G, Carlier PG. (1997) An interleaved heteronuclear NMRI-NMRS approach to non-invasive investigation of exercising human skeletal muscle. Cell. Mol. Biol. 1997;43:751-62.
23. Carlier PG, Bertoldi D. (2005) In vivo functional NMR imaging of resistance artery control. Am J Physiol Heart Circ Physiol.;288:H1028-36.
24. Baligand C, Gilson H, Ménard JC, Schakman O, Wary C, Thissen J-P, Carlier PG. Functional assessment of skeletal muscle in intact mice lacking myostatin by concurrent NMR imaging and spectroscopy. Gene Therapy.;17:328-37

Chapter 47
Hemoglobin and Myoglobin Contributions to Skeletal Muscle Oxygenation in Response to Exercise

Jessica Spires, Nicola Lai, Haiying Zhou, and Gerald M. Saidel

Abstract The quantitative contributions of hemoglobin and myoglobin oxygenation in skeletal muscle depend on physiological factors, especially muscle blood flow (Q_m) and capillary permeability-surface area (PS). Near-infrared spectroscopy (NIRS) can be used to quantify total heme oxidation, but it is unable to distinguish between hemoglobin and myoglobin. Therefore, a mechanistic computational model has been developed to distinguish the contributions of oxygenated hemoglobin and myoglobin to the total NIRS signal. Model simulations predict how Q_m and PS can affect oxygenated hemoglobin and myoglobin. Although both hemoglobin and myoglobin oxygenation decrease with impaired Q_m, simulations show that myoglobin provides a greater contribution to the overall NIRS signal. A decrease of PS primarily affects myoglobin oxygenation. Based on model simulations, the contribution of myoglobin oxygenation to the total NIRS signal can be significantly different under pathophysiological conditions, such as diabetes and peripheral arterial disorder.

47.1 Introduction

Muscle responses to exercise stimulus involve oxygen transport and metabolic processes characterized by dynamic responses of pulmonary oxygen uptake (VO_{2p}) and muscle oxygenation (SmO_2) measured by indirect calorimetry (IC) and NIRS. The NIRS measurement of heme oxygenation in perfused tissue is limited because NIRS cannot distinguish between hemoglobin and myoglobin. The relative contribution of myoglobin to the NIRS signal in tissue is still under investigation [1, 2, 3]. Several factors can affect the NIRS signal during muscle contraction. These include heterogeneity of muscle blood flow and oxygen utilization (UO_{2m}), capillary recruitment and fractional volume distribution of blood and muscle fibers. Also, during muscle contraction, the relative contributions of hemoglobin and myoglobin to the NIRS sig-

Department of Biomedical Engineering, Center for Modeling Integrated Metabolism Systems, Case Western Reserve University, Cleveland, OH
e-mail: nicola.lai@case.edu

J.C. LaManna et al. (eds.), *Oxygen Transport to Tissue XXXII*, Advances in Experimental Medicine and Biology 701, DOI 10.1007/978-1-4419-7756-4_47,

nal from tissue may change depending on oxygen delivery (convection and diffusion) and blood volume [4].

Pathophysiological conditions affect the central and peripheral processes responsible for the regulation of energy metabolism. At the peripheral level of skeletal muscle, SmO_2 dynamic responses can be slower in subjects with peripheral arterial disorder (PAD) than in healthy subjects [5]. At the whole body level of cardiorespiratory function, VO_{2p} dynamic responses are slower in PAD and diabetic subjects than in healthy subjects [6, 7]. In such disease states, muscle oxygen delivery may be impaired by reduced microvascular blood flow [7] and/or reduced diffusion from blood to tissue [5]. Moreover, PAD, diabetes and metabolic myopathies may impair UO_{2m} due to altered cellular metabolism [5, 8]. The effects of muscle blood flow and permeability-surface area on dynamic responses of oxygenated hemoglobin and myoglobin in muscle during exercise were studied using a mechanistic, computational model. With this model, which accounts for key transport and metabolic processes [4], muscle responses to exercise were simulated under normoxic and hypoxic conditions to distinguish the relative contributions of oxygenated hemoglobin and myoglobin to NIRS measurements.

47.2 Methods

Oxygen transport dynamics in capillary blood of skeletal muscle are modeled as spatially distributed from arterial to venous ports [4]. The total oxygen concentration $C^T_{O_2,b}(t, v)$ within capillary blood varies with time (t) and position, which is represented as cumulative muscle volume (v) from the arterial entrance (v=0) to the venous exit ($v = V_{mus}$):

$$\frac{\partial C^T_{O_2,b}}{\partial t} = -\frac{Q_m(t)}{f_{cap}(t)}\frac{\partial C^T_{O_2,b}}{\partial v} + D_b\frac{\partial^2 C^T_{O_2,b}}{\partial v^2} - \frac{PS(t)}{f_{cap}(t)}(C^F_{O_2,b} - C^F_{O_2,c}), \quad 0 < v < V_{mus}. \tag{47.1}$$

On the right side, the first term represents convective oxygen transport, where Q_m(t) is muscle blood flow and f_{cap}(t) is the ratio of capillary blood volume to total muscle volume. The second term represents axial dispersion of oxygen with the effective dispersion coefficient D_b. The third term represents oxygen transport between blood and tissue as determined by the permeability-surface area PS(t), and the difference of free oxygen concentration in blood $C^F_{O_2,b}(t, v)$ and in tissue cells$C^F_{O_2,c}$. In the blood, the total oxygen concentration is $C^T_{O_2,b} = C^F_{O_2,b} + C^B_{O_2,b}$, the sum of the free and bound oxygen concentrations, which are related under equilibrium conditions [4].

In extravascular tissue cells, the total oxygen concentration $C^T_{O_2,c}$ is assumed spatially uniform [4], but blood-tissue diffusion and metabolism produce a change with time according to

$$\frac{dC^T_{O_2,c}}{dt} = \frac{PS(t)\int_0^{V_{mus}}(C^F_{O_2,b} - C^F_{O_2,c})dv}{V_{tis}} - \varphi_{OxPhos}, \tag{47.2}$$

where φ_{OxPhos} is the flux of oxidative phosphorylation. The total muscle volume of blood and tissue, V_{mus}=V_{bl}+V_{tis}, consists of extravascular muscle cells (V_{tis}) and blood from arterioles, capillaries, and veins (V_{bl}=V_{art}+V_{cap}+V_{ven}). In muscle cells, the dynamic mass balances of ATP and PCr are related to metabolic fluxes [4]:

$$\frac{dC_{ATP}}{dt} = -\varphi_{ATPase} + \beta\varphi_{OxPhos} + \Delta\varphi_{CK}; \quad \frac{dC_{PCr}}{dt} = -\Delta\varphi_{CK}, \tag{47.3}$$

where the ATP utilization flux is $\phi_{ATPase} = k_{ATPase}C_{ATP}$ and k_{ATPase} depends on the energy demand, which can be related to the steady-state pulmonary oxygen uptake VO_{2p}. The stoichiometric coefficient β relates oxidative phosphorylation to ATP production. The net forward flux of the creatine kinase reaction $\Delta\phi_{CK}$ depends on a bi-bi reaction with C_{ATP} and C_{PCr} [9] and ϕ_{OxPhos} depends on $C^F_{O_2,c}$and C_{ATP} according to a Michaelis-Menten form [10]. The model does not include the contributions of anaerobic glycolysis to ATP production.

In response to a step increase in work rate from a steady-state warm up condition, the dynamic response of muscle blood flow Q_m at exercise is assumed to be exponential as is typical of cardiac output:

$$Q_m(t) = Q^0_m + \Delta Q[1 - \exp[-(t - t_0)/\tau_Q]], \quad (t > t_0), \tag{47.4}$$

where $\Delta Q = Q^{\max}_m - Q^0_m$ and Q^0_m and $Q^{\max}_m$ are the warm up and maximum muscle blood flow. The rate coefficient of capillary-tissue transport or PS(t) is assumed to increase in response to exercise similarly to blood flow. The change in muscle oxygenation depends on average oxygenated hemoglobin and myoglobin concentrations, $HbO_2(t)$and$MbO_2(t)$ [4]:

$$\begin{aligned} HbO_2(t) &= [\langle C^B_{O_2,cap}\rangle f_{cap}(t) + C^B_{O_2,art} f_{art}(t) + C^B_{O_2,ven} f_{ven}(t)], \\ MbO_2(t) &= [C^B_{O_2,c}\ f_{tis}(t)]/4, \end{aligned} \tag{47.5}$$

where the bound oxygen in arteries ($C^B_{O_2,art}$), spatially averaged capillaries ($< C^B_{O_2,cap} >$), veins ($C^B_{O_2,ven}$) and in muscle cells ($C^B_{O_2,c}$) have corresponding blood and tissue volume fractions (f_{art}, f_{ven}, f_{cap}, f_{tis}). The sum of the blood fractions f_x (x=art,cap,ven) represent the blood volume fraction in muscle (f_{bl}=1-f_{tis}). Bound and free oxygen concentrations are related by Hill-type equations:

$$C^B_{O_2,b} = \frac{4HctC_{Hb,rbc}K_{Hb}(C^F_{O_2,b})^n}{1 + K_{Hb}(C^F_{O_2,b})^n}; \quad C^B_{O_2,c} = \frac{W_{mc}C_{mc,Mb}K_{Mb}C^F_{O_2,c}}{1 + K_{Mb}C^F_{O_2,c}}, \tag{47.6}$$

where $C_{Hb,rbc}$ and $C_{mc,Mb}$ are the total concentrations of hemoglobin and myoglobin; K_{Hb} and K_{Mb} are Hill constants; and Hct and W_{mc} are the fractions of erythrocyte and myocyte in blood and tissue, respectively. To simulate oxygen responses to exercise as measured by NIRS, the relative change of the oxygenated forms in blood and tissue is normalized by the maximal change in the oxygenated Hb/Mb concentration variation observed during ischemia [4]:

$$\begin{aligned} \mathrm{g}\Delta HbMbO_2(\mathrm{t}) &= \mathrm{g}\Delta HbO_2(\mathrm{t}) + \Delta MbO_2(\mathrm{t}); \\ \Delta HbMb_{tot}(\mathrm{t}) &= \mathrm{g}\Delta HbMbO_2(\mathrm{t}) + \Delta HHbMb(\mathrm{t}). \end{aligned} \tag{47.7}$$

The change of total heme concentration $\Delta HbMb_{tot}(\mathrm{t})$ measured by NIRS can be represented by exponential functions during exercise. Such dynamic responses are related to changes in capillary blood volume V_{cap}. In this model, we assume that capillary blood volume increases as a double exponential function of $\Delta HbMb_{tot}(\mathrm{t})$. The increase of muscle volume during exercise affects arterioles, capillary and venules and tissue volume fractions $f_{art}(t)$, $f_{ven}(t)$, $f_{cap}(t)$, and $f_{tis}(t)$ [4].

47.3 Results

Characteristics of muscle oxygenation response to exercise in healthy and diseased states are analyzed by model simulations. These show the effects of reduced Q_m and PS on changes in oxygenated hemoglobin and myoglobin, ΔHbO_2 and ΔMbO_2 in working muscle under normoxia and hypoxia. When the blood flow is impaired, as indicated by a decrease in $Q_m^{\max}$, both ΔHbO_2 and ΔMbO_2 become more negative, but the extent of change is different in normoxia than in hypoxia. Under hypoxia, ΔHbO_2 is less negative and ΔMbO_2 is more negative (Fig. 1a). When the maximal permeability-surface area (PS^{max}) is decreased by impairment, ΔHbO_2 does not change significantly, but ΔMbO_2 becomes more negative and the difference becomes greater between normoxia and hypoxia (Fig. 1b).

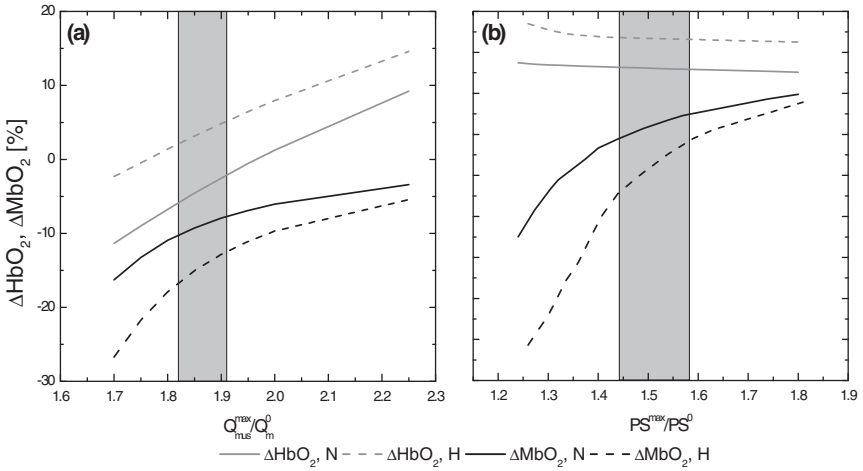

Fig. 47.1 (a) Effect of blood flow (Q_m) and (b) permeability-surface area (PS) on hemoglobin and myoglobin oxygenation during steady-state exercise, normalized to warm-up values, under normoxia (N) and hypoxia (H) arterial oxygen concentration. The grey region denotes the physiological range.

47.4 Discussion

The different responses of ΔHbO_2 and ΔMbO_2 indicate that the relative contribution of ΔMbO_2 to the change in the total NIRS signal may vary dramatically under pathophysiological conditions in which oxygen transport from mouth to muscle tissue is impaired as occurs in PAD and type 2 diabetes (T2DM). NIRS, however, cannot quantify the relative changes in hemoglobin and myoglobin oxygenation needed to evaluate the effect of oxygen delivery to the muscle distinctly from oxygen utilization. As an indirect method of evaluating oxygen utilization by muscle, pulmonary VO_{2p} kinetics used to represent UO_{2m} during exercise are valid only for quasi-steady-state conditions. A more general analysis of the underlying processes during dynamic responses to exercise requires a combination of model simulation and experimental NIRS data. Such a combination has the potential to distinguish ΔHbO_2(t) and ΔMbO_2(t) contributions to total oxygenation, $\Delta HbMbO_2$(t), under different physiological and pathophysiological conditions.

An NIRS study shows slower dynamic responses of $\Delta HbMbO_2$(t) to exercise in PAD subjects compared to healthy subjects [6]. This may indicate an impairment of oxygen utilization and/or reduced oxygen diffusion during exercise. Our model simulations (Fig. 1b) suggest that reduced permeability-surface area may cause significantly greater changes in ΔMbO_2(t) even for moderate exercise intensity in diseased states. Experimentally, VO_{2p} kinetics for T2DM subjects are slower than for healthy subjects, while the dynamic responses of $\Delta HHbMb$(t) to moderate exercise are similar in both populations [7]. This may indicate a slower dynamic response of the microvascular blood flow in T2DM associated with impaired O_2 delivery. Our model simulations (Fig. 1a) suggest that reduced muscle blood flow increases total $\Delta HbMbO_2$, associated with greater changes of ΔMbO_2 than ΔHbO_2.

These model simulations provide a quantitative analysis of Hb and Mb contributions to the NIRS signal under different experimental conditions; however, they rely on phenomenological functions to simulate PS, Q_m and intra and extra-vascular volume fractions (f_{art}, f_{ven}, f_{cap}, f_{tis}) changes during exercise. More mechanistic expressions of the physiological processes involving changes in the permeability-surface area can be tested with experimental data from muscle contraction studies [10]. To quantify the contributions of ΔHbO_2 and ΔMbO_2 in muscle oxygenation, mathematical modeling is needed to distinguish the effects of convection and diffusion on the impairment to oxygen utilization and delivery under pathological conditions. Noninvasive, *in vivo* studies using (1) NIRS to evaluate total heme oxidation and blood volume and (2) NMR imaging and spectroscopy to evaluate muscle perfusion, myoglobin oxygenation and ATP production can provide key data in the investigation of skeletal muscle energetics [11,12]. The information from these techniques can be substantially enhanced by computational mechanistic modeling. Consequently, hypotheses concerning characteristics of O_2 uptake dynamics and their limiting effects can be tested. Simulations with a validated mechanistic model can be used to predict ΔHbO_2(t) and ΔMbO_2(t) contributions to the NIRS signal and to quantify the effects of transport and metabolic parameters under a variety of physiological and pathophysiological conditions.

Acknowledgments

Supported in part by grants (P50 GM-66309, 1F31GM084682-01A1) from the National Institute of General Medical Sciences (NIH), and by a grant from the National Aeronautics and Space Administration (NNJ06HD81G).

References

1. Macdonald M, Tarnopolsky M, Green H et al (1999) Comparison of femoral blood gases and muscle near-infrared spectroscopy at exercise onset in humans. J Appl Physiol. 86(2):687–693.
2. Mancini D, Bolinger L, Li H et al (1994) Validation of near-infrared spectroscopy in humans. J Appl Physiol. 77(6):2740-2747.
3. Tran TK, Sailasuta N, Kreutzer U et al (1999) Comparative analysis of NMR and NIRS measurements of intracellular PO2 in human skeletal muscle. Am J Physiol. 276 (Regulatory Integrative Comp. Physiol. 45):R1682–R1690.
4. Lai N, Zhou H, Saidel M et al (2009) Modeling oxygenation in venous blood and skeletal muscle in response to exercise using near-infrared spectroscopy. J Appl Physiol. 106:1858-1874
5. Bauer T, Brass E, Nehler M et al (2004) Pulmonary VO2 dynamics during treadmill and arm exercise in peripheral arterial disease. J Appl Physiol. 97:627-634.
6. Bauer T, Brass E, Hiatt W (2004) Impaired muscle oxygen use at onset of exercise in peripheral arterial disease. J Vasc Surg. 40:488-93.
7. Bauer T, Levi M, Reusch J et al (2007) Skeletal muscle deoxygenation after the onset of moderate exercise suggests slowed microvascular blood flow kinetics in type 2 diabetes. Diabetes Care. 30:2880–2885.
8. Grassi B, Marzorati M, Lanfranconi F et al (2007) Impaired oxygen extraction in metabolic myopathies: detection and quantification by near-infrared spectroscopy. Muscle Nerve. 35:510–520.
9. Vicini P, Kushmerick M (2000) Cellular energetics analysis by a mathematical model of energy balance: estimation of parameters in human skeletal muscle. Am J Physiol Cell Physiol. 279:C213-C224.
10. Lai N, Saidel G, Grassi B, et al (2007) Model of oxygen transport and metabolism predicts effect of hyperoxia on canine muscle oxygen uptake dynamics. J Appl Physiol. 103:1366–1378
11. McCully K (2002) Near infrared spectroscopy in the evaluation of skeletal muscle disease. Muscle Nerve. 25(5):629-31.
12. Carlier P, Bertoldi D, Baligand C et al (2006) Muscle blood flow and oxygenation measured by NMR imaging and spectroscopy. NMR Biomed. 19: 954–967.

Chapter 48
Estimation of Muscle Fatigue Using Surface Electromyography and Near-Infrared Spectroscopy

Joachim Taelman, Joke Vanderhaegen, Mieke Robijns, Gunnar Naulaers, Arthur Spaepen, and Sabine Van Huffel

Abstract This study looks at various parameters, derived from surface electromyography (sEMG) and Near Infrared Spectroscopy (NIRS) and their relationship in muscle fatigue during a static elbow flexion until exhaustion as well as during a semidynamic exercise. We found a linear increasing trend for a corrected amplitude parameter and a linear decreasing slope for the frequency content of the sEMG signal. The tissue oxygenation index (TOI) extracted from NIRS recordings showed a four-phase response for all the subjects. A strong correlation between frequency content of the sEMG signal and TOI was established. We can conclude that both sEMG and NIRS give complementary information concerning muscle fatigue.

48.1 Introduction

Knowledge of myoelectric and oxygenation mechanisms in muscles is important to understand muscle fatigue [1]. A frequently used definition of muscle fatigue is the one established by Edwards, [2] "Fatigue is defined as a failure to maintain the required or expected force." As a consequence, a fatigued muscle can not continue the expected force and exhaustion occurs at a specific point in time. Note that the cause of muscle fatigue is not only located in the muscle. Neurological, physiological and circulatory changes influence the development of muscle fatigue. These changes already occur at the beginning of the contraction. At first, the changes can only be

Joachim Taelman and Sabine Van Huffel
ESAT/SCD, Dept. of Electrical Engineering, Katholieke Universiteit Leuven, Belgium
e-mail: joachim.taelman@faber.kuleuven.be

Joachim Taelman, Mieke Robijns, and Arthur Spaepen
Dept. of Biomedical Kinesiology, Katholieke Universiteit Leuven, Belgium

Joke Vanderhaegen and Gunnar Naulaers
Neonatal Intensive Care Unit, University Hospital Gasthuisberg, Katholieke Universiteit Leuven, Belgium

J.C. LaManna et al. (eds.), *Oxygen Transport to Tissue XXXII*, Advances in Experimental Medicine and Biology 701, DOI 10.1007/978-1-4419-7756-4_48,

measured with techniques such as surface electromyography (sEMG) for myoelectric changes and near-infrared spectroscopy (NIRS) for oxygenation changes.

sEMG measures the electrical activity of a muscle and is a good indicator of muscle force and fatigue [1]. Standard parameters from sEMG are extracted to analyze the electrical activity of the muscle. NIRS allows the direct and non-invasive measurement of local blood circulation, blood volume, and changes in oxygenated haemoglobin (Hb) and myoglobin (Mb) in working muscles [3]. Muscle oxygenation is the number of Hb saturated with oxygen (O_2) in the blood of the muscle. Oxygenation and blood volume decrease significantly and similarly during restriction of blood flow due to intramuscular pressure as, for example, when caused by exercise [4].

Although considerable research had been devoted to myoelectric or oxygenation changes during fatiguing exercises, rather less attention has been paid to the combination of myoelectric and oxygenation changes during development of muscle fatigue. The aim of this study is to investigate the relationship between sEMG and NIRS parameters in m. biceps brachii until exhaustion due to isometric static (STAT) and semidynamic (DYN) exercises. The parameters utilized are relevant for muscle fatigue and understanding their behaviour can lead to additional information in order to make a better assessment of muscle fatigue.

48.2 Methods

48.2.1 Experimental procedure

In total, 48 test subjects (24 male, 24 female, 21 $\pm$ 2.0 years) were requested to sit on a chair with the right upper arm relaxed against the body and elbow angle equal to 90°, forearm positioned in supination with hand palm up. A wooden handle attached with a solid rope to a load cell was held in the hand. The subject was instructed to bend his or her elbow using only arm muscles. This static isometric contraction caused activation of m. biceps brachii (BB).

sEMG electrodes and NIRS probe were placed in the direction of muscle fibres on BB symmetrically [5] of the line between medial acromion and fossa cubit at 1/3 from fossa cubit [6].

The exerted force on the load cell was amplified using a volt amplifier (HBM, Germany) and visual feedback of the force was given to the subject by a digital oscilloscope (Hewlett Packard, 54501A). sEMG signals (bipolar pre-gelled Ag/AgCl electrodes) were amplified. The NIRS probe (NIRO 300 ®, Hamamatsu Photonics K.K., Tokyo, Japan) was connected to the NIRO 300 measurement and display unit for visualization. All signals from sEMG, NIRO 300 and force transducer were digitised with an analog-to-digital converter (National Instruments, cDAQ, 24 bit) before storage on a personal computer.

Initially a maximal voluntary contraction (MVC) was measured. After 5 minutes of rest, the subject performed a static contraction (STAT) at 50% MVC until exhaustion. On the oscilloscope, a line was fixed, representing the target level of force output. At the moment the force of the subject decreased to 90% of the required force, the muscle was defined as exhausted. After a 20 min recuperation, a semi-dynamic contraction (DYN) was exerted in the static position. On the oscilloscope, two horizontal lines representing 20 and 60% MVC and time interval were displayed. Subject performed alternating 4s contractions at 20% MVC and 6s contractions at 60% MVC until exhaustion.

48.2.2 Muscle fatigue parameters

Surface electromyography (sEMG) is frequently used in kinesiology as an indicator of muscle activation, force production or fatigue index. This objective, non-invasive, and indirect method detects motor unit action potentials (MUAP) in the muscle fibre during muscle activity. The summation of the MUAPs of the underlying muscle detected by the electrodes provides the sEMG signal that results in the ability to estimate non visible phenomena in the muscle such as muscle fatigue [1]. In this study a closer look is taken at the following myoelectric parameters:

- *Root Mean Square* (RMS): statistical measure of the magnitude of a varying quantity, calculated in a window of 0.5s in the signal.

$$RMS(t) = \sqrt{\frac{1}{n}\sum_{i=0}^{n-1} E(t+i)^2},$$

  where $n =$ length of window; $E(x) =$ the EMG signal.
- *Mean Power Frequency* (MPF): windowed measure of frequency content

$$MPF(t) = \frac{\int_0^{f_s/2} f \cdot S_{E_{t\to t+n}}(f)}{\int_0^{f_s/2} S_{E_{t\to t+n}}(f)},$$

  where $n =$ length of window; $S(f) =$ the Power Spectral Density of EMG fragment $E(t \to t+n)$; $f_s =$ sampling frequency.
- *Activity* (ACT): proportional with the isometric contraction. This parameter has a lower sensitivity to a slowly changing baseline [7]

$$ACT(t+1) = p \cdot ACT(t) + |E(t+1) - E(t)|^{1/2},$$

  where $E(x)$ the EMG signal; $p =$ constant value of 0.9938.

Table 48.1 Duration of tests and MVC force[a]

	STAT time (s)	DYN time[b] (s)	MVC force (N)
Total	78 (20)	147 (46)	175 (7)
Men	73 (20)	123 (24)	235 (5)
Women	83 (19)	172 (51)	116 (3)

[a]Data are given as mean (SD)
[b]During DYN test 31 subjects were tested, 16 men and 15 women

- *RMS/ACT*: fatigue parameter, less dependent on produced force [7].

Near-infrared spectroscopy (NIRS) is a non-invasive technique that can be used for the measurement of tissue oxygenation. This method is based upon the relative transparency of biological tissue to light in the near-infrared (NIR) part of the light spectrum. Signal detection is based on levels of light directed through the muscle and picked up by the detector after the light has travelled through tissue. Tissue oxygenation index (TOI) is a NIRS parameter and indicates the dynamic balance between O_2 supply and O_2 consumption in tissue capillaries, arterioles, and venules [8, 9].

$$TOI = \frac{k \cdot HbO_2}{k \cdot HbO_2 + k \cdot HbR}$$

where k = constant scattering distribution; HbO_2 concentration in oxidized haemoglobin; HbR concentration in reduced haemoglobin.

48.3 Results and Discussion

All subjects successfully completed the protocol. The results are given in Table 1. MVC force produced by men was significantly larger than that produced by women ($p < 0.001$) and women could maintain the DYN test for a significantly longer period of time as compared with men ($p < 0.01$). The DYN test was significantly longer than the STAT test for all subjects ($p < 0.001$) indicating that local muscle exhaustion was reached faster during the STAT test.

Figure 1 shows the mean value of the sEMG parameters over all subjects during both tests (A: STAT, B: DYN). The time scale was normalised to the total contraction time until exhaustion.During both tests for all the subjects, we found increasing RMS and RMS/ACT slopes, a decreasing MPF slope and an almost stable ACT slope. The sEMG parameters confirm that muscle fatigue is an ongoing linear process that initiates from the very beginning of the contraction [7]. Both pictures show that RMS/ACT corrects for movement compensation during the fatigue test. The RMS/ACT curve is more of an increasing straight line as compared to the RMS curve, which is generally used in literature. This confirms the finding of [7] that RMS/ACT is a better parameter to estimate muscle fatigue. The RMS/ACT ratio and MPF are clear indicators for the myoelectric activity of local muscle fatigue.

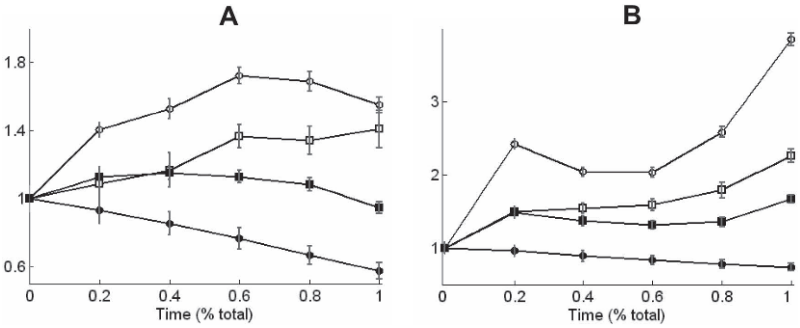

Fig. 48.1 Mean value of sEMG parameters over all subjects during the STAT test (A) and the DYN test (B) in normalized units. Confidence intervals (a = 0.025) are shown. • = RMS; • = RMS/ACT; • = ACT; • =MPF

Figure 2 shows the TOI response of a representative subject during the STAT (A) and the DYN test (B). The TOI showed a four-phase response during both tests, which was also demonstrated in earlier studies [5]. In the first phase, there is a small increase of the TOI during the first 2-3 seconds, indicating an increase in muscle oxygenation. Secondly, a fast linear decreasing phase was noticed (deoxygenation). The duration of this decline seems parallel with the use of phosphocreatine (CP) as energy source for the contraction, which lasted, according to the literature, for 15-30s [10]. The alteration for phase I and II was similar for both contraction modalities. In the third phase, the TOI is on group level almost constant and dependent on the type of contraction. There is a flat line for the STAT test, while the trace of the TOI during the DYN test is following the contraction intensity, indicating an increased supply of oxygen during the 20% MVC contraction, leading to recuperation. The energy during this third phase is probably mainly taken from glycogen in anaerobic glycolysis due to a deficit in oxygen because the mechanical obstruction of the blood flow in the muscle during a contraction limits the supply of enough oxygen. This leads to the accumulation of lactic acid followed by an oxygen debt resulting in muscle exhaustion [10]. The duration of phases I and II were similar during both tests for all the test subjects, while the length of the third phase was dependent on the length of the contraction. After the exercise, during the fourth phase, there is an overshoot of the TOI revealing an increase in oxygen supply for recuperation. Within the 20 minutes of recuperation between the STAT and the DYN test, TOI has recovered to the initial value at the beginning of the test.

The ΔTOI, which is the difference between the initial value during phase I and the constant value of phase III (the mean value is taken during the DYN test), correlates negatively with the total exertion time (STAT: $r = -0.56$, $p < 0.001$; DYN: $r = 0.66$, $p < 0.001$). Higher differences in the TOI value resulted in a shorter duration of exercise and, consequently, exhaustion occurs faster. Also, subjects with a small negative TOI slope in phase II could maintain both tests longer (STAT: $r = -0.64$, $p < 0.001$; DYN: $r = -0.74$, $p < 0.001$). The negative correlation between ΔTOI and total exertion time reveals that higher deoxygenation results in early exhaustion

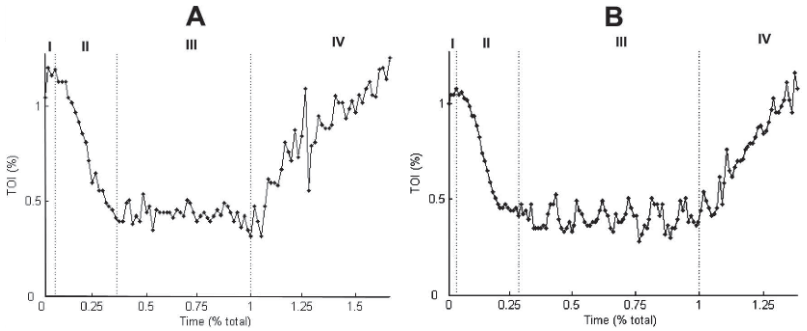

Fig. 48.2 TOI from a representative subject during the STAT test (A) and the DYN test (B) in normalized units.

of the muscle. A higher deoxygenation during phase II causes a larger oxygen debt resulting in a faster fatiguing process. Despite the evidence in sEMG that fatigue is an ongoing linear process, this is not revealed by NIRS. On the other hand, a NIRS parameter gives an indication of the velocity of the fatigue process.

The MPF and the TOI slope during phase 2 are significantly correlated during both the STAT and DYN test ($p > 0.001$). During the DYN test, a significant negative correlation between the TOI slope during phase II and the RMS/ACT ratio is seen ($p < 0.01$), however, this correlation was not significant during the STAT test. In earlier studies, a strong positive correlation was reported between muscle oxygenation and MPF [5, 8].

48.4 Conclusions

This study shows that although sEMG and NIRS measure two separate physiological phenomena of muscle fatigue, there is a link between both measurements. The MPF of the myoelectric signal is strongly correlated with the muscle oxygenation. On the other hand, only sEMG shows that muscle fatigue is an ongoing linear process that starts from the beginning of the contraction, while the duration of the contraction was correlated with a parameter from the TOI. We can conclude that both sEMG and NIRS give complementary information concerning muscle fatigue.

Acknowledgments

This research was supported by Research Council KUL (GOA-AMBioRICS, GOA-MANET CoE EF/05/006 Optimization in Engineering (OPTEC)) and FWO (Belgian Federal Science Policy Office IUAP P6/04 (DYSCO, “Dynamical systems, control and optimization,” 2007–2011)).

References

1. De Luca CJ (1997) The use of surface electromyography in biomechanics. J Appl Biomech 13: 135-163.
2. Edwards RHT (1981) Human muscle function and fatigue. Ciba Found Symp 82: 1-18.
3. Miura H, Araki H, Matoba H, et al. (2000) Relationship among oxygenation, myoelectric activity, and lactic accumulation in vastus lateralis muscle during exercise with constant work rate. Int J Sports Med 21: 180-184.
4. Yoshitake Y, Ue H, Miyazaki M, et al. (2001) Assessment of lower-back muscle fatigue using EMG, MMG and NIRS. Eur J Appl Physiol 84: 174-179.
5. Felici F, Quaresima V, Fattorini L, et al. (2009): Biceps bracii myoelectric and oxygenation changes during static and sinusoidal isometric exercises. J Electromyogr kinesiol 92:e1-e11
6. Hermens JH, Freriks B, Merletti B, et al. (1999) European recommendations for surface electromyography: Results of the Seniam Project (SENIAM). Roessingh research and development, ISBN 9075452152.
7. Hermans V, Spaepen AJ (1999) Relation between differences in EMG adaptations during static contractions and the muscle function. J Electromyogr Kinesiol 9: 253-261
8. Chance B, Marianne TD, Zhang C, et al. (1992) Recovery from exercise-induced desaturation in the quadriceps muscles of elite competition rowers. Am J Phys 268(3): c766-c775
9. Naulaers G: Non-invasive measurement of the neonatal cerebral and splanchnic circulation by near-infrared spectroscopy. Leuven University Press, 2003.
10. Albright JA, Brand RA (1984) The scientific basis of orthopaedics. Occupational biomechanics. New York: John Wiley & sons: 30-34

Erratum to:

Oxygen Transport to Tissue XXXII

Joseph C. LaManna, Michelle A. Puchowicz, Kui Xu, David K. Harrison, Duane F. Bruley

J.C. LaManna et al. (eds.), *Oxygen Transport to Tissue XXXII*, Advances in Experimental Medicine and Biology 701, DOI 10.1007/978-1-4419-7756-4_32,

10.1007/978-1-4419-7756-4_49

On page 248, the extraneous text "proteinsindex[sub]uncoupling" has been removed from the first paragraph.

Higher degrees of uncoupling are held to be beneficial and neuroprotective because they prevent excessive reduction of cytochromes and the accompanying generation of reactive oxygen species that occurs when the electron flux is not maintained. In parallel with different degrees of uncoupling known to operate in other parts of the body, such as the thyroid gland and brown fat where uncoupling is a factor involved in thermogenesis, the uncoupling proteins may contribute to individual differences of body-mass index, as well as to the variability of cerebral oxygen consumption rates in healthy human beings.

The wrong images were placed for Figure 32.1 (page 245), Figure 32.2 (page 245), Figure 32.3 (page 246), and Figure 32.4 (page 246); the corrected version of these images are as follows:

The original online version for this chapter can be found at http://dx.doi.org/10.1007/978-1-4419-7756-4_32

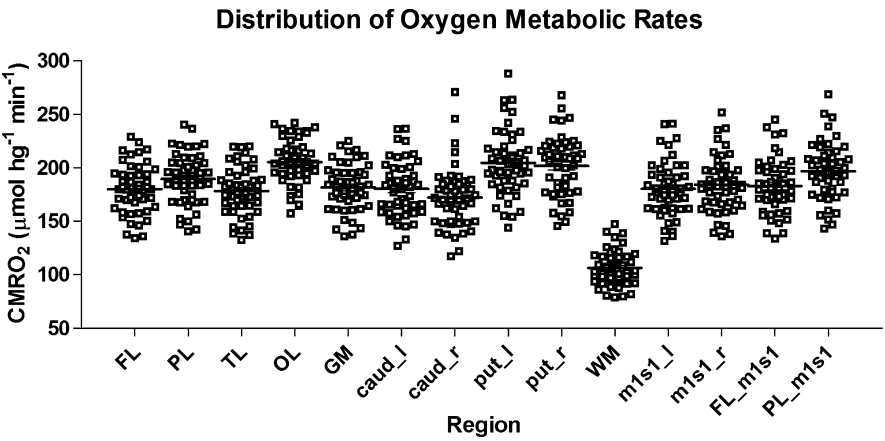

Fig. 32.1 $CMRO_2$ estimates of 49 healthy volunteers, adjusted to age 25 years. Regions are frontal (FL), parietal (PL), temporal (TL) and occipital (OL) lobes, gray and white matter (GM, WM), left and right caudate nuclei (caud_l, caud_r) and putamina (put_l, put_r), and left and right sensorimotor (m1s1_l, m1s1_r), precentral frontal (FL_m1s1) and postcentral parietal (PL_m1s1) cortices.

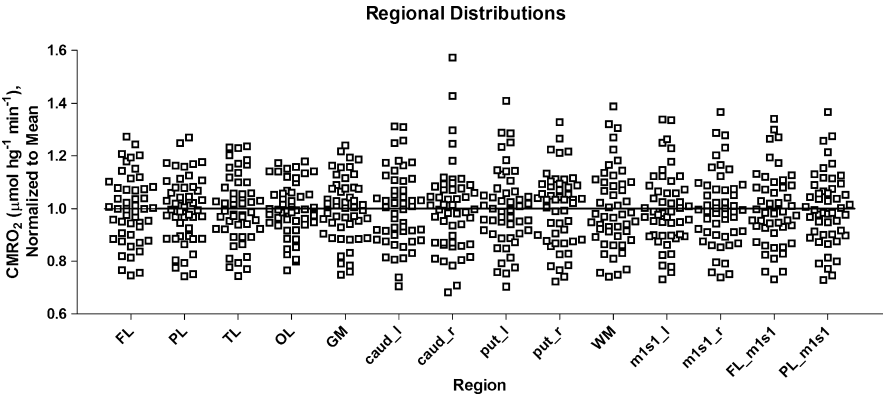

Fig. 32.2 $CMRO_2$ values normalized to population mean of every region.

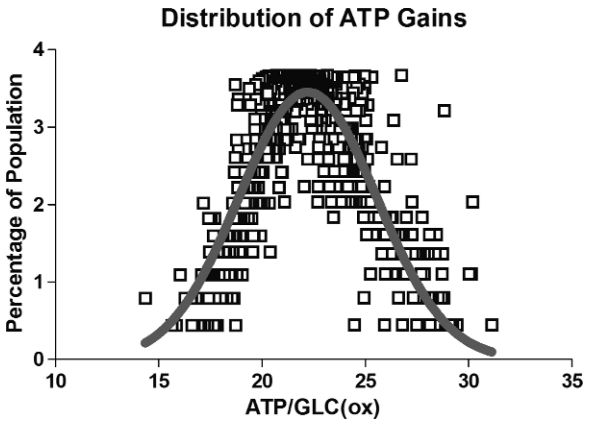

Fig. 32.3 Distribution of ATP gains (mol/mol glucose oxidized to CO_2).

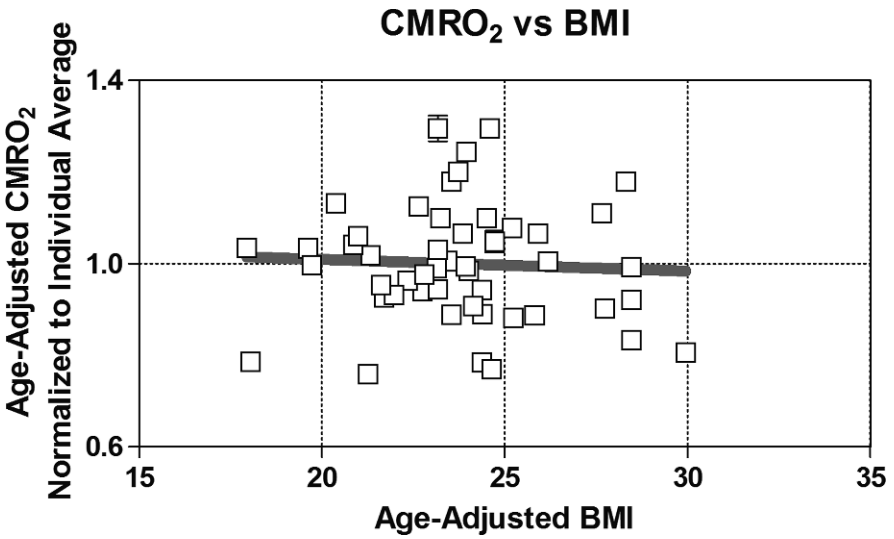

Fig. 32.4 Absent relation between age-adjusted BMI values and individual averages of $CMRO_2$ values normalized to regional population averages.

Erratum to:

Oxygen Transport to Tissue XXXII

Joseph C. LaManna, Michelle A. Puchowicz, Kui Xu, David K. Harrison, Duane F. Bruley

J.C. LaManna et al. (eds.), *Oxygen Transport to Tissue XXXII*, Advances in Experimental Medicine and Biology 701, DOI 10.1007/978-1-4419-7756-4_45,

10.1007/978-1-4419-7756-4_50

In Chapter 45, "Sufficient Oxygen Can Be Transported to Resting Skeletal Muscle via Arterialization of the Vein: Theoretical Considerations in a Rat Model", the second-listed author name was incorrectly printed as Tomiyasu Koyama. This error appeared on page xxx (30) of the front matter and also in Chapter 45 (p. 335).

The correct name should be 'Tadahiro Sasajima'.

The original online version for this chapter can be found at http://dx.doi.org/10.1007/978-1-4419-7756-4_45

Erratum to:

Oxygen Transport to Tissue XXXII

**Joseph C. LaManna, Michelle A. Puchowicz, Kui Xu,
David K. Harrison, Duane F. Bruley**

In the front matter (p. xii-xiii), the names are duplicated for the MH Knisely Award winners and the DW Lubbers Award winners; they should appear as follows:

Melvin H. Knisely Award Recipients:

1983 Antal G. Hudetz, Hungary
1984 Andras Eke, Hungary
1985 Nathan A. Bush, USA
1986 Karlfried Groebe, Germany
1987 Isumi Shibuya, Japan
1988 Kyung A. Kang, Korea/USA
1989 Sanja Batra, Canada
1990 Stephen J. Cringle, Australia
1991 Paul Okunieff, USA
1992 Hans Degens, Netherlands
1993 David A. Benaron, USA
1994 Koen van Rossem, Belgium
1995 Clare E. Elwell, UK
1996 Sergei A. Vinogradov, USA
1997 Chris Cooper, UK
1998 Martin Wolf, Switzerland
1999 Huiping Wu, USA
2000 Valentina Quaresima, Italy
2001 Fahmeed Hyder, Bangladesh
2002 Geofrey De Visscher, Belgium
2003 Mohammad N. Khan, USA
2004 Fredrick Palm, Sweden
2005 Nicholas Lintell, Australia
2006 No award was made
2007 Ilias Tachtsidis UK
2008 Kazuto Masamoto, Japan
2009 Rossana Occhipinti, USA

Dietrich W. Lubbers Award Recipients:

1994 Michael Dubina, Russia
1995 Philip E. James, UK/USA
1996 Resit Demit, Germany
1997 Juan Carlos Chavez, Peru
1998 Nathan A. Davis, UK
1999 Paola Pichiule, USA
2000 Ian Balcer, USA
2001 Theresa M. Busch, USA
2002 Link K. Korah, USA
2003 James E. Lee, USA
2004 Richard Olson, Sweden
2005 Charlotte Ives, UK
2006 Bin Hong, China/USA
2007 Helga Blocks, Belgium
2008 Joke Vanderhaegen, Belgium
2009 Matthew Bell, UK

The online version of the original text can be found at
http://dx.doi.org/10.1007/978-1-4419-7756-4-0

Author Index

J.C. LaManna et al. (eds.), *Oxygen Transport to Tissue XXXII*, Advances in Experimental Medicine and Biology 701, DOI 10.1007/978-1-4419-7756-4,

Subject Index